COPPE
UFRJ

**Instituto Alberto Luiz Coimbra de
Pós-Graduação e Pesquisa de Engenharia**

DYNAMIC PHASOR MODELING FOR SUBSYNCHRONOUS RESONANCE ANALYSIS

Lígia Rolim da Silva

Dissertação de Mestrado apresentada ao Programa de Pós-graduação em Engenharia Elétrica, COPPE, da Universidade Federal do Rio de Janeiro, como parte dos requisitos necessários à obtenção do título de Mestre em Engenharia Elétrica.

Orientadora: Tatiana Mariano Lessa de Assis

Rio de Janeiro

Junho de 2020

DYNAMIC PHASOR MODELING FOR SUBSYNCHRONOUS RESONANCE ANALYSIS

Lígia Rolim da Silva

DISSERTAÇÃO SUBMETIDA AO CORPO DOCENTE DO INSTITUTO ALBERTO LUIZ COIMBRA DE PÓS-GRADUAÇÃO E PESQUISA DE ENGENHARIA DA UNIVERSIDADE FEDERAL DO RIO DE JANEIRO COMO PARTE DOS REQUISITOS NECESSÁRIOS PARA A OBTENÇÃO DO GRAU DE MESTRE EM CIÊNCIAS EM ENGENHARIA ELÉTRICA.

Orientadora: Tatiana Mariano Lessa de Assis

Aprovada por: Profª. Tatiana Mariano Lessa de Assis, D.Sc.

                 Prof. Antônio Carlos Ferreira, Ph.D.

                 Eng. Fabricio Lucas Lirio, D.Sc.

                 Prof. Marcelo Aroca Tomim, Ph.D.

RIO DE JANEIRO, RJ – BRASIL

JUNHO DE 2020

Dedico esta dissertação aos meus
queridos pais, Beatriz e Aguimar.

"Whatever you do, work at it with all your heart, as working for the Lord, not for human masters."

Colossians 3:23

Agradecimentos

Primeiramente, agradeço a Deus pela vida, provisão e saúde para concluir este trabalho, diariamente iluminando os meus caminhos e renovando as minhas forças.

Agradeço à minha família, especialmente aos meus pais, Beatriz Rolim e Aguimar Moreira, pelo apoio constante, pelas incontáveis demonstrações de amor, e pela compreensão da minha ausência em diversos momentos ao longo dos três anos de desenvolvimento desta dissertação de mestrado.

Ao meu marido, Juan Rossi, devo um agradecimento especial por todo carinho, pelo grande incentivo, cuidado diário e paciência nesse período. Certamente, seu apoio e inspiração foram fundamentais para a conclusão desse trabalho.

À minha orientadora, professora Tatiana Assis, agradeço a orientação e contribuição com importantes sugestões nessa pesquisa. Agradeço também por disponibilizar tempo significativo para discorrer e revisar esta dissertação.

Aos pesquisadores do Cepel, Fabricio Lirio e Sergio Gomes, agradeço a orientação, disponibilidade e contribuições ao longo do desenvolvimento deste trabalho. Ao Thiago Masseram, Nícolas Netto e Leonardo Almeida pelas importantes discussões técnicas.

Ao Centro de Pesquisas de Energia Elétrica (Cepel) e à Universidade Federal do Rio de Janeiro (UFRJ), pela oportunidade e recursos para realização desta pesquisa.

Aos amigos do Cepel, em especial à Beatriz Levy, Paula Oliveira, Renan Fernandes e Eduardo Moutinho pelo companheirismo, amizade e apoio ao longo dessa jornada.

Resumo da Dissertação apresentada à COPPE/UFRJ como parte dos requisitos necessários para a obtenção do grau de Mestre em Ciências (M.Sc.)

DYNAMIC PHASOR MODELING FOR SUBSYNCHRONOUS RESONANCE ANALYSIS

Lígia Rolim da Silva

Junho/2020

Orientadora: Tatiana Mariano Lessa de Assis

Programa: Engenharia Elétrica

Este trabalho apresenta modelos matemáticos para representação da dinâmica dos componentes da rede elétrica para simulação não-linear de transitórios eletromecânicos e eletromagnéticos no domínio do tempo utilizando fasores dinâmicos e análise tensorial. As variáveis de estado dos componentes da rede são representadas como fasores dinâmicos de frequência fundamental nas equações que descrevem a dinâmica da rede, às quais aplica-se o método de integração trapezoidal para obter modelos de acompanhamento de fasores dinâmicos. A utilização desta modelagem em programas de análise de transitórios eletromecânicos amplia o escopo destas ferramentas, permitindo observar transitórios da faixa de frequência de fenômenos de Ressonância Subsíncrona (RSS). Portanto, modelos matemáticos de máquinas síncronas e para a representação do sistema mecânico do eixo turbina-gerador, apropriados para a análise de RSS, também são abordados neste trabalho. Os modelos de simulação baseados em fasores dinâmicos para a rede elétrica, máquina síncrona e eixo turbina-gerador são implementados no programa ANATEM, desenvolvido pelo Cepel. As implementações computacionais destes modelos são validadas com o PSCAD/EMTDC através de comparação dos resultados de simulação de sistemas testes. Finalmente, são apresentadas análises de resultados de simulações dinâmicas em um sistema de grande porte, demonstrando o potencial desta nova ferramenta em contribuir com informações importantes acerca da interação dinâmica entre os sistemas mecânicos do eixo turbina-gerador e a rede elétrica após grandes perturbações, o que pode acarretar torques de alta amplitude no rotor da máquina e danos ao eixo devido à fadiga mecânica.

Abstract of Dissertation presented to COPPE/UFRJ as a partial fulfillment of the requirements for the degree of Master of Science (M.Sc.)

DYNAMIC PHASOR MODELING FOR SUBSYNCHRONOUS RESONANCE ANALYSIS

Lígia Rolim da Silva

June/2020

Advisor: Tatiana Mariano Lessa de Assis

Department: Electrical Engineering

This work presents an electrical network modeling suitable for time-domain simulation of electromechanical and electromagnetic transients by using Dynamic Phasors and the tensorial analysis. The network modeling is developed by representing the state-variables of the network devices as dynamic phasors defined at the fundamental frequency, and by employing the trapezoidal integration method to obtain Dynamic Phasor Companion Models (DPCM). The application of the DPCM into electromechanical tools allows extending the simulation scope of these simulators into the range of Subsynchronous Resonance (SSR) analysis. Therefore, appropriate simulation models for SSR analysis are also presented for the synchronous machine and the mechanical system of the turbine-generator shaft, including the interface with the electrical network DPCM over the dynamic simulation. The dynamic phasor based models for both the electrical network, synchronous machine, and mechanical shaft system are implemented in the program ANATEM, which is developed by Cepel for traditional electromechanical studies in large-scale power systems. The ANATEM developments are validated with the PSCAD/EMTDC through test system simulations. Finally, simulation results of a large-scale power system demonstrate that the dynamic phasor-based models contribute with valuable information about interactions that may occur between the mechanical systems of the turbine-generator shaft and the electrical network following large disturbances, which can lead to high amplitude torques in the machine rotor, causing shaft damage due to mechanical fatigue.

Contents

List of Figures

List of Tables

List of Symbols

i	current.
v	voltage.
ψ	flux linkage.
j	unit imaginary number $\sqrt{-1}$.
f	electrical frequency.
ω	angular speed.
θ	phase angle in electrical degrees.
Δt	integration step.
T	period.
k	harmonic coefficient of a Fourier series.
τ	line travel time.
C	capacitance.
L	inductance.
Z	impedance.
R	resistance.
X	reactance.
Y	admittance.
G	conductance.
B	susceptance.
$\mathbf{Y}$	complex admittance matrix.
$\mathbf{Z}$	complex impedance matrix.
$\tilde{X}_k$	complex form of a dynamic phasor.
X_k^{Re}	real coefficients of a dynamic phasor.
X_k^{Im}	imaginary coefficient of a dynamic phasor.

π mathematical constant Pi$= 4 \cdot \arctan(1)$.

e Euler's number $e = 2.7182818284$.

pu   per unit system in terms of a base unit quantity.

List of Acronyms and Abbreviations

BIPS   Brazilian Interconnected Power System.

Cepel   Brazilian Electric Energy Research Center.

DC   Direct Current.

DP   Dynamic Phasors.

DPCM   Dynamic Phasor Companion Models.

DPTS   Dynamic Phasor Transient Simulator.

DSS   Direct Sparse Sover.

EMT   Electromagnetic Transient Programs.

EPS   Electrical Power System.

ESA   Electromechanical Stability Analysis.

FACTS   Flexible Alternating Current Transmission System.

FBM   First Benchmark Model.

GCSC   Gate-Controlled Series Capacitor.

HPS   Hydro Power Station.

HVDC   High Voltage Direct Current.

IGBT   Insulated-Gate Bipolar Transistor.

KCL   Kirchhoff's Current Law.

MKL	Math Kernel Library.
MMF	Magnetomotive Force.
ODE	Ordinary Differential Equation.
ONS	Operador Nacional do Sistema.
PAR	Plano de Ampliações e Reforços.
RMS	Root Mean Square.
SSO	Subsynchronous Oscillations.
SSR	Subsynchronous Resonance.
STATCOM	Static Synchronous Compensator.
SVC	Static Var Compensator.
TCSC	Thyristor-Controlled Series Capacitor.
TPS	Thermal Power Station.
UDC	User Defined Control.
VSC	Voltage Source Converter.

Notation

The following list describes the notation that will be later used in this thesis.

$\Re$ Denotes the real part of a complex number.

$\Im$ Denotes the imaginary part of a complex number.

v Lowercase italic letters are used to represent instantaneous signals.

V Capital italic letters denote phasors quantities.

$\mathbf{x}$ Lowercase bold letters denote vectors.

$\mathbf{Y}$ Capital bold letters denote matrices.

$\overline{v}$ Overline quantities denote per unit values.

l_{kk} Denotes self-inductance of winding k.

l_{km} Denotes mutual inductance between windings k and m.

Chapter 1

Introduction

1.1 General Background

The dynamic analysis of electrical power systems is a crucial issue in evaluating the safe operation of the system, electrical network reinforcements, and expansion planning. Essentially in the present context, where such systems continually evolve in load demand, with an increasing penetration level of renewable resources and significant application of power electronics devices. These features increase power system complexity in the range of dynamic interactions and phenomena that may occur, requiring simulation tools with the suitable analytical capability and inciting research approaching more powerful methods of analysis.

Time-domain simulation tools support the study of transient phenomena in Electrical Power System (EPS) under several frequency ranges and network dimensions. Traditional nonlinear time-domain tools are the Electromechanical Stability Analysis (ESA) and the Electromagnetic Transient Programs (EMT). The former allows evaluating slow frequency phenomena in the scope of electromechanical transients between 0.1 and 3 Hz [1], whereas the later is suitable for evaluating system behavior related to high-frequency phenomena, such as switching operations and lightning surges.

In general, standard simulation packages are focused on a specific subset of transient dynamics, according to each objective. Consequently, a set of useful simplifying assumptions may be considered to the equipment models, without compromising its primary purpose. The electrical network complexity and the required detail degree are determinant to select the analysis tool. Moreover, the available system data, the time frame of interest and the computational technology may also impact in the analyst choice.

The electromagnetic transient analysis uses detailed three-phase representation to model EPS components in order to analyze energy exchanges between magnetic and electric fields throughout the system devices. All associated devices, such as generation sources and their associated controls, Flexible Alternating Current Transmission System (FACTS), breakers, three-phase switching control systems, etc., usually require fully detailed mathematical models. The EMT precision degree allows high-frequency phenomena simulation with accurate system response. The instantaneous values of electrical variables are computed in time-domain with typical time step discretization in the order of tens of microseconds, although it may vary considerably according on the type of EMT phenomenon to be studied. Among the traditional EMT commercial packages are ATP [2], EMTP-RV [3], and PSCAD/EMTDC [4].

Electromechanical stability software provides time-domain simulation for the angular, voltage, and frequency stability assessment in large-scale EPS. The ability to handle large-scale power systems is a result of employing phasor domain analysis and neglecting high-frequency transients. This strategy reduces the number of equations that need to be solved. Hence, the electrical network is represented by its corresponding admittance matrix of positive sequence at the fundamental frequency. This representation is referred to as the quasi-steady state approach in the literature, by which the electrical network quantities are computed as Root Mean Square (RMS) phasors. On these premises, the main dynamic behavior of interest is related to synchronous machine rotational dynamics and its associated controls bandwidth. This investigation reveals which machines oscillate against each other and shows their interaction with other equipment and controls, as well as the exchange of energy between the rotating masses throughout the EPS. Among the traditional ESA commercial software are ANATEM [5], and Siemens PSS/E [6].

Simplifications assumed in the ESA modeling are based on the frequency range of the electromechanical transients, characterized by large time frames (10 - 20 seconds) and slow oscillation frequency (0.1 - 3 Hz) [1]. In this picture, electrical network transients can be neglected since their natural modes of oscillation occur in frequencies higher than those of interest, then, becoming unnecessary for analysis of slow electromechanical transients. Furthermore, equipment connected to the network shall use equivalents models describing their fundamental frequency response. Slower varying nature of the quantities involved in this analysis allows the simulation of large-scale power systems with a typical step size of milliseconds. Also, this type of modeling enables the linearization of the analytical equations and the data integration with linear analysis programs, which can infer unstable oscillations modes, poorly damped oscillations, and supports efficient controllers design to enhance system oscillation damping.

1.2   Motivation

After being subjected to a physical disturbance, the oscillatory nature of the EPS transients, ranging from a few hundred hertz up to several megahertz, are designated as **fast transients**; those covering tens of hertz are referred to as **subsynchronous oscillations**; and the **electromechanical transients** encompasses oscillations in the range of 0.1 Hz up to 3 Hz. The first two classes require detailed electrical network dynamics representation for the purpose of analysis, so they are traditionally assessed by EMT programs, while the last is studied by ESA programs, which have the ability to handle large-scale power systems.

From a broader perspective, a general set of transient phenomena observed in power systems is depicted in the schematic diagram of Figure 1.1, classified by their approximate timescales [7].
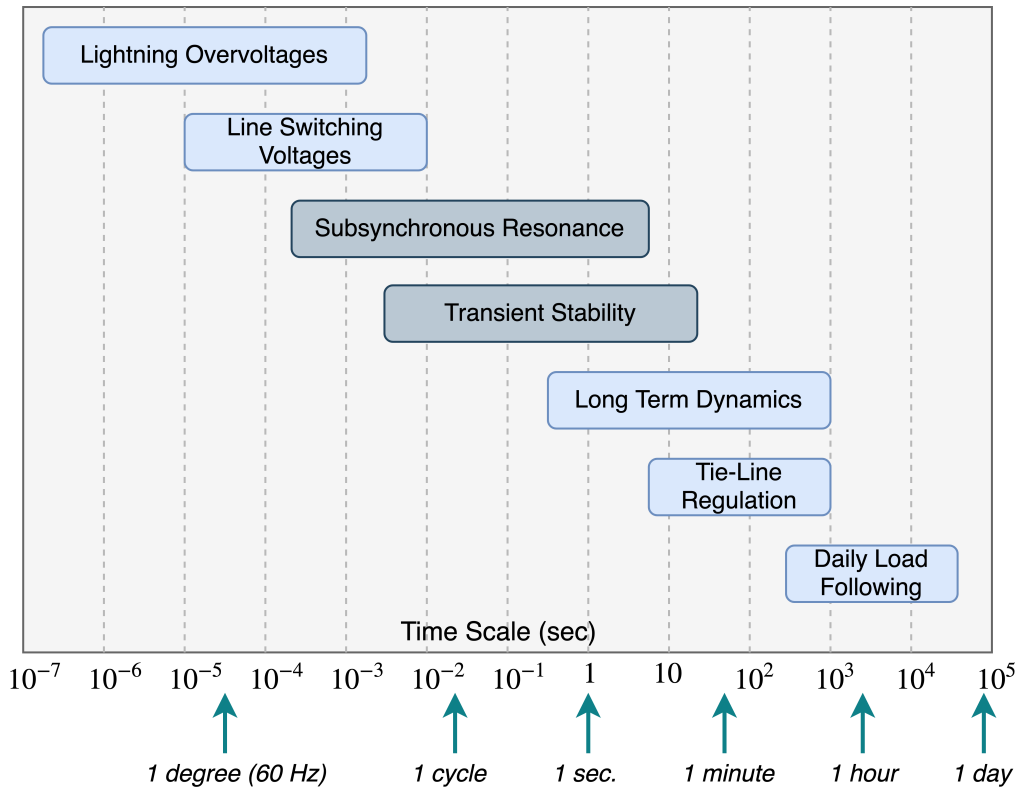
Figure 1.1: Frequency range of several dynamic phenomena

Regarding the level of detail needed for the EMT analysis, including the comprehensive electrical network data required by the mathematical models, and the reduced time step size demanded, this simulation technique is time-consuming and computationally costly. Thus, studies of this nature usually evaluate a short time frame, suitable for fast transients analysis. Also, given the refinement demanded on network data, extensive interconnected power system analysis with EMT tools becomes

3

impractical. Thus, a common practice in these studies is retaining an interest region for detailed analysis and the boundary buses of the interconnected system as equivalents. In complex cases, main difficulties are related to data preparation and acquiring accurate dynamic equivalent models to the interest region.

The use of dynamic equivalents involves difficulties associated with multiple operating conditions analysis since each dynamic equivalent is reliable near the original operating point. Hence, variations in the steady-state point imply new equivalent computation. Adjustments of controls in EMT tools are performed through a process of trial and error, making the identification of dynamic problems a huge challenge. Moreover, the parameters of controllers have to be tuned without integration with linear analysis tools.

In order to extend the frequency bandwidth of the phenomena studied by phasor domain simulation tools, previous work modeled transmission network dynamics through the concept of dynamic phasors [8]. This approach leads to nonlinear analytical models which, after linearization, derived models for linear analysis of electromagnetic transients [9–11]. Afterward, the gap due to the absence of an intermediary tool between nonlinear electromagnetic and electromechanical transient programs was target in [12] proposing a new simulator, the Dynamic Phasor Transient Simulator (DPTS). The DPTS aims to evaluate both nonlinear electromechanical and electromagnetic transients in networks containing switched devices, addressing the entire range of power system dynamics. The DPTS method ensures accurate nonlinear simulation of electromagnetic transients with the same steady-state operating point and dynamic database adopted in electromechanical studies. Furthermore, DPTS allows automatic initialization from steady-state operating point point, besides integration with linear analysis tools due to the use of compatible analytical models, enabling in-depth dynamic performance assessment of large-scale power systems.

Concerning DPTS approach to consider electrical network dynamics, holding the assumption of balanced three-phase system, it is possible to **evaluate the impact of modeling the electrical network dynamics in electromechanical transient stability simulations**. Furthermore, it is possible to increase the frequency scope of computational tools that use the inherent steady-state operating point and the dynamic database adopted in ESA programs. From Figure 1.1, one should note that the interest frequency band for subsynchronous oscillations is not substantially different from electromechanical stability range. Hence, most of the models used in electromechanical stability studies may be used in subsynchronous oscillation studies.

Usually, in electromechanical stability analysis, the turbine-generator shaft of the synchronous machine rotor is assumed to be made up of a single lumped mass. This rigid mass accounts for an equivalent inertia constant given by the sum of all individual inertia constants of shaft masses. This equivalent lumped model supports the study of synchronous machine oscillations against each other in the system, after being subjected to a disturbance that causes a mismatch between load demand and energy production. This oscillation nature corresponds to the electromechanical oscillation mode, which represents the aggregate oscillation of all individual masses of the rotor against the system.

Synchronous machines of thermal units consist of a complex mechanical structure with several masses connected by non-rigid shafts. During system disturbances, torsional oscillations arise between different sections of the turbine-generator shaft, which usually occur at frequencies below the synchronous frequency and are so-called *subsynchronous oscillations*. Turbogenerators account for a longer shaft than hydrogenerators, and they are also designed to operate at higher rotational speeds. For this reason, they are more susceptible to experience torsional oscillations. The frequency range of these oscillations may coincide with natural oscillation modes of the network when there are series compensated transmission lines. Therefore, in subsynchronous oscillation studies, the dynamic representation of the power grid as well as the stages and sections of the turbine-generator shaft are fundamental [1]. Indeed, Subsynchronous Resonance (SSR) studies require: (i) turbine-generator shaft model with individualized spring-mass representation; (ii) electrical network dynamics modeling; and (iii) representation of stator flux transients. Traditional modeling used in electromechanical transient analysis does not consider this degree of detail; consequently, it is inadequate for studies of this nature.

Given the required representation of electrical network dynamics for SSR studies and the available analysis tools, there is still an absence of an intermediary tool for both nonlinear electromagnetic and electromechanical transient analysis, which covers SSR study and accounts for steady-state automatic initialization. EMT programs include network dynamics and turbine-generator shaft representation but they are not suitable to analyze large-scale systems nor to use the electromechanical stability dynamic database. On the other hand, ESA programs are not suitable for SSR analysis due to its inherent modeling simplifications. These boundaries show that EMT and ESA tools do not effectively target the timescale range associated with both electrical network and mechanical subsystems.

Therefore, one may ask how to combine the available tools to make feasible nonlinear SSR analysis in large-scale power systems since it is not possible through EMT tools

yet. It would be interesting, then, to conceive the development of an intermediary analysis tool. This intermediary tool should be handier than EMT programs and with a more comprehensive analytical scope than those covered by ESA programs.

1.3   Objectives and Scope

This thesis presents detailed analytical development to represent electrical network dynamics using the dynamic phasor approach. In this concern, voltages and currents of lumped components are described as dynamic phasors at the fundamental frequency. Electrical quantities of transmission lines with distributed parameters are also expressed as dynamic phasors and solved by the method of characteristics. Ordinary differential equations (ODE) describing the dynamic behavior of lumped inductances and capacitances are integrated through the implicit trapezoidal integration rule, which is widely known for its numerical accuracy, efficiency, stability, and simplicity [13].

The mathematical models obtained in this thesis by using the DPTS method yields dynamic phasor companion models, whose structure is similar to the companion models proposed by H. Dommel in [14], i.e., both modelings result equivalent circuits comprising an admittance in pararell with a history source. The main difference between these two approaches is that the former regards the electrical network quantities as dynamic phasors, whereas the later considers instantaneous values. The network components addressed by DPTS modeling in this work include inductance, capacitance, and transmission lines with lumped and distributed parameters. By neglecting transmission line losses, an approximated representation for losses is carried by the Bergeron model, as it is provided in PSCAD/EMTDC [4].

The dynamic phasor companion models are derived from the tensor modeling approach [12]. The admittances are treated as *tensors* correlating real and imaginary coefficients of voltages and currents of the network components. These models also include a *"past term"* representing *history current sources* that enables the representation of the network dynamics. The history sources store memory dependent on past quantities, i.e., previous known variables from the network elements.

Whether voltages and currents are represented only by dynamic phasors in the fundamental frequency, EMT simulation can provide accurate results if the analyzed network is composed only by linear elements and sources at the same frequency. When nonlinear elements exist, there will be harmonic components in steady-state and, consequently, harmonic dynamic phasors. Even if there are harmonic components in the system, fundamental frequency models may be useful for some studies of

dynamic performance of electronic switching devices. In the scope of this work, electrical network dynamics are modeled only by dynamic phasors at the fundamental frequency.

The dynamic phasor companion models developed in this thesis are validated by implementing a prototype in MATLAB and comparing the dynamic response of each network component against the results acquired by using PSCAD/EMTDC. After DPTS validation, the electrical network dynamics is implemented in ANATEM software [5], which is a commercial ESA tool developed by the Brazilian Electric Energy Research Center (Cepel). Results of case studies acquired with ANATEM are also compared with simulations results obtained with PSCAD/EMTDC.

Therefore, the main objective of this thesis is implementing DPTS in ANATEM software allowing the study of broader frequency phenomena in a commercial tool traditionally applied for ESA simulations, widening the ANATEM application scope on its phenomena frequency range.

From Figure 1.1, one should note that the higher frequency range just after transient stability is the subsynchronous resonance frame. Hence, an appropriate machine model for subsynchronous oscillations study is also reviewed in this work for subsequent implementation in ANATEM. The turbine-generator shaft representation, along with network dynamics, allows evaluating the interaction between them in the range of SSR. DPTS approach enables a suitable interface between electrical network models and synchronous machine equations, as well as other equipment models. Thus, the present work also specifies a proper interface between DPTS model and the synchronous machine models for SSR studies.

The turbine-generator mechanical system is represented by a spring-mass model that holds the main masses as lumped masses connected by non-rigid shafts with neglected masses. The mass inertia and elasticity constants of the shaft sections relate the torques developed at the multiple machine stages with the torsional oscillations experienced by each individual masses. This representation enables analyzing the interaction between the electrical network natural oscillation modes and the machine torsional modes.

After the validation of electrical network dynamics and synchronous machine models, several simulations and analysis of SSR case studies are provided. In addition, it is proposed and implemented a feature that allows representing parts of the AC network statically and the remaining dynamically, resulting a hybrid configuration.

Throughout this work, several theoretical aspects are explored on the mathematical foundation of network dynamics and synchronous machines to allow the SSR study.

In summary, the scope of this thesis targets:

1. Development of mathematical models for the representation of the electrical network dynamics by using dynamic phasors and the tensor analysis;

2. Development of detailed dynamic phasor-based models for synchronous machines;

3. Development of a mathematical model for the mechanical system of the turbine-generator shaft;

4. Computational developments of network dynamics, dynamic phasor-based synchronous machines, and turbine-generator shaft models in the ANATEM software;

5. Validation of the electrical network dynamics, dynamic phasor-based synchronous machines, and turbine-generator shaft model against the PSCAD/EMTDC software;

6. Dynamic simulations and analysis of results from SSR case studies.

1.4   State of Art Review

Time-domain simulation of electromagnetic transients was widely assessed under the concept of companion models and nodal analysis [14–16]. The companion model technique builds the basis for a general solution method of electromagnetic transients in electrical networks. This technique allows finding instantaneous time response in arbitrary single and multi-phase networks with lumped and distributed parameters. In the range of electromechanical transients, considerable works have extensively studied and consolidated the theoretical foundations and efficient techniques for transient and dynamic stability simulations [17–20].

The companion model technique is employed in this thesis combined with the dynamic phasor approach [21] to describe the electrical network dynamics in an ESA software. The dynamic phasor approach is similar to the tensor modeling presented in [22]. The tensor modeling technique uses the concept of tensors to correlate electrical quantities, such as voltages and currents, in the frequency domain. This modeling describes the interaction between signals of different frequencies through its real and imaginary coefficients correlating frequencies. Mathematical models based on this method are analytical and, then, suitable to apply linear analysis and numerical methods for harmonic interaction evaluation.

The tensor modeling was applied in [23] to model synchronous machines and the

incremental behavior of nonlinear FACTS equipment in *s*-domain. This work also developed models and numerical methods for linear analysis of electromechanical stability, subsynchronous resonance, electromagnetic transients and harmonic interactions in electrical power systems. The tensor modeling is used in this thesis to represent synchronous machines regarding stator flux dynamics and the rotor subtransient saliency.

Previous work has shown substantial research on the analysis and design of power conversion circuits under the concept of *state-space averaging* to develop linear simulation models for small signal analysis [8, 24, 25]. The *averaging* technique evolved to the *dynamic phasor approach* [9, 21], which distinguishes from the former by providing a unique reconstruction of the original time-domain signals from its transformed (phasor) quantities. The dynamic phasor technique allows transforming a nonlinear time-varying system of equations into an autonomous nonlinear system. In this sense, the moving average operation is employed to obtain instantaneous Fourier coefficients of a generic waveform $x(\cdot)$ within a sliding time interval $(t - T, t]$. In this approach, the Fourier coefficients $X_k(t)$ are referred to as *dynamic phasors* as they are functions of time. The time interval under consideration for the averaging operation slides as a function of time over a window of length T, resulting in a *state-space model* for which the dynamic phasors are the state variables.

The dynamic phasor approach was applied in [26] to analyze lumped network dynamics together with the generator dynamics into a band-limited frequency range set up by a cut-off frequency and a convolution operation. In a different way, the present thesis replace voltages and currents of network components (lumped and distributed) directly by their corresponding time varying Fourier coefficients to obtain the analytical solution that yields companion models.

A dynamic phasor model for a Thyristor-Controlled Series Capacitor (TCSC) was developed in [9] applying the sliding window concept. This model was able to capture transients of higher frequencies than those from ESA range, encompassing subsynchronous resonance phenomena. This model was based on the representation of voltages and currents as time-varying Fourier series, and focus on short-term dynamics since the Fourier coefficients were restricted to the fundamental frequency components. This technique supports constructions of dynamic phasor models with modular characteristics and direct interface with other phasor models. This approach so far introduced an intermediate between the detailed TCSC time-domain representation and the quasi-static approximation that considers the TCSC as a variable reactance. Furthermore, these authors used this TCSC dynamic phasor model for SSR analysis and to obtain a proper linear model for eigenvalue analy-

sis [27]. This dynamic phasor model was constructed upon an averaging operation within a sliding window T to perform a hybrid system representation to incorporate both continuous-time dynamics (voltages and currents on elements) and discrete events (switching devices) [28].

The dynamic phasor theory was also applied in several works to acquire linear models of FACTS equipment suitable for linear analysis of electromagnetic transients. In [29] was introduced a new dynamic phasor model of the Static Var Compensator (SVC) suitable for high frequency analysis. A tensor modeling to represent the SVC and TCSC in s-domain was presented in [11] regarding the interaction between different frequencies. In [30] was presented both linear and nonlinear dynamic phasor based model for a Gate-Controlled Series Capacitor (GCSC). It must be highlighted that these dynamic phasor based models differ from the previous ones by not applying the sliding window concept while developing the equipment simulation models. Instead, these models describe the equipment dynamic behavior by replacing signals of interest (voltages, currents, switching functions) by their corresponding dynamic phasors. Thereafter, a numerical integration method may be applied to obtain time-domain analytical functions describing the equipment behavior with a high degree of accuracy. It performs a time-varying analytical transformation, likewise as the Park Transformation at the fundamental frequency. This thesis will follow this approach.

The comprehensive study of large-scale power systems covering fast electromagnetic transients and slow electromechanical transients involves a wide range of time constants. Regarding the electrical network, EMT programs consider high frequency dynamics, whereas ESA programs adopt the quasi-steady state approximation. The combined simulation of electromagnetic and electromechanical transients is an ambitious task. The possibility of studying both types of transients by an intermediary tool was the target of several works by using the dynamic phasor approach [31–34]. However, these previous researches made efforts on modeling electrical network dynamics and other equipment by using hybrid system representation and the dynamic phasors rooted in the averaging operation.

In [12] was introduced the *Dynamic Phasor Transient Simulator* (DPTS), a modeling methodology for time-domain electromagnetic transient simulation in large-scale power systems. This work focused on the analysis of electrical network dynamics and FACTS dynamic performance. The electrical network dynamic was modeled in DPTS by replacing instantaneous voltages and currents by their corresponding fundamental frequency dynamic phasors. Then, the ordinary differential equations describing the linear components dynamic behavior were solved through the implicit trapezoidal integration rule. This procedure yields tensor companion models referred

to as *Dynamic Phasor Companion Models*. This approach provides analytical models integrated with linear analysis tools and automatic steady-state initialization. Thus, DPTS approach allows using both *steady-state operating points* and *dynamic stability database* to perform EMT and ESA time-domain simulation.

In this thesis, the dynamic phasor companion models proposed in [12] will be implemented in ANATEM software to represent the electrical network dynamics. Important mathematical developments related to this technique will be discussed in Chapter 3. In addition, to extend the simulation scope to the range of SSR phenomena, an adequate machine model is also implemented to this analysis. This model must include the stator transients (usually neglected in ESA analysis) and also the turbine-generator shaft representation [1, 7, 35, 36]. Hence, this work will explore the electrical network dynamics interaction with torsional oscillation modes of the turbine-generator shaft. These jointly developments will provide the ability to the analysis of ESA and EMT electrical network transients and subsynchronous resonance analysis through a nonlinear time-domain commercial tool. It accounts for automatic initialization from a steady-state operating point, provided by ANAREDE software [37], also developed by Cepel. Additionally, it will adopt the database already utilized in ESA studies, i.e., no extra data is required so that, it is compatible to the analysis of large-scale power systems.

1.5   Thesis Structure

This thesis approaches comprehensive concepts related to the mathematical development of dynamic phasor companion models, model of synchronous machine for SSR studies, model of turbine-generator shaft system, and subsynchronous oscillations phenomena assessment. It also describes the computational developments, validation, and understanding of case studies associated to the theory examined. The document is organized into eight chapters, as follows:

This initial chapter introduces the motivations for developing a computational tool with a broader analysis field than traditional ESA tools, highlighting the context in which it is inserted and defining the scope and developments to be conferred in the following chapters. It makes a preliminary discussion on the subject, inserting subsynchronous oscillations in the general context of electrical power system transients. This chapter also exposes historical developments, presenting prominently associated references found in the literature.

Chapter 2 is devoted to present basic concepts and definitions, providing the necessary mathematical foundations to the understanding and development of suitable

models for electrical network components and synchronous machines. It is mainly related to dynamic phasor definitions, tensor modeling approach, and specifying the scope of stability studies.

Chapter 3 presents a comprehensive development of the Dynamic Phasor Companion Models for the representation of the electrical network dynamics. These models are acquired in a complex form, relating voltages and currents of the network components through a tensor of conductances and an associated history current source, which build modular blocks for general power system analysis. At this level, simulations models are presented for resistance, inductance, capacitance, transformers, and transmission lines (lumped and distributed).

Chapter 4 covers the synchronous machine theory, from its physical description to the proper model for SSR analysis. The needed mathematical tools for the simulation model development will also be detailed, such as the dq0 transformation, per unit system, direct and quadrature axis definition, and the swing equation. Equivalent circuits with fundamental and derived parameters are presented, as well as their relationships. The main differences between the SSR model and the model used in electromechanical studies are emphasized.

Chapter 5 introduces concepts related to the subsynchronous oscillation phenomena, including the mathematical modeling of the turbine-generator shaft and the swing equation adequacy with reference to an individualized shaft representation. The torsional natural frequencies and the interactions between turbine-generator shaft and series compensated transmission systems are discussed.

Chapter 6 details the solution methodology of the electrical network dynamics and the synchronous machine model for nonlinear SSR analysis. The computational developments performed in the ANATEM software involving the models presented in this thesis will be discussed. Finally, validations of the dynamic phasor models are performed through simulation comparison of simple test cases results against the PSCAD/EMTDC software.

Chapter 7 presents the simulation results and analysis of three case studies to evaluate nonlinear electromechanical and electromagnetic transients into small and large-scale power systems by using the Dynamic Phasor Companion Models, the synchronous machine model for SSR analysis, and the multi-mass model of the turbine-generator shaft.

Concluding remarks and directions for future researches, related to this thesis, are presented in Chapter 8.

Chapter 2

Basic Definitions and Theoretical Foundations

Time-domain simulation is an essential part concerning the analysis of slow and fast transient phenomena in EPS. It is generally difficult to make a clear distinction between transient phenomena since they evolve over time and change their characteristics. For instance, an electromagnetic transient in the transmission system may spread consequences and cause a nearby generator to fall out of step, extending into an electromechanical transient.

Using EMT programs to analyze fast transients involves a wide range of studies concerning transient overcurrents and overvoltages that may occur in the system after a disturbance. In general, EMT studies include the analysis of protection schemes, inrush currents, transient recovery voltages, switching surges, ferroresonance phenomenon, etc.

Despite the variety of EMT simulations, electromagnetic transients typically decay within a few cycles, and their area of propagation is usually confined nearby the faulty equipment. Therefore, the electrical network should be modeled in great detail for an accurate simulation. On the other hand, the dynamic of power plants associated with long-time constants is often represented by simplified models. Also, equipment located far away from the interest region may be represented by equivalents without loss of accuracy.

In another domain, the analysis of electromechanical transients through ESA programs allows a wide range of studies which are referred to as **stability simulation**. The electromechanical stability studies evaluate large-scale EPS and involve a wide range of phenomena with a broader nature and magnitude. Therefore, a variety of concepts and classification involved in electromechanical stability studies were

defined in several references [1, 38, 39].

This chapter presents basic concepts related to dynamic phasors and the tensor modeling applied to electrical networks. It also describes the general solution method introduced by H. Dommel [14] for nonlinear time-domain simulations of EMT by using companion models and nodal analysis. Furthermore, some basic terms and definitions for the study of electromechanical stability are presented, as well as the types of subsynchronous oscillation studies.

2.1   Dynamic Phasors

Conventional ESA simulators represent electrical power systems with sinusoidal steady-state response through the standard phasor analysis. The dynamic phasor technique is introduced in this chapter as a way of extending the ESA bandwidth by including the electrical network dynamics.

A dynamic phasor is simply a phasor whose magnitude and phase angle are allowed to vary over time, retaining information about fast and slow transients.

The use of dynamic phasors to obtain mathematical models for simulation is rooted in the fact that a **non-periodic** waveform $x(t)$ can be represented as a Fourier series with **time-varying coefficients** (2.1). The Fourier series of a **periodic** function is given by sinusoidal signals with **constant coefficients** and frequencies multiple of the inverse of the rated period.

$$x(t) = \sum_{k \in K} X_k^{Re}(t) \cdot \cos(k\omega t) - X_k^{Im}(t) \cdot \sin(k\omega t) \qquad k \geq 0 \qquad (2.1)$$

where $X_k^{Re}(t)$ and $X_k^{Im}(t)$ are the kth time-varying Fourier coefficients, also referred to as ***dynamic phasors***; K is the selected set of Fourier harmonic coefficients; ω is the angular speed at rated frequency, which is considered equal to the synchronous speed $\omega_0 = 2\pi f_0$.

In the complex form, a dynamic phasor may be expressed as follows:

$$x(t) = \Re\left\{ \sum_{k \in K} \tilde{X}_k(t) \cdot e^{jk\omega t} \right\} \qquad (2.2)$$

The expression $\tilde{X}_k(t)e^{jk\omega t}$ is denoted as the rotating dynamic phasor, as an extension of the rotating phasor defined in the classical theory of linear circuits [40].

As this notation serves as the basis for the remainder of this work, Dynamic Phasors

(DP) from this point forward may use the DP notation and it will refer to the real and imaginary coefficients related in (2.3).

$$\tilde{X}_k(t) = X_k^{Re}(t) + jX_k^{Im}(t) \tag{2.3}$$

Alternatively, the signal $x(t)$ can also be expressed as a sum of two imaginary dynamic phasors; likewise, those phasors defined in the classical circuits theory:

$$x(t) = \sum_{k \in K} \frac{\tilde{X}_k(t) \cdot e^{jk\omega t} + \tilde{X}_k^*(t) \cdot e^{-jk\omega t}}{2} \tag{2.4}$$

The time derivative of $x(t)$ in terms of the time-varying Fourier coefficients is given by (2.5), which may be easily obtained by differentiating (2.2).

$$\frac{dx(t)}{dt} = \Re\left\{ \sum_k \left(\frac{d\tilde{X}_k(t)}{dt} + jk\omega\tilde{X}_k(t) \right) \cdot e^{jk\omega t} \right\} \tag{2.5}$$

The notation adopted in this thesis considers:

- Symbol $\Re$ denotes the real part;

- Superscript * denotes complex conjugate value;

- Variables written in lowercase $x(t)$ represent time-domain quantities;

- Variables written in uppercase $X_k(t)$ represent the kth dynamic phasor.

Describing the state variables of the electrical system (such as voltages and currents) through DP allows representing these quantities as time-varying phasors, similarly to the phasors employed in ESA programs. The fundamental difference between these two approaches is that DP carries out higher frequency transients information. This feature enables representing electrical network dynamics since they are not neglected during analytical developments. On the contrary, ESA applications treat inductances and capacitances as fundamental frequency reactances. This approximation is referred to as quasi-steady state approximation from which the effects of disturbances instantaneously propagate throughout the electrical network.

Regarding an alternating current (AC) electrical network with linear components supplied by sinusoidal sources at the fundamental frequency (ω_0), voltages and currents shall be sinusoidal in steady-state. Hence, modeling linear networks supplied by sinusoidal sources through DP allows representing the state variables by constant phasors, either in polar (magnitude and phase) or rectangular coordinates (real and

imaginary components). When the system is subjected to a physical disturbance, DP quantities will vary over time, justifying its terminology. If the oscillations are stable, transients will decay, and the system will reach a new sinusoidal steady-state. In the presence of sinusoidal sources at the fundamental frequency and nonlinear components periodically switched, such as power electronic devices, the steady-state will be periodic non-sinusoidal with harmonic content.

Defining a dynamic phasor $\tilde{X}_k(t)$ by its magnitude $X_k(t)$ and phase θ in time t, it is possible to denote the DP by a complex number, as follows:

$$\tilde{X}_k(t) = X_k(t) \cdot e^{j\theta} \tag{2.6}$$

From (2.2), the real projection of a dynamic phasor is given by:

$$x(t) = \Re\left\{\sum_{k \in K} X_k(t) \cdot e^{j\theta} \cdot e^{j\omega t}\right\} = \sum_{k \in K} X_k(t) \cos(\theta + \omega t) \tag{2.7}$$

$$x(t) = \sum_k \left(\underbrace{X_k(t) \cdot \cos\theta}_{X_k^{Re}(t)} \cdot \cos(k\omega t) - \underbrace{X_k(t) \cdot \sin\theta}_{X_k^{Im}(t)} \cdot \sin(k\omega t) \right) \tag{2.8}$$

For $k = 1$, the **fundamental dynamic phasor** $\tilde{X}_1(t)$ is obtained, whereas other DP components $\tilde{X}_{(k \neq 1)}(t)$ are referred to as the **harmonic dynamic phasors**. A signal expressed strictly by its fundamental dynamic phasor is given by:

$$x(t) = X_1^{Re}(t) \cdot \cos(k\omega t) - X_1^{Im}(t) \cdot \sin(k\omega t) \tag{2.9}$$

Equation (2.9) reveals that the dynamic phasor domain transforms a set of non-linear time-variant equations into an autonomous nonlinear system in terms of DP coefficients [10]. This formulation is chosen in this thesis to describe currents (i) and voltages (v) from the electrical network equipment while developing the tensor models for simulation. Equation (2.10) exemplifies this application:

$$\begin{cases} v(t) = V_1^{Re}(t) \cdot \cos(\omega t) - V_1^{Im}(t) \cdot \sin(\omega t) \\ i(t) = I_1^{Re}(t) \cdot \cos(\omega t) - I_1^{Im}(t) \cdot \sin(\omega t) \end{cases} \tag{2.10}$$

Fundamental dynamic phasors will be used in Chapter 3 to derive mathematical models that describe electrical network dynamics, so-called Dynamic Phasor Com-

panion Models. It will be shown that using fundamental dynamic phasors provides an accurate simulation of high-frequency transients in linear and balanced electrical networks supplied by sources at fundamental frequency ω_0. Thereby, this dynamic phasor approach has no approximation since the relationships between state variables and their corresponding DP are instantaneous, i.e., there is no averaging operation to transform variables from time-domain to the phasor domain.

Harmonic dynamic phasors will be present in steady-state if the electrical network contains nonlinear equipment. Consequently, for an accurate modeling, such systems require a complete harmonic DP representation. The harmonic DP is analogous to the fundamental DP, whereas the harmonic DP frequency ω_k is the kth multiple of to the fundamental DP frequency ($k\omega_0$). Even if there are harmonic components in the system, previous research has shown that fundamental frequency models can be employed in practice as good approximations for some dynamic performance studies of switched components [9].

2.2 Tensor Modeling

The tensor modeling of electrical networks was introduced in [22] to study circuits operating in sinusoidal steady-state with a pulsating frequency ω. This modeling is conducted in frequency domain and it describes the relationship between voltages and currents of basic linear elements by a matrix denominated as **tensor**. In the case of passive linear circuits, the tensors correspond to the impedances (Z) and admittances (Y), which satisfy a symmetry property. This symmetry causes them to be equivalent to constant complexes (for a constant frequency), in a complex representation of sinusoidal AC quantities.

In order to explain elemental concepts concerning tensor modeling, let be the current and voltage of a static and passive linear element given by:

$$i(t) = I_{Re} \cos(\omega t) - I_{Im} \sin(\omega t) \tag{2.11}$$

$$v(t) = V_{Re} \cos(\omega t) - V_{Im} \sin(\omega t) \tag{2.12}$$

The complex representation of these quantities at frequency ω can be written as the real projection of complex phasors:

$$v(t) = \Re\left\{ \tilde{I} \cdot e^{j\omega t} \right\} \tag{2.13}$$

$$i(t) = \Re\left\{ \tilde{V} \cdot e^{j\omega t} \right\} \tag{2.14}$$

where:

$$\tilde{I} = I_{Re} + jI_{Im} \tag{2.15}$$

$$\tilde{V} = V_{Re} + jV_{Im} \tag{2.16}$$

From the general theory of linear circuits, these quantities are related by:

$$\tilde{I} = Y \cdot \tilde{V} \tag{2.17}$$

$$\tilde{V} = Z \cdot \tilde{I} \tag{2.18}$$

With Y and Z being constant complex numbers.

The tensor relationship between the rectangular coefficients $[I_{Re}, I_{Im}]$ and $[V_{Re}, V_{Im}]$ is given by a 2x2 complex admittance matrix ($\mathbf{Y}$), or a complex impedance matrix ($\mathbf{Z}$). These matrices are denominated tensors with a symmetry property, as follows:

$$\begin{bmatrix} I_{Re} \\ I_{Im} \end{bmatrix} = \begin{bmatrix} G & B \\ -B & G \end{bmatrix} \cdot \begin{bmatrix} V_{Re} \\ V_{Im} \end{bmatrix} \tag{2.19}$$

$$\begin{bmatrix} V_{Re} \\ V_{Im} \end{bmatrix} = \begin{bmatrix} R & -X \\ X & R \end{bmatrix} \cdot \begin{bmatrix} I_{Re} \\ I_{Im} \end{bmatrix} \tag{2.20}$$

Therefore, the association between voltage and current in linear circuits may be expressed by using complex numbers:

$$I_{Re} + jI_{Im} = (G - jB) \cdot (V_{Re} + jV_{Im}) \Rightarrow \tilde{I} = Y(\omega) \cdot \tilde{V} \tag{2.21}$$

$$V_{Re} + jV_{Im} = (R + jX) \cdot (I_{Re} + jI_{Im}) \Rightarrow \tilde{V} = Z(\omega) \cdot \tilde{I} \tag{2.22}$$

From (2.21) and (2.22), one should note that a linear time-invariant circuit supplied by sinusoidal voltage correlates with a corresponding sinusoidal current at the same frequency without interaction with components of different frequencies.

For the sake of illustration, consider the circuit of Figure 2.1 consisting of an ideal source connected in series with an inductance.
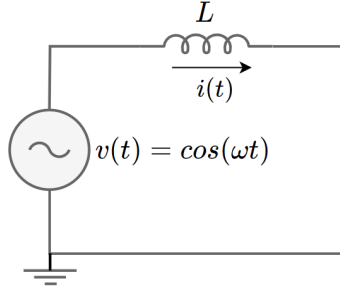
Figure 2.1: Ideal source connected in series with an inductance

where:

$$v(t) = L \cdot \frac{di(t)}{dt} \tag{2.23}$$

The voltage source is expressed through the phasor notation:

$$v(t) = \cos(\omega t) = \Re\left\{\tilde{V} \cdot e^{j\omega t}\right\} \tag{2.24}$$

The phasor $\tilde{V}$ is written as a complex number with a magnitude V and phase ϕ:

$$\tilde{V} = V \cdot e^{j\phi} \tag{2.25}$$

Thus:

$$v(t) = \cos(\omega t) = \Re\left\{V \cdot e^{j\phi} \cdot e^{j\omega t}\right\} = \Re\left\{V \cdot e^{j(\omega t + \phi)}\right\} \tag{2.26}$$

$$v(t) = \cos(\omega t) = \Re\left\{V\cos(\omega t + \phi) + jV\sin(\omega t + \phi)\right\} \tag{2.27}$$

$$\therefore v(t) = \cos(\omega t) = V\cos(\omega t + \phi) \Rightarrow \begin{cases} V = 1 \\ \phi = 0 \ (\text{in time } t = 0) \end{cases} \tag{2.28}$$

In a general form, the voltage may be written as:

$$v(t) = V\cos(\omega t + \phi) = V\cos\phi\cos(\omega t) - V\sin\phi\sin(\omega t) \tag{2.29}$$

The projections of the complex number $\tilde{V}$ are given by:

$$V_{Re} = V\cos\phi \tag{2.30}$$

$$V_{Im} = V\sin\phi \tag{2.31}$$

Then, the voltage source is expressed as follows:

$$v(t) = V_{Re} \cos(\omega t) - V_{Im} \sin(\omega t) \tag{2.32}$$

The circuit current is calculated from the following expression:

$$i(t) = \frac{1}{L} \int_0^t v(\tau) d\tau \tag{2.33}$$

Substituting (2.32) in (2.33), in terms of voltage projections, gives:

$$i(t) = \frac{1}{L} \int_0^t V_{Re} \cos(\omega \tau) - V_{Im} \sin(\omega \tau) \, d\tau$$

$$i(t) = \frac{1}{\omega L} \left[V_{Re} \sin(\omega t) + V_{Im} \cos(\omega t) - V_{Re} \underbrace{\sin(0)}_{0} - V_{Im} \underbrace{\cos(0)}_{1} \right]$$

$$i(t) = \frac{1}{\omega L} \left[V_{Re} \sin(\omega t) + V_{Im} \cos(\omega t) - V_{Im} \right]$$

$$i(t) = \frac{1}{\omega L} \left[V_{Re} \sin(\omega t) + V_{Im} \cos(\omega t) - V \sin\phi \right]$$

At time $t = 0$, the phase $\phi = 0$, thus:

$$i(t) = \frac{1}{\omega L} \left[V_{Re} \sin(\omega t) + V_{Im} \cos(\omega t) \right] \tag{2.34}$$

Considering:

$$i(t) = I_{Re} \cos(\omega t) - I_{Im} \sin(\omega t) \tag{2.35}$$

and substituting (2.35) in (2.34) yields:

$$I_{Re} \cos(\omega t) - I_{Im} \sin(\omega t) = \frac{1}{\omega L} \left[V_{Re} \sin(\omega t) + V_{Im} \cos(\omega t) \right] \tag{2.36}$$

Identifying the terms associated to the sine and cosine functions in (2.36), the tensor model is achieved:

$$\begin{bmatrix} I_{Re} \\ I_{Im} \end{bmatrix} = \begin{bmatrix} 0 & \frac{1}{\omega L} \\ -\frac{1}{\omega L} & 0 \end{bmatrix} \cdot \begin{bmatrix} V_{Re} \\ V_{Im} \end{bmatrix} \Rightarrow \tilde{I} = \mathbf{Y}(\omega) \cdot \tilde{V} \tag{2.37}$$

$$\begin{bmatrix} V_{Re} \\ V_{Im} \end{bmatrix} = \begin{bmatrix} 0 & -\omega L \\ \omega L & 0 \end{bmatrix} \cdot \begin{bmatrix} I_{Re} \\ I_{Im} \end{bmatrix} \Rightarrow \tilde{V} = \mathbf{Z}(\omega) \cdot \tilde{I} \tag{2.38}$$

In a similar way, a basic circuit consisting of an ideal sinusoidal source connected in series with resistance R and inductance L yields the following tensor model:

$$\begin{bmatrix} V_{Re} \\ V_{Im} \end{bmatrix} = \begin{bmatrix} R & -\omega L \\ \omega L & R \end{bmatrix} \cdot \begin{bmatrix} I_{Re} \\ I_{Im} \end{bmatrix} \tag{2.39}$$

In the presence of nonlinear components, the incremental behavior of such circuits is modeled by the general tensor notation:

$$\begin{bmatrix} I_{Re} \\ I_{Im} \end{bmatrix} = \begin{bmatrix} y_{11} & y_{12} \\ y_{21} & y_{22} \end{bmatrix} \cdot \begin{bmatrix} V_{Re} \\ V_{Im} \end{bmatrix} \tag{2.40}$$

In this representation, the coefficients y_{ij} of the admittance matrix do not exhibit the symmetry observed in (2.19) and (2.20). It should be noted that without this feature, it is not possible to utilize complex numbers to correlate the phasors of voltage and current, as seen in (2.21) and (2.22). As a result, nonlinear circuits supplied by sinusoidal sources will produce harmonic components in steady-state.

The tensor modeling and the dynamic phasor approach are similar in their analytical developments so far. However, these methods present some conceptual differences: the tensor modeling describes the electrical quantities in the frequency domain by its real and imaginary coefficients, whereas the dynamic phasor technique regards these coefficients in time-domain to obtain the dynamic response. In this thesis, the dynamic phasor approach is chosen to develop the companion models representing the electrical network dynamics.

2.3 Numerical Solution of Electromagnetic Transients

A numerical solution method for time-domain simulation of electromagnetic transients was introduced by H. Dommel [14, 41] to support EMT analysis of electrical power systems with generic topology. This modeling applies nodal analysis, trapezoidal rule of integration, and the method of characteristics to represent basic elements, such as resistors, inductors, capacitors, and transmission lines. These basic models are discussed in this subsection introducing the concept of companion models, which builds the basis for the methodology presented in Chapter 3.

The central idea concerning the companion model approach is depicted in the following steps:

1. Consider a basic linear component whose terminal voltage across and current through the device are related by an ODE:

$$v_{km}(t) = L \cdot \frac{di_{km}(t)}{dt} \qquad\qquad i_{km}(t) = C \cdot \frac{dv_{km}(t)}{dt}$$
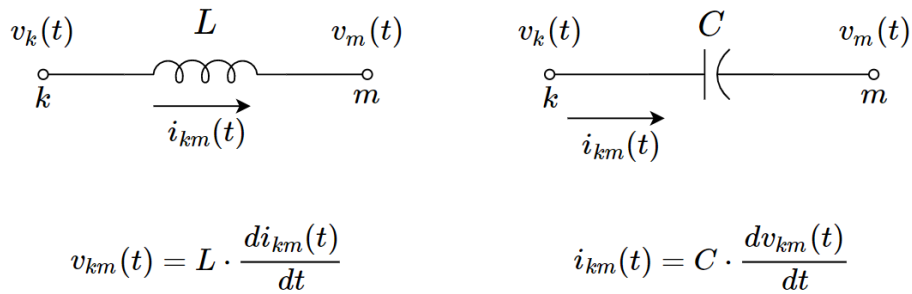
Figure 2.2: Basic linear components

2. A numerical integration method (such as the trapezoidal rule) may be applied within a discrete interval $[t - \Delta t, t]$ to acquire a discrete difference equation describing the time-domain solution;

3. Then, the difference equation may be rearranged to explicit the current at time t revealing a discrete relationship between the voltage and current;

4. As a result, the discrete relationship expressing the current through the device accounts for a part multiplying the voltage (conductance), and a part depending on past information (history source);

5. This relationship may be used to express the element as a discrete Norton equivalent (Figure 2.3) that can be used in agreement with the nodal analysis technique.
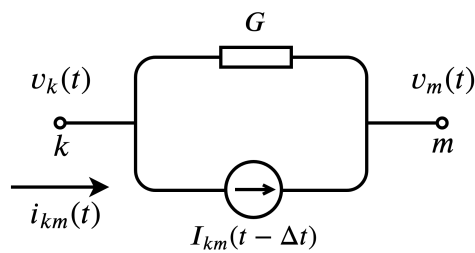
Figure 2.3: Discrete Norton equivalent of a Companion Model

Time-domain simulation of electromagnetic transients cannot reproduce a continuous history of dynamic phenomena. Hence, a sequence of snapshot frames at discrete intervals Δt are determined step-by-step. The implicit trapezoidal rule was chosen for numerical integration due to its accuracy, stability, and simplicity [42]. Although the trapezoidal method does not give accurate approximations for large step sizes, its error will not exponentially grow since this method is A-stable, ensuring that simulations of stable continuous systems will be numerically stable [13].

Trapezoidal Integration Method

The trapezoidal integration method uses linear interpolation to integrate an ordinary differential equation numerically at discrete intervals Δt over time. It expresses the integral by approximating the solution within a specific interval $[t - \Delta t, t]$ by the trapezoid area between two subsequent solutions (as a function of Δt).

For the sake of illustration, Figure 2.4 graphically exemplifies the trapezoidal rule.
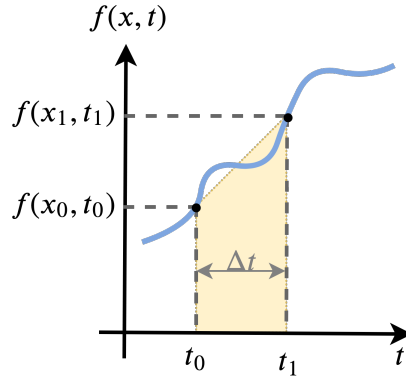
Figure 2.4: Illustration of the Trapezoidal Integration Method

Considering a generic differential equation given by:

$$f(x,t) = \frac{dx(t)}{dt} \qquad \text{with } x = x_0 \text{ at } t = t_0 \qquad (2.41)$$

Integrating (2.41) from $t_0 = t_1 - \Delta t$ to t_1, the solution for x_1 may be expressed as:

$$x_1 = x_0 + \int_{t_0}^{t_1} f(x, \tau)d\tau \qquad (2.42)$$

The step-by-step solution of (2.42) is approximated by a sequence of discrete trapezoid area under the function $f(x, t)$, as depicted in Figure 2.4. This integration rule is given by:

$$x_1 = x_0 + \left[\frac{f(x_0, t_0) + f(x_1, t_1)}{2} \right] \cdot \Delta t \qquad (2.43)$$

The trapezoidal integration method may be summarized into the following practical rule to algebrize differential equations towards a discrete system of algebraic difference equations:

1. Consider a generic first order differential equation:

$$f(x,t) = \frac{dx(t)}{dt} \tag{2.44}$$

2. In order to transform this differential equation into a discrete algebraic expression, replace derivative terms $\left[\frac{dx(t)}{dt}\right]$ and algebraic functions $f(x,t)$ by:

$$\frac{dx(t)}{dt} \implies \left[\frac{x(t) - x(t-\Delta t)}{\Delta t}\right] \tag{2.45}$$

$$f(x,t) \implies \left[\frac{f(t) + f(t-\Delta t)}{2}\right] \tag{2.46}$$

3. Therefore, employing the trapezoidal integration rule into (2.44) allows writing this ODE through the following algebraic equation:

$$\left[\frac{x(t) - x(t-\Delta t)}{\Delta t}\right] = \left[\frac{f(t) + f(t-\Delta t)}{2}\right] \tag{2.47}$$

2.4 Companion Models for EMT Simulation

Dynamic simulation models for linear and time-invariant passive components, such as reactors, capacitors, transmission lines, and unsaturated transformers, can be represented by a combination of basic linear components (R, L, C). In developing these models, typical state variables of interest are capacitor voltages $v_C(t)$ and inductor currents $i_L(t)$.

The companion models of branches with lumped parameters are acquired by using the trapezoidal rule for numerical integration, while branches with distributed parameters are analyzed with the method of characteristics. In this sense, the resulting difference equations are rearranged so that each branch yields an equivalent circuit comprising a **conductance** and a **history source**. This branch model is called **companion model**, which is a function of the circuit parameters and step interval Δt. Therefore, it remains unchanged as long as the step size and the network topology remains unchanged. In the case of nonlinear branches, the equivalent conductance may change over the simulation.

The following subsections show the mathematical development of companion models for EMT simulations. The lumped models discussed here include inductance, capacitance, and resistance. Series, parallel, and any generic association of these elemental components are obtained by a systematic combination of each companion

model. Transmission lines with distributed parameters are examined by using the method of characteristic (Bergeron's method). Neglecting transmission line losses, the Bergeron's method presents an exact solution. However, for general purpose, a diffuse model that considers the losses into concentrated points through the line length is also inferred.

Computationally, the electrical network model is constructed by connecting each branch through its appropriate companion model in accordance with the grid topology. This procedure is performed in this thesis by using the nodal analysis to build the admittance matrix from the modular companion models.

2.4.1 Inductance

Consider an inductance L between nodes k and m of a generic branch illustrated in Figure 2.5:
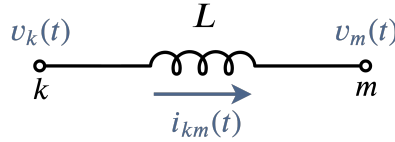
Figure 2.5: Inductance branch

The inductor current $i_{km}(t)$ and the voltage $v_{km}(t)$ are associated by the following ODE:

$$v_k(t) - v_m(t) = L\frac{di_{km}(t)}{dt} \tag{2.48}$$

Regarding instantaneous values and discretization Δt, the numerical integration by trapezoidal rule yields:

$$i_{km}(t) - i_{km}(t - \Delta t) = \frac{1}{L}\int_{t-\Delta t}^{t} v_{km}(\tau)d\tau \tag{2.49}$$

$$i_{km}(t) = i_{km}(t - \Delta t) + \frac{1}{L}\left[\frac{v_{km}(t - \Delta t) + v_{km}(t)}{2} \cdot \Delta t\right] \tag{2.50}$$

Rearranging (2.50) to explicit the current i_{km} at time t, gives:

$$i_{km}(t) = i_{km}(t - \Delta t) + \frac{\Delta t}{2L}v_{km}(t - \Delta t) + \frac{\Delta t}{2L}v_{km}(t) \tag{2.51}$$

The term $\left[\frac{\Delta t}{2L}\right]$ multiplying voltage $v_{km}(\cdot)$ is referred to as a *conductance*. Grouping

the terms calculated in the previous step $(t - \Delta t)$ allows one to define the following equivalent *history current source*:

$$I_{km}(t - \Delta t) = i_{km}(t - \Delta t) + \frac{\Delta t}{2L} v_{km}(t - \Delta t) \tag{2.52}$$

This history source provides past information about the inductor, which influences on the present time.

Equation (2.53) presents the **inductance companion model** as a function of the conductance and the history current source.

$$\boxed{i_{km}(t) = I_{km}(t - \Delta t) + \frac{\Delta t}{2L} v_{km}(t)} \tag{2.53}$$

An equivalent impedance network corresponding to the inductance companion model is shown in Figure 2.6.
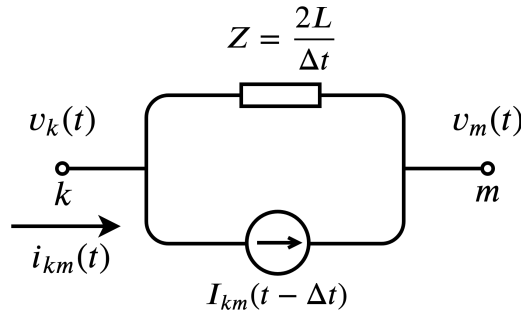
Figure 2.6: Companion model of an inductance

2.4.2 Capacitance

For a capacitance C between nodes k and m of a generic branch illustrated in Figure 2.7:
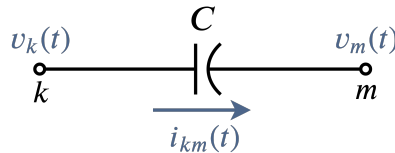
Figure 2.7: Capacitance branch

The capacitor current $i_{km}(t)$ and the voltage $v_{km}(t)$ are associated by the following

ODE:

$$i_{km}(t) = C\frac{d(v_k(t) - v_m(t))}{dt} \tag{2.54}$$

Integrating (2.54) from $(t - \Delta t)$ to (t):

$$v_{km}(t) = v_{km}(t - \Delta t) + \frac{1}{C}\int_{t-\Delta t}^{t} i_{km}(\tau)d\tau \tag{2.55}$$

and applying the trapezoidal rule with regular discretization step Δt yields:

$$v_{km}(t) = v_{km}(t - \Delta t) + \frac{\Delta t}{2C}\left[i_{km}(t - \Delta t) + i_{km}(t)\right] \tag{2.56}$$

Rearranging (2.56) to explicit the current $i_{km}(t)$, gives:

$$i_{km}(t) = -i_{km}(t - \Delta t) - \frac{2C}{\Delta t}v_{km}(t - \Delta t) + \frac{2C}{\Delta t}v_{km}(t) \tag{2.57}$$

The term $\left[\frac{2C}{\Delta t}\right]$ multiplying voltage $v_{km}(\cdot)$ is referred to as a *conductance*. Grouping the terms calculated in the previous step $(t - \Delta t)$ allows one to define the following equivalent *history current source*:

$$I_{km}(t - \Delta t) = -i_{km}(t - \Delta t) - \frac{2C}{\Delta t}v_{km}(t - \Delta t) \tag{2.58}$$

Equation (2.59) presents the **capacitance companion model** as a function of the conductance and the history current source.

$$\boxed{i_{km}(t) = I_{km}(t - \Delta t) + \frac{2C}{\Delta t}v_{km}(t)} \tag{2.59}$$

An equivalent impedance network corresponding to the capacitance companion model is shown in Figure 2.8.

$$Z = \frac{\Delta t}{2C}$$
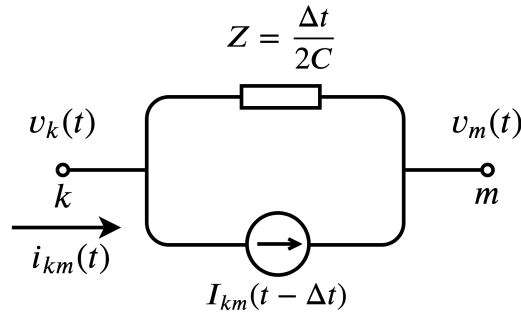
Figure 2.8: Companion model of a capacitance

2.4.3 Resistance

For complete approach of the elemental companion models, consider a resistance between generic nodes k and m:
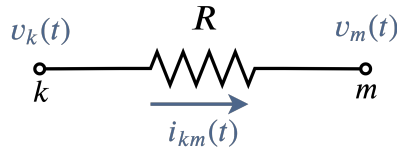
Figure 2.9: Resistance branch

In this case, the relationship between the voltage across and current through the branch does not involve differential equations, so that trapezoidal rule is not necessary.

Thus, the algebraic equation for the resistance branch is directly given by:

$$i_{km}(t) = \frac{1}{R} v_{km}(t) \qquad (2.60)$$

Therefore, the equivalent impedance network corresponding to the resistance companion model is given in Figure 2.10.
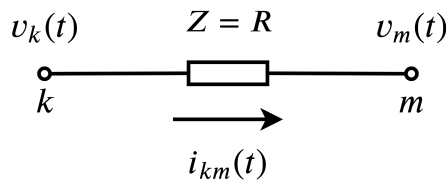
Figure 2.10: Companion model of a resistance

Since this basic device has no dependence on past information, it has no history source but the impedance relating the voltage and current at the present instant.

2.4.4 Transmission Line

Simulation models of transmission lines generally consist of four basic parameters to denote their characteristics. These basic parameters are the **series impedance** consisting of resistance R' and inductance L' per units of length, and the **shunt admittance** consisting of conductance G' and capacitance C' per units of length. The shunt conductance is usually neglected because it gives a small contribution to shunt admittance. General equations relating voltage and current on a transmission line are a function of its basic parameters, from which are inferred general equations and quadripole models.

The series impedance and shunt admittance are **uniformly distributed** along the line. However, **lumped parameters** provide satisfying accuracy for short lines and lines of medium length. If an overhead line is classified as *short-length*, shunt capacitance is so small that it can be entirely omitted with little loss of accuracy, and it is acceptable to consider only the total series resistance R and inductance L both lumped. A *medium-length* line can be represented sufficiently well by its total series impedance R and L, and half of the total shunt capacitance at each line end, both as lumped parameters as depicted in Figure 2.11a. Total shunt conductance G is usually neglected in overhead transmission lines models for the purpose of voltage and current calculation.

(a) π-equivalent parameters (b) π-equivalent companion model
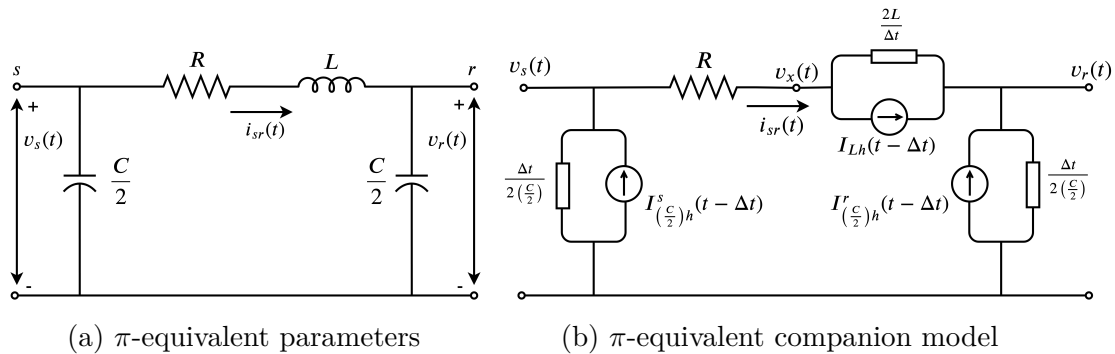
Figure 2.11: Equivalents circuits of a medium-line length

Models of short and medium-length transmission lines are made up of lumped parameters. Consequently, their equivalent companion models are intuitively built by simple substitution of each component by its corresponding companion model. For instance, Figure 2.11b depicts the equivalent companion model of a medium-length line.

Open-wire AC transmission lines operating at 60 Hz configure short lines until less than about 80 km. Medium-lines are typically encompassed between 20 km and 240 km length. Lines longer than 240 km require calculation in terms of distributed

parameters if a high precision degree is required. Otherwise, a lumped-parameters representation may be used for lines up to 320 km [43]. Regarding long overhead transmission lines, the method of Bergeron is considered to obtain the companion model of *long-length* lines since it is widely applied for EMT analysis with an acceptable accuracy level [4].

Consider the transmission line illustrated in Figure 2.12 with distributed parameters R', L' and C' per unit of length. This thesis is not devoted to present an exhaustive deduction of transmission line models since several references already comprehend detailed mathematical development of voltage and current equations and quadripole models [16, 44, 45].
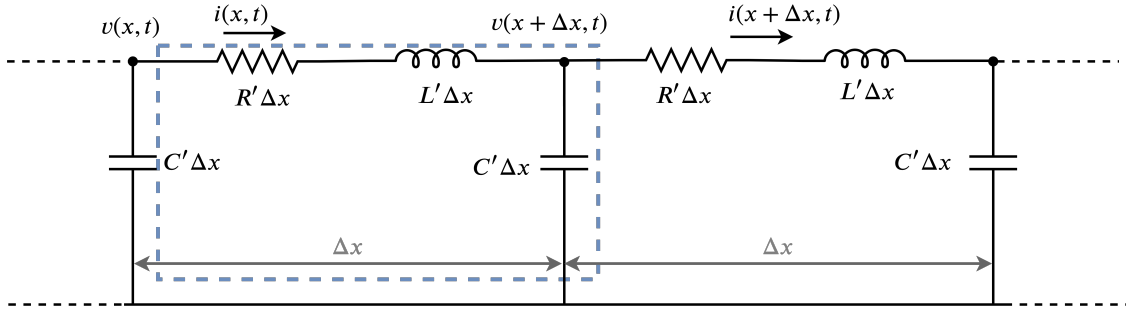
Figure 2.12: Model of a distributed parameter tramission line

Voltage and current vary along an elemental line length of Δx as specified by:

$$v(x,t) - v(x + \Delta x, t) = R'\Delta x \cdot i(x,t) + L'\Delta x \cdot \frac{\partial i(x,t)}{\partial t} \tag{2.61}$$

$$i(x,t) - i(x + \Delta x, t) = C'\Delta x \cdot \frac{\partial v(x + \Delta x, t)}{\partial t} \tag{2.62}$$

The ordinary differential equations (2.61) and (2.62) of the method of characteristic are not directly integrable [14]. Therefore, at this stage, transmission line losses are neglected ($R' \rightarrow 0$) and an exact model is developed for lossless lines.

2.4.4.1 Lossless Transmission Lines

A lossless line with inductance L' and capacitance C' per unit length relates voltage and current at a generic point x along the line by (2.63) and (2.64).

$$-\frac{\partial v(x,t)}{\partial t} = L' \cdot \frac{\partial i(x,t)}{\partial t} \tag{2.63}$$

$$-\frac{\partial i(x,t)}{\partial t} = C' \cdot \frac{\partial v(x,t)}{\partial t} \tag{2.64}$$

The general solution of these equations is given by:

$$i(x,t) = f_1(x - \nu t) + f_2(x + \nu t) \tag{2.65}$$

$$v(x,t) = Z \cdot f_1(x - \nu t) + Z \cdot f_2(x + \nu t) \tag{2.66}$$

where $f_1(x - \nu t)$ and $f_2(x + \nu t)$ are arbitrary functions of the variables $(x - \nu t)$ and $(x + \nu t)$. These functions shall be determined from the initial and contour conditions of the problem. The parameters Z and ν are respectively referred to as the *surge impedance* and the *phase velocity*, defined by:

$$Z = \sqrt{\frac{L'}{C'}} \tag{2.67}$$

$$\nu = \frac{1}{\sqrt{L'C'}} \tag{2.68}$$

The term $f_1(x - \nu t)$ can be interpreted as a traveling wave at speed ν towards the line receiving-end, whereas $f_2(t + \nu t)$ represents a wave that travels in the opposite direction up to the sending-end.

Multiplying (2.65) by $2Z$ and adding it to (2.66), yields:

$$v(x,t) + Zi(x,t) = 2Z \cdot f_1(x - \nu t) \tag{2.69}$$

In the same manner, multiplying (2.65) by $2Z$ and subtracting it to (2.66), gives:

$$v(x,t) - Zi(x,t) = -2Z \cdot f_1(x + \nu t) \tag{2.70}$$

One should note that the expression $(v + Zi)$ in (2.69) remains constant as long as the argument $(x - \nu t)$ remains constant. Similarly, the term $(v - Zi)$ in (2.70) is constant while $(x + \nu t)$ is constant. This feature may be noticed by a fictitious observer who travels along the line at velocity ν. The expressions $(x - \nu t) = \text{constant}$ and $(x + \nu t) = \text{constant}$ are termed as *characteristics* of the differential equations, justifying Bergeron's method terminology.

Consider the lossless line of Figure 2.13 with node k as the sending-end, node m as the receiving-end and line length ℓ.
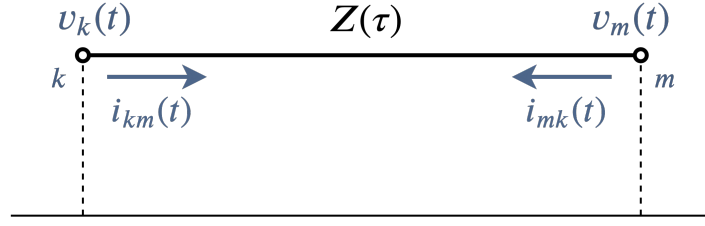
Figure 2.13: Lossless transmission line

The travel time τ is defined as the total interval that a wave gets from one line-end to another. This parameter is calculated by (2.71):

$$\tau = \frac{\ell}{\nu} = \ell\sqrt{L'C'} \tag{2.71}$$

The value of expression $v(x,t) + Zi(x,t)$ at the sending-end k and instant $(t - \tau)$ is integrally reproduced at the receiving-end m and instant t (Figure 2.14).
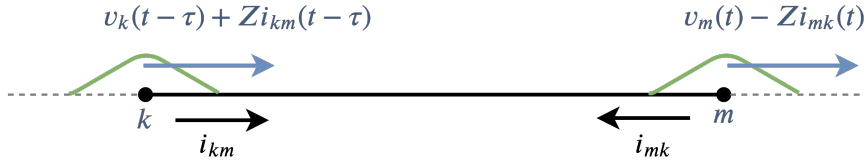
Figure 2.14: Progressive wave

In other words, the value of expression $(v + Zi)$ seen by an observer when he leaves node k at instant $(t - \tau)$ must be identical to the value found when he arrives at node m at instant t.

The signal of terminal currents assumes positive convention for currents flowing from node k to node m. Hence, equations relating voltages and currents between the line ends are given by:

$$v_k(t - \tau) + Zi_{km}(t - \tau) = v_m(t) - Zi_{mk}(t) \tag{2.72}$$

$$v_m(t - \tau) + Zi_{mk}(t - \tau) = v_k(t) - Zi_{km}(t) \tag{2.73}$$

Dividing (2.72) and (2.73) by Z, and defining the following history sources:

$$b_k(t - \tau) = \frac{v_m(t - \tau)}{Z} + i_{mk}(t - \tau) \qquad (2.74)$$

$$b_m(t - \tau) = \frac{v_k(t - \tau)}{Z} + i_{km}(t - \tau) \qquad (2.75)$$

After some basic algebraic manipulations, the two-port equations for $i_{km}(t)$ and $i_{mk}(t)$ may be written as:

$$\boxed{i_{km}(t) = \frac{v_k(t)}{Z} - b_k(t - \tau)} \qquad \boxed{i_{mk}(t) = \frac{v_m(t)}{Z} - b_m(t - \tau)} \qquad (2.76)$$

The equivalent current sources $b_k(t - \tau)$ and $b_m(t - \tau)$ represent terminal *history sources*, which are completely known at time t from the past history $(t - \tau)$. Consequently, the ideal lossless line companion model consists of two branches at each line-end uncoupling terminal currents and voltages at time t.

The equivalents conductance and history sources are illustrated in Figure 2.15 and the two-port representation of the lossless line quadripole is shown in Figure 2.16.
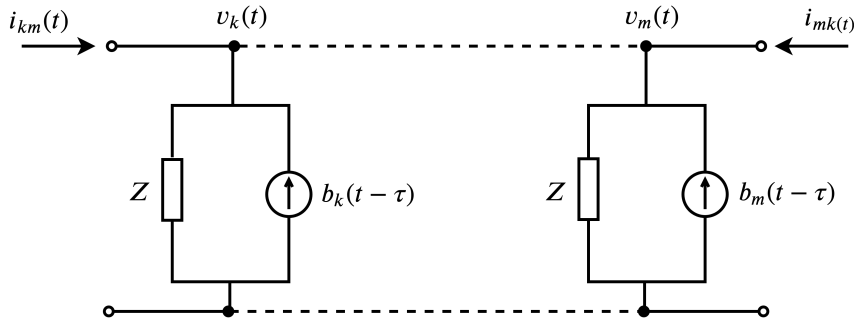
Figure 2.15: Equivalent companion model of a lossless line
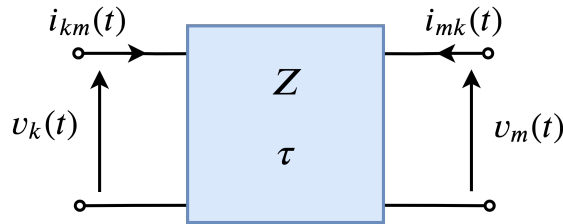
Figure 2.16: Lossless line quadripole

2.4.4.2 Lossy Transmission Line

Power losses in transmission lines depend on electrical resistances distributed over the entire length of line conductors. In practice, line losses are frequency-dependent (due to the skin effect) [46]. An approximate way to study resistance losses by using the Bergeron model will be presented. In this modeling, the following assumptions are made:

1. The transmission line is divided into ideal lossless sections;

2. Each lossless sections are evaluated with the Bergeron's method;

3. Then, a limited number of divisions of the total resistance are added as constants and concentrated values along the line length between lossless sections;

4. The sum of the lumped resistances along the lossless sections corresponds to the total line resistance (R).

Treating the line as a unique lossless section and adding lumped resistances at both line-ends yields the quadripole presented in Figure 2.17.
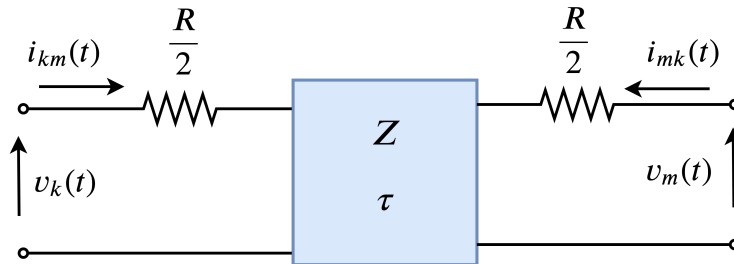
Figure 2.17: Approximate lossy line with lumped resistances at both line-ends

The lumped resistances may be inserted within many points along the line when the total length is divided into many line sections. Nevertheless, previous research has shown no noticeable difference between lumped resistances inserted into a few or many points [14].

A traditional and convenient form adopted in EMT programs lumps ($R/4$) at both line-ends and ($R/2$) in the middle of the line. Indeed, this model can be seen as:

1. Series connection of two lossless sections, each one corresponding to half of the total line length;

2. Each half-section accounts for a total resistance equal to ($R/2$) since the entire line resistance corresponds to R;

3. The half section resistance $R/2$ must be divided into both terminals ($R/4$).

This configuration is adopted in the program PSCAD/EMTDC and it is depicted in Figure 2.18.
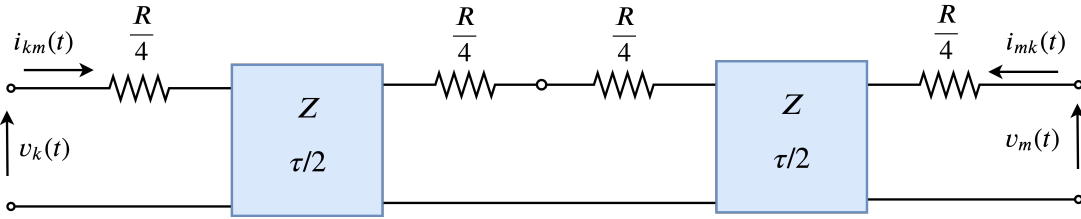
Figure 2.18: Approximate lossy line with lumped resistances and lossless sections

Comparing to a lossless line of length ℓ, each lossless sections have the same surge impedance Z and half of the travel time $\tau/2$ since each section has a total length equal to $\ell/2$. The surge impedance does not change as it remains being calculated through (2.67).

The approximate model of Figure 2.18 is considered in this work to obtain the lossy line companion model. Hence, the desired quadripole should relate terminal voltages and currents. Taking the equivalent network shown in Figure 2.19 to obtain the expressions relating terminal quantities, these equations shall be reduced toward the final equivalent quadripole.
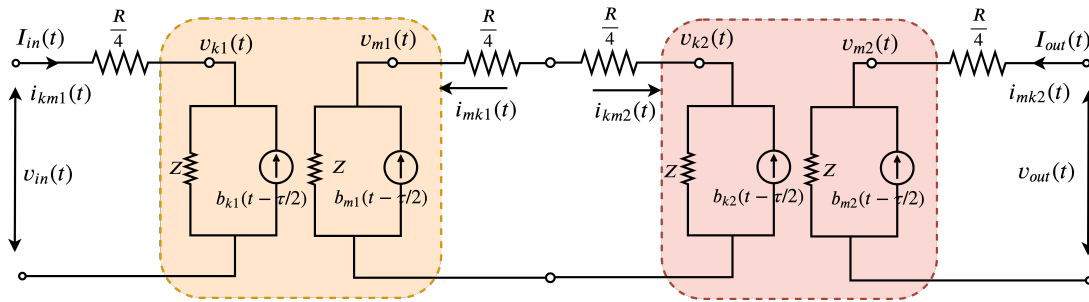
Figure 2.19: Cascade connection of lossless line companion models and lumped resistances

In this sense, intermediary variables of the two lossless sections must be eliminated in order to acquire an equivalent companion model as depicted in Figure 2.20

35
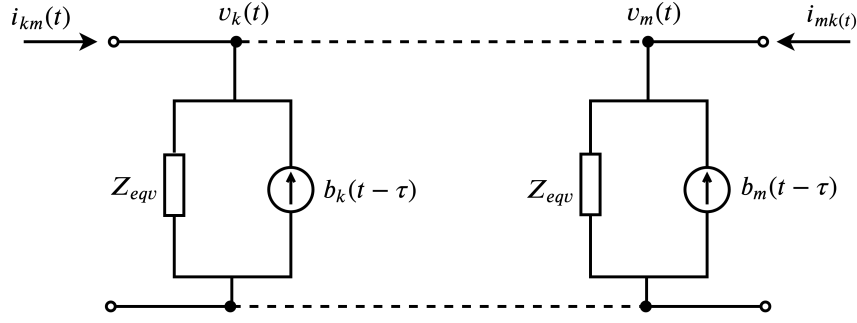
Figure 2.20: Equivalent companion model of an approximated lossy line

The equivalent quadripole is obtained by cascading the lossless line companion model and adding lumped resistances in series connection. Each ideal lossless line segment represents half of the transmission line. From this circuit, currents of interest at both line-ends are:

$$I_{in}(t) = i_{km1}(t) \tag{2.77}$$

$$I_{out}(t) = i_{mk2}(t) \tag{2.78}$$

Relating terminal quantities yields:

$$i_{km1}(t) = \frac{v_{k1}(t)}{Z} - b_{k1}(t) \tag{2.79}$$

$$i_{mk2}(t) = \frac{v_{m2}(t)}{Z} - b_{m2}(t) \tag{2.80}$$

The intermediary voltages may be written as:

$$v_{k1}(t) = v_{in}(t) - \frac{R}{4}i_{km1}(t) \tag{2.81}$$

$$v_{m2}(t) = v_{out}(t) - \frac{R}{4}i_{mk2}(t) \tag{2.82}$$

The history current sources at each section end are defined as follows:

$$
\begin{aligned}
b_{k1}(t) &= \frac{1}{Z}v_{m1}(t - \tau/2) + i_{mk1}(t - \tau/2) \\
b_{k2}(t) &= \frac{1}{Z}v_{m2}(t - \tau/2) + i_{mk2}(t - \tau/2) \\
b_{m1}(t) &= \frac{1}{Z}v_{k1}(t - \tau/2) + i_{km1}(t - \tau/2) \\
b_{m2}(t) &= \frac{1}{Z}v_{k2}(t - \tau/2) + i_{km2}(t - \tau/2)
\end{aligned}
\tag{2.83}
$$

Substituting (2.81) into (2.79), comes:

$$i_{km1}(t) = \frac{v_{in}(t) - \dfrac{R}{4}i_{km1}(t)}{Z} - b_{k1}\left(t - \tau/2\right)$$

$$i_{km1}(t) = \frac{v_{in}(t)}{Z + R/4} - \left(\frac{Z}{Z + R/4}\right)b_{k1}\left(t - \tau/2\right) \qquad (2.84)$$

Analogously, substituting (2.82) into (2.80), gives:

$$i_{mk2}(t) = \frac{v_{out}(t)}{Z + R/4} - \left(\frac{Z}{Z + R/4}\right)b_{k2}\left(t - \tau/2\right) \qquad (2.85)$$

Equation (2.83) shows that the history sources from (2.84) and (2.85) depend on intermediary voltages and currents evaluated at time $(t - \tau/2)$. As a result, the intermediary circuit must be evaluated at time $t = t - \tau/2$. The resulting circuit is shown in Figure 2.21.
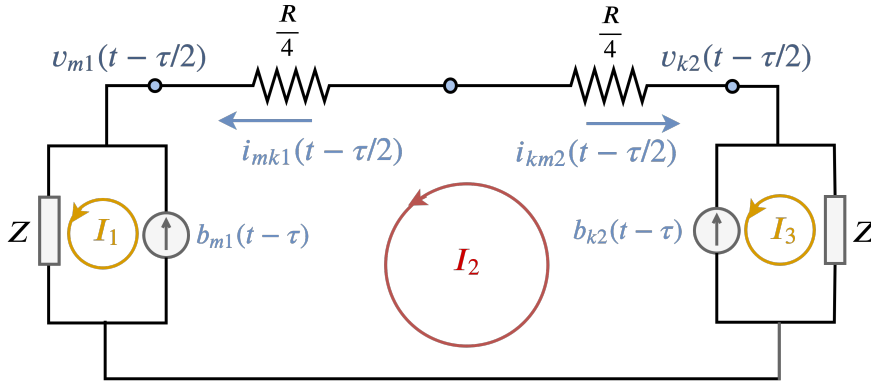
Figure 2.21: Intermediary circuit of the lossy line companion model

From the intermediary circuit, the following mesh currents are defined:

$$I_1 = b_{m1}\left(t - \tau\right) = \frac{v_{k1}\left(t - \tau\right)}{Z} + i_{km1}\left(t - \tau\right) \qquad (2.86)$$

$$I_3 = b_{k2}\left(t - \tau\right) = \frac{v_{m2}\left(t - \tau\right)}{Z} + i_{mk2}\left(t - \tau\right) \qquad (2.87)$$

Substituting (2.81) and (2.82) into (2.86) and (2.87), respectively, comes that:

$$I_1 = b_{m1}(t - \tau) = \frac{v_{in}(t - \tau) - \frac{R}{4}i_{km1}(t - \tau)}{Z} + i_{km1}(t - \tau)$$

$$I_3 = b_{k2}(t - \tau) = \frac{v_{out}(t - \tau) - \frac{R}{4}i_{mk2}(t - \tau)}{Z} + i_{mk2}(t - \tau)$$

$$\begin{aligned}
I_1 = b_{m1}(t - \tau) &= \frac{v_{in}(t - \tau)}{Z} + \left[\frac{Z - R/4}{Z}\right] i_{km1}(t - \tau) \\
I_3 = b_{k2}(t - \tau) &= \frac{v_{out}(t - \tau)}{Z} + \left[\frac{Z - R/4}{Z}\right] i_{mk2}(t - \tau)
\end{aligned} \tag{2.88}$$

The current equation of the principal mesh is given by:

$$Z \cdot I_1 + I_2 \cdot \left[2Z + \frac{R}{2}\right] - Z \cdot I_3 = 0 \tag{2.89}$$

$$I_2 = \frac{Z(-I_1 + I_3)}{2Z + R/2} \tag{2.90}$$

Substituting (2.88) into (2.90), yields:

$$I_2 = \frac{-v_{in}(t - \tau) - (Z - R/4)\,i_{km1}(t - \tau) + v_{out}(t - \tau) + (Z - R/4)\,i_{mk2}(t - \tau)}{2Z + R/2} \tag{2.91}$$

The voltages $v_{m1}(t - \tau/2)$ and $v_{k2}(t - \tau/2)$ can be written as a function of the mesh currents as:

$$v_{m1}(t - \tau/2) = Z \cdot (I_1 + I_2) \tag{2.92}$$

$$v_{k2}(t - \tau/2) = Z \cdot (I_3 - I_2) \tag{2.93}$$

The history sources given by (2.84) and (2.85) may also be written as a function of the mesh currents, resulting in:

$$b_{k1}(t) = \frac{1}{Z}v_{m1}(t - \tau/2) + \overbrace{i_{mk1}(t - \tau/2)}^{I_2} \tag{2.94}$$

$$b_{m2}(t) = \frac{1}{Z}v_{k2}(t - \tau/2) + \underbrace{i_{km2}(t - \tau/2)}_{-I_2} \tag{2.95}$$

Substituting (2.92) and (2.93) into (2.94) and (2.95), respectively, yields:

$$b_{k1}(t) = I_1 + 2I_2 \tag{2.96}$$

$$b_{m2}(t) = I_3 - 2I_2 \tag{2.97}$$

$$b_{k1}(t) = \frac{v_{in}(t-\tau)}{Z} + \left[\frac{Z - R/4}{Z}\right] i_{km1}(t-\tau) +$$

$$+ \left[\frac{-v_{in}(t-\tau) - (Z - R/4)\, i_{km1}(t-\tau) + v_{out}(t-\tau) + (Z - R/4)\, i_{mk2}(t-\tau)}{Z + R/4}\right]$$

$$b_{m2}(t) = \frac{v_{out}(t-\tau)}{Z} + \left[\frac{Z - R/4}{Z}\right] i_{mk2}(t-\tau) +$$

$$- \left[\frac{-v_{in}(t-\tau) - (Z - R/4)\, i_{km1}(t-\tau) + v_{out}(t-\tau) + (Z - R/4)\, i_{mk2}(t-\tau)}{Z + R/4}\right]$$

After some basic algebraic manipulations, the following expressions describe the equivalents history sources of the line ends shown in Figure 2.20:

$$\boxed{b_k(t) = b_{k1}(t) = \left[\frac{R/4}{Z(Z + R/4)}\right] v_{in}(t-\tau) + \left[\frac{(R/4)(Z - R/4)}{Z(Z + R/4)}\right] i_{km1}(t-\tau) \\ + \left[\frac{1}{Z + R/4}\right] v_{out}(t-\tau) + \left[\frac{Z - R/4}{Z + R/4}\right] i_{mk2}(t-\tau)}$$

$$\tag{2.98}$$

$$\boxed{b_m(t) = b_{m2}(t) = \left[\frac{1}{Z + R/4}\right] v_{in}(t-\tau) + \left[\frac{Z - R/4}{Z + R/4}\right] i_{km1}(t-\tau) \\ + \left[\frac{R/4}{Z(Z + R/4)}\right] v_{out}(t-\tau) + \left[\frac{(R/4)(Z - R/4)}{Z(Z + R/4)}\right] i_{mk2}(t-\tau)}$$

$$\tag{2.99}$$

Finally, the equivalent companion model of the lossy line is expressed in a compact form as follows:

$$\boxed{\begin{aligned} i_{km}(t) &= \frac{v_k(t)}{Z_{eqv}} - b_k(t) \\[2em] i_{mk}(t) &= \frac{v_m(t)}{Z_{eqv}} - b_m(t) \end{aligned}}$$

$$\tag{2.100}$$

$$b_k(t) = A \cdot \left[\frac{v_k(t-\tau)}{Z_{eqv}} + h \cdot i_{km}(t-\tau) \right] + B \cdot \left[\frac{v_m(t-\tau)}{Z_{eqv}} + h \cdot i_{mk}(t-\tau) \right]$$

$$b_m(t) = B \cdot \left[\frac{v_k(t-\tau)}{Z_{eqv}} + h \cdot i_{km}(t-\tau) \right] + A \cdot \left[\frac{v_m(t-\tau)}{Z_{eqv}} + h \cdot i_{mk}(t-\tau) \right]$$

$$(2.101)$$

where:

$$Z_{eqv} = Z + \frac{R}{4}; \quad h = \frac{Z - R/4}{Z + R/4}; \quad A = \frac{R}{4Z_{eqv}}; \quad B = \frac{Z}{Z_{eqv}} \qquad (2.102)$$

2.5   Nodal Analysis Formulation

The nodal analysis is a convenient method in the study of electrical networks since it forms the basis for world-leading EMT applications, such as ATP, EMTP-RV, and PSCAD/EMTDC. The nodal analysis supports the study of generic networks consisting of linear components by adding the currents injected and flowing away from each network node according to the Kirchhoff's Current Law (KCL). This approach is simple and flexible because it requires a minimal amount of data regarding the system topology to formulate a set of algebraic equations, which can naturally be written in a matrix form. The solution technique presented here applies to time-invariant linear networks. In the presence of nonlinear elements (such as circuit breakers, transformer saturation, and nonlinear resistance), the linear network matrix and the nonlinear equations will require solution schemes through simultaneous or alternating iterative algorithms [18, 20].

Consider a generic node k of the basic network depicted in Figure 2.22.
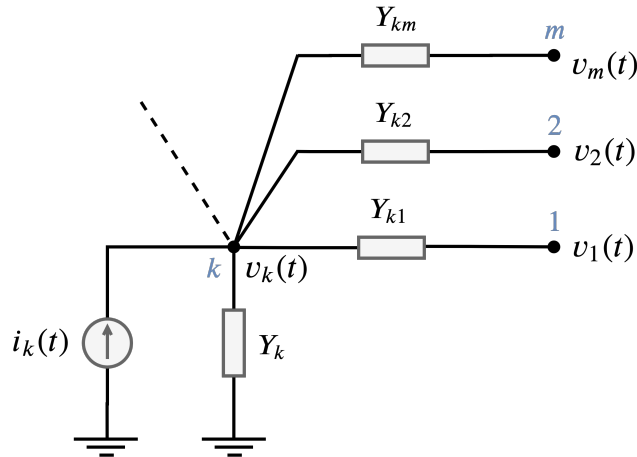
Figure 2.22: Elements connected to node k

where $Y_{km} = G_{km} + jB_{km}$ is the branch admittance.

Applying the first Kirchhoff's law, the net current injected into node k must be equal to the sum of all currents flowing away from node k, resulting in:

$$i_k = (v_k - v_1)\,Y_{k1} + (v_k - v_2)\,Y_{k2} + V_k Y_{kk} + \cdots + (v_k - v_m)\,Y_{km}$$
$$i_k = -v_1 Y_{k1} - v_2 Y_{k2} + \cdots + (Y_{k1} + Y_{k2} + Y_{kk} + \cdots + Y_{km})\,v_k + \cdots - v_m Y_{km}$$

$$(2.103)$$

It should be pointed out that the time argument t is omitted in (2.103) for notation simplicity. This formulation extended to the other nodes leads to the nodal admittance matrix, which relates current and voltage in each node of the network at time t, as follows:

$$\tilde{i}(t) = \mathbf{Y}\tilde{v}(t) \tag{2.104}$$

With:

$\tilde{i}(t)$: column vector of node currents at time t. If node k has no current source connected to it, then $i_k(t) = 0$;

$\tilde{v}(t)$: column vector of node voltages at time t;

$\mathbf{Y}$: nodal admittance matrix.

The following expression illustrates the admittance matrix:

$$
\begin{bmatrix} i_1 \\ \vdots \\ i_k \\ \vdots \\ i_m \end{bmatrix}
=
\begin{bmatrix}
y_{11} & \cdots & y_{1k} & \cdots & y_{1m} \\
\vdots & \ddots & \vdots & \cdots & \vdots \\
y_{k1} & \cdots & y_{kk} & \cdots & y_{km} \\
\vdots & \cdots & \vdots & \ddots & \vdots \\
y_{m1} & \cdots & y_{mk} & \cdots & y_{mm}
\end{bmatrix}
\times
\begin{bmatrix} v_1 \\ \vdots \\ v_k \\ \vdots \\ v_m \end{bmatrix}
\tag{2.105}
$$

where:

$$y_{k1} = y_{1k} = -Y_{k1}$$

$$y_{kk} = Y_{k1} + Y_{k2} + \cdots + Y_{kk}$$

$$y_{km} = y_{mk} = -Y_{km}$$

2.5.1 Nodal Analysis Using Companion Models

The nodal analysis technique will be applied to the system of Figure 2.23, taking into account the companion models developed in the previous subsections. This approach allows the construction of a nodal equation system, where:

1. The conductances of the companion models are considered to build the admittance matrix;

2. The nodal currents vector includes the history sources in addition to the node sources.

This procedure is flexible since the only requirement for the companion models equivalents is that they must be represented as conductances and history sources.
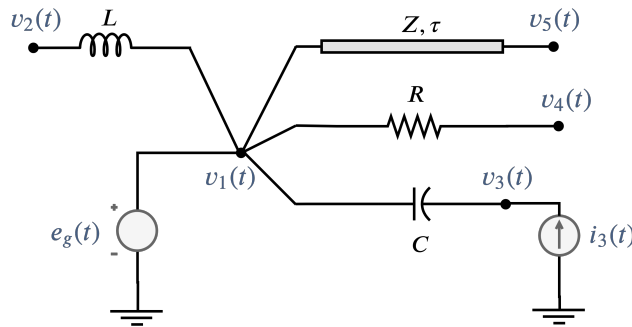
Figure 2.23: Generic electrical network

Substituting the elements R, L, C, and Z by their corresponding companion models yields the following equivalent network:
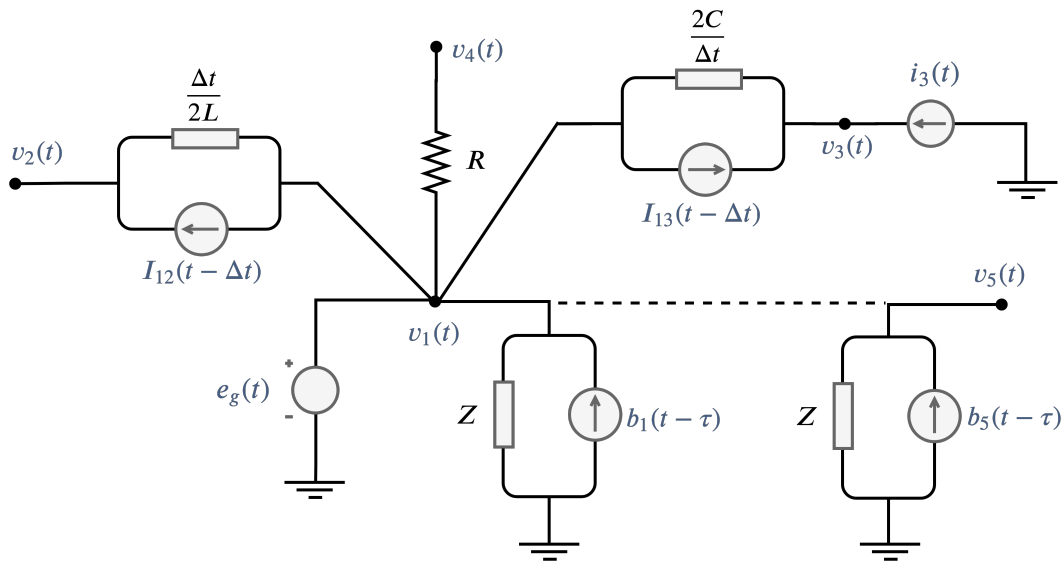
Figure 2.24: Generic network modeled by companion models

42

For the sake of simplicity, the following notation is assumed:

$$I_{km}^h = I_{km}(t - \Delta t)$$

$$b_k^h = b_k(t - \tau)$$

and also omitting the time argument (t), gives:

$$
\begin{bmatrix}
b_1^h - I_{12}^h - I_{13}^h \\
I_{12}^h \\
i_3 + I_{13}^h \\
0 \\
b_5
\end{bmatrix}
=
\begin{bmatrix}
\frac{2C}{\Delta t} + \frac{1}{R} + \frac{\Delta t}{2L} + \frac{1}{Z} & -\frac{\Delta t}{2L} & -\frac{2C}{\Delta t} & -\frac{1}{R} & 0 \\
-\frac{\Delta t}{2L} & \frac{\Delta t}{2L} & 0 & 0 & 0 \\
-\frac{2C}{\Delta t} & 0 & \frac{2C}{\Delta t} & 0 & 0 \\
-\frac{1}{R} & 0 & 0 & \frac{1}{R} & 0 \\
0 & 0 & 0 & 0 & \frac{1}{Z}
\end{bmatrix}
\times
\begin{bmatrix}
v_1 = e_g \\
v_2 \\
v_3 \\
v_4 \\
v_6
\end{bmatrix}
$$

$$(2.106)$$

In a matrix form, the following system of nodal equations is obtained for the solution of generic networks [14, 16]:

$$\tilde{i}(t) + \tilde{I}(t - \Delta t) = \mathbf{Y}\tilde{v}(t) \tag{2.107}$$

or:

$$\tilde{i}'(t) = \mathbf{Y}\tilde{v}(t) \tag{2.108}$$

where:

$\mathbf{Y}$: nodal conductance matrix;

$\tilde{i}(t)$: column vector of currents associated with active sources;

$\tilde{I}(t - \Delta t)$: known column vector of currents associated with the past history of the companion models;

$\tilde{v}(t)$: column vector of node voltages at time t;

$\tilde{i}'(t)$: column vector of total currents including active sources and history terms.

2.5.1.1 Solution Methodology of Electromagnetic Transients

In (2.108) part of the node voltages may be known (specified from voltage sources) and the others unknown. Let the nodes be subdivided into a subset U of nodes with unknown voltages and a subset K of nodes with known voltages [14]. Rearranging

the nodal equations to obtain vectors and matrices accordingly divided, yields the following form:

$$
\begin{bmatrix} \tilde{i}'_K \\ \tilde{i}'_U \end{bmatrix} = \left[\begin{array}{c|c} \mathbf{Y}_{KK} & \mathbf{Y}_{KU} \\ \hline \mathbf{Y}_{UK} & \mathbf{Y}_{UU} \end{array} \right] \cdot \begin{bmatrix} \tilde{v}_K \\ \tilde{v}_U \end{bmatrix}
\tag{2.109}
$$

The system of equations is manipulated to determine the unknown voltages $v_U(t)$:

$$
\tilde{i}'_U = \mathbf{Y}_{UK} \cdot \tilde{v}_K + \mathbf{Y}_{UU} \cdot \tilde{v}_U
\tag{2.110}
$$

$$
\mathbf{Y}_{UU} \cdot \tilde{v}_U = \tilde{i}'_U - \mathbf{Y}_{UK} \cdot \tilde{v}_K
\tag{2.111}
$$

$$
\boxed{\tilde{v}_U = \left[\mathbf{Y}_{UU} \right]^{-1} \cdot \left[\tilde{i}'_U - \mathbf{Y}_{UK} \cdot \tilde{v}_K \right]}
\tag{2.112}
$$

The vector $\tilde{i}'_U$ includes currents injected by generators and history sources dependent on the previous time step, so it is fully determined within each iteration loop. In the same way, the voltage vector $\tilde{v}_K$ is also known. The submatrices $\mathbf{Y}_{UU}$ and $\mathbf{Y}_{UK}$ do not change as long as the network topology and the step size Δt do not change. Therefore, (2.112) allows determining unknown node voltages along the simulation from known quantities.

It is noteworthy that the alternating solution scheme is adopted in this thesis to calculate network voltages and equipment current injections through Norton equivalents and Nodal Analysis. Figure 2.25 illustrates the interface between active sources and the electrical network.
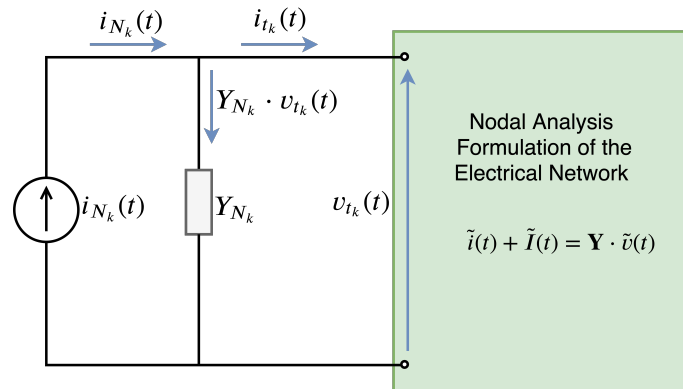
Figure 2.25: Interface between active sources and the electrical network

where:

k is the network interface bus index considered in the nodal analysis formulation;

$v_{t_k}(t)$ is the terminal voltage at bus k;

$i_{N_k}(t)$ is the Norton equivalent current of the active source connected at bus k;

$i_{t_k}(t)$ is the terminal current injected by the active source into the network bus k;

$Y_{N_k}(t)$ is the Norton sensitivity admittance to be added into the network nodal analysis formulation.

The Norton sensitivity admittance and the terminal current injected by the active source must be added into the network nodal analysis formulation. The alternating solution scheme to determine unknown voltages of electrical network and injections of active sources over the time-domain simulation is enumerated below:

1. Initialization of history sources and equipment models regarding the electrical network topology and the steady-state operating point. Start the time-domain simulation with $t = 0$;

2. Build nodal matrix regarding companion models of linear components;

3. Perform ordination and triangular factorization of the admittance matrix using sparsity techniques in order to optimize computation time and storage;

4. Check the electrical network for changes and/or disturbances. If any of these have occurred, return to step 2;

5. Increment the actual time t: $t = t + \Delta t$

6. Reset the iteration counters;

7. Execute the following alternating procedure while $t < t_{max}$; If $t = t_{max}$, the simulation stops successfully.

8. Execute the alternating solution scheme comprising the liner electrical network, active sources, and nonlinear equipment models. Increment the iteration counter: $\mathrm{iter} = \mathrm{iter} + 1$;

9. While solving unknown voltages of the electrical network, currents injected by generators and other active sources remain constant;

10. Likewise, network voltages remain unchanged while solving equipment current injections;

11. Steps 8, 9 and 10 are solved alternatively and iteratively within each time step Δt until interface errors between these solution loops are below a specified

tolerance ϵ. Therefore, return to step 8 while interface erros are above ϵ and iter $<$ iter$_{max}$;

12. If iter $>$ iter$_{max}$ and the convergence was not achieved, the simulation stops before t_{max} without success;

13. Otherwise, if the iterative loops 9 and 10 reach convergence, return to step 4.

2.6 Electromechanical Transient Modeling

In this section, important concepts related to the electromechanical stability modeling traditionally employed in ESA time-domain simulation tools are reviewed. A comprehensive understanding of these concepts is necessary to develop EMT network models suitable to interface general electromechanical modeling within ESA software. Therefore, a brief summary of this modeling and associated studies are provided to form the basis upon which the electrical network and synchronous machine models should be built. A more extensive discussion about the topics presented in the following subsections can be found in several references in the literature [1, 47].

After remarking simplifying assumptions adopted in ESA modeling, the subsequent chapters present detailed EMT models for the network components and the synchronous machine to expand the simulation scope of ESA tools into the range of subsynchronous resonance analysis.

2.6.1 State Space Representation of the Electrical Network

In the study of electromechanical transient phenomena, the EPS dynamic behavior may be studied by using the *state-space* representation, which describes the *system state* through a set of n first order nonlinear ordinary differential equations in the following form:

$$\dot{x}_i = f_i\left(x_1, x_2, \cdots, x_n; u_1, u_2, \cdots, u_r; t\right) \qquad i = 1, 2, \cdots, n \qquad (2.113)$$

where n is the order of the system and r is the number of inputs. The *system state* refer to the operating conditions of the system, and the *state variables* are the minimum set of variables $x_1, x_2, \cdots, x_n$ which completely define the *system state*. The output variables of interest may be expressed in terms of the state variables and the input variables by algebraic equations in the form:

$$y_m = f_i\left(x_1, x_2, \cdots, x_n; u_1, u_2, \cdots, u_r\right) \qquad (2.114)$$

Thus, the following column vectors are defined:

$$\mathbf{x} = \begin{bmatrix} x_1 \\ x_2 \\ \vdots \\ x_n \end{bmatrix}; \quad \mathbf{u} = \begin{bmatrix} u_1 \\ u_2 \\ \vdots \\ u_r \end{bmatrix}; \quad \mathbf{y} = \begin{bmatrix} y_1 \\ y_2 \\ \vdots \\ y_m \end{bmatrix}; \quad \mathbf{f} = \begin{bmatrix} f_1 \\ f_2 \\ \vdots \\ f_n \end{bmatrix} = \begin{bmatrix} \dot{x}_1 \\ \dot{x}_2 \\ \vdots \\ \dot{x}_n \end{bmatrix}; \quad \mathbf{g} = \begin{bmatrix} g_1 \\ g_2 \\ \vdots \\ g_m \end{bmatrix}$$

$$(2.115)$$

where:

    $\mathbf{x}$: column vector formed by n state variables, so-called *state vector*;

    $\mathbf{u}$: column vector formed by r input variables;

    $\mathbf{y}$: column vector formed by m output variables;

    $\mathbf{f}$: column vector formed by n ordinary differential equations, representing the derivatives of the state variables;

    $\mathbf{g}$: column vector formed by m algebraic equations.

If the derivatives of the state variables (denoted by $\dot{x}$) are not explicit functions of time, the system is *autonomous* and the set of state space equations simplifies to:

$$\begin{aligned} \dot{\mathbf{x}} &= \mathbf{f}(\mathbf{x}, \mathbf{u}) \\ \mathbf{y} &= \mathbf{g}(\mathbf{x}, \mathbf{u}) \end{aligned}$$

$$(2.116)$$

where bold letters represent vectors.

Equilibrium point

A curve $x(t)$ encompassing system states in consecutive time instants is referred to as *system trajectory*. The *equilibrium points* $[\mathbf{x_0}]$ are the states where all the derivatives $[\dot{\mathbf{x}}_0]$ are simultaneously zero (no movement). Therefore, the following expression must be satisfied in the equilibrium points:

$$\dot{\mathbf{x}} = \mathbf{f}(\mathbf{x_0}) = 0 \qquad (2.117)$$

with $\mathbf{x}_0$ being the state vector at the equilibrium point. The vector $\mathbf{x_0}$ is also referred to as the *equilibrium set*.

A nonlinear system may have more than one equilibrium point since nonlinear equations may have more than one solution. In the case of linear systems, according to

Cramer theorem [48], there exist only one equilibrium state if the system matrix $\mathbf{A}$ is nonsingular ($\det \mathbf{A} \neq 0$). Where $\mathbf{A}$ is a square matrix of constant coefficients that correlates the state variables and its derivatives in the following form:

$$\dot{\mathbf{x}} = \mathbf{A} \cdot \mathbf{x} \tag{2.118}$$

Electrical Power System Equations

The power system modeling by using the state space realization yields into two sets of nonlinear equations in the form of (2.116). Figure 2.26 depicts the general structure of the power system model considered in electromechanical stability studies.
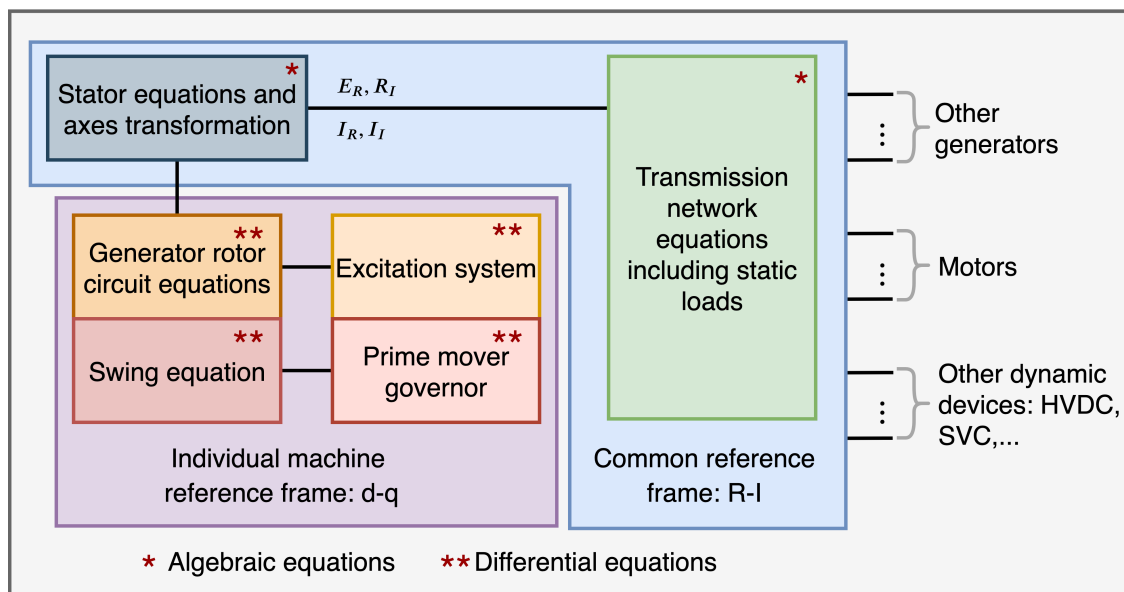
Figure 2.26: Structure of the EPS model for ESA applications

The first set of functions $\mathbf{f}(\mathbf{x}, \mathbf{u})$ includes differential equations describing the dynamic behavior of synchronous machines and their associate controls, as well as other dynamic devices (such as motors, HVDC, FACTS, etc.). The functions $\mathbf{g}(\mathbf{x}, \mathbf{u})$ encompasses algebraic equations describing the steady-state behavior of the network, including static load models, and the algebraic equations of dynamic equipment (for instance, the stator algebraic equations).

The discrete computation of $\mathbf{x}$ and $\mathbf{y}$ produce a sequence of snapshots at intervals Δt. Interpolation assumptions are usually made on $\mathbf{x}$ to define the state between the discrete points. The discretization of differential equations by an implicit integration method provides a set of algebraic difference equations. This set, along with the algebraic equations, must be resolved step-by-step through a simultaneous or alternating scheme, using the same procedure stated in Section 2.5 for EMT

solution.

In ANATEM program, the set of algebraic difference equations (discretized by the implicit trapezoidal rule) and the algebraic equations are resolved in time-domain by the alternating solution scheme.

Therefore, the general system of equations consists of: (i) a set of differential equations of all dynamic equipment combined with (ii) all algebraic equations of the network and other equipment. These two sets of equations are expressed as the following:

1. A set of first-order ordinary differential equations describing the dynamic behavior of the power system components:

$$\dot{\mathbf{x}} = \mathbf{f}\left(\mathbf{x}, \mathbf{u}\right) \;\; \Rightarrow \;\; \dot{\mathbf{x}} = \mathbf{f}\left(\mathbf{x}, \mathbf{V}\right) \tag{2.119}$$

2. A set of algebraic equations representing the quasi-steady state behavior of the electrical network:

$$\mathbf{I} = \mathbf{g}\left(\mathbf{x}, \mathbf{u}\right) \;\; \Rightarrow \;\; \mathbf{Y} \cdot \mathbf{V} = \mathbf{I}(\mathbf{x}, \mathbf{V}) \tag{2.120}$$

where:

$\mathbf{x}$ = column vector of system state variables;
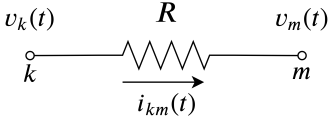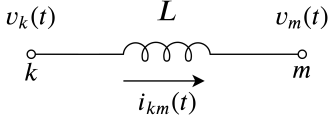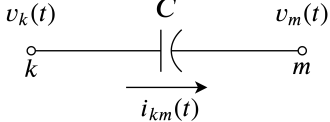
$\mathbf{I}$ = column vector of currents associated with active sources;

$\mathbf{V}$ = column vector of node voltages;

$\mathbf{Y}$ = nodal admittance matrix at the fundamental frequency.

The formation rule for the admittance matrix is the same presented in Section 2.5. However, it differs from the EMT modeling since the network dynamics are neglected. The nodal admittance matrix is formed from the system parameters and topology assuming reactances at fundamental frequency ($\omega = \omega_s$) following the structure presented in Table 2.1.

Table 2.1: Impedances and Admitances of Basic Linear Components

Linear Component	v_{km} X i_{km}	Impedance	Admittance
$v_k(t)$ R $v_m(t)$ k ~~~~~ m $i_{km}(t)$	$v_{km} = R \cdot i_{km}$	$Z_{km} = R$	$Y_{km} = \dfrac{1}{R}$
$v_k(t)$ L $v_m(t)$ k ~~~~~ m $i_{km}(t)$	$v_{km} = jX_L \cdot i_{km}$	$Z_{km} = j\omega L$	$Y_{km} = -\dfrac{j}{\omega L}$
$v_k(t)$ C $v_m(t)$ k ——|(—— m $i_{km}(t)$	$v_{km} = jX_C \cdot i_{km}$	$Z_{km} = -\dfrac{j}{\omega C}$	$Y_{km} = j\omega C$

2.6.2   Introduction to Power System Stability

This subsection provides a brief review of power system stability, according to the definitions conferred in a CIGRE/IEEE joint task force [39]. The evaluation of power system transients after being subjected to a disturbance forms the basis for a wide range of stability studies. In general, stability is a condition of equilibrium between opposing forces. Depending on the network topology, initial operating condition, and the disturbance nature, different sets of opposing forces may occur in the power system leading to varying types of sustained imbalance and instability. A formal definition of this problem extracted from [39] is:

> ***Power system stability*** *is the ability of an electric power system, for a given initial operating condition, to regain a state of operating equilibrium after being subjected to a physical disturbance, with most system variables bounded so that practically the entire system remains intact.*

This formal definition refers to the bulk power system as a whole. However, it might also be of interest to assess whether individual generators or dynamic devices are stable. For instance, an individual generator can lose stability (synchronism) without collapsing the whole system. In the EPS stability assessment, it is typically considered that the system is initially in a steady-state operating condition. Then, a stable condition after a disturbance is assumed if the power system reaches a new equilibrium state with the system integrity preserved, i.e., with almost all devices

connected to it. In other words, a stable condition admits some equipment disconnection in order to isolate or clear faulted elements for preserving the continuity of the bulk system operation.

As a dynamic system, the EPS is constantly varying due to daily fluctuations in load demand, control device switching, and eventual disturbance occurrence. The states of a dynamic system, apart from the equilibrium points, present the derivatives $\dot{\mathbf{x}} \neq \mathbf{0}$. *Disturbance* means a random (intentional or unintentional) event affecting the system. Disturbances affecting the power system may be modeled as changes in nodal admittance matrix elements, or by shifts in the inputs. Power systems are subjected to a wide range of disturbances classified as small or large:

Small disturbances occur continually in the form of small variations in loads, parameters, or inputs. The system must be able to support these daily fluctuations successfully. A disturbance is considered to be *small* if the linearization of the system of nonlinear equations brings a meaningful response, which remains valid for the purpose of analysis nearby the operating point.

Large disturbances include severe faults, such as short-circuit in the transmission system, loss of generation, and structural changes in the network topology. This type of disturbance exhibits significant nonlinear response. Consequently, it requires the use of nonlinear models for effective analysis. After the occurrence of this type of event, the system must also be able to regain a new equilibrium point or return to the original operating condition.

In the sense of Lyapunov [49], the stability of a dynamic system is defined by investigating the state variables trajectory around the equilibrium point after a disturbance. Power system stability, from a particular equilibrium point $\mathbf{x_0}$, may be stable for a given large disturbance, and unstable for another. For this reason, it is complex and costly to design power systems to be stable for every set of disturbances at overall possible initial conditions. Then, contingencies are selected based on the system planning guidelines, e.g., probability of occurrence or N-1 criterion. Therefore, large disturbance stability always refers to a specified set of disturbances and initial operating conditions.

In the case of linear systems, stability does not depend on the size of a disturbance. Hence if a linear system is stable for a small disturbance, it should also be globally stable for any large disturbance. On the contrary, nonlinear system stability depends on the size of a disturbance, since it may be stable for a small disturbance but unstable for a large one.

In control system theory, it is common practice to classify the stability of a nonlinear

system into the following categories, depending on the region of state space on which the state vector ranges [1]:

- *Local stability or stability in the small:* the system is said to be locally stable about an equilibrium point if, when subjected to small variations, it remains within a small region surrounding the equilibrium point. Local stability can be studied by using linear analysis.

- *Finite stability:* If the state of a system remains within a finite region ϵ, it is said to be stable within ϵ. Furthermore, if it returns to the original equilibrium point from any point within ϵ, it is said to be *asymptotically stable* within the finite region ϵ.

- *Global stability or stability in the large:* The system is said to be globally stable if ϵ includes the entire finite space.

The EPS is a high order multivariable nonlinear system which operates in a changing environment, making it difficult to identify all individual factors that contribute to instability and its different forms. The following aspects outline the key factors employed in the classification of stability into its appropriate divisions:

- The physical nature of the resulting instability;

- The initial operating condition and electrical network topology;

- The magnitude of the disturbance considered;

- The equipment models and timescale considered to investigate a given type of stability;

- The most appropriate solution method and tool for stability prediction.

Regarding the power system complexity and the features above-mentioned, simplifying assumptions are made to analyze specific types of instabilities that may occur in different timeframes. Figure 2.27 depicts the categories and subdivisions defined to analyze the stability problem.

As power systems stability depends on both the initial conditions and the size of a disturbance, consequently, angle and voltage stability can be divided into: *small-disturbance* stability and *large-disturbance* stability.

Power system stability is mainly associated with the electromechanical phenomena. However, it is also affected by fast electromagnetic phenomena and slow thermodynamic phenomena. Consequently, depending on the type of phenomena, one can refer to the stability problem as: *short-term* stability and *long-term* stability.
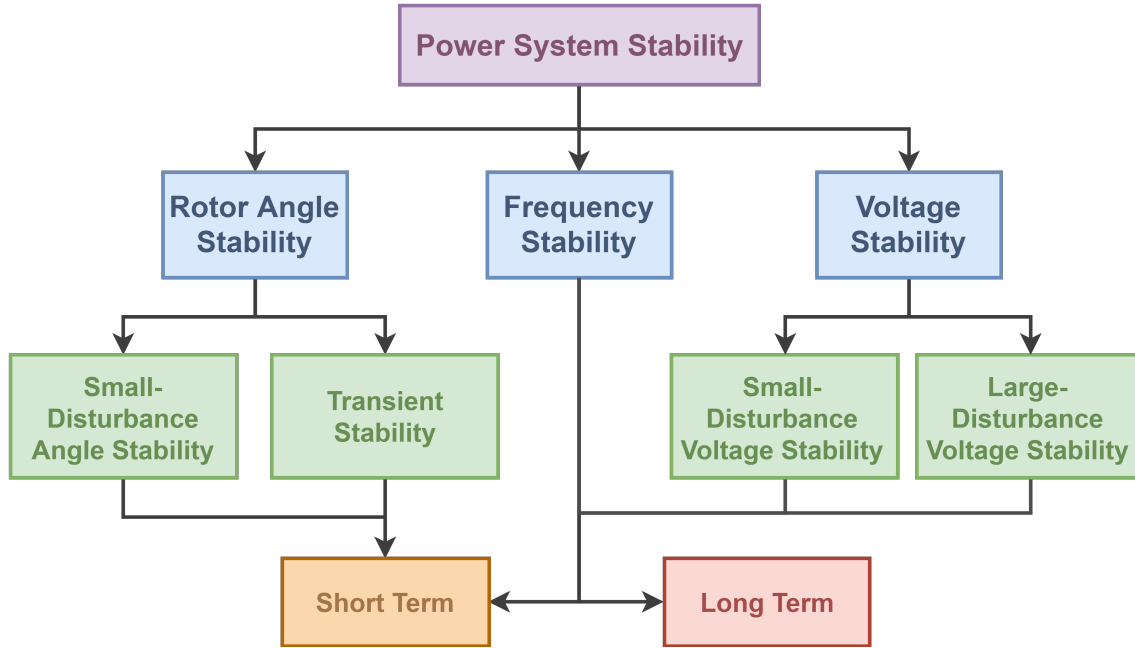
Figure 2.27: Classification of power system stability adapted from [1]

Three essential quantities for power system operation are evaluated in this context: (i) displacement angles of nodal voltages δ, also called power or load angles; (ii) electrical frequency f; and (iii) nodal voltage magnitudes V. Hence, according to the formal definitions extracted from [39], power system stability can be divided into:

*(i) **Rotor angle stability** refers to the ability of synchronous machines of an interconnected power system to remain in synchronism after being subjected to a disturbance. It depends on the ability to maintain and restore equilibrium between electromagnetic torque and mechanical torque of each synchronous machine in the system.*

*(ii) **Voltage stability** refers to the ability of a power system to accommodate steady voltages at all buses in the system after being subjected to a disturbance. It depends on the ability to restore and sustain the equilibrium between load demand and energy production.*

*(iii) **Frequency stability** refers to the ability of a power system to maintain steady frequency after being subjected to a severe system upset, resulting in a significant imbalance between generation and load demand. It depends on the ability to maintain and restore equilibrium between system generation and load, with minimum unintentional loss of load.*

Chapter 3

Electrical Network Modeling

In this chapter, the electrical network modeling suitable for time-domain simulation of electromechanical and electromagnetic transients is developed by using tensor modeling and the dynamic phasor technique, regarding the electrical network state-variables as fundamental dynamic phasors. First, the traditional ESA modeling is characterized through the quasi steady-state approximation, which neglects network dynamics and carries out the traditional fundamental phasor modeling.

Afterward, mathematical models suitable for EMT dynamic analysis are presented by representing voltages and currents of the basic network components as fundamental dynamic phasors. Subsequently, the ordinary differential equations describing linear device dynamics are discretized by means of the trapezoidal integration rule resulting in *Dynamic Phasor Companion Models* in a tensor form.

In the scope of this thesis, a positive-sequence network representation is employed under the premise of a three-phase balanced system. In this scenario, the EMT dynamic phasor modeling allows accurate simulation of fast transients induced in the network as a result of balanced faults. However, a detailed EMT analysis of unbalanced networks or fast transients following unbalanced faults can also be addressed by applying a three-phase dynamic phasor representation, either using positive, negative, and zero sequence components or *abc* phase components, as proposed in [50].

3.1   General Dynamic Phasor Modeling

In the mathematical developments of ESA and EMT simulation models approaching dynamic phasors, the following common procedure is performed for each linear device of the network:

1. Consider a generic network branch composed by a linear device between nodes

k and m:
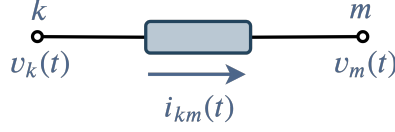
Figure 3.1: Linear branch

2. The nodal voltages $v_k(t)$ and $v_m(t)$, and the current $i_{km}(t)$ are treated in Section 2.4 as instantaneous values. Now these quantities must be replaced by fundamental dynamic phasors, as illustrated in Figure 3.2. For the sake of simplicity, the subscript "1" used in Section 2.1 to denote fundamental DP is omitted; instead, the subscripts of voltages and currents specify the bus index considered in the network nodal analysis formulation.
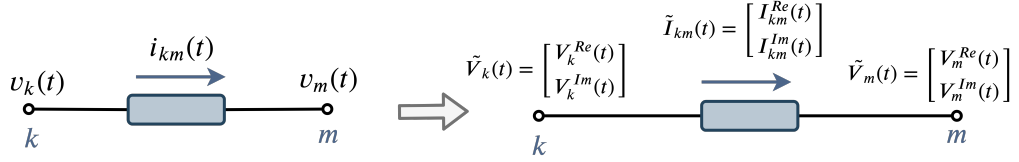
Figure 3.2: Representation of voltages and currents through DP

where:

$\tilde{V}_{km}(t) = V_{km}^{Re}(t) + jV_{km}^{Im}(t) =$ complex DP of voltage $v_{km}(t)$;

$\tilde{I}_{km}(t) = I_{km}^{Re}(t) + jI_{km}^{Im}(t) =$ complex DP of current $i_{km}(t)$;

$V_{km}^{Re}(t), V_{km}^{Im}(t) =$ real and imaginary DP components of voltage $v_{km}(t)$;

$I_{km}^{Re}(t), I_{km}^{Im}(t) =$ real and imaginary DP components of current $i_{km}(t)$.

3. The instantaneous values of the state-variables can be reconstituted from the DP, as follows:

$$v_{km}(t) = V_{km}^{Re}(t)\cos(\omega t) - V_{km}^{Im}(t)\sin(\omega t) \tag{3.1}$$

$$i_{km}(t) = I_{km}^{Re}(t)\cos(\omega t) - I_{km}^{Im}(t)\sin(\omega t) \tag{3.2}$$

4. The ordinary differential equations describing the transient behavior of dynamic components are treated in a tensor form, according to the modeling depicted in Section 2.2.

5. At this stage, the network transients are neglected in the ESA modeling and maintained in the EMT analysis. Because of this, the trapezoidal integration

rule is employed in the EMT modeling to describe the dynamic relationship between voltages and currents throughout equivalent discrete-time simulation models.

6. Therefore, whether ESA or EMT, the dynamic phasor modeling allows the construction of modular equivalent circuits for dynamic simulation of general networks. The basic structure of these equivalent circuits accounts for a 2x2 admittance matrix called **_tensor_**, which relates real and imaginary components of voltage and currents within each network branch. The EMT equivalent model also includes a *"past term"* representing a **_history current source_** that describes the linear device dynamic behavior .

7. After building dynamic simulation models for the basic components, their interface with other equipment is constructed upon the nodal analysis formulation consistent with (2.108). In this sense, a solution scheme to determine the unknown nodal voltages along the dynamic simulation is also discussed in this chapter.

From (3.1) and (3.2), one should note that the DP are functions of time, transformed from the nonlinear time-varying network equations into an autonomous nonlinear system. Therefore, the DP approach yields simulation models that are able to carry out fast transient information, likewise the instantaneous time-domain modeling. Naturally, both approaches demand the adoption of an adequate step size Δt to ensure the observation of electromagnetic transient phenomena within the desired frequency bandwidth.

3.2 ESA Network Modeling using Dynamic Phasors

Simulation models of electrical network components suitable for the analysis of electromechanical oscillations typically neglect fast electromagnetic transients. Therefore, the network transient behavior within each time step is approximated to the steady-state final value solution, i.e., the derivative terms are supposed to be zero, which is referred to as the *quasi-steady state approximation.*

For illustrative purposes, the quasi-steady state approximation is characterized in terms of the series RLC circuit presented in Figure 3.3.
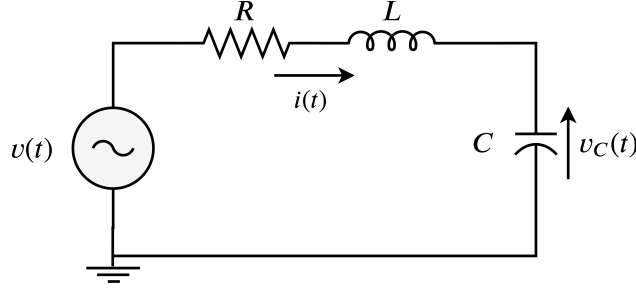
Figure 3.3: RLC circuit

The dynamic behavior of this circuit is described by the following differential equations:

$$v(t) = Ri(t) + L\frac{di(t)}{dt} + v_c(t) \tag{3.3}$$

$$i(t) = C\frac{dv_c(t)}{dt} \tag{3.4}$$

The voltage and current of this RLC circuit are expressed by fundamental dynamic phasors, as follows:

$$v(t) = V^{Re}(t)\cos(\omega t) - V^{Im}(t)\sin(\omega t) \tag{3.5}$$

$$i(t) = I^{Re}(t)\cos(\omega t) - I^{Im}(t)\sin(\omega t) \tag{3.6}$$

$$v_c(t) = V_c^{Re}(t)\cos(\omega t) - V_c^{Im}(t)\sin(\omega t) \tag{3.7}$$

Omitting the time argument (t) for the sake of simplicity, and substituting (3.5), (3.6), and (3.7) above into (3.3) and (3.4) yields:

$$
\begin{aligned}
V^{Re}\cos(\omega t) - V^{Im}\sin(\omega t) = & RI^{Re}\cos(\omega t) - RI^{Im}\sin(\omega t) \\
& + L\frac{d}{dt}\left[I^{Re}\cos(\omega t) - I^{Im}\sin(\omega t)\right] \\
& + V_c^{Re}\cos(\omega t) - V_c^{Im}\sin(\omega t)
\end{aligned}
\tag{3.8}
$$

$$I^{Re}\cos(\omega t) - I^{Im}\sin(\omega t) = C\frac{d}{dt}\left[V_c^{Re}\cos(\omega t) - V_c^{Im}\sin(\omega t)\right] \tag{3.9}$$

Employing the chain-rule differentiation, gives:

$$V^{Re}\cos(\omega t) - V^{Im}\sin(\omega t) = RI^{Re}\cos(\omega t) - RI^{Im}\sin(\omega t) + V_c^{Re}\cos(\omega t) - V_c^{Im}\sin(\omega t) +$$

$$L\frac{dI^{Re}}{dt}\cos(\omega t) - \omega LI^{Re}\sin(\omega t) - L\frac{dI^{Im}}{dt}\sin(\omega t) - \omega LI^{Im}\cos(\omega t) \tag{3.10}$$

$$I^{Re}\cos(\omega t) - I^{Im}\sin(\omega t) = C\frac{dV_c^{Re}}{dt}\cos(\omega t) - \omega CV_c^{Re}\sin(\omega t)$$

$$-C\frac{dV_c^{Im}}{dt}\sin(\omega t) - \omega CV_c^{Im}\cos(\omega t) \tag{3.11}$$

Identifying and grouping the terms related to $\sin(\omega t)$ and $\cos(\omega t)$ in (3.10) and (3.11), results in:

$$\begin{cases} V^{Re} &= RI^{Re} + V_c^{Re} + L\dfrac{dI^{Re}}{dt} - \omega LI^{Im} \\[2mm] V^{Im} &= RI^{Im} + V_c^{Im} + \omega LI^{Re} + L\dfrac{dI^{Im}}{dt} \end{cases} \tag{3.12}$$

$$\begin{cases} V_c^{Re} &= -\dfrac{1}{\omega}\dfrac{dV_c^{Im}}{dt} + \dfrac{1}{\omega C}I^{Im} \\[2mm] V_c^{Im} &= \dfrac{1}{\omega}\dfrac{dV_c^{Re}}{dt} - \dfrac{1}{\omega C}I^{Re} \end{cases} \tag{3.13}$$

Substituting (3.13) into (3.12) yields:

$$V^{Re} = RI^{Re} + L\frac{dI^{Re}}{dt} - \omega LI^{Im} - \frac{1}{\omega}\frac{dV_c^{Im}}{dt} + \frac{1}{\omega C}I^{Im} \tag{3.14}$$

$$V^{Im} = RI^{Im} + \omega LI^{Re} + L\frac{dI^{Im}}{dt} + \frac{1}{\omega}\frac{dV_c^{Re}}{dt} - \frac{1}{\omega C}I^{Re} \tag{3.15}$$

Neglecting the network dynamics, (3.14) and (3.15) give rise to the DP modeling of the RLC branch suitable for ESA analysis. Thus, it can be written in a matrix form, as follows:

$$\begin{bmatrix} V^{Re} \\ V^{Im} \end{bmatrix} = \begin{bmatrix} R & -\omega L + \dfrac{1}{\omega C} \\[3mm] \omega L - \dfrac{1}{\omega C} & R \end{bmatrix} \cdot \begin{bmatrix} I^{Re} \\ I^{Im} \end{bmatrix} \longrightarrow \tilde{V} = \mathbf{Z}(\omega)\tilde{I} \tag{3.16}$$

And the circuit current is calculated by:

$$\begin{bmatrix} I^{Re} \\ I^{Im} \end{bmatrix} = \frac{1}{R^2 + \left(\omega L + \dfrac{1}{\omega C}\right)^2} \begin{bmatrix} R & \omega L - \dfrac{1}{\omega C} \\[3mm] -\omega L + \dfrac{1}{\omega C} & R \end{bmatrix} \cdot \begin{bmatrix} V^{Re} \\ V^{Im} \end{bmatrix} \longrightarrow \tilde{I} = \mathbf{Y}(\omega)\tilde{V} \tag{3.17}$$

If this series RLC circuit is seen as a network branch, the equivalent admittance matrix (or tensor) $\mathbf{Y}(\omega)$ should be employed in the nodal analysis formulation to build the nodal admittance matrix in a tensor form. Alternatively, considering each linear device of the circuit depicted in Figure 3.3 as an individual branch, the nodes 1, 2, and 3 can be defined according to Figure 3.4.
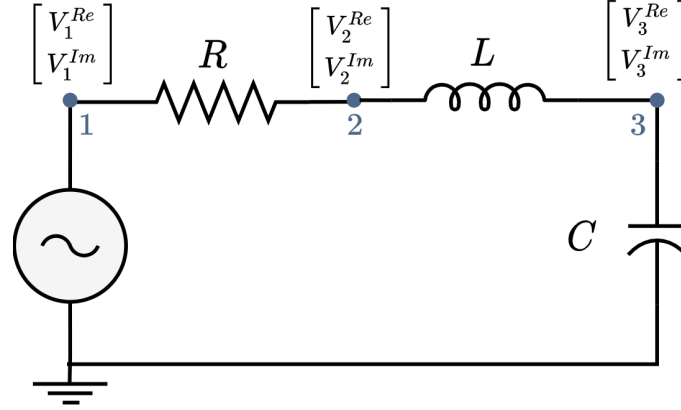
Figure 3.4: RLC circuit nodes

In this case, each linear component shall constitute an equivalent tensor with the symmetry property depicted in (2.19). This symmetry allows representing the admittance and the relationship between voltage and current through the complex numbers defined in (2.21) and repeated below:

$$I_{km}^{Re} + jI_{km}^{Im} = (G_{km} + jB_{km}) \cdot \left(V_{km}^{Re} + jV_{km}^{Im}\right) \Rightarrow \underbrace{\tilde{I}_{km} = \mathbf{Y}_{km}(\omega) \cdot \tilde{V}_{km}}_{\substack{\text{Tensor} \\ \text{modeling}}} \qquad (3.18)$$

From (3.18), one should note that using the tensor modeling, the complex admittance $Y_{km} = G_{km} + jB_{km}$ may be written as a tensor $\mathbf{Y}_{km}$, which allows building an equivalent circuit for each linear branch in the format illustrated in Figure 3.5:
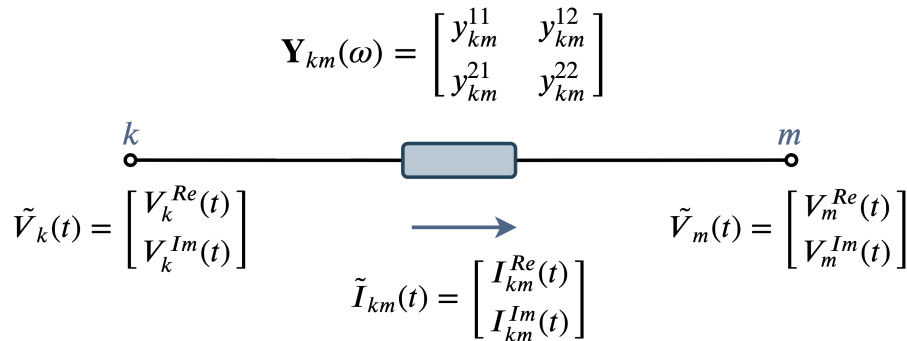
Figure 3.5: ESA equivalent model of a linear branch

where the elements of $\mathbf{Y}_{km}$ are given by:

$$\mathbf{Y}_{km}(\omega) = \begin{bmatrix} G_{km} & B_{km} \\ -B_{km} & G_{km} \end{bmatrix} \tag{3.19}$$

Employing the tensor nodal analysis for the RLC circuit of Figure 3.4, the following system of equations is obtained:

$$\begin{bmatrix} I_1^{Re} \\ I_1^{Im} \\ I_2^{Re} \\ I_2^{Im} \\ I_3^{Re} \\ I_3^{Im} \end{bmatrix} = \begin{bmatrix} y_{11}^{11} & y_{11}^{12} & y_{12}^{11} & y_{12}^{12} & y_{13}^{11} & y_{13}^{12} \\ y_{11}^{21} & y_{11}^{22} & y_{12}^{21} & y_{12}^{22} & y_{13}^{21} & y_{13}^{22} \\ y_{21}^{11} & y_{21}^{12} & y_{22}^{11} & y_{22}^{12} & y_{23}^{11} & y_{23}^{12} \\ y_{21}^{21} & y_{21}^{22} & y_{22}^{21} & y_{22}^{22} & y_{22}^{21} & y_{22}^{22} \\ y_{31}^{11} & y_{31}^{12} & y_{32}^{11} & y_{32}^{12} & y_{33}^{11} & y_{33}^{12} \\ y_{31}^{21} & y_{31}^{22} & y_{32}^{21} & y_{32}^{22} & y_{33}^{11} & y_{33}^{12} \end{bmatrix} \cdot \begin{bmatrix} V_1^{Re} \\ V_1^{Im} \\ V_2^{Re} \\ V_2^{Im} \\ V_3^{Re} \\ V_3^{Im} \end{bmatrix} \tag{3.20}$$

or

$$\tilde{I}(t) = \mathbf{Y}(\omega) \cdot \tilde{V}(t) \tag{3.21}$$

where each 2x2 block of the tensor admittance matrix $\mathbf{Y}(\omega)$ is built in consonance with to the following formation rule:

$$\begin{bmatrix} y_{kk}^{11} & y_{kk}^{12} \\ y_{kk}^{21} & y_{kk}^{22} \end{bmatrix} = \sum_m \mathbf{Y}_{km} \qquad \qquad \begin{bmatrix} y_{km}^{11} & y_{km}^{12} \\ y_{km}^{21} & y_{km}^{22} \end{bmatrix} = -\mathbf{Y}_{km} \tag{3.22}$$

From (3.20), one should note that the vector of nodal currents $\tilde{I}(t)$ does not account for any history source since the network dynamics are neglected. Therefore, the ESA modeling does not depend on past information of electrical network devices, which are treated as static components.

The interface between the active source at bus "1" and the electrical network may be carried out through the equivalent Norton circuit depicted in Figure 2.25. A proper interface between synchronous generators and the electrical network is also detailed in Section 4.6.3 since the interaction between these models comprehends the main scope of this thesis.

3.3 Dynamic Phasor Companion Model for EMT Analysis

The mathematical formulation of Dynamic Phasor Companion Models (DPCM) is developed in this section to analyze fast transients of the electrical network components based on the methodology introduced in [12]. This modeling employs fundamental dynamic phasors to describe state-variables of the electrical network, following the general procedure depicted in Section 3.1, which is suitable for time-domain simulation of electromagnetic transients in linear electrical networks.

In this thesis, the mathematical development of DPCM include: resistance, inductance, capacitance, transformer, short transmission line (lumped parameters), and long transmission line (Bergeron model). By developing the equivalent DPCM circuit, a structure similar to that acquired in the ESA modeling is obtained (Figure 3.5). In addition to the ESA equivalent circuit, the DPCM branch also comprises a *history current source* in parallel with the 2x2 admittance matrix $\mathbf{Y}_{km}$.

Regarding a dynamic linear component with **lumped parameters**, the DPCM equivalent circuit may be expressed through the general structure presented in Figure 3.6.
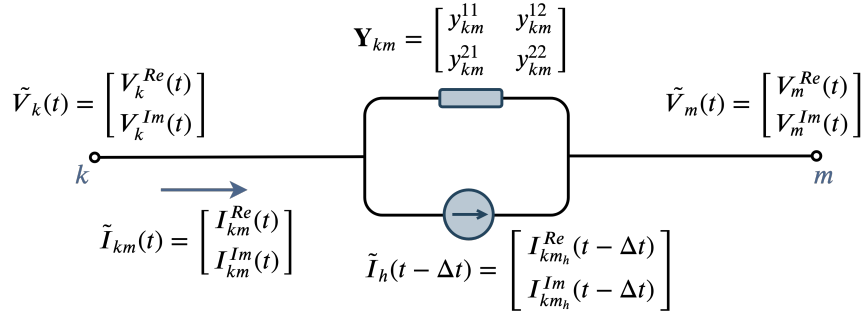
Figure 3.6: Equivalent DPCM structure of a linear network branch

From which the mathematical model (3.23) is written in terms of complex DP.

$$\tilde{I}_{km}(t) = \tilde{I}_{km_h}(t - \Delta t) + \mathbf{Y}_{km} \cdot \tilde{V}_{km}(t) \tag{3.23}$$

In terms of real and imaginary components of DP yields:

$$\begin{bmatrix} I_{km}^{Re}(t) \\ I_{km}^{Im}(t) \end{bmatrix} = \begin{bmatrix} I_h^{Re}(t - \Delta t) \\ I_h^{Im}(t - \Delta t) \end{bmatrix} + \begin{bmatrix} y_{km}^{11} & y_{km}^{12} \\ y_{km}^{21} & y_{km}^{22} \end{bmatrix} \cdot \begin{bmatrix} V_{km}^{Re}(t) \\ V_{km}^{Im}(t) \end{bmatrix} \tag{3.24}$$

where the history current source $\tilde{I}_h(t - \Delta t)$ depends on variables that are known from the previous time-domain solutions (past or historical terms) enabling the representation of the network dynamics. The elements of the tensor $\mathbf{Y}_{km}$ are built from the simulation and circuit parameters and are detailed in the following subsections.

The equivalent DPCM are given in terms of real and imaginary DP using the tensor modeling of (3.24). This selection allows a direct interface with other equipment models, such as the synchronous machine modeling (described in Chapter 4).

3.3.1 Resistance

Consider a resistance R between generic nodes k and m, described in terms of instantaneous voltages and current values in (3.25).
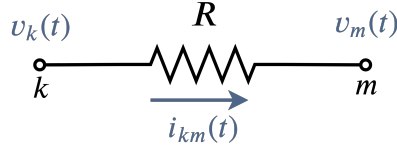
Figure 3.7: Resistance

$$v_{km}(t) = R \cdot i_{km}(t) \tag{3.25}$$

Expressing the voltage $v_{km}(t)$ and the current $i_{km}(t)$ as a function of the DP defined in (3.1) and (3.2) yields:

$$V_{km}^{Re}(t)\cos(\omega t) - V_{km}^{Im}(t)\sin(\omega t) = R\left[I_{km}^{Re}(t)\cos(\omega t) - I_{km}^{Im}(t)\sin(\omega t)\right] \tag{3.26}$$

Identifying and grouping the terms associated with the trigonometric functions $\sin(\omega t)$ and $\cos(\omega t)$ yields:

$$V_{km}^{Re}(t) = R \cdot I_{km}^{Re}(t) \tag{3.27}$$
$$V_{km}^{Im}(t) = R \cdot I_{km}^{Im}(t) \tag{3.28}$$

Equation (3.29) presents the DPCM of a resistance branch in a tensor form:

$$\begin{bmatrix} I_{km}^{Re}(t) \\ I_{km}^{Im}(t) \end{bmatrix} = \begin{bmatrix} \dfrac{1}{R} & 0 \\ 0 & \dfrac{1}{R} \end{bmatrix} \cdot \begin{bmatrix} V_{km}^{Re}(t) \\ V_{km}^{Im}(t) \end{bmatrix} \tag{3.29}$$

Alternatively, (3.29) may be rewritten, as follows:

$$\tilde{I}_{km}(t) = \mathbf{Y}^R \cdot \tilde{V}_{km}(t) \tag{3.30}$$

From (3.29), one should note that the transient behavior of a resistance branch does not depend on past quantities, neither presents a cross-coupling between real and imaginary DP components of voltage and current at the present time (t).

3.3.2 Inductance

Consider the ODE (3.31) describing the dynamic behavior of an inductance L between generic nodes k and m:
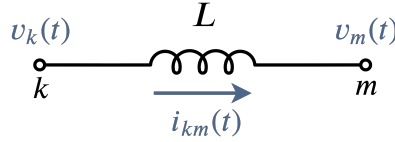
Figure 3.8: Inductance

$$v_k(t) - v_m(t) = L\frac{di_{km}(t)}{dt} \tag{3.31}$$

Substituting the voltage $v_{km}(t)$ (3.1) and the current $i_{km}(t)$ (3.2) into (3.31), gives:

$$V_{km}^{Re}(t)\cos(\omega t) - V_{km}^{Im}(t)\sin(\omega t) = L\frac{d}{dt}\left(I_{km}^{Re}(t)\cos(\omega t) - I_{km}^{Im}(t)\sin(\omega t)\right) \tag{3.32}$$

Employing the chain-rule differentiation into (3.32) yields:

$$V_{km}^{Re}(t)\cos(\omega t) - V_{km}^{Im}(t)\sin(\omega t) = L\left(\frac{dI_{km}^{Re}(t)}{dt}\cos(\omega t) - I_{km}^{Re}(t)\omega \cdot \sin(\omega t)\right) \tag{3.33}$$
$$-L\left(\frac{dI_{km}^{Im}(t)}{dt}\sin(\omega t) + I_{km}^{Im}(t)\omega \cdot \cos(\omega t)\right)$$

Identifying and grouping the terms associated with the trigonometric functions $\sin(\omega t)$ and $\cos(\omega t)$, results in:

$$\begin{cases} V_{km}^{Re}(t) = L\dfrac{dI_{km}^{Re}(t)}{dt} - \omega L \cdot I_{km}^{Im}(t) \\[3mm] V_{km}^{Im}(t) = L\dfrac{dI_{km}^{Im}(t)}{dt} + \omega L \cdot I_{km}^{Re}(t) \end{cases} \tag{3.34}$$

In order to obtain the inductance discrete DPCM model, the trapezoidal integration rule must be applied into (3.34), which allows to explicit the real and imaginary

63

coefficients of the current $\tilde{I}_{km}(t)$, resulting in:

$$I_{km}^{Re}(t) = I_{km}^{Re}(t - \Delta t) + \frac{\Delta t}{2L} \cdot \left[V_{km}^{Re}(t - \Delta t) + V_{km}^{Re}(t) + \omega L I_{km}^{Im}(t - \Delta t) + \omega L I_{km}^{Im}(t) \right] \quad (3.35)$$

$$I_{km}^{Im}(t) = I_{km}^{Im}(t - \Delta t) + \frac{\Delta t}{2L} \cdot \left[V_{km}^{Im}(t - \Delta t) + V_{km}^{Im}(t) - \omega L I_{km}^{Re}(t - \Delta t) - \omega L I_{km}^{Re}(t) \right] \quad (3.36)$$

Rearranging (3.35) and (3.36) by grouping the previous time step $(t - \Delta t)$ dependent terms, the tensor current $\tilde{I}_{km}(t)$ may be rewritten, as follows:

$$I_{km}^{Re}(t) = C_h^{Re}(t - \Delta t) + \frac{\Delta t}{2L} \cdot \left[V_{km}^{Re}(t) + \omega L I_{km}^{Im}(t) \right] \quad (3.37)$$

$$I_{km}^{Im}(t) = C_h^{Im}(t - \Delta t) + \frac{\Delta t}{2L} \cdot \left[V_{km}^{Im}(t) - \omega L I_{km}^{Re}(t) \right] \quad (3.38)$$

where the real and imaginary historical terms $\tilde{C}_h(t - \Delta t)$ are given by:

$$C_h^{Re}(t - \Delta t) = I_{km}^{Re}(t - \Delta t) + \frac{\Delta t}{2L} \cdot \left[V_{km}^{Re}(t - \Delta t) + \omega L I_{km}^{Im}(t - \Delta t) \right] \quad (3.39)$$

$$C_h^{Im}(t - \Delta t) = I_{km}^{Im}(t - \Delta t) + \frac{\Delta t}{2L} \cdot \left[V_{km}^{Im}(t - \Delta t) - \omega L I_{km}^{Re}(t - \Delta t) \right] \quad (3.40)$$

From (3.37) and (3.38), one should note that real and imaginary components of current $\tilde{I}_{km}(t)$ present a time cross-coupling. Consequently, these equations are not consistent with the general DPCM structure presented in Figure 3.6, where $I_{km}^{Re}(t)$ and $I_{km}^{Im}(t)$ should depend only on past terms $(t - \Delta t)$ and nodal voltages at time t. As a result, some basic algebraic manipulations are required to eliminate this time cross-coupling.

It is also important to emphasize that the historical terms denoted by C_h in (3.39) and (3.40) are not the final history current source of the inductance DPCM model yet. Instead, it represents an intermediate-term defined during the development of the inductance history source in conformity with Figure 3.6.

Regarding the real component $I_{km}^{Re}(t)$, its interdependence with $I_{km}^{Im}(t)$ is eliminated by substituting (3.38) into (3.37), as follows:

$$I_{km}^{Re}(t) = C_h^{Re}(t - \Delta t) + \frac{\Delta t}{2L} V_{km}^{Re}(t) + \frac{\Delta t}{2L} \omega L \left[C_h^{Im}(t - \Delta t) + \frac{\Delta t}{2L} \left[V_{km}^{Im}(t) - \omega L I_{km}^{Re}(t) \right] \right]$$
$$(3.41)$$

In a similar way, the imaginary current $I_{km}^{Im}(t)$ is obtained by substituting (3.37)

into (3.38):

$$I_{km}^{Im}(t) = C_h^{Im}(t - \Delta t) + \frac{\Delta t}{2L}V_{km}^{Im}(t) - \frac{\omega \Delta t}{2}\left[C_h^{Re}(t - \Delta t)\right] - \frac{\omega \Delta t^2}{4L} \cdot \left[V_{km}^{Re}(t) + \omega L I_{km}^{Im}(t)\right]$$

(3.42)

With some algebraic manipulations over (3.41) and (3.42), the following terms are defined:

$$I_{km}^{Re}(t) = \underbrace{\left[\frac{2}{4 + \omega^2 \Delta t^2}\right]}_{K_1} \cdot \left[\frac{\Delta t}{L}\right] \cdot \left[\frac{2L}{\Delta t}C_h^{Re}(t - \Delta t) + \omega L C_h^{Im}(t - \Delta t) + V_{km}^{Re}(t) + \frac{\omega \Delta t}{2}V_{km}^{Im}(t)\right]$$

$$I_{km}^{Re}(t) = \underbrace{K_1 \cdot \left[2C_h^{Re}(t - \Delta t) + \omega \Delta t C_h^{Im}(t - \Delta t)\right]}_{I_h^{Re}(t - \Delta t)} + K_1\frac{\Delta t}{L}\left[V_{km}^{Re}(t) + \frac{\omega \Delta t}{2}V_{km}^{Im}(t)\right]$$

(3.43)

$$I_{km}^{Im}(t) = \underbrace{\left[\frac{2}{4 + \omega^2 \Delta t^2}\right]}_{K_1}\left[2C_h^{Im}(t - \Delta t) - \omega \Delta t\left[C_h^{Re}(t - \Delta t)\right] + \frac{\Delta t}{L}V_{km}^{Im}(t) - \frac{\omega \Delta t^2}{2L} \cdot \left[V_{km}^{Re}(t)\right]\right]$$

$$I_{km}^{Im}(t) = \underbrace{K_1 \cdot \left[2C_h^{Im}(t - \Delta t) - \omega \Delta t\left[C_h^{Re}(t - \Delta t)\right]\right]}_{I_h^{Im}(t - \Delta t)} + K_1\frac{\Delta t}{L}\left[V_{km}^{Im}(t) - \frac{\omega \Delta t}{2} \cdot \left[V_{km}^{Re}(t)\right]\right]$$

(3.44)

Therefore, from (3.43) and (3.44), the DPCM of an inductance is obtained:

$$\begin{bmatrix} I_{km}^{Re}(t) \\ I_{km}^{Im}(t) \end{bmatrix} = \underbrace{\begin{bmatrix} I_h^{Re}(t - \Delta t) \\ I_h^{Im}(t - \Delta t) \end{bmatrix}}_{\text{(i) history current source } \tilde{I}_h(t - \Delta t)} + K_1\frac{\Delta t}{L}\underbrace{\begin{bmatrix} 1 & \frac{\omega \Delta t}{2} \\ -\frac{\omega \Delta t}{2} & 1 \end{bmatrix}}_{\text{(ii) tensor}} \cdot \begin{bmatrix} V_{km}^{Re}(t) \\ V_{km}^{Im}(t) \end{bmatrix}$$

(3.45)

Alternatively, (3.45) may be rewritten, as follows:

$$\tilde{I}_{km}(t) = \tilde{I}_{km_h}(t - \Delta t) + \mathbf{Y}^L \cdot \tilde{V}_{km}(t)$$

(3.46)

where:

$$K_1 = \frac{2}{4 + \omega^2 \Delta t^2}$$
$$I_h^{Re}(t - \Delta t) = K_1 \left[2C_h^{Re}(t - \Delta t) + \omega \Delta t \left[C_h^{Im}(t - \Delta t) \right] \right] \qquad (3.47)$$
$$I_h^{Im}(t - \Delta t) = K_1 \left[2C_h^{Im}(t - \Delta t) - \omega \Delta t \left[C_h^{Re}(t - \Delta t) \right] \right]$$

Equation (3.45) gives the tensor modeling of an inductance in accordance with the DPCM equivalent circuit of Figure 3.6. In this expression, the term (i) represents the history current source, and the term (ii) is related to the tensor $\mathbf{Y}_{km}$.

3.3.3   Capacitance

Consider a capacitance branch between generic nodes k and m, whose dynamic behavior is expressed by the following ODE:
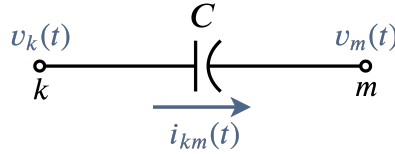
Figure 3.9: Capacitance

$$i_{km}(t) = C \frac{d(v_k(t) - v_m(t))}{dt} \qquad (3.48)$$

Representing the voltage $v_{km}(t)$ and current $i_{km}(t)$ by DP, (3.48) becomes:

$$I_{km}^{Re}(t)\cos(\omega t) - I_{km}^{Im}(t)\sin(\omega t) = C\frac{d}{dt}\left(V_{km}^{Re}(t)\cos(\omega t) - V_{km}^{Im}(t)\sin(\omega t) \right) \qquad (3.49)$$

Employing the chain-rule differentiation into (3.49), gives:

$$I_{km}^{Re}(t)\cos(\omega t) - I_{km}^{Im}(t)\sin(\omega t) = C\left(\frac{dV_{km}^{Re}(t)}{dt}\cos(\omega t) - \omega V_{km}^{Re}(t)\sin(\omega t) \right) \qquad (3.50)$$

$$-C\left(\frac{dV_{km}^{Im}(t)}{dt}\sin(\omega t) + \omega V_{km}^{Im}(t)\cos(\omega t) \right)$$

Identifying and grouping the terms associated with $\sin(\omega t)$ and $\cos(\omega t)$ yields:

$$
\begin{cases}
I_{km}^{Re}(t) = C\dfrac{dV_{km}^{Re}(t)}{dt} - \omega C V_{km}^{Im}(t) \\[2mm]
I_{km}^{Im}(t) = C\dfrac{dV_{km}^{Im}(t)}{dt} + \omega C V_{km}^{Re}(t)
\end{cases}
\tag{3.51}
$$

In order to obtain the capacitance discrete DPCM model, the trapezoidal integration rule is applied to (3.51), resulting in:

$$
V_{km}^{Re}(t) = V_{km}^{Re}(t - \Delta t) + \frac{\Delta t}{2C}\left[I_{km}^{Re}(t) + I_{km}^{Re}(t - \Delta t) + \omega C V_{km}^{Im}(t) + \omega C V_{km}^{Im}(t - \Delta t)\right]
\tag{3.52}
$$

$$
V_{km}^{Im}(t) = V_{km}^{Im}(t - \Delta t) + \frac{\Delta t}{2C}\left[I_{km}^{Im}(t) + I_{km}^{Im}(t - \Delta t) - \omega C V_{km}^{Re}(t) - \omega C V_{km}^{Re}(t - \Delta t)\right]
\tag{3.53}
$$

From (3.52) and (3.53), the real and imaginary DP components of current $\tilde{I}_{km}(t)$ are obtained:

$$
I_{km}^{Re}(t) = \underbrace{-\frac{2C}{\Delta t}V_{km}^{Re}(t - \Delta t) - I_{km}^{Re}(t - \Delta t) - \omega C V_{km}^{Im}(t - \Delta t)}_{I_h^{Re}(t - \Delta t)} + \frac{2C}{\Delta t}V_{km}^{Re}(t) - \omega C V_{km}^{Im}(t)
$$

$$
\tag{3.54}
$$

$$
I_{km}^{Im}(t) = \underbrace{-\frac{2C}{\Delta t}V_{km}^{Im}(t - \Delta t) - I_{km}^{Im}(t - \Delta t) + \omega C V_{km}^{Re}(t - \Delta t)}_{I_h^{Im}(t - \Delta t)} + \frac{2C}{\Delta t}V_{km}^{Im}(t) + \omega C V_{km}^{Re}(t)
$$

$$
\tag{3.55}
$$

Therefore, the DPCM of a capacitance is given by:

$$
\begin{bmatrix} I_{km}^{Re}(t) \\ I_{km}^{Im}(t) \end{bmatrix} = \begin{bmatrix} I_h^{Re}(t - \Delta t) \\ I_h^{Im}(t - \Delta t) \end{bmatrix} + \frac{2C}{\Delta t}\begin{bmatrix} 1 & -\dfrac{\omega\Delta t}{2} \\[2mm] \dfrac{\omega\Delta t}{2} & 1 \end{bmatrix} \cdot \begin{bmatrix} V_{km}^{Re}(t) \\ V_{km}^{Im}(t) \end{bmatrix}
\tag{3.56}
$$

Alternatively, (3.56) may be rewritten, as follows:

$$
\tilde{I}_{km}(t) = \tilde{I}_{km_h}(t - \Delta t) + \mathbf{Y}^C \cdot \tilde{V}_{km}(t)
\tag{3.57}
$$

where:

$$
I_h^{Re}(t - \Delta t) = -\frac{2C}{\Delta t}V_{km}^{Re}(t - \Delta t) - I_{km}^{Re}(t - \Delta t) - \omega C V_{km}^{Im}(t - \Delta t)
\tag{3.58}
$$

$$
I_h^{Im}(t - \Delta t) = -\frac{2C}{\Delta t}V_{km}^{Im}(t - \Delta t) - I_{km}^{Im}(t - \Delta t) + \omega C V_{km}^{Re}(t - \Delta t)
\tag{3.59}
$$

3.3.4 Lumped Parameter Transmission Lines

The companion models presented in Section 2.4.4 to represent transmission lines in EMT dynamic simulations are specified in terms of the line length. From this perspective, the representation of short and medium-length lines through lumped parameter models are considered accurate enough for nodal voltages and currents calculation [44]. Then, corresponding DPCM models are built by a direct combination of the basic DPCM models developed for R, L, and C related to the total line length.

In this regard, several DPCM line branches are developed to provide a suitable interface with lumped parameter line models that are commonly found in traditional power flow analysis software, which supplies the initial steady-state operating point for dynamic simulation in ESA software.

Therefore, the lumped line models addressed in the following subsections include: series RL branch, series RC branch, and the *nominal-π* model. The first two models are traditionally used to describe short-length lines, whereas the last is mostly employed to medium-length lines. However, it is also customary (in ESA analysis) to represent long transmission lines through the lumped *equivalent-π* model, which gives accurate calculation of terminal voltages and currents in steady-state analysis. The equivalent-π model is obtained from the nominal-π model by employing some hyperbolic correction factors over the nominal-π parameters [46].

3.3.4.1 Series RL Branch

Consider the series RL branch presented in Figure 3.10.
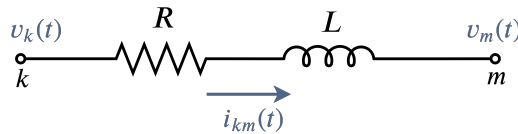
Figure 3.10: RL Branch

The ODE describing the dynamic relationship between current and voltage in this branch is given by:

$$v_{km}(t) = L\frac{di_{km}(t)}{dt} + R \cdot i_{km}(t) \tag{3.60}$$

Representing the voltage $v_{km}(t)$ and current $i_{km}(t)$ by DP yields:

$$V_{km}^{Re}(t)\cos(\omega t) - V_{km}^{Im}(t)\sin(\omega t) = L\frac{d}{dt}\left(I_{km}^{Re}(t)\cos(\omega t) - I_{km}^{Im}(t)\sin(\omega t)\right) + $$
$$R\left(I_{km}^{Re}(t)\cos(\omega t) - I_{km}^{Im}(t)\sin(\omega t)\right) \qquad (3.61)$$

Employing the chain-rule differentiation into (3.61), gives:

$$V_{km}^{Re}(t)\cos(\omega t) - V_{km}^{Im}(t)\sin(\omega t) = L\left(\frac{dI_{km}^{Re}(t)}{dt}\cos(\omega t) - I_{km}^{Re}(t)\omega \cdot \sin(\omega t)\right)$$
$$-L\left(\frac{dI_{km}^{Im}(t)}{dt}\sin(\omega t) + I_{km}^{Im}(t)\omega \cdot \cos(\omega t)\right) + $$
$$R \cdot \left(I_{km}^{Re}(t)\cos(\omega t) - I_{km}^{Im}(t)\sin(\omega t)\right) \qquad (3.62)$$

Then, identifying and grouping the terms associated with $\sin(\omega t)$ and $\cos(\omega t)$, comes that:

$$\begin{cases} V_{km}^{Re}(t) = L\dfrac{dI_{km}^{Re}(t)}{dt} - \omega L \cdot I_{km}^{Im}(t) + R \cdot I_{km}^{Re}(t) \\ V_{km}^{Im}(t) = L\dfrac{dI_{km}^{Im}(t)}{dt} + \omega L \cdot I_{km}^{Re}(t) + R \cdot I_{km}^{Im}(t) \end{cases} \qquad (3.63)$$

In order to obtain a discrete DPCM model for the RL branch, the trapezoidal integration rule is applied into (3.63), resulting in:

$$I_{km}^{Re}(t) = I_{km}^{Re}(t - \Delta t) + \frac{\Delta t}{2L} \cdot \left[\begin{array}{l} V_{km}^{Re}(t - \Delta t) + \omega L I_{km}^{Im}(t - \Delta t) - R \cdot I_{km}^{Re}(t - \Delta t) + \\ V_{km}^{Re}(t) + \omega L I_{km}^{Im}(t) - R \cdot I_{km}^{Re}(t) \end{array} \right]$$

$$I_{km}^{Im}(t) = I_{km}^{Im}(t - \Delta t) + \frac{\Delta t}{2L} \cdot \left[\begin{array}{l} V_{km}^{Im}(t - \Delta t) - \omega L I_{km}^{Re}(t - \Delta t) - R \cdot I_{km}^{Im}(t - \Delta t) + \\ V_{km}^{Im}(t) - \omega L I_{km}^{Re}(t) - R \cdot I_{km}^{Im}(t) \end{array} \right]$$

$$(3.64)$$

Therefore, after some basic algebraic manipulations to eliminate the time cross-coupling between real and imaginary DP currents, the equivalent DPCM model of the RL branch is obtained:

$$\begin{bmatrix} I_{km}^{Re}(t) \\ I_{km}^{Im}(t) \end{bmatrix} = \begin{bmatrix} I_h^{Re}(t - \Delta t) \\ I_h^{Im}(t - \Delta t) \end{bmatrix} + K_1 \cdot a \cdot \frac{\Delta t}{L} \begin{bmatrix} 1 & a \cdot \dfrac{\omega \Delta t}{2} \\ -a \cdot \dfrac{\omega \Delta t}{2} & 1 \end{bmatrix} \cdot \begin{bmatrix} V_{km}^{Re}(t) \\ V_{km}^{Im}(t) \end{bmatrix} \qquad (3.65)$$

Alternatively, (3.65) may be rewritten, as follows:

$$\tilde{I}_{km}(t) = \tilde{I}_{km_h}(t - \Delta t) + \mathbf{Y}^{RL} \cdot \tilde{V}_{km}(t) \tag{3.66}$$

where:

$$a = \frac{1}{\left(1 + R \cdot \dfrac{\Delta t}{2L}\right)} \tag{3.67}$$

$$K_1 = \frac{2}{4 + a^2 \cdot \omega^2 \Delta t^2} \tag{3.68}$$

$$I_h^{Re}(t - \Delta t) = k_1 \left[2a \cdot C_h^{Re}(t - \Delta t) + a^2 \cdot \omega \Delta t C_h^{Im}(t - \Delta t)\right] \tag{3.69}$$

$$I_h^{Im}(t - \Delta t) = k_1 \left[2a \cdot C_h^{Im}(t - \Delta t) - a^2 \cdot \omega \Delta t C_h^{Re}(t - \Delta t)\right] \tag{3.70}$$

$$C_h^{Re}(t - \Delta t) = I_{km}^{Re}(t - \Delta t) + \frac{\Delta t}{2L} \cdot \left[V_{km}^{Re}(t - \Delta t) + \omega L I_{km}^{Im}(t - \Delta t) - R \cdot I_{km}^{Re}(t - \Delta t)\right] \tag{3.71}$$

$$C_h^{Im}(t - \Delta t) = I_{km}^{Im}(t - \Delta t) + \frac{\Delta t}{2L} \cdot \left[V_{km}^{Im}(t - \Delta t) - \omega L I_{km}^{Re}(t - \Delta t) - R \cdot I_{km}^{Im}(t - \Delta t)\right] \tag{3.72}$$

The algebraic operations for obtaining (3.65) from (3.64) are quite exhaustive, and therefore only the result of the final expressions has been presented. However, it follows the same line of thought along the development of the inductance DPCM model depicted in Section 3.3.2.

It is important to emphasize that the equivalent RL model draws a generalization for the basic resistance and inductance DPCM models previously developed since the RL model can also be employed to describe both basic elements. One should note that (3.65) turns into (3.45) when R equals zero, i.e., becoming identical to the inductance DPCM model. Similarly, if L is equal to zero, (3.65) turns into the resistance tensor model (3.29).

3.3.4.2 Series RC Branch

Consider the series RC branch between generic nodes k and m:
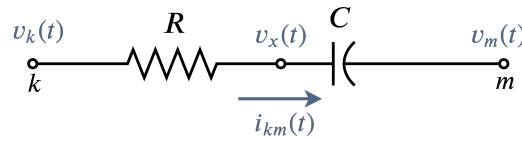
Figure 3.11: RC Branch

Defining an intermediate node x, the voltage $v_x(t)$ can be written in terms of the

terminal quantities, as follows:

$$v_x(t) = v_k(t) - R \cdot i_{km}(t) \tag{3.73}$$

Then, the ODE describing the dynamic relationship between voltage and current in this branch is given by:

$$i_{km}(t) = C \cdot \frac{d}{dt}(v_x(t) - v_m(t)) \tag{3.74}$$

Substituting (3.73) into (3.74), gives:

$$i_{km}(t) = C \cdot \frac{d}{dt}(v_{km}(t) - R \cdot i_{km}(t)) \tag{3.75}$$

Representing the voltage $v_{km}(t)$ and the current $i_{km}(t)$ through DP, gives:

$$\begin{aligned}
I_{km}^{Re}(t)\cos(\omega t) - I_{km}^{Im}(t)\sin(\omega t) = & C \cdot \frac{d}{dt}\Big[V_{km}^{Re}(t)\cos(\omega t) - V_{km}^{Im}(t)\sin(\omega t) \\
& - R \cdot \big(I_{km}^{Re}(t)\cos(\omega t) - I_{km}^{Im}(t)\sin(\omega t)\big)\Big]
\end{aligned} \tag{3.76}$$

Employing the chain-rule differentiation into (3.76) and grouping the terms associated with $\sin(\omega t)$ and $\cos(\omega t)$, follows that:

$$\begin{cases}
I_{km}^{Re} = C\dfrac{dV_{km}^{Re}}{dt} - \omega C V_{km}^{Im} - RC\dfrac{dI_{km}^{Re}}{dt} + \omega RC I_{km}^{Im} \\[3mm]
I_{km}^{Im} = C\dfrac{dV_{km}^{Im}}{dt} + \omega C V_{km}^{Re} - RC\dfrac{dI_{km}^{Im}}{dt} - \omega RC I_{km}^{Re}
\end{cases} \tag{3.77}$$

Applying the trapezoidal integration rule into (3.77) yields:

$$\begin{aligned}
\frac{\Delta t}{2}[I_{km}^{Re}(t) + I_{km}^{Re}(t - \Delta t)] = & C[V_{km}^{Re}(t) - V_{km}^{Re}(t - \Delta t)] - \omega C\frac{\Delta t}{2}[V_{km}^{Im}(t) + V_{km}^{Im}(t - \Delta t)] \\
& - RC[I_{km}^{Re}(t) - I_{km}^{Re}(t - \Delta t)] + \omega RC\frac{\Delta t}{2}[I_{km}^{Im}(t) + I_{km}^{Im}(t - \Delta t)]
\end{aligned} \tag{3.78}$$

$$\begin{aligned}
\frac{\Delta t}{2}[I_{km}^{Im}(t) + I_{km}^{Im}(t - \Delta t)] = & C[V_{km}^{Im}(t) - V_{km}^{Im}(t - \Delta t)] + \omega C\frac{\Delta t}{2}[V_{km}^{Re}(t) + V_{km}^{Re}(t - \Delta t)] \\
& - RC[I_{km}^{Im}(t) - I_{km}^{Im}(t - \Delta t)] - \omega RC\frac{\Delta t}{2}[I_{km}^{Re}(t) + I_{km}^{Re}(t - \Delta t)]
\end{aligned} \tag{3.79}$$

Rearranging (3.78) and (3.79) and rewriting these expressions in a matrix form, gives:

$$\frac{\Delta t}{2} \cdot \mathbf{A} \begin{bmatrix} I_{km}^{Re}(t) \\ I_{km}^{Im}(t) \end{bmatrix} = C \cdot \begin{bmatrix} 1 & -\omega\frac{\Delta t}{2} \\ \omega\frac{\Delta t}{2} & 1 \end{bmatrix} \begin{bmatrix} V_{km}^{Re}(t) \\ V_{km}^{Im}(t) \end{bmatrix} + \begin{bmatrix} C_h^{Re}(t-\Delta t) \\ C_h^{Im}(t-\Delta t) \end{bmatrix} \tag{3.80}$$

where by definition:

$$\mathbf{A} = \begin{bmatrix} \frac{2}{\Delta t}RC + 1 & -\omega RC \\ \omega RC & \frac{2}{\Delta t}RC + 1 \end{bmatrix} \tag{3.81}$$

$$
\begin{aligned}
C_h^{Re}(t-\Delta t) = & -C \cdot V_{km}^{Re}(t-\Delta t) - \omega C\frac{\Delta t}{2}V_{km}^{Im}(t-\Delta t) \\
& + \left[RC - \frac{\Delta t}{2}\right]I_{km}^{Re}(t-\Delta t) + \omega RC\frac{\Delta t}{2}I_{km}^{Im}(t-\Delta t)
\end{aligned}
\tag{3.82}
$$

$$
\begin{aligned}
C_h^{Im}(t-\Delta t) = & \ \omega C\frac{\Delta t}{2}V_{km}^{Re}(t-\Delta t) - C \cdot V_{km}^{Im}(t-\Delta t) \\
& -\omega RC\frac{\Delta t}{2}I_{km}^{Re}(t-\Delta t) + \left[RC - \frac{\Delta t}{2}\right]I_{km}^{Im}(t-\Delta t)
\end{aligned}
\tag{3.83}
$$

Therefore, after some algebraic manipulations, the equivalent DPCM model of a series RC branch is obtained:

$$\begin{bmatrix} I_{km}^{Re}(t) \\ I_{km}^{Im}(t) \end{bmatrix} = \begin{bmatrix} I_{km}^{Re}(t-\Delta t) \\ I_{km}^{Im}(t-\Delta t) \end{bmatrix} + \mathbf{A}^{-1} \cdot \frac{2C}{\Delta t} \begin{bmatrix} 1 & -\omega\frac{\Delta t}{2} \\ \omega\frac{\Delta t}{2} & 1 \end{bmatrix} \begin{bmatrix} V_{km}^{Re}(t) \\ V_{km}^{Im}(t) \end{bmatrix} \tag{3.84}$$

where:

$$\mathbf{A}^{-1} = \frac{1}{\left(\frac{2}{\Delta t}RC + 1\right)^2 + (\omega RC)^2} \cdot \begin{bmatrix} \frac{2}{\Delta t}RC + 1 & \omega RC \\ -\omega RC & \frac{2}{\Delta t}RC + 1 \end{bmatrix} \tag{3.85}$$

$$\begin{bmatrix} I_{km}^{Re}(t-\Delta t) \\ I_{km}^{Im}(t-\Delta t) \end{bmatrix} = A^{-1} \cdot \frac{2}{\Delta t} \begin{bmatrix} C_h^{Re}(t-\Delta t) \\ C_h^{Im}(t-\Delta t) \end{bmatrix} \tag{3.86}$$

Alternatively, (3.84) may be rewritten, as follows:

$$\tilde{I}_{km}(t) = \tilde{I}_{km_h}(t-\Delta t) + \mathbf{Y}^{RC} \cdot \tilde{V}_{km}(t) \tag{3.87}$$

One should note that the equivalent DPCM model of the RC branch draws a gen-

eralization for the resistance and capacitance DPCM models, i.e., if R is equal to zero, (3.84) becomes identical to (3.56). Similarly, if C equals zero, (3.84) turns into (3.29).

3.3.4.3   Nominal-π model

The nominal-π model depicted in Figure 3.12 is adopted in this thesis to represent medium-length lines. This model is composed by a concentrated series impedance R and L, and half of the total shunt capacitance C placed at each line end, both as lumped parameters.
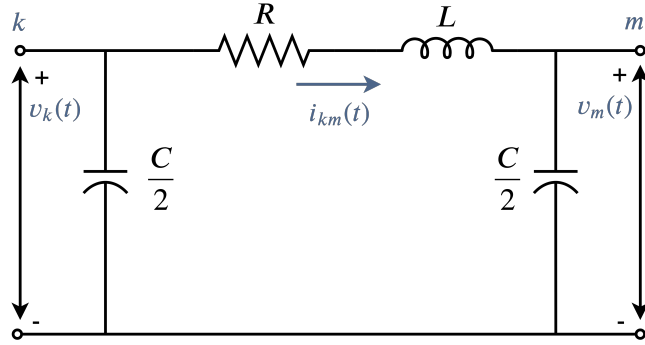
Figure 3.12: Equivalent impedance network of the nominal-π line model

In this framework, the equivalent DPCM circuit of the nominal-π model is intuitively built by a systematic substitution of each linear component (R, L, C) by its individual DPCM model, as shown in Figure 3.13.
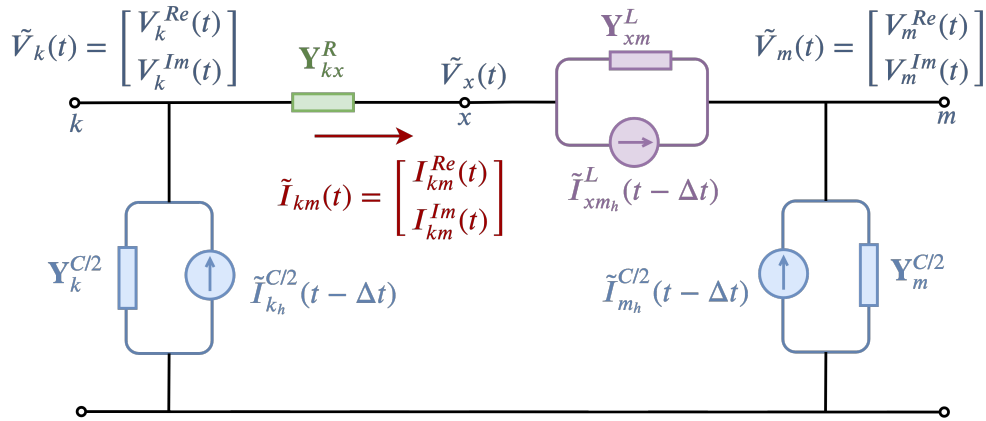
Figure 3.13: Equivalent DPCM circuit of the nominal-π line model

Therefore, there is no need to reduce this model into a two-port equivalent DPCM circuit since, in practical dynamic simulation, each element may be solved through its respective DPCM model, already presented in the previous subsections. Another

practical aspect of this modeling is that the series impedance parameter is replaced by the RL branch model described by (3.65), instead of using individual R and L representations.

3.3.5   Distributed Parameter Transmission Lines

An accurate representation of long transmission lines in EMT analysis must take into consideration the line parameters uniformly distributed per unit of line length (R', L', and C'). In this thesis, the Bergeron's method is employed to obtain DPCM of (i) lossless transmission lines by neglecting the series resistance; and (ii) approximated lossy line model assuming lossless line sections and concentrated fractions of the total resistance lumped in the middle ($R/2$) and at both line-ends ($R/4$).

These models have been approached in Section 2.4.4 by using instantaneous voltage and current. Now, they are addressed by using dynamic phasors to support the development of corresponding DPCM.

3.3.5.1   Lossless Line

Consider the lossless line of Figure 3.14 with node k as the sending-end, node m as the receiving-end and line length ℓ.
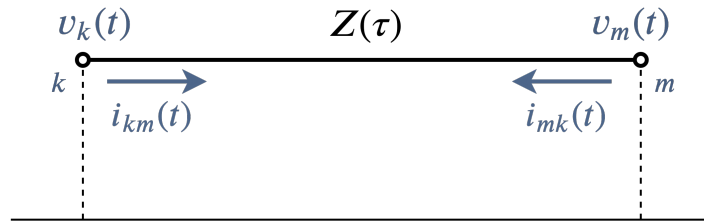
Figure 3.14: Lossless transmission line

where:

$$Z = \sqrt{\frac{L'}{C'}} \quad \text{is the surge impedance;}$$

$$\nu = \frac{1}{\sqrt{L'C'}} \quad \text{is the phase velocity of a progressive wave;}$$

$\tau = \ell\sqrt{L'C'}$ is the travel time for a progressive wave go through one line-end to the other.

According to the mathematical formulation developed in Section 2.4.4, the relationship between voltage and current at the sending-end k and instant $(t - \tau)$ is integrally reproduced at the receiving-end m and instant (t) (Figure 3.15).
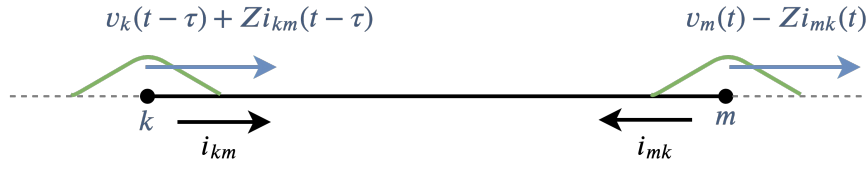
Figure 3.15: Progressive wave

Considering a wave which travels from node k to node m, follows that:

$$v_k(t - \tau) + Z i_{km}(t - \tau) = v_m(t) - Z i_{mk}(t) \tag{3.88}$$

Similarly, considering a wave which travels from node m to node k yields:

$$v_m(t - \tau) + Z i_{mk}(t - \tau) = v_k(t) - Z i_{km}(t) \tag{3.89}$$

Equations (3.88) and (3.89) describe, in terms of instantaneous quantities, the relationship between voltage and current as progressive waves traveling toward the line-ends in opposite directions. In order to obtain the DPCM model of a lossless transmission line, voltages and currents given in time (t) and $(t - \tau)$ are expressed through the following DP expressions:

$$
\begin{aligned}
v(t) &= V^{Re}(t)\cos(\omega t) - V^{Im}(t)\sin(\omega t) \\
i(t) &= I^{Re}(t)\cos(\omega t) - I^{Im}t)\sin(\omega t) \\
v(t - \tau) &= V^{Re}(t - \tau)\cos\left(\omega(t - \tau)\right) - V^{Im}(t - \tau)\sin(\omega(t - \tau)) \\
i(t - \tau) &= I^{Re}(t - \tau)\cos\left(\omega(t - \tau)\right) - I^{Im}(t - \tau)\sin(\omega(t - \tau))
\end{aligned}
\tag{3.90}
$$

Substituting (3.90) into (3.88), gives:

$$
\begin{aligned}
&V_k^{Re}(t - \tau)\cos\left(\omega(t - \tau)\right) - V_k^{Im}(t - \tau)\sin(\omega(t - \tau)) + \\
&+ Z\left[I_{km}^{Re}(t - \tau)\cos(\omega(t - \tau)) - I_{km}^{Im}(t - \tau)\sin(\omega(t - \tau))\right] = \\
&V_m^{Re}(t)\cos(\omega t) - V_m^{Im}(t)\sin(\omega t) - Z\left[I_{mk}^{Re}(t)\cos(\omega t) - I_{mk}^{Im}(t)\sin(\omega t)\right]
\end{aligned}
\tag{3.91}
$$

Similarly, substituting (3.90) into (3.89), results in:

$$
\begin{aligned}
&V_m^{Re}(t - \tau)\cos\left(\omega(t - \tau)\right) - V_m^{Im}(t - \tau)\sin(\omega(t - \tau)) + \\
&+ Z\left[I_{mk}^{Re}(t - \tau)\cos(\omega(t - \tau)) - I_{mk}^{Im}(t - \tau)\sin(\omega(t - \tau))\right] = \\
&V_k^{Re}(t)\cos(\omega t) - V_k^{Im}(t)\sin(\omega t) - Z\left[I_{km}^{Re}(t)\cos(\omega t) - I_{km}^{Im}(t)\sin(\omega t)\right]
\end{aligned}
\tag{3.92}
$$

Then, the following trigonometric identities are considered:

$$\cos\left(\omega t - \omega\tau\right) = \cos(\omega t)\cos(\omega\tau) + \sin(\omega t)\sin(\omega\tau) \tag{3.93}$$

$$\sin\left(\omega t - \omega\tau\right) = \sin(\omega t)\cos(\omega\tau) - \sin(\omega\tau)\cos(\omega t) \tag{3.94}$$

Therefore, substituting (3.93) and (3.94) into (3.91) and rearranging this expression to explicit the real and imaginary DP components of $\tilde{I}_{mk}(t)$ yields:

$$
\begin{aligned}
I_{mk}^{Re}(t)\cos(\omega t) - I_{mk}^{Im}(t)\sin(\omega t) = \quad & \frac{V_m^{Re}(t)}{Z}\cos(\omega t) - \frac{V_m^{Im}(t)}{Z}\sin(\omega t) \\
& - \frac{V_k^{Re}(t-\tau)}{Z}\left(\cos(\omega t)\cos(\omega\tau) + \sin(\omega t)\sin(\omega\tau)\right) \\
& + \frac{V_k^{Im}(t-\tau)}{Z}\left(\sin(\omega t)\cos(\omega\tau) - \cos(\omega t)\sin(\omega\tau)\right) \\
& - I_{km}^{Re}(t-\tau)\left(\cos(\omega t)\cos(\omega\tau) + \sin(\omega t)\sin(\omega\tau)\right) \\
& + I_{km}^{Im}(t-\tau)\left(\sin(\omega t)\cos(\omega\tau) - \cos(\omega t)\sin(\omega\tau)\right)
\end{aligned}
\tag{3.95}
$$

Analogously, substituting (3.93) and (3.94) into (3.92), and rearranging to explicit the DP components of $\tilde{I}_{km}(t)$, follows that:

$$
\begin{aligned}
I_{km}^{Re}(t)\cos(\omega t) - I_{km}^{Im}(t)\sin(\omega t) = \quad & \frac{V_k^{Re}(t)}{Z}\cos(\omega t) - \frac{V_k^{Im}(t)}{Z}\sin(\omega t) \\
& - \frac{V_m^{Re}(t-\tau)}{Z}\left(\cos(\omega t)\cos(\omega\tau) + \sin(\omega t)\sin(\omega\tau)\right) \\
& + \frac{V_m^{Im}(t-\tau)}{Z}\left(\sin(\omega t)\cos(\omega\tau) - \cos(\omega t)\sin(\omega\tau)\right) \\
& - I_{mk}^{Re}(t-\tau)\left(\cos(\omega t)\cos(\omega\tau) + \sin(\omega t)\sin(\omega\tau)\right) \\
& + I_{mk}^{Im}(t-\tau)\left(\sin(\omega t)\cos(\omega\tau) - \cos(\omega t)\sin(\omega\tau)\right)
\end{aligned}
\tag{3.96}
$$

Identifying and grouping the terms associated with $\sin(\omega t)$ and $\cos(\omega t)$ in (3.95) and (3.96) yields:

$$
\begin{cases}
\begin{aligned}
I_{mk}^{Re}(t) = \;& \frac{V_m^{Re}(t)}{Z} - \frac{V_k^{Re}(t-\tau)}{Z}\left(\cos(\omega\tau)\right) - \frac{V_k^{Im}(t-\tau)}{Z}\left(\sin(\omega\tau)\right) + \\
& - I_{km}^{Re}(t-\tau)\left(\cos(\omega\tau)\right) - I_{km}^{Im}(t-\tau)\left(\sin(\omega\tau)\right)
\end{aligned} \\[4mm]
\begin{aligned}
I_{mk}^{Im}(t) = \;& \frac{V_m^{Im}(t)}{Z} + \frac{V_k^{Re}(t-\tau)}{Z}\left(\sin(\omega\tau)\right) - \frac{V_k^{Im}(t-\tau)}{Z}\left(\cos(\omega\tau)\right) + \\
& I_{km}^{Re}(t-\tau)\left(\sin(\omega\tau)\right) - I_{km}^{Im}(t-\tau)\left(\cos(\omega\tau)\right)
\end{aligned}
\end{cases}
\tag{3.97}
$$

$$
\begin{cases}
I_{km}^{Re}(t) = \dfrac{V_k^{Re}(t)}{Z} - \dfrac{V_m^{Re}(t-\tau)}{Z}\left(\cos(\omega\tau)\right) - \dfrac{V_m^{Im}(t-\tau)}{Z}\left(\sin(\omega\tau)\right) + \\
\qquad\quad -I_{mk}^{Re}(t-\tau)\left(\cos(\omega\tau)\right) - I_{mk}^{Im}(t-\tau)\left(\sin(\omega\tau)\right) \\[2mm]
I_{km}^{Im}(t) = \dfrac{V_k^{Im}(t)}{Z} + \dfrac{V_m^{Re}(t-\tau)}{Z}\left(\sin(\omega\tau)\right) - \dfrac{V_m^{Im}(t-\tau)}{Z}\left(\cos(\omega\tau)\right) + \\
\qquad\quad I_{mk}^{Re}(t-\tau)\left(\sin(\omega\tau)\right) - I_{mk}^{Im}(t-\tau)\left(\cos(\omega\tau)\right)
\end{cases}
\tag{3.98}
$$

Therefore, the DPCM model of a lossless transmission line is obtained from these expressions and may be written in a tensor form, as follows:

$$
\begin{bmatrix}
I_{km}^{Re}(t) \\
I_{km}^{Im}(t) \\
\hline
I_{mk}^{Re}(t) \\
I_{mk}^{Im}(t)
\end{bmatrix}
=
\begin{bmatrix}
\frac{1}{Z} & & & \\
& \frac{1}{Z} & & \\
\hline
& & \frac{1}{Z} & \\
& & & \frac{1}{Z}
\end{bmatrix}
\cdot
\begin{bmatrix}
V_k^{Re}(t) \\
V_k^{Im}(t) \\
\hline
V_m^{Re}(t) \\
V_m^{Im}(t)
\end{bmatrix}
-
\begin{bmatrix}
b_k^{Re}(t-\tau) \\
b_k^{Im}(t-\tau) \\
\hline
b_m^{Re}(t-\tau) \\
b_m^{Im}(t-\tau)
\end{bmatrix}
\tag{3.99}
$$

Alternatively, (3.99) may be rewritten, as follows:

$$
\tilde{\mathbf{I}}(t) = \mathbf{Y}^Z \cdot \tilde{\mathbf{V}}(t) - \tilde{\mathbf{b}}(t-\tau)
\tag{3.100}
$$

where:

$$
\begin{bmatrix}
b_k^{Re}(t) \\
b_k^{Im}(t) \\
\hline
b_m^{Re}(t) \\
b_m^{Im}(t)
\end{bmatrix}
=
\begin{bmatrix}
\mathbf{A} & \\
\hline
& \mathbf{A}
\end{bmatrix}
\cdot
\left\{
\mathbf{Y} \cdot
\begin{bmatrix}
V_m^{Re}(t) \\
V_m^{Im}(t) \\
\hline
V_k^{Re}(t) \\
V_k^{Im}(t)
\end{bmatrix}
+
\begin{bmatrix}
I_{mk}^{Re}(t) \\
I_{mk}^{Im}(t) \\
\hline
I_{km}^{Re}(t) \\
I_{km}^{Im}(t)
\end{bmatrix}
\right\}
\tag{3.101}
$$

The transformation matrix $\mathbf{A}$ and the tensor admittance matrix $\mathbf{Y}$ are defined, as follows:

$$
\mathbf{A} =
\begin{bmatrix}
\cos(\omega\tau) & \sin(\omega\tau) \\
\hline
-\sin(\omega\tau) & \cos(\omega\tau)
\end{bmatrix}
\qquad
\mathbf{Y} =
\begin{bmatrix}
\frac{1}{Z} & & & \\
& \frac{1}{Z} & & \\
\hline
& & \frac{1}{Z} & \\
& & & \frac{1}{Z}
\end{bmatrix}
\tag{3.102}
$$

From (3.99), one should note that the equivalent DPCM model of a lossless line

results in uncoupled real and imaginary DP equations of voltages and currents, as well as an uncoupling between quantities related to the sending-end k and the receiving-end m. Indeed, the relationship between these quantities are given by the memory vector $\tilde{\mathbf{b}}(t - \tau)$, which represents a history current source for each line-end whose past quantities refers to time $(t - \tau)$, i.e., it presents a delay equal to the progressive wave travel time τ.

Figures 3.16 and 3.17 present the real and imaginary DPCM circuits of a lossless transmission line modeled by DP, highlighting the associated uncoupled feature. It is worth mentioning that real and imaginary DP of current may be determined by independent equivalent circuits, and terminal quantities uncoupled by a travel time τ.
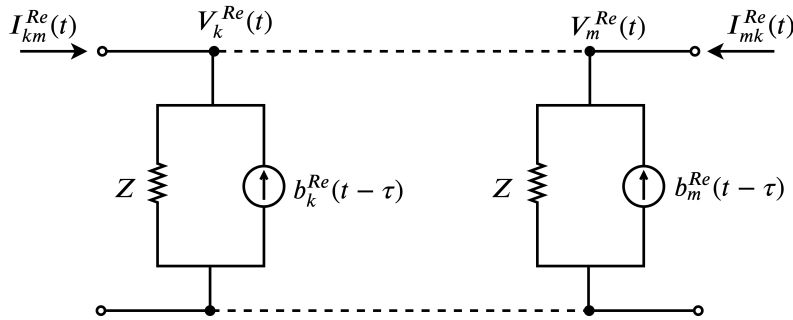
Figure 3.16: Real DPCM circuit of a lossless line
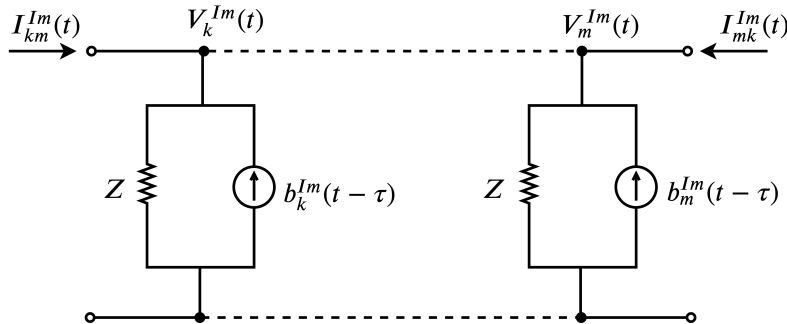
Figure 3.17: Imaginary DPCM circuit of a lossless line

It is important to emphasize that, in the case of lumped elements, the history current sources only depend on one previous time step $(t - \Delta t)$, whereas distributed parameter lines (whether lossless or lossy models) should hold a memory vector whose delay must date back over the number of time steps that fits into the line travel time (τ).

3.3.5.2 Lossy Line

Distributed losses have been neglected in the method of characteristic to allow a direct integration of expressions (2.61) and (2.62). Therefore, transmission line losses are evaluated in this thesis by the approximated model described in Section 2.4.4.2, where the two-port equivalent of the lossy line model is developed through a cascade connection of lumped resistances and lossless line sections.

Figure 3.18 illustrates the traditional lossy line model adopted in EMT analysis that considers two half lossless line sections and the losses are take into account through a lumped resistance $R/2$ in the middle of the line and $R/4$ at both line-ends. This modeling is sufficiently accurate for the purpose of voltage and current calculation in EMT simulations.
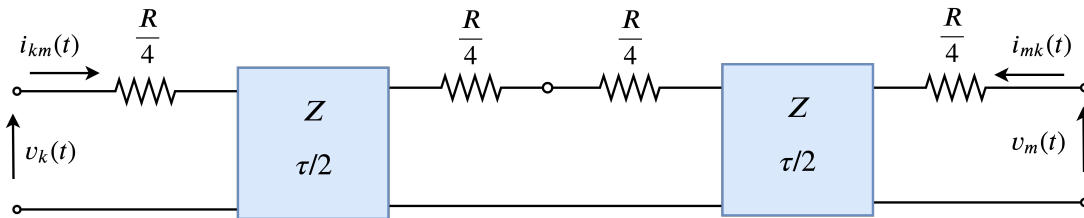
Figure 3.18: Approximate lossy line with lumped resistances and lossless sections

The equivalent DPCM quadripole is obtained by cascading the lossless line and lumped resistances DPCM models, as shown in Figure 3.19. One should note that this connection gives a direct interface between real and imaginary DPCM circuits due to the uncoupled characteristic of both models, which also exist in the lossy DPCM equivalent model.
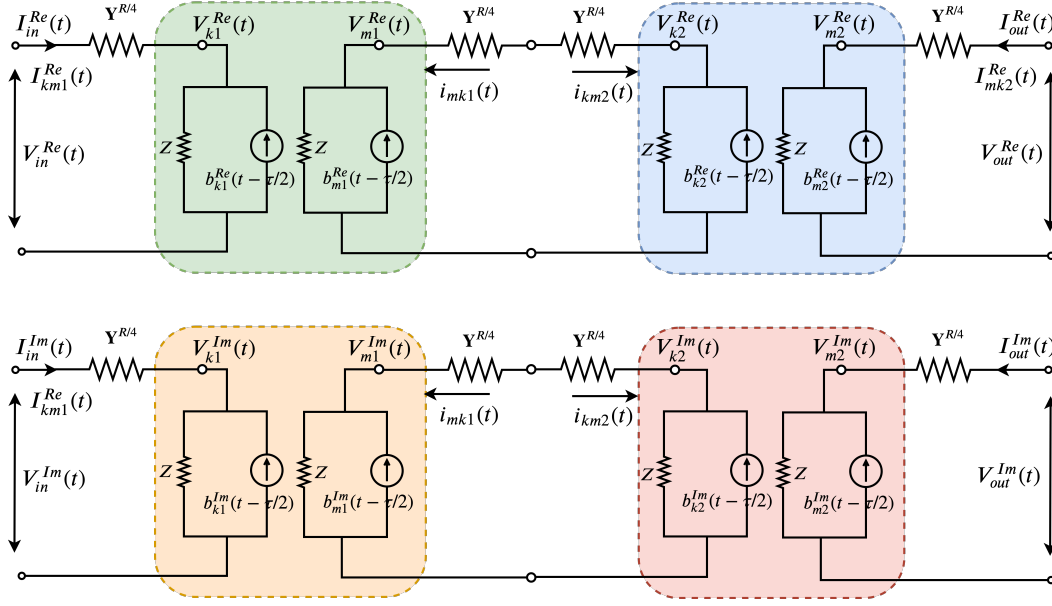
Figure 3.19: Cascade connection of uncoupled real and imaginary DPCM models of lossless line sections and lumped resistances

In order to obtain the equivalent DPCM model of a lossy line, some algebraic manipulations are required similar to that deductions detailed in Section 2.4.4.2 to eliminate the intermediary circuit of Figure 3.19. After this development, the following DPCM is obtained for the lossy line:

$$
\begin{bmatrix}
I_{km}^{Re}(t) \\
I_{km}^{Im}(t) \\
\hline
I_{mk}^{Re}(t) \\
I_{mk}^{Im}(t)
\end{bmatrix}
=
\begin{bmatrix}
\dfrac{1}{Z_{eqv}} & & & \\
& \dfrac{1}{Z_{eqv}} & & \\
\hline
& & \dfrac{1}{Z_{eqv}} & \\
& & & \dfrac{1}{Z_{eqv}}
\end{bmatrix}
\cdot
\begin{bmatrix}
V_k^{Re}(t) \\
V_k^{Im}(t) \\
V_m^{Re}(t) \\
V_m^{Im}(t)
\end{bmatrix}
-
\begin{bmatrix}
b_k^{Re}(t-\tau) \\
b_k^{Im}(t-\tau) \\
b_m^{Re}(t-\tau) \\
b_m^{Im}(t-\tau)
\end{bmatrix}
\quad (3.103)
$$

The history sources $\tilde{b}_k$ and $\tilde{b}_m$ of each line-end are given in (3.104) and (3.105) as functions of time t.

$$
\begin{aligned}
b_k^{Re}(t) = \ & A \cdot \left[\left(\frac{V_k^{Re}(t)}{Z_{eqv}} + h \cdot I_{km}^{Re}(t) \right) \cos(\omega\tau) + \left(\frac{V_k^{Im}(t)}{Z_{eqv}} + h \cdot I_{km}^{Im}(t) \right) \sin(\omega\tau) \right] + \\
+ \ & B \cdot \left[\left(\frac{V_m^{Re}(t)}{Z_{eqv}} + h \cdot I_{mk}^{Re}(t) \right) \cos(\omega\tau) + \left(\frac{V_m^{Im}(t)}{Z_{eqv}} + h \cdot I_{mk}^{Im}(t) \right) \sin(\omega\tau) \right]
\end{aligned}
$$

$$
\begin{aligned}
b_k^{Im}(t) = \ & A \cdot \left[\left(\frac{V_k^{Re}(t)}{Z_{eqv}} + h \cdot I_{km}^{Re}(t) \right) \sin(\omega\tau) - \left(\frac{V_k^{Im}(t)}{Z_{eqv}} + h \cdot I_{km}^{Im}(t) \right) \cos(\omega\tau) \right] + \\
+ \ & B \cdot \left[\left(\frac{V_m^{Re}(t)}{Z_{eqv}} + h \cdot I_{mk}^{Re}(t) \right) \sin(\omega\tau) - \left(\frac{V_m^{Im}(t)}{Z_{eqv}} + h \cdot I_{mk}^{Im}(t) \right) \cos(\omega\tau) \right]
\end{aligned}
$$

$$(3.104)$$

$$
\begin{aligned}
b_m^{Re}(t) = \ & B \cdot \left[\left(\frac{V_k^{Re}(t)}{Z_{eqv}} + h \cdot I_{km}^{Re}(t) \right) \cos(\omega\tau) + \left(\frac{V_k^{Im}(t)}{Z_{eqv}} + h \cdot I_{km}^{Im}(t) \right) \sin(\omega\tau) \right] + \\
+ \ & A \cdot \left[\left(\frac{V_m^{Re}(t)}{Z_{eqv}} + h \cdot I_{mk}^{Re}(t) \right) \cos(\omega\tau) + \left(\frac{V_m^{Im}(t)}{Z_{eqv}} + h \cdot I_{mk}^{Im}(t) \right) \sin(\omega\tau) \right]
\end{aligned}
$$

$$
\begin{aligned}
b_m^{Im}(t) = \ & B \cdot \left[\left(\frac{V_k^{Re}(t)}{Z_{eqv}} + h \cdot I_{km}^{Re}(t) \right) \sin(\omega\tau) - \left(\frac{V_k^{Im}(t)}{Z_{eqv}} + h \cdot I_{km}^{Im}(t) \right) \cos(\omega\tau) \right] + \\
+ \ & A \cdot \left[\left(\frac{V_m^{Re}(t)}{Z_{eqv}} + h \cdot I_{mk}^{Re}(t) \right) \sin(\omega\tau) - \left(\frac{V_m^{Im}(t)}{Z_{eqv}} + h \cdot I_{mk}^{Im}(t) \right) \cos(\omega\tau) \right]
\end{aligned}
$$

$$(3.105)$$

where Z_{eqv}, h, A, and B are constant defined by:

$$
\begin{aligned}
Z_{eqv} = Z + \frac{R}{4} \qquad\qquad & h = \frac{Z - R/4}{Z + R/4} \\
A = \frac{R}{4Z_{eqv}} \qquad\qquad & B = \frac{Z}{Z_{eqv}}
\end{aligned}
$$

$$(3.106)$$

Alternatively, (3.103) may be rewritten, as follows:

$$
\tilde{\mathbf{I}}(t) = \mathbf{Y}^{Z_{eqv}} \cdot \tilde{\mathbf{V}}(t) - \tilde{\mathbf{b}}(t - \tau) \tag{3.107}
$$

Figures 3.20 and 3.21 show the uncoupled real and imaginary DPCM circuits of a lossy transmission line, according to (3.103).
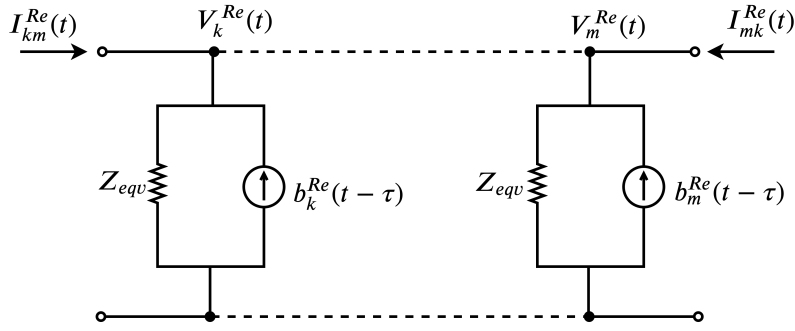
Figure 3.20: Real DPCM circuit of a lossy line
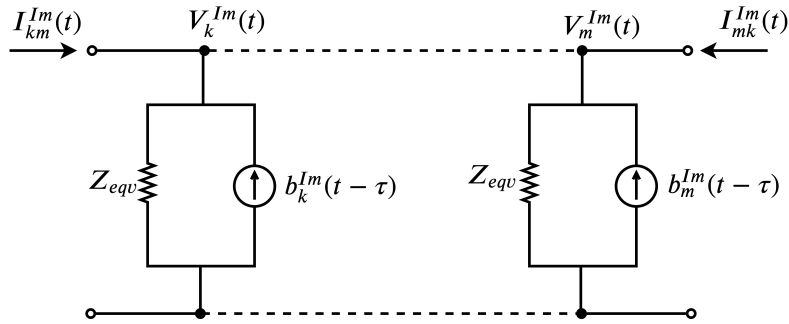
Figure 3.21: Imaginary DPCM circuit of a lossy line

The values of the history source $\tilde{b}_k$ and $\tilde{b}_m$ at $(t - \tau)$ are obtained from a memory vector that must delay back the number of time step that fit into the line travel time, as performed for the lossless line model.

If the travel time τ is not a multiple of the step Δt, then an interpolation method must be used to determine the past terms values at time $(t - \tau)$. The linear interpolation method (described in Appendix A.2) is employed in this work for computational development of this DPCM model into a ESA software that is discussed in Chapter 6.

3.4 Electrical Network Solution Methodology

A solution methodology for electromagnetic transients through the nodal analysis technique has been reviewed in Section 2.5 in terms of instantaneous quantities by employing the companion models proposed in [14]. In this present subsection, the solution of electrical network transients is developed upon the dynamic phasor companion models. This methodology is referred to as *Dynamic Phasors Transient Simulation* (DPTS) [12].

In developing the DPTS methodology, the nodal analysis is employed by applying the KCL to each network node in order to obtain a set of algebraic equations, which can naturally be written in matrix form.

For the sake of illustration, let one consider the generic electrical network depicted in Figure 3.22 comprising n buses.
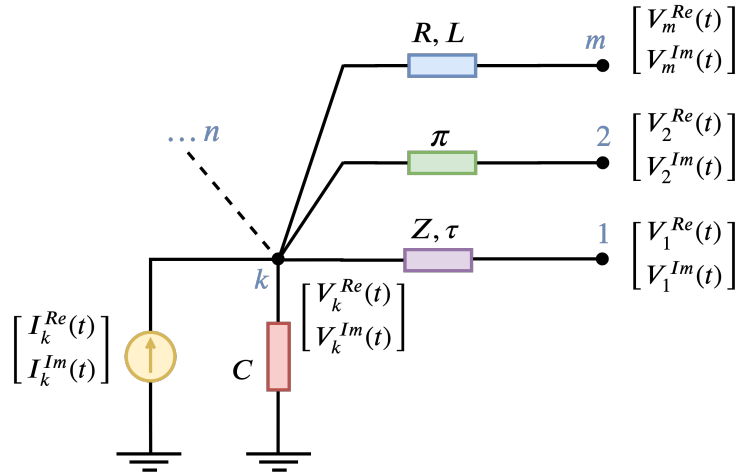
Figure 3.22: Generic electrical network with n buses

Representing voltages and currents of this circuit as dynamic phasors, and its basic network components by tensors in parallel with their respective history current sources, the equivalent DPCM circuit of Figure 3.23 is obtained:
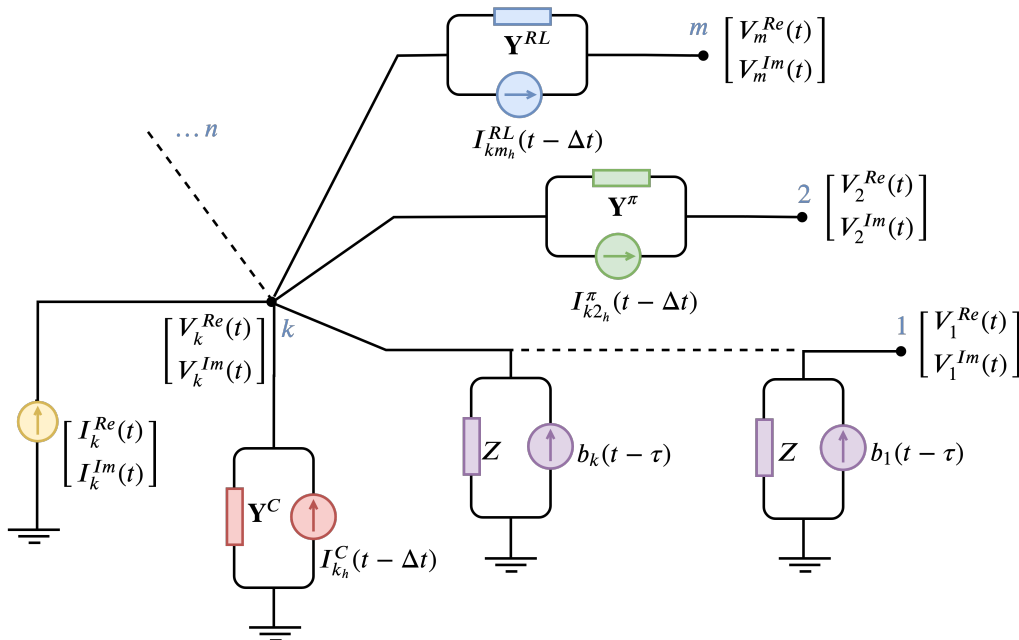
Figure 3.23: Generic network represented by DPCM models

One should note that, when the KCL is applied to this network, the history current source $I_{km_h}^{RL}(t - \Delta t)$ of the RL branch shall account for both k and m positions of the nodal history vector. Following the convention established in Chapter 2, it accounts subtracting for node k and adding for node m.

Therefore, employing the KCL in the network of Figure 3.23, grouping constant coefficients relative to the same state-variable, and omitting the time argument (t), the resulting expression can be written in a matrix form, as follows:

$$
\begin{bmatrix} I_1^{Re} \\ I_1^{Im} \\ \vdots \\ I_k^{Re} \\ I_k^{Im} \\ \vdots \\ I_m^{Re} \\ I_m^{Im} \\ \vdots \\ I_n^{Re} \\ I_n^{Im} \end{bmatrix}
-
\begin{bmatrix} I_{1_h}^{Re} \\ I_{1_h}^{Im} \\ \vdots \\ I_{k_h}^{Re} \\ I_{k_h}^{Im} \\ \vdots \\ I_{m_h}^{Re} \\ I_{m_h}^{Im} \\ \vdots \\ I_{n_h}^{Re} \\ I_{n_h}^{Im} \end{bmatrix}
=
\begin{bmatrix}
y_{11}^{11} & y_{11}^{12} & \cdots & y_{1k}^{11} & y_{1k}^{12} & \cdots & y_{1m}^{11} & y_{1m}^{12} & \cdots & y_{1n}^{11} & y_{1n}^{12} \\
y_{11}^{21} & y_{11}^{22} & \cdots & y_{1k}^{21} & y_{1k}^{22} & \cdots & y_{1m}^{21} & y_{1m}^{22} & \cdots & y_{1n}^{21} & y_{1n}^{22} \\
\vdots & & & & & & & & & & \\
y_{k1}^{11} & y_{k1}^{12} & \cdots & y_{kk}^{11} & y_{kk}^{12} & \cdots & y_{km}^{11} & y_{km}^{12} & \cdots & y_{kn}^{11} & y_{kn}^{12} \\
y_{k1}^{21} & y_{k1}^{22} & \cdots & y_{kk}^{21} & y_{kk}^{22} & \cdots & y_{km}^{21} & y_{km}^{22} & \cdots & y_{kn}^{21} & y_{kn}^{22} \\
\vdots & & & & & & & & & & \\
y_{m1}^{11} & y_{m1}^{12} & \cdots & y_{mk}^{11} & y_{mk}^{12} & \cdots & y_{mm}^{11} & y_{mm}^{12} & \cdots & y_{mn}^{11} & y_{mn}^{12} \\
y_{m1}^{21} & y_{m1}^{22} & \cdots & y_{mk}^{21} & y_{mk}^{22} & \cdots & y_{mm}^{21} & y_{mm}^{22} & \cdots & y_{mn}^{21} & y_{mn}^{22} \\
\vdots & & & & & & & & & & \\
y_{n1}^{11} & y_{n1}^{12} & \cdots & y_{nk}^{11} & y_{nk}^{12} & \cdots & y_{nm}^{11} & y_{nm}^{12} & \cdots & y_{nn}^{11} & y_{nn}^{12} \\
y_{n1}^{21} & y_{n1}^{22} & \cdots & y_{nk}^{21} & y_{nk}^{22} & \cdots & y_{nm}^{21} & y_{nm}^{22} & \cdots & y_{nn}^{21} & y_{nn}^{22}
\end{bmatrix}
\cdot
\begin{bmatrix} V_1^{Re} \\ V_1^{Im} \\ \vdots \\ V_k^{Re} \\ V_k^{Im} \\ \vdots \\ V_m^{Re} \\ V_m^{Im} \\ \vdots \\ V_n^{Re} \\ V_n^{Im} \end{bmatrix}
$$

$$(3.108)$$

where each 2x2 block of the nodal admittance matrix is obtained following the formation rule:

$$
\begin{bmatrix} y_{kk}^{11} & y_{kk}^{12} \\ y_{kk}^{21} & y_{kk}^{22} \end{bmatrix} = \sum_m \mathbf{Y}_{km}
\qquad
\begin{bmatrix} y_{km}^{11} & y_{km}^{12} \\ y_{km}^{21} & y_{km}^{22} \end{bmatrix} = -\mathbf{Y}_{km}
\qquad (3.109)
$$

In a compact form, (3.108) may be rewritten, as follows:

$$
\tilde{\mathbf{I}}(t) - \tilde{\mathbf{I}}_{\mathbf{h}}(t - \Delta t) = \mathbf{Y} \cdot \tilde{\mathbf{V}}(t) \qquad (3.110)
$$

where:

$\tilde{\mathbf{I}}(t)$: nodal current vector with real and imaginary DP components;

$\tilde{\mathbf{I}}_{\mathbf{h}}(t - \Delta t)$: nodal history source vector with real and imaginary DP;

$\mathbf{Y}$: nodal admittance matrix obtained from (3.109);

$\tilde{\mathbf{V}}(t)$: nodal voltage vector with real and imaginary DP components.

It is important to emphasize that, in this formulation, the equivalent tensors of each network component are considered to build the nodal admittance matrix, whereas the nodal current vector must be subtracted from the history sources vector. Moreover, this formulation can also be applied to the ESA network solution by neglecting the history source vector and building the nodal admittance matrix following the notation depicted in Section 3.2.

Completing the description of the DPTS solution methodology, the general procedure for determining unknown network voltages detailed in Section 2.5.1.1 is fully applied to (3.110) in terms of DP. As a result, this approach constitutes a suitable interface for application into ESA software, enabling the analysis of the network transients, which allows extending the simulation scope of this tool toward the subsynchronous resonance range. In Chapter 6, it is detailed the computational implementation and validation of the DPTS modeling into a commercial ESA software.

The network interface with other equipment models should be performed through the real ($\Re$) and imaginary ($\Im$) reference frame. Thus, the connection with equipment models that are given in other coordinate systems, such as the dq coordinate system of synchronous machines simulation models (Chapter 4), should be intermediated by a transform matrix to convert the equipment state-variables so as to allow a direct interface with the network reference frame.

Validation Results Using MATLAB

In order to validate the DPCM equations formulated in this chapter, the network solution algorithm for the time-domain analysis of fast transients has been implemented in the MATLAB software. Thus, simulation results obtained with MATLAB are compared to the results of PSCAD/EMTDC, which is assumed as the reference for validation purposes. It is shown that the DPCM representation allows incorporating changes in the network topology along with the dynamic simulation through piecewise linear approximations, requiring time steps smaller than typically adopted in ESA studies.

For the sake of simplicity, both instantaneous and dynamic phasor approaches are implemented in MATLAB assuming zero initial conditions. Hence, results obtained with the dynamic phasor technique are referred to as `MATLAB-DPCM`, whereas results from the instantaneous modeling are denoted as `MATLAB-Dommel`. Besides, the test systems simulations are also carried out using PSCAD/EMTDC.

Let one consider the test system A presented in Figure 3.24 whose interest variables are the inductor current $i_L(t)$ and the capacitor voltage $v_C(t)$.
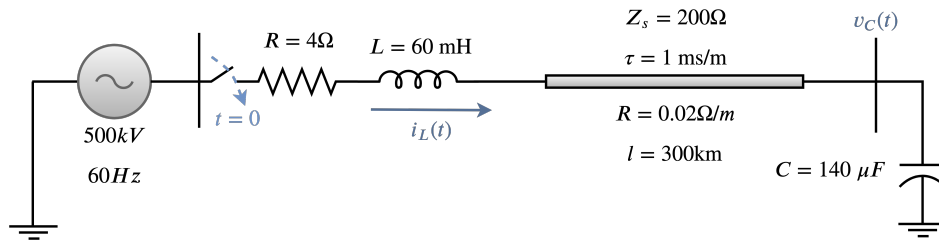
Figure 3.24: Test system A

Following the circuit energization at $t = 0$, the instantaneous inductor current and capacitor voltage waveforms present the dynamic behavior are shown in Figures 3.25 and 3.26, respectively. The time step adopted in the simulations is 20 μs, and the voltage source angle is zero at the switching instant.
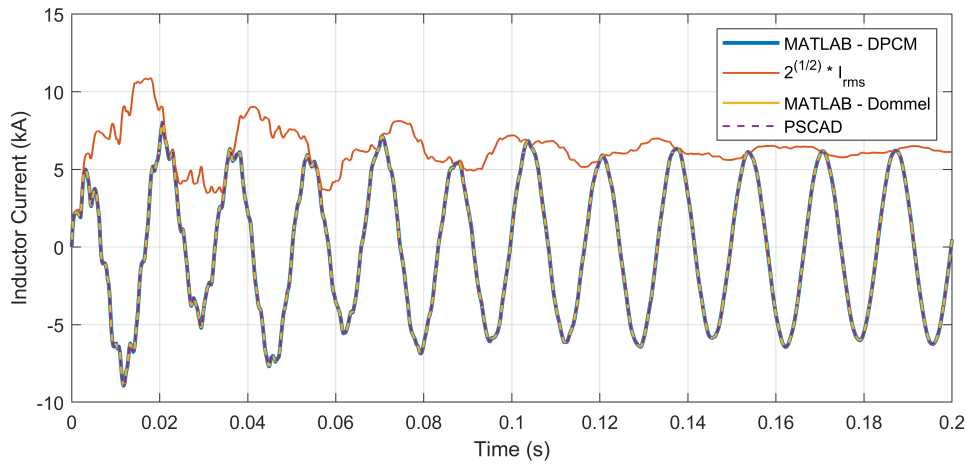
Figure 3.25: Test system A: inductor current in kA
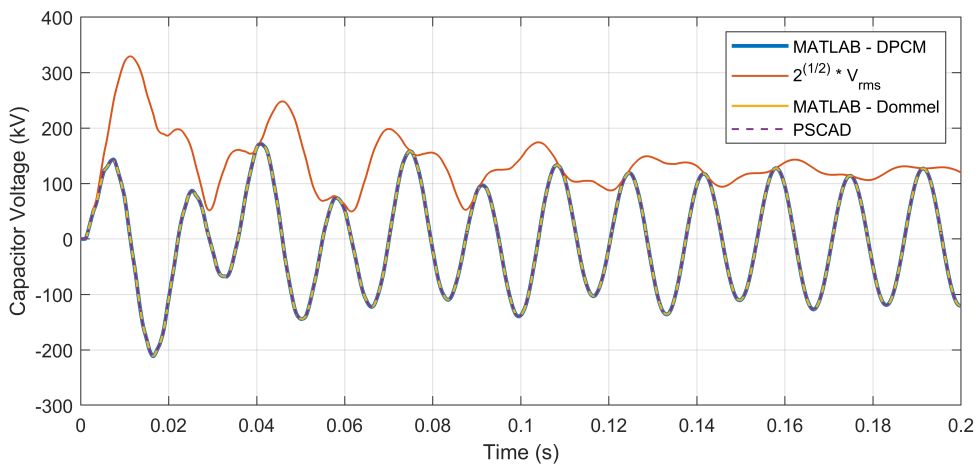
Figure 3.26: Test system A: capacitor voltage in kV

The simulations demonstrate that the DPCM equations provide results in good

agreement with the PSCAD results. The RMS current and voltage are also provided and multiplied by $\sqrt{2}$ to highlight the envelope dynamic behavior of these quantities. In this case, the resistance losses are considered through the equations given in Section 3.3.5.2. The following example show an alternative way to represent long transmission line losses.

The test system B illustrated in Figure 3.27 is modified from the test system 2a of reference [12]. In this case, the resistance losses are modeled externally to the Bergeron model, using lumped resistances and the lossless line model of Section 3.3.5.1.
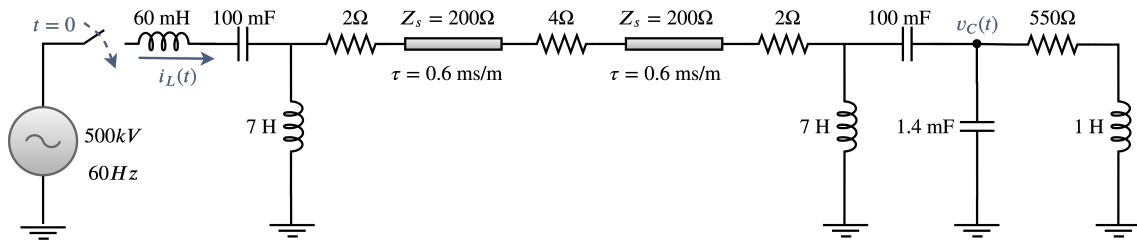
Figure 3.27: Test system B

Figures 3.28 and 3.29 presents the simulation results of System B for the instantaneous inductor current and capacitor voltage waveforms, respectively. The simulation parameters adopted for this system are the same employed for Test System A, but the time frame is reduced to 150 ms to provide a clearer perception of the waveforms since they present a more oscillatory transient.
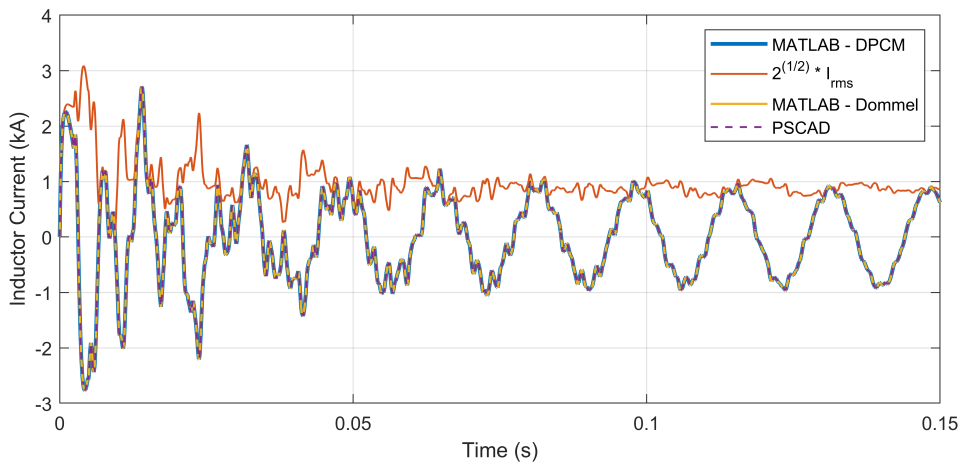
Figure 3.28: Test system B: inductor current in kA
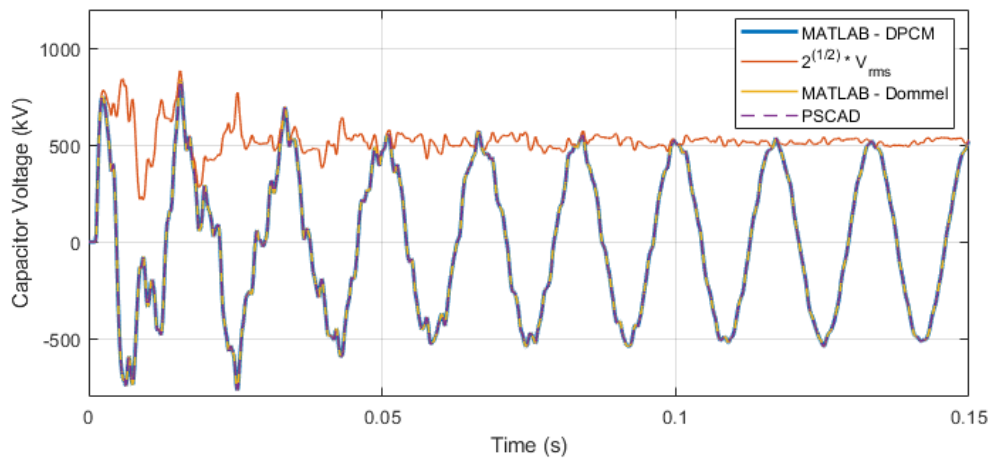
Figure 3.29: Test system B: capacitor voltage in kV

From the results of System B, it is shown that both representations of resistance losses give time-domain results in accordance with the PSCAD. Therefore, once the DPCM equations and the network solution methodology are validated, their implementation in ANATEM software is described in Chapter 6, considering steady-state initialization, as well as the electrical and mechanical equations of the synchronous machine to be discussed in the following chapters.

Chapter 4

Synchronous Machine Theory

This chapter reviews the mathematical developments of the synchronous machine model appropriate for subsynchronous resonance and electromechanical stability studies. This model presents a suitable interface with the DPCM methodology presented in Chapter 3 for the analysis of electrical network dynamics.

The synchronous generator model studied in this thesis is modular and convenient for representation in multi-machine systems. It provides a direct interface to couple *electrical equations* associated with the generator and *mechanical equations* associated with the turbine-generator shaft (described in Chapter 5). The main difference between the machine model adopted in SSR and ESA studies is related to the alternative of considering or not the stator flux variation, so-called the transformer effect. Representing the stator flux dynamics is a fundamental feature to make the machine model consistent with the study of electrical network dynamics. Consequently, this interface enables the analysis of interactions between *transients of the electrical transmission system* and *torsional oscillations of the turbine-generator shaft*. Additionally, in this analysis, the machine model should consider the variation of machine voltages and parameters with frequency.

In order to review the synchronous machine models adopted in time-domain simulations, associated deductions are presented upon the physical laws that describe relevant phenomena related to fluxes, voltages, currents, and rotational speed. Readers familiar with these basic concepts can skip directly to Section 4.6, where the synchronous machine simulation models for SSR analysis are depicted. This modeling is rooted in the broadly used Park Transformation (dq0 Transformation) to project the stator quantities (voltages, currents, and fluxes) onto rotor coordinate (dq-axes). The advantage of this transformation is that the resultant machine's inductance matrix comprises constant coefficients expressed into an appropriate per

unit (pu) system. A more detailed description of synchronous machine theory can be found in several references in the literature [1, 47, 51, 52].

4.1 Physical Description

The synchronous machine consists of two basic structures: the *rotor* and the *stator*. A schematic diagram of a three-phase synchronous machine with one pair of field poles is depicted in Figure 4.1. The three-phase windings of the stator (or armature) are uniformly distributed and placed 120 degrees apart in space [1].
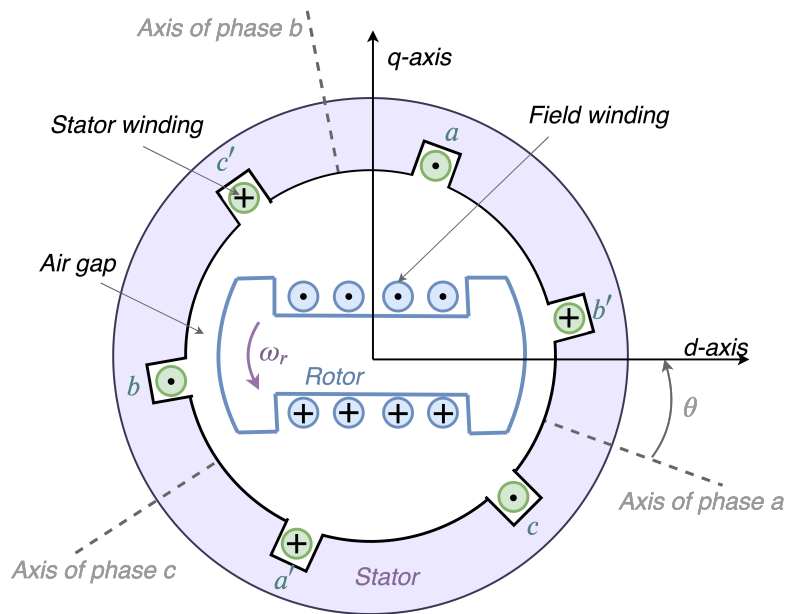
Figure 4.1: Schematic diagram of a three-phase synchronous machine

The rotor has a primary field (fd) winding connected to a source of direct current (DC), which provides the excitation voltage e_{fd} and the field current i_{fd}. As the rotor revolves at synchronous speed (ω_s), the field windings produce a rotating magnetic field, which induces alternating voltages 120 electrical degrees displaced in the three-phase stator windings. If the machine supplies a three-phase balanced load, the armature will carry balanced three-phase AC currents. These currents produce a rotating magnetic field in the air-gap at synchronous speed. The interaction between those two (rotor and stator) magnetic fields produces the *electromagnetic torque* applied to the rotor and stator. In steady-state operating condition, the resultant electromagnetic torque is constant and rotates along the stator's periphery at speed ω_s.

The machine basic equations are the same despite the number of pole pairs since the armature windings are uniformly distributed within multiple sets of coils. Because

of that, the general synchronous machine equations are written in terms of electrical degrees, where 180 electrical degrees correspond to the angle between two adjacent north and south poles. The relationship between electrical (θ_{ele}) and mechanical (θ_{mec}) degrees is given by:

$$\theta_{\text{ele}} = \frac{p_f}{2} \cdot \theta_{\text{mec}} \tag{4.1}$$

where p_f is the number of field poles. It should be noted that one pole pair ($p_f/2$) covers 2π radians or 360 electrical degrees. The mechanical speed of the machine rotor is obtained from the number of field poles and the electrical frequency of stator currents, as follows:

$$n = \frac{120 \cdot f}{p_f} \tag{4.2}$$

where n is the mechanical rotational speed in rpm, and f is the electrical frequency in Hz.

The machine rotor is classified into two construction types depending on its physical characteristics and designed rotational speed: (i) salient (or projecting) poles rotor, more appropriate to operate with low rotational speeds; and (ii) cylindrical (or round) rotor, adequate to operate at high rotational speeds.

Hydraulic turbines operate at low speeds and, therefore, require a large number of poles to produce the rated frequency. For this reason, a structure with salient poles is more appropriate. Generally, they are also equipped with short-circuit damper (or amortisseurs) windings located in the pole faces, whose primary purpose is to increase the damping of electromechanical oscillations. On the other hand, steam or gas turbines (called turbogenerators) are designed to operate at high speeds, so a two or four-pole cylindrical structure is recommended. The intrinsic design features of round rotors do not allow the use of damping windings. However, its solid steel rotor structure provides multiple paths for eddy currents, whose effect is equivalent to the representation of damping windings on direct and quadrature axes [1].

In regard to the symmetry around the polar and inter-polar axes of the rotor magnetic circuits (depicted in Figure 4.1), the following coordinate reference is defined:

d-axis: direct axis, magnetically centered in the north pole;

q-axis: quadrature axis, 90 electrical degrees ahead of d-axis, counterclockwise direction.

Rotating Magnetic Field

The three-phase currents (i_a, i_b, i_c) in the stator windings produce corresponding magnetomotive forces (MMF) described as follows:

$$\text{MMF}_a = K i_a \cos \alpha$$
$$\text{MMF}_b = K i_b \cos (\alpha - 2\pi/3) \qquad (4.3)$$
$$\text{MMF}_c = K i_c \cos (\alpha + 2\pi/3)$$

where α is the angle along stator's periphery with respect to the center of the magnetic axis of phase a, and K is a constant. It should be noted that each MMF is a stationary wave, displaced 120 electrical degrees apart from each other, with a magnitude proportional to the associated instantaneous current.

Consider balanced three-phase currents and time origin at the instant where i_a reaches its maximum instantaneous value (I_m). Therefore, the phase currents are expressed, as follows:

$$i_a = I_m \sin (\omega_s t)$$
$$i_b = I_m \sin (\omega_s t - 2\pi/3) \qquad (4.4)$$
$$i_c = I_m \sin (\omega_s t + 2\pi/3)$$

where $\omega_s = 2\pi f$ = angular frequency of stator currents in electrical rad/s.

The net MMF wave due to the three-phase currents in the stator windings is:

$$\text{MMF}_{\text{total}} = \text{MMF}_a + \text{MMF}_b + \text{MMF}_c$$
$$\text{MMF}_{\text{total}} = K i_a \cos \alpha + K i_b \cos (\alpha - 2\pi/3) + K i_c \cos (\alpha + 2\pi/3) \qquad (4.5)$$

Substituting (4.4) into (4.5), and after some basic algebraic manipulations, results:

$$\text{MMF}_{\text{total}} = K I_m \cos (\alpha - \omega_s t) \qquad (4.6)$$

One should note that the net MMF wave presents a sinusoidal spatial distribution and travels with constant angular speed at ω_s electrical rad/s along the stator's periphery.

It is also worth noting that the electromagnetic torque on the rotor acts in a direction so as to align both (stator and rotor) rotational magnetic fields. The machine load has a fundamental influence on the rotating MMF magnitude and relative angular displacement with respect to the rotor's MMF wave. Operating as a generator, the

rotor magnetic field leads the stator field so that the electromagnetic torque acts opposite to the rotational direction. On the contrary, operating as a motor, the rotor magnetic field lags the stator field, and the torque acts in the same rotational direction. As a result, a generator must be supplied by a forward torque of a prime mover in the rotor, whereas a motor is fed by AC currents which produce a forward magnetic field in the stator.

4.2 Basic Electrical Equations

The synchronous machine mathematical model comprises two basic sets of voltages and flux linkage equations related to the stator and rotor circuits. The stator circuit accounts for three-phase armature equations, whereas the rotor circuits contribute with field and damper equations. The damper circuits do not exist physically and take different forms based on the rotor type (cylindrical or salient poles). For analytical purposes, currents flowing in damper windings may be represented by a limited number of fictitious closed circuits in each rotor axis. The subscripts kd and kq are respectively used to denote damper circuits in d- and q-axis. For ESA and SSR studies, it is common practice considering: (i) one damper in d-axis (kd) and one damper in q-axis (kq) for a salient pole rotor; (ii) one damper in d-axis (kd) and two dampers in q-axis ($kq1$ and $kq2$) for a cylindrical rotor [1].

A major concern in SSR studies is related to the performance of turbogenerators, so that machine equations are developed here considering the presence of two damper windings in q-axis. Figure 4.2 exhibit the basic circuits of a synchronous machine.
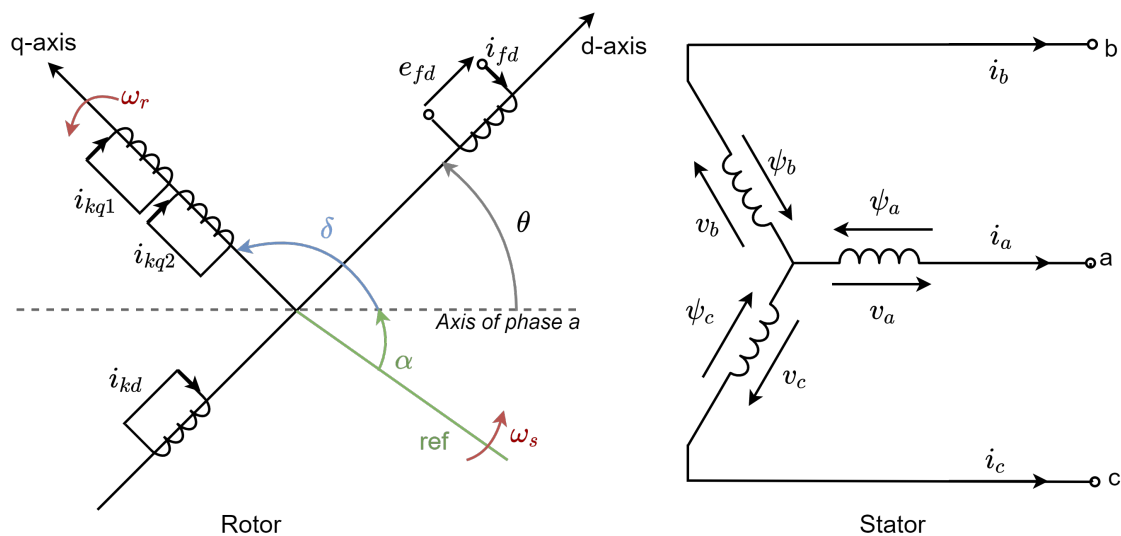
Figure 4.2: Stator and rotor circuits of a synchronous machine

In formulating electrical equations of a synchronous machine, a broad set of symbols

and subscripts are involved. Thus, the following notation must be specified [1]:

$$v_a, v_b, v_c \quad = \quad \text{instantaneous stator phase-to-neutral voltages}$$

$$i_a, i_b, i_c \quad = \quad \text{instantaneous stator currents}$$

$$\psi_a, \psi_b, \psi_c \quad = \quad \text{instantaneous stator flux linkages}$$

$$e_{fd} \quad = \quad \text{instantaneous field voltage}$$

$$i_{fd}, i_{kd}, i_{kq1}, i_{kq2} \quad = \quad \text{instantaneous field and damper circuit currents}$$

$$r_{fd}, r_{kd}, r_{kq1}, r_{kq2} \quad = \quad \text{rotor circuit resistances}$$

$$l_{aa}, l_{bb}, l_{cc} \quad = \quad \text{self-inductances of stator windings}$$

$$l_{ab}, l_{bc}, l_{ca} \quad = \quad \text{mutual inductances between stator windings}$$

$$l_{ifd}, l_{ikd}, l_{ikq} \quad = \quad \text{mutual inductances between stator and rotor } (i = a, b, c)$$

$$L_{ffd}, L_{kkd}, L_{kkq1}, L_{kkq2} \quad = \quad \text{self-inductances of rotor circuits}$$

$$r_a \quad = \quad \text{stator resistance per phase}$$

For the sake of simplicity, it is also convenient to define the differential operator (p):

$$p = \frac{d}{dt}$$

In Figure 4.2, θ is the angle in electrical degrees by which the d-axis leads the magnetic axis of phase a. Therefore it varies linearly in time along with the machine rotor speed, denoted ω_r. In order to use a common reference for all machines in the system, the angle θ is given in (4.7) as a function of synchronous speed ω_s. The angle δ represents the initial displacement between q-axis and the network synchronous reference.

$$\theta = \omega_r t = \omega_s t - \delta + \pi/2 \tag{4.7}$$

If the rotor speed remains equal to ω_s, the angle δ remains constant. Otherwise, it will vary in time. The derivative of δ is equal to the difference between synchronous and the rotor speed, i.e.:

$$\frac{d\delta}{dt} = \omega_s - \omega_r \tag{4.8}$$

4.2.1   Voltage and Flux Linkage Equations - abc Reference

The stator and rotor windings are magnetically coupled as a function of the rotor position [47]. In developing the basic electrical equations, the instantaneous terminal

voltage v of any winding is given by:

$$v = \pm \sum ri \pm p\psi \tag{4.9}$$

where ψ is the flux linkage, r is the winding resistance and i is the current. The generator convention is adopted, so that positive directions of stator currents flow out of the machine terminals, whereas positive direction of field and damper currents flow into the machine.

The voltage equations with respect to stator and rotor windings may be expressed in a matrix form, as follows:

$$
\begin{bmatrix} v_a \\ v_b \\ v_c \\ e_{fd} \\ 0 \\ 0 \\ 0 \end{bmatrix}
=
\begin{bmatrix}
r_a & & & & & & \\
& r_a & & & & & \\
& & r_a & & & & \\
& & & r_{fd} & & & \\
& & & & r_{kd} & & \\
& & & & & r_{kq1} & \\
& & & & & & r_{kq2}
\end{bmatrix}
\cdot
\begin{bmatrix} -i_a \\ -i_b \\ -i_c \\ i_{fd} \\ i_{kd} \\ i_{kq1} \\ i_{kq2} \end{bmatrix}
+ p
\begin{bmatrix} \psi_a \\ \psi_b \\ \psi_c \\ \psi_{fd} \\ \psi_{kd} \\ \psi_{kq1} \\ \psi_{kq2} \end{bmatrix}
\quad [\text{V}] \quad (4.10)
$$

In a compact form, voltage equations may be divided into two subsets respective to stator and rotor quantities, as follows:

$$
\begin{bmatrix} \mathbf{V}_{abc} \\ \hline \mathbf{V}_R \end{bmatrix}
=
\begin{bmatrix} \mathbf{R}_{abc} & \mathbf{0} \\ \hline \mathbf{0} & \mathbf{R}_R \end{bmatrix}
\cdot
\begin{bmatrix} -\mathbf{I}_{abc} \\ \hline \mathbf{I}_R \end{bmatrix}
+ p
\begin{bmatrix} \mathbf{\Psi}_{abc} \\ \hline \mathbf{\Psi}_R \end{bmatrix}
\quad [\text{V}] \tag{4.11}
$$

where upercase variables denote matricial quantities.

The flux linkages coupling stator and rotor circuits are related through an inductance

matrix, as follows:

$$
\begin{bmatrix} \psi_a \\ \psi_b \\ \psi_c \\ \psi_{fd} \\ \psi_{kd} \\ \psi_{kq1} \\ \psi_{kq2} \end{bmatrix} = \left[\begin{array}{ccc:cccc} l_{aa} & l_{ab} & l_{ac} & l_{afd} & l_{akd} & l_{akq1} & l_{akq2} \\ l_{ba} & l_{bb} & l_{bc} & l_{bfd} & l_{bkd} & l_{bkq1} & l_{bkq2} \\ l_{ca} & l_{cb} & l_{cc} & l_{cfd} & l_{ckd} & l_{ckq1} & l_{ckq2} \\ \hdashline l_{fda} & l_{fdb} & l_{fdc} & L_{ffd} & L_{fkd} & & \\ l_{kda} & l_{kdb} & l_{kdc} & L_{fkd} & L_{kkd} & & \\ l_{kq1a} & l_{kq1b} & l_{kq1c} & & & L_{kkq1} & L_{kq12} \\ l_{kq2a} & l_{kq2b} & l_{kq2c} & & & L_{kq12} & L_{kkq2} \end{array} \right] \cdot \begin{bmatrix} -i_a \\ -i_b \\ -i_c \\ i_{fd} \\ i_{kd} \\ i_{kq1} \\ i_{kq2} \end{bmatrix} \quad \text{[Wb]} \quad (4.12)
$$

In a compact form:

$$
\left[\begin{array}{c} \boldsymbol{\Psi}_{abc} \\ \hdashline \boldsymbol{\Psi}_R \end{array} \right] = \left[\begin{array}{c:c} \mathbf{L}_{abc} & \mathbf{0} \\ \hdashline \mathbf{0} & \mathbf{L}_R \end{array} \right] \cdot \left[\begin{array}{c} -\mathbf{I}_{abc} \\ \hdashline \mathbf{I}_R \end{array} \right] \quad \text{[Wb]} \quad (4.13)
$$

The flux linkages, inductances, voltages and currents are respectively expressed in webers [Wb], henrys [H], volts [V] and amperes [A].

In the cylindrical rotor, mutual inductances between stator and rotor circuits vary in time as functions of the rotor position. On the contrary, the mutual and self-inductances between rotor circuits, as well as mutual and self-inductances relating to stator quantities, are constant due to the cylindrical structure of the stator.

The derivative flux linkage term $(p\psi)$ in (4.9) is computed as follows:

$$
\frac{d\psi}{dt} = \frac{d(Li)}{dt} = L\frac{di}{dt} + \frac{dL}{dt}i \quad (4.14)
$$

Therefore, regarding three-phase quantities, the expressions of stator voltages become complicated since mutual and self-inductances of stator circuits vary with rotor position θ. Table 4.1 provides expressions for the calculation of self and mutual inductances between stator windings, whereas Table 4.2 contains expressions of mutual inductances between stator and rotor circuits. A deeper explanation about these expressions can be found in excellent detail in [1].

In these expressions, symbols in lowercase denote inductances that vary with the rotor position, whereas capital letters imply constant coefficients of stator and rotor inductances.

Table 4.1: Stator Self and Mutual Inductances in henry [H]

Self-Inductances	Mutual Inductances
$l_{aa} = L_{aa0} + L_{aa2}\cos 2\left(\theta\right)$	$l_{ab} = l_{ba} = -L_{ab0} - L_{ab2}\cos\left(2\theta + \pi/3\right)$
$l_{bb} = L_{aa0} + L_{aa2}\cos 2\left(\theta - 2\pi/3\right)$	$l_{bc} = l_{cb} = -L_{ab0} - L_{ab2}\cos\left(2\theta - \pi\right)$
$l_{ca} = L_{aa0} + L_{aa2}\cos 2\left(\theta + 2\pi/3\right)$	$l_{ac} = l_{ba} = -L_{ab0} - L_{ab2}\cos\left(2\theta - \pi/3\right)$

Table 4.2: Mutual Inductances between Stator and Rotor Windings [H]

Stator (abc) and Field (fd)	Stator (abc) and Amortisseur (kd)
$l_{afd} = L_{afd}\cos\theta$	$l_{akd} = L_{akd}\cos\theta$
$l_{bfd} = L_{afd}\cos\left(\theta - 2\pi/3\right)$	$l_{bkd} = L_{akd}\cos\left(\theta - 2\pi/3\right)$
$l_{cfd} = L_{afd}\cos\left(\theta + 2\pi/3\right)$	$l_{ckd} = L_{akd}\cos\left(\theta + 2\pi/3\right)$
Stator (abc) and Amortisseur ($kq1$)	Stator (abc) and Amortisseur ($kq2$)
$l_{akq1} = -L_{akq1}\sin\theta$	$l_{akq2} = -L_{akq2}\sin\theta$
$l_{bkq1} = -L_{bkq1}\sin\left(\theta - 2\pi/3\right)$	$l_{bkq2} = -L_{bkq2}\sin\left(\theta - 2\pi/3\right)$
$l_{ckq1} = -L_{ckq1}\sin\left(\theta + 2\pi/3\right)$	$l_{ckq2} = -L_{ckq2}\sin\left(\theta + 2\pi/3\right)$

4.2.2 The dq0 Transformation

The voltage and flux linkage equations of stator and rotor windings form the *basic set of electrical equations* that completely describe the dynamic behavior of a synchronous machine. However, the three-phase reference used in the previous subsections for stator quantities yields an inductance matrix (4.12) composed by elements that vary with rotor position and, consequently, with time. For instance, substituting the inductances expressions given in Tables 4.1 and 4.2 into the rotor flux linkage equations yields:

$$\psi_{fd} = L_{ffd}i_{fd} + L_{fkd}i_{kd} - L_{afd}\left[i_a\cos\theta + i_b\cos\left(\theta - \frac{2\pi}{3}\right) + i_c\cos\left(\theta + \frac{2\pi}{3}\right)\right]$$

$$\psi_{kd} = L_{fkd}i_{fd} + L_{kkd}i_{kd} - L_{akd}\left[i_a\cos\theta + i_b\cos\left(\theta - \frac{2\pi}{3}\right) + i_c\cos\left(\theta + \frac{2\pi}{3}\right)\right] \quad (4.15)$$

$$\psi_{kq1} = L_{kkq1}i_{kq1} + L_{kq12}i_{kq2} + L_{akq1}\left[i_a\sin\theta + i_b\sin\left(\theta - \frac{2\pi}{3}\right) + i_c\sin\left(\theta + \frac{2\pi}{3}\right)\right]$$

$$\psi_{kq2} = L_{kkq2}i_{kq2} + L_{kq12}i_{kq1} + L_{akq2}\left[i_a\sin\theta + i_b\sin\left(\theta - \frac{2\pi}{3}\right) + i_c\sin\left(\theta + \frac{2\pi}{3}\right)\right]$$

From (4.15), observe that the self-inductances of rotor circuits and mutual induc-

tances between each other do not vary with the rotor position [1]. Only mutual inductances between rotor and stator vary periodically with θ, as shown in Table 4.2. Additionally, in these flux linkage equations, one can see that the stator currents combine in a convenient form in d-q axis in relation to the rotor position. This peculiarity leads to the definition of two new variables, which represent the stator currents referred to the rotor coordinates:

$$
\begin{cases}
i_d = k_d & \left[i_a \cos\theta + i_b \cos\left(\theta - \frac{2\pi}{3}\right) + i_c \cos\left(\theta + \frac{2\pi}{3}\right) \right] \\
i_q = -k_q & \left[i_a \sin\theta + i_b \sin\left(\theta - \frac{2\pi}{3}\right) + i_c \sin\left(\theta + \frac{2\pi}{3}\right) \right]
\end{cases}
\tag{4.16}
$$

Assuming k_d and k_q equal to 2/3, the peak values of currents i_d and i_q (for balanced sinusoidal conditions) become equal to the peak value (I_m) of the stator currents. This choice for these constants is considered in several references [1, 52] and it is also adopted here.

For a comprehensive degree of freedom, a third component should be included so that the three-phase currents may be transformed into three variables. However, the third variable must produce no magnetic field in the air-gap, since the currents i_d and i_q produce a field equivalent to that produced by the stator currents. Thus, a suitable third variable is the zero sequence current i_0 from the symmetrical components theory [43]:

$$
i_0 = \frac{1}{3} \left(i_a + i_b + i_c \right)
\tag{4.17}
$$

Equations (4.16) and (4.17) project the stator quantities, given in *abc* reference, on the rotor coordinate axes (dq0), eliminating any dependency with rotor position. It is referred to as the dq0 or **Park Transformation** [53]. Equation (4.18) presents the Park transformation matrix:

$$
\mathbf{P} = \frac{2}{3}
\begin{bmatrix}
\cos\theta & \cos\left(\theta - \frac{2\pi}{3}\right) & \cos\left(\theta + \frac{2\pi}{3}\right) \\
-\sin\theta & -\sin\left(\theta - \frac{2\pi}{3}\right) & -\sin\left(\theta + \frac{2\pi}{3}\right) \\
\frac{1}{2} & \frac{1}{2} & \frac{1}{2}
\end{bmatrix}
\implies \left[\mathbf{I}_{dq0} \right] = [\mathbf{P}] \cdot [\mathbf{I}_{abc}]
\tag{4.18}
$$

The inverse transformation matrix, which takes *dq0* quantities to the *abc* reference,

is given by:

$$\mathbf{P}^{-1} = \begin{bmatrix} \cos\theta & -\sin\theta & 1 \\ \cos\left(\theta - \frac{2\pi}{3}\right) & -\sin\left(\theta - \frac{2\pi}{3}\right) & 1 \\ \cos\left(\theta + \frac{2\pi}{3}\right) & -\sin\left(\theta + \frac{2\pi}{3}\right) & 1 \end{bmatrix} \implies [\mathbf{I}_{abc}] = [\mathbf{P}]^{-1} \cdot \left[\mathbf{I}_{dq0}\right] \quad (4.19)$$

The same transformation could be performed over flux linkage and voltage equations, i.e., the three-phase voltages v_a, v_b, v_c may also be converted into v_d, v_q, v_0 components and vice-versa.

The dq0 transformation gives a clearer physical representation concerning the influence of stator currents in d- and q-axes. Assuming balanced currents at frequency ω_s in the stator, and the rotor revolving at angular speed ω_r, currents i_d and i_q are given by:

$$\begin{aligned} i_d &= I_m \sin\left(\omega_s t - \omega_r' t + \phi\right) \\ i_q &= -I_m \cos\left(\omega_s t - \omega_r' t + \phi\right) \end{aligned} \quad (4.20)$$

where $\theta = \omega' t - \phi$ is the angle by which d-axis leads the magnetic center of phase a, as defined in Figure 4.1. If the stator currents and the rotor operate in synchronism, then $\omega_s = \omega_r$ and (4.20) becomes:

$$\begin{aligned} i_d &= I_m \sin\left(\phi\right) \\ i_q &= -I_m \cos\left(\phi\right) \end{aligned} \quad (4.21)$$

Equation (4.21) reveals that the components i_d and i_q behave as DC (constant) quantities in the case of balanced stator currents at the synchronous frequency. Thus, the resulting MMF wave rotates at the same rotor speed and, relative to the rotor, it appears to be stationary. Alternatively, when $\omega_s \neq \omega_r$, the currents i_d and i_q will vary sinusoidally at the slip frequency $(\omega_s - \omega_r)$.

4.2.3 Flux Linkage Equations - dq0 Reference

Applying the dq0 transformation to the *abc* quantities of (4.12) and rearranging the trigonometric functions, the following stator flux linkage equation is obtained in

terms of dq0 components:

$$
\begin{bmatrix} \psi_d \\ \psi_q \\ \psi_0 \\ \psi_{fd} \\ \psi_{kd} \\ \psi_{kq1} \\ \psi_{kq2} \end{bmatrix} = \begin{bmatrix} L_d & & & L_{afd} & L_{akd} & & \\ & L_q & & & & L_{akq1} & L_{akq2} \\ & & L_0 & & & & \\ \text{\textonehalf} L_{afd} & & & L_{ffd} & L_{fkd} & & \\ \text{\textonehalf} L_{akd} & & & L_{fkd} & L_{kkd} & & \\ & \text{\textonehalf} L_{akq1} & & & & L_{kkq1} & L_{kq12} \\ & \text{\textonehalf} L_{akq2} & & & & L_{kq12} & L_{kkq2} \end{bmatrix} \cdot \begin{bmatrix} -i_d \\ -i_q \\ -i_0 \\ i_{fd} \\ i_{kd} \\ i_{kq1} \\ i_{kq2} \end{bmatrix} \quad (4.22)
$$

The inductances L_d, L_q, and L_0 are defined, as follows:

$$
\begin{aligned}
L_d &= L_{aa0} + L_{ab0} + \text{\textthreequarters}\!/\!\text{\texttwo}\, L_{aa2} \\
L_q &= L_{aa0} + L_{ab0} - \text{\textthreequarters}\!/\!\text{\texttwo}\, L_{aa2} \\
L_0 &= L_{aa0} - 2L_{ab0}
\end{aligned} \quad (4.23)
$$

From (4.23), it is worth noting that all transformed inductances are constant. Therefore, in dq0 reference, the stator flux linkages are related to the stator and rotor currents through inductances that are independent of rotor position and, consequently, independent of time.

This result can be physically interpreted as if the three-phase stator windings were replaced by dummy *dq*0 windings in the rotor. These windings should rotate together with the rotor, inasmuch as the mutual inductances between those and the rotor windings are constant. Additionally, winding 0 is completely decoupled from the other windings and it can be disregarded under balanced conditions, where $i_a + i_b + i_c = 0$.

Therefore, the flux linkage equations in dq0 coordinates consist of three uncoupled systems, which allows dividing (4.22) into three subsets corresponding exclusively

of each dq0 circuit, as follows:

$$
\begin{bmatrix} \psi_d \\ \psi_{fd} \\ \psi_{kd} \\ \psi_q \\ \psi_{kq1} \\ \psi_{kq2} \\ \psi_0 \end{bmatrix} = \begin{bmatrix} L_d & L_{afd} & L_{akd} & & & & \\ \frac{3}{2}L_{afd} & L_{ffd} & L_{fkd} & & & & \\ \frac{3}{2}L_{akd} & L_{fkd} & L_{kkd} & & & & \\ & & & L_q & L_{akq1} & L_{akq2} & \\ & & & \frac{3}{2}L_{akq1} & L_{kkq1} & L_{kq12} & \\ & & & \frac{3}{2}L_{akq2} & L_{kq12} & L_{kkq2} & \\ & & & & & & L_0 \end{bmatrix} \cdot \begin{bmatrix} -i_d \\ i_{fd} \\ i_{kd} \\ -i_q \\ i_{kq1} \\ i_{kq2} \\ -i_0 \end{bmatrix} \quad (4.24)
$$

The inductance matrix of (4.24) is not symmetrical in terms of mutual inductance between the stator and rotor. This issue is resolved by adopting an appropriate per unit system as described in Section 4.3.

4.2.4 Voltage Equations - dq0 Reference

Transforming stator voltages of (4.10) into dq0 components, gives:

$$
v_d = p\psi_d - \psi_q p\theta - r_a i_d \tag{4.25}
$$

$$
v_q = p\psi_q + \psi_d p\theta - r_a i_q \tag{4.26}
$$

$$
v_0 = p\psi_0 - r_a i_0 \tag{4.27}
$$

The term $p\theta$ represents the rotor angular speed ω_r in electrical rad/s. It corresponds to the synchronous speed $\omega_s = 2\pi f$ in steady-state condition. The angle θ was previously defined in Figure 4.1 as the displacement between the axis of phase a and d-axis.

Equations (4.25), (4.26), and (4.27) are similar to the voltage equation of a static coil, except for the $-p\theta\psi_q$ and $p\theta\psi_d$ terms, resulting from the rotor motion. From these equations, the following terms are defined:

- $p\theta\psi_q = \omega_r\psi_q$ and $p\theta\psi_d = \omega_r\psi_d$ are referred to as **speed voltages**. These terms result from the flux change in space, and they represent dominant components of the stator voltages;

- $p\psi_d$ and $p\psi_q$ terms are called the **transformer voltages** resulting from the flux change in time. Under steady-state conditions, with sinusoidal and balanced stator currents, ψ_d and ψ_q, as well as v_d, v_q, i_d, i_q behave as constant quantities, so that $p\psi_d$ and $p\psi_q$ are zero. In ESA studies, these terms are typ-

ically neglected in the machine model. However, in SSR analysis, these terms have substantial influence and cannot be ignored.

Equation (4.28) exhibits the complete set of stator and rotor voltage equations in a matrix form with dq0 components.

$$
\begin{bmatrix} v_d \\ v_q \\ v_0 \\ e_{fd} \\ 0 \\ 0 \\ 0 \end{bmatrix} = \begin{bmatrix} r_a & & & & & & \\ & r_a & & & & & \\ & & r_a & & & & \\ & & & r_{fd} & & & \\ & & & & r_{kd} & & \\ & & & & & r_{kq1} & \\ & & & & & & r_{kq2} \end{bmatrix} \cdot \begin{bmatrix} -i_d \\ -i_q \\ -i_0 \\ i_{fd} \\ i_{kd} \\ i_{kq1} \\ i_{kq2} \end{bmatrix} + p \begin{bmatrix} \psi_d \\ \psi_q \\ \psi_0 \\ \psi_{fd} \\ \psi_{kd} \\ \psi_{kq1} \\ \psi_{kq2} \end{bmatrix} + p\theta \begin{bmatrix} -\psi_q \\ \psi_d \\ 0 \\ 0 \\ 0 \\ 0 \\ 0 \end{bmatrix}
$$

$$(4.28)$$

4.2.5 Electrical Power and Torque

At any time, the instantaneous three-phase power in the synchronous machine terminals is given by:

$$
P_t = [v_a i_a + v_b i_b + v_c i_c] \tag{4.29}
$$

In terms of dq0 components, the instantaneous power may be written as:

$$
P_t = \frac{3}{2} \left[v_d i_d + v_q i_q + 2 v_0 i_0 \right] \tag{4.30}
$$

Under steady-state condition with sinusoidal and balanced stator currents, $i_0 = 0$ and $v_0 = 0$, therefore:

$$
P_t = \frac{3}{2} \left[v_d i_d + v_q i_q \right] \tag{4.31}
$$

The electromagnetic torque is obtained from the power transferred across the air-gap, which is obtained by substituting the dq0 stator voltages (4.25), (4.26), and (4.27) into (4.30), as follows:

$$
P_t = \frac{3}{2} \left[i_d \left(\frac{d\psi_d}{dt} - \psi_q \frac{d\theta}{dt} - r_a i_d \right) + i_q \left(\frac{d\psi_q}{dt} + \psi_d \frac{d\theta}{dt} - r_a i_q \right) + i_0 \left(\frac{d\psi_0}{dt} - r_a i_0 \right) \right]
$$

$$(4.32)$$

After grouping the terms multiplying w_r, r_a, and $p\psi$, the following components of

the instantaneous power are recognized:

$$P_t = \overbrace{\frac{3}{2}\left(i_d \frac{d\psi_d}{dt} + i_q \frac{d\psi_q}{dt} + i_0 \frac{d\psi_0}{dt}\right)}^{\text{(i) Rate of magnetic energy change in the stator}} + \underbrace{\frac{3}{2}\left(i_q \psi_d - i_d \psi_q\right)\omega_r}_{\substack{\text{(ii) Power transferred} \\ \text{across the air-gap}}} - \overbrace{\frac{3}{2}r_a\left(i_d^2 + i_q^2 + i_0^2\right)}^{\substack{\text{(iii) Armature} \\ \text{resistance losses}}}$$

(4.33)

The electromagnetic torque T_e is derived from the term (ii) in (4.33), dividing the power transferred across the air-gap by the rotor angular speed in mechanical rad/s, as follows:

$$T_e = \frac{3}{2}\left(i_q\psi_d - i_d\psi_q\right) \cdot \frac{\omega_r}{\omega_{\text{mech}}}$$
$$T_e = \frac{3}{2}\left(i_q\psi_d - i_d\psi_q\right) \cdot \frac{pf}{2}$$

(4.34)

In summary, (4.22) and (4.28) describe voltages and flux linkages of stator and rotor circuits. Equations (4.30) and (4.34) provide the instantaneous three-phase power and the electromagnetic torque expressions. These equations completely specify the electrical dynamic behavior of a synchronous machine in terms of dq0 components. This set of equations are referred to as Park's equations [53], which are individually recap in Table 4.3.

Table 4.3: Voltage and flux linkage equations of the rotor and stator in dqo components

	Voltage [V]	Flux Linkage [Wb]
stator	$v_d = p\psi_d - \psi_q p\theta - r_a i_d$ $v_q = p\psi_q + \psi_d p\theta - r_a i_q$ $v_0 = p\psi_0 - r_a i_0$	$\psi_d = -L_d i_d + L_{afd} i_{fd} + L_{akd} i_{kd}$ $\psi_q = -L_q i_q + L_{akq1} i_{kq1} + L_{akq2} i_{kq2}$ $\psi_0 = -L_0 i_0$
rotor	$e_{fd} = p\psi_{fd} + r_{fd} i_{fd}$ $0 = p\psi_{kd} + r_{kd} i_{kd}$ $0 = p\psi_{kq2} + r_{kq1} i_{kq1}$ $0 = p\psi_{kq2} + r_{kq2} i_{kq2}$	$\psi_{fd} = L_{ffd} i_{fd} + L_{fkd} i_{kd} - \tfrac{3}{2} L_{afd} i_d$ $\psi_{kd} = L_{fkd} i_{fd} + L_{kkd} i_{kd} - \tfrac{3}{2} L_{akd} i_d$ $\psi_{kq1} = L_{kkq1} i_{kq1} + L_{kq12} i_{kq2} - \tfrac{3}{2} L_{akq} i_{q1}$ $\psi_{kq2} = L_{kq12} i_{kq2} + L_{kq12} i_{kq1} - \tfrac{3}{2} L_{akq} i_{q2}$
	Three-Phase Power [W]	Electromagnetic Torque [N.m]
	$P_t = \tfrac{3}{2}\left[v_d i_d + v_q i_q + v_0 i_0 \right]$	$T_e = \tfrac{3}{2}\left(i_q \psi_d - i_d \psi_q \right) \cdot \frac{p_f}{2}$

4.3 Per Unit System

The fundamental purpose of developing a per unit (pu) system for synchronous machines is describing the basic equations in terms of equivalent circuits without requiring ideal transform ratios between quantities of different windings (stator and rotor). The previous subsection presented the basic equations considering electrical variables and parameters in physical units (amperes, volts, henrys, etc.). From now on, a per unit system is assigned, using the formulation presented in [52], to specify a normalized system of equations. This procedure requires the following steps:

1. Definition of base values for stator quantities;

2. Express the machine equations in dq0 reference as per unit values, dividing the machine variables and parameters by their appropriate base quantities:

$$\text{per unit quantity} = \frac{\text{physical quantity}}{\text{compatible base quantity}}$$

3. The kVA base choice for the rotor is established to obtain *reciprocal per unit*

mutual inductances between rotor and stator in the flux linkage equations;

4. The base currents of rotor circuits are also established in order to acquire reciprocal per unit mutual inductances between the stator and rotor circuits in each axis. This system is referred to as the L_{ad}-*base reciprocal per unit system.*

It should be emphasized that primary base quantities (for example: voltage, current, and frequency) may be arbitrarily chosen at first. Afterwards, fundamental circuit equations automatically establish the bases for remaining variables and circuit parameters (such as flux linkages, resistance, inductance, et cetera).

Let one define the following primary base values for the stator:

$$\boldsymbol{v_{s_{base}}} \quad = \quad \text{peak value of rated phase-to-neutral voltage, volts [V]}$$

$$\boldsymbol{i_{s_{base}}} \quad = \quad \text{peak value of rated phase current, amperes [A]}$$

$$\boldsymbol{f_{base}} \quad = \quad \text{rated frequency, hertz [Hz]}$$

The remaining secondary bases are determined, as follows:

$$\boldsymbol{\omega_{base}} \quad = \quad 2\pi f_{base} = \text{synchronous angular speed, [elec rad/s]}$$

$$\boldsymbol{\omega_{m_{base}}} \quad = \quad \omega_{base} \cdot \frac{2}{p_f} = \text{mechanical angular speed, [mech rad/s]}$$

$$\boldsymbol{Z_{s_{base}}} \quad = \quad \frac{v_{s_{base}}}{i_{s_{base}}} = \text{impedance, ohms } [\Omega]$$

$$\boldsymbol{\psi_{s_{base}}} \quad = \quad L_{s_{base}} i_{s_{base}} = \frac{v_{s_{base}}}{\omega_{base}} = \text{flux linkage, webers-turns}$$

$$\boldsymbol{V_{RMS_{base}}} \quad = \quad \frac{v_{s_{base}}}{\sqrt{2}} = \text{RMS phase-to-neutral voltage, volts [V]}$$

$$\boldsymbol{I_{RMS_{base}}} \quad = \quad \frac{i_{s_{base}}}{\sqrt{2}} = \text{RMS phase current, amperes [A]}$$

$$\boldsymbol{S_{base}} \quad = \quad 3 V_{RMS_{base}} I_{RMS_{base}} = 3\frac{v_{s_{base}}}{\sqrt{2}}\frac{i_{s_{base}}}{\sqrt{2}}$$

$$= \quad \frac{3}{2} v_{s_{base}} i_{s_{base}} = \text{three-phase power, volt-amperes [VA]}$$

$$\boldsymbol{T_{base}} \quad = \quad \frac{S_{base}}{\omega_{m_{base}}} = \frac{3}{2} \cdot \frac{p_f}{2} \cdot \psi_{s_{base}} i_{s_{base}}$$

$$= \quad \text{electromagnetic torque, newton-meters [N.m]}$$

Due to the symmetry between stator circuits, a unified per unit system can be specified for all three-phase stator windings. Differently, each rotor winding must account for its own base quantities, since they are unequally coupled with each

other. Therefore, the base choice for each rotor circuit should be made following the same premises adopted in the transformer model, aiming to eliminate the ideal transformer ratio between different coils. Also, the base choice for rotor quantities must assure reciprocal mutual inductances in per unit between all windings in each axis. The fundamental principle in this choice is that the volt-ampere base must be the same for all machine windings, so that the equivalent per unit circuit yields reciprocal mutual inductances.

4.3.1 Per Unit Voltage Equations

The Park's equations presented in Table 4.3 are converted into a per unit system of equations by employing the base values properly chosen. In the resulting set of equations, overline quantities $(\overline{v}, \overline{i}, \overline{\psi}, \overline{\omega}, \overline{r}, \overline{L})$ denote per unit values.

Let one first consider (4.25):

$$v_d = p\psi_d - \psi_q p\theta - r_a i_d$$

Dividing by $v_{s_{base}}$, gives:

$$\overline{v}_d = \frac{v_d}{v_{s_{base}}} = \frac{p\psi_d}{(v_{s_{base}})} - \frac{\psi_q}{v_{s_{base}}} p\theta - \frac{r_a i_d}{v_{s_{base}}} \tag{4.35}$$

Recognizing that $v_{s_{base}} = \omega_{base} \psi_{s_{base}} = Z_{s_{base}} i_{s_{base}}$, and $p\theta = \omega_r$. Equation (4.35) may be rewritten as:

$$\overline{v}_d = p\left(\frac{1}{\omega_{base}} \frac{\psi_d}{\psi_{s_{base}}}\right) - \frac{\psi_q}{\psi_{s_{base}}} \frac{\omega_r}{\omega_{base}} - \frac{r_a}{Z_{s_{base}}} \frac{i_d}{i_{s_{base}}}$$

$$\therefore \overline{v}_d = \frac{1}{\omega_{base}} p\overline{\psi}_d - \overline{\psi}_q \overline{\omega}_r - \overline{r}_a \overline{i}_d \tag{4.36}$$

Equation (4.36) regards time in seconds. Alternatively, it is also common practice to normalize the entire expression by defining the following base time, which represents the time required for the rotor to move one electrical radian at synchronous speed:

$$t_{base} = \frac{1}{\omega_{base}} = \frac{1}{2\pi f_{base}} = \text{base time, [s]} \tag{4.37}$$

Using t_{base}, it is possible to define the per unit derivative $\overline{p}$, as follows:

$$\overline{p} = \frac{d}{d\overline{t}} = \frac{1}{\omega_{base}} \frac{d}{dt} = \frac{1}{\omega_{base}} p \tag{4.38}$$

Therefore, with time in per unit, and performing similar normalization for stator voltages (4.26) and (4.27), follows that:

$$\overline{v}_d = \overline{p}\overline{\psi}_d - \overline{\psi}_q\overline{\omega}_r - \overline{r}_a\overline{i}_d \tag{4.39}$$

$$\overline{v}_q = \overline{p}\overline{\psi}_q + \overline{\psi}_d\overline{\omega}_r - \overline{r}_a\overline{i}_q \tag{4.40}$$

$$\overline{v}_0 = \overline{p}\overline{\psi}_d - \overline{r}_a\overline{i}_0 \tag{4.41}$$

At this stage, the base values for rotor quantities were not specified. It will be defined when addressing the normalization of flux linkage equations. Besides that, it is already known that each rotor winding must have its own per unit system. Hence, dividing each rotor voltage equation by its respective base voltage yields the following per unit voltage equations for the rotor circuits:

$$\overline{v}_{fd} = \overline{p}\overline{\psi}_{fd} + \overline{r}_{fd}\overline{i}_{fd} \tag{4.42}$$

$$0 = \overline{p}\overline{\psi}_{kd} + \overline{r}_{kd}\overline{i}_{kd} \tag{4.43}$$

$$0 = \overline{p}\overline{\psi}_{kq1} + \overline{r}_{kq1}\overline{i}_{kq1} \tag{4.44}$$

$$0 = \overline{p}\overline{\psi}_{kq2} + \overline{r}_{kq2}\overline{i}_{kq2} \tag{4.45}$$

Therefore, the complete set of per unit voltage equations may be written in a matrix form, as follows:

$$
\begin{bmatrix} \overline{v}_d \\ \overline{v}_q \\ \overline{v}_0 \\ \overline{v}_{fd} \\ 0 \\ 0 \\ 0 \end{bmatrix}
=
\begin{bmatrix} \overline{r}_a & & & & & & \\ & \overline{r}_a & & & & & \\ & & \overline{r}_a & & & & \\ & & & \overline{r}_{fd} & & & \\ & & & & \overline{r}_{kd} & & \\ & & & & & \overline{r}_{kq1} & \\ & & & & & & \overline{r}_{kq2} \end{bmatrix}
\cdot
\begin{bmatrix} -\overline{i}_d \\ -\overline{i}_q \\ -\overline{i}_0 \\ \overline{i}_{fd} \\ \overline{i}_{kd} \\ \overline{i}_{kq1} \\ \overline{i}_{kq2} \end{bmatrix}
+ \overline{p}
\begin{bmatrix} \overline{\psi}_d \\ \overline{\psi}_q \\ \overline{\psi}_0 \\ \overline{\psi}_{fd} \\ \overline{\psi}_{kd} \\ \overline{\psi}_{kq1} \\ \overline{\psi}_{kq2} \end{bmatrix}
+ \overline{\omega}
\begin{bmatrix} -\overline{\psi}_q \\ \overline{\psi}_d \\ 0 \\ 0 \\ 0 \\ 0 \\ 0 \end{bmatrix}
\tag{4.46}
$$

4.3.2 Per Unit Flux Linkage Equations

The flux linkage expressions of stator and rotor circuits presented in (4.22) describe flux linkages, inductances and currents in physical units. In this regard, the normalization of flux linkage equations demands definition of a per unit system for mutual and self-inductances. This development is detailed in this subsection, including the main concepts related to the L_{ad}-reciprocal per unit system [52].

Dividing the stator flux linkage equations in dq0 components by $\psi_{s_{base}}$ yields:

$$\overline{\psi}_d = \left(-L_d i_d + L_{afd} i_{fd} + L_{akd} i_{kd}\right) \cdot \frac{1}{\psi_{s_{base}}} \tag{4.47}$$

$$\overline{\psi}_q = \left(-L_q i_q + L_{akq1} i_{kq1} + L_{akq2} i_{kq2}\right) \cdot \frac{1}{\psi_{s_{base}}} \tag{4.48}$$

$$\overline{\psi}_0 = \left(-L_0 i_0\right) \cdot \frac{1}{\psi_{s_{base}}} \tag{4.49}$$

Let one take $\overline{\psi}_d$ as example, recognizing that $\psi_{s_{base}} = L_{s_{base}} i_{s_{base}}$. Multiplying and dividing some terms of (4.47) by convenient bases yields the following per unit equation:

$$\underbrace{\frac{\psi_d}{\psi_{s_{base}}}}_{\overline{\psi}_d} = -\underbrace{\frac{L_d}{L_{s_{base}}}}_{\overline{L}_d} \underbrace{\frac{i_d}{i_{s_{base}}}}_{\overline{i}_d} + \underbrace{\frac{L_{afd}}{L_{s_{base}}} \frac{i_{fd_{base}}}{i_{s_{base}}}}_{\overline{L}_{afd}} \underbrace{\frac{i_{fd}}{i_{fd_{base}}}}_{\overline{i}_{fd}} \tag{4.50}$$

Performing similar algebraic manipulations over (4.48) and (4.49), and identifying per unit terms, the following per unit mutual inductances *between stator and rotor windings* are defined:

$$\overline{L}_{afd} = \frac{L_{afd}}{L_{s_{base}}} \frac{i_{fd_{base}}}{i_{s_{base}}} \qquad \overline{L}_{akd} = \frac{L_{akd}}{L_{s_{base}}} \frac{i_{kd_{base}}}{i_{s_{base}}}$$

$$\overline{L}_{akq1} = \frac{L_{akq1}}{L_{s_{base}}} \frac{i_{kq1_{base}}}{i_{s_{base}}} \qquad \overline{L}_{akq2} = \frac{L_{akq2}}{L_{s_{base}}} \frac{i_{kq2_{base}}}{i_{s_{base}}} \tag{4.51}$$

Self-inductances of stator windings in dq0 reference are given by:

$$\overline{L}_d = \frac{L_d}{L_{s_{base}}} \qquad \overline{L}_q = \frac{L_q}{L_{s_{base}}} \qquad \overline{L}_0 = \frac{L_0}{L_{s_{base}}} \tag{4.52}$$

The self-inductances L_d and L_q may be divided into two components: (i) a leakage inductance in d-axis (L_{ld}) and q-axis (L_{lq}) respective to the flux that does not link any rotor circuit, (ii) and a mutual component in d-axis (L_{ad}) and q-axis (L_{aq}) due to the magnetizing flux linking stator and rotor windings. The leakage components in d and q-axis are nearly equal in both axes, so that they are assumed to be equal L_l. Therefore, the following per unit components are defined:

$$\overline{L}_d = \overline{L}_{ld} + \overline{L}_{ad} = \overline{L}_l + \overline{L}_{ad} \tag{4.53}$$

$$\overline{L}_q = \overline{L}_{lq} + \overline{L}_{aq} = \overline{L}_l + \overline{L}_{aq} \tag{4.54}$$

The per unit magnetizing inductances $\overline{L}_{ad}$ and $\overline{L}_{aq}$ are important quantities to be

employed when defining the rotor per unit system, in as much as $\overline{L}_{ad}$ is assumed to be equal the per unit mutual inductances between all windings in d-axis, and $\overline{L}_{aq}$ draw the same function in q-axis. This base choice provides the foundation for the L_{ad}-reciprocal per unit system.

The following notation is adopted for the base quantities of the rotor:

- Field winding: $\psi_{fd_{base}} = L_{fd_{base}} i_{fd_{base}}$

- Damper winding in d-axis: $\psi_{kd_{base}} = L_{kd_{base}} i_{kd_{base}}$

- First damper winding in q-axis: $\psi_{kq1_{base}} = L_{kq1_{base}} i_{kq1_{base}}$

- Second damper winding in q-axis: $\psi_{kq2_{base}} = L_{kq2_{base}} i_{kq2_{base}}$

Dividing the flux linkage of each rotor winding by its respective base value, yields:

$$\overline{\psi}_{fd} = \frac{\psi_{fd}}{\psi_{fd_{base}}}; \qquad \overline{\psi}_{kd} = \frac{\psi_{kd}}{\psi_{kd_{base}}}; \qquad \overline{\psi}_{kq1} = \frac{\psi_{kq1}}{\psi_{kq1_{base}}}; \qquad \overline{\psi}_{kq2} = \frac{\psi_{kq2}}{\psi_{kq2_{base}}} \qquad (4.55)$$

Taking the field flux linkage $\overline{\psi}_{fd}$ as example, the following steps are performed:

$$\overline{\psi}_{fd} = \frac{\psi_{fd}}{\psi_{fd_{base}}} = \left(L_{ffd} i_{fd} + L_{fkd} i_{kd} - \frac{3}{2} L_{afd} i_d \right) \cdot \frac{1}{\psi_{fd_{base}}} \qquad (4.56)$$

Understanding that $\psi_{fd_{base}} = L_{fd_{base}} i_{fd_{base}}$ and including convenient terms into the expression (4.56) yields the following per unit flux linkage equation:

$$\underbrace{\frac{\psi_{fd}}{\psi_{fd_{base}}}}_{\overline{\psi}_{fd}} = \underbrace{\frac{L_{ffd}}{L_{fd_{base}}}}_{\overline{L}_{ffd}} \underbrace{\frac{i_{fd}}{i_{fd_{base}}}}_{\overline{i}_{fd}} + \underbrace{\frac{L_{fkd}}{L_{fd_{base}}} \frac{i_{kd_{base}}}{i_{fd_{base}}}}_{\overline{L}_{fkd}} \underbrace{\frac{i_{kd}}{i_{kd_{base}}}}_{\overline{i}_{kd}} - \underbrace{\frac{3}{2} \frac{L_{afd}}{L_{fd_{base}}} \frac{i_{s_{base}}}{i_{fd_{base}}}}_{\overline{L}_{fda}} \underbrace{\frac{i_d}{i_{s_{base}}}}_{\overline{i}_d} \qquad (4.57)$$

Equation (4.57) defines a new set of per unit mutual inductances related to field and other windings in d-axis. In a similar way, dividing the flux linkage equations of the remaining rotor windings (dampers of d and q-axis), the following per unit multual inductances *between rotor windings* are defined:

$$\overline{L}_{fkd} = \frac{L_{fkd}}{L_{fd_{base}}} \frac{i_{kd_{base}}}{i_{fd_{base}}} \qquad \overline{L}_{kfd} = \frac{L_{fkd}}{L_{kd_{base}}} \frac{i_{fd_{base}}}{i_{kd_{base}}}$$

$$\overline{L}_{kq12} = \frac{L_{kq12}}{L_{kq1_{base}}} \frac{i_{kq2_{base}}}{i_{kq1_{base}}} \qquad \overline{L}_{kq21} = \frac{L_{kq12}}{L_{kq2_{base}}} \frac{i_{kq1_{base}}}{i_{kq2_{base}}} \qquad (4.58)$$

Also, the following per unit mutual inductances *between rotor and stator windings*

are defined:

$$\overline{L}_{fda} = \frac{3}{2} \frac{L_{afd}}{L_{fd_{base}}} \frac{i_{s_{base}}}{i_{fd_{base}}} \qquad \overline{L}_{kda} = \frac{3}{2} \frac{L_{akd}}{L_{kd_{base}}} \frac{i_{s_{base}}}{i_{kd_{base}}}$$

$$\overline{L}_{kq1a} = \frac{3}{2} \frac{L_{akq1}}{L_{kq1_{base}}} \frac{i_{s_{base}}}{i_{kq1_{base}}} \qquad \overline{L}_{kq2a} = \frac{3}{2} \frac{L_{akq2}}{L_{kq2_{base}}} \frac{i_{s_{base}}}{i_{kq2_{base}}}$$

(4.59)

It is important to notice that mutual inductances between stator and rotor (4.51) differ from the expressions relating mutual inductances between rotor and stator (4.59). Hence, a proper per unit system for the rotor shall be developed to overcome this feature and assure numerical reciprocal mutual inductances.

Writing the flux linkage equations of stator and rotor circuits in a matrix form, yields:

$$
\begin{bmatrix}
\overline{\psi}_d \\
\overline{\psi}_q \\
\overline{\psi}_0 \\
\overline{\psi}_{fd} \\
\overline{\psi}_{kd} \\
\overline{\psi}_{kq1} \\
\overline{\psi}_{kq2}
\end{bmatrix}
=
\begin{bmatrix}
\overline{L}_d & & & \overline{L}_{afd} & \overline{L}_{akd} & & \\
& \overline{L}_q & & & & \overline{L}_{akq1} & \overline{L}_{akq2} \\
& & \overline{L}_0 & & & & \\
\overline{L}_{fda} & & & \overline{L}_{ffd} & \overline{L}_{fkd} & & \\
\overline{L}_{kda} & & & \overline{L}_{kfd} & \overline{L}_{kkd} & & \\
& \overline{L}_{kq1a} & & & & \overline{L}_{kkq1} & \overline{L}_{kq12} \\
& \overline{L}_{kq2a} & & & & \overline{L}_{kq21} & \overline{L}_{kkq2}
\end{bmatrix}
\cdot
\begin{bmatrix}
-\overline{i}_d \\
-\overline{i}_q \\
-\overline{i}_0 \\
\overline{i}_{fd} \\
\overline{i}_{kd} \\
\overline{i}_{kq1} \\
\overline{i}_{kq2}
\end{bmatrix}
$$

(4.60)

Furthermore, (4.60) may be expressed in a compact form, as follows:

$$
\begin{bmatrix}
\overline{\boldsymbol{\Psi}}_S \\
\overline{\boldsymbol{\Psi}}_R
\end{bmatrix}
=
\begin{bmatrix}
\overline{\boldsymbol{L}}_S & \overline{\boldsymbol{L}}_{M_{SR}} \\
\overline{\boldsymbol{L}}_{M_{RS}} & \overline{\boldsymbol{L}}_R
\end{bmatrix}
\cdot
\begin{bmatrix}
-\overline{\boldsymbol{I}}_S \\
\overline{\boldsymbol{I}}_R
\end{bmatrix}
$$

(4.61)

The sub-matrix $\overline{\boldsymbol{L}}_{M_{SR}}$ should be equal $\overline{\boldsymbol{L}}_{M_{RS}}^T$ after employing a reciprocal mutual per unit system. Also, to highlight the uncoupled characteristic between dq0 windings, the matrix form of flux linkage equations may be rewritten, grouping the dq0

quantities, as follows:

$$
\begin{bmatrix}
\overline{\psi}_d \\
\overline{\psi}_{fd} \\
\overline{\psi}_{kd} \\
\overline{\psi}_q \\
\overline{\psi}_{kq1} \\
\overline{\psi}_{kq2} \\
\overline{\psi}_0
\end{bmatrix}
=
\begin{bmatrix}
\overline{L}_d & \overline{L}_{afd} & \overline{L}_{akd} & & & & \\
\overline{L}_{fda} & \overline{L}_{ffd} & \overline{L}_{fkd} & & & & \\
\overline{L}_{kda} & \overline{L}_{kfd} & \overline{L}_{kkd} & & & & \\
& & & \overline{L}_q & \overline{L}_{akq1} & \overline{L}_{akq2} & \\
& & & \overline{L}_{kq1a} & \overline{L}_{kkq1} & \overline{L}_{kq12} & \\
& & & \overline{L}_{kq2a} & \overline{L}_{kq21} & \overline{L}_{kkq2} & \\
& & & & & & \overline{L}_0
\end{bmatrix}
\cdot
\begin{bmatrix}
-\overline{i}_d \\
\overline{i}_{fd} \\
\overline{i}_{kd} \\
\overline{i}_{kq1} \\
\overline{i}_{kq2} \\
-\overline{i}_q \\
-\overline{i}_0
\end{bmatrix}
\tag{4.62}
$$

4.3.3 Rotor Per Unit System

The base quantities of rotor circuits are defined with the purpose of simplifying flux linkage equations and fulfill the following premises:

(i) The per unit mutual inductances between different windings have to be reciprocal so as to allow the synchronous machine modeling through equivalent circuits without ideal tranformer ratios. In short:

$$
\overline{L}_{afd} = \overline{L}_{fda} \qquad \overline{L}_{fkd} = \overline{L}_{kfd} \qquad \overline{L}_{akd} = \overline{L}_{kda}
$$
$$
\overline{L}_{akq1} = \overline{L}_{kq1a} \qquad \overline{L}_{akq2} = \overline{L}_{kq2a} \qquad \overline{L}_{kq12} = \overline{L}_{kq21}
$$

(ii) All per unit inductances between stator and rotor windings in the same axis must be equal L_{ad} in d-axis, and equal to L_{aq} in q-axis, i.e.:

$$
\overline{L}_{ad} = \overline{L}_{afd} = \overline{L}_{akd} \qquad\qquad \overline{L}_{aq} = \overline{L}_{akq1} = \overline{L}_{akq2}
$$

Defining the VA Base of Rotor Circuits

For reciprocal mutual inductances between rotor windings in per unit, the expressions of $\overline{L}_{fkd}$ and $\overline{L}_{kfd}$ in (4.58) should be numerically identical, resulting in:

$$
\frac{L_{fkd}}{L_{fd_{base}}} \frac{i_{kd_{base}}}{i_{fd_{base}}} = \frac{L_{fkd}}{L_{kd_{base}}} \frac{i_{fd_{base}}}{i_{kd_{base}}}
\tag{4.63}
$$

Rearranging (4.63), gives:

$$
L_{fd_{base}} i_{fd_{base}}^2 = L_{kd_{base}} i_{kd_{base}}^2
\tag{4.64}
$$

Multiplying both sides by ω_{base} and using the identity $v_{base} = \omega_{base} L_{base} i_{base}$ yields:

$$e_{fd_{base}} i_{fd_{base}} = v_{kd_{base}} i_{kd_{base}} \tag{4.65}$$

Equation (4.65) confirms that to obtain reciprocal mutual inductances between any **rotor winding**, **the volt-ampere base adopted for each rotor circuit must be the same**. Afterward, for reciprocal mutual inductances between **field** and **stator** windings, the inductances $\overline{L}_{afd}$ and $\overline{L}_{fda}$ determined in (4.51) and (4.59) must satisfy the following equality:

$$\overline{L}_{afd} = \overline{L}_{fda}$$

$$\frac{L_{afd}}{L_{s_{base}}} \frac{i_{fd_{base}}}{i_{s_{base}}} = \frac{3}{2} \frac{L_{afd}}{L_{fd_{base}}} \frac{i_{s_{base}}}{i_{fd_{base}}} \tag{4.66}$$

Multiplying (4.66) by ω_{base} and considering that $v_{base} = \omega_{base} L_{base} i_{base}$, follows that:

$$\frac{3}{2} v_{s_{base}} i_{s_{base}} = e_{fd_{base}} i_{fd_{base}} \tag{4.67}$$

Therefore, (4.67) establishes that for reciprocal mutual inductances between **stator** and **rotor** windings, the **power base of rotor windings must be equal to the three-phase VA base selected for the stator windings**.

Defining the Current Base of Rotor Circuits

The current base values are to be specified for each rotor winding in order to accomplish numerically identical mutual inductances between stator and rotor windings in each axis. The per unit mutual inductances in d-axis are supposed to be equal to L_{ad}, whereas in q-axis the mutual inductances are supposed to be equal to L_{aq}.

In order to build equivalents circuits without ideal transform ratios between windings, the L_{ad}-reciprocal per unit system stipulates:

$$\overline{L}_{ad} = \overline{L}_{afd} = \overline{L}_{akd} \tag{4.68}$$

$$\overline{L}_{aq} = \overline{L}_{akq1} = \overline{L}_{akq2} \tag{4.69}$$

Substituting the terms for $\overline{L}_{afd}$ and $\overline{L}_{akd}$ into (4.68), follows that:

$$\overline{L}_{ad} = \frac{L_{ad}}{L_{s_{base}}} = \overline{L}_{afd} = \frac{L_{afd}}{L_{s_{base}}} \frac{i_{fd_{base}}}{i_{s_{base}}} \tag{4.70}$$

$$= \overline{L}_{akd} = \frac{L_{akd}}{L_{s_{base}}} \frac{i_{kd_{base}}}{i_{s_{base}}} \tag{4.71}$$

Performing similar manipulations over (4.69) to assure per unit reciprocal mutual inductances in q-axis, gives:

$$\overline{L}_{aq} = \frac{L_{aq}}{L_{s_{base}}} = \overline{L}_{akq1} = \frac{L_{akq1}}{L_{s_{base}}} \frac{i_{kq1_{base}}}{i_{s_{base}}} \tag{4.72}$$

$$= \overline{L}_{akq2} = \frac{L_{akq2}}{L_{s_{base}}} \frac{i_{kq2_{base}}}{i_{s_{base}}} \tag{4.73}$$

Then, it is possible to define the following current bases for rotor circuits:

$$i_{fd_{base}} = \frac{L_{ad}}{L_{afd}} i_{s_{base}} \tag{4.74}$$

$$i_{kd_{base}} = \frac{L_{ad}}{L_{akd}} i_{s_{base}} \tag{4.75}$$

$$i_{kq1_{base}} = \frac{L_{ad}}{L_{akq1}} i_{s_{base}} \tag{4.76}$$

$$i_{kq2_{base}} = \frac{L_{ad}}{L_{akq2}} i_{s_{base}} \tag{4.77}$$

This choice for rotor base currents concludes the deductions of all base quantities related to the stator and rotor circuits of a synchronous machine, according to the L_{ad}-reciprocal per unit system. Using this system, the flux linkage equations may be written in the following matrix form:

$$
\begin{bmatrix}
\overline{\psi}_d \\
\overline{\psi}_q \\
\overline{\psi}_0 \\
\overline{\psi}_{fd} \\
\overline{\psi}_{kd} \\
\overline{\psi}_{kq1} \\
\overline{\psi}_{kq2}
\end{bmatrix}
=
\begin{bmatrix}
\overline{L}_d & & & \overline{L}_{ad} & \overline{L}_{ad} & & \\
& \overline{L}_q & & & & \overline{L}_{aq} & \overline{L}_{aq} \\
& & \overline{L}_0 & & & & \\
\overline{L}_{ad} & & & \overline{L}_{ffd} & \overline{L}_{ad} & & \\
\overline{L}_{ad} & & & \overline{L}_{ad} & \overline{L}_{kkd} & & \\
& \overline{L}_{aq} & & & & \overline{L}_{kkq1} & \overline{L}_{aq} \\
& \overline{L}_{aq} & & & & \overline{L}_{aq} & \overline{L}_{kkq2}
\end{bmatrix}
\cdot
\begin{bmatrix}
-\overline{i}_d \\
-\overline{i}_q \\
-\overline{i}_0 \\
\overline{i}_{fd} \\
\overline{i}_{kd} \\
\overline{i}_{kq1} \\
\overline{i}_{kq2}
\end{bmatrix}
\tag{4.78}
$$

The per unit mutual inductance between field and damper windings in d-axis was assumed to be equal to the mutual inductance between rotor and stator windings. The reason for this assumption is further explained in Section 4.4.1.

The flux linkage equations may be written in a compact form, as follows:

$$
\begin{bmatrix} \overline{\boldsymbol{\Psi}}_S \\ \overline{\boldsymbol{\Psi}}_R \end{bmatrix} = \begin{bmatrix} \overline{\boldsymbol{L}}_S & \overline{\boldsymbol{L}}_M \\ \overline{\boldsymbol{L}}_M^T & \overline{\boldsymbol{L}}_R \end{bmatrix} \cdot \begin{bmatrix} -\overline{\boldsymbol{I}}_S \\ \overline{\boldsymbol{I}}_R \end{bmatrix}
\tag{4.79}
$$

4.3.4 Per Unit Power and Torque

The three-phase instantaneous power given by (4.30):

$$
P_t = \frac{3}{2} \left[v_d i_d + v_q i_q + v_0 i_0 \right]
$$

Is normalized by dividing this equation by the three-phase VA base:

$$
S_{base} = \frac{3}{2} v_{s_{base}} i_{s_{base}}
$$

This operation yields the following per unit three-phase power equation:

$$
\overline{P} = \overline{v}_d \overline{i}_d + \overline{v}_q \overline{i}_q + 2\overline{v}_0 \overline{i}_0
\tag{4.80}
$$

The expression of electromagnetic torque presented in (4.34):

$$
T_e = \frac{3}{2} \left(i_q \psi_d - i_d \psi_q \right) \cdot \frac{pf}{2}
$$

Is also normalized by using the torque base:

$$
T_{base} = \frac{3}{2} \cdot \frac{p_f}{2} \cdot \psi_{s_{base}} i_{s_{base}}
$$

From which, the following per unit torque equation is obtained:

$$
\overline{T} = \overline{i}_q \overline{\psi}_d - \overline{i}_d \overline{\psi}_q
\tag{4.81}
$$

4.4 Basic Mechanical Equations

The basic equations of rotational motion are developed regarding the turbine-generator shaft as a single lumped mass modeled by a rigid body with an equivalent inertia. This model is adopted in ESA studies for the analysis of oscillations within multi-machine systems, and it allows observing the electromechanical mode of rotor

oscillation, typically in the range of 0.1 to 3 Hz. The equation of motion adopted in SSR analysis will be subsequently assigned in Section 5.3.

In a synchronous generator, the acceleration (or deceleration) torque is given by the unbalance between the mechanical, electromagnetic and damping torques applied to the rotor:

$$T_a = T_m - T_e - T_D \tag{4.82}$$

where:

T_a = Accelerating torque, [N.m]

T_m = Mechanical torque, [N.m]

T_e = Electromagnetic torque, [N.m]

T_D = Damping torque, [N.m]

The mechanical equation governing the rotational dynamic behavior of a rigid body states that the acceleration torque (T_a) is given by the product between the rotor moment of inertia (J) and its angular acceleration (α):

$$J \cdot \alpha = T_a \tag{4.83}$$

The equivalent moment of inertia of the turbine-generator system is modeled by a rigid body that suffers the unbalance between the applied torques [47]. The equation of motion relating these quantities is given by:

$$J\frac{d\omega_m}{dt} = J\frac{d\theta_m^2}{dt^2} = T_a = T_m - T_e - T_D \text{ [N.m]} \tag{4.84}$$

where:

J = combined moment of inertia of the turbine-generator shaft, $[\text{kg} \cdot \text{m}^2]$

ω_m = rotational angular speed of the rotor, [mech rad/s]

θ_m = angular position of the rotor, [mech rad]

The motion equation may be normalized in terms of the **inertia constant** (H), defined as the ratio between the stored kinetic energy in the rotor at rated speed given in $W.s$, and the machine VA base:

$$H = \frac{1}{2}\frac{J\omega_{0m}^2}{\text{VA}_{base}} \tag{4.85}$$

with ω_{0m} being the rated angular speed in mech rad/s.

Representing the moment of inertia J in terms of H and substituting the resulting expression into (4.84), gives:

$$\frac{2H}{\omega_{om}^2}\text{VA}_{base}\frac{d\omega_m}{dt} = T_m - T_e - T_D \tag{4.86}$$

Which can be conveniently rearranged, as follows:

$$2H\frac{d}{dt}\frac{\omega_m}{\omega_{0m}} = \frac{T_a - T_e - T_D}{\text{VA}_{base}/\omega_{0m}} \tag{4.87}$$

Recognizing that $T_{base} = \text{VA}_{base}/\omega_{0m}$ and that:

$$\overline{\omega}_r = \frac{\omega_m}{\omega_{0m}} = \frac{\omega_r}{\omega_0} \tag{4.88}$$

The per unit motion equation is:

$$\boxed{2H\frac{d\overline{\omega}_r}{dt} = \overline{T}_m - \overline{T}_e - \overline{T}_D} \tag{4.89}$$

where ω_r is the rotational angular speed of the rotor in elec rad/s.

Defining the load angle δ as the angular position of the rotor in elec rad/s with respect to a synchronously rotating reference:

$$\delta = \omega_r t - \omega_0 t + \delta_0 \tag{4.90}$$

where δ_0 is the load angle value at time $t = 0$. The time derivative of (4.90) yields:

$$\frac{d\delta}{dt} = \omega_r - \omega_0 = \Delta\omega_r \tag{4.91}$$

and

$$\frac{d^2\delta}{dt^2} = \frac{d\omega_r}{dt} = \frac{d(\Delta\omega_r)}{dt} = \omega_0\frac{d\overline{\omega}_r}{dt} = \omega_0\frac{d(\Delta\overline{\omega}_r)}{dt} \tag{4.92}$$

Substituting (4.92) into (4.89) and expressing the damping torque T_D as a term proportional to the speed deviation, gives:

$$\frac{2H}{\omega_0}\frac{d\delta^2}{dt^2} = \overline{T}_m - \overline{T}_e - D\Delta\overline{\omega}_r \tag{4.93}$$

116

where D is the damping factor or coefficient in pu torque/pu speed deviation.

From (4.91), one should note that:

$$\Delta\overline{\omega}_r = \frac{\Delta\omega_r}{\omega_0} = \frac{1}{\omega_0}\frac{d\delta}{dt} \tag{4.94}$$

Therefore, (4.93) may be rewritten as:

$$\frac{2H}{\omega_0}\frac{d\delta^2}{dt^2} = \overline{T}_m - \overline{T}_e - \frac{D}{\omega_0}\frac{d\delta}{dt} \tag{4.95}$$

Equation (4.95) is referred to as the *swing equation* of the synchronous machine rotor since it reflects the oscillations of angle δ in a condition of unbalance between the torques applied to the rotor [1].

The state-space representation of the equations of motion are expressed as a set of first order differential equations, in the following form:

$$\frac{d\Delta\overline{\omega}_r}{dt} = \frac{1}{2H}\left(\overline{T}_m - \overline{T}_e - D\Delta\overline{\omega}_r\right) \tag{4.96}$$

$$\frac{d\delta}{dt} = \omega_0\Delta\overline{\omega}_r \tag{4.97}$$

with t in seconds, δ in elec radians and $\omega_0 = 2\pi f$.

Figure 4.3 depicts the block diagram representation of expressions (4.96) and (4.97):
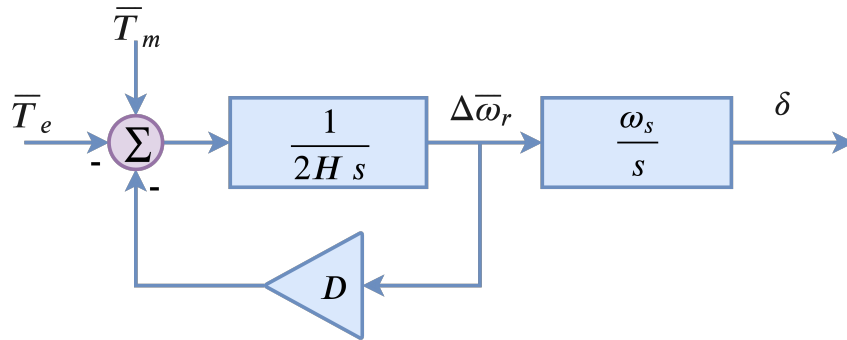
Figure 4.3: Block diagram of the synchronous machine swing equations

4.4.1 Equivalent Circuits for Direct and Quadrature Axis

The dynamic behavior of synchronous machines can be analyzed directly from the per unit equations developed previously; however, expressing these equations by equivalent circuits provides a clear understanding of its physical meaning [1].

The equivalent circuits of Figures 4.4 and 4.5 represent the complete set of equations describing the relationship between flux linkages, voltages, and currents in d- and q-axis in terms of dq0 components. From this point forward, the per unit variables shall be written without the overline notation since all quantities are to be expressed in per unit values.
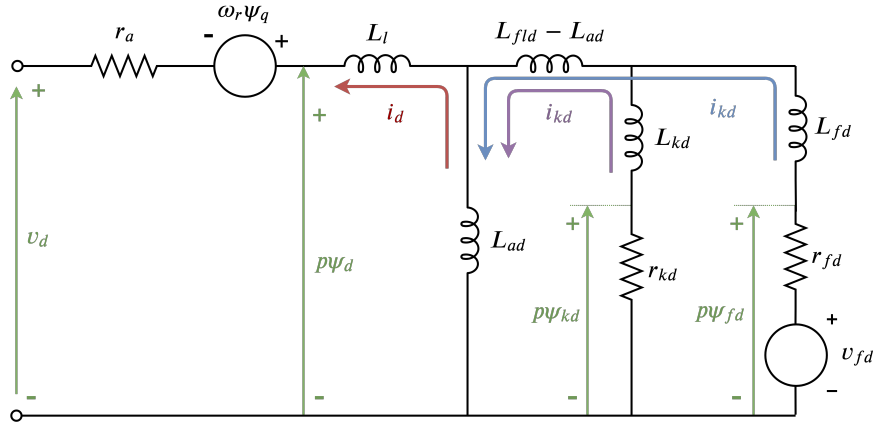
Figure 4.4: d-axis equivalent circuit of a synchronous machine
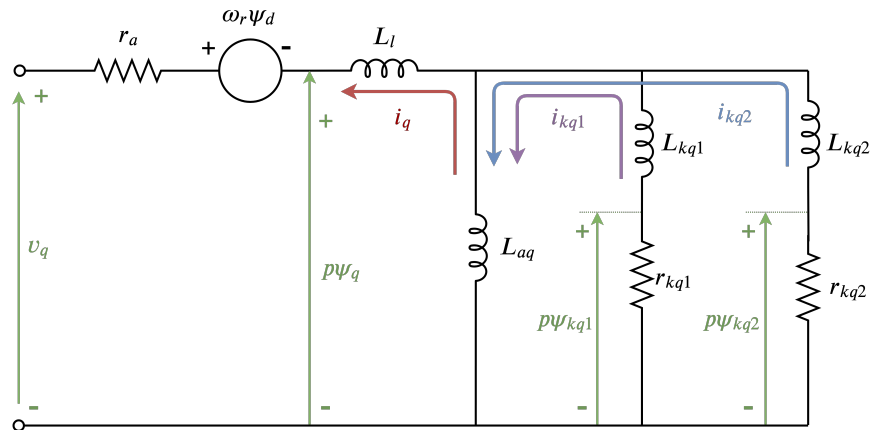
Figure 4.5: q-axis equivalent circuit of a synchronous machine

The series inductance $(L_{fld} - L_{ad})$ in d-axis between the stator and rotor circuits represents the flux linking only field and damper windings without linking the stator. This term is usually small and, therefore, it is typically neglected in ESA and SSR studies. For this reason, the per unit mutual inductance between the field and damper windings is supposed to be equal to L_{ad} in (4.78). In respect of q-axis, the stator and damper windings are assumed to link a single mutual flux represented by the inductance L_{aq}.

As defined for stator windings, the self-inductances of rotor circuits can be split into a magnetizing inductance L_{ad} or L_{aq}, and a leakage inductance. The per unit

leakage inductances of rotor circuits are defined, as follows:

$$L_{fd} = L_{ffd} - L_{fld} \approx L_{ffd} - L_{ad}$$

$$L_{kd} = L_{kkd} - L_{fld} \approx L_{ffd} - L_{ad}$$

$$L_{kq1} = L_{kkq1} - L_{aq}$$ (4.98)

$$L_{kq2} = L_{kkq2} - L_{aq}$$

Under a variety of transient and steady-state conditions, the behavior of a synchronous machine may be examined from the equations represented by these equivalent circuits and additional equations representing the armature and the overall power system.

4.5   Operational Parameters

The basic equations developed in Section 4.3 entirely describe the dynamic behavior of a synchronous machine in terms of resistances and inductances of rotor and stator circuits, which are referred to as *fundamental or basic parameters*. However, a practical determination of these parameters from short-circuit and open-circuit tests cannot feasibly be obtained from measurements of the machine terminal quantities.

Considerable insight may be achieved by reducing these equations with some simplifications of transient effects as one looks at them in terms of final and initial value solutions. These reductions lead to the definition of *derived or operational parameters* of the synchronous machine, which are usually provided by manufacturers and widely used in ESA and SSR studies. It includes transient and subtransient reactances, short-circuit and open-circuit time constants.

The operational parameters are obtained from the basic parameters considering linear relationships between incremental terminal quantities of the stator and field circuits [52]. Hence, performing some algebraic manipulations over the basic per unit equations, the stator incremental flux linkages $\Delta\psi_d(s)$ and $\Delta\psi_q(s)$ may be expressed in terms of $\Delta e_{fd}(s)$, $\Delta i_d(s)$ and $\Delta i_q(s)$, according to the following equations:

$$\Delta\psi_d(s) = G(s)\Delta e_{fd}(s) - L_d(s)\Delta i_d(s)$$ (4.99)

$$\Delta\psi_q(s) = -L_q(s)\Delta i_q(s)$$ (4.100)

where:

Δ represents incremental quantities;

119

s is the Laplace operator;

$G(s)$ is the stator to field transfer function;

$L_d(s)$ is the d-axis operational inductance;

$L_q(s)$ is the q-axis operational inductance.

Equations (4.99) and (4.100) are suitable to the equivalents circuits of Figures 4.4 and 4.5. These circuits are applicable for several studies when an accurate calculation of rotor currents (i_{fd}, i_{kd}, i_{kq}) are necessary. In the case of ESA and SSR studies, dependent variables, such as rotor currents, may be eliminated from the basic electrical equations leading to operational expressions relating field voltage, stator flux linkages, and stator currents. Figure 4.6 draws the relationship between these expressions and terminal quantities of the machine.
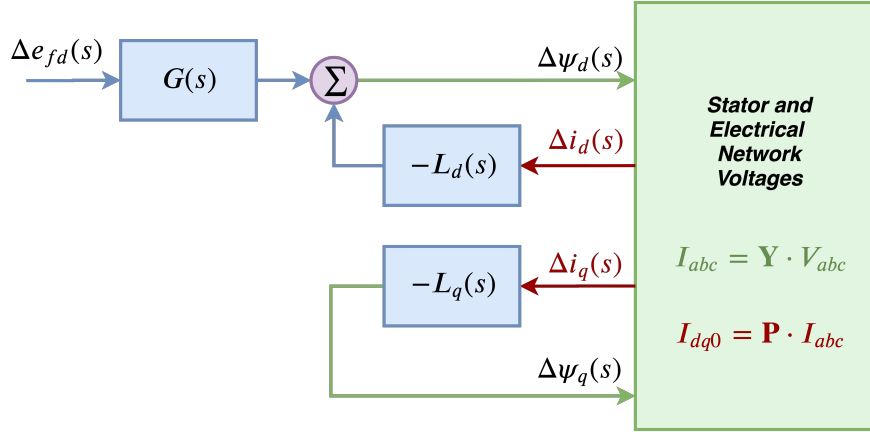
Figure 4.6: Operational diagram of a synchronous machine

The operational expressions $G(s)$, $L_d(s)$ and $L_q(s)$ are transfer functions that may be written as a ratio of polynomials in s, whose denominator order is equal to the number of rotor circuits considered in the respective axis. In addition, these transfer functions can be factored to explicit important time constants of transient response, as follows:

$$G(s) = G_0 \frac{(1 + sT_{kd})}{(1 + sT'_{d0})(1 + sT''_{d0})} \tag{4.101}$$

$$L_d(s) = L_d \frac{(1 + sT'_d)(1 + sT''_d)}{(1 + sT'_{d0})(1 + sT''_{d0})} \tag{4.102}$$

$$L_q(s) = L_q \frac{(1 + sT'_q)(1 + sT''_q)}{(1 + sT'_{q0})(1 + sT''_{q0})} \tag{4.103}$$

where:

L_d : d-axis synchronous inductance

L_q : q-axis synchronous inductance

T_d' : d-axis short-circuit transient time constant

T_d'' : d-axis short-circuit subtransient time constant

T_{d0}' : d-axis open-circuit transient time constant

T_{d0}'' : d-axis open-circuit subtransient time constant

T_q' : q-axis short-circuit transient time constant

T_q'' : q-axis short-circuit subtransient time constant

T_{q0}' : q-axis open-circuit transient time constant

T_{q0}'' : q-axis open-circuit subtransient time constant

These time constants are obtained from open-circuit and short-circuit tests and they are classified according to the machine dynamic response, split into subtransient, transient, and synchronous regimes. The analytical process for determining these constants by using the basic parameters of the synchronous machine is quite laborious [52], and these deductions are out of scope of this thesis. For the sake of simplicity, only final expressions for the calculation of operational parameters are presented:

$$
\begin{aligned}
&T_{d0}' = \frac{1}{\omega_{base}}\left(T_1 + T_2\right) &&T_d' = \frac{1}{\omega_{base}}\left(T_4 + T_5\right) \\
&T_{d0}'' = \frac{1}{\omega_{base}}\left(\frac{T_1 T_3}{T_1 + T_2}\right) &&T_d'' = \frac{1}{\omega_{base}}\left(\frac{T_4 T_6}{T_4 + T_5}\right) \\
&G_0 = \frac{L_{ad}}{R_{fd}} &&T_{kd} = \frac{1}{\omega_{base}}\left(\frac{L_{kd}}{R_{kd}}\right)
\end{aligned}
\tag{4.104}
$$

where:

$$
\begin{aligned}
&T_1 = \frac{L_{ad} + L_{fd}}{R_{fd}} &&T_2 = \frac{L_{ad} + L_{kd}}{R_{kd}} \\
&T_3 = \frac{1}{R_{kd}}\left(L_{kd} + \frac{L_{ad}L_{fd}}{L_{ad} + L_{fd}}\right) &&T_4 = \frac{1}{R_{fd}}\left(L_{fd} + \frac{L_{ad}L_l}{L_{ad} + L_l}\right) \\
&T_5 = \frac{1}{R_{kd}}\left(L_{kd} + \frac{L_{ad}L_l}{L_{ad} + L_l}\right) &&T_6 = \frac{1}{R_{kd}}\left(L_{kd} + \frac{L_{ad}L_{fd}L_l}{L_{ad}L_l + L_{ad}L_{fd} + L_{fd}L_l}\right)
\end{aligned}
\tag{4.105}
$$

For the quadrature axis, similar expressions are obtained by exchanging the subscript

121

kd for $kq1$ and fd for $kq2$. In these expressions, time constants are given in seconds and inductances in per unit values.

Following a disturbance, the response of components with fast dynamics are influenced by **subtransient parameters** and rapidly decay after a few cycles. **Transient parameters** influence slower components and last a few seconds. The **synchronous parameters** are related to sustained response and influence the steady-state regime.

The synchronous machine behavior is typically described in terms of inductances (or reactances) seen from the machine terminals, which are related to the fundamental frequency currents during sustained, transient, and subtransient periods. Time constants associated with these inductances are also specified to determine the rate of decay of currents and voltages. This set of data is referred to as the *standard parameters* that are defined by manufacturers to specify the synchronous machine dynamic behavior. The transient and subtransient inductances are defined below as a function of the basic parameters and in terms of operational time constants:

$$L'_d = L_l + \frac{L_{ad}L_{fd}}{L_{ad} + L_{fd}} \triangleq L_d \left(\frac{T'_d}{T'_{d0}} \right) \tag{4.106}$$

$$L''_d = L_l + \frac{L_{ad}L_{fd}L_{kd}}{L_{ad}L_{fd} + L_{ad}L_{kd} + L_{fd}L_{kd}} \triangleq L_d \left(\frac{T'_d T''_d}{T'_{d0} T''_{d0}} \right) \tag{4.107}$$

$$L'_q = L_l + \frac{L_{aq}L_{kq1}}{L_{aq} + L_{kq1}} \triangleq L_q \left(\frac{T'_q}{T'_{q0}} \right) \tag{4.108}$$

$$L''_q = L_l + \frac{L_{aq}L_{kq1}L_{kq2}}{L_{aq}L_{kq1} + L_{aq}L_{kq2} + L_{kq1}L_{kq2}} \triangleq L_q \left(\frac{T'_q T''_q}{T'_{d0} T''_{d0}} \right) \tag{4.109}$$

where:

L'_d : d-axis transient inductance

L''_d : d-axis subtransient inductance

L'_q : q-axis transient inductance

L''_q : q-axis subtransient inductance

4.6 Synchronous Machine Simulation Modeling

This subsection encompasses simulation models of synchronous machines suitable for subsynchronous resonance analysis. These models are expressed in terms of the operational parameters (L_d, L'_d, L''_d, etc.) instead of basic parameters of rotor and stator equivalent circuits (L_{ad}, L_l, L_{fd}, etc.). To review the notation employed in the

mathematical developments of these models, the following symbols are recapitulated:

v_d, v_q = direct and quadrature stator voltages;

i_d, i_q = direct and quadrature stator currents;

r_a = stator resistance;

ω_r = stator angular speed in per unit;

ω_s = rated angular speed in per unit = 1 pu, since $\omega_{base} = \omega_s$;

ω_0 = rated angular speed in elec rad/s = $2\pi f_0$ elec rad/s;

f_0 = rated electrical frequency in hertz;

E_d', E_d'' = transient and subtransient voltages of direct axis;

E_q', E_q'' = transient and subtransient voltages of quadrature axis;

ψ_d', ψ_d'' = transient and subtransient voltages of direct axis;

ψ_q', ψ_q'' = transient and subtransient voltages of quadrature axis;

L_l, X_l = leakage inductance and reactance;

L_d, L_q = synchronous inductance of direct and quadrature axes;

L_d', L_d'' = transient and subtransient inductances of direct axis;

L_q', L_q'' = transient and subtransient inductances of quadrature axis;

X_d, X_q = synchronous reactance of direct and quadrature axes;

X_d', X_d'' = transient and subtransient reactances of direct axis;

X_q', X_q'' = transient and subtransient reactances of quadrature axis;

The following relationship between stator voltages and flux linkages must be defined [52]:

$$
\begin{aligned}
E_d' &= \omega_r \cdot \psi_q' & E_d'' &= \omega_r \cdot \psi_q'' \\
E_q' &= \omega_r \cdot \psi_d' & E_q'' &= \omega_r \cdot \psi_d''
\end{aligned}
\tag{4.110}
$$

Greater emphasis is given to the cylindrical rotor machine model since it is mostly adopted for thermal units, which are more probable to experience subsynchronous

oscillations. Still, a brief summary concerning the salient pole machine model is also provided.

In electromecanical stability studies, the angular speed of the rotor is assumed to remain nearby the synchronous speed ($\omega_r \approx 1$ pu), so that it is traditionally considered constant ($\omega_r = 1$ pu). It is important to note that, with the hypothesis of $\omega_r = 1$ pu, the inductances L and reactances $X = \omega L$ have the same per unit value; Therefore, it is common to represent the synchronous machine model in terms of reactances X and voltages v, instead of inductances L and flux linkages ψ. However, in SSR studies this simplifying assumption cannot be made, since the speed variation of the multiple rotor sections are substantial for this analysis.

Representation of Magnetic Saturation

Magnetic saturation effects are considered negligible in the development of the machine model thus far. Now the magnetic saturation may be considered to influence only the mutual inductances L_{ad} and L_{aq}. Therefore, the magnetic saturation shall be examined exclusively over the air-gap flux linkage [52].

Defining an internal voltage, proportional do the field current:

$$E_I = \omega L_{ad} i_{fd} \tag{4.111}$$

One should note that $E_I = 1.0$ pu, when $i_{fd} = 1/X_{ad}$. If the magnetic saturation can be neglected, the phase voltage $v_a = E_I$ in per unit. In addition, the field voltage e_{fd} is also proportional to the field current i_{fd}, as follows:

$$i_{fd} = \frac{e_{fd}}{r_{fd}} \tag{4.112}$$

Substituting (4.112) into (4.111), yields:

$$E_I = \frac{\omega L_{ad}}{r_{fd}} i_{fd} \tag{4.113}$$

The magnetic saturation relationship between the air-gap flux linkage and the rotating MMF under loaded and no-load conditions is assumed to be the same. Therefore, a saturation curve may be constructed from the open-circuit test to represent the saturation characteristics of the machine. The pattern of the synchronous generator saturation curve is illustrated in Figure 4.7.
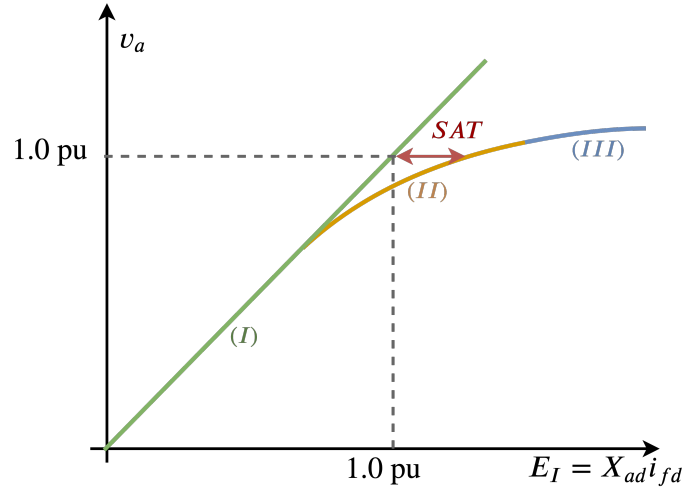
Figure 4.7: Representation of the synchronous machine saturation characteristic

The saturation curve may be divided into three segments: unsaturated segment (I), nonlinear segment (II), and fully saturated segment (III). The straight line extending the unsaturated segment (I) is referred to as the *air-gap line*. The nonlinear segment (II) may be expressed by an exponential function, as follows:

$$SAT = A \cdot e^{B|\psi''|-C} \tag{4.114}$$

where A, B, and C are constant and depend on the generator saturation characteristic over the segment (II) [1].

4.6.1 Cylindrical Rotor Synchronous Generator Model

In this thesis, the mathematical model of a synchronous generator with cylindrical rotor is developed regarding four rotor windings: one damper and one field winding on d-axis; and two damper windings on q-axis. The relationship between the electrical quantities of this machine is presented through the state-space block diagram of d- and q-axis in Figure 4.8. The construction of this generator model is presented in great detail in [52].
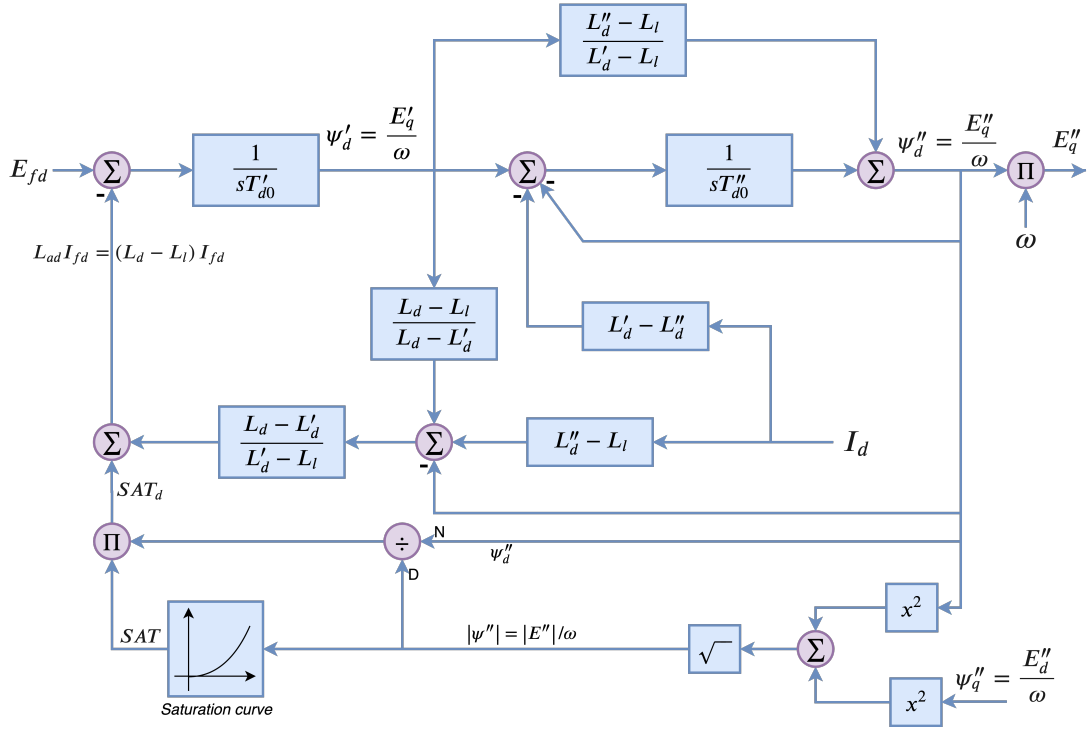
(a) State-space block diagram of d-axis
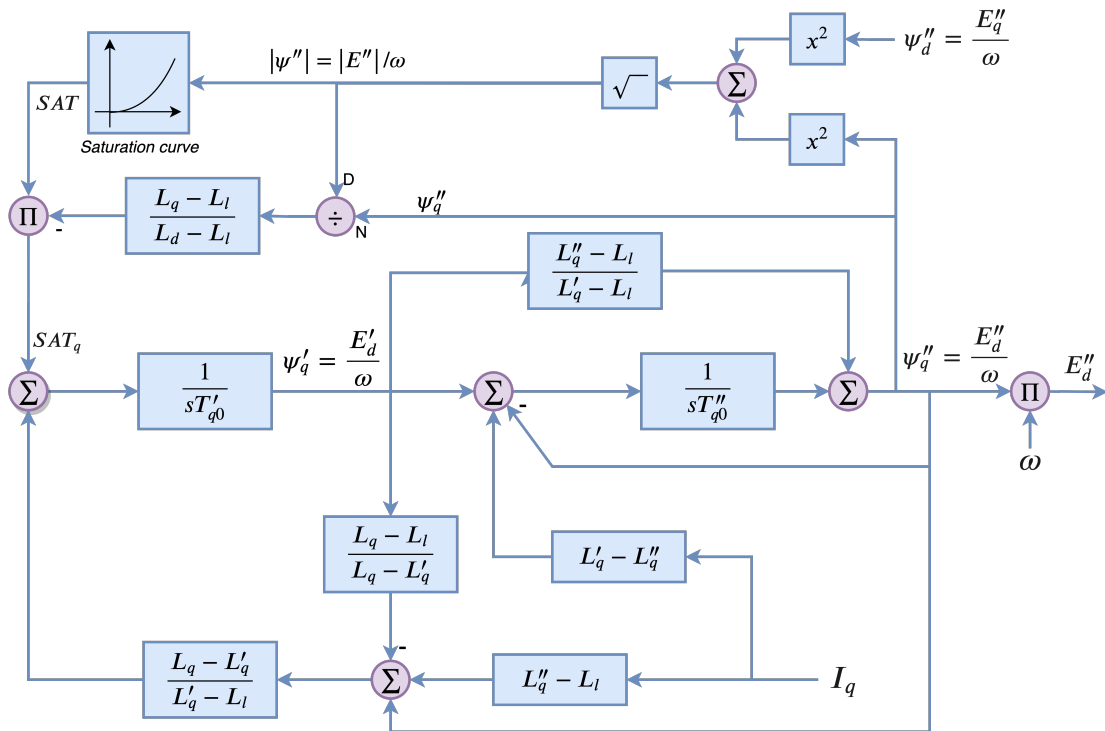
(b) State-space block diagram of q-axis

Figure 4.8: Model of a cylindrical rotor synchronous generator

From the block diagram of d-axis (Figure 4.8a), the following state-space equations

are written in terms of flux linkages and inductances:

$$\psi'_d = \frac{E'_q}{\omega} = \frac{1}{sT'_{d0}} \left[E_{fd} - SAT_d - \left(\frac{L_d - L'_d}{L'_d - L_l} \right) \cdot \left(-\psi''_d + \left(\frac{L_d - L_l}{L_d - L'_d} \right) \psi'_d + \left(L''_d - L_l \right) i_d \right) \right]$$

(4.115)

$$\psi''_d = \frac{E''_q}{\omega} = \frac{1}{sT''_{d0}} \left[\psi'_d - \psi''_d - \left(L'_d - L''_d \right) i_d \right] + \left(\frac{L''_d - L_l}{L'_d - L_l} \right) \psi'_d$$

(4.116)

In a similar way, for q-axis (Figure 4.8b) the following state-space equations are written:

$$\psi'_q = \frac{E'_d}{\omega} = \frac{1}{sT'_{q0}} \left[SAT_q + \left(\frac{L_q - L'_q}{L'_q - L_l} \right) \left(\psi''_q - \frac{L_q - L_l}{L_q - L'_q} \psi'_q + \left(L''_q - L_l \right) i_q \right) \right]$$

(4.117)

$$\psi''_q = \frac{E''_d}{\omega} = \frac{1}{sT''_{q0}} \left[\psi'_q - \psi''_q + \left(L'_q - L''_q \right) i_q \right] + \left(\frac{L''_q - L_l}{L'_q - L_l} \right) \psi'_q$$

(4.118)

Therefore, the following subset of differential equations describes the dynamic electrical behavior of a cylindrical rotor synchronous generator:

$$\frac{d\psi'_d}{dt} = \frac{1}{T'_{d0}} \left[E_{fd} - SAT_d - \left(\frac{L_d - L'_d}{L'_d - L_l} \right) \cdot \left(-\psi''_d + \left(\frac{L_d - L_l}{L_d - L'_d} \right) \psi'_d + \left(L''_d - L_l \right) i_d \right) \right]$$

(4.119)

$$\frac{d\psi'_q}{dt} = \frac{1}{T'_{q0}} \left[SAT_q + \left(\frac{L_q - L'_q}{L'_q - L_l} \right) \left(\psi''_q - \frac{L_q - L_l}{L_q - L'_q} \psi'_q + \left(L''_q - L_l \right) i_q \right) \right]$$

(4.120)

$$\frac{d\psi''_d}{dt} = \frac{1}{T''_{d0}} \left[\psi'_d - \psi''_d - \left(L'_d - L''_d \right) i_d \right] + \left(\frac{L''_d - L_l}{L'_d - L_l} \right) \frac{d\psi'_d}{dt}$$

(4.121)

$$\frac{d\psi''_q}{dt} = \frac{1}{T''_{q0}} \left[\psi'_q - \psi''_q + \left(L'_q - L''_q \right) i_q \right] + \left(\frac{L''_q - L_l}{L'_q - L_l} \right) \frac{d\psi'_q}{dt}$$

(4.122)

The magnetic saturation on d-axis (SAT_d) and q-axis (SAT_q) is represented by the following expressions:

$$SAT_d = \frac{\psi''_q}{|\psi''|} \cdot SAT$$

(4.123)

$$SAT_q = -\frac{L_q - L_l}{L_d - L_l} \cdot \frac{\psi''_q}{|\psi''|} \cdot SAT$$

(4.124)

where:

$$SAT = A \cdot e^{B \cdot |\psi''| - C}$$

(4.125)

$$|\psi''| = \sqrt{(\psi''_d)^2 + (\psi''_q)^2}$$

(4.126)

4.6.2 Salient Pole Synchronous Generator Model

The mathematical model of the synchronous generator with salient pole rotor is developed regarding three rotor windings: one damper and one field winding on d-axis; and one damper winding on q-axis. The relationship between the electrical quantities of this machine model is presented through the state-space block diagram of d- and q-axis in Figure 4.9 in terms of inductances and flux linkages:
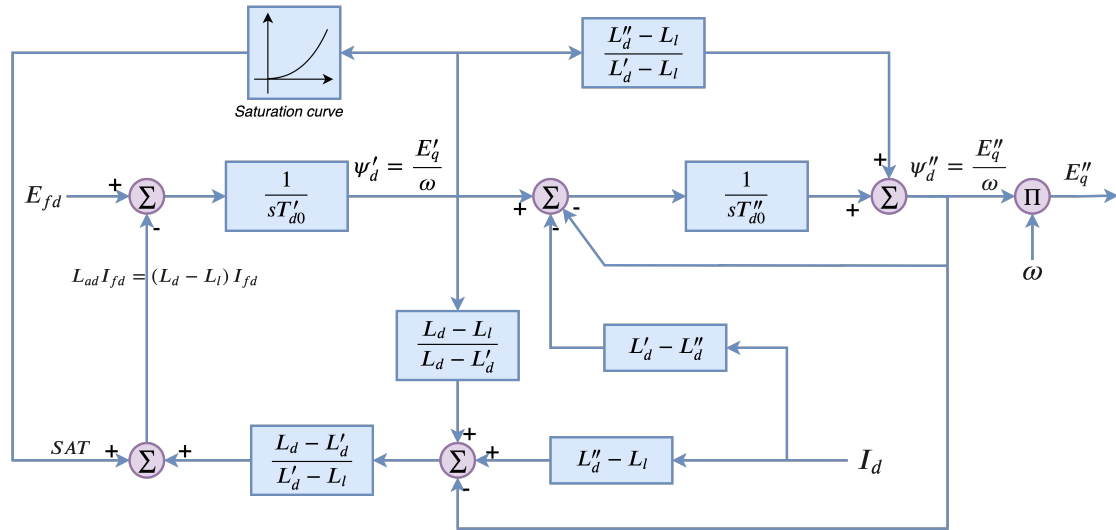
(a) State-space block diagram of d-axis
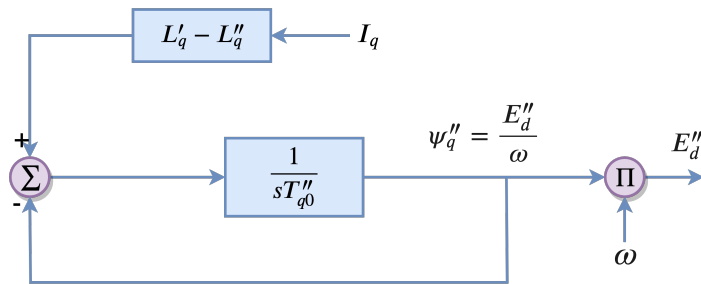
(b) State-space block diagram of q-axis

Figure 4.9: Model of a salient pole rotor synchronous generator

The following subset of differential equations describes the dynamic electrical be-

havior of a salient pole rotor synchronous generator:

$$\frac{d\psi'_d}{dt} = \frac{1}{T'_{d0}} \left[E_{fd} - SAT - \left(\frac{L_d - L'_d}{L'_d - L_l} \right) \cdot \left(-\psi''_d + \left(\frac{L_d - L_l}{L_d - L'_d} \right) \psi'_d + \left(L''_d - L_l \right) i_d \right) \right]$$

(4.127)

$$\frac{d\psi''_d}{dt} = \frac{1}{T''_{d0}} \left[\psi'_d - \psi''_d - \left(L'_d - L''_d \right) i_d \right] + \left(\frac{L''_d - L_l}{L'_d - L_l} \right) \frac{d\psi'_d}{dt}$$

(4.128)

$$\frac{d\psi''_q}{dt} = \frac{1}{T''_{q0}} \left[-\psi''_q + \left(L'_q - L''_q \right) i_q \right]$$

(4.129)

where the magnetic saturation is given by:

$$SAT = A \cdot e^{B \cdot |\psi'_q| - C}$$

(4.130)

4.6.3 Interface with Electrical Network Modeling

The magnetic flux linkage of the stator for both cylindrical and salient rotor models are calculated from the subtransient fluxes by the following equations [52]:

$$\psi_d = \psi''_d - i_d L''_d$$
$$\psi_q = -\psi''_q - i_q L''_q$$

(4.131)

The stator voltages v_d and v_q have been defined in (4.39) and (4.40) as a function of the flux linkages, as follows:

$$v_d = p\psi_d - \omega\psi_q - r_a i_d$$
$$v_q = p\psi_q + \omega\psi_d - r_a i_q$$

(4.132)

As the main purpose of this thesis relates to the evaluation of torsional interactions between the turbine-generator shaft and the network dynamics, then, a proper interface between the synchronous machine model and the electrical network suitable for SSR analysis is developed. In spite of that, an appropriated model for ESA analysis may be easily derived from this model by employing some simplifying assumptions [1], briefly summarized below:

1. Neglect subtransient salience: $L''_d \approx L''_q$;

2. Neglect stator flux linkage dynamics, i.e., the transformer voltage terms: $p\psi_d$ and $p\psi_q$;

3. Consider rotor angular speed constant: $\omega \approx 1$ pu;

4. Since the angular speed is considered equal 1 pu, the electrical equations may be expressed in terms of voltages and reactances, instead of flux linkages and inductances.

It is important to emphasize that, in this work, these simplifying assumptions are not considered. Therefore, applying the trapezoidal rule directly into (4.132), results:

$$\frac{[v_d(t) + v_d(t - \Delta t)]}{2} = \frac{[\psi_d(t) - \psi_d(t - \Delta t)]}{\Delta t} - \omega \frac{[\psi_q(t) + \psi_q(t - \Delta t)]}{2} - r_a \frac{[i_d(t) + i_d(t - \Delta t)]}{2}$$

$$\frac{[v_q(t) + v_q(t - \Delta t)]}{2} = \frac{[\psi_q(t) - \psi_q(t - \Delta t)]}{\Delta t} + \omega \frac{[\psi_d(t) + \psi_d(t - \Delta t)]}{2} - r_a \frac{[i_q(t) + i_q(t - \Delta t)]}{2}$$

Identifying and rearranging the historical terms, which are known from the previous time step numerical solution, gives:

$$v_d(t) = \frac{2}{\Delta t}\psi_d(t) - \omega\psi_q(t) - r_a i_d(t) - V_{dh}(t)$$

$$v_q(t) = \frac{2}{\Delta t}\psi_q(t) + \omega\psi_d(t) - r_a i_q(t) - V_{qh}(t)$$

(4.133)

where V_{dh} and V_{qh} are defined as:

$$V_{dh}(t) = v_d(t - \Delta t) + \frac{2}{\Delta t}\psi_d(t - \Delta t) + \omega\psi_q(t - \Delta t) + r_a i_d(t - \Delta t)$$

$$V_{qh}(t) = v_q(t - \Delta t) + \frac{2}{\Delta t}\psi_q(t - \Delta t) - \omega\psi_d(t - \Delta t) + r_a i_q(t - \Delta t)$$

Substituting (4.131) into (4.133) and performing some basic algebraic manipulations, then, (4.133) may be rewritten in a matrix form as a function of the subtransient voltages, as follows:

$$\begin{bmatrix} r_a + \dfrac{2}{\Delta t}L_d'' & -\omega L_q'' \\ \omega L_d'' & r_a + \dfrac{2}{\Delta t}L_q'' \end{bmatrix}\begin{bmatrix} i_d \\ i_q \end{bmatrix} = \begin{bmatrix} 1 & \dfrac{2}{\Delta t \cdot \omega} \\ -\dfrac{2}{\Delta t \cdot \omega} & 1 \end{bmatrix}\begin{bmatrix} E_d'' \\ E_q'' \end{bmatrix} - \begin{bmatrix} v_d \\ v_q \end{bmatrix} - \begin{bmatrix} V_{dh} \\ V_{qh} \end{bmatrix}$$

(4.134)

Finally, the stator current injected by the synchronous machine model into the electrical network in the dq reference frame is given by:

$$\begin{bmatrix} i_d \\ i_q \end{bmatrix} = \mathbf{Y}\begin{bmatrix} \dfrac{2}{\Delta t}\dfrac{E_q''}{\omega} + E_d'' \\ -\dfrac{2}{\Delta t}\dfrac{E_d''}{\omega} + E_q'' \end{bmatrix} - \mathbf{Y}\begin{bmatrix} v_d \\ v_q \end{bmatrix} - \mathbf{Y}\begin{bmatrix} V_{dh} \\ V_{qh} \end{bmatrix}$$

(4.135)

where:

$$\mathbf{Y} = \frac{1}{\left(r_a + \dfrac{2}{\Delta t}L_d''\right) \cdot \left(r_a + \dfrac{2}{\Delta t}L_q''\right) + \omega^2 X_d'' X_q''} \begin{bmatrix} r_a + \dfrac{2}{\Delta t}L_q'' & \omega L_q'' \\[2ex] -\omega L_d'' & r_a + \dfrac{2}{\Delta t}L_d'' \end{bmatrix}$$

(4.136)

Equation (4.135) allows one to build a Norton equivalent circuit to couple the synchronous generator model with the electrical network DPCM modeling through a consistent and modular interface. However, a previous conversion must be performed over the stator currents i_d, i_q, and the sensitivity matrix $\mathbf{Y}$ since they are expressed in a dq reference frame, whereas the DPCM is developed in a rectangular reference frame $\Re - \Im$. The required transformations to couple the synchronous generator model and the electrical network quantities are depicted in Figure 4.10:
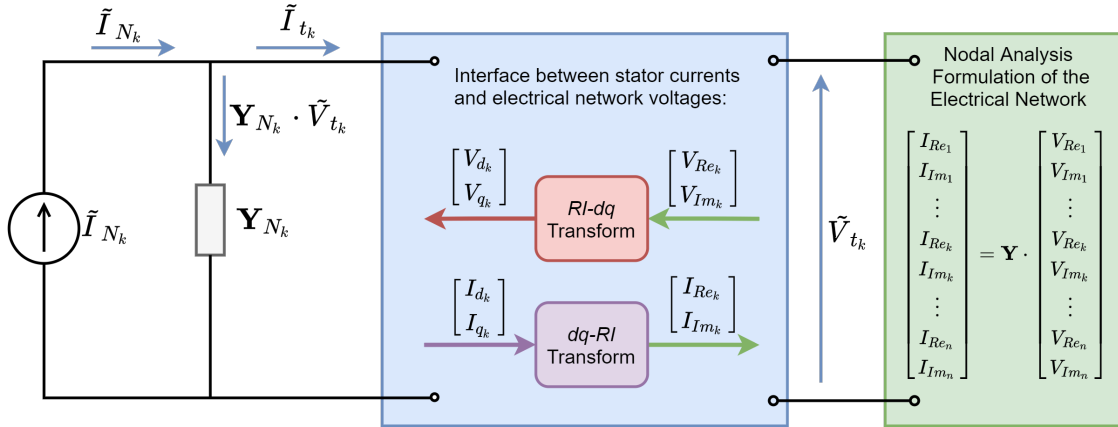
Figure 4.10: Interface between the synchronous generator model and the electrical network

Regarding an alternating solution scheme described in Section 2.5, the voltages V_{Re_k} and V_{Im_k} of the network interface bus k are made constant while solving the generator stator currents I_{d_k} and I_{q_k}, which in turn are made constant while solving unknown voltages of the electrical network. In short, this iterative process is repeated within each time step solution until the interface error between the generator and network model is below a specified tolerance.

The dq0 reference frame rotates with the machine rotor at angular speed ω_r. The relationship between the dq0 reference frame and the network reference is depicted in Figure 4.11.
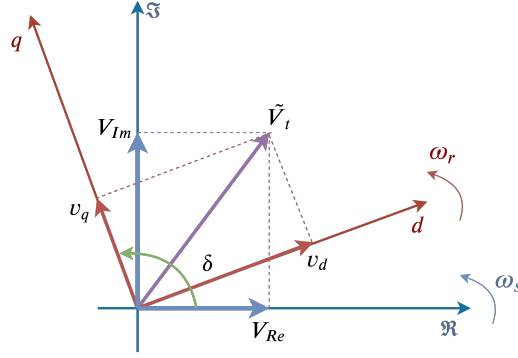
Figure 4.11: Reference frame of transformation from dq to $\Re - \Im$ axes

With δ being the angle between the q-axis and the real axis ($\Re$) in a common synchronous rotating reference for the electrical network. From Figure 4.11, the following *dq-RI* transformation matrix must be employed to convert dq quantities into the network reference frame:

$$\begin{bmatrix} V_d \\ V_q \end{bmatrix} = \begin{bmatrix} \sin(\delta) & -\cos(\delta) \\ \cos(\delta) & \sin(\delta) \end{bmatrix} \cdot \begin{bmatrix} V_{Re} \\ V_{Im} \end{bmatrix} \longrightarrow \begin{bmatrix} V_{dq} \end{bmatrix} = [T] [V_{RI}] \qquad (4.137)$$

The inverse *dq-RI* transformation to transform real and imaginary quantities to the machine dq reference is given by:

$$\begin{bmatrix} V_{Re} \\ V_{Im} \end{bmatrix} = \begin{bmatrix} \sin(\delta) & \cos(\delta) \\ -\cos(\delta) & \sin(\delta) \end{bmatrix} \cdot \begin{bmatrix} V_d \\ V_q \end{bmatrix} \longrightarrow [V_{RI}] = [T]^{-1} \begin{bmatrix} V_{dq} \end{bmatrix} \qquad (4.138)$$

4.6.4 Interface between Electrical and Mechanical Equations

The interface between the electrical and mechanical equations is established through the equations of motion described in Section 4.4, where the unbalance between the mechanical and electromagnetic torques yields acceleration or deceleration torque over the machine rotor. Equation (4.96) describing the rotor acceleration is repeated below:

$$\frac{d\omega_r}{dt} = \frac{1}{2H} (T_m - T_e - D\Delta\omega_r)$$

Substituting the electromagnetic torque T_e into this expression results:

$$\frac{d\omega_r}{dt} = \frac{1}{2H} \left(T_m - (i_q\psi_d - i_d\psi_q) - D\Delta\omega_r \right) \qquad (4.139)$$

132

Equation (4.139) provides the interface between the mechanical and electrical sub-systems of the synchronous machine.

The next chapter describes the turbine-generator shaft model considering the speed deviation of each turbine section as a function of the unbalance experienced between the input and output torque of each individual mass of the turbine-generator mechanical system.

Chapter 5

Subsynchronous Resonance

This chapter reviews basic definitions and physical aspects involved in the analysis of *subsynchronous oscillations* in the electrical power systems, with the main focus on the mathematical development of simulation models suitable for time-domain analysis of *subsynchronous resonance* (SSR) phenomena. From this perspective, Figure 5.1 highlights the interface between several subsystems of a turbogenerator unit (for instance, a boiler-turbogenerator unit) demanded in the scope of SSR analysis.
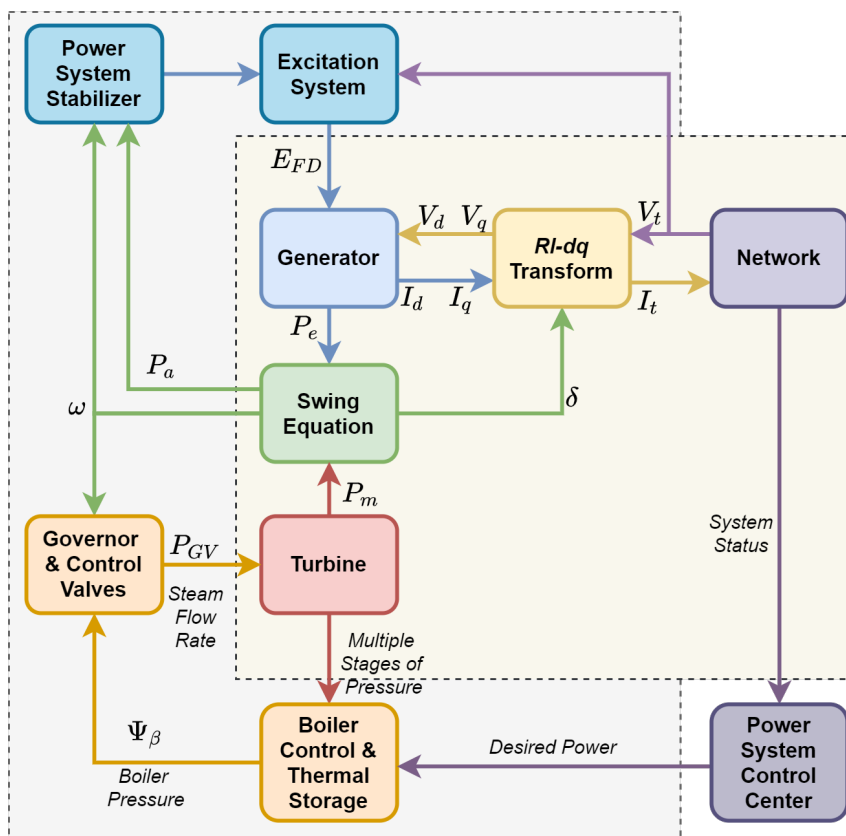
Figure 5.1: Interface between subsystems of a turbogenerator unit

In this regard, the previous chapters have already fulfilled some requirements: Chapter 3 has presented a detailed electrical network modeling to reveal its natural oscillation frequencies associated with fast transients; and Chapter 4 has described the synchronous generator model including the stator flux dynamics to allow the analysis of interactions between the network and stator transients. The system to rotor reference frame transformation gives the interface between the state-variables from the electrical network and the synchronous generator model. The interface between the electrical and mechanical equations of the generator has been carried out by the swing equation (4.95), correlating the unbalance between the torques applied to the turbine, represented as a rigid body so far.

For a comprehensive modeling of the elements shown in Figure 5.1, this chapter provides a detailed discussion about terms, symbols, and definitions related to SSR theory, supporting the understanding toward the mathematical formulation of the turbine-generator mechanical system. Readers familiar with the basic theory related to SSR can skip directly to Section 5.3, where the individualized simulation modeling of the synchronous generator rotor mechanical system is presented.

In the scope of this thesis, special attention is given to the analysis of subsynchronous interactions between the turbine-generator shaft and series compensated transmission systems, thereby the interface between the turbine sections and the synchronous generator is detailed through the *individualized spring-mass model*. This modeling is widely employed in the study of natural torsional oscillations modes of the rotor system, which may interact with the subsystems of Figure 5.1.

5.1 Introduction to Subsynchronous Oscillations

In the development of the synchronous generator mechanical equations presented in Chapter 4, the turbine-generator rotor shaft has been assumed to be composed by a single lumped mass, with an equivalent inertia (H) and damping factor (D). However, the mechanical system of a turbogenerator shaft is not effectively rigid, instead it is composed by a long complex axis with several dominant rotating masses connected by shafts of limited stiffness [1].

In practice, the turbine-generator rotor accounts for several torsional oscillation modes (frequencies) below and above the synchronous frequency, which are respectively referred to as **subsynchronous** and **supersynchronous** oscillation modes. Adverse interactions between the turbine-generator mechanical shaft and the electrical network dynamics are more prone to occur in the subsynchronous range, thereby an individualized spring-mass model is necessary to represent the synchronous ma-

chine rotor in SSR studies [7].

Figure 5.2 shows an individualized representation of a steam turbine-generator shaft system, where each predominant turbine section is modeled as a *lumped mass*. This example considers six masses representing the rotors of the generator (GEN), two low-pressure turbine sections (LPA and LPB), an intermediate-pressure turbine section (IP), and a high-pressure (HP) turbine section [1].
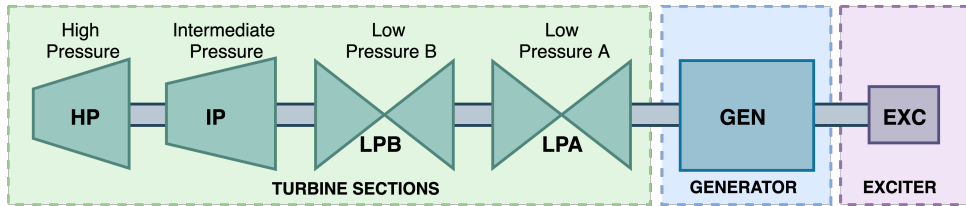
Figure 5.2: Individualized lumped-mass model of a multi-stage thermal unit

Following a disturbance, each rotor mass oscillates against each other at one or more natural oscillation modes with associated damping factors. In general terms, a turbine-generator shaft composed by n individualized masses has $(n-1)$ torsional oscillation modes and one electromechanical oscillation mode due to the entire rigid body oscillation against the rest of the system. While the oscillation frequency of the electromechanical mode is typically between 0.1 and 3 Hz, the torsional modes range up to a few tens of Hertz and are referred to as *Subsynchronous Oscillations* (SSO). A formal definition of SSO was provided by IEEE [35]:

> **Subsynchronous oscillation** *is an electric power system condition where the electric network exchanges significant energy with a turbine-generator at one or more of the natural frequencies of the combined system below the synchronous frequency of the system following a disturbance from equilibrium. The above excludes the rigid body modes of the turbine-generator rotors.*

Oscillations of the turbine-generator shaft in the subsynchronous range may occur as a result of interaction between the rotor mechanical system with network passive components, such as series capacitors; or between the rotor and the control system of active transmission equipment, such as HVDC or SVC. The electrical network presents natural oscillation frequencies that are function of the inherent system characteristics (described in Section 5.2). Likewise, active power system controls introduce forced oscillation modes in the EPS. In this regard, both natural and forced subsynchronous oscillation frequencies may interact with torsional modes of the turbine-generator shaft system. In order to analyze subsynchronous oscillations, special committees were created to establish nomenclatures, component modeling, and assessment methods [35, 54, 55].

136

Electromechanical oscillations in the rotor induce torques between adjacent rotor sections, so that if these torques coincide with a subsynchronous torsional mode, it may lead to an unstable situation. Besides that, if these torques are of greater magnitude than the restorative torques, the shaft fatigue can cause irreparable deformation or shaft rupture [7]. The most common problems related to SSO are defined in [1], as follows:

1. **Torsional interaction** with power system controls, which can introduce negative damping torques in the subsynchronous frequency range, causing instability of torsional modes;

2. **Subsynchronous resonance** resulting from the interaction between the electrical and mechanical systems of the synchronous generator at an oscillation mode close to a natural electrical frequency of series capacitor-compensated electrical networks;

3. **Torsional fatigue** due to electrical network switching or large disturbances. This phenomenon is related to the transient torques originated in the synchronous generator shaft following a disturbance in the transmission system.

The first two problems can be evaluated by using linear and nonlinear analysis tools, while the third requires the use of nonlinear models since it is related to large disturbances or maneuvers in the EPS, such as transmission line faults or energization. The subsynchronous resonance phenomenon is the one that stands out most in the literature [7, 54, 56]. The characteristics of oscillations associated with SSR are defined as [35]:

> *Subsynchronous resonance* *encompasses the oscillatory attributes of electrical and mechanical variables associated with turbine-generators when coupled to a series capacitor compensated transmission system where the oscillatory energy interchange is* **lightly damped**, **undamped***, or even* **negatively damped** *and* **growing***.*

Abnormal operation following the application of series capacitors in power systems were first reported in 1937, over the occurrence of electrical self-excitation in synchronous and induction machines [57]. In that instance, subsynchronous currents of large amplitude have originated in the machine's stator under unfavorable circumstances, resulting in pulsating torques in the rotor. Later, a more detailed analysis of the problem pointed out that electromechanical oscillations and self-excitation in electrical machines were associated phenomena, so that their separate analysis would only be drawn considering the different time constants involved with these phenomena [58]. Afterwards, several other topics were published on the subject, but

without due attention from the electrical industry until the 1970s.

In 1970, it has occurred the first shaft failure of a turbogenerator at the Mohave Generating Station, in Southern California [59]. In those circumstances, a short-circuit was developed in the shaft section between the generator and exciter at the main generator collector due to torsional fatigue. After a deep analysis, it was concluded that the shaft suffered excessive heating due to mechanical oscillations produced by an adverse interaction with the series-compensated transmission system. However, this problem was only recognized as subsynchronous resonance after the second shaft failure, in 1971 [60]. After these occurrences, a comprehensive research related to the phenomena involving torsional aspects of the machines provided a significant improvement in the degree of knowledge of power engineers and a more consolidated theory on the subject [61]. Subsequently, tests were conducted in Mohave to identify the torsional characteristics of the electromechanical system, such as the natural oscillation frequencies of the shaft and their corresponding modal damping coefficients [62].

Against this background, the following subsections address this theory by using very simplified models, in order to illustrate the basic concepts that govern the SSR phenomenon in series capacitor compensated transmission systems.

5.2 Series Capacitor-Compensated Systems

Series capacitors are widely employed on transmission systems to compensate a portion of the transmission line inductive reactance. This application increases the maximum power transfer capability of the compensated circuit. Additionally, it can contribute to improve the system voltage profile, enhance transient stability, increase the damping of power oscillations, and balance power sharing between parallel circuits [63]. On the other hand, series compensation introduces natural electrical oscillation frequencies in the subsynchronous range. This intrinsic characteristic of the electrical power system is illustrated in this subsection.

Let one consider the radial system of Figure 5.3 composed by a thermal generation unit connected through a step-up transformer and a compensated transmission line with lumped parameters to an infinite bus.
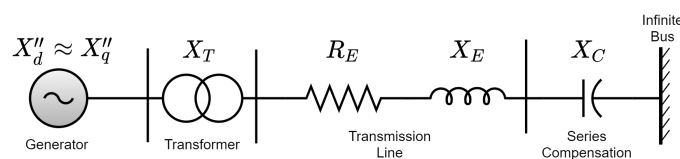
Figure 5.3: Series capacitor-compensated system

At this stage, for a basic understanding of the subject, the reactances are calculated at the synchronous frequency ω_0:

$X_d'' = \omega_0 \cdot L_d''$ $\rightarrow$ is the d-axis subtransient reactance of the generator [ohms];

$X_T = \omega_0 \cdot L_T$ $\rightarrow$ is the step-up transformer reactance [ohms];

$X_E = \omega_0 \cdot L_E$ $\rightarrow$ is the transmission line reactance [ohms];

$X_C = 1/(\omega_0 \cdot L_C)$ $\rightarrow$ is the series capacitor reactance [ohms];

The total inductive reactance X_L includes the line, the transformer, and the generator subtransient reactance, as follows:

$$X_L = X_d'' + X_T + X_E \tag{5.1}$$

This electrical system is the simplest resonant circuit and yields a single **electrical resonant** or **natural oscillation frequency** (ω_n), given by:

$$\omega_n = \frac{1}{\sqrt{LC}} = \frac{\omega_0}{\sqrt{(\omega_0 L)(\omega_0 C)}} = \omega_0 \sqrt{\frac{X_C}{X_L}} \qquad [\text{rad/s}] \tag{5.2}$$

or:

$$f_n = f_0 \sqrt{\frac{X_C}{X_L}} \qquad [\text{Hz}] \tag{5.3}$$

where:

f_0 is the synchronous base frequency [Hz];

f_n is the natural or resonant frequency of the electrical system [Hz];

The electrical natural oscillation frequencies (f_n) introduced in the power grid by series capacitor compensation are also referred to as *subsynchronous natural frequencies*, inasmuch as the value of X_C is always smaller than X_E. In other words, the series capacitance only compensates a portion of the inductive line reactance, resulting natural frequencies always below the synchronous frequency ω_0, which is easily inferred from (5.2).

After a disturbance in the electrical network, components of transient stator current at natural frequency (f_n) induce rotor currents at the slip frequency (f_r):

$$f_r = f_0 \pm f_n \tag{5.4}$$

Therefore, both subsynchronous $(f_0 - f_n)$ and supersynchronous $(f_0 + f_n)$ current components result in the machine rotor, respectively representing positive and negative sequence components of rotor currents [7]. From a review of the shaft torsional response, the supersynchronous components are reasonably well damped [60], while the subsynchronous components are lightly damped and more prone to interact with series-compensated network [1].

The subsynchronous electrical natural frequency and the subsynchronous rotor slip frequency are said to be complementary since their sum is equal to the synchronous frequency. If the complement of a torsional mode of the rotor is close to any natural frequency of the electrical network, they may interact with a strong coupling exchanging energy in the subsynchronous frequency range. The origin of these interactions is didactically approached in [64] through a deep analysis of the relationship between mechanical and electromagnetic torques acting in a simple electromechanical system.

Table 5.1 illustrates the natural frequency of the network and the subsynchronous slip rotor frequency as a function of the series compensation degree. For the sake of simplicity, the reactances frequency-dependent characteristic is neglected in this simplified example. A detailed method to determine these impedances as a function of the capacitive compensation is employed in frequency scanning programs [65].

Table 5.1: Electrical network natural frequency and slip rotor frequency

$(X_C/X_L) \cdot 100$ (%)	Natural frequency f_n (Hz)	Slip frequency f_r (Hz)
10	18	42
25	30	30
30	32.6	27.4
40	38	22
50	42.4	17.6

As the use of series capacitors is a simple, economical and efficient way to increase the transmission capability and improve the dynamic performance of the electrical system, the development of mitigating measures is needed to prevent the adverse effects of their use. Many alternatives have been proposed [66], but the application of a specific measure depends on technical analysis of the problem and economical issues.

5.2.1 Types of Subsynchronous Resonance

The following items describe different mechanisms of subsynchronous resonance that can be derived from the interaction between series-compensated transmission networks and synchronous generators [7]. In general terms, the following steps can trigger SSR mechanisms:

1. **Subsynchronous currents** flowing in the electrical network **produce subsynchronous rotor torques**;

2. The subsynchronous rotor torques **induce subsynchronous rotor currents**;

3. These subsynchronous rotor currents **produce subsynchronous armature voltages components**;

4. The subsynchronous armature voltages **sustain or enhance the subsynchronous network currents** that first originate these voltage components;

The cyclical mechanism aforementioned is referred to as **self-excitation**, and it can be triggered in different sequence order. For example, an oscillation in a turbine section at a torsional mode frequency can induce subsynchronous rotor torques that produce subsynchronous stator voltages, giving rise to subsynchronous stator currents that enhance the subsynchronous torque at the original torsional mode. These sustained or enhanced subsynchronous currents may be damped, sustained or negatively damped depending on mechanical and electrical damping sources.

For ease of analysis, the self-excitation mechanism is divided into: (i) strictly electrical phenomenon of interaction between the electrical network and the synchronous generator; and (ii) mechanical interaction between the turbine-generator shaft and electrical network dynamics. Alternatively, these two effects may also appear in the power system as a combined phenomenon.

Additionally, there have several references approaching torsional mode instability due to interaction with excitation systems, speed governor controls, and with controls of HVDC converters and FACTS equipment [1, 27, 67]. These control systems, designed to improve the power system dynamic performance, can interact adversely with the torsional modes of the turbine-generator shaft, affecting their performance. In general, any device located close to a turbogenerator and that responds to power or speed variations in the subsynchronous frequency range can interact adversely with the electrical and mechanical systems of the synchronous machine. The causes and methods of analyzing such torsional instability problems are out of the scope of this thesis. Therefore, the focus of this thesis is devoted to the analysis of subsynchronous interactions of turbine-generator systems with series compensated trans-

mission system whose origin mechanisms are described below.

Induction Generator Effect

The induction generator effect is a phenomenon of strictly electrical origin, which is caused by the self-excitation of the electrical system associated with the generator. Figure 5.4 depicts a simplified equivalent circuit of the synchronous generator seen from its terminals by subsynchronous stator currents $i_s(t)$. At this point, the synchronous generator saliency is neglected, so that its equivalent circuit becomes similar to that employed in the analysis of induction motors.
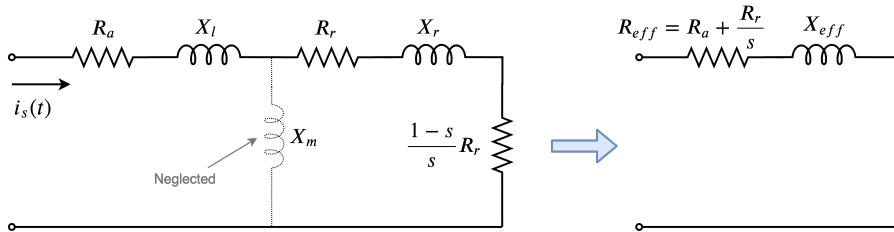
Figure 5.4: Simplified equivalent circuit of a synchronous generator viewed from its terminals by subsynchronous stator currents

The effective resistance R_{eff} of this equivalent circuit is obtained as a function of the slip frequency:

$$R_{eff} = R_a + \frac{R_r}{s} \tag{5.5}$$

$$s = \frac{f_n - f_0}{f_n} \tag{5.6}$$

where s is the slip between the synchronous and subsynchronous speeds. The resulting slip (5.6) has a negative value in the presence of subsynchronous currents since the main rotor field runs faster than the MMF produced by the subsynchronous currents in the stator ($f_n < f_0$). Consequently, the rotor effective resistance R_{eff} seen by subsynchronous currents is also negative. This feature is similar to the operation of an induction machine.

In series-compensated transmission systems with a high degree of compensation, this negative effective resistance can exceed the network resistance at the subsynchronous frequency f_n resulting in an RLC circuit with a negative equivalent resistance. Under this condition, the electrical system becomes self-excited, causing voltage and current oscillations with growing amplitudes over time. Once this form of self-excitation is a fundamentally electrical phenomenon, it does not depend on the characteristics of the turbine-generator axis [1].

Torsional Interaction

In contrast with the induction generator effect, torsional interaction involves both the electrical system and the mechanical system associated with the turbine-generator shaft.

The mechanical system of the turbine-generator shaft has several natural torsional oscillation frequencies (f_{rt}), generally located in the subsynchronous range. These oscillations are responsible for modulating voltages in the stator at the slip frequency $(f_s = f_0 \pm f_{rt})$, which are reflected in the electrical network. If one of these complement frequencies (f_s) is close to any of the resonant frequencies f_n, a small induced voltage in the stator might result in large subsynchronous currents. These currents in the stator of the generator induce electromagnetic torques that amplify the primary torsional rotor oscillations. If these torques exceed the damping torques inherent in the mechanical system, the subsynchronous currents are sustained or growing, and the system becomes self-excited [35]. In general, phenomena of this nature have catastrophic consequences for the turbogenerator shaft. Even if the system is not unstable, minor disturbances can result in torsional stresses of great magnitude, causing loss of shaft life due to cyclic fatigue.

There is still a possibility of a combined occurrence of torsional interaction and the induction generator effect. In general, torsional interaction dominates when the sybsynchronous rotor torque frequency (the complement of the subsynchronous torsional frequency $f_s = f_0 - f_{rt}$) is close to one of the electrical natural frequencies (f_n), whereas the induction generator effect dominates when the subsynchronous slip frequency (which produces rotor torque $f_s = f_0 - f_n$) is isolated from any of the rotor torsional frequencies (f_{rt}). These mechanisms are distinctively classified for ease of analysis since there is no method to completely separate these two phenomena.

Shaft Torque Amplification

This type of phenomenon results from large disturbances or switching in the system, such as transmission line faults or energization. These sudden network changes give rise to transient currents that impose transient torques on the rotors of the synchronous generators. In a transmission system without series compensation, these transients are DC, and they always decay to zero over a time constant given by the ratio of the inductance to resistance. In the presence of series capacitors, the currents caused by these disturbances are oscillatory and may contain components at different subsynchronous frequencies. If the complement of any of these subsynchronous frequencies $(f_s = f_0 - f_n)$ is close to a torsional frequency of the turbine-generator shaft (f_{rt}), large pulsating torques can result, amplifying the effect of the original

torques [7]. The resulting transient torques cause torsional stresses on the turbogenerator shafts, which may contribute to the loss of the torsional fatigue life, especially in the presence of series capacitors.

5.2.2   Analytical Tools for SSR Studies

In dealing with the SSR mechanisms discussed in Section 5.2.1, the mathematical modeling adopted in the study of the first two problems might consider linear models for small signal analysis. In contrast, the third problem requires nonlinear models since it involves large disturbances. The following items provide a brief description of the most frequent analytical tools employed in the study of SSR mechanisms.

- **Frequency Scanning**: this method is rooted in the linear analysis and it is mainly employed in the study of the induction generator effect, as a preliminary analysis of the problem. This method computes the equivalent resistance and inductance viewed from the internal buses of the generators looking into the network, as a function of frequency [1]. This analytical method gives information about the natural frequencies of the system at which the equivalent inductance is zero and the resistance is negative, so that subsynchronous oscillations are self-sustained by virtue of the induction generator effect. This technique is fast and simple, requiring reduced computational burden when compared to nonlinear methods. Thus, it can be useful in identifying regions of the system that do not interact in the SSR range and, therefore, can be omitted or represented by equivalents in detailed studies of torque amplification and torsional interaction.

- **Eigenvalue Analysis**: this method is a powerful analytical tool for the study of the power system dynamic behavior under small disturbances. This technique allows the study of large scale power systems and support efficient designing and tunning of control parameters. The mathematical formulation employed in this analysis considers the power system components and their control system models linearized at the equilibrium operating point [1]. The linearized system of equations gives information about the natural oscillation modes and their associated damping. However, this tool is limited to study small disturbances nearby the steady-state operating point. On the other hand, in the analysis of shaft torque amplification phenomenon, the linearized models are not representative since the power system nonlinearities become significant. In this case, a detailed nonlinear representation is required for the power system equipment and control models.

- **Time-Domain Analysis**: the numerical integration of the power system

nonlinear differential equations provides detailed information about the state-variables dynamic behavior over time. Therefore, the occurrence of SSR problems, such as transient shaft torques amplification due to network changes, can be inferred by the observation of torques, currents, and voltages through the dynamic simulation. In this framework, both three-phase representation (employed in EMT programs), and the DP modeling (adopted in this thesis) can carry out the study of adverse interactions between the turbine-generator shaft and series-compensated transmission systems. It is worth emphasizing that the three-phase representation is limited to the analysis of small systems due to the computational burden associated and also for the absence of the required data. In contrast, the DP approach can handle large-scale power systems and it allows automatic initialization from a steady-state operating point.

In this thesis, the nonlinear time-domain analysis of torsional interactions between the natural oscillation modes of the turbine-generator shaft and the electrical natural frequencies of the network is explored through the DP modeling. Hence, the following subsection presents a steam turbine-generator shaft modeling that gives a direct interface with the DPCM models presented in Chapter 3 for the electrical network components.

5.3 Turbine-Generator Shaft Model

The equations of motion presented in Section 4.4 allows the analysis of rotor oscillations involving the entire turbine-generator shaft relative to other generators since the rotor has been assumed to be composed of a single lumped-mass. This subsection presents the mathematical formulation of the turbine-generator shaft by using the *individualized spring-mass model*, suitable for SSR studies. While the electromechanical modeling gives information about the rigid body oscillation mode ranging from 0.1 up to 3 Hz, the individualized simulation model reveals torsional oscillation modes, which take place between the multiple sections of the turbine-generator shaft [7].

In this context, it is necessary to model the predominant rotor masses interconnected by shaft sections, likewise the steam turbine-generator model illustrated in Figure 5.2. Considering that example, Figure 5.5 gives the *spring-mass model* corresponding to this six masses turbine-generator shaft.
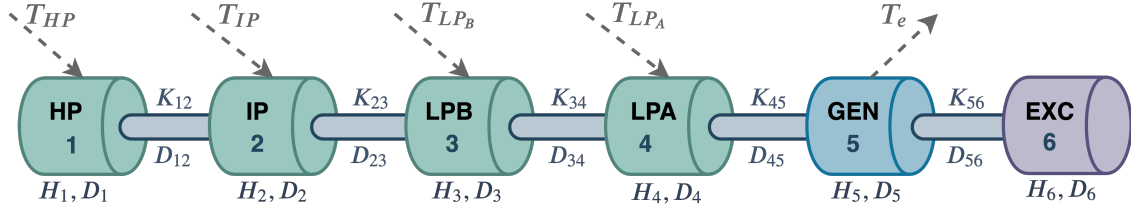
Figure 5.5: Individualized lumped-mass model of a steam turbine-generator shaft

In general terms, a turbine-generator shaft is composed by n individualized masses, where each rotor mass i is defined by a inertia constant H_i and damping factor D_i; and each shaft section (i,j) between masses i and j is modeled by a finite torsional stiffness K_{ij} and damping factor D_{ij}.

Therefore, the overall symbols and notations employed in the mathematical development of the individualized rotor swing equations are outlined in Table 5.2.

Table 5.2: Parameters of the turbine-generator shaft system

Symbol	Description	Unit
T_i	Mechanical torque developed by mass i, if it is a turbine section, otherwise $T_i = 0$	pu
T_e	Generator air-gap torque	pu
T_m	Total mechanical torque	pu
H_i	Inertia constant of the rotor mass i	MW.s/MVA
p_i	Percent of the total turbine mechanical torque (T_m) developed by mass i	%
δ_i	Angular position of mass i with respect to a synchronously rotating common reference	elec. rad
D_i	Damping factor (or coefficient) of mass i	pu torque/ pu speed deviation
$D_{i,j}$	Damping factor (or coefficient) of the shaft section connecting masses i and j	pu torque/ pu speed deviation
K_i	Torsional stiffness of mass i	pu torque/elec. rad
$K_{i,j}$	Torsional stiffness of the shaft section connecting masses i and j	pu torque/elec. rad

The inertia constant H_i related to each rotor mass represents a fraction of the total shaft inertia constant given in (4.85), whereas the torsional stiffness K_{ij} assigned

to the shaft between masses i and j can be obtained from (5.7) (for a shaft with uniform cross-section).

$$K = \frac{GF}{l} \tag{5.7}$$

where G is the rigidity modulus of the shaft material, F is the form factor associated with the shaft geometry property, and l is the shaft length. In practice, the inertia and stiffness constants are obtained from the constructive characteristics of the turbine-generator shaft provided by the manufacturers and they can predict the natural oscillation frequencies with a good level of accuracy [7].

The torsional torques (T_s) that cause elastic strain into each shaft section are written in terms of its torsional stiffness (K_{ij}) and angular twist (θ_{ij}), as follows:

$$T_s = K_{ij} \cdot \theta_{ij} \tag{5.8}$$

with the torque, torsional stiffness, and angular twist being expressed in [N·m], [N·m/rad], and [mech. rad], respectively.

The normalization of the turbine-generator shaft torque equations is performed in terms of the torque base:

$$T_{base} = \frac{S_{base}}{\omega_{0m}} = S_{base} \cdot \frac{p_f}{2\omega_0} \tag{5.9}$$

where p_f is the number of field poles, ω_{0m} is the rated angular speed in mech rad/s, and ω_0 is the rated angular speed in elec rad/s. Thus, dividing the torsional torque (5.8) by (5.9) yields:

$$K \text{ [pu torque/elec rad]} = \frac{K \text{ [N·m/mech rad]}}{S_{base}} \left(\frac{4\omega_0}{p_f^2} \right) \tag{5.10}$$

The restorative sources that contribute to the damping of torsional oscillations include steam forces, shaft material hysteresis and electrical sources. These sources are very small and difficult to measure [1]. Thus, in the individualized spring-mass modeling, the damping torques associated with each rotor mass (D_i) and shaft section (D_{ij}) are represented in terms of torque components, which are proportional to the speed deviations of each rotor section.

5.3.1 Mechanical Equations of the Shaft System

The development of the swing equations associated with each rotor mass is assigned in this subsection, considering the specific example of the turbine-generator shaft shown in Figure 5.5. Subsequently, a general shaft modeling is conferred to allow SSR studies of generic turbine-generator shafts composed of n masses.

The per unit equations of motion for the rotor mass i, are given by:

$$T_{a_i}(t) = 2H_i \frac{d\Delta\omega_i(t)}{dt} = T_{input_i}(t) - T_{output_i}(t) - T_{damping_i}(t) \qquad i = 1, \dots, n$$

$$\frac{d\delta_i(t)}{dt} = \omega_0 \cdot \Delta\omega_i(t)$$

(5.11)

Thus, the various torque components in (5.11) are defined, as follows:

- $\boldsymbol{T_{a_i}(t)} \rightarrow$ denotes the acceleration (or deceleration) torque over the rotor mass i;

- $\boldsymbol{T_{input_i}(t)} \rightarrow$ denotes the **input torques** of mass i, decomposed into the following components:

  $\boldsymbol{T_{i-1,i}(t)}$: mechanical torque developed by the previous turbine rotors and transmitted throughout the shaft section between masses $(i-1)$ and i, given by:
  $$T_{i-1,i}(t) = K_{i-1,i} \cdot (\delta_{i-1}(t) - \delta_i(t))$$
  (5.12)

  $\boldsymbol{T_i(t)}$: mechanical torque developed by mass i (if it belongs to a turbine section). It can be expressed as a portion p_i of the total mechanical torque T_m, as follows:
  $$T_i(t) = p_i \cdot T_m(t)$$
  (5.13)

- $\boldsymbol{T_{output_i}(t)} \rightarrow$ denotes the **output torques** of mass i, decomposed into the following components:

  $\boldsymbol{T_e(t)}$: electromagnetic air-gap torque. This component only takes place in the rotor mass of the generator.

  $\boldsymbol{T_{i,i+1}(t)}$: output mechanical torque transmitted throughout the shaft section between masses i and $(i+1)$ toward the rotor mass $(i+1)$.

  $$T_{i,i+1}(t) = K_{i,i+1} \cdot (\delta_i(t) - \delta_{i+1}(t))$$
  (5.14)

148

- $\boldsymbol{T_{damping_i}(t)} \rightarrow$ denotes the **damping torques** of mass i, decomposed into the following components:

$\boldsymbol{T_{D_i}(t)}$: damping torque associated with the rotor mass i:

$$T_{D_i}(t) = D_i \cdot \Delta\omega_i(t) \qquad (5.15)$$

$\boldsymbol{T_{D_{i-1,i}}(t)}$: damping torque associated with the shaft section between masses $(i-1)$ and i:

$$T_{D_{i-1,i}}(t) = D_{i-1,i} \cdot (\Delta\omega_i(t) - \Delta\omega_{i-1}(t)) \qquad (5.16)$$

$\boldsymbol{T_{D_{i,i+1}}(t)}$: damping torque associated with the shaft section between masses i and $(i+1)$:

$$T_{D_{i,i+1}}(t) = D_{i,i+1} \cdot (\Delta\omega_i(t) - \Delta\omega_{i+1}(t)) \qquad (5.17)$$

For the sake of simplicity, the time argument (t) is omitted in the mathematical development presented from this point forward.

5.3.1.1 Equations of Motion - Especific Case

Considering the specific lumped-mass model of Figure 5.5 composed by six masses, the various components of torques over the rotors of the generator (GEN) and the low pressure turbine section A (LPA) are depicted in Figure 5.6.
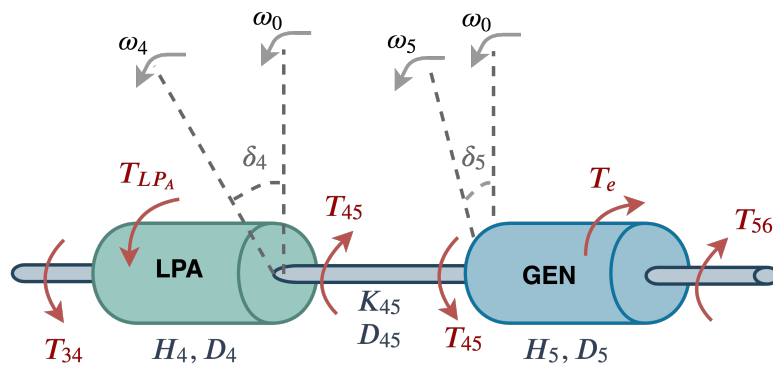
Figure 5.6: Components of torques over the rotor sections LPA and GEN

For the turbine section LPA, the input, output and damping torque components are given by:

$$T_{input_4} \quad = \quad T_{LPA} + T_{34} = T_{LPA} + K_{34} \cdot (\delta_3 - \delta_4)$$

$$T_{output_4} \quad = \quad T_{45} = K_{45} \cdot (\delta_4 - \delta_5) \tag{5.18}$$

$$T_{damping_4} \quad = \quad T_{D_4} + T_{D_{34}} + T_{D_{45}}$$

$$= \quad D_4 \left(\Delta \omega_4 \right) + D_{34} \left(\Delta \omega_4 - \Delta \omega_3 \right) + D_{45} \left(\Delta \omega_4 - \Delta \omega_5 \right)$$

Substituting (5.18) into (5.11) yields:

$$2H_4 \frac{d \left(\Delta \omega_4 \right)}{dt} = T_{LPA} + K_{34} \left(\delta_3 - \delta_4 \right) - K_{45} \left(\delta_4 - \delta_5 \right) - D_4 \left(\Delta \omega_4 \right) \tag{5.19}$$

$$- D_{34} \left(\Delta \omega_4 - \Delta \omega_3 \right) - D_{45} \left(\Delta \omega_4 - \Delta \omega_5 \right)$$

Similarly, the components of torques over the generator mass are given by:

$$T_{input_5} \quad = \quad T_{45} = K_{45} \cdot (\delta_4 - \delta_5)$$

$$T_{output_5} \quad = \quad T_e + T_{56} = T_e + K_{56} \cdot (\delta_5 - \delta_6) \tag{5.20}$$

$$T_{damping_5} \quad = \quad T_{D_5} + T_{D_{45}} + T_{D_{56}}$$

$$= \quad D_5 \left(\Delta \omega_5 \right) + D_{45} \left(\Delta \omega_5 - \Delta \omega_4 \right) + D_{56} \left(\Delta \omega_5 - \Delta \omega_6 \right)$$

Once the generator mass does not develop mechanical torque, this input component is omitted on its respective swing equation. Besides, the generator mass accounts for the air-gap torque into its output torque components. Thus, substituting (5.20) into (5.11), gives:

$$2H_5 \frac{d \left(\Delta \omega_5 \right)}{dt} = K_{45} \left(\delta_4 - \delta_5 \right) - T_e - K_{56} \left(\delta_5 - \delta_6 \right) - D_5 \left(\Delta \omega_5 \right) \tag{5.21}$$

$$- D_{45} \left(\Delta \omega_5 - \Delta \omega_4 \right) - D_{56} \left(\Delta \omega_5 - \Delta \omega_6 \right)$$

Performing a similar procedure for each rotor mass of the specific turbine-generator shaft of Figure 5.5, it is obtained the following set of swing equations:

Mass 1: HP

$$2H_1 \frac{d \left(\Delta \omega_1 \right)}{dt} = T_{HP} - K_{12} \left(\delta_1 - \delta_2 \right) - D_1 \left(\Delta \omega_1 \right) - D_{12} \left(\Delta \omega_1 - \Delta \omega_2 \right) \tag{5.22}$$

$$\frac{d \left(\delta_1 \right)}{dt} = \left(\Delta \omega_1 \right) \omega_0 \tag{5.23}$$

Mass 2: IP

$$2H_2\frac{d\left(\Delta\omega_2\right)}{dt} = T_{IP} + K_{12}\left(\delta_1 - \delta_2\right) - K_{23}\left(\delta_2 - \delta_3\right) - D_2\left(\Delta\omega_2\right) \tag{5.24}$$
$$- D_{12}\left(\Delta\omega_2 - \Delta\omega_1\right) - D_{23}\left(\Delta\omega_2 - \Delta\omega_2\right)$$

$$\frac{d\left(\delta_2\right)}{dt} = \left(\Delta\omega_2\right)\omega_0 \tag{5.25}$$

Mass 3: LPB

$$2H_3\frac{d\left(\Delta\omega_3\right)}{dt} = T_{LPB} + K_{23}\left(\delta_2 - \delta_3\right) - K_{34}\left(\delta_3 - \delta_4\right) - D_3\left(\Delta\omega_3\right) \tag{5.26}$$
$$- D_{23}\left(\Delta\omega_3 - \Delta\omega_2\right) - D_{34}\left(\Delta\omega_3 - \Delta\omega_4\right)$$

$$\frac{d\left(\delta_3\right)}{dt} = \left(\Delta\omega_3\right)\omega_0 \tag{5.27}$$

Mass 4: LPA

$$2H_4\frac{d\left(\Delta\omega_4\right)}{dt} = T_{LPA} + K_{34}\left(\delta_3 - \delta_4\right) - K_{45}\left(\delta_4 - \delta_5\right) - D_4\left(\Delta\omega_4\right) \tag{5.28}$$
$$- D_{34}\left(\Delta\omega_4 - \Delta\omega_3\right) - D_{45}\left(\Delta\omega_4 - \Delta\omega_5\right)$$

$$\frac{d\left(\delta_4\right)}{dt} = \left(\Delta\omega_4\right)\omega_0 \tag{5.29}$$

Mass 5: GEN

$$2H_5\frac{d\left(\Delta\omega_5\right)}{dt} = K_{45}\left(\delta_4 - \delta_5\right) - T_e - K_{56}\left(\delta_5 - \delta_6\right) - D_5\left(\Delta\omega_5\right) \tag{5.30}$$
$$- D_{45}\left(\Delta\omega_5 - \Delta\omega_4\right) - D_{56}\left(\Delta\omega_5 - \Delta\omega_6\right)$$

$$\frac{d\left(\delta_5\right)}{dt} = \left(\Delta\omega_5\right)\omega_0 \tag{5.31}$$

Mass 6: EXC

$$2H_6\frac{d\left(\Delta\omega_6\right)}{dt} = K_{56}\left(\delta_5 - \delta_6\right) - D_6\left(\Delta\omega_6\right) - D_{56}\left(\Delta\omega_6 - \Delta\omega_5\right) \tag{5.32}$$

$$\frac{d\left(\delta_6\right)}{dt} = \left(\Delta\omega_6\right)\omega_0 \tag{5.33}$$

5.3.1.2 Equations of Motion - General Model

Let one consider the generic turbine-generator shaft shown in Figure 5.7. The inertia constant (H_i), damping factors (D_i, D_{ij}), and torsional stiffness (K_{ij}) associated with this model are defined in Table 5.2:
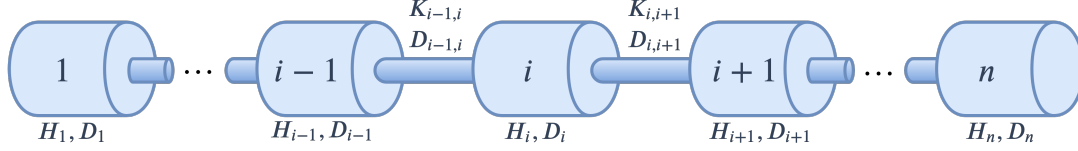
Figure 5.7: General structure of a individualized lumped-mass model

The general equations of motion for each rotor mass i, is given by:

$$2H_i \frac{d\Delta\omega_i}{dt} = T_i - T_e - K_{i-1,i}(\delta_i - \delta_{i-1}) - K_{i,i+i}(\delta_i - \delta_{i+1}) + \tag{5.34}$$
$$- D_i\Delta\omega_i - D_{i-1,i}(\Delta\omega_i - \Delta\omega_{i-1}) - D_{i,i+i}(\Delta\omega_i - \Delta\omega_{i+1})$$

$$\frac{d\delta_i}{dt} = (\Delta\omega_i(t))\,\omega_0 \tag{5.35}$$

The following items point out some specific modifications that must be made over (5.34) in particular cases:

- If the mass i does not belong to the turbine section, the corresponding term T_i must be zero in (5.34) since it does not develop mechanical torque;

- If the mass i is located at the shaft left-end, its corresponding swing equation simplifies to:

$$2H_i \frac{d\Delta\omega_i}{dt} = T_i - T_e - K_{i,i+i}(\delta_i - \delta_{i+1}) - D_i\Delta\omega_i - D_{i,i+i}(\Delta\omega_i - \Delta\omega_{i+1}) \tag{5.36}$$

- If the mass i is located at the shaft rigth-end, its corresponding swing equation simplifies to:

$$2H_i \frac{d\Delta\omega_i}{dt} = T_i - T_e - K_{i-1,i}(\delta_i - \delta_{i-1}) - D_i\Delta\omega_i - D_{i-1,i}(\Delta\omega_i - \Delta\omega_{i-1}) \tag{5.37}$$

- If the mass i is the generator rotor, the air-gap torque T_e must be included in the swing equation. Moreover, as it does not develop mechanical torque, its

corresponding swing equation simplifies to:

$$2H_i \frac{d\Delta\omega_i}{dt} = -T_e - K_{i-1,i}\left(\delta_i - \delta_{i-1}\right) - K_{i,i+i}\left(\delta_i - \delta_{i+1}\right) + \qquad (5.38)$$
$$-D_i\Delta\omega_i - D_{i-1,i}\left(\Delta\omega_i - \Delta\omega_{i-1}\right) - D_{i,i+i}\left(\Delta\omega_i - \Delta\omega_{i+1}\right)$$

It is worth mentioning that the electromagnetic torque T_e is determined by solving the generator electrical equations presented in Section 4.6, and its interface with the mechanical shaft modeling is given by the generator swing equation. Furthermore, the mechanical torques developed by each turbine stage depends on the steam turbine dynamics and its respective governor system.

5.3.2 Solution of the Shaft Mechanical Equations

In this thesis, the time-domain solution methodology of the turbine-generator shaft system is developed by employing the trapezoidal integration rule over the first order differential equations of motion. In this context, the state-variables of interest are the rotational speeds of each shaft section $\omega_i(t)$ and its respective angular position $\delta_i(t)$ with respect to a synchronously rotating common reference for the electrical network.

Thus, considering the swing equations of mass i :

$$2H_i \frac{d\Delta\omega_i(t)}{dt} = T_i(t) - T_e(t) - D_i\Delta\omega_i(t) \qquad (5.39)$$
$$- K_{i-1,i}\left(\delta_i(t) - \delta_{i-1}(t)\right) - K_{i,i+i}\left(\delta_i(t) - \delta_{i+1}(t)\right) +$$
$$- D_{i-1,i}\left(\Delta\omega_i(t) - \Delta\omega_{i-1}(t)\right) - D_{i,i+i}\left(\Delta\omega_i(t) - \Delta\omega_{i+1}(t)\right)$$

$$\frac{d\delta_i(t)}{dt} = \omega_0 \cdot \left(\Delta\omega_i(t)\right) \qquad (5.40)$$

The trapezoidal integration rule is applied into (5.39), resulting in:

$$2H_i\left[\omega_i(t) - \omega_i(t - \Delta t)\right] = \frac{\Delta t}{2}\left[T_i(t) - T_e(t) - D_i\Delta\omega_i(t)\right. \qquad (5.41)$$
$$- K_{i-1,i}\left(\delta_i(t) - \delta_{i-1}(t)\right) - K_{i,i+i}\left(\delta_i(t) - \delta_{i+1}(t)\right) +$$
$$\left. - D_{i-1,i}\left(\Delta\omega_i(t) - \Delta\omega_{i-1}(t)\right) - D_{i,i+i}\left(\Delta\omega_i(t) - \Delta\omega_{i+1}(t)\right)\right] +$$
$$\frac{\Delta t}{2}\left[T_i(t - \Delta t) - T_e(t - \Delta t) - D_i\Delta\omega_i(t - \Delta t)\right.$$
$$- K_{i-1,i}\left(\delta_i(t - \Delta t) - \delta_{i-1}(t - \Delta t)\right) - K_{i,i+i}\left(\delta_i(t - \Delta t) - \delta_{i+1}(t - \Delta t)\right) +$$
$$\left. - D_{i-1,i}\left(\Delta\omega_i(t - \Delta t) - \Delta\omega_{i-1}(t - \Delta t)\right) - D_{i,i+i}\left(\Delta\omega_i(t - \Delta t) - \Delta\omega_{i+1}(t - \Delta t)\right)\right]$$

Grouping the historical terms depending on the previous time step $(t - \Delta t)$, the memory term $B_1(t - \Delta t)$ is defined:

$$
\begin{aligned}
B_1(t - \Delta t) =& T_i(t - \Delta t) - T_e(t - \Delta t) - D_i \Delta\omega_i(t - \Delta t) \\
& - K_{i-1,i}\left(\delta_i(t - \Delta t) - \delta_{i-1}(t - \Delta t)\right) - K_{i,i+i}\left(\delta_i(t - \Delta t) - \delta_{i+1}(t - \Delta t)\right) + \\
& - D_{i-1,i}\left(\Delta\omega_i(t - \Delta t) - \Delta\omega_{i-1}(t - \Delta t)\right) - D_{i,i+i}\left(\Delta\omega_i(t - \Delta t) - \Delta\omega_{i+1}(t - \Delta t)\right)
\end{aligned}
\tag{5.42}
$$

Performing some basic algebraic manipulations over (5.41) to explicit the rotational speed of the rotor mass i, gives:

$$
\begin{aligned}
\omega_i(t) = \ & K_2 \bigg[T_i(t) - T_e(t) - K_3 \cdot \delta_i(t) + K_{i-1,i} \cdot \delta_{i-1}(t) + K_{i,i+i} \cdot \delta_{i+1}(t) + \\
& + D_{i-1,i} \cdot \Delta\omega_{i-1}(t) + D_{i,i+i} \cdot \Delta\omega_{i+1}(t) \bigg] + K_2 \cdot B_1(t - \Delta t) + \omega_i(t - \Delta t)
\end{aligned}
\tag{5.43}
$$

where:

$$
\begin{aligned}
K_0 &= \frac{\Delta t}{4H_i} \\
K_1 &= 1 + \left(D_i + D_{i-1,i} + D_{i,i+i}\right) \cdot K_0 \\
K_2 &= \frac{K_0}{K_1} \\
K_3 &= K_{i-1,i} + K_{i,i+i}
\end{aligned}
\tag{5.44}
$$

Similarly, employing the trapezoidal integration rule into (5.40), gives:

$$
[\delta_i(t) - \delta_i(t - \Delta t)] = \frac{\Delta t}{2}\omega_0\left[\Delta\omega_i(t)\right] + \frac{\Delta t}{2}\omega_0\left[\Delta\omega_i(t - \Delta t)\right]
\tag{5.45}
$$

Grouping the historical terms depending on the previous time step $(t - \Delta t)$, the memory term $B_2(t - \Delta t)$ is defined:

$$
B_2(t - \Delta t) = \frac{\Delta t}{2}\omega_0\left[\Delta\omega_i(t - \Delta t)\right] + \delta_i(t - \Delta t)
\tag{5.46}
$$

Therefore, the position of the rotor mass i in respect with a synchronously rotating common reference in the network is given by:

$$
\delta_i(t) = \frac{\Delta t}{2}\omega_0\left[\Delta\omega_i(t)\right] + B_2(t - \Delta t)
\tag{5.47}
$$

154

The interface between the turbine-generator equations and the DPCM models of the electrical network allows determining the initial values respective to the mechanical torques developed by each turbine section, and the angular rotor position of each mass i, from the steady-state operating point.

5.3.3   Initialization of the Shaft Mechanical Equations

The initial conditions of the turbine-generator shaft are computed from a steady-state operating point provided by a power flow solution of the system. This initialization process is detailed in this subsection assuming the electrical network as a balanced three-phase system.

Therefore, the mechanical torque of each rotor mass i is obtained as a portion (p_i) of the total mechanical torque T_m developed by the entire turbine mechanical system:

$$T_i = p_i \cdot T_m \tag{5.48}$$

Considering the turbine-generator shaft of Figure 5.5, the mechanical torques developed by each mass are expressed, as follows:

$$
\begin{aligned}
T_1 &= p_1 \cdot T_m \\
T_2 &= p_2 \cdot T_m \\
T_3 &= p_3 \cdot T_m \\
T_4 &= p_4 \cdot T_m \\
T_5 &= 0 \\
T_6 &= 0
\end{aligned}
\tag{5.49}
$$

For steady-state operating condition $(T_{a_i} = 0)$, the total mechanical torque is assumed to be equal to the electromagnetic torque T_e. In addition, the derivatives of the equations of motion are assumed to be zero, as well as the speed deviation of the rotor sections. In this extent, (5.34) turns into the following expression:

$$0 = T_i - T_e - K_{i-1,i} \left(\delta_i - \delta_{i-1} \right) - K_{i,i+i} \left(\delta_i - \delta_{i+1} \right) \tag{5.50}$$

Writing the expression (5.50) for each rotor mass of Figure 5.5, results in:

$$
\begin{aligned}
T_1 &= K_{12}\left(\delta_1 - \delta_2\right) \\
T_2 &= K_{12}\left(\delta_2 - \delta_1\right) + K_{23}\left(\delta_2 - \delta_3\right) \\
T_3 &= K_{23}\left(\delta_3 - \delta_2\right) + K_{34}\left(\delta_3 - \delta_4\right) \\
T_4 &= K_{34}\left(\delta_4 - \delta_3\right) + K_{45}\left(\delta_4 - \delta_5\right) \\
-T_e &= K_{45}\left(\delta_5 - \delta_4\right) + K_{56}\left(\delta_5 - \delta_6\right) \\
0 &= K_{56}\left(\delta_6 - \delta_5\right)
\end{aligned}
\tag{5.51}
$$

Expressing (5.51) in a matrix form by grouping associated terms, gives:

$$
\begin{bmatrix}
T_1 \\
T_2 \\
T_3 \\
T_4 \\
-T_e \\
0
\end{bmatrix}
=
\begin{bmatrix}
K_{12} & -K_{12} & & & & \\
-K_{12} & K_{12}+K_{23} & -K_{23} & & & \\
& -K_{23} & K_{23}+K_{34} & -K_{34} & & \\
& & -K_{34} & K_{34}+K_{45} & -K_{45} & \\
& & & -K_{45} & K_{45}+K_{56} & -K_{56} \\
& & & & -K_{56} & K_{56}
\end{bmatrix}
\cdot
\begin{bmatrix}
\delta_1 \\
\delta_2 \\
\delta_3 \\
\delta_4 \\
\delta_5 \\
\delta_6
\end{bmatrix}
\tag{5.52}
$$

One should note that the linear system (5.52) has infinite possible solutions since it is linearly dependent. Therefore, once the angular displacement $(\delta_i - \delta_j)$ is satisfied, any constant added to each δ_i is also a solution for this linear system.

In this sense, an additional equation is added in (5.52) to settle the initial position of the generator rotor equals to the value obtained in the solution of the synchronous generator electrical equations:

$$
\delta_5 = \delta_{\text{gen}_0}
\tag{5.53}
$$

Therefore, the following system of linear equations is obtained:

$$
\begin{bmatrix}
T_1 \\
T_2 \\
T_3 \\
T_4 \\
\mathbf{0} \\
0 \\
\hline
\delta_{\text{gen}_0}
\end{bmatrix}
=
\left[
\begin{array}{cccccc|c}
K_{12} & -K_{12} & & & & & \\
-K_{12} & K_{12}+K_{23} & -K_{23} & & & & \\
& -K_{23} & K_{23}+K_{34} & -K_{34} & & & \\
& & -K_{34} & K_{34}+K_{45} & -K_{45} & & \\
& & & -K_{45} & K_{45}+K_{56} & -K_{56} & -1 \\
& & & & -K_{56} & K_{56} & \\
\hline
& & & & 1 & & 0
\end{array}
\right]
\cdot
\begin{bmatrix}
\delta_1 \\
\delta_2 \\
\delta_3 \\
\delta_4 \\
\delta_5 \\
\delta_6 \\
\hline
-T_e
\end{bmatrix}
\tag{5.54}
$$

156

Equation (5.3.3) allows a complete definition of the initial angular position of each individual rotor mass relative to a common synchronously rotating reference in the network.

5.3.4 Torsional Natural Frequencies and Mode Shapes

After being subjected to a physical disturbance, the individual rotor masses oscillate against each other at one or more natural frequencies of the turbine-generator shaft mechanical model. These natural oscillation frequencies are referred to as *torsional mode frequencies*, which are dependent on the disturbance nature and the initial operating point. If the system reaches the steady-state condition, and the mechanical shaft remains oscillating at one of the natural frequencies, the relative amplitude and phase of the individual turbine-generator rotor modes are fixed, and they are called the *mode shapes* of torsional motion [35].

The natural torsional frequencies and mode shapes can be determined by using the modal analysis [1] through linearized models. In this regard, the determination of the most active components, concerning an individual oscillatory mode, provides the mode-shapes which give substantial information about the system, such as variables of significant excitation, and coherence of oscillations between different machine groups.

The modal analysis requires the development of the state-space equations of the turbine-generator shaft in the following form:

$$\dot{\mathbf{x}} = \mathbf{A}\mathbf{x} \tag{5.55}$$

In this analysis the state variables that compose the state vector $\mathbf{x}$ are the speed deviations $\Delta\omega_i$, and the rotor angle $\Delta\delta_i$, for $i = 1 \ldots 6$. Therefore, linearizing the equations of motion of each rotor mass yields a linear system of equations in the form of (5.55), where the constant coefficients of matrix $\mathbf{A}$ depend on the shaft system parameters $(H_i, D_i, D_{ij}, K_{ij})$ and the generator synchronizing coefficient.

Assuming constant mechanical torque developed by each turbine section, the linearized equations of the shaft system can be written by inspection from (5.22) to (5.33). Thus, the eigenvalues of $\mathbf{A}$ represent the *natural oscillation frequencies* of the shaft system, and the corresponding eigenvectors provide the *mode shapes*, i.e., the relative activity of a state variable for a given mode [1]. For the sake of qualitative illustration, Figure 5.8 provides a graphical example of the mode shapes,

arranged from the lowest to the highest value of the shaft modes. In this analysis, one should note that the mode order indicates the number of mode reversals. It gives information about the rotational displacement and the oscillation magnitude of each rotor mass when a specific mode is excited.
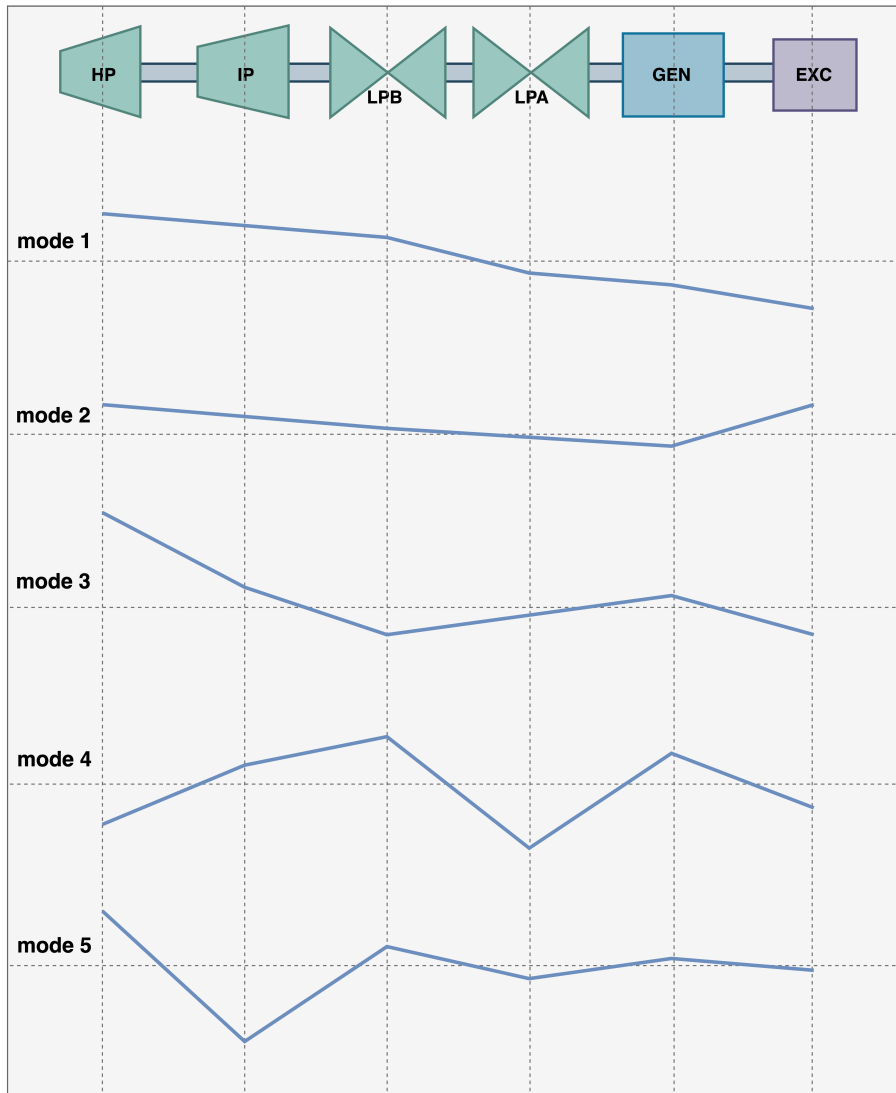

Figure 5.8: Mode shapes of the natural oscillation modes

In a general case, a rotor with n masses will present $n-1$ torsional modes. Hence, the ith torsional mode holds the ith highest torsional frequency (arranging in crescent order), and its mode shape (eigenvector) reveals i polarity reversals.

Altough the modal analysis of the shaft system is not the main concern of this thesis, the PacDyn [68], developed by Cepel for small signal analysis, will be employed as a complement for the SSR analysis in Chapter 7.

Chapter 6

Computational Developments and Validations

This chapter presents the computational developments and validation results of the mathematical models formulated in the previous chapters into the commercial software ANATEM©, which is a comprehensive ESA tool developed by CEPEL [5] for nonlinear analysis of electromechanical stability in large-scale power systems.

The developments detailed in this chapter include the representation of the electrical network dynamics, stator transients of synchronous machines, and the individualized turbine-generator shaft model. Incorporating these models allows widening the ANATEM simulation scope toward the subsynchronous frequency range since it reveals the interactions between shaft torsional modes and electrical resonant frequencies of the power system.

In this purpose, this chapter is divided into three main sections detailing the developments and validations through simplified models of the (i) electrical network, (ii) synchronous machine electrical equations, and (iii) the individualized turbine-generator equations of motion. The ANATEM simulation results are compared with reference solutions obtained by the PSCAD/EMTDC software [4], which is assumed as the validation tool.

The ANATEM dynamic models and simulation parameters are specified through a main "**st**a**b**ility" file (`*.STB`) written in a proper syntax with fixed columns for each type of input data. In addition to that, a **sav**ecase file (`*.SAV`) with a converged steady-state operating point must be provided by the ANAREDE software [37], which is used as the initial condition for the time-domain simulation. In this context, the **execution codes** are the main commands that specify equipment models and controls, for the association of these models with electrical network equipment, and

for the definition of simulation parameters, output variables and simulation events. Complementary, the **execution options** modify fundamental characteristics of the execution codes, such as the simulation context (ESA or EMT analysis). Both **execution codes** and **options** are defined in ANATEM by mnemonics composed of four letters. Some important mnemonics, for the scope of this thesis, are described below:

`DEVT` - Execution code to specify chronological simulation events, such as network switching and faults over the simulation window;

`DPLT` - Execution code to specify output variables to be monitored over time, such as nodal voltages, line currents, control variables, etc.;

`DSIM` - Execution code to define the simulation parameters, such as the time step Δt size, and the maximum simulation time t_{max};

`EXSI` - Execution code to begin the time-domain simulation using the alternated trapezoidal implicit solution scheme. The traditional ANATEM simulation context is the ESA analysis, so that in this thesis the SSR scope is enabled through new execution options, which are detailed in the following subsection.

In general terms, the following subsections detail the **execution codes** and **options** developed in this thesis to represent the electrical network (Figure 6.1), synchronous machines (Figure 6.2), and additional features related to output variables and simulation events (Figure 6.3). The description of the mnemonics for execution codes are explained in the following items. The details of the implementations is provided in this thesis in order to instruct the users about these new features and to allow reproducing the results.
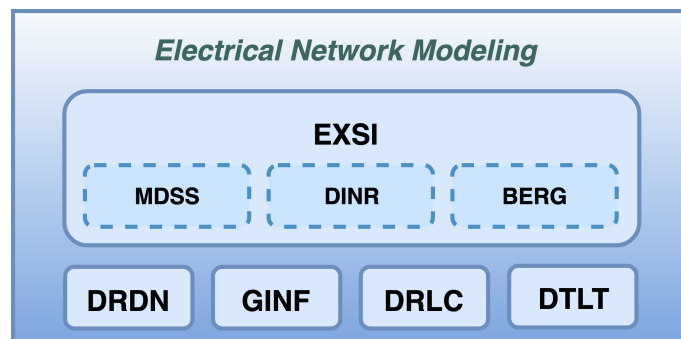

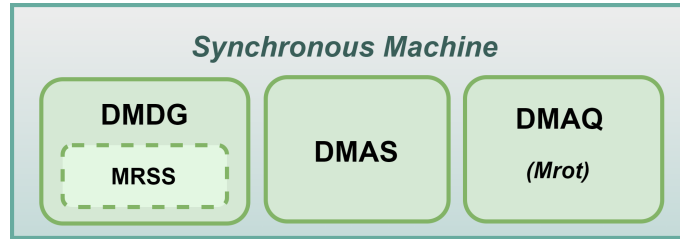Figure 6.1: ANATEM developments for electrical network modeling

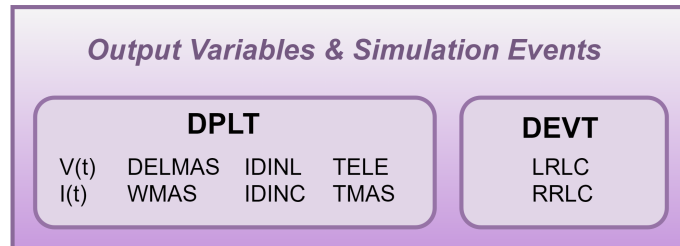Figure 6.2: ANATEM developments for synchronous machine modeling

Figure 6.3: ANATEM developments for output variables and simulation events

In Figures 6.1 to 6.3, the execution codes are delineated by continuous lines, whereas the execution options are bounded by dashed lines.

6.1 Electrical Network Modeling

In this subsection, the DPTS approach is employed in ANATEM software for the representation of electrical network dynamics, with automatic steady-state initialization, considering loads as balanced three-phase impedances in each abc phase as positive sequence impedances. In this development, the steady-state operating point is provided by ANAREDE software, whereas the dynamic database shall be the same adopted for traditional ANATEM simulations of ESA analysis.

6.1.1 Computational Developments

The ANATEM software is developed in FORTRAN, so that the computational developments of the network dynamics through the DPCM models are implemented in the same language by using the Direct Sparse Solver (DSS) Interface Routines of INTEL© Math Kernel Library (MKL). These routines are employed to reorder and factorize the network admittance matrix built in a compatible form, and to solve the electrical network system of equations. The DSS interface is composed by a set of user-callable routines that are used in the step-by-step iterative solving process and utilizes a general matrix format for solving sparse systems of linear equations. More information about the DSS description and implementation details can be obtained in [69].

Figure 6.4 shows a typical structure of the DSS interface routines applied to the time-domain solution of linear systems.
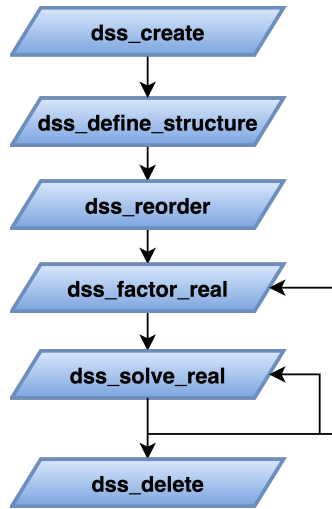

Figure 6.4: DSS interface routines

Each DSS routine depicted in Figure 6.4 accounts for some input and output parameters, and it provides return values, which are described in detail in [69]. Usually, this structure is employed to perform the mathematical solution of the matrix-vector equation, $\mathbf{A} \cdot \mathbf{x} = \mathbf{b}$, where the matrix $\mathbf{A}$ is referred to as the *coefficient matrix*, and the vectors $\mathbf{x}$ and $\mathbf{b}$ represent the *solution* and the *independent vector*, respectively. In this thesis, these routines are applied to the electrical network iterative solution, considering the following expression:

$$\mathbf{Y} \cdot \tilde{\mathbf{V}}(t) = \tilde{\mathbf{I}}(t) - \tilde{\mathbf{I}}_{\mathbf{h}}(t - \Delta t) \tag{6.1}$$

Equation (6.1) has been introduced in Section 3.4, where the nodal admittance matrix $\mathbf{Y}$ is constructed from the DPCM tensors and it remains unchanged as long as the simulation time step size remains unchanged; the nodal current vector $\tilde{\mathbf{I}}(t)$ and the nodal history source vector $\tilde{\mathbf{I}}_{\mathbf{h}}(\mathbf{t})$ are determined in the beginning of the time step and are kept constant within each Δt for the iterative (in the presence of nonlinear elements, such as voltage or frequency dependent loads) or direct (linear networks) solution of the nodal voltage vector $\tilde{\mathbf{V}}(t)$.

The overall structure of the solution algorithm implemented in ANATEM by using the DPTS approach via DSS interface routines is depicted in Figure 6.5.
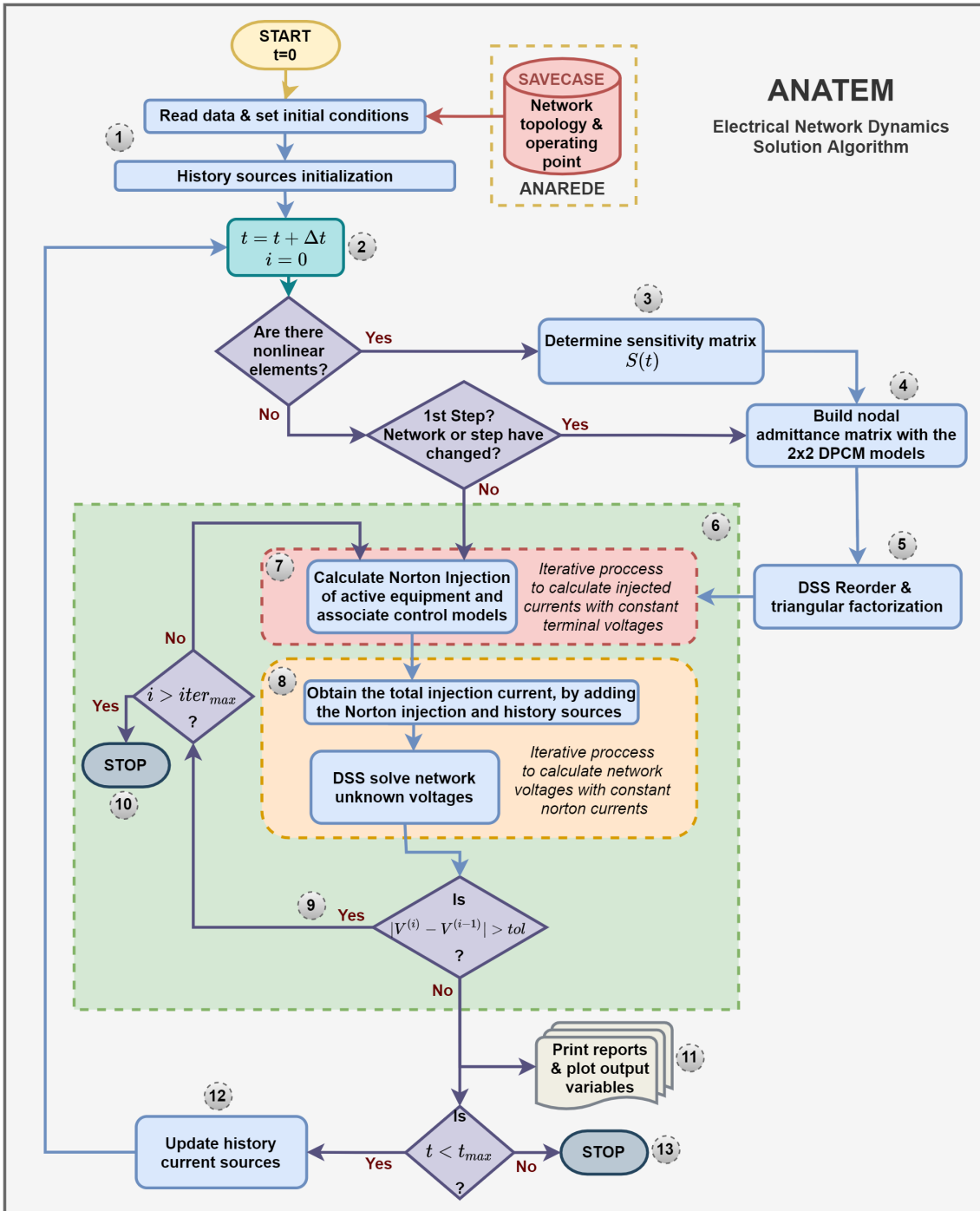
Figure 6.5: ANATEM solution algorithm for the electrical network dynamics by using the DPTS approach and the DSS interface routines

In greater detail, the dynamic simulation algorithm portrayed through the flowchart of Figure 6.5 carries out the following steps:

1. At $t = 0$, the simulation begins and the electrical network topology and operating point is obtained from the ANAREDE savecase, where the initial conditions of algebraic and state-variables are determined. At this point, the history current sources from the DPCM models are also obtained;

2. Reset iteration counters ($i = 0$) and increment the actual time ($t = t + \Delta t$);

3. In the presence of nonlinear elements, build the Norton sensitivity matrix $\boldsymbol{S}(t)$ to be considered in the network nodal analysis formulation;

4. If it is the first integration step, or if there has been any change in the network or in the integration step-size, or if there are any non-linear elements, then, build the nodal admittance matrix using the 2x2 DPCM equivalent tensors described in Chapter 3;

5. Employ the DSS interface routine to reorder and factorize the network system of equations, and also to execute the following alternating procedure while $t < t_{max}$; If $t = t_{max}$, then, the simulation stops successfully;

6. Execute the alternating solution scheme comprising the electrical network, active sources, and nonlinear equipment models. Increment the iteration counter: i = i + 1;

7. While solving unknown voltages of the electrical network, currents injected by generators and other active sources remain constant;

8. Likewise, network voltages remain unchanged while solving equipment current injections;

9. Steps 6, 7 and 8 are solved alternatively and iteratively within each time step Δt until interface errors between these solution loops are below a specified tolerance *tol*. Therefore, return to step 7 while interface errors are above *tol* and i < iter$_{max}$;

10. If i > iter$_{max}$ and the convergence is not achieved, the simulation stops before t_{max} without success;

11. Otherwise, if the iterative loops 7 and 8 reach convergence, plot output variables and print reports;

12. While $t < t_{max}$, update the history current sources for usage in the next step and return to step 2;

13. If $t = t_{max}$, the dynamic simulation finishes successfully.

The following items detail the new execution codes and options developed in this thesis to modify the context of the `EXSI` execution code, which originally enables the traditional ESA simulation scope in the ANATEM software.

DSS Interface Routines

In the first development stage, the application of the DSS interface routines has been implemented in ANATEM through the following command:

> `MDSS` - This execution option must be used jointly with the `EXSI` execution code to enable the ESA electrical network solution by using the DSS interface routines of the MKL library.

The validation of the simulation results obtained by using the `MDSS` execution option is carried out with the well known IEEE 14-bus test system. In this regard, Figure 6.6 shows the comparison between the `MDSS` mode and the traditional ANATEM simulation of a three-phase short-circuit fault in the middle of the line between bus 2 and bus 3, followed by a generation reduction at bus 1, and a load shedding scheme tripping.
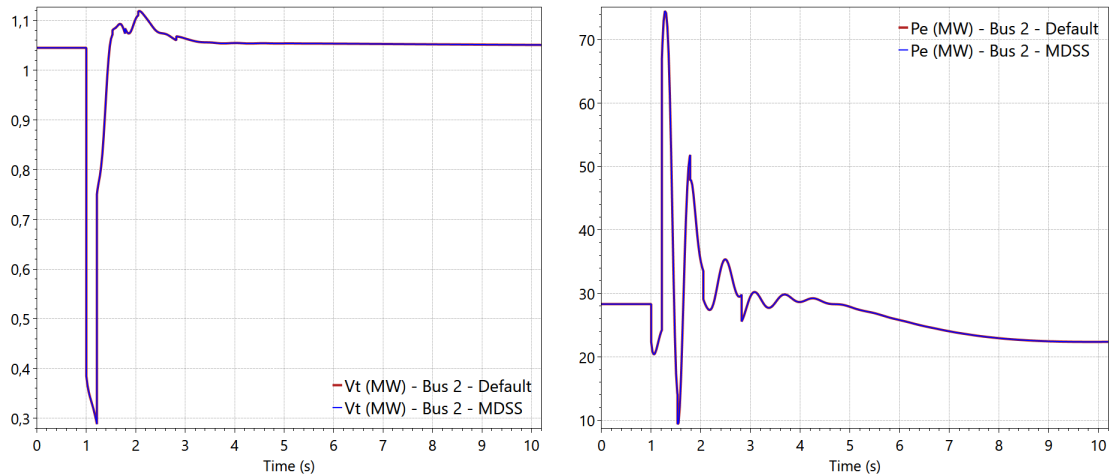
(a) RMS voltage at bus 2 in pu   (b) Electrical power of the generator at bus 2 in MW

Figure 6.6: Comparison between the Default and MDSS simulation results

The dynamic data corresponding to the equipment models and controls employed in this analysis, as well as the simulation events used to perform this simulation are detailed in Appendix B.1.

Figures 6.6a and 6.6b respectively illustrate the RMS voltage at bus 2 in pu, and the active electrical power injected by the generator at bus 2 in MW. These results validate the computational development of the DSS interface routines (`MDSS`) since it provides results in agreement with the ANATEM traditional simulation (default).

DPCM Developments

Once the DSS structure is established, the implementation of the DPCM equations for the representation of the electrical network dynamics is provided in ANATEM through the new execution option `DINR`, which is described below:

> `DINR` - This execution option enables the representation of the electrical network dynamics through the DPCM models, considering the solution algorithm depicted in Figure 6.5. It uses the DSS interface routines (likewise the `MDSS` option uses) due to its modularity and direct compatibility with the tensor equations given in Chapter 3. It is important to emphasize that this new feature keeps compatibility with the ANATEM dynamic database; thus far, no additional data is needed. Furthermore, the history sources of the DPCM models are determined at the beginning of the simulation, considering steady-state initialization from the operating point provided by the ANAREDE software.

Employing the execution option `DINR` with the execution code `EXSI`, automatically converts lumped components of the electrical network, such as short line branches modeled by L, C, RL or RC components, into their respective DPCM models, as illustrated in Figure 6.7. The validation results of these DPCM models are later shown in Section 6.1.2.
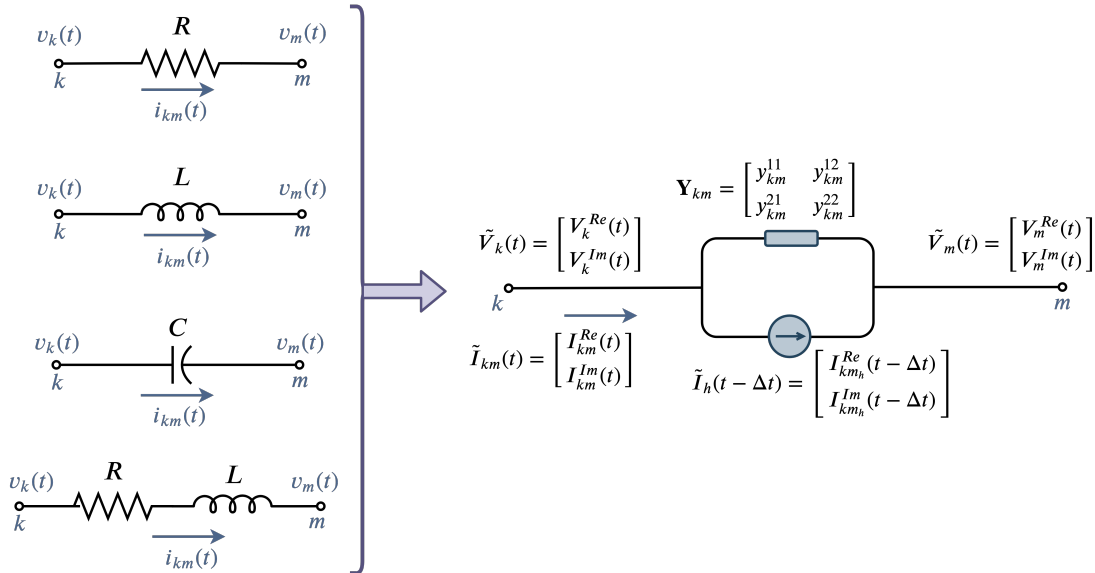

Figure 6.7: Direct conversion of lumped components into DPCM model

It should be pointed out that by using the `DINR` execution option, the default procedure is to consider all circuits (medium and long-length lines) through the nominal-π model. However, long transmission lines can also be represented by the Bergeron model. Indeed, in the steady-state savecase, they may be represented through the

equivalent-π models, i.e. considering hyperbolic correction factors over the line nominal parameters. This particularity is discussed in more detail in the following sections.

Distributed Parameter Line

In this item, it is described the execution codes and options implemented in the programs ANATEM and ANAREDE to allow representing long transmission lines by the Bergeron model (the selection of lossless or lossy model depends on the existence of series resistance). It is important to recall that enabling the `DINR` execution option in ANATEM automatically converts all circuits to their corresponding lumped parameter DPCM model. Therefore, to change it toward enabling the distributed-parameter model for long transmission lines, it is also needed to add the following command:

`BERG` - This execution option can be used in the `EXSI`+`DINR` context to enable the representation of all long transmission lines through the Bergeron model, as illustrated in Figure 6.8. The identification of long transmission lines includes all circuits whose respective travel time τ is above a `MINTAU` parameter multiplied by the step size Δt (`MINTAU` $\cdot \Delta t$). Circuits that do not fulfill this criterion are still modeled as nominal-π lines though;

`MINTAU` - Simulation parameter that represents the minimum number of step sizes (`MINTAU` $\cdot \Delta t$) that a given line travel time τ must accommodate so as to be modeled through the Bergeron model. The default value of `MINTAU` is settled as 10 times the step size, but it can be modified through a specific execution code (`DCTE`).
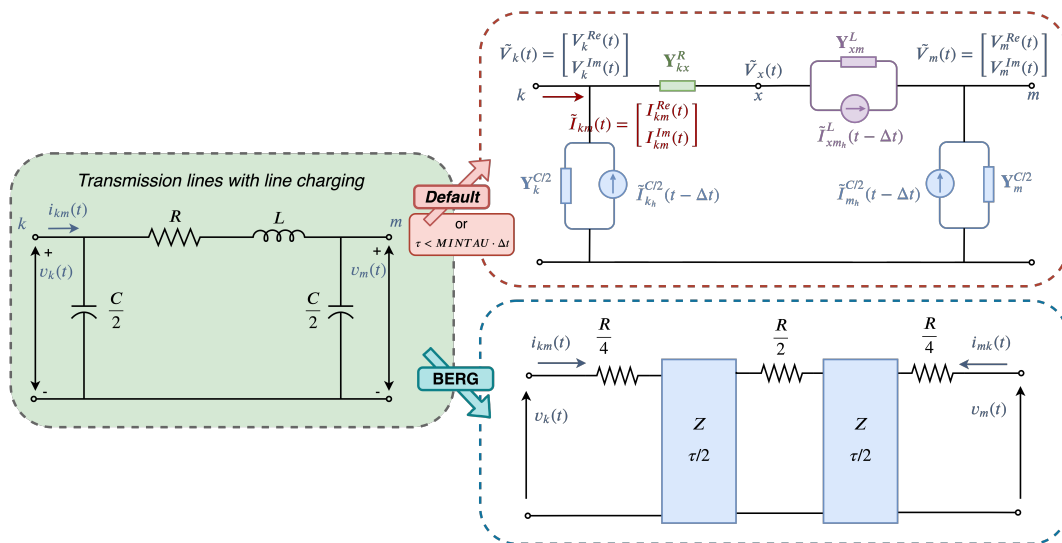

Figure 6.8: Selection of DPCM model for transmission lines with line charging

Process to Adequate the Bergeron Model in the Power Flow Solution

Once long transmission lines data are usually represented in steady-state power flow programs through their respective equivalent-π models, i.e., considering **hyperbolic correction factors** over their nominal parameters, the default procedure adopted by the `BERG` execution option is to employ an iterative method, referred to as `PARNOM` [70], to **retrieve the line nominal parameters** from the hyperbolic corrected ones. Then, the nominal parameters are considered in the initialization of the historical terms, and also for the calculation of the Bergeron model parameters.

Appendix A.1 presents the equations implemented in ANATEM for an adequate initialization of the Bergeron model by using the methodology proposed in [71]. These equations have also been implemented in the program ANAREDE under the execution option `DINR` to allow the power flow solution considering the quadripole line model in conformity with the lossy Bergeron model given in Section 3.3.5.2.

Flexible Definition of Transmission Line Models

The execution options `DINR` and `DINR+BERG` have been approached in the previous items, respectively, to allow the representation of all long transmission lines by models with lumped or distributed (if $\tau > $ `MINTAU` $\cdot \Delta t$) parameters.

For the sake of flexibility, it would be interesting to have the feasibility of studying a combined configuration. In other words, it can be valuable to represent some circuits through the nominal-π model, and others by the Bergeron model. In that respect, the following execution code has been implemented:

> `DTLT` - Execution code to specify the transmission line models. Figure 6.9 gives an application example of this execution code.

```
DTLT
( Fr ) ( To ) Nc (Type) ( MinTau )
   1     3    1    PI
   1     4    1    BERG      1e-3
999999
```

Figure 6.9: `DTLT` execution code

It should be recalled that this execution code follows the traditional fixed column format of the ANATEM software. Thus, Table 6.1 describes the function of the parameters illustrated in Figure 6.9.

Table 6.1: Description of the `DTLT` parameters

Parameter	Description
Fr	Identification number of bus `FROM`
To	Identification number of bus `TO`
Nc	Identification number of the parallel circuit
Type	Model definition: `PI` (lumped) or `BERG` (distributed)
MinTau	Minimum τ value in seconds to consider the Bergeron model

To illustrate the application of this execution code, let one consider the generic network illustrated in Figure 6.10.
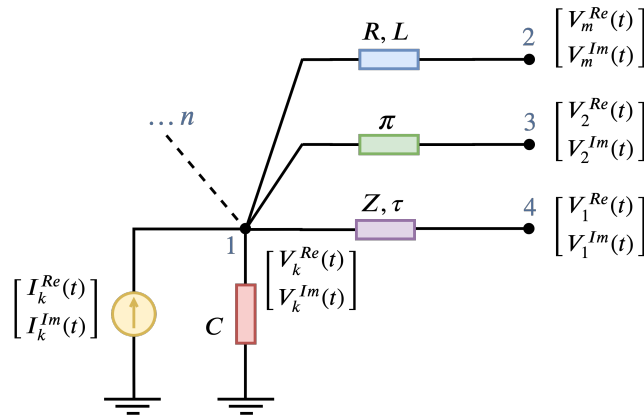

Figure 6.10: Generic electrical network

In this particular case, if the `DTLT` of Figure 6.9 is applied to this system, the circuit `1-3` would be modeled by the nominal-π model, whereas the circuit `1-4` would be modeled by the Bergeron model. In addition, the remaining circuits (which are not explicit in this `DTLT` example) would be represented by default through the nominal-π model. Alternatively, if the execution options `DINR+BERG` are both enabled, the default treatment adopted for the remaining circuits would be the employment of the Bergeron model.

Bergeron Model - Linear Interpolation

It is worth mentioning that in the case of lumped elements, the history current sources only depend on one previous time step $(t - \Delta t)$, whereas distributed parameter lines (whether lossless or lossy models) should hold a **memory vector** whose delay must date back over the number of time steps that fits into the line travel time $(t - \tau)$, as shown in Figure 6.11.
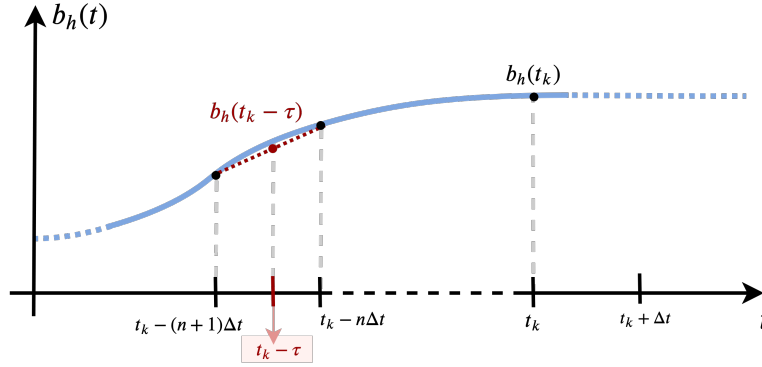
Figure 6.11: Illustration of linear interpolation

As an example, let one consider a long transmission line with a given travel time τ, which conforms x multiples of the time step size, as follows:

$$x = \frac{\tau}{\Delta t} \tag{6.2}$$

From Figure 6.11, one should note that if x is not an integer number, the travel time τ would not be a common multiple of Δt. As a consequence, the line historical term $b_h(t_k - \tau)$ should be placed between two subsequent discrete solutions at the instants $[t_k - (n+1) \cdot \Delta t]$ and $[t_k - n \cdot \Delta t]$, where $n = \lfloor x \rfloor$ and t_k is the current simulation time. In such circumstances, a sufficiently precise time-domain solution for the Bergeron model is obtained by employing the linear interpolation technique (described in Appendix A.2), so that this interpolation method is adopted in this thesis. In Section 6.1.2, it is shown that the linear interpolation provides simulation results in accordance with the PSCAD/EMTDC.

Representation of Generation Buses

At this point, the validation of the DPCM developments in ANATEM is carried out considering the individual behavior of these models, so that the generators are modeled as infinite buses. This assumption holds before the synchronous machines developments compatible with the network dynamics are presented. However, the ANATEM did not have an option to do this automatically. To overcome this limitation and to allow for this conversion to occur automatically, the following execution code has also been developed:

> `GINF` - This execution code automatically converts all generation buses without dynamic modeling into infinite buses, i.e., these buses will present constant voltage magnitude and constant frequency over the dynamic simulation. This execution code does not require additional data.

170

To exemplify the `GINF` operation, let one consider the generic generation bus i illustrated in Figure 6.12.
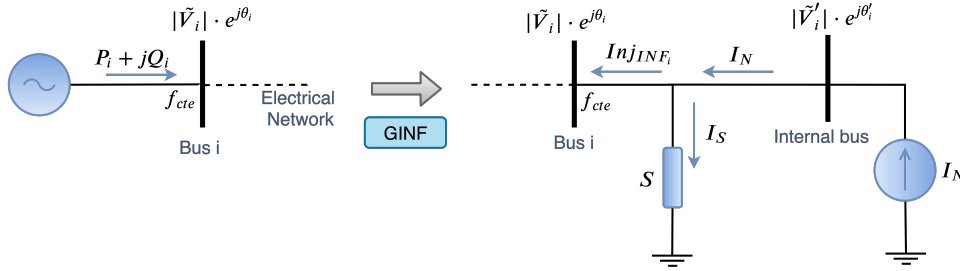

Figure 6.12: Infinite bus conversion through the `GINF` execution code

In the dynamic simulation of this system, if the execution code `GINF` is enabled and no dynamic model is assigned to bus i, then, its respective generation will automatically be converted to a discrete equivalent Norton model, which accounts for a injected current I_N, and an infinitesimal sensitivity conductance S. Thereafter, the net injected current Inj_{INF_i} is determined through the alternated scheme of Figure 6.5, and it must be included into the vector of nodal injected currents. As well, the sensitivity conductance is considered in the construction of the network admittance matrix. Hence, in order to ensure that the voltage and frequency at bus i are kept constant, an additional equation assigning the voltage at bus i equal to its initial value is incorporated into the network linear system solution.

Retaining the Dynamic Region for DPCM Representation

For large-scale power systems, representing some section of the electrical network with dynamics by using the DPCM models, and the remainder with the conventional ESA modeling would be an interesting approach. The network retained for dynamic modeling is referred to as the influence zone, i.e., the region with significant impact on the dynamic behavior of the variables of interest. In this definition, the determination of the influence zone is a complex task, which is out of the scope of this thesis, but an object for future work. However, at this point, the following execution code is proposed to allow such a hybrid modeling:

> `DRDN` - Execution code to define the network region retained for dynamic representation by using the DPCM models. This definition is carried out by making use of a proper selection rule syntax rooted in the set theory, which is exemplified in Figure 6.13.

```
DRDN
(tp) ( no) C (tp) ( no) C (tp) ( no) C (tp) ( no)
BARR      1 A BARR   80
BARR    100 A BARR  150
999999
```

Figure 6.13: Example of usage of the DRDN execution code

In this example, all buses whose identification number takes place between 1 and 80, and also the buses between 100 and 150 will be included in the influence zone. On the other side, the external network region will be represented statically by using the ESA modeling. It should be pointed out that a future study would determine the dynamic region by gradually increasing the retained region. In greater level of detail, the parameters of the DRDN execution code are described in Figure 6.14.
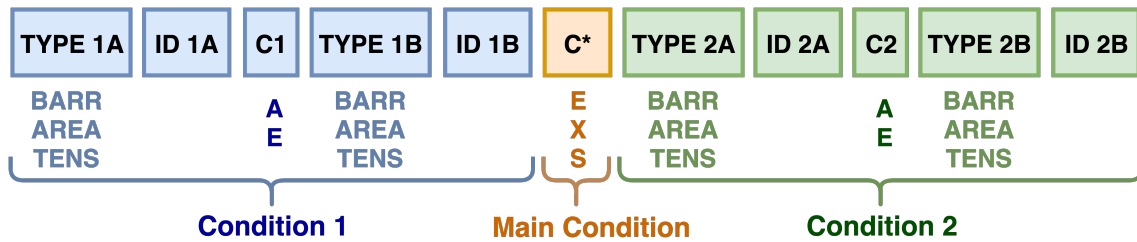

Figure 6.14: Selection language to retain the network region for dynamic modeling

The function of the DRDN parameters highlighted in Figure 6.14 are described in Table 6.2.

Table 6.2: Description of the DRDN parameters

Parameter	Description
Type	Type of equipment A or B to be employed in condition 1 or 2
ID	Identification number of equipment A or B for condition 1 or 2
C	Condition 1 or 2
C*	Main condition

Additionally, Table 6.3 presents the options for filling in the `DRDN` execution code:

Table 6.3: Options for filling in the selection language syntax

Parameter	Option	Description
Type	BARR	Identification number of the network bus
	AREA	Electrical area defined in the power flow savecase
	TENS	Voltage level defined in the power flow savecase
C1 or C2	A	Define an addition operation
	E	Define an interval operation
C	E	Intersection condition
	X	Difference condition
	S	Union condition

One should note that the `DRDN` execution code enables the **hybrid ESA and EMT simulation environment within a compatible dynamic phasor interface**. This feature allows to evaluate the impact of modeling the electrical network dynamics in electromechanical transient stability programs, as long as it uses the steady-state operating point and the dynamic database of the overall electrical network.

Defining Elements for Dynamic Switching

In validating the DPCM developments, the simulation events executed in ANATEM and PSCAD/EMTDC include the switching of load groups. In this thesis, these load groups are referred to as "RLC groups", which might be composed by a parallel or series connection of inductance, capacitance, and resistance. Therefore, to allow this formulation in a generic bus of the electrical network, the `DRLC` execution code has been developed in ANATEM, as follows:

> `DRLC` - Execution code to define RLC groups for dynamic switching along the time-domain simulation through the `DEVT` execution code. Therefore, once a RLC group is defined in the `DRLC` context, its respective switch is open at the beginning of the simulation (as shown in Figure 6.15). Then, it can be turned on by using the `LRLC` event, and subsequently turned off by the `RRLC` event. These simulation events must be provided in the scope of the `DEVT` execution code, and they are detailed in the following items.

For the sake of illustration, let one consider a network bus identified by the number "1" in Figure 6.15. This electrical bus contains groups of loads identified by the switches "10", "20", and "30".
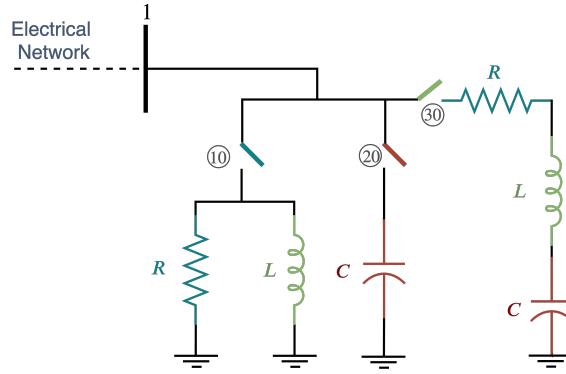
Figure 6.15: RLC groups at bus "1"

In particular, the RLC groups illustrated in Figure 6.15 would be modeled in ANATEM through the DRLC execution code, as follows:

```
DRLC
( Nb ) (Gp) (U) (Vdef) (    R    ) (    L    ) (    C    ) (T)
   1    10   P   1.0      1000       1000                    P
   1    20   P   1.0                              1000
   1    30   P   1.0       500        500         1000       S
999999
```

Figure 6.16: Example of usage of the DRLC execution code

It it important to highlight that the values of resistance, inductance and capacitance are given in units of power, i.e. in MW for the resistance, and in Mvar for the inductance and capacitance. In this respect, it represents the power supplied by these elements at the specified voltage (informed in the parameter Vdef in pu), and at the default base power (100 MVA).

Alternatively, the RLC values can also be provided in electrical units by choosing the option "E" in the field (U). In this case, the field (Vdef) means the base voltage in kV that shall be used for the parameters normalization.

Table 6.4 describes the function of the `DRLC` parameters shown in Figure 6.16.

Table 6.4: Description of the `DRLC` parameters

Parameter	Description
Nb	Identification number of the network bus
Gp	Identification number of the RLC group
U	Type of data (`P` = values are given as power ; `E` = electrical units)
Vdef	Specified voltage in pu for which the RLC power is determined
R	Resistance value
L	Inductance value
C	Capacitance value
T	Connection type (`P` = parallel; `S` = series)

New Simulation Events

The following **simulation events** have been implemented in the scope of the `DEVT` execution code to allow the connection and removal of the RLC groups defined by the `DRLC` code.

LRLC - This simulation event turns on a RLC group previously defined in the `DRLC` execution code;

RRLC - This simulation event turns off a RLC group previously defined in the `DRLC` execution code, which had already been turned on during the simulation.

Figure 6.17 gives an example of usage for this execution code. It illustrates the connection (`LRLC`) of the RLC group "10" of bus "1" at 0.05 s, followed by its removal (`RRLC`) at 0.15 s.

```
DEVT
(Tp) ( Tempo)( El )( Pa)Nc( Ex) ( % ) (ABS ) Gr Und
LRLC   0.0500   1                              10
RRLC   0.1500   1                              10
999999
```

Figure 6.17: Example of usage of the `LRLC` and `RRLC` simulation events

New Output Variables

In ANATEM software, the choice of output variables is performed through the the execution code `DPLT`. Thereby, to allow observing instantaneous quantities over time,

the following new output variables have been developed in the context of the `DPLT` execution code:

$\boxed{\texttt{V(t)}}$ - Instantaneous bus voltage in pu;

$\boxed{\texttt{IL(t)}}$ - Instantaneous current of a circuit in pu;

$\boxed{\texttt{IDINL}}$ - Instantaneous history source of an inductive load;

$\boxed{\texttt{IDINC}}$ - Instantaneous history source of a capacitive load.

In addition, a scale factor has also been included in the `DPLT` execution code to allow plotting these signals in electrical units (or other scales) by multiplying the per-unit quantities by their respective base values.

Figure 6.18 shows a example of application of the `DPLT` execution code, where the instantaneous voltage at bus 1 and the instantaneous current of the circuit between buses 1 and 2 are required as output variables over the dynamic simulation.

```
DPLT
(Tipo)M( El ) ( Pa) Nc Gp ( Br) Gr ( Ex) (Bl) P
V(t)      1
IL(t)     2     1    1
999999
```

Figure 6.18: Example of usage of the `DPLT` execution code

6.1.2   Validation Results

In this subsection, simulation results using the DPCM models are provided by using simplified models in order to validate the network dynamics against the PSCAD/EMTDC results. Therefore, the following items show the results for the dynamic switching of individual components, such as resistance, inductance, and capacitance, in systems with lumped and distributed-parameter components.

It is worth mentioning that, in all test systems evaluated in this subsection, a PSCAD/EMTDC simulation has been previously carried out to obtain the `snapshot file` in order to analyze the disturbances from a steady-state operating point. On the other hand, the ANATEM software executes a steady-state initialization from a power flow solution provided by the ANAREDE software, so that a previous dynamic simulation running is not required.

6.1.2.1 Resistance

Consider the single-load infinite-bus system shown in Figure 6.19.
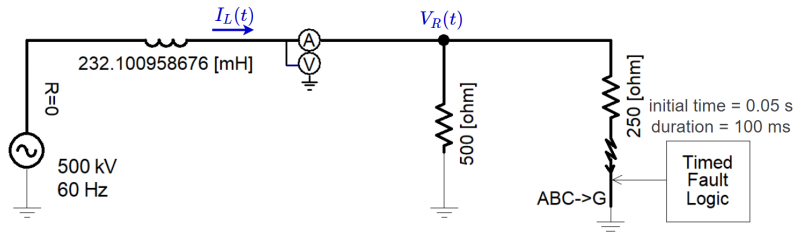

Figure 6.19: Resistive fault in a single-load infinite-bus system

This system is modeled in PSCAD/EMTDC and ANATEM considering the voltage source as an infinite bus. For this representation, the execution code `GINF` is enabled in ANATEM. Furthermore, all the ANATEM developments detailed in the previous subsection, except for the `BERG` option, are explored in this example. The ANATEM dynamic data used in this basic system is given in Appendix B.2.

A balanced three-phase short-circuit fault through a resistance of 250 Ω is simulated at the load terminal to ground, followed by the fault clearance after 100 ms. This disturbance is also simulated in ANATEM by using the events `LRLC` and `RRLC` for the switching of a load of 1000 MW, considering the base voltage as 500 kV RMS line-to-line, and the base power as 100 MVA. The fault resistance has been previously defined through the `DRLC` execution code. Table 6.5 details the parameters and events specified for the ANATEM simulation.

Table 6.5: ANATEM simulation parameters and events

Parameter	Description	Value
Base values	base frequency	60 Hz
	base voltage	500 kV RMS L-L
	base power	100 MVA
Voltage source	magnitude	1 pu
(infinite bus)	angle	0° (cosinusoidal reference)
Line reactance	X_L	0.035 pu
Resistive load	defined at 1 pu	500 MW
Fault resistance	defined at 1 pu	1000 MW
Fault sequence	initial status	no fault
	at $t = 0.05$ s	three-phase fault (`LRLC`)
	at $t = 0.15$ s	fault clearance (`RRLC`)

For this simulation, the variables of interest are the instantaneous values of the load voltage $V_R(t)$ and the line current $I_L(t)$ highlighted in Figure 6.19. The simulation results for these quantities are shown in Figure 6.20, where the ANATEM results are given as curves thicker than the PSCAD/EMTDC ones.
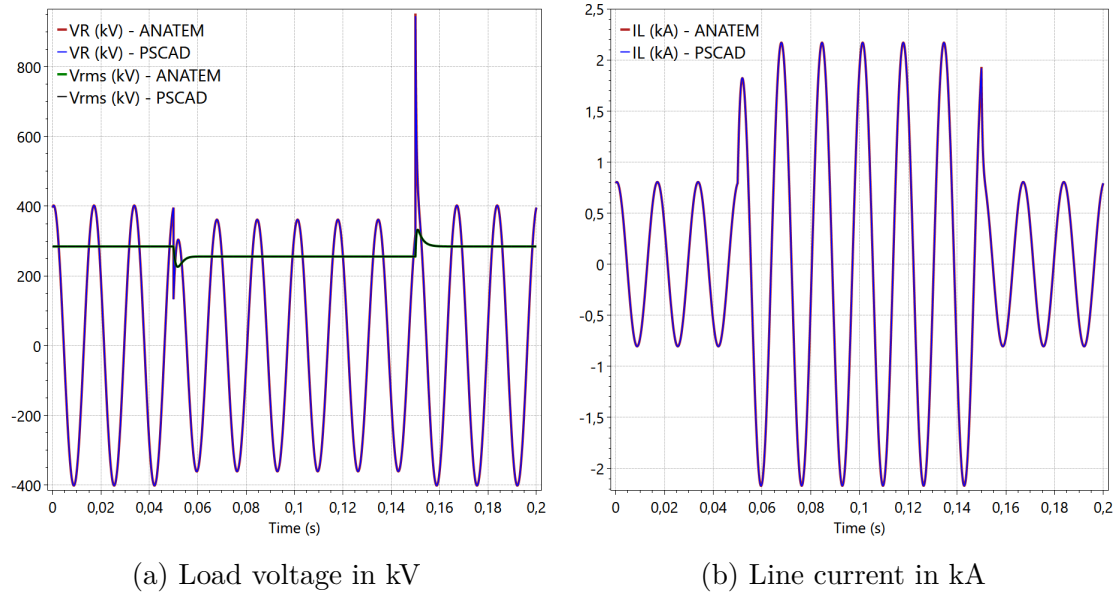

(a) Load voltage in kV
(b) Line current in kA

Figure 6.20: Three-phase short-circuit fault through a resistance

Figures 6.20a and 6.20b present the results as instantaneous values, and also the RMS voltage at the load terminal. From these graphics, it is observed that the ANATEM and PSCAD/EMTDC results are in good agreement and, therefore, validating the DPCM developments.

6.1.2.2 Inductance

The system to be analyzed in this item is depicted in Figure 6.21. In this case, a balanced three-phase short-circuit fault through an inductance at the load terminal is simulated, followed by the fault clearance after 100 ms.

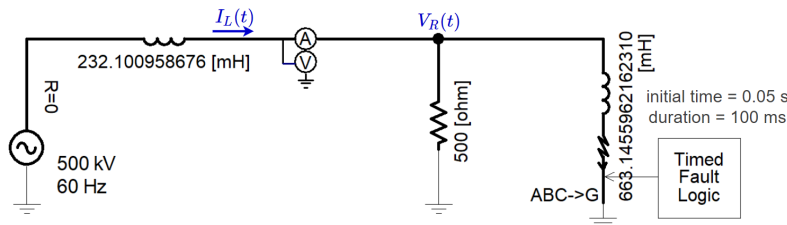Figure 6.21: Inductive fault in a single-load infinite-bus system

The sequence of events employed in ANATEM to simulate this disturbance is show in Table 6.6.

Simulation Event	Description	Value
Fault reactance	defined at 1 pu	1000 Mvar
Fault sequence	initial status	no fault
	at $t = 0.05$ s	three-phase fault (`LRLC`)
	at $t = 0.15$ s	fault clearance (`RRLC`)

As a result, the instantaneous load voltage $V_R(t)$, line current $I_L(t)$, and the RMS load voltage are shown in Figure 6.22.
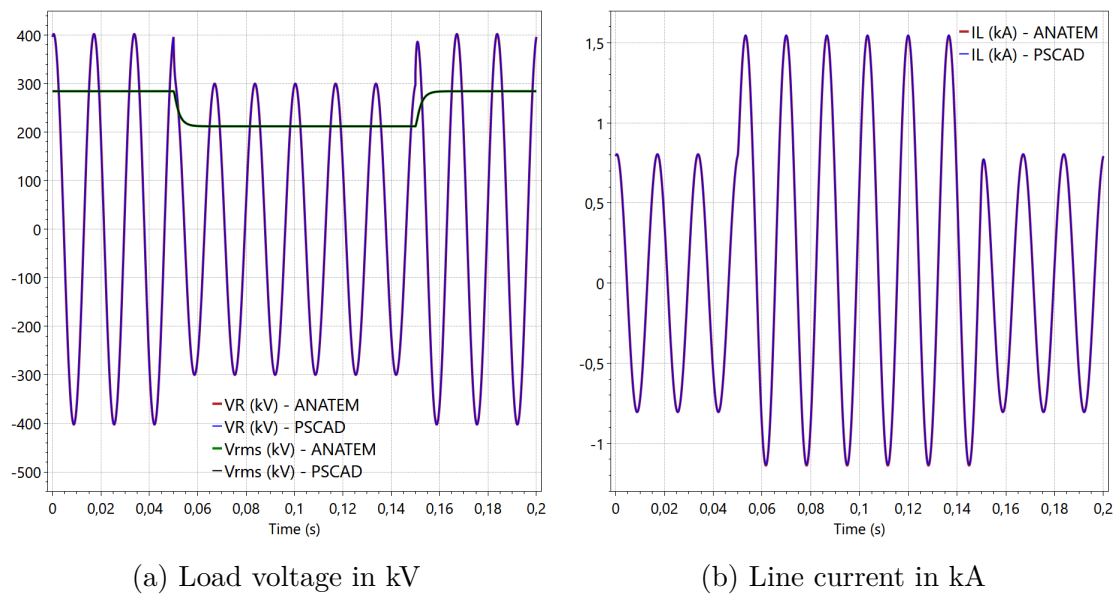

(a) Load voltage in kV

(b) Line current in kA

Figure 6.22: Three-phase short-circuit fault through an inductance

From a comparison with the PSCAD/EMTDC reference solution in Figures 6.22a and 6.22b, it can be seen that the inductance DPCM model provides accurate results.

6.1.2.3 Capacitance

For a complete validation of the elemental DPCM models, this item is concerned with the simulation of a capacitor switching at the load terminal, as shown in Figure 6.23.
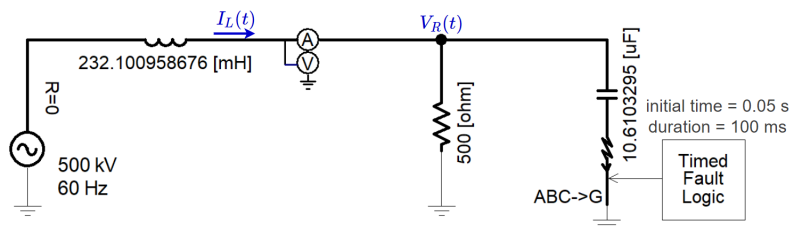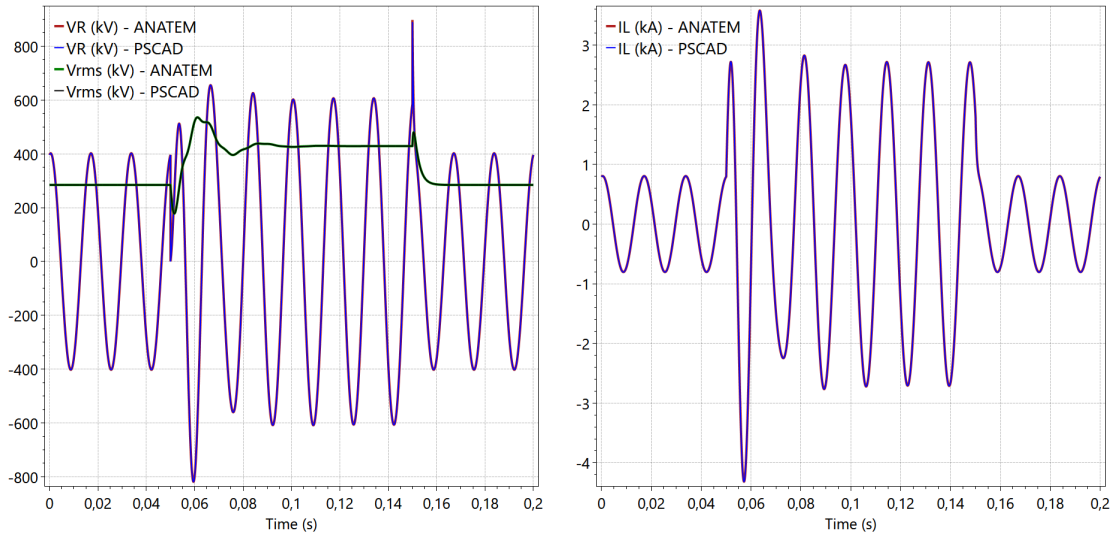

Figure 6.23: Switching of a shunt capacitor

The sequence of events employed in ANATEM to simulate this disturbance is show in Table 6.7.

Table 6.7: ANATEM simulation events

Simulation Event	Description	Value
Shunt capacitor	defined at 1 pu	1000 Mvar
Event sequence	initial status	no fault
	at $t = 0.05$ s	Shunt capacitor energizing (`LRLC`)
	at $t = 0.15$ s	Capacitor removal (`RRLC`)

The instantaneous load voltage $V_R(t)$, line current $I_L(t)$, and the RMS load voltage are shown in Figure 6.24.

(a) Load voltage in kV

(b) Line current in kA

Figure 6.24: Switching of a shunt capacitor

From Figures 6.24a and 6.24b, it is observed that the ANATEM results are in consonance with the PSCAD/EMTDC reference solution.

6.1.2.4 Compensated RL Branch

Consider the system of Figure 6.25 comprising a single-load infinite-bus system with a RL-series branch and a compensation capacitor. The parameters are shown in electrical units, as well as in per unit value considering the base values previously specified in Table 6.5.
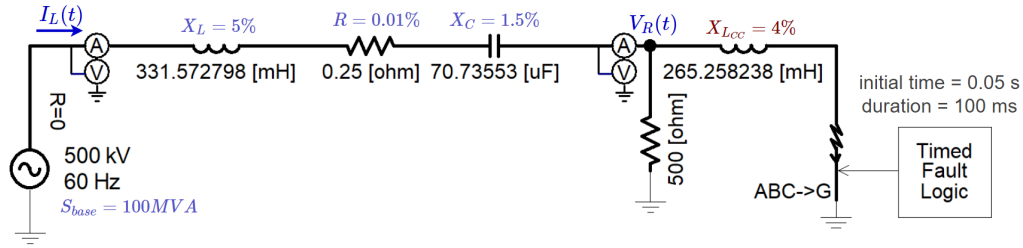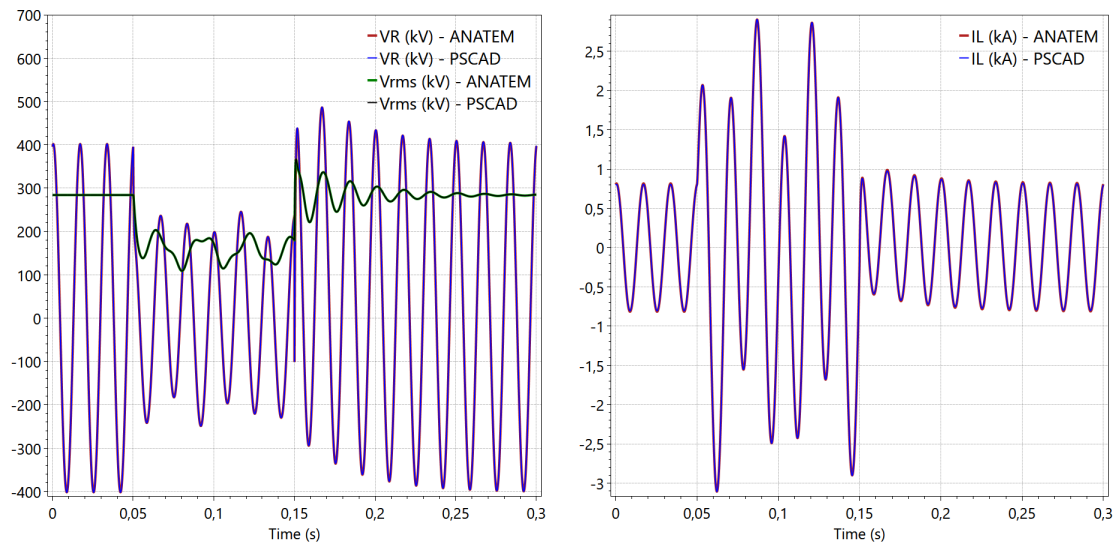
Figure 6.25: Inductive fault in a series compensated system

This system is modeled in ANATEM and PSCAD/EMTDC. Then, it is simulated the balanced three-phase short-circuit fault through an inductance at the load terminal. Table 6.8 details the sequence of events employed in ANATEM to simulate this disturbance.

Table 6.8: ANATEM simulation events

Simulation Event	Description	Value
Fault reactance	defined at 1 pu	2500 Mvar
Fault sequence	initial status	no fault
	at $t = 0.05$ s	three-phase fault (`LRLC`)
	at $t = 0.15$ s	fault clearance (`RRLC`)

Resulting from this simulation, the graphics of Figure 6.25 depicts the instantaneous load voltage $V_R(t)$, line current $I_L(t)$, and the RMS load voltage.

(a) Load voltage in kV

(b) Line current in kA

Figure 6.26: Inductive fault in a series compensated system

Figures 6.26a and 6.26b demonstrate that the instantaneous and RMS waveforms of ANATEM are in good agreement with the PSCAD/EMTDC results.

6.1.2.5 Nominal-π model

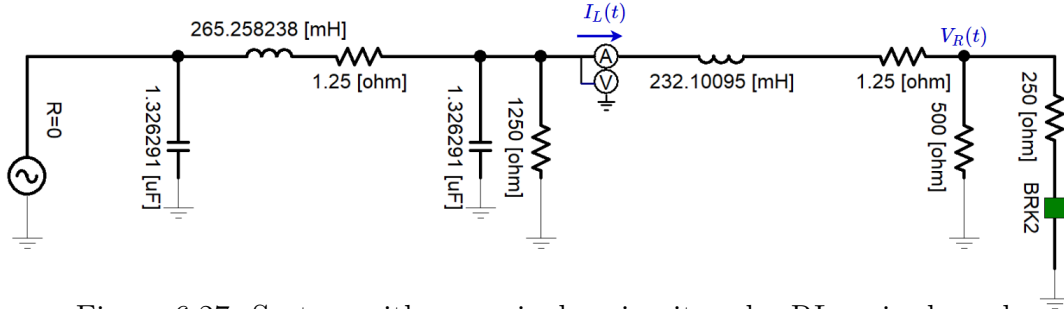Let one consider the system of Figure 6.27 with lumped-parameter components, including a nominal-π circuit.

Figure 6.27: System with a nominal-π circuit and a RL-series branch

A balanced three-phase short-circuit fault through a resistance of 250 Ω is simulated at the load terminal to ground, with 100 ms duration. The simulation data represented in ANATEM to analyze this disturbance are detailed in Table 6.9.

Table 6.9: ANATEM simulation parameters and events

Parameter	Description	Value
Base values	base frequency	60 Hz
	base voltage	500 kV RMS L-L
	base power	100 MVA
Voltage source	magnitude	1 pu
(infinite bus)	angle	0°
Nominal-π line	series reactance X_L	0.04 pu
	series resistance R_L	0.0005 pu
	line charging B_{sh}	250 Mvar
Resistive load 1 (1250Ω)	defined at 1 pu	200 MW
RL-series branch	series reactance X_L	0.035 pu
	series resistance R_L	0.0005 pu
Resistive load 2 (500Ω)	defined at 1 pu	500 MW
Fault resistance	defined at 1 pu	1000 MW
Fault sequence	initial status	no fault
	at $t = 0.05$ s	three-phase fault (`LRLC`)
	at $t = 0.15$ s	fault clearance (`RRLC`)

Figure 6.25 illustrates the instantaneous and RMS load voltage $V_R(t)$, and the instantaneous line current $I_L(t)$ resulting from this simulation.
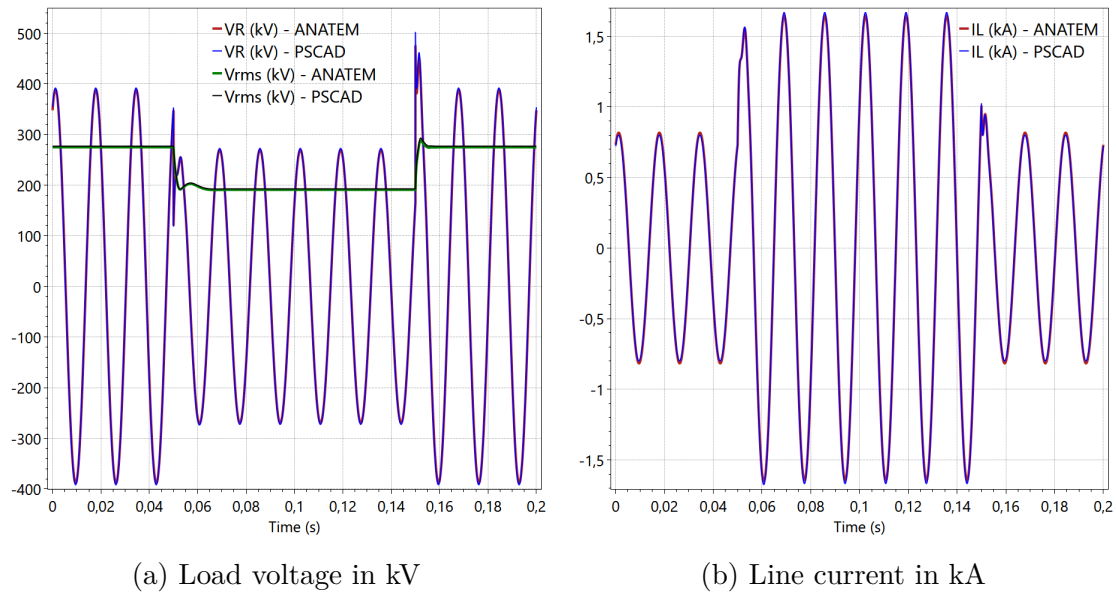

(a) Load voltage in kV

(b) Line current in kA

Figure 6.28: Resistive fault in a system with a nominal-π line

Figures 6.28a and 6.28b show that the ANATEM results are in accordance with the PSCAD/EMTDC results.

6.1.2.6 Bergeron Line

The system of Figure 6.29 accounts for the same set of parameters used in the nominal-π line example. However, in this case, the transmission line with line charging is represented through the Bergeron model by using the BERG execution option in ANATEM.
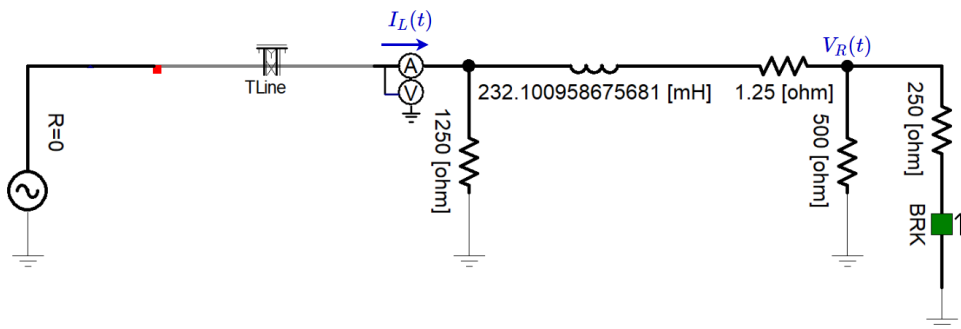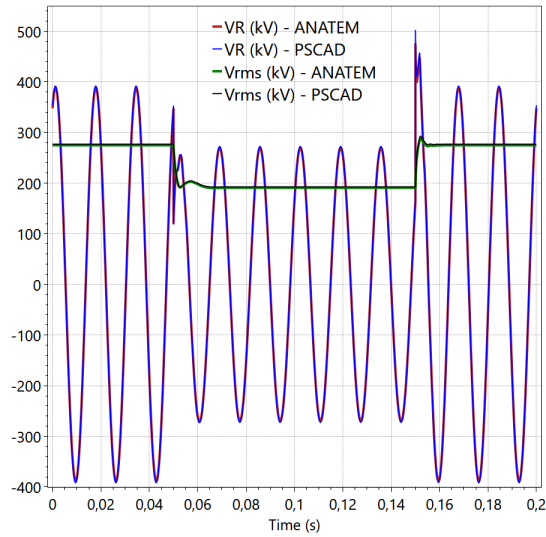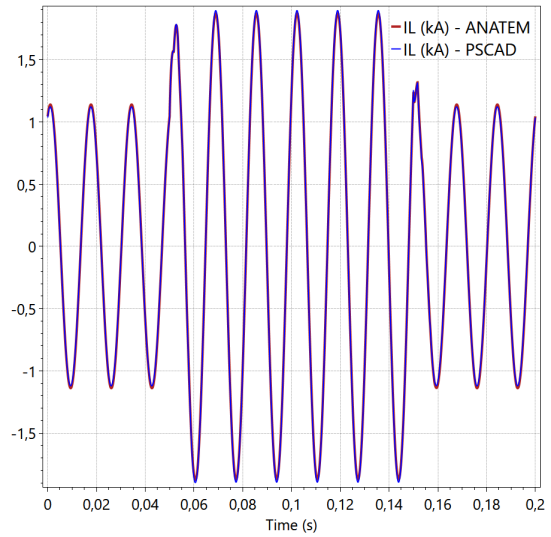

Figure 6.29: System with a Bergeron line and a RL-series branch

In this case, the simulation results obtained for the instantaneous and RMS load voltage $V_R(t)$, and also for the instantaneous line current $I_L(t)$ are shown in Figure 6.30.

(a) Load voltage in kV

(b) Line current in kA

Figure 6.30: Resistive fault in a system with a Bergeron line

Concluding the validation of the network DPCM models, Figures 6.30a and 6.30b demonstrate that the ANATEM results are aligned with the PSCAD/EMTDC results.

6.2 Synchronous Machine Modeling

In this subsection, it is presented the ANATEM developments related to the synchronous machine models (cylindrical rotor and salient poles) suitable for subsynchronous resonance analysis. At this stage, the developments are focused on the electrical equations of the machine, so as to provide a compatible interface with the electrical network DPCM equations validated in Section 6.1.2.

6.2.1 Computational Developments

The synchronous machine models currently existing in the ANATEM software assume the traditional premises of electromechanical stability studies described in Chapter 4, i.e., they consider the electrical frequency close to its nominal value and neglect the stator flux dynamics and the subtransient saliency. However, these premises are not valid for subsynchronous resonance analysis. In this regard, the detailed models approached in Section 4.6 have also been implemented in the ANATEM software, and now they are detailed and validated against the PSCAD/EMTDC.

Before the presentation of the new synchronous machine modeling, it is important to introduce the following execution codes and options that are required when specifying synchronous machine models in the ANATEM `stability file`.

`DMDG` - Execution code to define synchronous generator models to be utilized in the dynamic simulation. In this environment, the generator model is not associate yet to an electrical bus of the network. Instead, a generator model is created through the specification of its parameters, such as the inertia constant, inductances, armature resistance, time constants, damping factor, and power base.

The construction type of the generator rotor has to be assigned within the `DMDG` scope by employing the execution options `MD01`, `MD02`, or `MD03`, defined below.

Classic Machine Model

`MD01` - Execution option to use classic generators or infinite buses models. Figure 6.31 illustrates the utilization of this execution option. In this example, the generator model identified by the number "10" is represented as an infinite bus, whereas the generator "20" is defined as a classic model, i.e., an ideal source behind a transient reactance.

```
DMDG MD01
(No)   (L'd)(Ra )( H )( D )(MVA)Fr C
  10                           60
  20    25.0 0.5  5.0  0.2  200 60
999999
```

Figure 6.31: `DMDG MD01`: Definition of an infinite bus and a classic generator model

Table 6.10 describes the parameters of the `DMDG` execution code that are required when employing the `MD01` execution option.

Table 6.10: Description of the `DMDG MD01` parameters

Parameter	Description
No	Identification number of the generator model
Ld'	Transient inductance in %
Ra	Armature resistance in %
H	Inertia constant in seconds
D	Damping coefficient in pu torque/pu speed deviation
MVA	MVA base power used for the machine parameter normalization
Fr	Synchronous frequency in Hz.
	If it is not filled, the default value is 60 Hz
C	Correction of the parameters with frequency: `S` = yes; `N` = no

Salient-Pole Synchronous Generator

`MD02` - Execution option to specify the parameters of a salient-pole synchronous generator model. Figure 6.32 gives an example of usage of this execution option where the generator identified by the number "30" is modeled with the parameters detailed in Table 6.11.

```
DMDG MD02
(No)   (CS) (Ld )(Lq )(L'd)     (L"d)(Ll )(T'd)     (T"d)(T"q)
  30   0100 93.59 59.0 40.0     21.5 18.5 5.60      .020 .050
(No)   (Ra )( H )( D )(MVA)Fr C
  30    0.25 5.0  0.2 200.0
999999
```

Figure 6.32: `DMDG MD02`: Definition of a salient-pole synchronous generator model

Table 6.11: Description of the `DMDG MD02` parameters

✦ First line of input data

Parameter	Description
No	Identification number of the generator model
CS	Identification number of the saturation curve
Ld	Synchronous inductance of direct axis in %
Lq	Synchronous inductance of quadrature axis in %
Ld'	Transient inductance of direct axis in %
Ld"	Subtransient inductance of direct axis in %
Ll	Leakage inductance in %
Tdo'	d-axis open-circuit transient time constant in seconds
Tdo"	d-axis open-circuit subtransient time constant in seconds
Tqo"	q-axis open-circuit subtransient time constant in seconds

✦ Second line of input data

Parameter	Description
No	Identification number of the generator model
Ra	Armature resistance in %
H	Inertia constant in seconds
D	Damping coefficient in pu torque/pu speed deviation
MVA	MVA base power used for the machine parameter normalization
Fr	Synchronous frequency in Hz.
	If it is not filled, the default value is 60 Hz
C	Correction of the parameters with frequency: `S` = yes; `N` = no

Round Rotor Synchronous Generator

`MD03` - Execution option to specify the parameters of a cylindrical-rotor synchronous generator model. Figure 6.33 gives a usage example of this modeling for the definition of the generator identified by "40".

```
DMDG MD03
(No)    (CS) (Ld )(Lq )(L'd)(L'q)(L"d)(Ll )(T'd)(T'q)(T"d)(T"q)
  40         101.4 77  31.4 22.8  28   163. 6.55  .85 .039 .071
(No)    (Ra )( H )( D )(MVA)Fr C
  40    .517 2.894        100
999999
```

Figure 6.33: `DMDG MD03`: Definition of a cylindrical-rotor synchronous generator model

The parameters of this model are quite similar to the salient-pole machine, except for the fact that the round-rotor synchronous machine accounts for transient effects on the q-axis. Therefore, the common parameters described in Table 6.11 are also valid to this model.

Synchronous Machine Modeling for Subsynchronous Resonance Analysis

The detailed synchronous machine model presented in Section 4.6 has been implemented in the ANATEM software, and it can be enabled if the network dynamics is also enabled by using the `DINR` execution option along with `EXSI` execution code.

Thus, the generator model for SSR analysis can be applied in the dynamic simulation by using the new execution option `MRSS`:

`MRSS` - Execution option to enable the synchronous machine model for SSR analysis. This model represents the stator flux dynamics, the variation of the rotor speed and the subtransient saliency. This execution option can be provided in the scope of the `DMDG` execution code. Figure 6.34 shows an example of usage of this execution option for the definition of the generator identified by "50".

```
DMDG MD03 MRSS
(No)    (CS) (Ld )(Lq )(L'd)(L'q)(L"d)(Ll )(T'd)(T'q)(T"d)(T"q)
  50         101.4 77  31.4 22.8 28   163. 6.55  .85  .039 .071
(No)    (Ra )( H )( D )(MVA)Fr C (L"q)
  50    .517 2.894       100       37.5
999999
```

Figure 6.34: `DMDG MD03 MRSS`: Definition of a cylindrical-rotor synchronous genera-
tor for SSR studies

Considering the effect of the subtransient saliency in SSR studies, a new data field
(`L"q`) has also been added in the joint usage of the `MD03+MRSS` execution options,
as illustrated in Figure 6.34. This parameter corresponds to the value of the q-axis
subtransient inductance. In ESA studies, this value is considered equal to the d-
axis subtransient inductance. Alternatively, in the network dynamics context (using
the `DINR` execution option), the q-axis subtransient inductance can be considered
different from the d-axis subtransient inductance.

New Output Variables

In ESA studies, the premise of close to nominal rotor speed ($\omega_r \approx 1$ pu) and also
by neglecting the stator flux dynamics lead to the approximation that considers
the electromagnetic torque equal to the internal electrical power in per unit values.
However, if these simplification are not regarded, the per unit electromagnetic torque
(T_e) shall be determined by (6.3) in terms of the direct and quadrature currents
(i_d, i_q) and flux linkages (ψ_d, ψ_q), as described in Chapter 4.

$$T_e = i_q \psi_d - i_d \psi_q \tag{6.3}$$

Therefore, the following output variable has been added into the ANATEM to allow
the validation of the synchronous machine model against the PSCAD/EMTDC:

 $\boxed{\text{TELE}}$ - This variable enables the output of the electromagnetic torque of the
 synchronous generator in per unit over the dynamic simulation.

189

6.2.2 Validation Results

In this subsection, the validation of the ANATEM developments related to the dynamic phasor synchronous machine models is performed by the comparison of simulation results from PSCAD/EMTDC. The steady-state numerical initialization is considered in the dynamic phasor modeling.

In this framework, the ANATEM simulations have been executed according to the following procedure:

(i) Specify the system parameters in the power flow software (ANAREDE) to obtain the initial operation point for dynamic simulation;

(ii) Add dynamic models of the synchronous machine, and specify simulation parameters, disturbances, and output variables in the ANATEM stability file;

(iii) Execute the time-domain simulation from the steady-state operating point considering numeric initialization of the state-variables and history terms.

An equivalent system is also represented in the PSCAD/EMTDC, for validation purposes. Therefore, the adjustment of the initial conditions and the dynamic simulations have been carried out in the following steps:

(i) Specify the system data, including the electrical network and the machine parameters;

(ii) Define the initial conditions in the synchronous machine terminals: voltage magnitude, voltage phase angle, active output power, reactive output power; The initial conditions must be settled identical to that obtained by the power flow solution in the ANAREDE software;

(iii) Execute a simulation assuming zero initial conditions to record a snapshot file relative to the steady-state operating point. In this simulation, the machine should start as an ideal source, and after the circuit energizing, the transition from the ideal source to the synchronous machine model must be made regarding only the electrical equations. Thus, once the steady-state is reached with the machine electrical equations, the swing equations of the machine might also be enabled, and the snapshot shall be recorded;

(iv) Run the dynamic simulation from the snapshot file in order to study the system dynamic behavior following a disturbance.

On this matter, the following items present the validation results of the salient and the cylindrical rotor synchronous machine models developed in Section 4.6 by using

fundamental dynamic phasors and the trapezoidal integration method.

6.2.2.1 Salient-Pole Synchronous Machine

Let one consider the system of Figure 6.35 composed by a synchronous generator connected to a passive electrical network. At this stage, this system is employed to evaluate the computational developments of the salient-pole synchronous machine model in the ANATEM software.
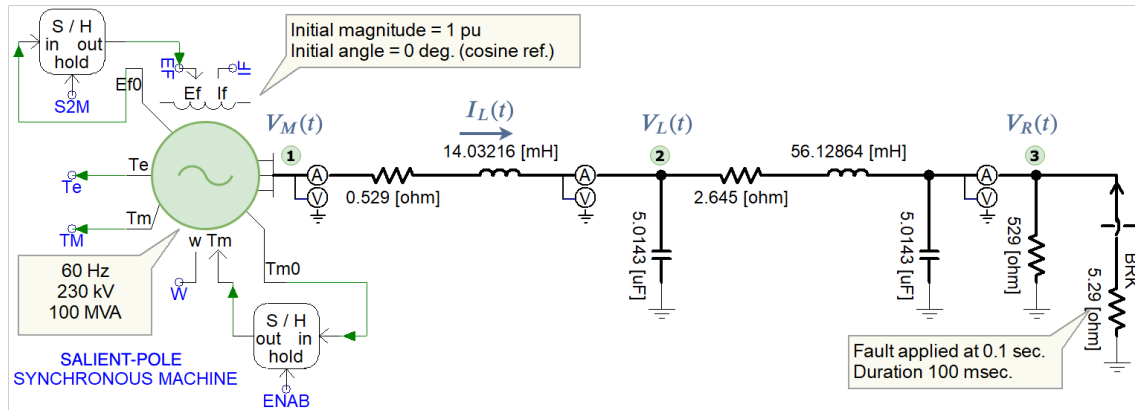

Figure 6.35: System with a salient-pole synchronous machine

The variable "S2M" depicted in Figure 6.35 represents the control variable to release the machine electrical equations, whereas the variable "ENAB" releases the machine mechanical equations. When these variables are enabled, the initial field voltage (E_{f0}), and the initial mechanical torque (T_{m0}) are used to determine the internal variables of the machine.

Table 6.12 contains the operational parameters of the salient-pole synchronous machine in per unit on the system MVA base at the nominal frequency (60Hz).

Table 6.12: Salient-pole synchronous machine parameters

Parameter	Value	Parameter	Value	Parameter	Value
Base MVA	100 MVA	H	5.0 s	R_a	0.0025 pu
Base voltage	230 kV	X_l	0.185 pu	X_d	0.9359 pu
Base frequency	60 Hz	X_q	0.59 pu	L'_d	0.40 pu
L''_d	0.215 pu	L''_q	0.215 pu	T'_{do}	5.6 s
T''_{do}	0.02 s	T''_{qo}	0.05 s		

The system of Figure 6.35 is represented in the ANATEM simulations through the parameters given in Table 6.13:

Table 6.13: System parameters utilized in the ANATEM

Parameter	Description	Value
Base values	base frequency	60 Hz
	base voltage	230 kV RMS L-L
	base power	100 MVA
Synchronous Machine (initial conditions)	magnitude	1 pu
	angle	0° (cosine ref.)
RL-series branch	series reactance X_L	0.01 pu
	series resistance R_L	0.001 pu
Nominal-π line	series reactance X_L	0.04 pu
	series resistance R_L	0.005 pu
	line charging B_{sh}	200 Mvar
Resistive load (529Ω)	defined at 1 pu	100 MW

A balanced three-phase short-circuit fault through a resistance of 5.29 Ω is simulated at the load terminal to ground, with 100 ms duration. The simulation data represented in ANATEM to analyze this disturbance is detailed in Table 6.14.

Table 6.14: ANATEM simulation event

Simulation Event	Description	Value
Fault resistance (5.29Ω)	from node 3 to ground	0.01 pu
Fault sequence	initial status	no fault
	at $t = 0.10$ s	three-phase fault
	at $t = 0.20$ s	fault clearance

For validation purposes, the interest variables of the electrical network (indicated in Figure 6.35) are the instantaneous and the RMS voltage of the machine $V_M(t)$, and load $V_R(t)$ terminals, and the instantaneous current $I_L(t)$, which are illustrated in Figures 6.36 to 6.38, respectively.
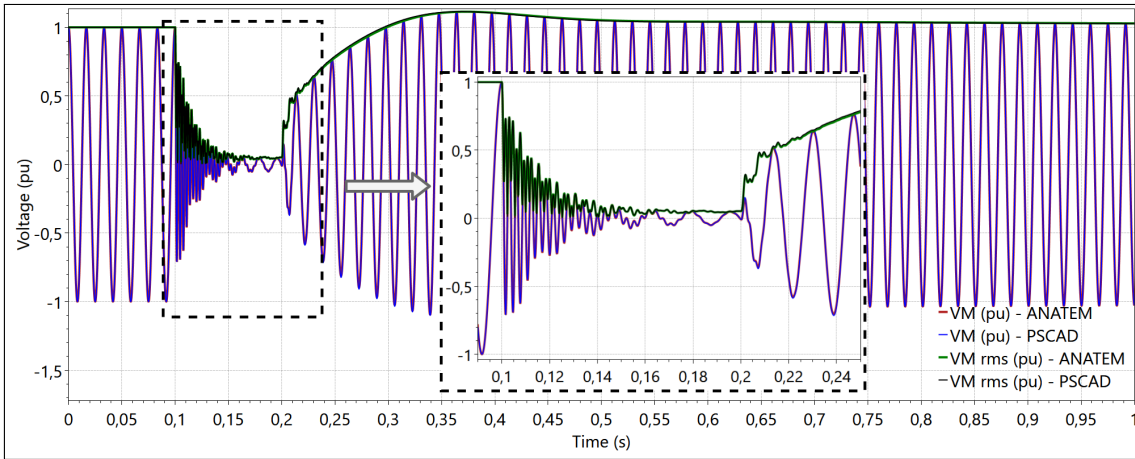
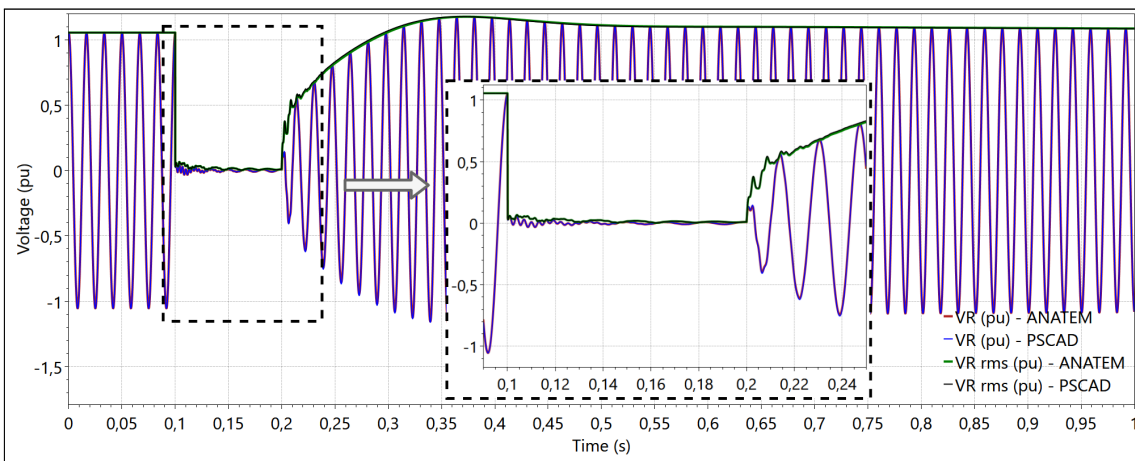Figure 6.36: Comparison of the stator voltage (pu) following a three-phase fault

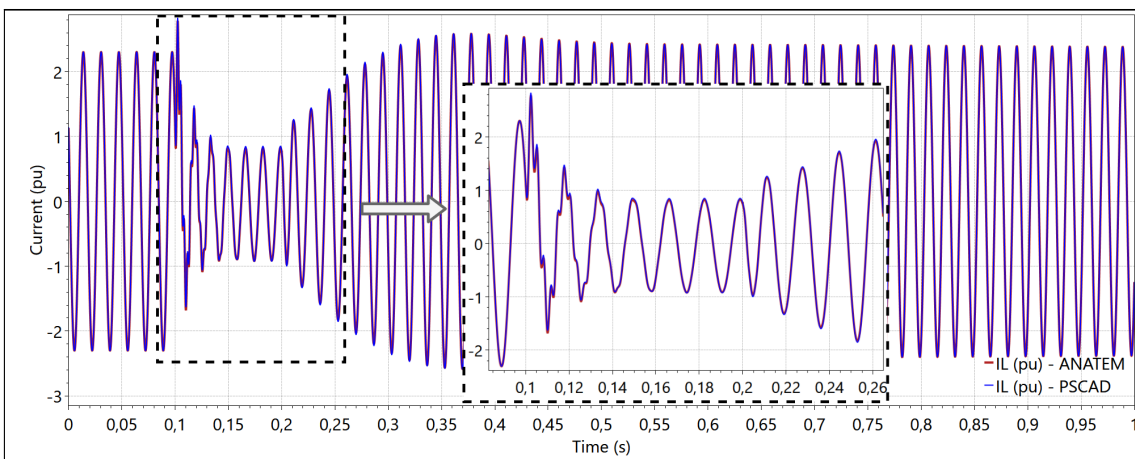Figure 6.37: Comparison of the load voltage (pu) following a three-phase fault

Figure 6.38: Comparison of the line current (pu) following a three-phase fault

It should be pointed out that the base values adopted for the instantaneous voltage and current normalization are chosen in order to obtain per unit peak values coin-

ciding with the RMS envelope. Additionally, a zoom graphic is provided along with the results in an effort to explicit the dynamic response of the curves in the most oscillatory simulation period, i.e., right after the fault application. The expanded graphics allow a clearer view of the aligned dynamic behavior of the two programs.

The variables associated with the synchronous machine model are illustrated in Figures 6.39 to 6.41. In this respect, the machine terminal electrical power, the electromagnetic torque, and the rotor frequency are chosen for comparison and validation of the dynamic phasor machine model against the instantaneous representation of the PSCAD/EMTDC.
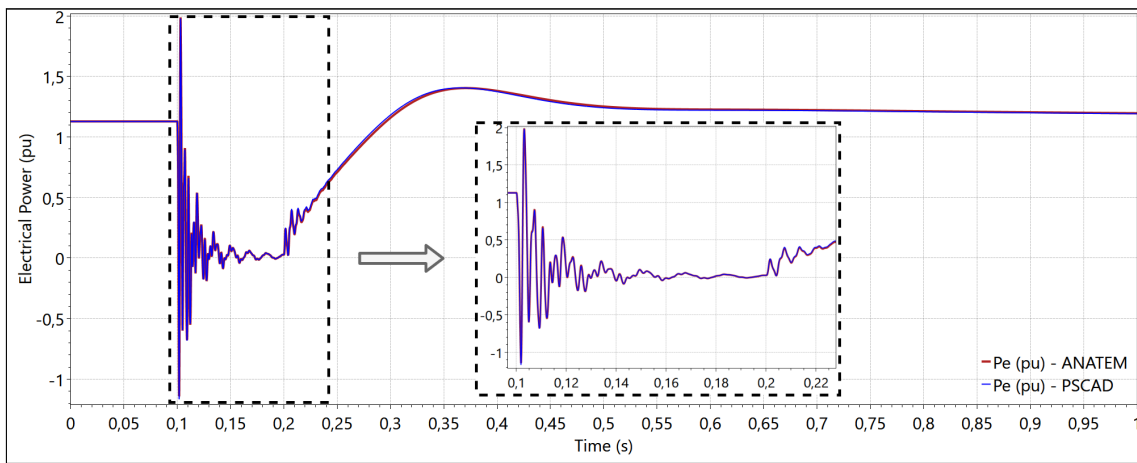
Figure 6.39: Comparison of the terminal electrical power (pu)
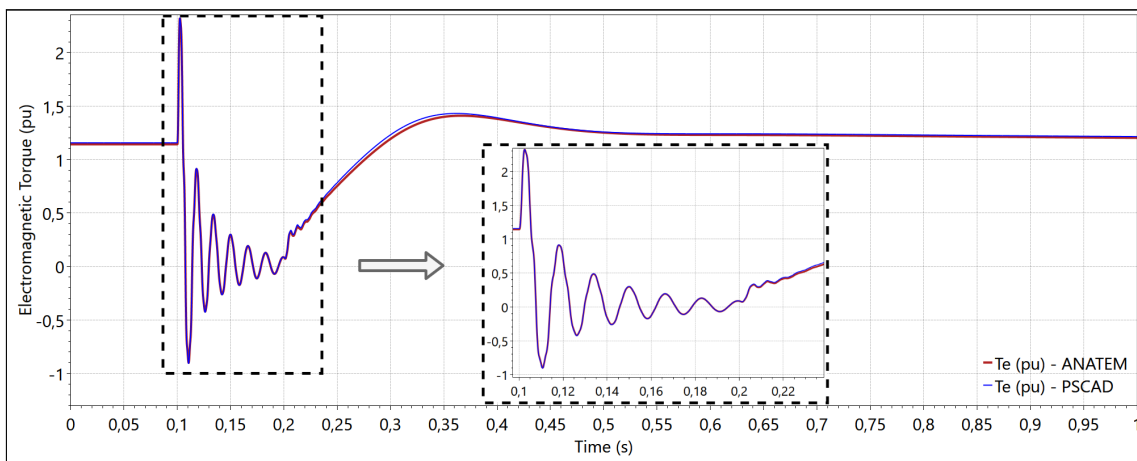
Figure 6.40: Comparison of the electromagnetic torque (pu)

Figures 6.39 and 6.40 demonstrate that the terminal electrical power $P_e(t)$ and the electromagnetic torque $T_e(t)$ are in consonance with the instantaneous modeling of the PSCAD/EMTDC. One should note that the relationship between these variables does not provide the rotor frequency $w_r(t)$ (shown in Figure 6.41) since the $P_e(t)$

194

contains a component relative to the rate of magnetic energy change in the stator, and it deducts the armature resistance losses (4.33). On the other side, the electromagnetic torque $T_e(t)$ is directly determined by the power transferred across the air-gap (4.81). As a result, the electromagnetic torque presents a smoother dynamic behavior in comparison to the electrical power transients.
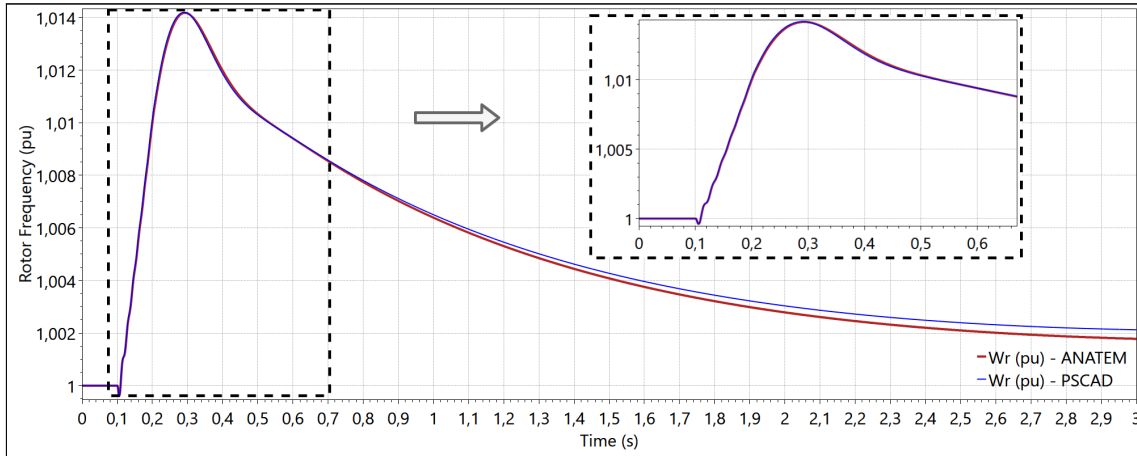

Figure 6.41: Comparison of the rotor frequency (pu)

The electrical network and the machine quantities shown in this item demonstrate that the dynamic phasor model of the salient-pole synchronous generator implemented in ANATEM is in good agreement with the PSCAD/EMTDC representation.

However, these results reveal that there are some differences in the machine modeling of the two programs, which is most evidenced in the rotor frequency. Because of this accumulating difference in the rotor frequency over time, the time frame of this particular graphic has been extended to a three-second duration. These differences have been exhaustively examined, and part of the reason for the variation stands in the fact that the steady-state operating point obtained in the PSCAD/EMTDC is slightly different from the ANATEM, which naturally reflects in the machine model initialization. Discrepancies due to truncation errors in the parameters are expected to be negligible as 16 decimal digits have been adopted for data entry. Despite the rotor frequency deviation, the synchronous machine dynamic behavior, as well as the network variables, maintain alignment with the PSCAD/EMTDC results.

Due to the vertical axis scale employed in Figure 6.36, the difference in the initialization of the machine terminal voltage are not apparent. Therefore, Figure 6.42 gives a vertical axis zoom so as to provide a better visualization of the differences in the initialization of the field voltage (Figure 6.42a) and in the terminal voltage (Figure 6.42b). More specifically, the initial values of the machine terminal and field
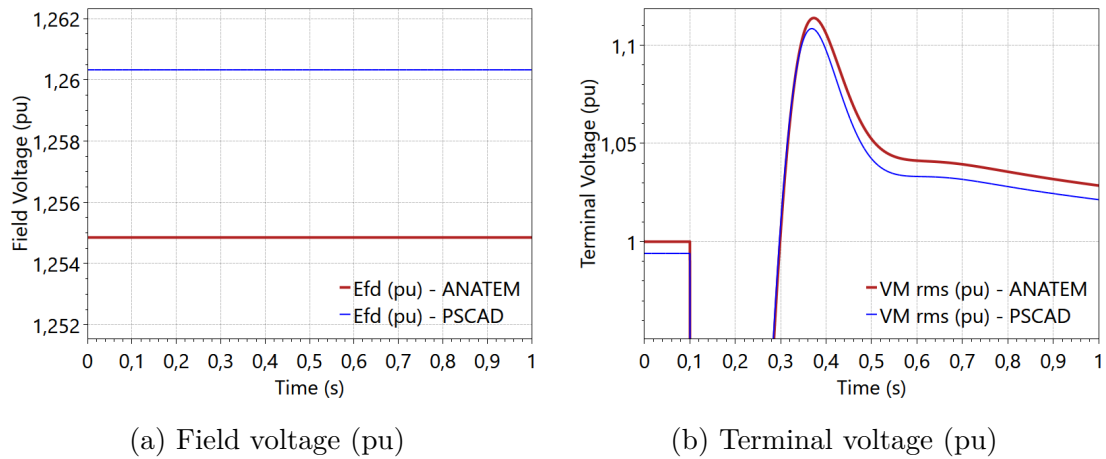
voltage are also described in Table 6.15.

(a) Field voltage (pu)

(b) Terminal voltage (pu)

Figure 6.42: Initial conditions of the salient-pole synchronous machine

Table 6.15: Initial conditions of the salient-pole synchronous machine

Variable	ANATEM	PSCAD
Initial field voltage (pu)	1.25485	1.26032
Initial terminal voltage (pu)	1.0	0.994057

Although the terminal voltage of the machine has been settled as 1.0 pu for the simulation in the PSCAD/EMTDC, from Table 6.15 one can see that this specification has not been respected in the simulation following the circuit energizing and the synchronous machine initialization. It is noteworthy that the field voltage, as well as the mechanical torque are kept constant in this didactic case since it is desired to validate the machine model without influence of such controllers.

6.2.2.2 Cylindrical-Rotor Synchronous Machine

In this present item, the computational developments of the ANATEM software corresponding to the dynamic phasor model of the cylindrical-pole synchronous machine are evaluated through the system of Figure 6.43.
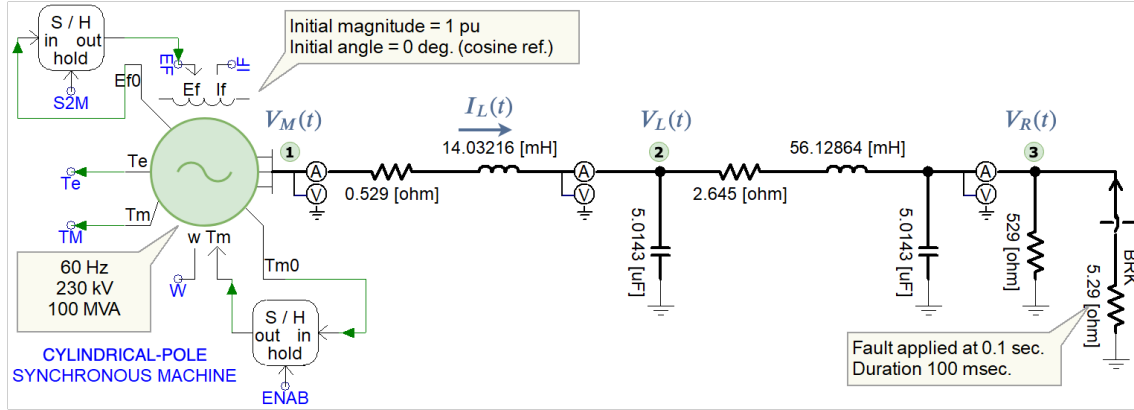

Figure 6.43: System with a cylindrical-pole synchronous machine

The operational parameters of the cylindrical-pole synchronous machine used in the simulations are specified in Table 6.16 in per unit on the system MVA base at the nominal frequency (60Hz).

Table 6.16: Cylindrical-pole synchronous machine parameters

Parameter	Value	Parameter	Value	Parameter	Value
Base MVA	100 MVA	H	5.0 s	R_a	0.0025 pu
Base voltage	230 kV	X_l	0.185 pu	X_d	0.9359 pu
Base frequency	60 Hz	X_q	0.59 pu	X'_d	0.40 pu
X'_q	0.35 pu	X''_d	0.215 pu	X''_q	0.215 pu
T'_{do}	5.6 s	T'_{qo}	0.66 s	T''_{do}	0.02 s
T''_{qo}	0.05 s				

The electrical network parameters and the three-phase balanced fault applied in this analysis are the same as those adopted in the previous item.

Thus, the simulation results following the disturbance are shown in Figures 6.44 to 6.46. These graphics present the RMS and instantaneous voltage waveform of the machine $V_M(t)$ and load $V_R(t)$ terminals, and the line current $I_L(t)$ highlighted in Figure 6.43.

Concerning the electrical network quantities, it is demonstrated that the cylindrical-pole synchronous machine development is validated as it provides results consistent

with the three-phase instantaneous representation of the PSCAD/EMTDC.
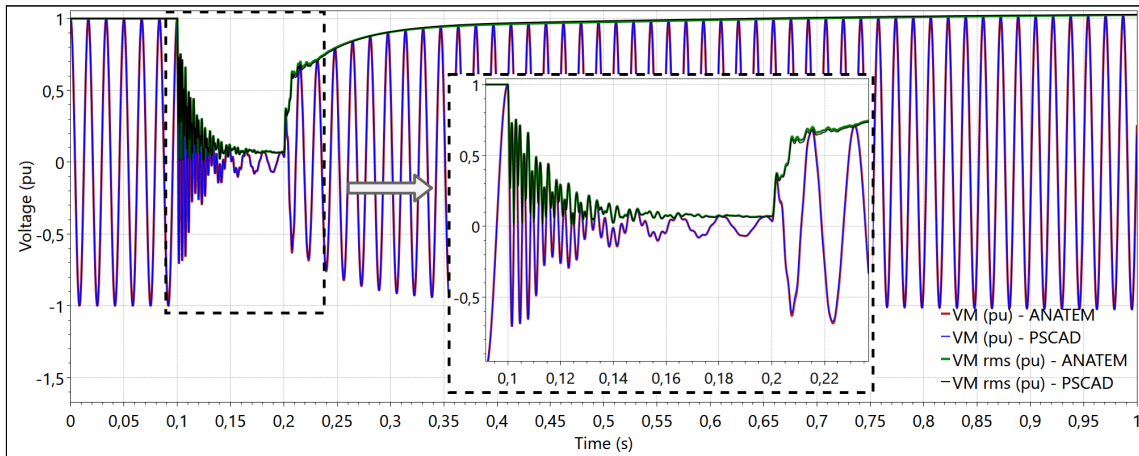

Figure 6.44: Comparison of the stator voltage (pu) following a three-phase fault
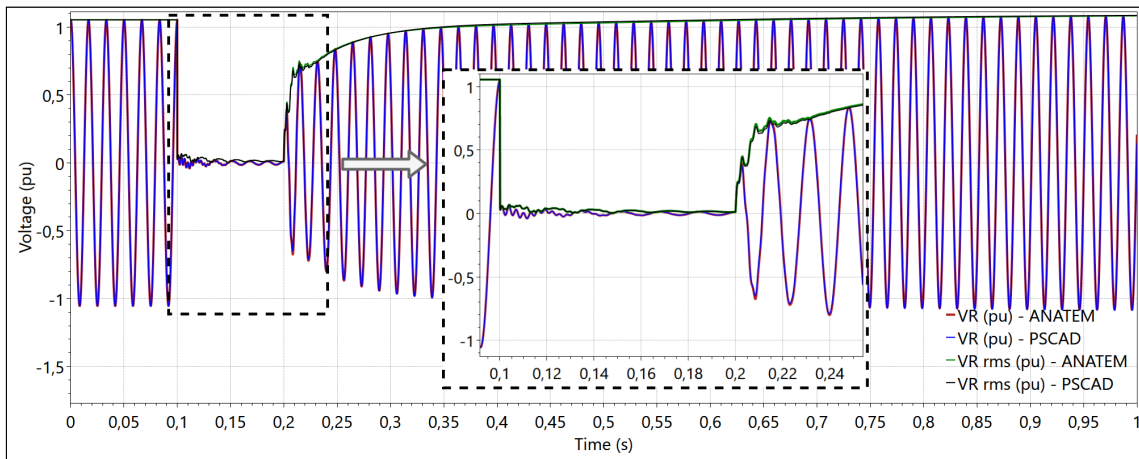

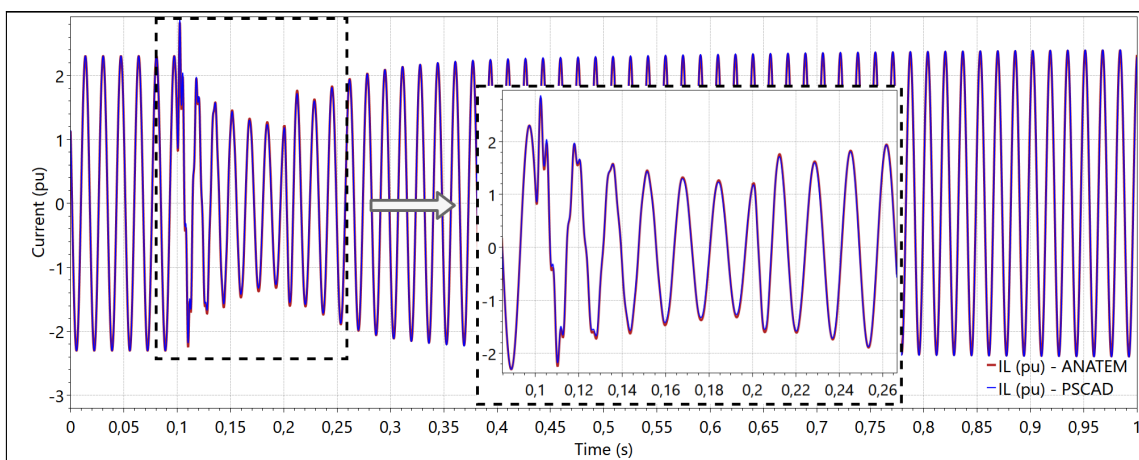Figure 6.45: Comparison of the load voltage (pu) following a three-phase fault

Figure 6.46: Comparison of the line current (pu) following a three-phase fault

For the analysis of the synchronous machine modeling, Figures 6.47 to 6.49 present

the comparison of the terminal electrical power, the electromagnetic torque, and the rotor frequency, following the three-phase balanced short-circuit.
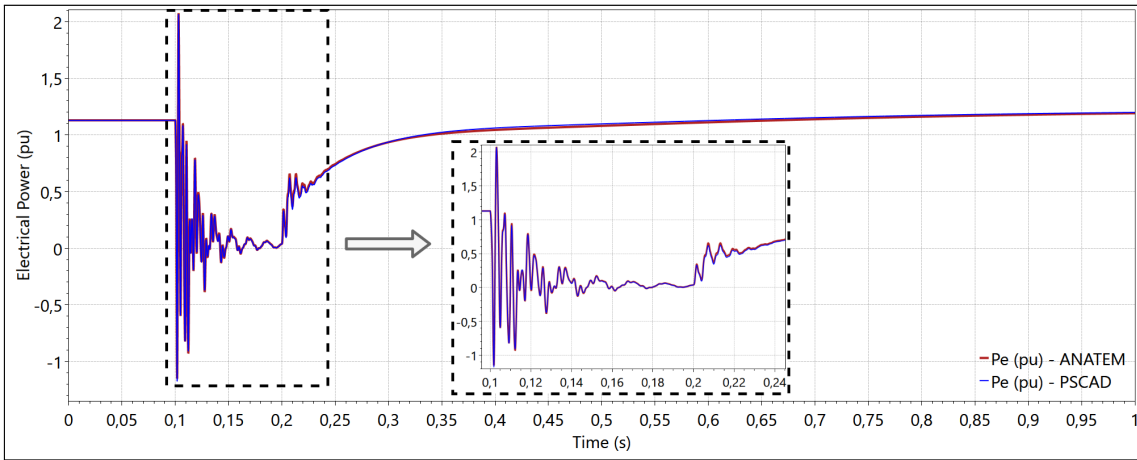
Figure 6.47: Comparison of the terminal electrical power (pu)
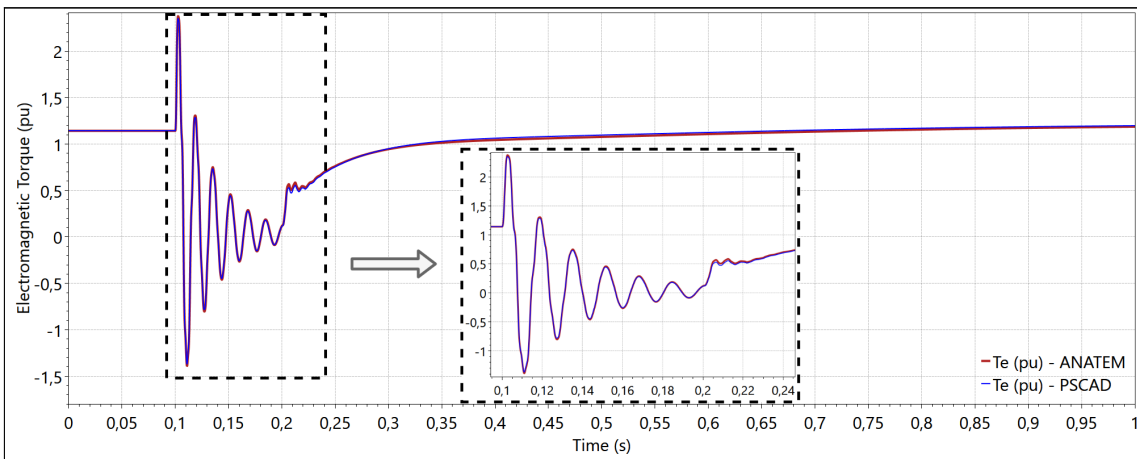

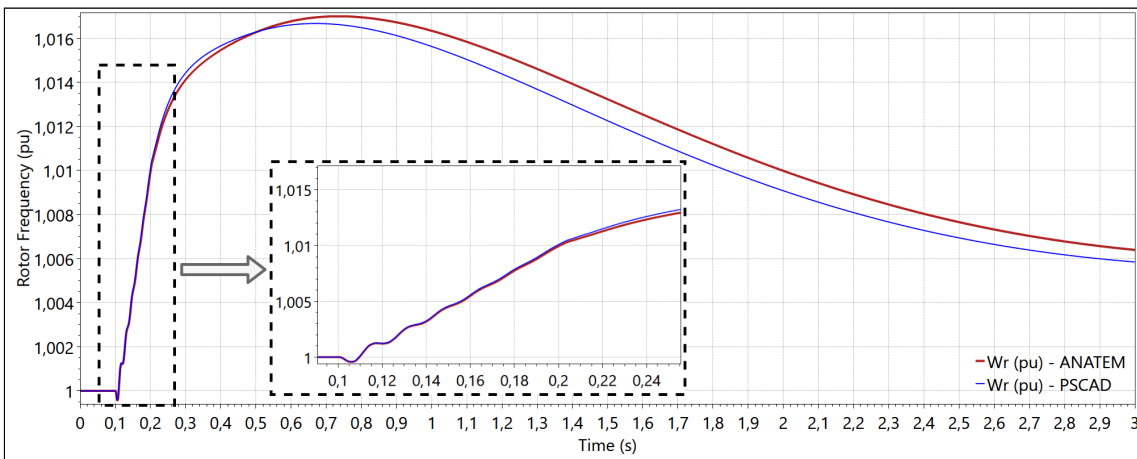Figure 6.48: Comparison of the electromagnetic torque (pu)

Figure 6.49: Comparison of the rotor frequency (pu)

Figures 6.47 and 6.48 evidence that both the terminal electrical power and the electromagnetic torque exhibit sufficiently close dynamic behavior. Likewise observed in the salient-pole machine validation, Figure 6.49 reveals a difference in the rotor frequency, suggesting that there are still some differences in the modeling adopted in the two programs. Due to the lack of detailed information about the internal machine equations of the PSCAD/EMTDC, this work considers that the present results validate the dynamic phasor models developed in ANATEM. However, a further investigation of this difference can still be conducted in future works.

6.3 Turbine-Generator Shaft

This section describes the ANATEM computational developments associated with the *individualized spring-mass model* for the representation of the synchronous machine mechanical shaft system through the mathematical modeling provided in Chapter 5. This modeling is widely employed in subsynchronous oscillations studies for the analysis of interactions between the turbine-generator shaft and series-compensated transmission systems.

As illustrated in Figure 6.50, the solution methodology for the dynamic phasor based synchronous machine is modular and convenient for simulation of multi-machine systems. This feature allows a direct coupling between the electrical equations associated with the generator "k" and the mechanical equations associated with its respective turbine-generator shaft.
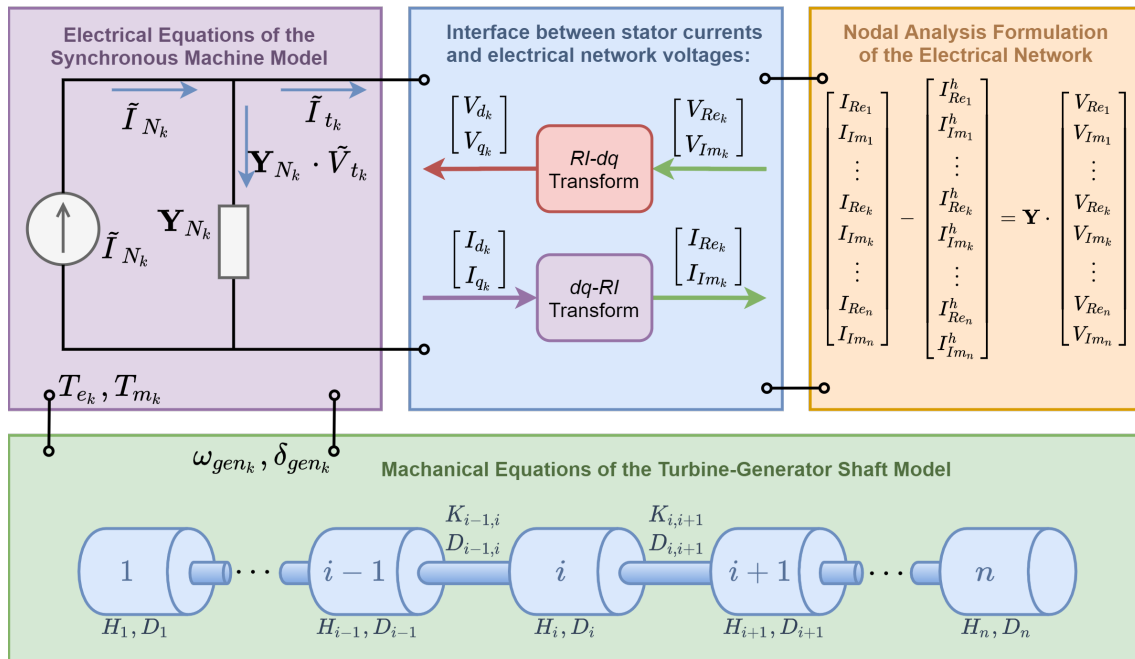

Figure 6.50: Interface solution of the synchronous machine electrical and mechanical equations and the electrical network modeling

6.3.1 Computational Developments

In the ESA simulation scope of the ANATEM software, the synchronous machine mechanical system has been modeled as a rigid body with an equivalent inertia constant. Thus far, when defining a synchronous machine model, only the following models have been required: (i) the *synchronous machine model* defined in the `DMDG` execution code; (ii) and the *machine controllers* defined in associated structures, for instance, the exciter, speed governor, and power system stabilizer. Afterward, these models (machine and controllers) should be associated to a network generation bus by using the following execution code:

> `DMAQ` - Execution code to associate a synchronous machine model and its respective controllers to the generation buses of the electrical network through the identification bus number defined in the ANAREDE savecase. Figure 6.51 shows an example of the usage of the `DMAQ` execution code.

```
DMAQ
( Nb)   Gr (P) (Q) Und ( Mg ) ( Mt )u( Mv )u( Me )u(Xvd)(Nbc)
   1    10            3    40    140    240u   340
999999
```

Figure 6.51: Example of usage of the `DMAQ` execution code

In this example, the synchronous machine model identified by "40" (in the `DMDG` context) is associated to a network generation bus defined in the power flow savecase as the node "1". As well, the exciter, speed governor, and stabilizer models, respectively defined by the identification numbers "140", "240", and "340", are also associated to this generation bus. The parameter `(u)` of the `DMAQ` execution code should be filled with the character "u" if the controller is represented by a user-defined controller structure, instead of using the ANATEM built-in models. However, such structure will not be explored in-depth as it is out of the scope of this thesis.

In general, the parameters required in the `DMAQ` execution code are detailed in Table 6.17:

Table 6.17: Description of the `DMAQ` parameters

Parameter	Description
Nb	Identification number of the electrical network generation bus to be modeled as a power plant with synchronous generators
Gr	Identification number of the generator group in this network bus
P	Percentage of the active electrical power supplied by this group
Q	Percentage of the reactive electrical power supplied by this group
Und	Units of synchronous machines in operation
Mg	Identification number of the generator model
Mt	Identification number of the exciter model
Mv	Identification number of the speed governor model
Me	Identification number of the power system stabilizer model
Xvd	Drop compensation reactance
Nbc	Identification number of the network controlled bus

Turbine-Generator Shaft Individualized Model

In this thesis, the new SSR module has been developed in the ANATEM software to allow the representation of the turbine-generator mechanical shaft system through the spring-mass model described in Section 5.3. Therefore, to enable this simulation context, it is necessary to specify the parameters of each rotor mass and shaft section that composes the synchronous machine mechanical system.

The SSR analysis module keeps the compatibility with the existing electromechanical stability database of the ANATEM. The main difference in relation to the traditional ESA module is that the data related to the individual masses must be provided by using the following `DMAS` execution code, which has been developed in this thesis.

`DMAS` - Execution code to define the individualized masses data set. Similarly to the `DMDG`, this execution code specifies a generic turbine-generator shaft without associating it to a synchronous machine group. Therefore, this shaft model must subsequently be connected to a network generation bus within the `DMAQ` scope.

Figure 6.52 illustrates an application example of the `DMAS` execution code. In this example, it is defined a turbine-generator shaft composed by six predominant masses in conformity with the shaft model shown in Figure 5.5. One should note that the generator (referred to as `"GEN"`) and the exciter (`"EXC"`) masses do not develop mechanical torque, so that the field `"Tmec"`, which corresponds to the percentage of the total mechanical torque that is developed by mass "i", is null for these two masses.

```
DMAS
( No ) (     Name    )
10     turbogenerator
( Ident ) ( Hmass  ) ( Dmass  ) ( Tmec ) ( Kshaf ) ( Dshaf )
HP          0.092897   0.10500      0.30    19.303       0.0
IP          0.155589   0.05850      0.26    34.929       0.0
LPA         0.858670   0.01970      0.22    52.038       0.0
LPB         0.884215   0.00233      0.22    70.858       0.0
GEN         0.868495   0.02480               2.822       0.0
EXC         0.0342165  0.01020
FIMMAS
999999
```

Figure 6.52: Example of usage of the `DMAS` execution code

It should also be highlighted that the spring-mass data set must necessarily be provided in the `DMAS` environment following the order depicted in the generic shaft model of Figure 6.53, i.e., from the first left mass up to the last right mass. This order is imperative because the shaft parameters "ij" are respective to the **shaft between the mass "i" that is provided in the same line and the mass "j" that comes next**. Additionally, the generator mass is required to be identified by the string `"GEN"` since this is how the ANATEM software shall identify the generator mass, which constitutes the initial interface between the electrical and mechanical equations of the synchronous machine.
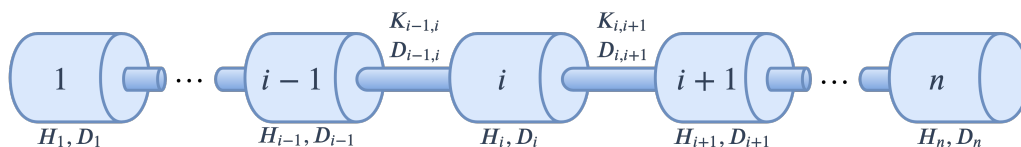

Figure 6.53: General structure of a individualized lumped-mass model

Table 6.18 describes the parameters that are required in the `DMAS` execution code:

Table 6.18: Description of the `DMAS` parameters

Parameter	Description
No	Identification number of the turbine-generator shaft model
Name	Identification name of the turbine-generator
Ident	Identification name of the mass i
Hmass	Inertia constant of the rotor mass i in MW.s/MVA
Dmass	Damping coefficient or factor of the rotor mass i, in pu torque/pu speed deviation
Tmec	Percentage of the mechanical torque developed by this rotor section
Kshaf	Torsional stiffness of the rotor shaft between the rotor mass i and $i+1$, in pu torque/rad
Dshaf	Damping coefficient of the rotor shaft section associated with the rotor mass i and $i+1$, in pu torque/pu speed deviation

After defining the individualized mass model, this structure shall be associated to a network generation bus, along with the other synchronous machine models within the `DMAQ` environment. Therefore, a new parameter referred to as "Mrot" has been added in the `DMAQ` execution code to associate the shaft model defined in the `DMAS` scope. Figure 6.54 gives an application example of this new parameter, where the shaft model identified by "10" is associated to the network bus "1".

```
DMAQ
( Nb)   Gr (P) (Q) Und ( Mg ) ( Mt )u( Mv )u( Me )u(Xvd)(Nbc) (Mrot)
    1   10          10    103                                    10
999999
```

Figure 6.54: Example of usage of the `DMAQ` execution code with the new parameter "Mrot"

New Output Variables

For validation purposes, the following new output variables associated with the rotor mechanical system have been developed:

DELMAS - This variable enables the output of the angular position in degrees of the rotor masses in relation to the generator mass. The angular position

of the generator mass is determined in respect to a common synchronously rotating reference in the electrical network.

WMAS - This variable enables the output of the angular frequency of each rotor mass in pu.

TMAS - This variable enables the output of the mechanical torque in all the shaft sections in pu.

Figure 6.55 shows an application example of these new output variables. In this case, the variables related to the turbine-generator shaft associated in the bus "1" by the group "10" are required over the time-domain simulation.

```
DPLT
(Tipo)M( El ) ( Pa) Nc Gp ( Br) Gr ( Ex) (Bl) P
TMAS       1          10
DELMAS     1          10
WMAS       1          10
999999
```

Figure 6.55: Example of usage of the turbine-generator shaft output variables

6.3.2 Validation Results

The computational developments associated with the turbine-generator shaft mechanical system are validated in this subsection considering the system illustrated in Figure 6.56.
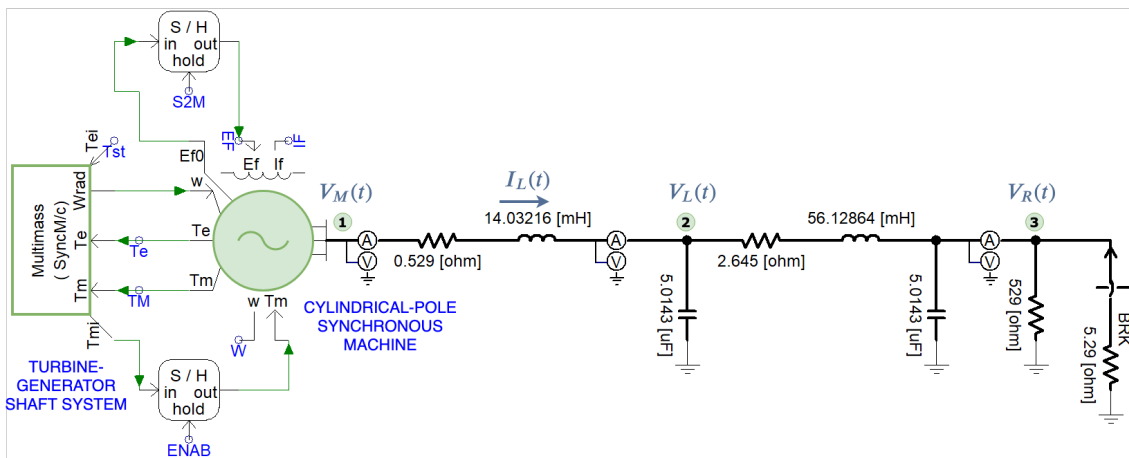
Figure 6.56: Cylindrical-pole synchronous machine with the representation of the turbine-generator shaft mechanical system

Table 6.19 contains the parameters of the turbine-generator shaft system employed in the simulations.

Table 6.19: Parameters of the turbine-generator shaft system

Rotor Mass i	Inertia H_i (s)	Damping D_i (pu/pu)	Mechanical Torque (%)	Shaft Section ij	Stiffness K_{ij} (pu/rad)
HP	0.092897	0.10500	30%	HP-IP	19.303
IP	0.155589	0.05850	26%	IP-LPA	34.929
LPA	0.858670	0.01970	22%	LPA-LPB	52.038
LPB	0.884215	0.00233	22%	LPB-GEN	70.858
GEN	0.868495	0.02480		GEN-EXC	2.822
EXC	0.0342165	0.01020			

The electrical network and the synchronous machine parameters considered here are the same as those adopted in Section 6.2.2.2 for the validation of the electrical equations of the cylindrical-pole synchronous machine. Then, it is simulated a balanced three-phase short-circuit fault through a resistance of 5.29 Ω at the load terminal with 100 ms duration.

The dynamic behavior of the electrical network variables are illustrated in Figures 6.57 to 6.59. These results show that the voltage of the synchronous machine terminals $V_M(t)$, the load voltage $V_L(t)$, and the line current $I_L(t)$ are in good agreement with the PSCAD/EMTDC.
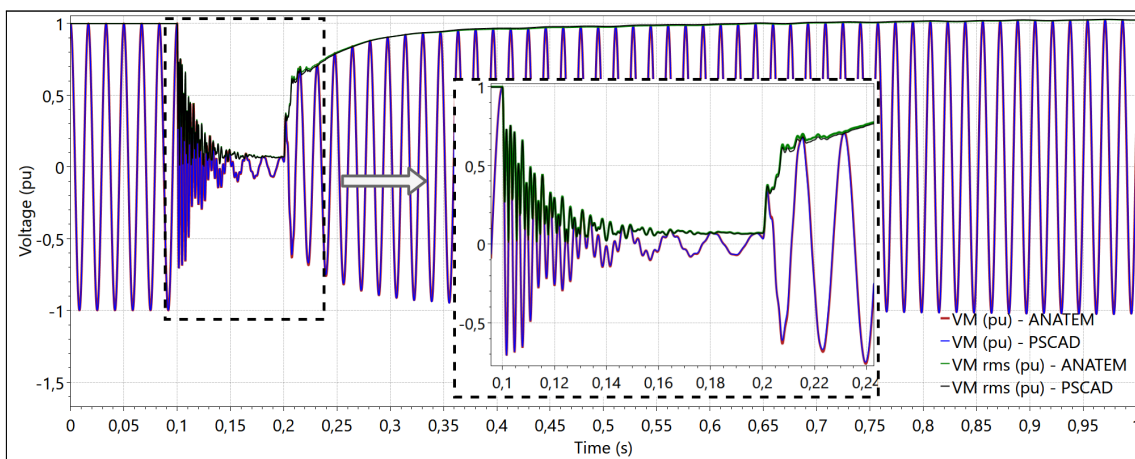
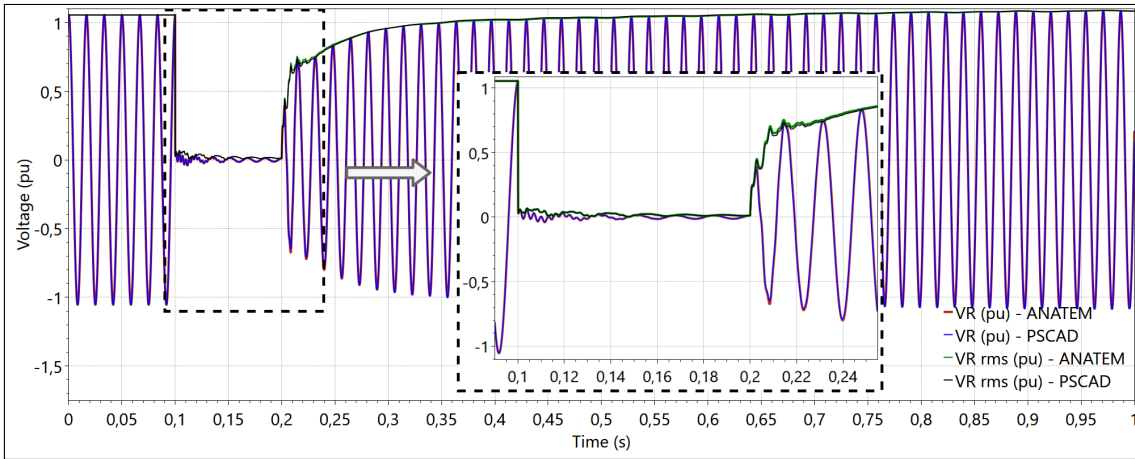Figure 6.57: Comparison of the stator voltage (pu) following a three-phase fault

Figure 6.58: Comparison of the load voltage (pu) following a three-phase fault
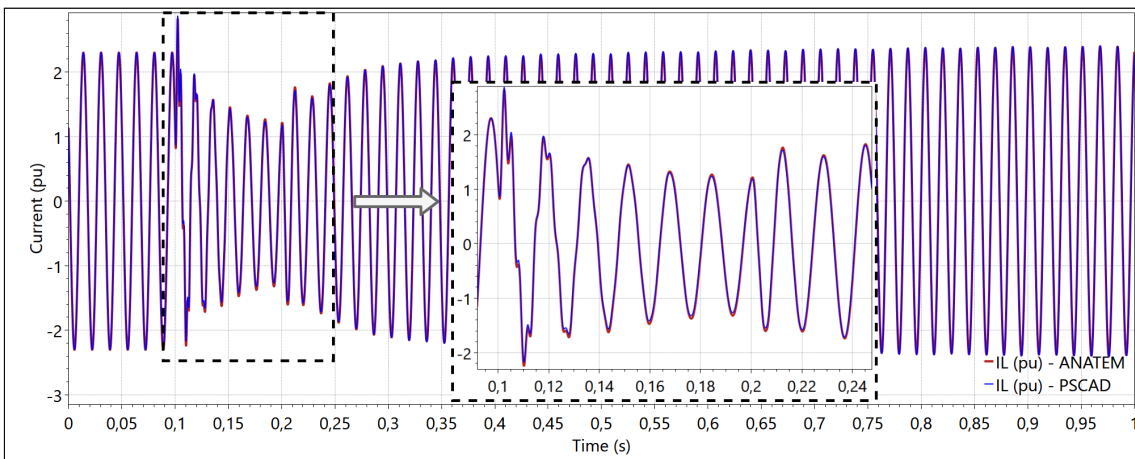

Figure 6.59: Comparison of the line current (pu) following a three-phase fault

Regarding the variables of the synchronous machine modeling, the simulation results of the terminal electrical power and the electromagnetic torque are shown in Figures 6.60 and 6.61, respectively.
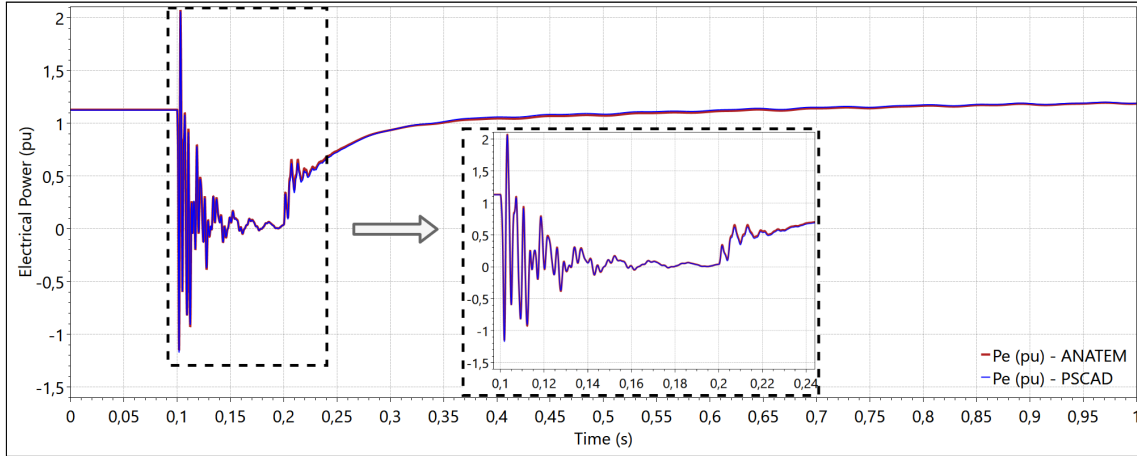

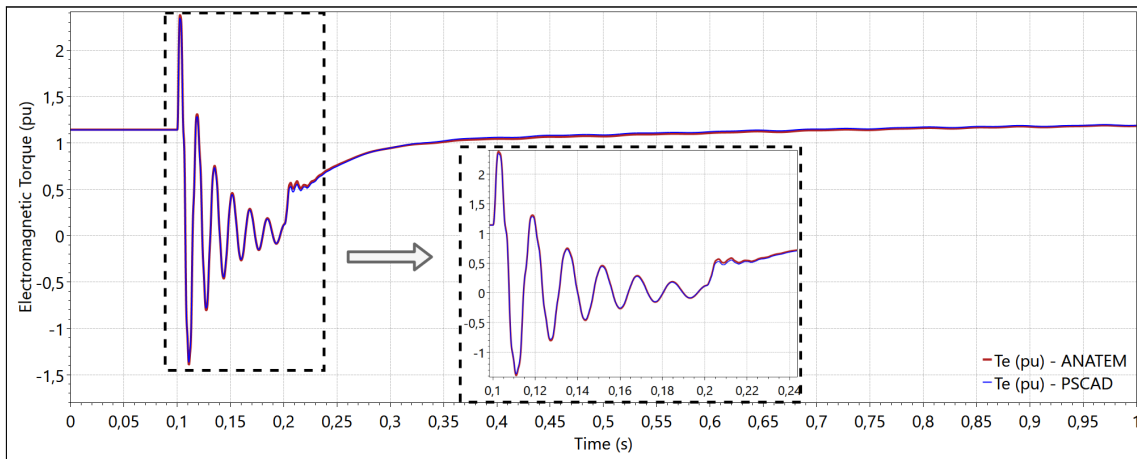Figure 6.60: Comparison of the terminal electrical power (pu)

Figure 6.61: Comparison of the electromagnetic torque (pu)

In validating the computational developments related to the turbine-generator shaft, the relative position of the rotor masses $\delta_i(t)$ in respect with the generator mass $\delta_{gen}(t)$, the speed of each rotor mass ω_i, and the torque of shaft between adjacent masses T_{ij} have been chosen for comparison against the PSCAD/EMTDC.

In this regard, Figure 6.62 presents the transient behavior of the rotor masses position in degrees. One should note that following the three-phase balanced short-circuit, the deviation of the rotor masses position with respect to the generator mass is in consonance with the reference results from PSCAD/EMTDC.
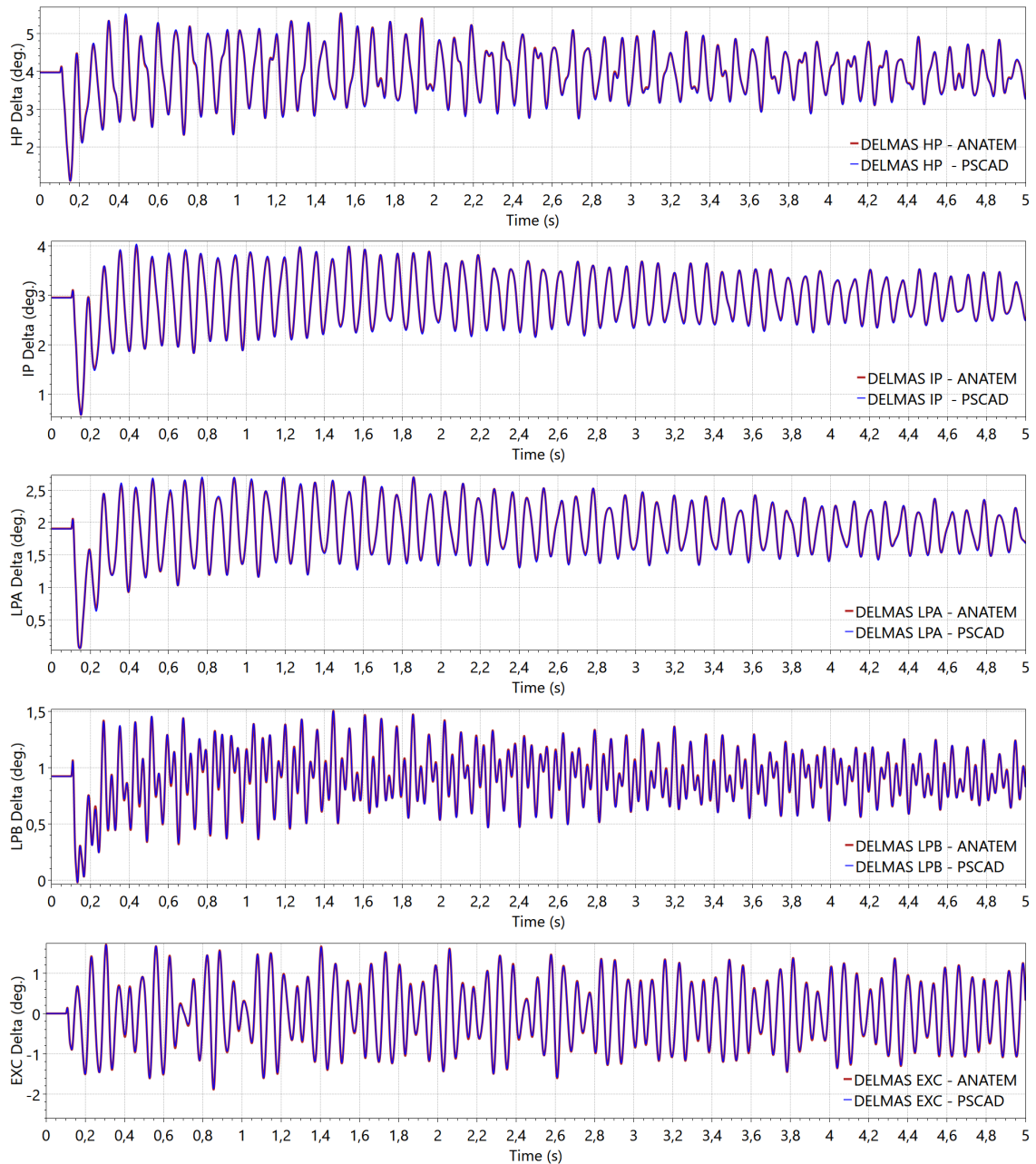
Figure 6.62: Comparison of the shaft masses position in respect to the generator mass

Figure 6.63 presents the rotor speed respective to the six masses that composes the turbine-generator shaft system. It is noted that the curves are in conformity throughout the 5-second time-frame, validating the individualized shaft modeling implemented in this thesis. The differences observed in this variable follow the same pattern noticed in the generator frequency when considering a rigid rotor, so that it is potentially resultant from the same reasons mentioned in Section 6.2.2.2.
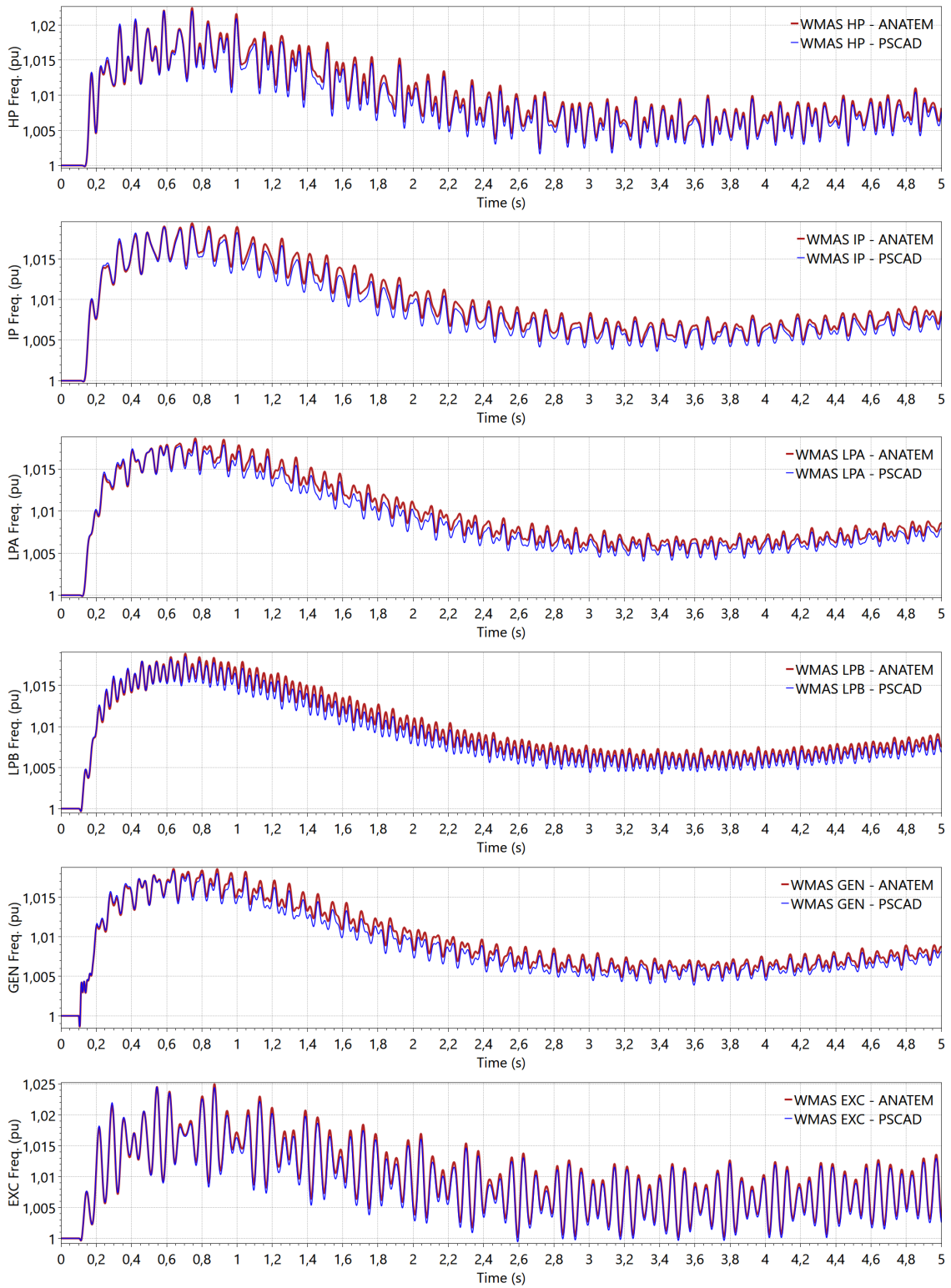
Figure 6.63: Comparison of the rotor masses speed following the fault

The mechanical torque on the several turbine shaft sections between adjacent masses is illustrated in Figure 6.64. Based on this simulation results, it is evidenced that both curves are maintained into alignment.
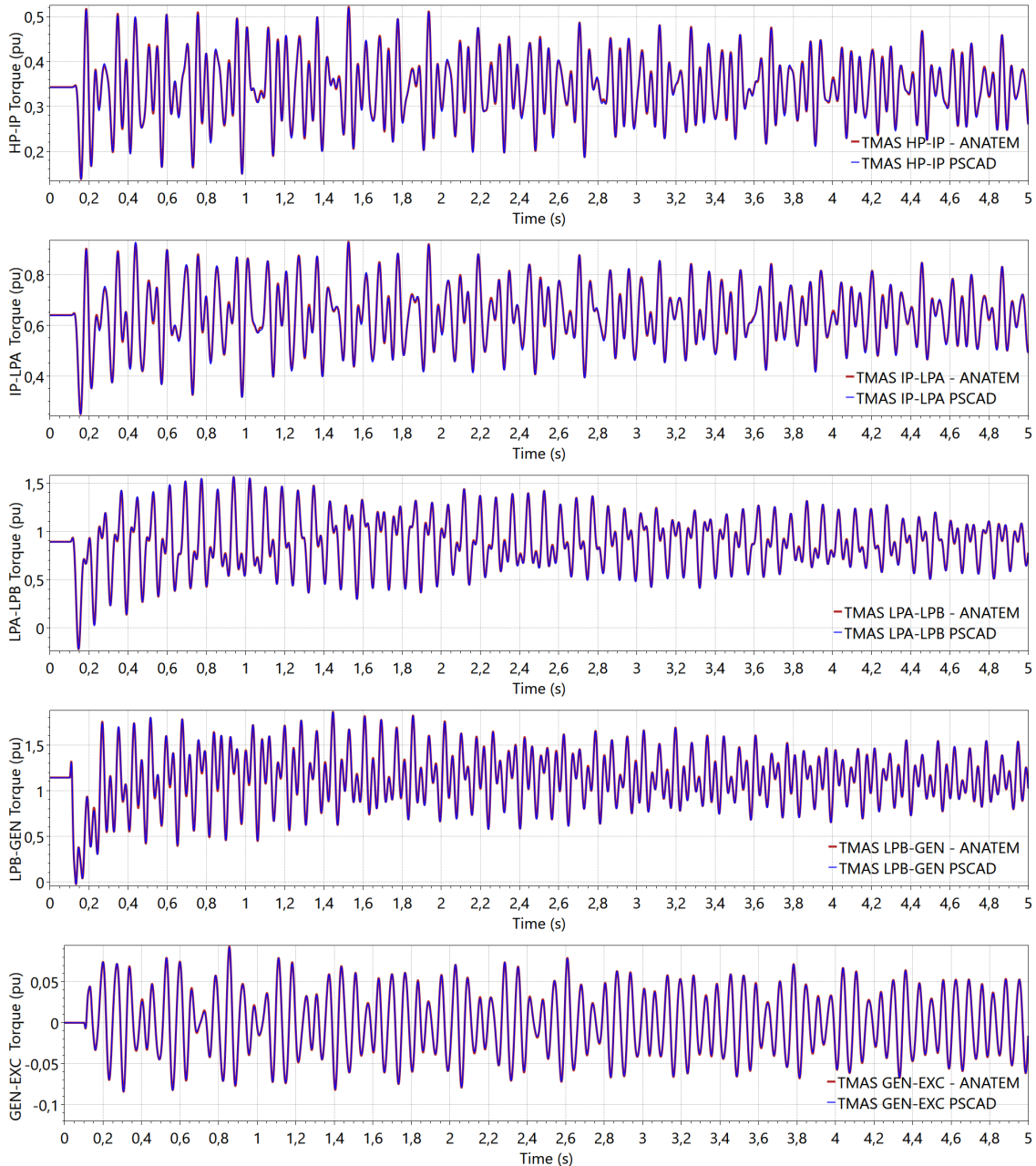

Figure 6.64: Comparison of the shaft torque following the fault

The simulation results demonstrate that the turbine-generator shaft model implemented in the ANATEM is adequate for subsynchronous resonance studies as it provides the dynamic behavior of the synchronous machine and the electrical network in good agreement with the PSCAD/EMTDC software.

Chapter 7

Case Study Simulation and Analysis

In this chapter, three case studies are presented to study nonlinear electromechanical and electromagnetic transients in electrical power systems by using the DPCM models of the electrical network components described in Chapter 3. Furthermore, the subsynchronous resonance phenomenon associated with interactions between the turbine-generator shaft and series compensated transmission systems is evaluated by employing the dynamic phasor-based synchronous machine model presented in Chapter 4, and the turbine-generator shaft model described in Chapter 5.

The first case to be studied is the IEEE First Benchmark Model for subsynchronous resonance analysis, where both linear and nonlinear results are presented in order to validate the simulation models implemented in the ANATEM software. The second case study includes the ESA model of a Voltage Source Converter to examine the influence of the network dynamics representation in the time-domain simulation of electrical networks containing power electronic devices. The third one presents the investigation of the network dynamics representation and a nonlinear SSR analysis with a detailed representation of multiple synchronous machines and their associated controllers in a large-scale power system.

To this extent, dynamic simulations are carried out with the ANATEM software by using the new `DINR` and `MRSS` modules, which have been implemented in this thesis. Moreover, the PacDyn software [68], which is integrated with the ANATEM to perform the linear analysis of the electrical system, is also used here to provide valuable SSR analysis by revealing specific forms of interactions between the torsional modes of the turbine and the natural oscillation frequencies of the electrical network.

7.1 IEEE First Benchmark for SSR Analysis

In this section, the subsynchronous resonance phenomena associated with series-compensated systems is studied through the IEEE First Benchmark Model [56] proposed in a IEEE task force of the Subsynchronous Resonance Working Group.

7.1.1 System Description

The IEEE First Benchmark Model (FBM) is based on the transmission system of the Navajo power plant [72]. The single-line diagram of this system is shown in Figure 7.1, which consists of a 892.4 MVA synchronous generator connected to an infinite bus through a series-compensated transmission line.
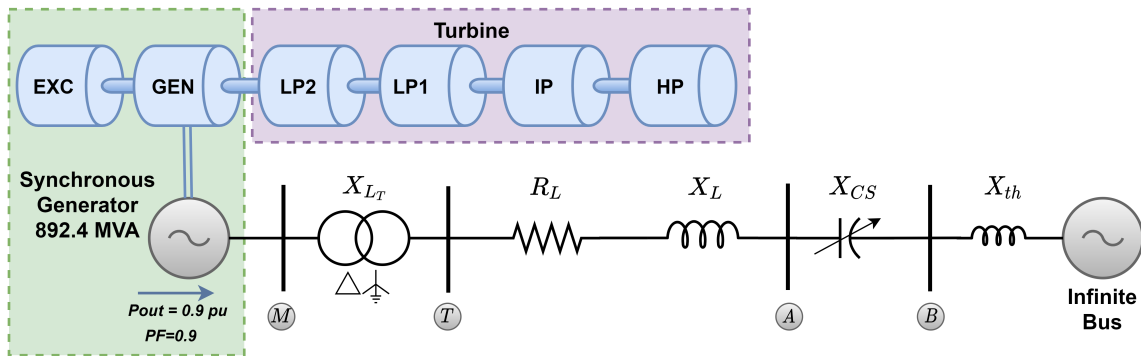

Figure 7.1: IEEE First Benchmark Model for SSR Analysis

Table 7.1 contains the operational parameters of the synchronous machine in per unit on the machine base power.

Table 7.1: Operational parameters of the synchronous generator

Parameter	Value	Parameter	Value	Parameter	Value
Base power	892.4 MVA	Base voltage	26 kV	Base frequency	60 Hz
R_a	0 pu	X_l	0.13 pu	X_d	1.79 pu
X_q	1.71 pu	X'_d	0.169 pu	X'_q	0.228 pu
X''_d	0.135 pu	X''_q	0.200 pu	T'_{do}	4.3 s
T'_{qo}	0.85 s	T''_{do}	0.032 s	T''_{qo}	0.05 s

Table 7.2 describes the operating point of the system under study, and the equipment parameters expressed in pu at the generator base power (892.4 MVA) and nominal frequency (60 Hz). At this stage, no control systems are associated with the generator. Thus, both field voltage and mechanical torque remain constant over the time-domain simulation.

Table 7.2: Parameters of the IEEE FBM study case for SSR analysis

Parameter	Description	Value
Synchronous generator Initial conditions	base power	892.4 MVA
	magnitude	1.0 pu / 26 kV RMS L-L
	angle	$-9.7°$ (cosine ref.)
	output electrical power	0.9 pu
	power factor	0.9 (lag.)
Step-up transformer	base power	892.4 MVA
	base voltage on primary side	26 kV RMS L-L
	base voltage on secondary side	539 kV RMS L-L
	reactance X_{L_T}	0.14 pu
Transmission line	series reactance X_L	0.50 pu
	series resistance R_L	0.02 pu
Series compensation	capacitive reactance X_{CS}	-0.35 pu
Thévenin reactance	equivalent reactance X_{th}	0.06 pu
Infinite bus	magnitude	0.885 pu
	angle	$0°$ (cosine ref.)
	frequency	60 Hz

Table 7.3 contains the parameters of the mechanical system of the turbine-generator shaft. It also describes the fraction of the total mechanical torque that is developed by each turbine section.

Table 7.3: Parameters of the turbine-generator shaft system

Rotor Mass i	Inertia H_i (s)	Damping D_i (pu/pu)	Mechanical Torque (%)	Shaft Section ij	Stiffness K_{ij} (pu/rad)
HP	0.092897	0.40500	30%	HP-IP	19.303
IP	0.155589	0.09850	26%	IP-LPA	34.929
LPA	0.858670	0.03970	22%	LPA-LPB	52.038
LPB	0.884215	0.00433	22%	LPB-GEN	70.858
GEN	0.868495	0.04480		GEN-EXC	2.822
EXC	0.0342165	0.02020			

It is known that the damping constants of the individual rotor masses are dependent on the operating condition of the system and that they should be obtained

from the modal damping factors, as described in [7, 64]. For simplicity, and with the purpose of time-domain simulation, the damping factors of the shaft masses are determined to provide positive damping for all torsional modes considering a capacitive compensation of 0.35 pu.

7.1.2 Simulation Results and Analysis

Dynamic Performance Following a Step Change in the Mechanical Torque

In this item, dynamic simulations are performed in the ANATEM software to compare the time-domain response of the IEEE FBM test system, considering the representation of the turbine-generator shaft: (i) an equivalent single lumped mass, which is referred to as `"RIGID SHAFT"` (blue curve) in the simulation results; and (ii) the individualized multi-mass shaft described in Table 7.3, which is referred to as `"MULTI-MASS"` (red curve). It is noteworthy that both simulations include the electrical network dynamics, as well as the synchronous machine stator flux dynamics.

It is simulated a positive step change of 0.1 pu in the mechanical torque of the synchronous generator, considering a total simulation time of $10s$, and $\Delta t = 10\mu s$ as the time step size for both `"RIGID SHAFT"` and `"MULTI-MASS"` simulations. Figure 7.2 illustrates the frequency of the generator mass, following this disturbance.
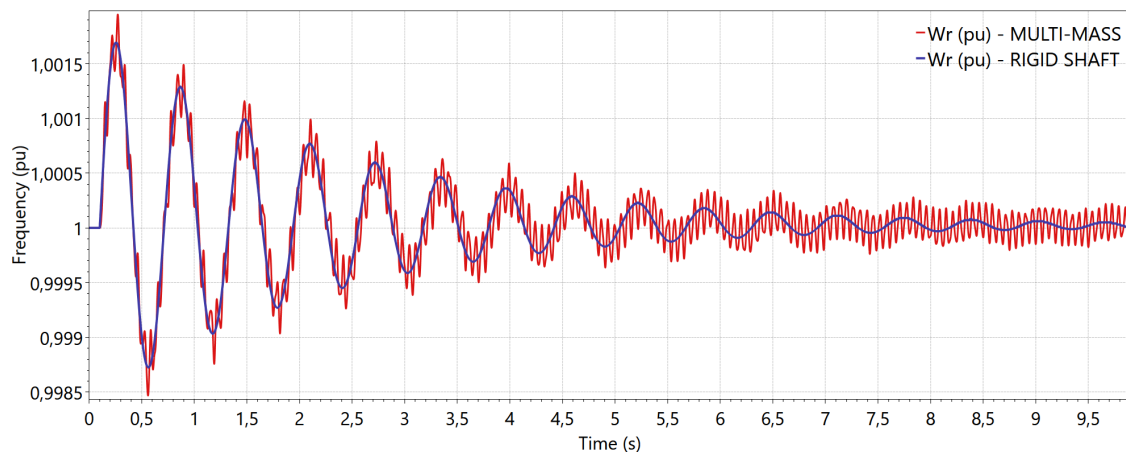

Figure 7.2: Comparison of the frequency (pu) of the generator mass following a step change of 0.1 pu in the mechanical torque - multi-mass x rigid shaft

Figure 7.3 illustrates the electromagnetic torque of the synchronous machine, while Figure 7.4 presents the RMS voltages at the machine terminal and at point A (identified in Figure 7.1) following a step change of 0.1 pu in the mechanical torque. For the voltages, the simulation window is reduced to 5 seconds to allow a clearer view of the differences between the two curves.
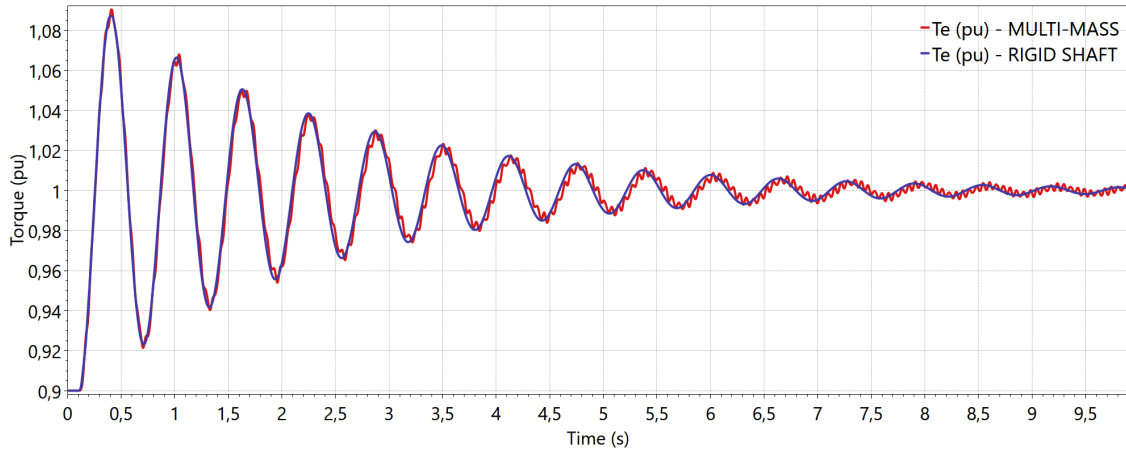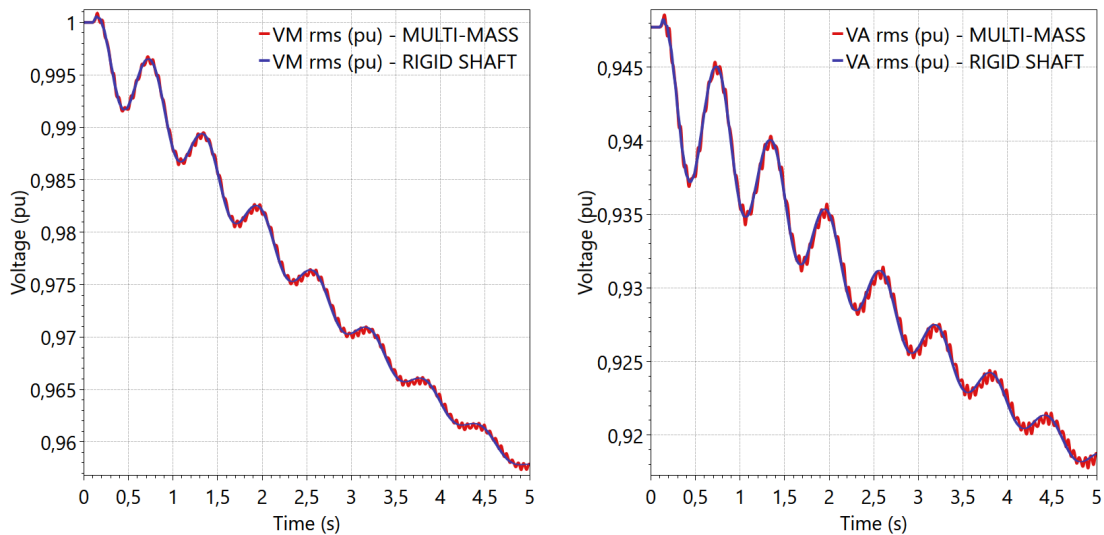
Figure 7.3: Electromagnetic torque (pu) following a step change of 0.1 pu in the mechanical torque

(a) Voltage (pu) at the machine terminal

(b) Voltage (pu) at terminal A

Figure 7.4: Comparison of the RMS voltage (pu) following a step change of 0.1 pu in the mechanical torque of the synchronous generator - multi-mass x rigid shaft

Figure 7.2 demonstrates that the electromechanical oscillation mode can be observed in both configurations of the rotor shaft. This oscillation mode can approximately be determined as the inverse of the period between two successive peaks of the rotor frequency. Therefore, considering the period between $t = 4.5837s$ and $t = 5.2161s$, an approximate frequency of **1.6 Hz** is obtained for the electromechanical oscillation mode. On the other hand, higher oscillation frequencies can only be observed in the multi-mass shaft representation since they arise from the interaction between the individualized shaft model and the electrical network dynamics. Analogously, by inspecting the generator frequency resultant from the multi-mass model, one of the torsional oscillation frequencies can be determined approximately as the inverse

of the period between $t = 8.33679s$ and $t = 8.27464s$, resulting in a torsional mode around **16 Hz**. It is recognized that this six-mass rotor shaft presents one electromechanical and five torsional modes, but the other torsional modes cannot directly be determined through the time-domain response. Thus, the following item shows a detailed analysis of the oscillation mode frequencies of the FBM system using linear analysis tools, which are also employed to confirm the frequency of the electromechanical mode around 1.6 Hz and the torsional mode of 16 Hz.

Figures 7.3 and 7.4 show that both electromagnetic torque and voltages present smaller observability of the torsional modes, i.e., the identification of torsional oscillations in these variables is less apparent than in the generator frequency.

Figure 7.5 illustrates the frequency (pu) of each rotor mass following the step of 0.1 pu in the mechanical torque.
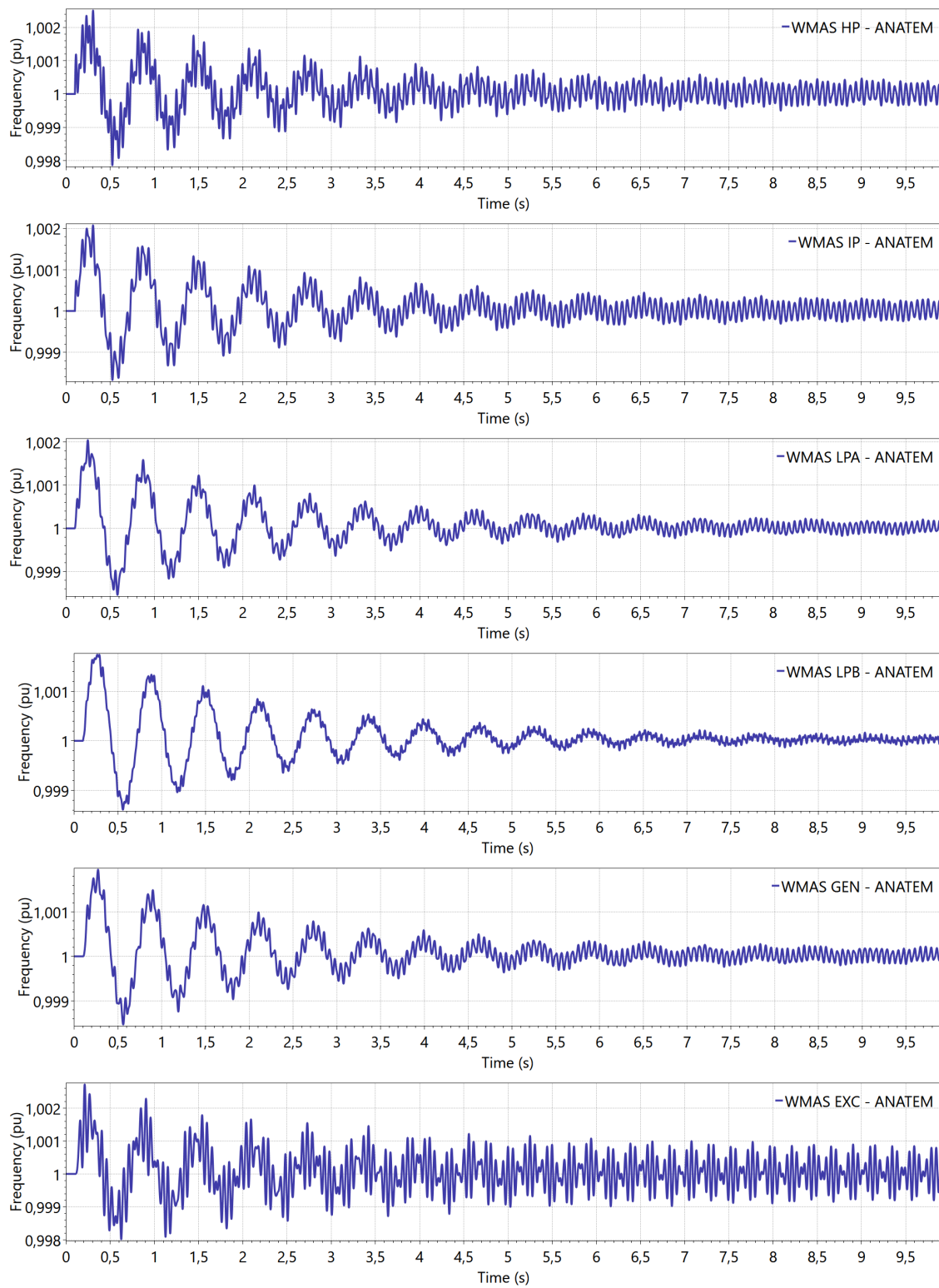

Figure 7.5: Frequency (pu) of the rotor masses following a step of 0.1 pu in the mechanical torque

In addition, the dynamic behavior of the other specific shaft variables, such as the shaft torques and the position of the multiple rotor sections, can also be observed in the ANATEM to support the nonlinear analysis of the SSR phenomenon. Figure 7.6 illustrates the position of the rotor masses in relation to the generator mass following a step change of 0.1 pu in the mechanical torque.
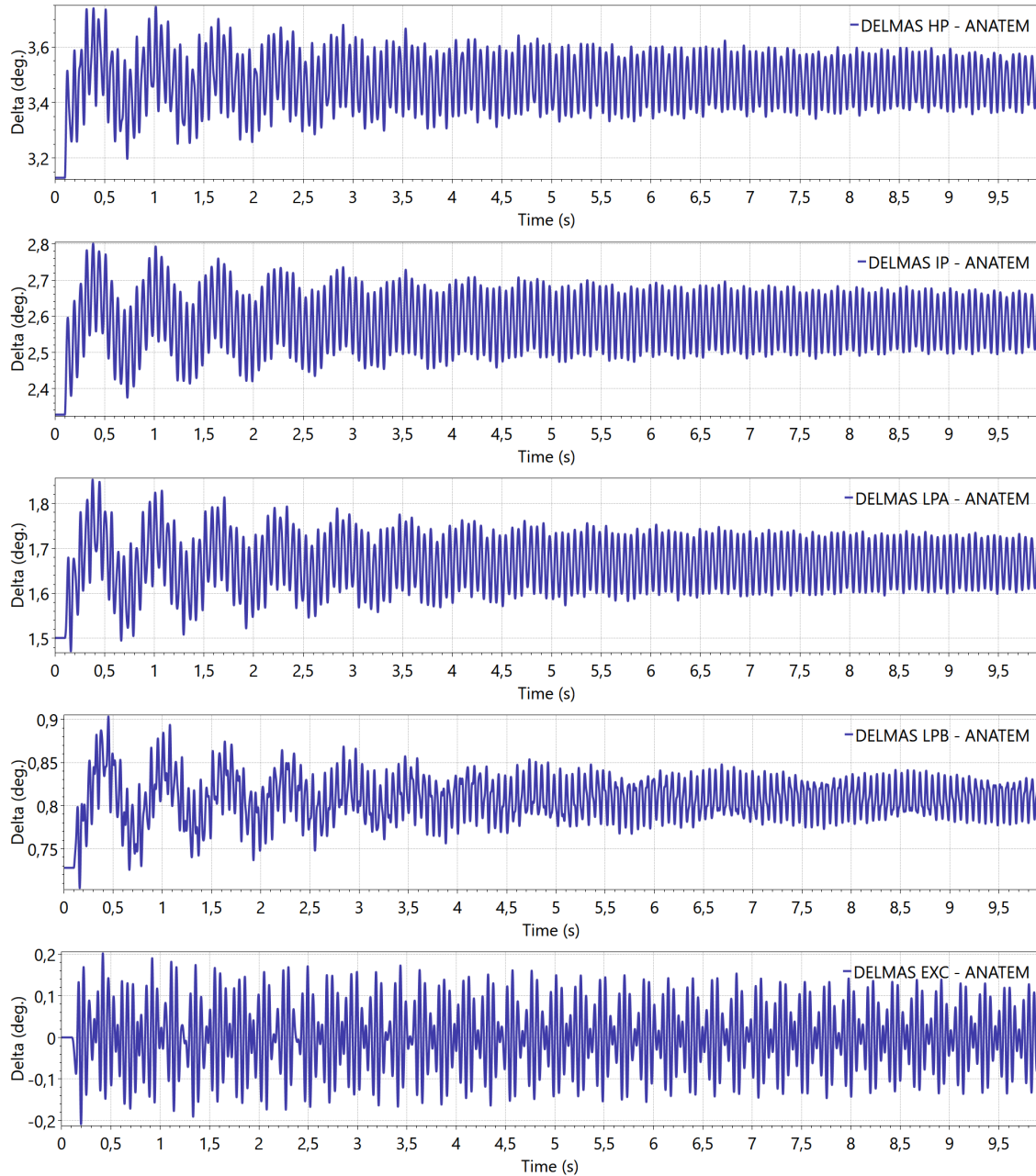
Figure 7.6: Position of the rotor masses (degrees) in respect to the generator mass following a step of 0.1 pu in the mechanical torque

Figure 7.7 illustrates the torque on the shaft sections following a step change of 0.1 pu in the mechanical torque.
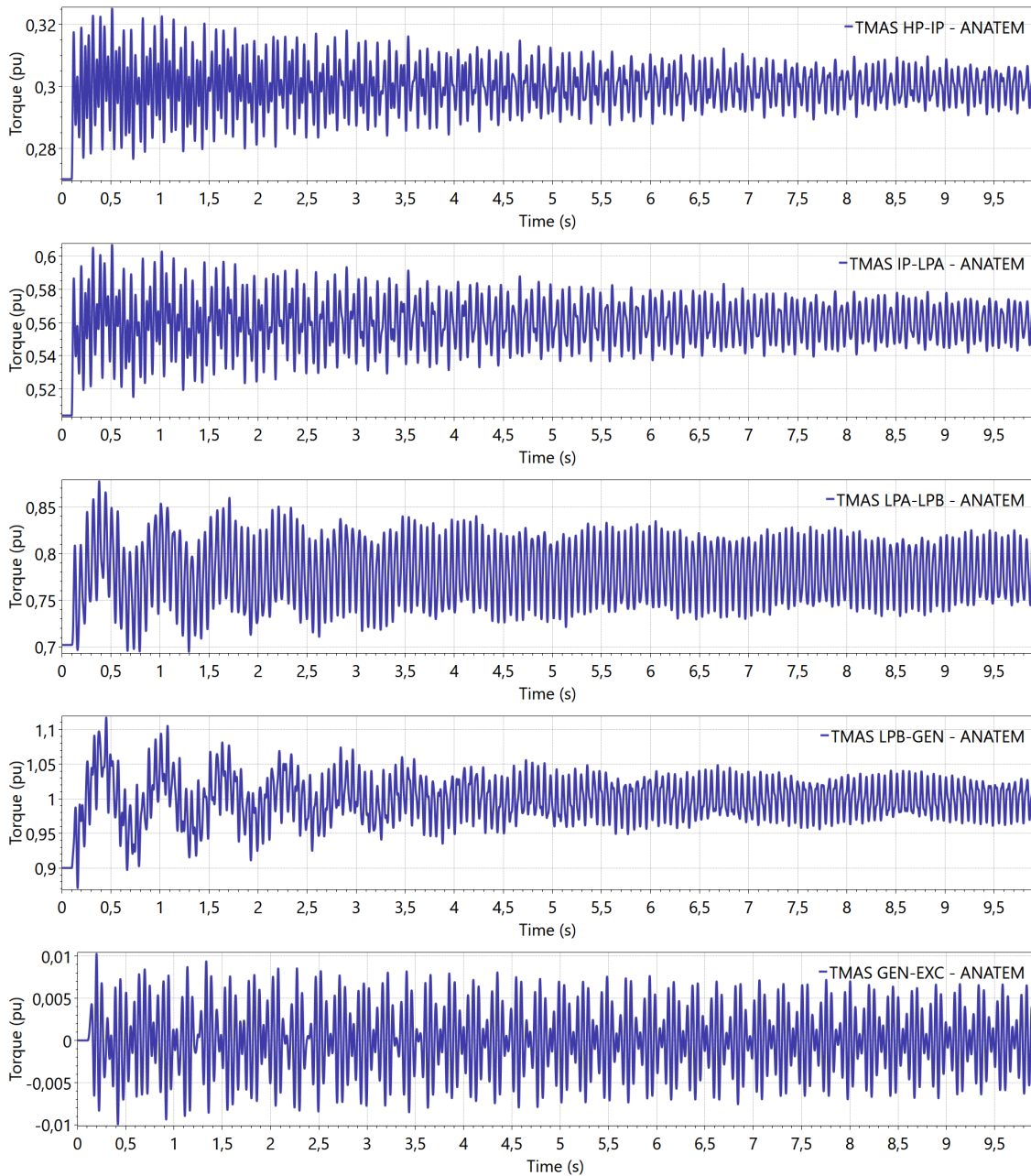

Figure 7.7: Torque (pu) on the shaft sections following a step change of 0.1 pu in the mechanical torque

Figures 7.5 to 7.7 show that both the electromechanical and the torsional modes are poorly damped. The torsional oscillations can be observed in the individual shaft variables. However, the distinction between the different natural oscillation frequencies is not evident since the application of the disturbance excites all torsional modes simultaneously.

The nonlinear time-domain analysis of the SSR phenomenon does not intend to

substitute the SSR linear analysis, but rather they constitute complementary tools. Furthermore, it allows the identification of unstable oscillations in the electrical quantities due to **adverse interaction with the transmission system following an electrical network switching or large disturbances**. In this regard, it can reveal the nonlinear interaction between the turbine-generator shaft and the network equipment, which can cause torsional fatigue on the mechanical system due to transient torques originated in the synchronous generator shaft.

Linear Analysis of the IEEE FBM System

In this item, the linear analysis of the IEEE FBM system is presented in order to identify specific characteristics of the torsional oscillation modes. Table 7.4 presents the eigenvalues of the FBM system with their respective damping factors, obtained with the PacDyn software [68]. The nature of the eigenvalues has been determined from the analysis of the participation factors [1]: the electrical network modes (supersynchronous and subsynchronous) present a higher participation factor in relation to the network variables, whereas the higher participation factors of the torsional modes are related to the mechanical variables of the turbine-generator shaft.

Table 7.4: Engeinvalues of the IEEE FBM system - $X_{CS} = 0.35$ pu

Description	Eigenvalue	Module	Freq. (Hz)	Damp. (%)
Torsional	$-0.05597 \pm j \ 202.79$	202.79	32.275	0.02760
Torsional	$-0.08494 \pm j \ 127.22$	127.22	20.248	0.06676
Torsional	$-0.1037 \pm j \ 99.783$	99.783	15.881	0.1039
Torsional	$-0.3897 \pm j \ 298.17$	298.18	47.456	0.1307
Torsional	$-0.5411 \pm j \ 160.29$	160.29	25.510	0.3376
Supersynchronous	$-4.6236 \pm j \ 616.62$	616.64	98.138	0.7498
Subsynchronous	$-3.3390 \pm j \ 136.81$	136.85	21.774	2.4399
Electromechanical	$-0.4990 \pm j \ 10.318$	10.330	1.6421	4.8303
Generator	-41.202	41.202	0.	100.00
Generator	-25.425	25.425	0.	100.00
Generator	-3.0751	3.0751	0.	100.00
Generator	-0.2479	0.2479	0.	100.00

In this radial system, the natural electrical frequency can approximately be determined from (5.3), as follows:

$$f_n = f_0 \sqrt{\frac{X_C}{X_L}} = 60 \sqrt{\frac{0.35}{0.17 + 0.14 + 0.5 + 0.06}} \approx 38.1 Hz \qquad (7.1)$$

with the reactance X_L being the sum of the inductive reactance of this radial system and the machine subtransient reactance (to this extent, the average of the direct and quadrature subtransient reactances has been considered); and X_C is the capacitive reactance.

From the natural oscillation frequency of the network, two distinct poles appear in the dq rotating reference frame. The first network mode is given by the complement of the synchronous frequency ($60 - 38.1 \approx 21.9$ Hz), which is referred to as **subsynchronous mode**. The second one is given by the sum of the network mode and the synchronous frequency ($60 + 38.1 \approx 98.1$ Hz), so-called **supersynchronous mode**. These results are in consonance with the frequencies listed in Table 7.4.

As expected, a rotor shaft composed by n masses introduces $n-1$ torsional oscillation modes in the system and one electromechanical oscillation mode due to the entire rigid body oscillation against the rest of the system. In the FBM case, the subsynchronous oscillation frequencies due to the torsional modes are 15.9 Hz, 20.2 Hz, 25.5 Hz, 32.3 Hz, and 47.5 Hz. This analysis confirms the existence of a torsional mode around 16 Hz, which could be observed by inspection of the time-response of the generator frequency. Likewise, the electromechanical oscillation mode corresponds to the oscillation frequency of 1.6 Hz, which has also been identified through the nonlinear analysis. Furthermore, the electromechanical and torsional modes present a low damping factor, justifying the slow decline tendency over their associated oscillations in the time-domain response.

Figure 7.8 shows the mode-shapes of the rotor speed for the electromechanical and torsional modes, ordered from the lowest to the highest frequency. The mode-shapes give information about how the masses oscillate between them in relation to a specific mode. The mode-shape is built by the components of the right eigenvector (associated with the respective eigenvalue), in the positions of the interest variables [1], which in this case are the rotational speed of the shaft sections (HP, IP, LPA, LPB, GEN, and EXC). In this regard, each eigenvector component is normalized by using the highest speed activity as the reference. In this case, the mode-shapes are represented in a histogram format, assuming positive (coherent oscillation) or negative (in opposite polarity) values, depending on how the masses oscillate against each other.

(a) Mode 0: $-0.4990 \pm j10.318$
(1.64 Hz)

(b) Mode 1: $-0.1037 \pm j99.783$
(15.88 Hz)

(c) Mode 2: $-0.08494 \pm j127.22$
(20.25 Hz)

(d) Mode 3: $-0.5411 \pm j160.29$
(25.51 Hz)

(e) Mode 4: $-0.05597 \pm j202.79$
(32.28 Hz)

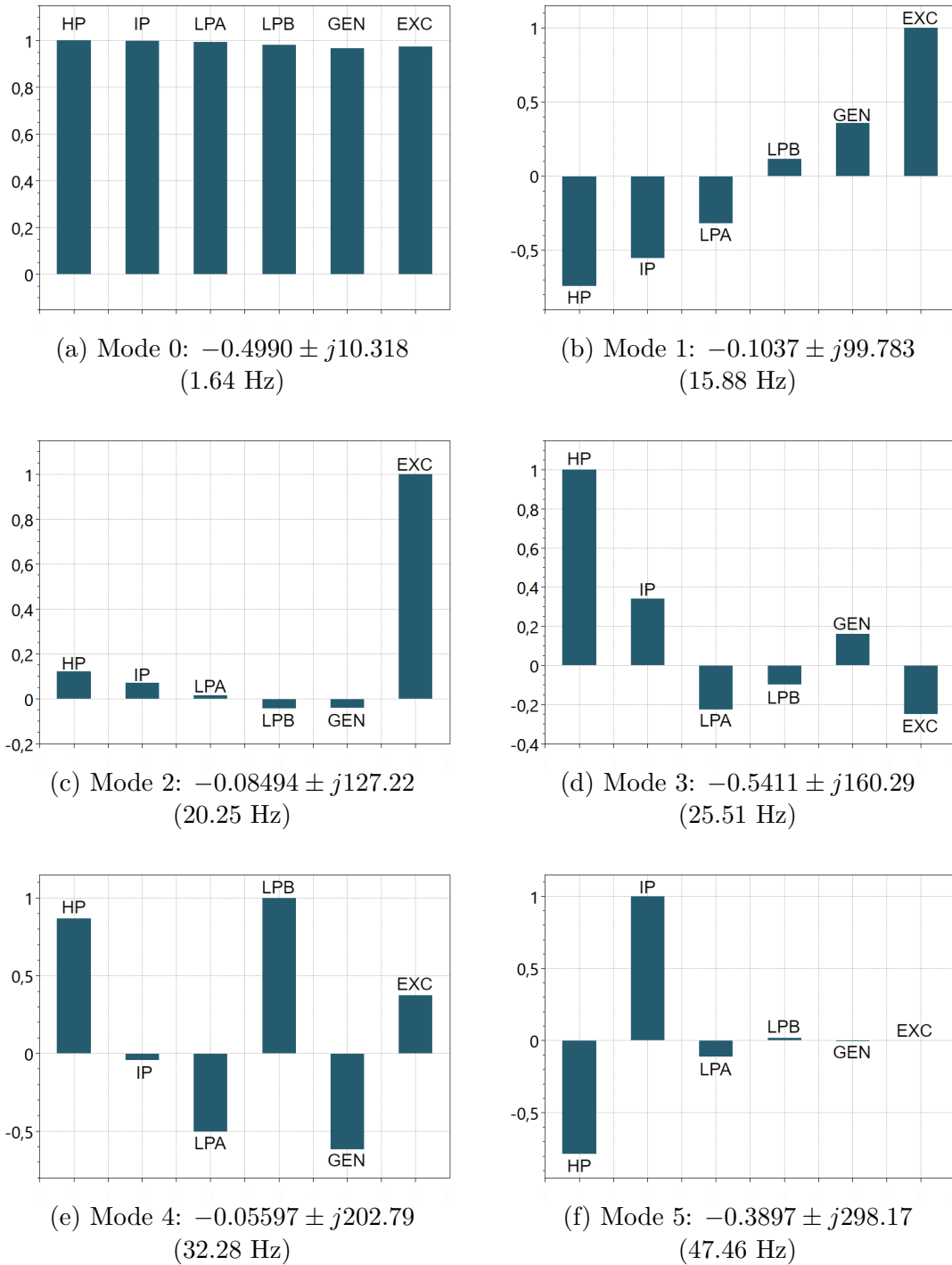(f) Mode 5: $-0.3897 \pm j298.17$
(47.46 Hz)

Figure 7.8: Mode-shapes of the natural frequencies of the turbine-generator shaft

From Figure 7.8a, one should note that the mode-shape of the electromechanical mode (1.64 Hz) presents a similar amplitude for all rotor masses indicating that, in this frequency, they oscillate coherently (in phase). This behavior is confirmed in Figure 7.5, where the electromechanical oscillation mode appears in a similar shape in the time-response of all rotor frequencies. This oscillation mode could also be observed by representing the rotor as a single lumped mass since it corresponds to

the rigid body oscillation against the power system. The other oscillation frequencies shown in Figures 7.8b to 7.8f are the torsional modes of the turbine-generator shaft, and they reveal that some masses oscillate in opposition to others. For instance, the frequency of 15.88 Hz presents one polarity reversal. This is a torsional mode in which the left masses oscillate against the masses on the right, where the end masses oscillating with a higher amplitude. On the other hand, the frequency of 20.2 Hz is an oscillation mode predominantly of the exciter mass, and it presents two polarity reversals. It is important to highlight that the nth oscillation mode presents n polarity reversals. This is shown in Figure 7.8f, where the mode-shape of the fifth torsional mode presents five oscillation reversals.

Figure 7.9 presents the root-locus of the eigenvalues of the FBM system in the s-domain for varying values of the series capacitor reactance X_{CS} from 0.035 pu to 0.7 pu, i.e., from 5% to 100% of the total inductive reactance. The supersynchronous and the subsynchronous poles of the electrical network, as well as the electromechanical and the torsional poles, are also identified in this graphic.
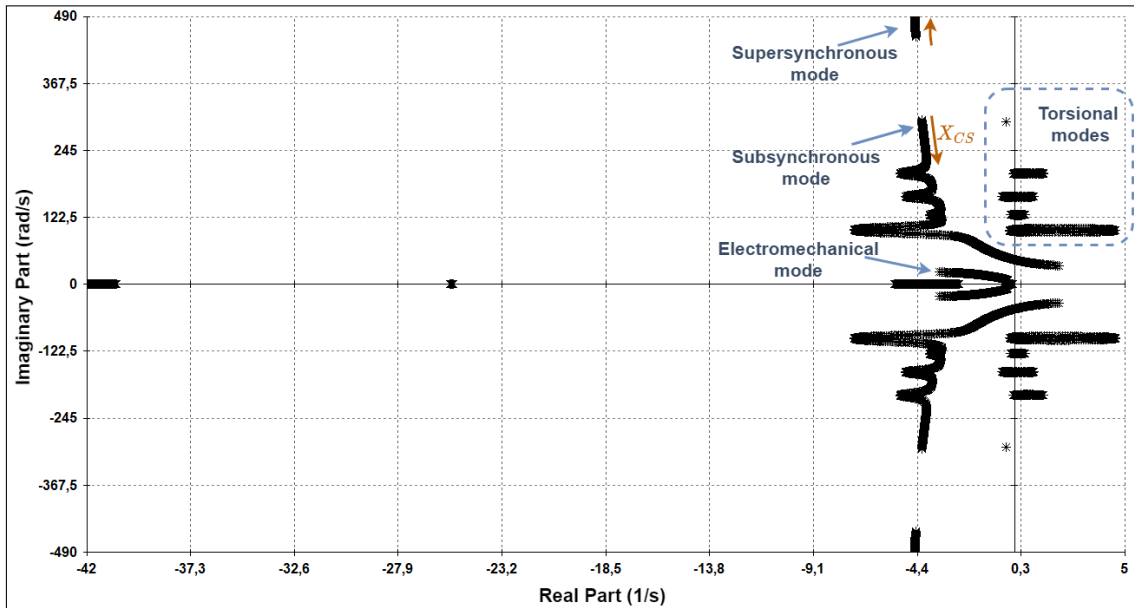
Figure 7.9: Root-locus varying the series compensation from 0.035 pu to 0.7 pu

One should note that when increasing the series capacitor reactance, the frequency of the supersynchronous mode increases, whereas the frequency of the subsynchronous mode reduces toward the frequency range of the torsional modes. As the frequency of the subsynchronous mode approaches the frequency of the torsional modes, there is a strong interaction between them, causing the torsional modes to be shifted to the right in the complex plane. This adverse interaction characterizes the subsynchronous resonance phenomenon by means of the torsional interaction mechanism.

For certain critical values of series compensation, this occurs with higher intensity, as illustrated in Figure 7.10.
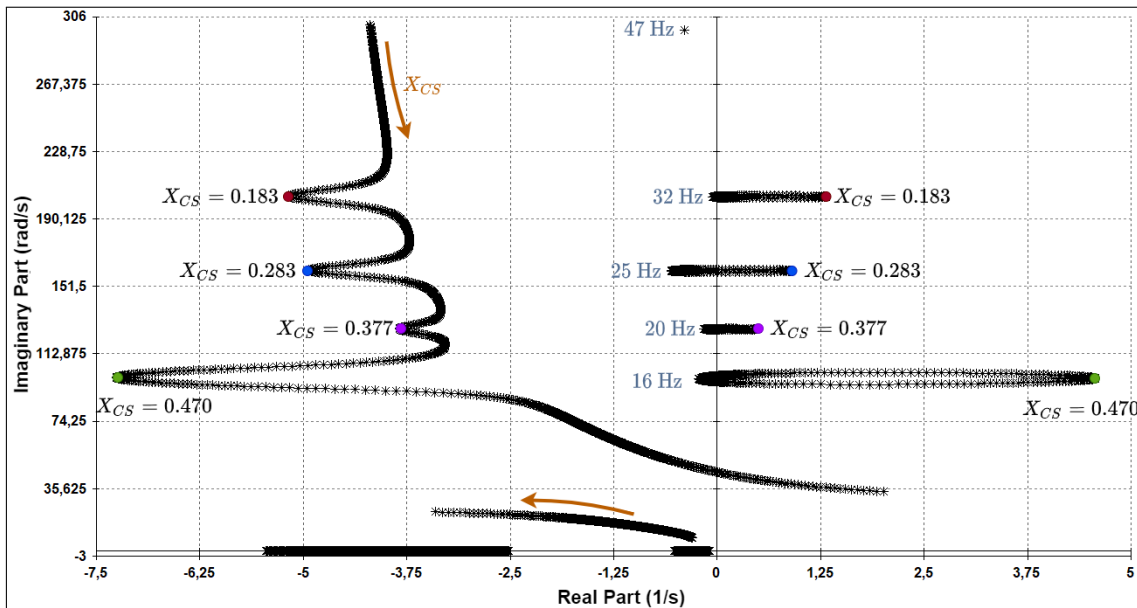

Figure 7.10: Root-locus - subsynchronous, electromechanical and torsional modes

The SSR phenomenon limits the level of series compensation that can be employed in the system. Otherwise, it can provoke excessive torsional stress on the shaft, causing loss of shaft lifetime due to torsional fatigue or even more severe shaft damage. Therefore, the effects of varying the series capacitor reactance are explored in the following item to investigate the SSR phenomenon in several compensation levels.

Analysis of the FBM System Considering Different Levels of Series Compensation

Figure 7.11 shows the nonlinear time-domain response of the electromagnetic torque of the synchronous generator following a step change of 0.1 pu in the mechanical power, considering a compensation level of 54.2% ($X_{CS} = 0.38$ pu).
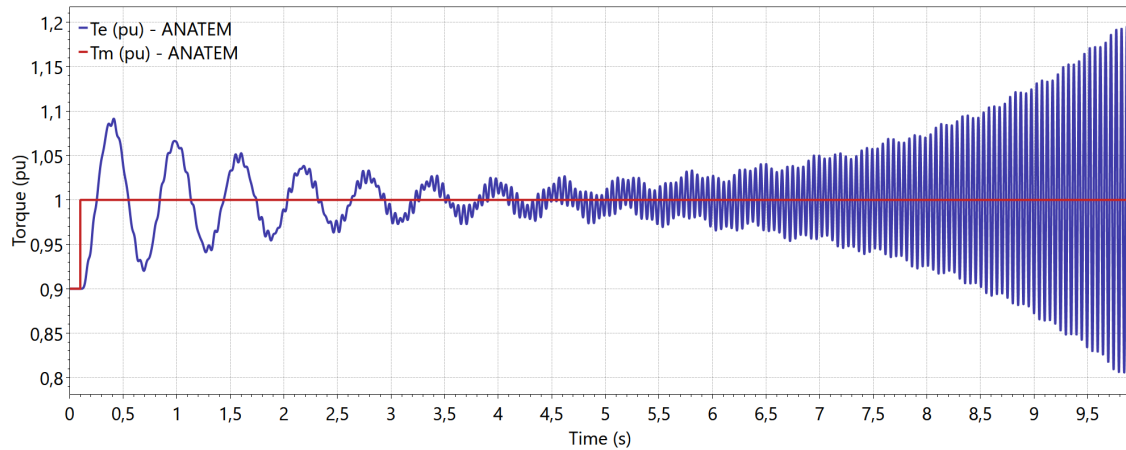
Figure 7.11: Electromagnetic torque (pu) of the synchronous generator following a step change of 0.1 pu in the mechanical torque - FBM System with $X_{CS} = 0.38$ pu

Considering this same compensation level and disturbance, the frequency of the multiple masses of the shaft is illustrated in Figure 7.12.
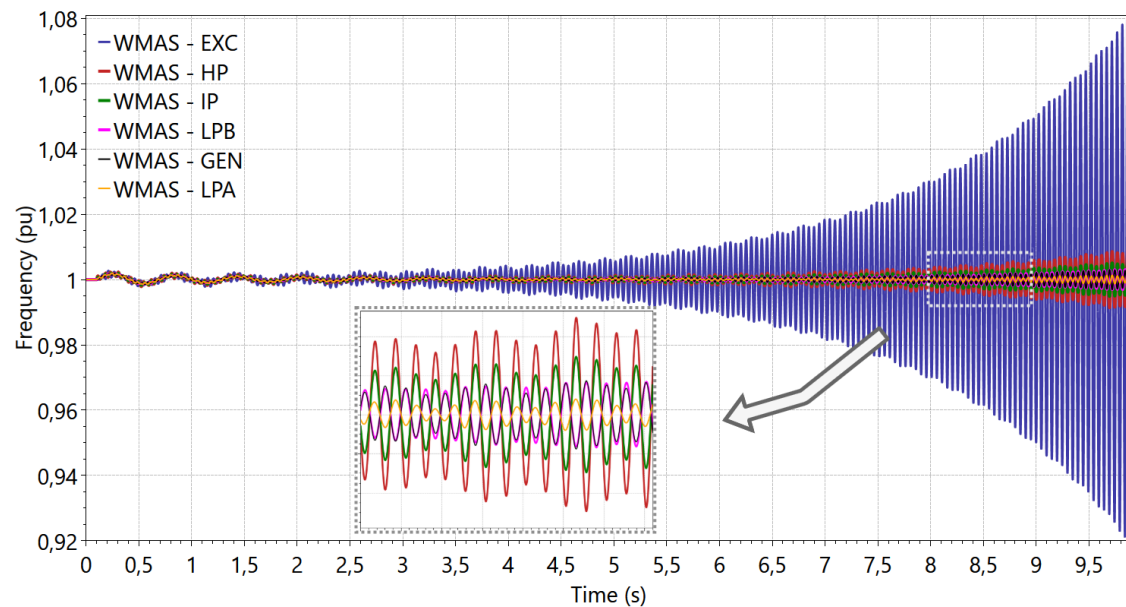
Figure 7.12: Frequencies of the multiple shaft masses following the disturbance

According to the root-locus presented in Figure 7.10, by increasing the level of series compensation from 50% ($X_{CS} = 0.35$ pu) to 54% ($X_{CS} = 0.38$ pu) results in

instability of the second torsional mode (20 Hz). Table 7.5 presents the eigenvalues of the FBM system for $X_{CS} = 0.38$ pu, confirming that the torsional oscillation mode of 20 Hz presents negative damping at this compensation level.

Table 7.5: Poles of the IEEE FBM system - $X_{CS} = 0.38$ pu

Description	Eigenvalue	Module	Freq. (Hz)	Damp. (%)
Torsional	$0.4829 \pm j\ 126.91$	126.91	20.198	-0.3805
Torsional	$-0.05606 \pm j\ 202.81$	202.81	32.278	0.02764
Torsional	$-0.03383 \pm j\ 100.11$	100.11	15.934	0.03380
Torsional	$-0.3897 \pm j\ 298.17$	298.18	47.456	0.1307
Torsional	$-0.5509 \pm j\ 160.37$	160.37	25.523	0.3435
Supersynchronous	$-4.6304 \pm j\ 626.68$	626.70	99.739	0.7389
Subsynchronous	$-3.8269 \pm j\ 126.61$	126.67	20.151	3.0212
Electromechanical	$-0.5403 \pm j\ 10.708$	10.721	1.7042	5.0394
Generator	-41.287	41.287	0.	100.00
Generator	-25.431	25.431	0.	100.00
Generator	-3.1475	3.1475	0.	100.00
Generator	-0.2685	0.2685	0.	100.00

As predicted in the mode-shapes, subsynchronous oscillations at 20 Hz (Figure 7.8c) are observed with higher intensity in the frequency of the exciter mass (EXC). This feature can be clearly seen in Figure 7.12. Another important information obtained through the mode-shape of the 20 Hz mode, is that the HP, IP, LPA, and EXC masses oscillate in phase, which is also confirmed in the amplified region highlighted in Figure 7.12. On the other hand, this set of masses oscillate in opposite polarity with respect to the LPB and GEN masses. Additionally, the oscillation magnitude of each shaft mass follows the proportion shown in the mode-shape.

Figure 7.13 presents the comparison of the generator frequency considering three different levels of series capacitive compensation: 25.7% ($X_{CS} = 0.18$ pu), 34.3% ($X_{CS} = 0.24$ pu), and 40% ($X_{CS} = 0.28$ pu). In these simulations, it is also applied a step change of 0.1 pu in the mechanical torque.
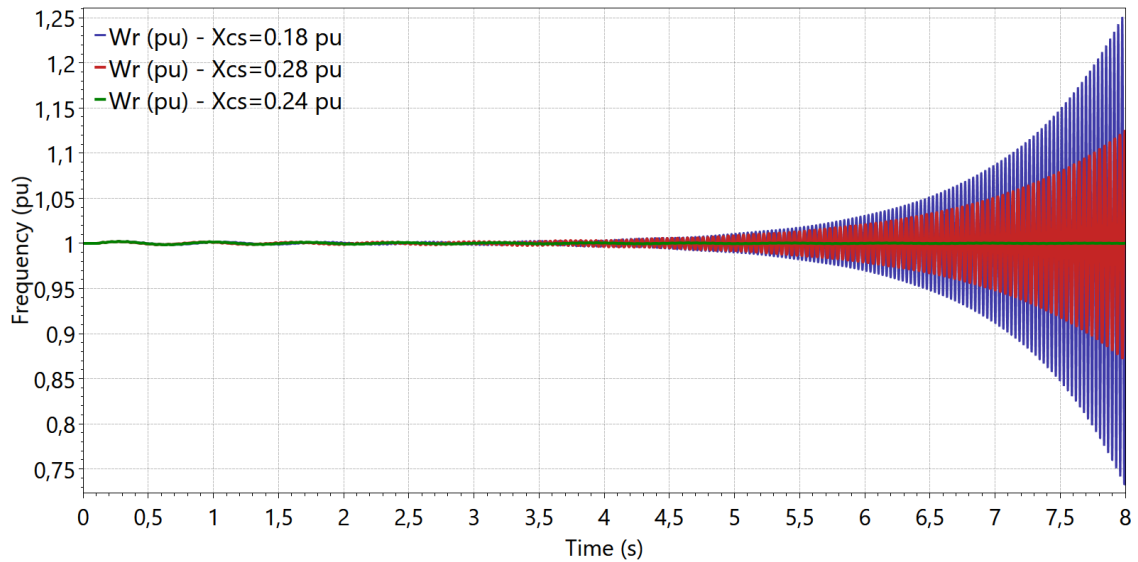

Figure 7.13: Comparison of the generator frequency considering different levels of series compensation: 25.7% (0.18 pu), 34.3% (0.24 pu), and 40% (0.28 pu)

One should note that the nonlinear time-domain response confirms the subsynchronous resonance phenomenon at the same compensation levels identified in the root-locus (0.18 pu and 0.28 pu), whereas the application of a capacitive reactance with a intermediary value equals 0.24 pu does not cause instability of the torsional modes.

From the root-locus shown in Figure 7.10, it is identified that employing a capacitive reactance of 0.18 pu causes instability of the torsional mode 4 (32.28 Hz). Figure 7.14 presents the frequency of the shaft masses following the disturbance. From this graphic, one can see that the oscillation amplitude for each mass follows the proportion described in the mode-shape of Figure 7.8e. Therefore, the frequency of the LPB mass presents the highest oscillation amplitude, whereas the frequency of the IP mass presents the smallest activity when this torsional mode is excited.
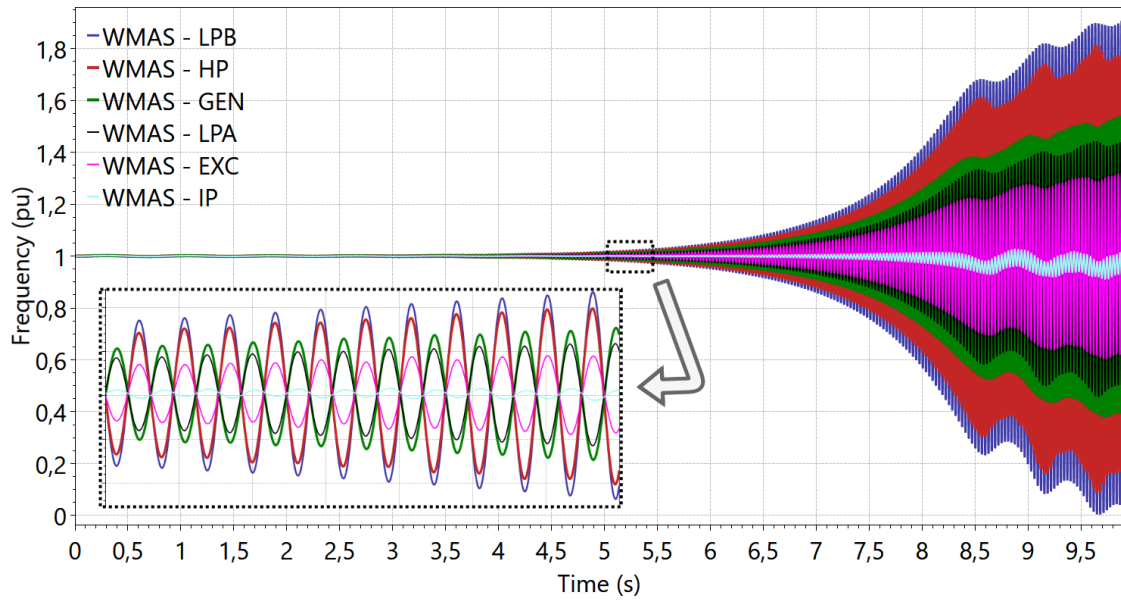
Figure 7.14: Comparison of the frequencies (pu) of the six shaft masses considering $X_{CS} = 0.18$ pu

Similarly, Figure 7.15 presents the frequency of the generator mass following a step change of 0.1 pu in the mechanical torque, considering a different range of series capacitive compensation: 38.5% ($X_{CS} = 0.27$ pu), 50% ($X_{CS} = 0.35$ pu), and 54.3% ($X_{CS} = 0.38$ pu).
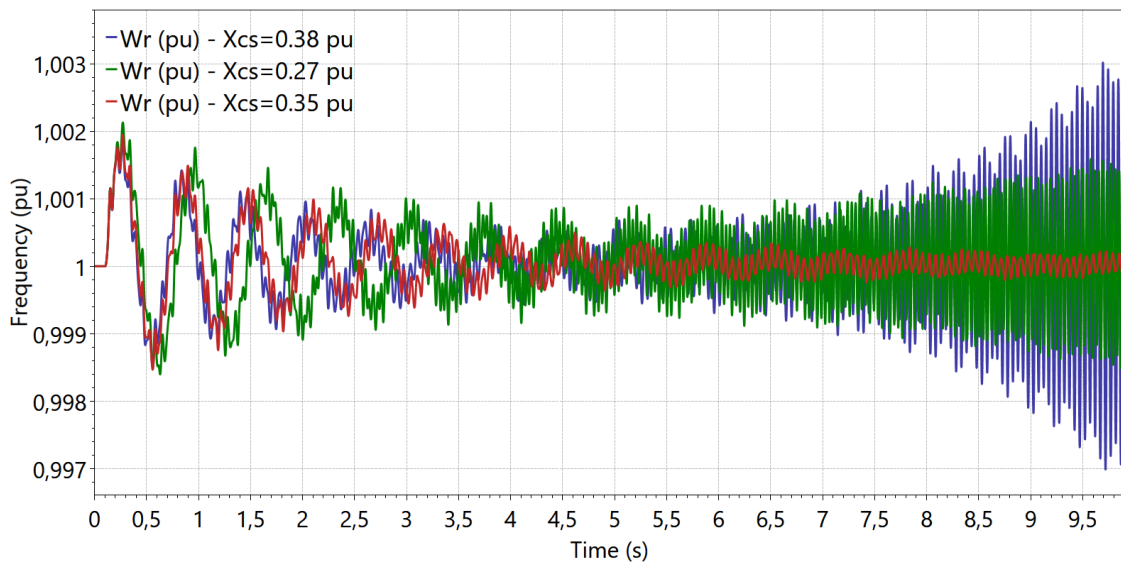

Figure 7.15: Comparison of the generator frequency considering different levels of series compensation: 38.5% (0.27 pu), 50% (0.35 pu), and 54.3% (0.38 pu)

One should note that the series capacitive compensation of 0.27 pu causes an SSR instability in the torsional mode of 25.5 Hz, while a series compensation of 0.38 pu

provokes instability in the torsional frequency of 20 Hz. These simulation results verify the behavior expected from the linear analysis.

Analysis of the FBM System with Controllers

The original IEEE FBM system does not consider any controls associated with the synchronous generator. As discussed in [1], the level of torsional damping can vary with steam conditions and power unit output, but in most cases, it is not affected by the network controls. However, the detailed representation of electrical power system controllers is an important aspect concerning nonlinear time-domain simulations of electromechanical stability. In this picture, Automatic Voltage Regulators (AVR), Speed Governors (GOV), and Power System Stabilizers (PSS) are controllers associated with the synchronous machine, which for certain parameter settings [73], may originate torsional mode instability due to adverse interactions. Therefore, this item presents the inclusion of controls in the IEEE FBM case and shows an example of torsional interaction between the turbine and a PSS associated with the synchronous generator. It should be pointed out that all controllers employed in this example are available in the FBM sample case of the PacDyn software [68].

In Figure 7.4, it has been observed that the voltage profile of the FBM system does not recover following the disturbance in the mechanical torque since the excitation voltage E_{fd} of the generator model has been assumed constant over the simulation. Therefore, a simplified AVR, illustrated in Figure 7.16, is incorporated in the synchronous machine to improve the voltage control by varying the excitation voltage E_{fd}. The inputs V_{ref} and V_t are, respectively, the reference and the measured voltages at the machine terminal, and the input V_{PSS} is a stabilization signal that may be provided by a PSS.
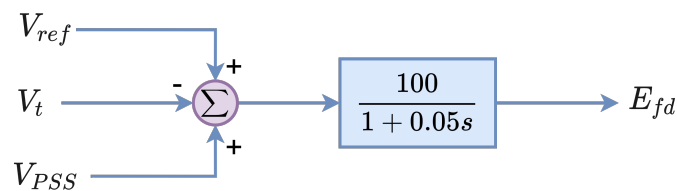

Figure 7.16: Block diagram of the AVR model employed in the FBM system

The inclusion of this rapid response AVR model introduces a negative damping component in the FBM system, as illustrated Figures 7.17 and 7.18. These graphics respectively present the generator frequency and the voltage at the machine terminal following a step of 0.1 pu in the mechanical torque, comparing the original FBM system and the modified case with the AVR insertion.
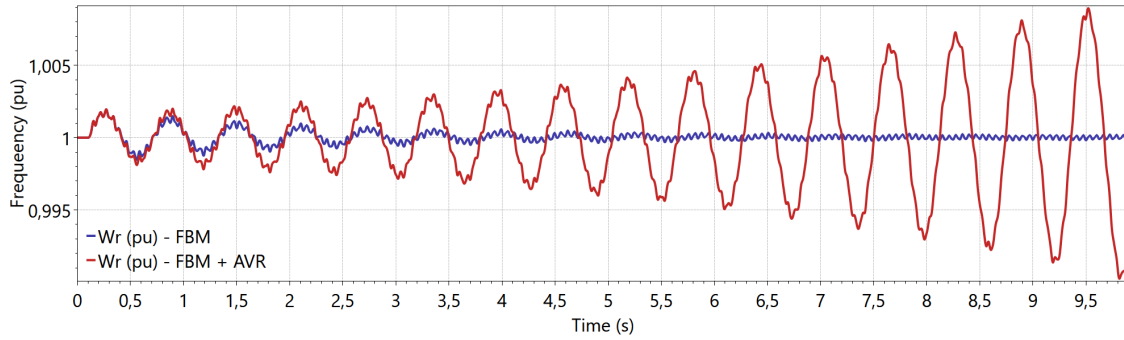
Figure 7.17: Comparison of the frequency (pu) of the generator following a step change of 0.1 pu in the mechanical torque
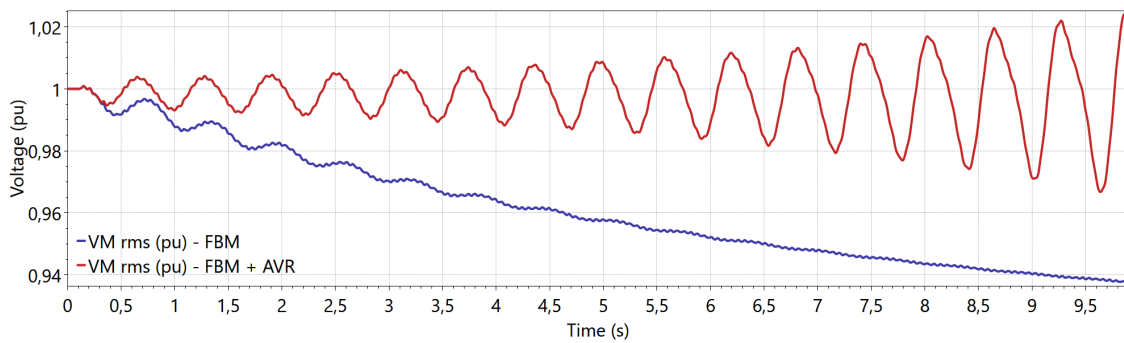

Figure 7.18: Comparison of the terminal voltage (pu) of the synchronous generator following a step change of 0.1 pu in the mechanical torque

It is observed that as the AVR attempts to regulate the terminal voltage of the synchronous machine around a reference value, it causes increasing oscillations in the frequency of the electromechanical mode. Therefore, the PSS model depicted Figure 7.19 is also incorporated into this system in order to increase the damping of the electromechanical oscillation mode.
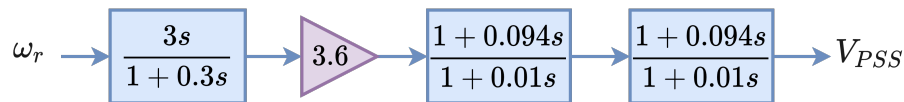
Figure 7.19: Block diagram of the PSS model employed in the FBM system

At this point, it is considered the AVR model of Figure 7.16, and the PSS model shown in Figure 7.19. Thereby, it is simulated a step change of 0.1 pu in the mechanical torque. Figure 7.20 compares the simulation result of the generator frequency, regarding (i) the multi-mass model of the turbine-generator (red curve); and (ii) the rigid shaft representation (blue curve).
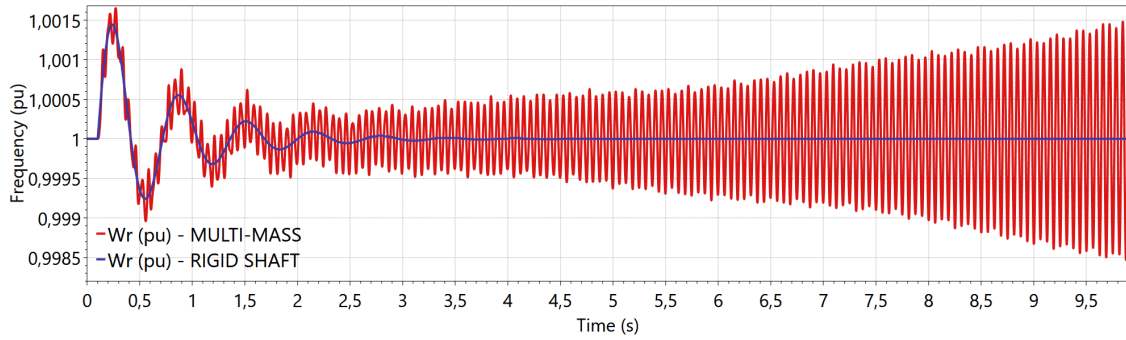
Figure 7.20: Comparison of the generator frequency (pu) - Rigid Shaft x Multi-mass - FBM case with PSS and AVR

One can recognize that the PSS signal increases the damping of the electromechanical oscillation, but at the same time, it causes an adverse interaction with the torsional mode of 15.9 Hz. An approximated calculation could determine this unstable oscillation frequency by considering the period between two successive peaks of the time-domain response obtained with the individualized shaft representation.

Figure 7.21 illustrates the frequency of the multiple masses of the turbine-generator shaft.
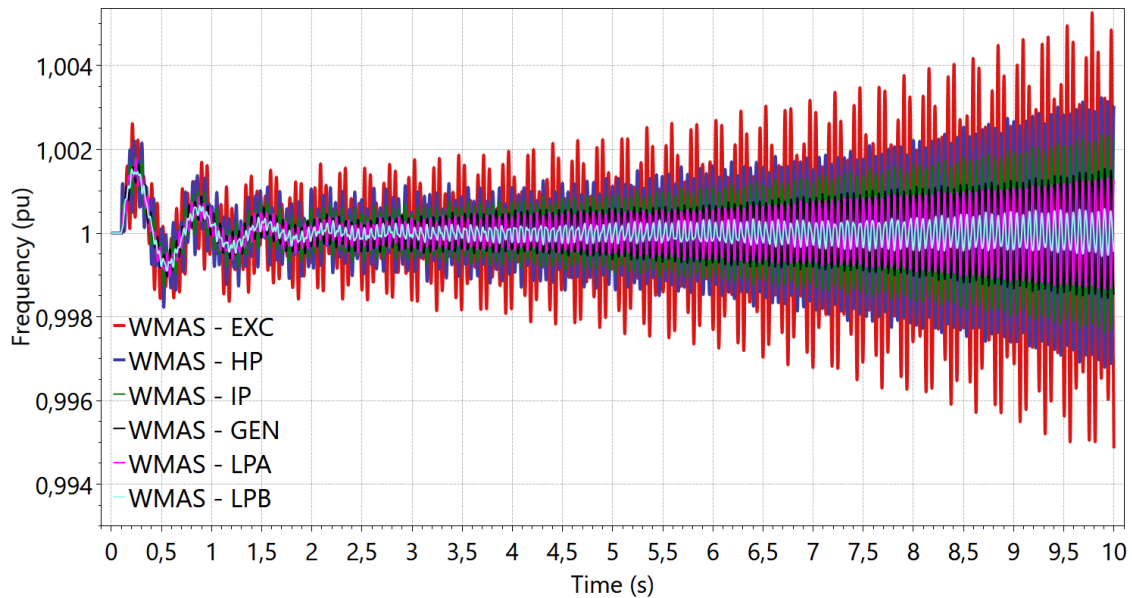
Figure 7.21: Frequency (pu) of the multiple shaft masses - FBM case with PSS and AVR

It is noted that the exciter mass (EXC) performs the greater activity following this disturbance, as expected from the mode shape of the torsional frequency of 15.9 Hz (Figure 7.8b).

232

Table 7.6 presents the eigenvalues of the FBM system with the multi-mass shaft representation, AVR, and PSS. From this result, it is confirmed that the mode frequency of 15.9 Hz presents a negative damping factor, whereas the electromechanical oscillation is well damped. At this point, the real poles of the generator model have been omitted from this table since they are inherently damped and do not vary significantly with the inclusion of machine controllers.

Table 7.6: Engeinvalues of the FBM system with AVR and PSS - $X_{CS} = 0.35$ pu

Description	Eigenvalue	Module	Freq. (Hz)	Damp. (%)
Torsional	$0.09377 \pm j\ 100.42$	100.42	15.982	-0.09338
Torsional	$-0.00747 \pm j\ 127.34$	127.34	20.267	0.00587
Torsional	$-0.03720 \pm j\ 202.77$	202.77	32.272	0.01835
Torsional	$-0.3897 \pm j\ 298.17$	298.18	47.456	0.1307
Torsional	$-0.5329 \pm j\ 160.19$	160.19	25.495	0.3327
Supersynchronous	$-4.6202 \pm j\ 616.62$	616.64	98.139	0.7493
Subsynchronous	$-3.4553 \pm j\ 136.52$	136.56	21.728	2.5301
Electromechanical	$-1.5086 \pm j\ 9.8247$	9.9398	1.5636	15.177
AVR	$-8.0961 \pm j\ 13.384$	15.643	2.1302	51.757
PSS	$-102.02 \pm j\ 10.578$	102.57	1.6836	99.467

Therefore, the PSS of Figure 7.19 is modified in order to minimize the torsional interaction due to the action of the stabilizer. This is achieved by adding the torsional filter depicted in Figure 7.22, which attenuates the input signal of the PSS in the frequency range of the torsional modes [68].
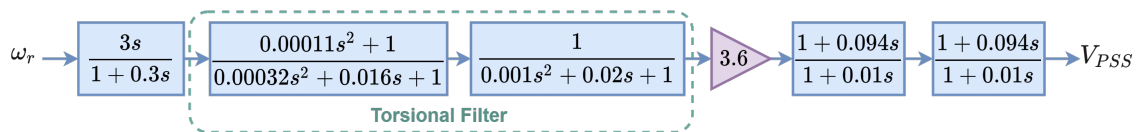

Figure 7.22: Block diagram of the PSS with torsional filter

Considering a step change of 0.1 pu in the mechanical torque, Figure 7.23 presents the comparison of the nonlinear simulation results of the following cases: (i) original FBM system (green curve); (ii) FBM system with AVR and PSS (red curve); and (iii) FBM system with AVR, PSS, and torsional filter.
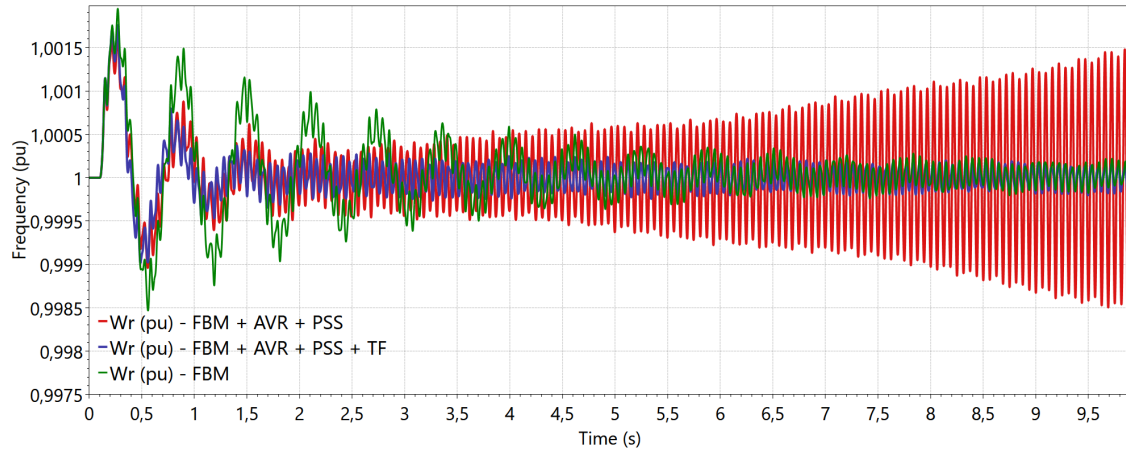
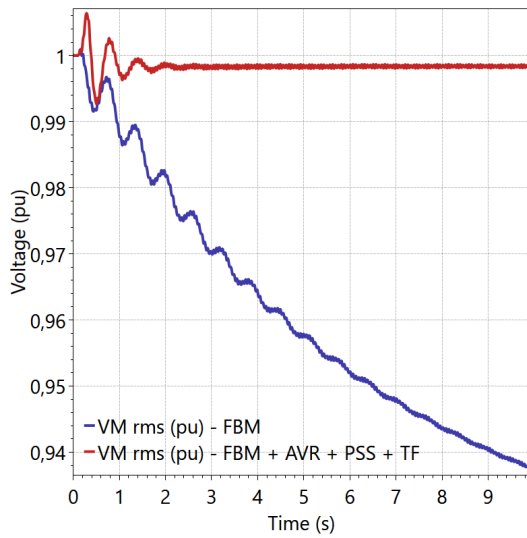Figure 7.23: Comparison of the generator frequency (pu) including a torsional filter in the PSS model

It is noticed that, including a torsional filter, the electromechanical mode is still well-damped, and there is no adverse interaction between the PSS control and the torsional modes. Table 7.7 presents the eigenvalues of the FBM system with AVR, PSS, and torsional filter, confirming that all torsional modes present positive damping factor in this configuration.

Table 7.7: Engeinvalues of the IEEE FBM system with AVR, PSS and torsional filter - $X_{CS} = 0.35$ pu

Description	Eigenvalue	Module	Freq. (Hz)	Damp. (%)
Torsional	$-0.05618 \pm j\ 202.79$	202.79	32.275	0.02770
Torsional	$-0.08634 \pm j\ 127.22$	127.22	20.248	0.06787
Torsional	$-0.1083 \pm j\ 99.782$	99.782	15.881	0.1086
Torsional	$-0.3897 \pm j\ 298.17$	298.18	47.456	0.1307
Torsional	$-0.5417 \pm j\ 160.29$	160.29	25.511	0.3379
Supersynchronous	$-4.6229 \pm j\ 616.62$	616.64	98.138	0.7497
Subsynchronous	$-3.2882 \pm j\ 136.80$	136.84	21.773	2.4030
Electromechanical	$-2.1446 \pm j\ 10.310$	10.530	1.6408	20.366
AVR	$-6.3147 \pm j\ 14.372$	15.698	2.2873	40.227
PSS	$-12.265 \pm j\ 27.717$	30.310	4.4113	40.467
PSS	$-24.636 \pm j\ 49.499$	55.291	7.8781	44.556
PSS	$-100.35 \pm j\ 3.3108$	100.41	0.5269	99.946

Figure 7.24 presents the simulation results following a step change of 0.1 pu in the mechanical torque of the synchronous generator, considering: (i) the original FBM
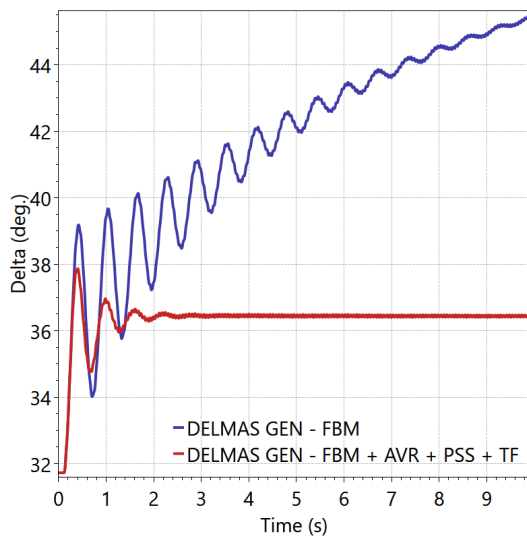
system without controllers (blue curve); and (ii) the FBM system with the inclusion of the AVR, PSS, and torsional filter (red curve).
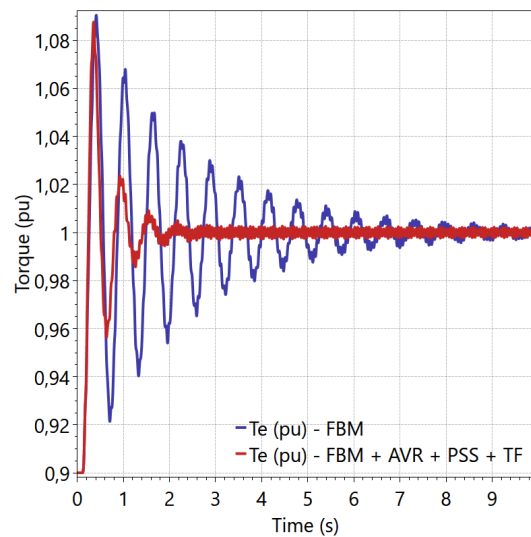

(a) Terminal voltage (pu) of the generator
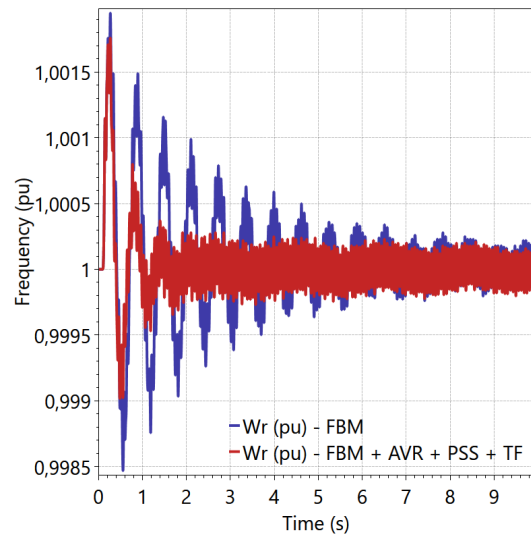
(b) Generator frequency (pu)

(c) Generator rotor position (deg.)

(d) Electromagnetic torque (pu)

Figure 7.24: Comparison of the FBM system dynamic behavior with AVR, PSS, and torsional filter following a step change of 0.1 pu in the mechanical torque

These simulation results show that the inclusion of the AVR, PSS, and torsional filter improves the dynamic performance of the FBM system. The AVR action on the field voltage allows recovering the terminal voltage of the machine after the disturbance, but without a stabilization signal, it introduces a negative damping component in the electromechanical frequency. The inclusion of the PSS with a torsional filter causes the electromechanical oscillations visibly damped and does not present the problem of subsynchronous resonance. Therefore, a comprehensive representation of the machine controllers is essential for an accurate evaluation of

adverse interactions between them and the torsional modes of the turbine-generator shaft.

Dynamic Performance Following a Short-Circuit

In this item, it is simulated a balanced three-phase short-circuit fault through a resistance of 0.1 pu at the terminal A (identified in Figure 7.1) with 100 ms duration. The simulation results of the original FBM system (blue curve) and the FBM system with controllers (red curve) are compared considering a series compensation of 0.35 pu. The FBM case with controllers includes the AVR, PSS, and torsional filter.

Figure 7.25 illustrate the RMS voltage at the terminal A following the short-circuit. The simulation results of the terminal voltage of the machine, and the electromagnetic torque are presented in Figures 7.26 and 7.27, respectively.
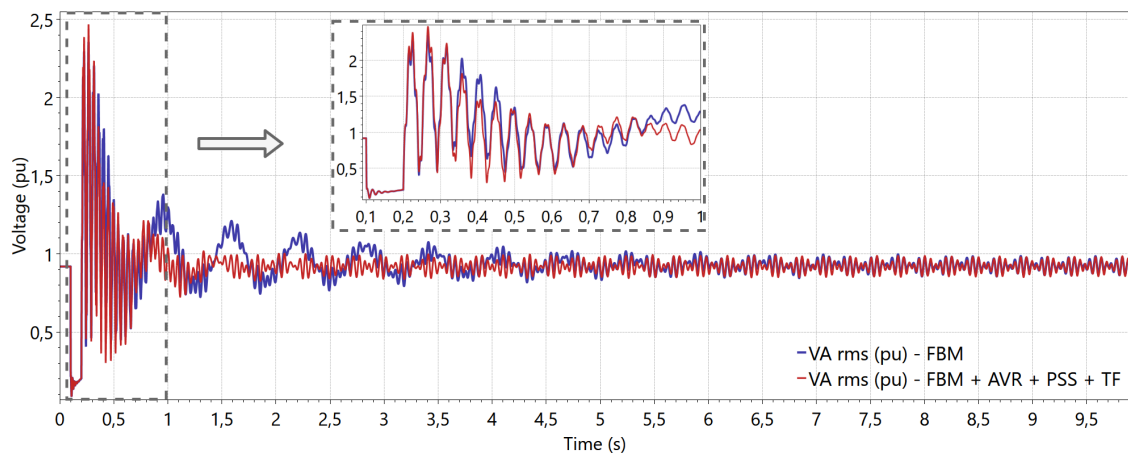

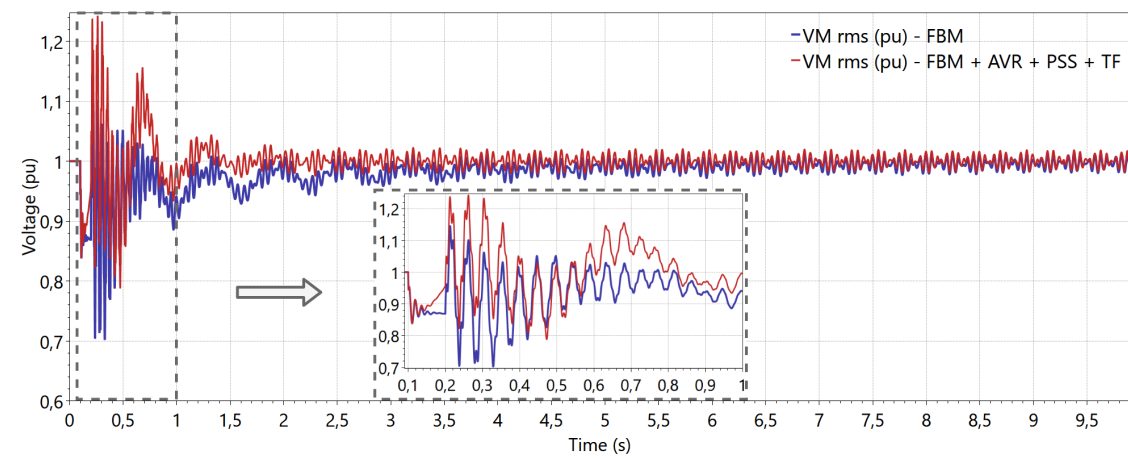Figure 7.25: Voltage at the terminal A following a short-circuit at the terminal A

Figure 7.26: Terminal voltage of the synchronous generator following a short-circuit at the terminal A
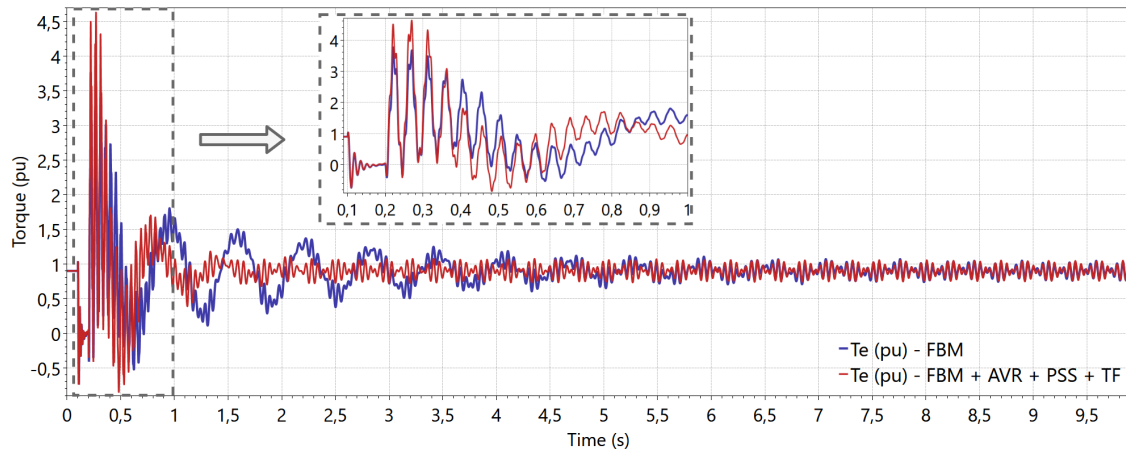
Figure 7.27: Electromagnetic torque (pu) following a short-circuit at the terminal A

In these graphics, it is also provided an amplified picture nearby the fault occurrence to provide a clearer visualization of the electromagnetic transients. It is shown that the representation of the network dynamics, the machine stator flux dynamics, the multi-mass turbine-generator shaft, and the machine controllers into an integrated simulation tool allows studying phenomena of multiple frequency ranges.

Figure 7.28 presents the angular position of the rotor in degrees with respect to a synchronously rotating reference following the short-circuit.
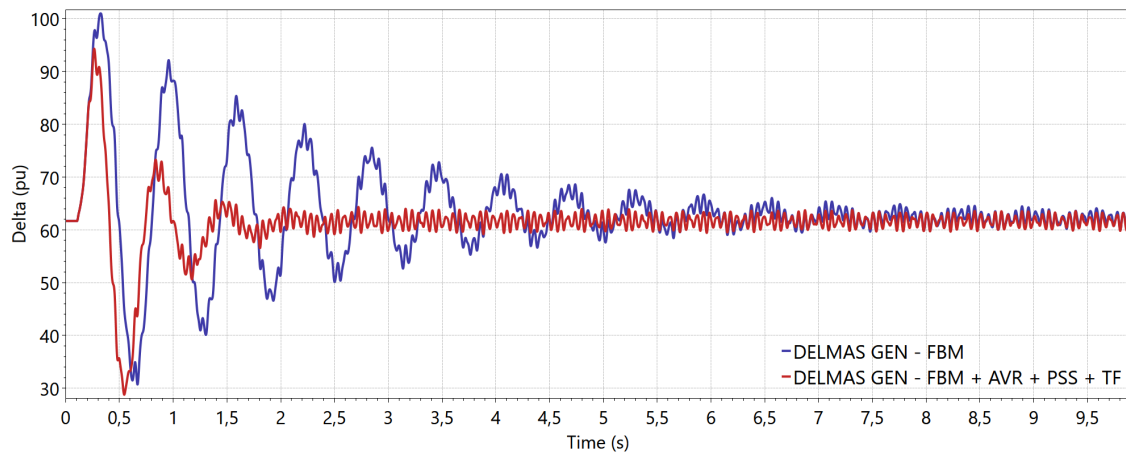

Figure 7.28: Rotor position (degrees) following a short-circuit at terminal A

The torsional oscillations of the turbine shaft are inherently lightly damped [1], which is seen in Figure 7.28. The subsynchronous oscillations present a slow decay, but they are not in crescent tendency following the temporary short-circuit simulated in this item. In addition, the controllers included in this system also improved dynamic performance compared to the original IEEE FBM system response.

7.2 System with a Voltage Source Converter

In this subsection, a test system comprising a Voltage Source Converter (VSC) is used to analyze the influence of the network dynamics representation in the time-domain simulation of electrical networks containing power electronic devices. In this regard, simulation results obtained with the ANATEM software are compared with the PSCAD/EMTDC.

7.2.1 System Description

Figure 7.29 illustrates the single-line diagram of the system to be studied, which is composed by a VSC connected to an infinite bus through a step-up transformer and a transmission line. In this case, the VSC operates as a Static Synchronous Compensator (STATCOM), which regulates the AC voltage at bus 1 by injecting appropriate reactive power. Harmonic filters for the fifth and seventh harmonics are also added at the high-voltage side.
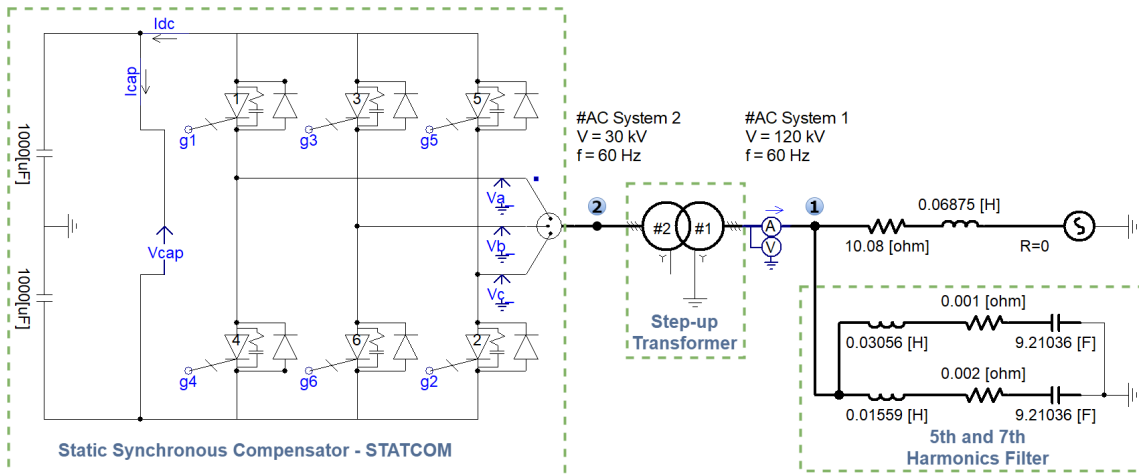

Figure 7.29: Test system with a STATCOM

The STATCOM model employed in the dynamic simulations is a two-level IGBT converter (non PWM type), whose control strategy is validated and described in great level of detail in [74, 75]. At this stage of development, the ANATEM software holds a hybrid ESA and EMT simulation environment within a compatible dynamic phasor interface, i.e., the electrical network modeling considers fast transients via the `DINR` execution option, whereas the STATCOM uses a fundamental frequency model proposed in [74] for ESA analysis. Therefore, concerning the DPTS approach to represent the electrical network dynamics, with the assumption of balanced three-phase system, it is possible to evaluate the impact of the electrical network dynamics in the transient response of other equipment that use electromechanical models.

Table 7.8 contains the parameters of the system utilized in the dynamic simulations.

Table 7.8: Parameters of the system with a STATCOM

Parameter	Description	Value
Step-up transformer	base power	100 MVA
	base voltage on primary side	120 kV RMS L-L
	base voltage on secondary side	30 kV RMS L-L
	reactance X_T	0.05 pu
Infinite bus	magnitude	1.0 pu
	angle	0° (cosine ref.)
	frequency	60 Hz
RL-series branch	series reactance X_L	0.07 pu
	series resistance R_L	0.18 pu
STATCOM	inductive/capacitive range	-100/+100 Mvar
	controlled AC bus	bus 1
	control strategy	two-level IGBT converter

The STATCOM control system employed in the simulations is shown in Figures 7.30 and 7.31. This control strategy regulates the RMS voltage of the AC bus 1 (V_{rms1}) nearby a reference value (V_{ref}) by varying the capacitor DC voltage (V_{cap}), which is controlled by changing the firing angle (ψ) of the IGBTs. This equipment provides the AC system with a highly dynamic and adjustable reactive power support within a given operating range. Besides, it and can inject its maximum rated current capacity at low voltage levels [74].
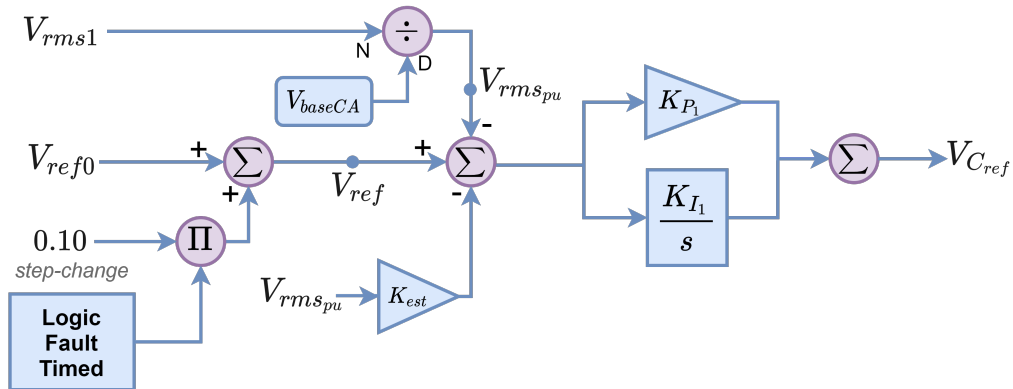

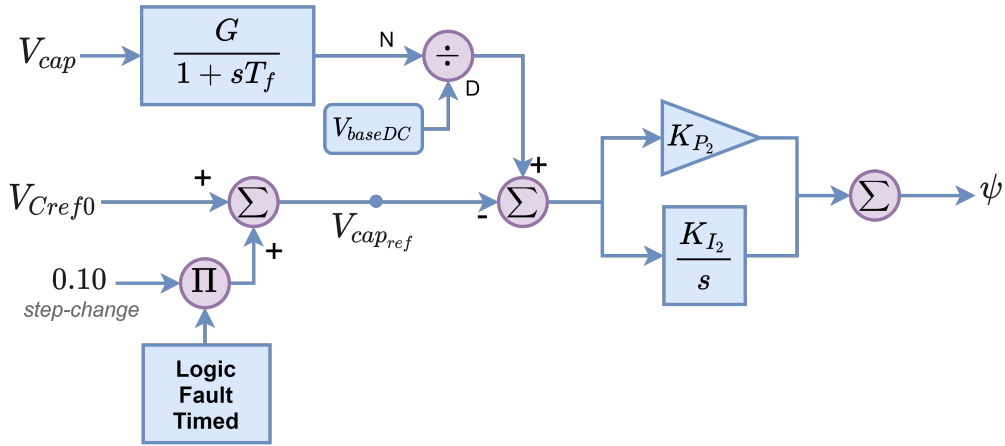Figure 7.30: Control of the AC RMS voltage of bus 1

Figure 7.31: Control of the firing angle of the IGBTs

Reference [75] has demonstrated, through the comparison of simulation results of the PSCAD/EMTDC, ANATEM, and MATLAB software, that representing the network dynamics approximates the nonlinear time-domain response of the STATCOM model. In that work, a fundamental frequency STATCOM model has been implemented in MATLAB, considering the network dynamics. Then, this MATLAB model has been validated against the three-phase STATCOM model represented in the PSCAD/EMTDC. Subsequently, the network dynamics have been neglected in the MATLAB algorithm and, then, the simulation results presented a good agreement with the two-level STATCOM model of the ANATEM. Now, considering the network dynamics developed in this thesis in the ANATEM software through the `DINR` module, these simulation results are confirmed.

The simulations are performed in the ANATEM according to the following procedure:

(i) Specify the positive sequence parameters in the power flow software (ANAREDE) to obtain the initial operation point for dynamic simulation; It is worth mentioning that, as ANAREDE does not have a STATCOM model, it is necessary to represent this equipment by using a SVC model in the network bus and, then, associate it to a STATCOM model in the ANATEM;

(ii) Add the dynamic model of the STATCOM, and specify simulation parameters, disturbances, and output variables in the ANATEM stability file; The dynamic database utilized to simulate this system in the ANATEM is illustrated in Appendix B.4;

(iii) Execute the time-domain simulation from the steady-state operating point considering numeric initialization of the state-variables and history terms.

In the PSCAD, the adjustment of the initial conditions and the dynamic simulations has been carried out in the following steps:

(i) Specify the system data, including the electrical network, infinite bus, and the STATCOM parameters. The PSCAD/EMTDC considers detailed three-phase representation for the STATCOM and electrical network components and computes the time-domain simulation regarding the instantaneous quantities of the electrical network variables.

(ii) Execute the simulation assuming null initial conditions. The analysis of simulation events is performed after the steady-state operating point is reached.

The STATCOM model and its associated control systems are fully integrated with the nodal analysis method for power system simulation. The approach employed in the ANATEM software does not decouple the solution of the electrical network and other dynamic equipment (for instance, synchronous machines, VSC, SVC, HVDC). Instead, they are solved by an alternating and iterative process in each time step integration throughout the time-domain simulation. At each time step, the updated DPCM solution of the electrical network models is utilized for the solution of the STATCOM model and its associated control systems. Likewise, the electrical network is iteratively updated considering the STATCOM solution until the interface errors between these two loops reach the convergence. This solution strategy is robust and the simulation results do not accumulate interface errors, as long as this method updates all of the network variables and dynamic equipment models at each time step.

7.2.2   Simulation Results and Analysis

Steady-State Initialization

Figure 7.32 compares the initialization of the test system of Figure 7.29 in the ANATEM and PSCAD/EMTDC, using 20 μs as the integration time step size. Figure 7.32a shows the RMS voltage in pu of bus 1, and Figure 7.32b illustrates the capacitor DC voltage. In this simulation, no disturbance is applied since the purpose here is to validate the ANATEM steady-state initialization.
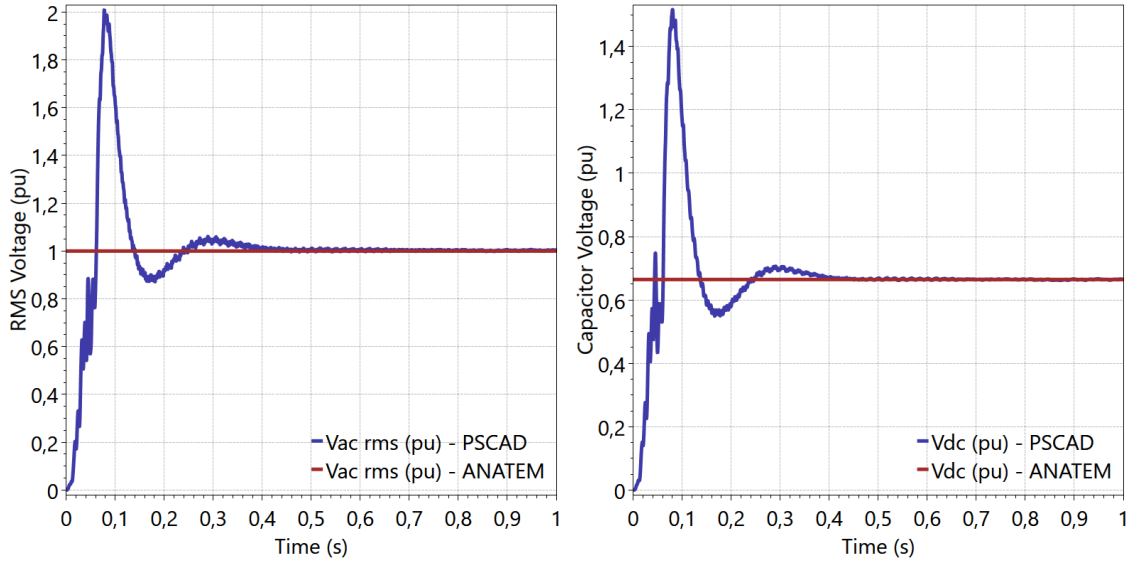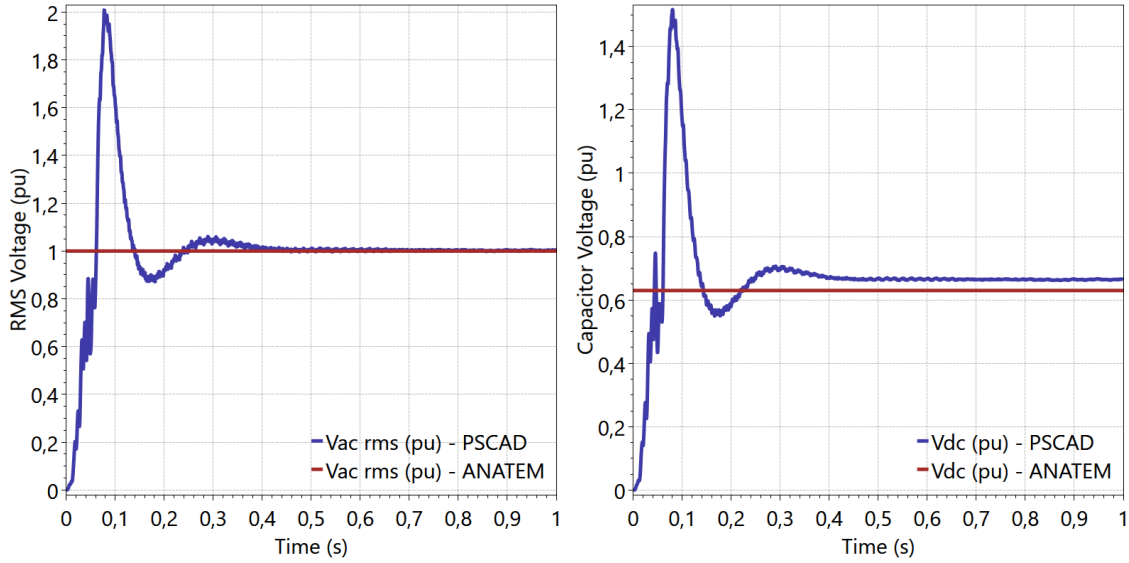
(a) RMS voltage (pu) of bus 1   (b) Capacitor voltage (pu)

Figure 7.32: Initialization considering the step-up transformer reactance equal to 0.05 pu

The simulations results show that both the AC RMS voltage of bus 1 and the capacitor DC voltage present steady-state values in good agreement in the two programs. One should note that the initialization with null initial conditions in the PSCAD/EMTDC demands a certain simulation time until the steady-state regime is reached, whereas the ANATEM initializes at time $t = 0s$ from the operating point calculated by the ANAREDE software. The results of the PSCAD/EMTDC present some noise in the voltage waveforms resulting from the harmonic components, which can be observed in the network due to its detailed three-phase representation. On the other hand, the positive sequence and the fundamental dynamic phasor model employed in the ANATEM for the electrical network neglect these harmonic components, which yields simulation results with a smoother dynamic behavior.

It is worth mentioning that the STATCOM model of the ANATEM includes the representation of the VSC step-up transformer, i.e., the transformer is not modeled as an external electrical network component. Therefore, the dynamics of the transformer leakage inductance is not considered via the `DINR` option, as the VSC equipment still uses the ESA representation. This peculiarity reveals some differences between the results of the ANATEM and PSCAD when using higher values for the step-up transformer reactance. In this regard, Figure 7.33 demonstrates the effect, in the ANATEM initialization, of increasing the transformer reactance from 0.05 pu to 0.10 pu.

(a) RMS voltage (pu) of bus 1

(b) Capacitor voltage (pu)

Figure 7.33: Initialization considering the step-up transformer reactance equal to 0.1 pu

Figure 7.33a shown that the initialization of the AC RMS voltage is identical to the previous case, as it presents the value determined in the power flow solution so that it is not affected by increasing the reactance of the step-up transformer. The transformer reactance affects only the initialization of the variables associated with the STATCOM model since it is treated as an internal parameter of this equipment. The difference in the initialization is illustrated in Figure 7.33b, evidencing that higher values of the transformer reactance provokes a more significant difference in the initialization of the two programs because the STATCOM model employed in the ANATEM still neglects the dynamics of the transformer inductance.

Step Change in the RMS Reference Voltage

In this item, the dynamic performance of the STATCOM model of the PSCAD/EMTDC is compared with the following two approaches of the ANATEM software: (i) considering the electrical network dynamics through the `DINR` execution option; and (ii) neglecting the network dynamics by using the traditional ESA modeling.

For that purpose, it is simulated a 10% step-change in the RMS reference voltage of the STATCOM control system, both positive and negative variations are evaluated. The time step size employed in this simulation is $\Delta t = 20 \mu s$, and the simulation event is applied at the instant $t = 5.1s$ to assure that the PSCAD/EMTDC has reached the steady-state operating point. Figures 7.34a and 7.34b, respectively,

show the simulations results of the AC RMS voltage at bus 1 and the capacitor DC voltage, following a positive 10% step change in the RMS reference voltage.

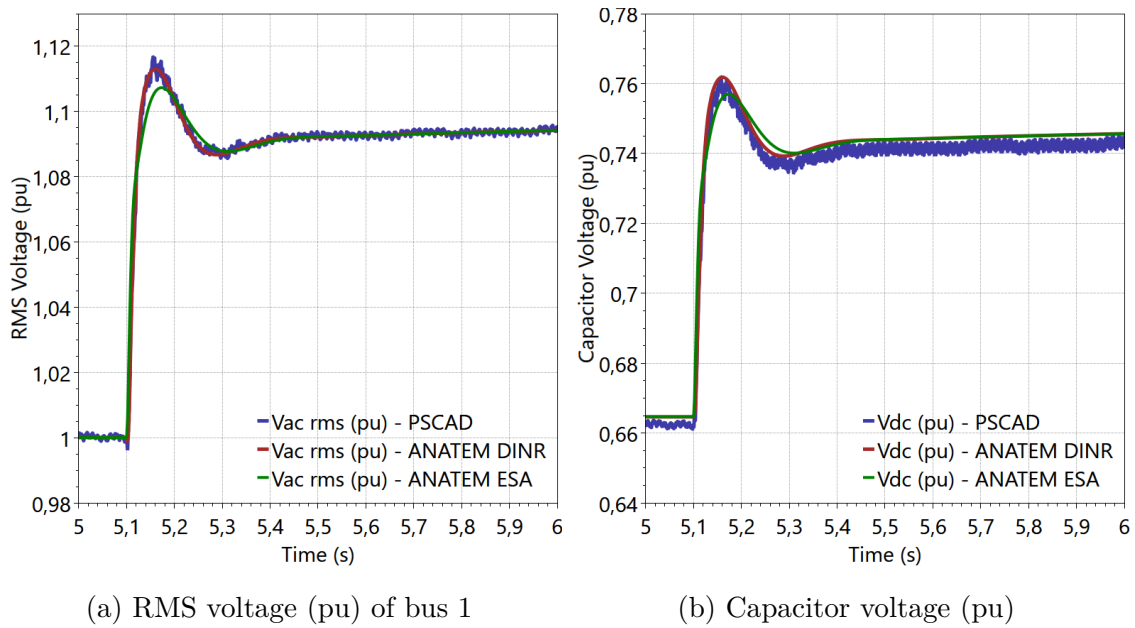(a) RMS voltage (pu) of bus 1

(b) Capacitor voltage (pu)

Figure 7.34: Dynamic performance following a positive 10% step change in the reference voltage

Likewise, Figures 7.35a and 7.35b respectively show the simulations results of the AC RMS voltage at bus 1 and the capacitor DC voltage, following a negative 10% step change in the reference voltage.

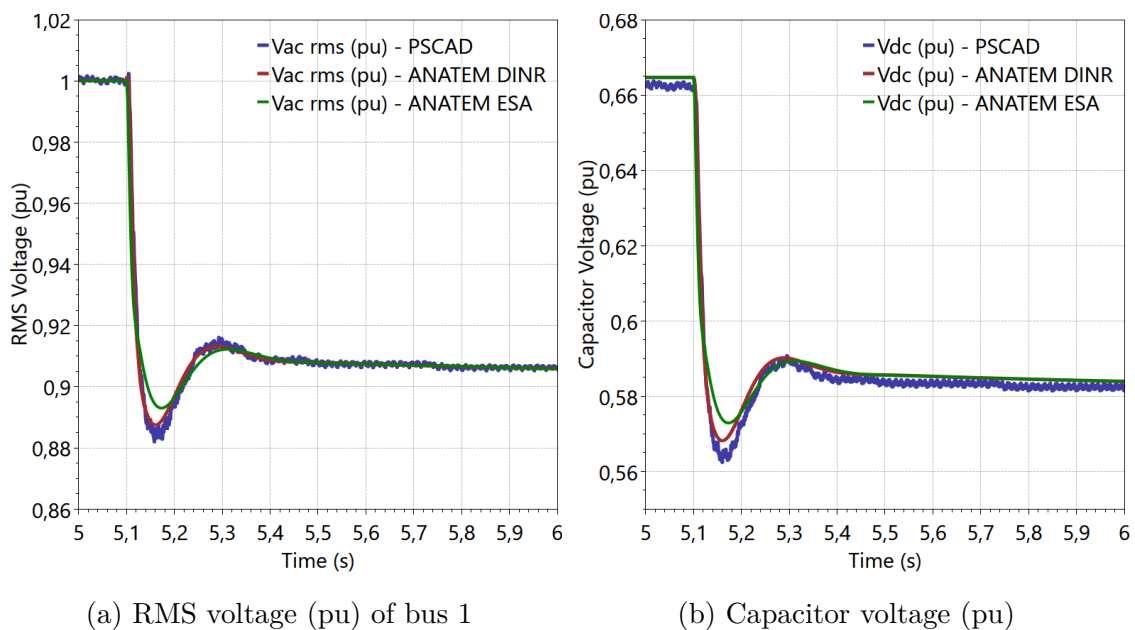(a) RMS voltage (pu) of bus 1

(b) Capacitor voltage (pu)

Figure 7.35: Dynamic performance following a negative 10% step change in the reference voltage

Figures 7.34 and 7.35 demonstrate that development of the DPCM models in this thesis to represent the electrical network dynamics in the ANATEM improved the simulation results of the STATCOM model, as it approximates to the PSCAD/EMTDC dynamic response.

Dynamic Performance Following a Voltage Dip

In order to evaluate the STATCOM dynamic response and the influence of the electrical network dynamics following a voltage dip, a temporary reduction of the AC voltage is simulated by reducing the reference voltage to 0.5 pu during 200 ms from $t = 5.1s$ to $t = 5.3s$. Figures 7.36a and 7.36b, respectively, illustrate the AC RMS voltage at bus 1 and the capacitor DC voltage following the voltage dip.

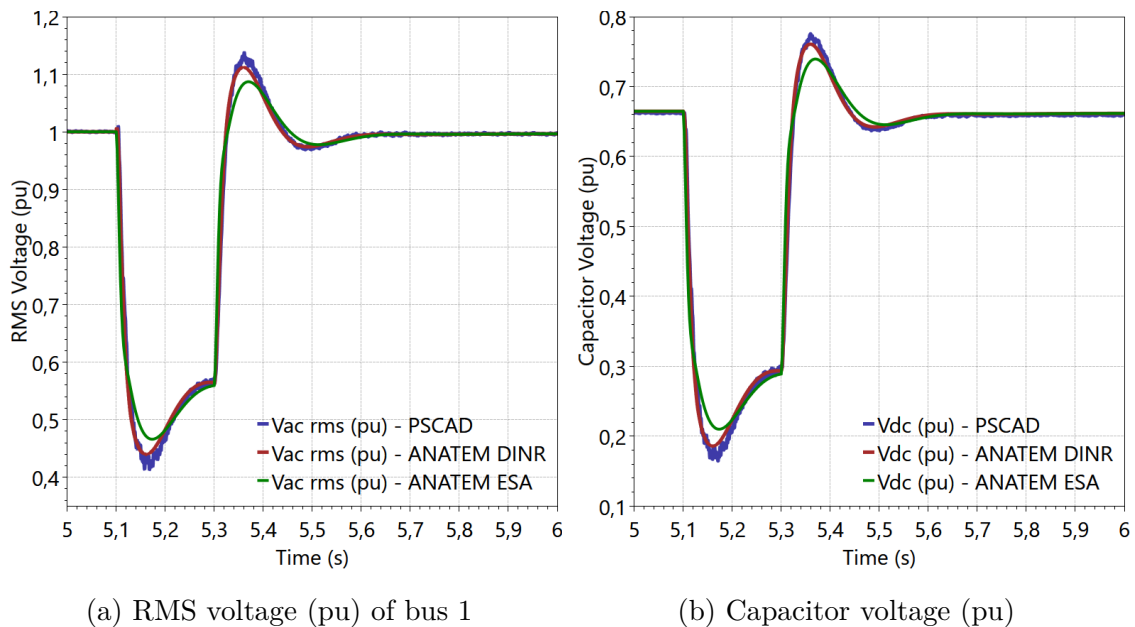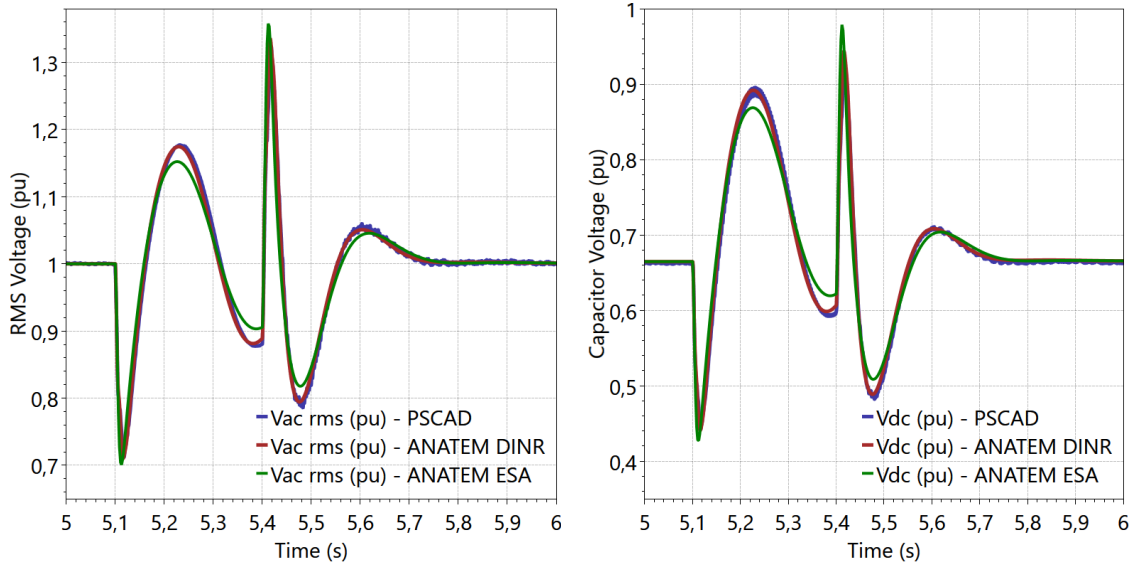(a) RMS voltage (pu) of bus 1   (b) Capacitor voltage (pu)

Figure 7.36: Comparison of the AC RMS voltage of bus 1 and capacitor DC voltage following a temporary step change in the reference voltage

From Figure 7.36, it is observed that the ANATEM results are in consonance with the PSCAD/EMTDC when the electrical network dynamic is considered via the DPCM.

Dynamic Performance Following a Short-Circuit

In this item, it is simulated a balanced three-phase short-circuit fault through a resistance of 72Ω at the bus 1 with 300 ms duration. Figures 7.37a and 7.37b, respectively, illustrate the AC RMS voltage at bus 1 and the capacitor DC voltage following the short-circuit.

(a) RMS voltage (pu) of bus 1   (b) Capacitor voltage (pu)

Figure 7.37: Comparison of the AC RMS voltage of bus 1 and capacitor DC voltage following a balanced resistive three-phase short-circuit

This case study demonstrates that the representation of the network dynamics approximates the dynamic response of the STATCOM to the PSCAD/EMTDC results. Similarly, other dynamic equipment, yet using the ESA model, will also have a closer response to that obtained in the EMT approach when the electrical network dynamic is represented. This hybrid simulation environment can extend to the electrical network by using the `DRDN` execution code to limit a boundary region to be represented by the DPCM, and that research can be the subject of future work.

7.3 Brazilian Interconnected Power System

This section presents the simulation results of a large-scale power system adapted from the Brazilian Interconnected Power System (BIPS). In this study, the network dynamics and the synchronous machine models for SSR analysis are applied in a modified power system, which is conceived from the Expansion and Reinforcement Planning (PAR, in Portuguese) referring to the 2023 horizon [76]. The original case study and the ESA Dynamic Database, utilized in this analysis, are provided by the *Operador Nacional do Sistema* (ONS, the Brazilian Independent System Operator) [77]. Figure 7.38 illustrates the BIPS transmission system, outlining the North-Northeast Interconnection, which is the interest area for the present SSR analysis.
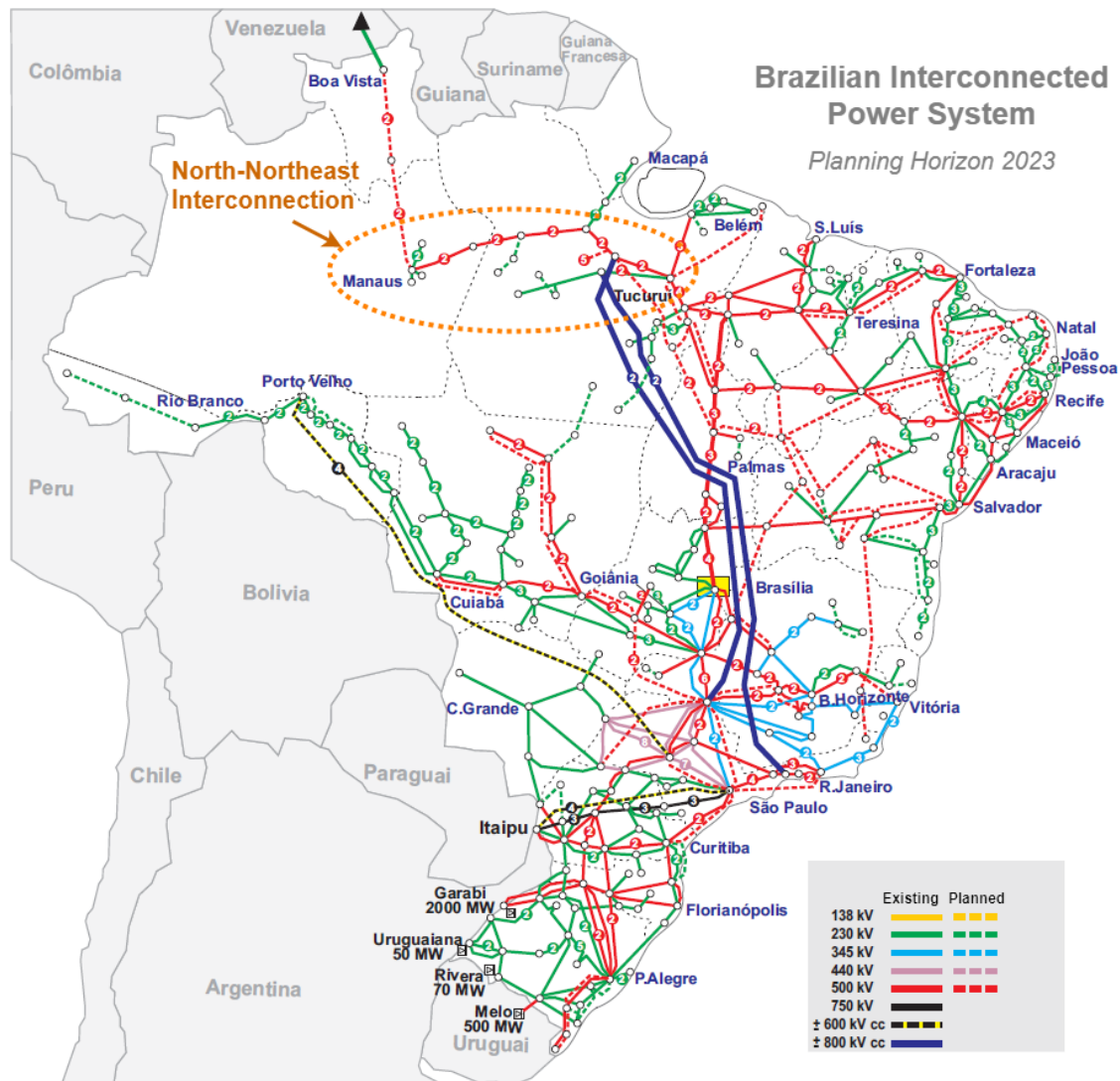

Figure 7.38: Brazilian Interconnected Power System - PAR 2023 (Source: ONS)

The objective of this case study is to perform a nonlinear subsynchronous resonance analysis regarding the detailed representation of multiple synchronous machines and

their associated controllers in a large-scale power system.

7.3.1 Electrical Power System Modeling

The power system scenario to be studied is adapted from the PAR 2023 operating scenario for the summer medium-load forecast, elaborated by the ONS. This case study is broadly employed for the steady-state and the ESA analysis through the ANAREDE and ANATEM software. Table 7.9 describes the power system dimension, including most of the network buses, circuits, transformers, generation buses, and power plants contained in the original PAR 2023 scenario.

Table 7.9: Dimension of the large-scale power system

Equipment	Dimension
AC Bus	6972
Transmission Lines	6244
Generation Bus	1247
Transformers	3844
Shunt Reactors	1230
Synchronous Power Plants	279
User Defined Controllers	1102

The electrical network dynamics and the synchronous machine models suitable for SSR analysis are evaluated assuming the following premises in the dynamic simulations:

- Two distinct configurations for the long transmission lines are studied: (i) with lumped parameters through a single equivalent-π circuit; and (ii) through the Bergeron model;

- Loads are modeled by a parallel association of resistors, capacitors and inductors by using the DPCM models. Similarly, shunt reactors and capacitors are represented through their respective inductance and capacitance equivalent DPCM models;

- Hydro and thermal units of synchronous generators are represented with detailed synchronous machine models, including the stator flux dynamics (the transformer effect) and the rotor speed variation;

- Control systems of the synchronous machines are represented, in the ANATEM, through a detailed User Defined Controls (UDC) structure, pro-

vided by the ONS in the Electromechanical Stability Database of March 2019 [77]. Therefore, the detailed models of AVR, GOV, and PSS are associated with the synchronous generators.

- The dynamic representation of wind and photovoltaic sources are simplified, at this stage, since the present UDC models corresponding to these sources do not provide an adequate interface with the network dynamics. Therefore, wind and photovoltaic generators have been modeled as synchronous machines with an inertia constant equal to 1 second. On this matter, the adequacy of a hybrid ESA representation for these sources by using DP, coupled with the network dynamics, may also be the subject of a future work.

7.3.2 Description of the Study Area

In this section, the network dynamics and a hypothetical subsynchronous resonance study are evaluated in the North region of the BIPS by varying the series capacitive compensation of the North-Northeast Interconnection. This area comprises numerous Thermal Power Stations connected to the BIPS through a long compensated transmission system, forming an interesting arrangement for SSR analysis. Figure 7.39 illustrates the single-line diagram of the North-Northeast Interconnection, between the substations Tucurui 500 kV and Manaus 230 kV.
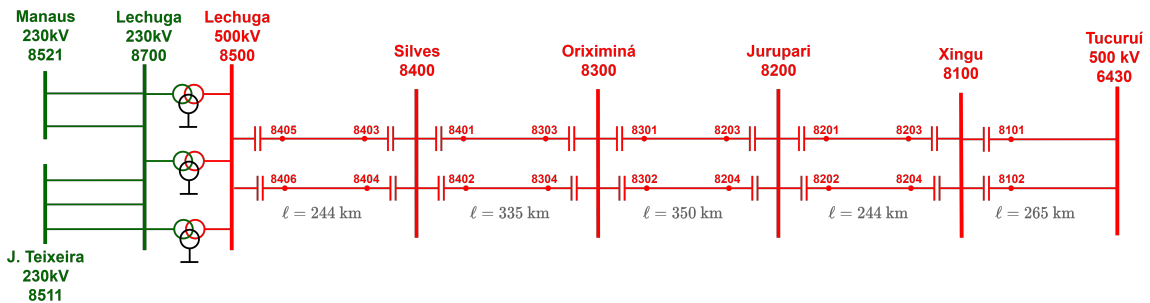

Figure 7.39: Tucuruí 500 kV - Manaus 230 kV Interconnection

The parameters of the 500 kV transmission lines, illustrated in Figure 7.39, are detailed in Table 7.10. The line parameters are specified in per unit values at the system nominal frequency, considering the base power of 100 MVA, and the base voltage of 500 kV.

Table 7.10: Parameters of the transmission lines from Lechuga 500 kV to Tucuruí 500 kV

Transmission Line	R_L (pu)	X_L (pu)	B_{sh} (Mvar)
Lechuga 500 kV - Silves 500 kV	0.001673	0.023478	354.09
Silves 500 kV - Oriximiná 500 kV	0.002415	0.034509	534.21
Oriximiná 500 kV - Jurupari 500 kV	0.002484	0.036388	555.85
Jurupari 500 kV - Xingu 500 kV	0.001793	0.025821	384.04
Xingu 500 kV - Tucuruí 500 kV	0.001935	0.027960	417.73

Table 7.11 describes the series capacitive reactance X_{CS} and the associated compensation percentage of the 500 kV transmission lines in relation to their respective series inductive reactance X_L. It is observed that this interconnection accounts for approximately 70% of the series compensation for each transmission line. In particular, between the AC buses Lechuga 500 kV and Xingu 500 kV, the compensation takes place in each line-end, i.e., each terminal includes a series capacitor whose reactance compensates around 35% of the line inductive reactance.

Table 7.11: Series compensation of the 500 kV transmission lines - $X_{CS} \approx 70\%$

Transmission Line	X_{CS} (pu)	(X_{CS}/X_L) (%)
Lechuga 500 kV - Silves 500 kV	-0.01643	70.0 %
Silves 500 kV - Oriximiná 500 kV	-0.02416	70.0 %
Oriximiná 500 kV - Jurupari 500 kV	-0.02606	71.6 %
Jurupari 500 kV - Xingu 500 kV	-0.01848	71.6 %
Xingu 500 kV - Tucuruí 500 kV	-0.01957	70.0 %

Figure 7.40 presents a fragment of the single-line diagram of the Northern transmission system, illustrating the connection of multiple Thermal Power Stations (TPS), and a Hydro Power Station (HPS), in this region. The active and reactive powers supplied by the power plants are also depicted in Figure 7.40, concerning the operating point to be evaluated in the following items.
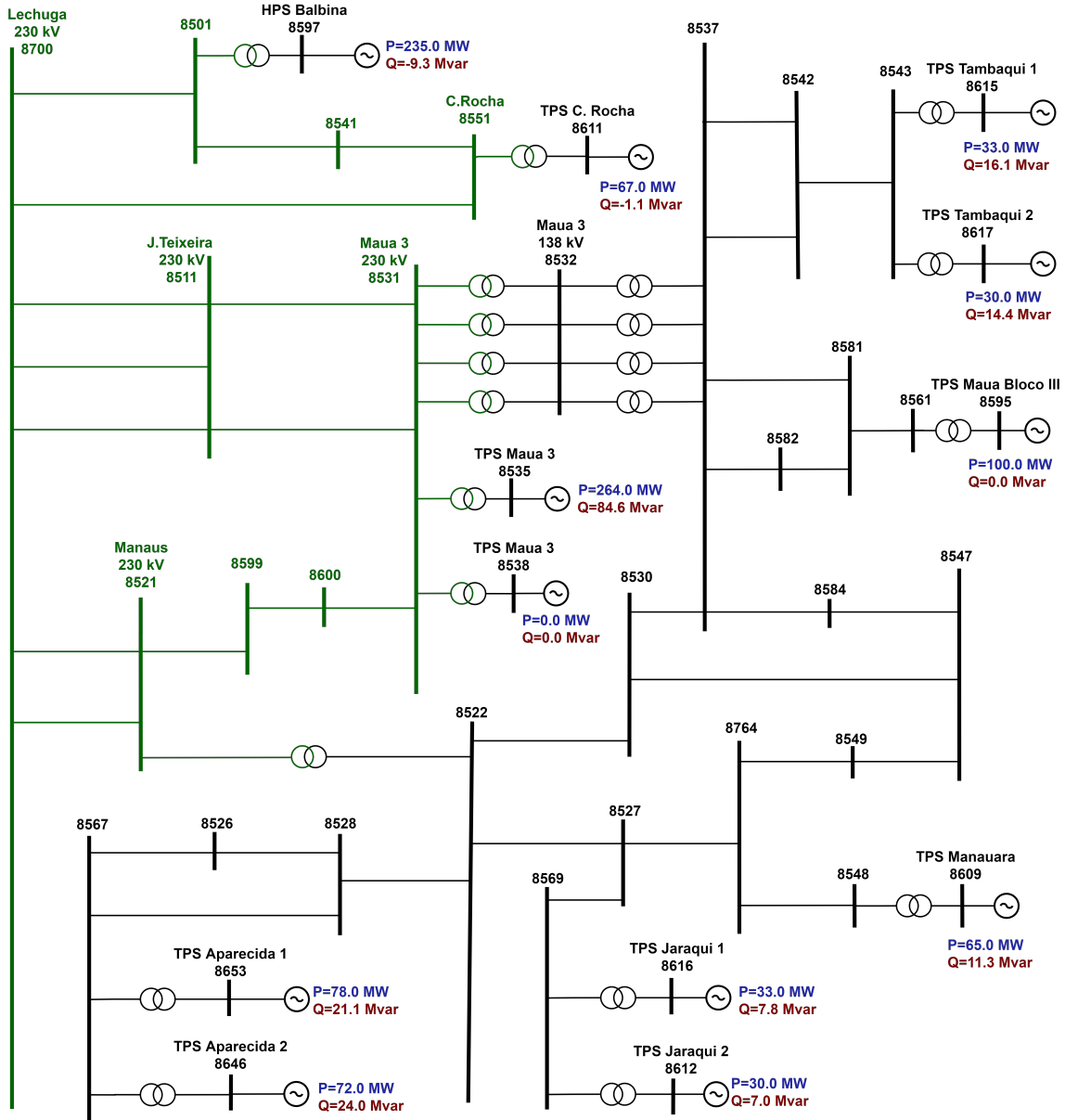

Figure 7.40: Connection of power stations in the Northern transmission system

7.3.3 Simulation Results and Analysis

In the following sections, the DPCM models for the electrical network (Chapter 3), the dynamic phasor-based synchronous machine (Chapter 4), and the individualized turbine-generator shaft (Chapter 5), developed in the ANATEM software, are incorporated in the BIPS case study. It is important to emphasize that the dynamic simulations performed here do not consider network equivalents, but rather the entire 6972-bus power system based on the premises detailed in Section 7.3.1.

Analysis of Electromagnetic Transients

This item presents the comparison of the ANATEM simulation results considering: (i) electromagnetic transients, referred to as EMT (blue curves); (ii) traditional electromechanical analysis, referred to as ESA (red curves). At this point, long transmission lines are represented through the equivalent-π model with DPCM as lumped parameters. The dynamic simulations from the EMT analysis are performed with time step size $\Delta t = 10 \ \mu s$, whereas the electromechanical simulations are carried out with $\Delta t = 1.0 \ ms$. Both the EMT and the ESA dynamic simulations initialize from the steady-state operating point provided by the ANAREDE software.

It is simulated a balanced three-phase short-circuit fault through a resistance of 0.01 pu at the AC bus 8500 (Lechuga 500 kV). The fault is applied at the instant $t = 0.02s$, and it is cleared after $100 \ ms$. Figure 7.41 presents the RMS voltage (pu) at the AC bus Lechuga 500 kV and Tucuruí 500 kV, following this disturbance.
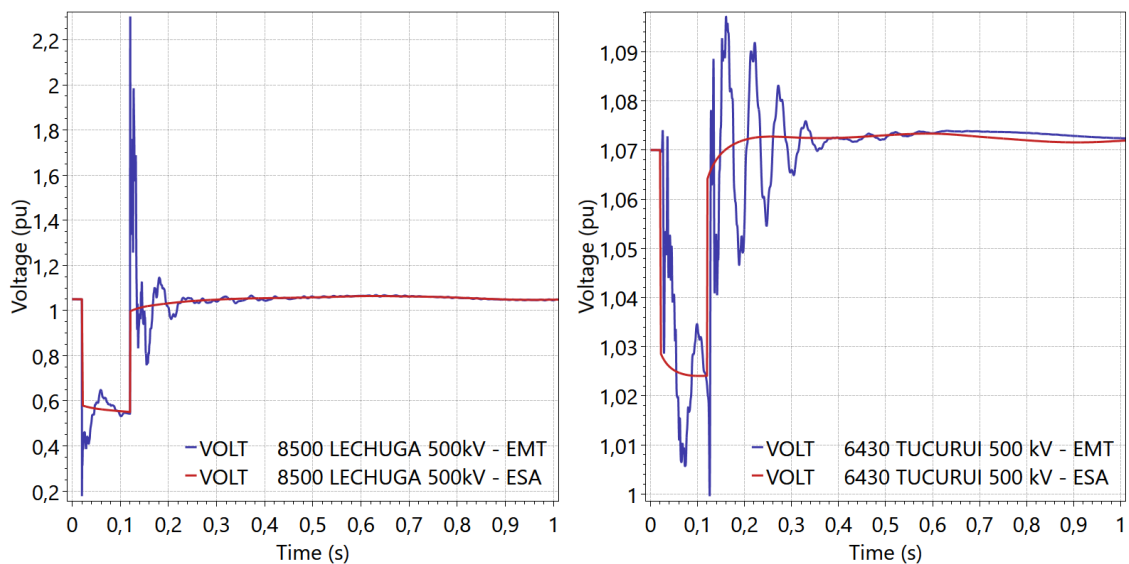
(a) Voltage (pu) at Lechuga 500 kV

(b) Voltage (pu) at Tucurui 500 kV

Figure 7.41: EMT x ESA: RMS voltage (pu) at the 500 kV buses following a short-circuit at Lechuga 500 kV

One should note that the peak voltage at Lechuga 500 kV occurs after the fault clearance; this dynamic behavior is not captured by the static representation of the electric network. Therefore, the representation of the network dynamics provides valuable information concerning transient overvoltages that the network equipment may experience following sudden events.

Figure 7.41 presents the RMS voltage (pu) at the TPS Mauá 3 and at the HPS Balbina, following the short-circuit at Lechuga 500 kV.

(a) Voltage (pu) at the TPS Mauá 3
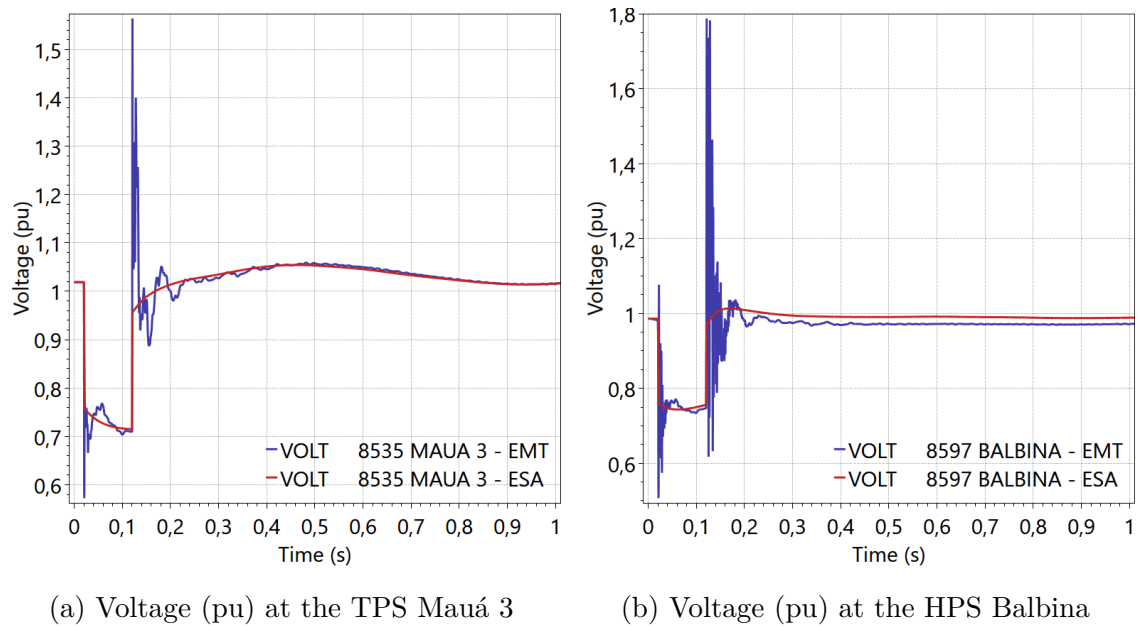
(b) Voltage (pu) at the HPS Balbina

Figure 7.42: EMT x ESA: RMS voltage (pu) at the power stations following a short-circuit at Lechuga 500 kV

Comparing the EMT and the ESA analysis, it is noted that the voltage level at the HPS Balbina presents a visible difference at $t = 1s$. The representation of the network dynamics has led the AVR of the HPS Balbina to reach a different setpoint for the terminal voltage of this synchronous machine after the fault clearance. In both simulations, the TPS Mauá 3 and the HPS Balbina, as well as the other generation stations, include detailed AVR and GOV in the dynamic simulation. The representation of fast transients of the network may interact with rapid response controls (static exciter systems), which impact the long-term dynamics of the synchronous machines. In addition, fast transients influence the action of quick protection systems that may also be included in the analysis.

Let one compare the dynamic behavior of the internal variable of the synchronous machine model, in order to observe the influence of the stator transients and the variation of the rotor speed against the traditional ESA modeling. Figure 7.43 presents the direct and quadrature stator currents, the subtransient voltage of quadrature

253

axis, and the field voltage of each generation unit at the TPS Mauá 3, following the
short-circuit at Lechuga 500 kV. It is noteworthy that, in this case study, there are
two generation units in operation at the TPS Mauá 3, each one with an apparent
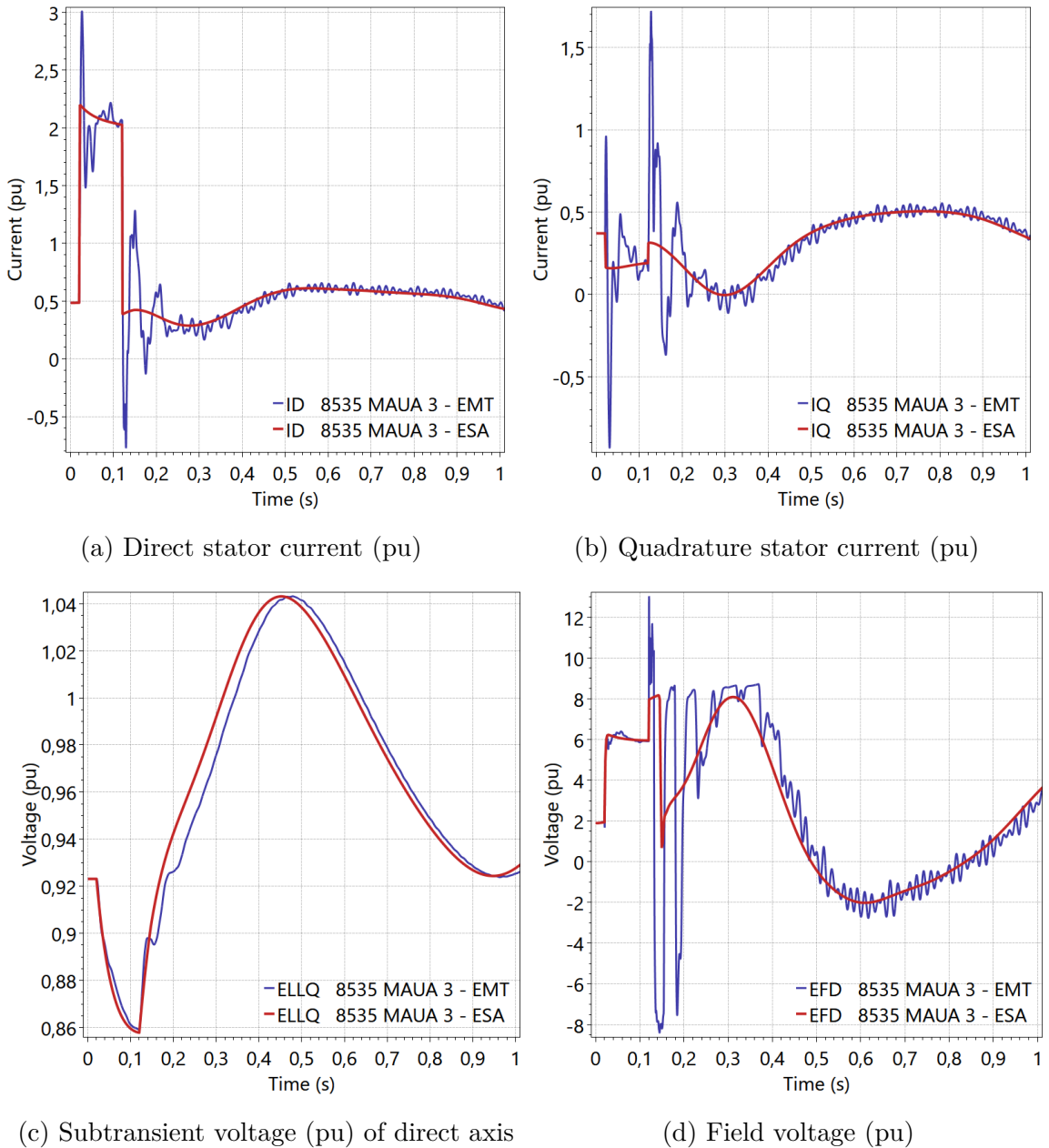power capacity of 223 MVA.

(a) Direct stator current (pu)

(b) Quadrature stator current (pu)

(c) Subtransient voltage (pu) of direct axis

(d) Field voltage (pu)

Figure 7.43: Internal variables of the cylindrical rotor synchronous generator units
at the TPS Mauá 3, following a short-circuit at Lechuga 500 kV

In Figure 7.43, the synchronous machine quantities are given in per unit concerning
the L_{ad}-*reciprocal per unit system* that has been approached in Chapter 4. One
should note that the detailed synchronous machine model reveals fast transients in
its internal variables, which are not captured with the traditional ESA modeling.

However, in both representations, the slow transients of the synchronous machine exhibit a coherent dynamic response.

Figure 7.44 illustrates the voltage profile at multiple AC buses in order to show that the new EMT module of the ANATEM software supports the analysis of electromagnetic transients of the electrical network in a large-scale power system with a detailed representation of synchronous machines and their associated controllers.
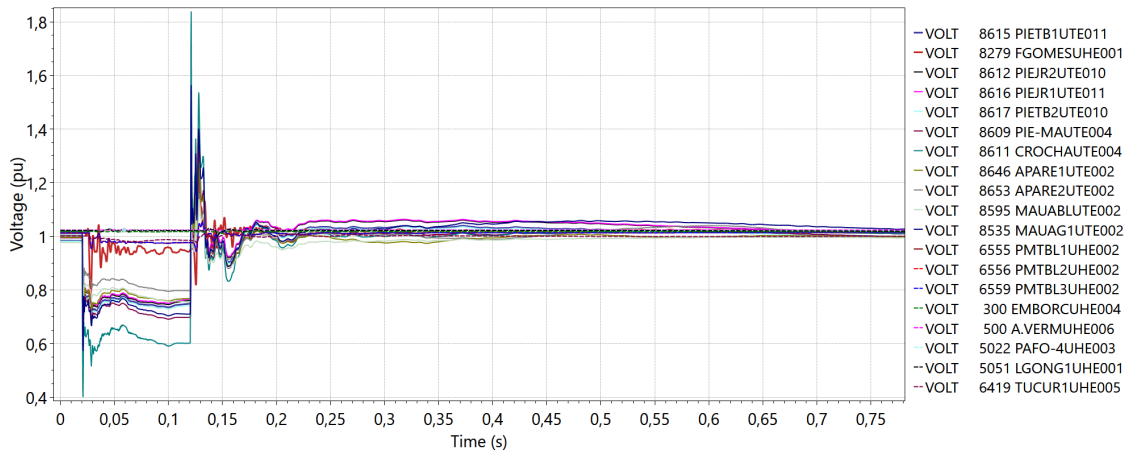

Figure 7.44: Voltage profile at multiple AC buses following a short-circuit at the AC bus Lechuga 500 kV

Figures 7.41 and 7.42 presented a simulation window of 1 second to provide a clearer view of the fast transients after the fault. Now, Figure 7.45 presents a wider view of the voltages at Lechuga 500 kV and at the TPS Mauá 3 to show that these variables reach a new steady-state operating point following the fault clearance.
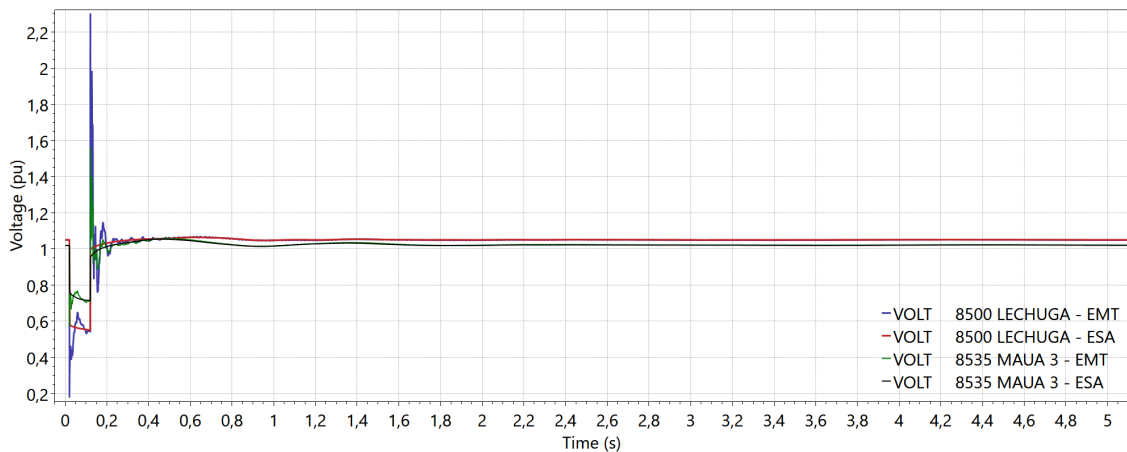

Figure 7.45: Voltage at Lechuga 500 kV (8500) and at the TPS Mauá 3 (8535) following a short-circuit at the AC bus Lechuga 500 kV

Figure 7.46 illustrates the RMS current (pu) at the circuits Lechuga-Silves 500 kV, and Lechuga-J.Teixeira 230 kV, and Figures 7.47 and 7.48, respectively, illustrates the instantaneous current (pu) at the circuits Lechuga-Silves 500 kV and Lechuga-J.Teixeira 230 kV, following the short-circuit at Lechuga 500 kV.
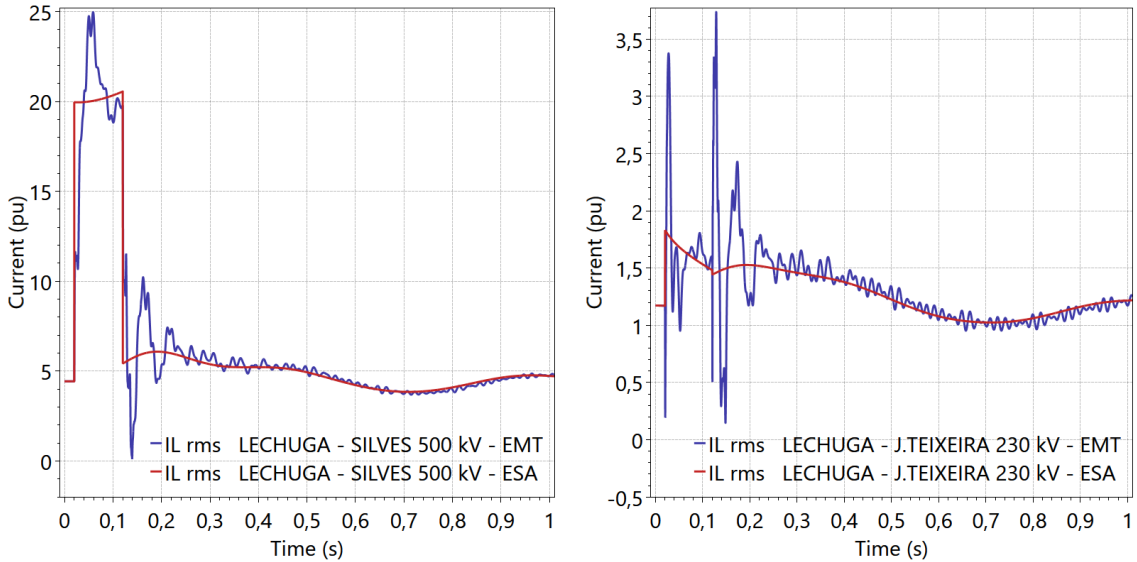
(a) Current at Lechuga-Silves 500 kV   (b) Current at Lechuga-J.Teixeira 230 kV

Figure 7.46: RMS currents (pu) following a short-circuit at Lechuga 500 kV

The instantaneous values of the currents shown in Figures 7.47 and 7.48 are obtained from the real and imaginary components of the dynamic phasor according to (3.2). In the ESA analysis, the fundamental DP represents the electromechanical transients but does not encompass the electrical network transients, whereas the EMT analysis also carries information on the fast transients of the electrical network components through the history sources aggregated to the DPCM.
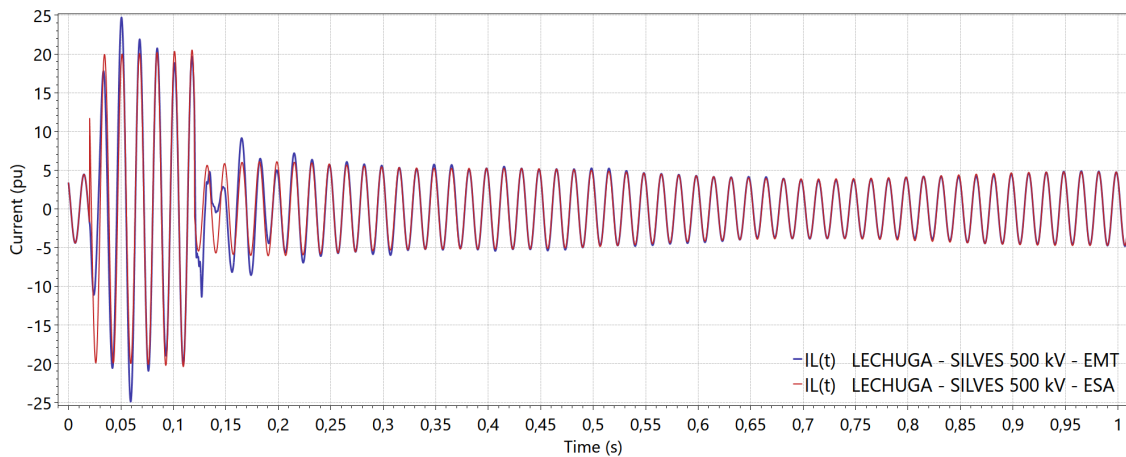

Figure 7.47: Instantaneous current (pu) at the circuit Lechuga-Silves 500 kV following a short-circuit at the AC bus Lechuga 500 kV
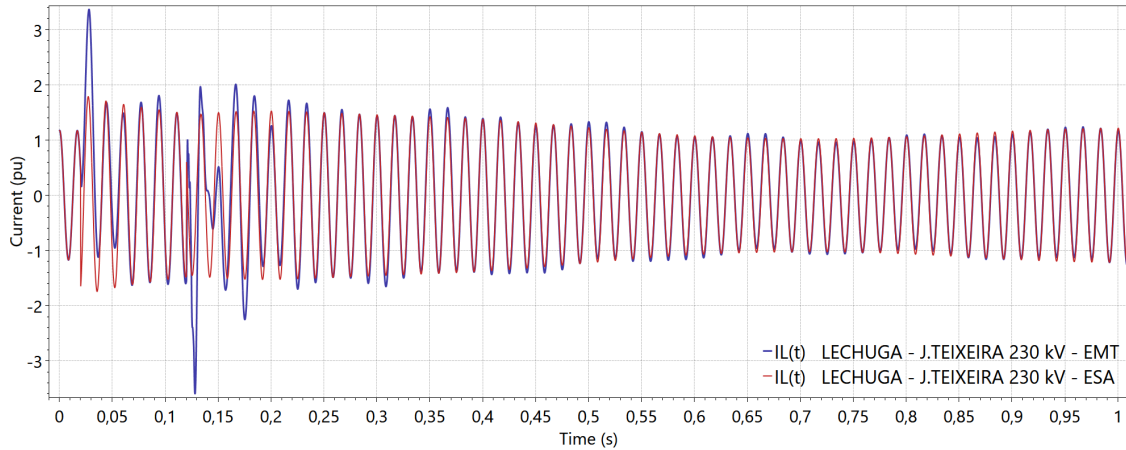
256

Figure 7.48: Instantaneous current (pu) at the circuit Lechuga-J.Teixeira 230 kV following a short-circuit at the AC bus Lechuga 500 kV

Figures 7.46 to 7.48 show that the representation of the network dynamics reveals transient overcurrents that are not captured by the ESA representation. The study of transient overcurrents constitutes an important part for the design of protection systems associated with the power system equipment. After the fast transients, the dynamic behavior of the currents in the circuits are in good agreement concerning both the ESA and the EMT representation.

In order to evaluate the long-term dynamics due to the electromechanical transients, the simulation time is increased to 10 seconds. Figures 7.49 and 7.50, respectively, present the active power and the frequency of the TPS Mauá 3, following the short-circuit at Lechuga 500 kV. In these graphics, it is also provided an amplified picture nearby the fault occurrence to provide a clearer visualization of the fast transients.
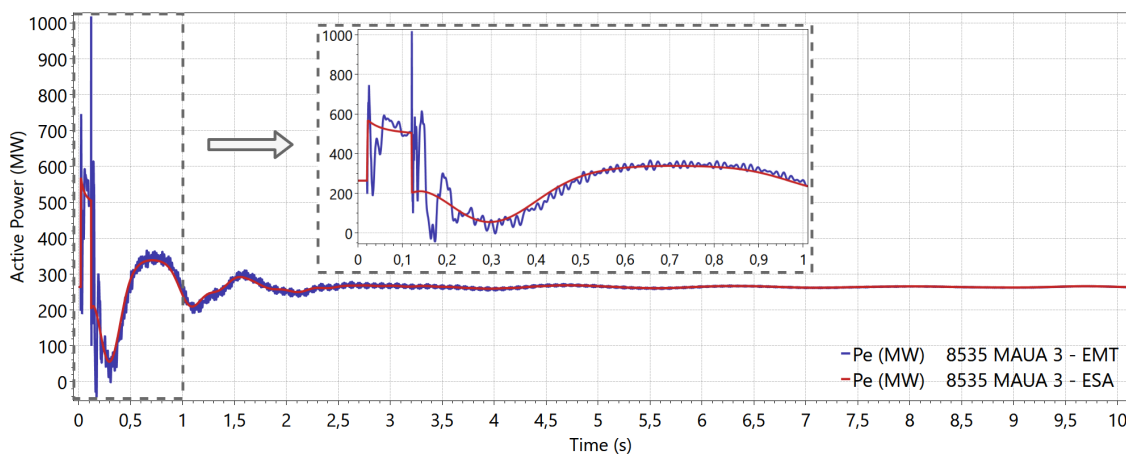

Figure 7.49: Active power (MW) of the TPS Mauá 3 following a short-circuit at the AC bus Lechuga 500 kV
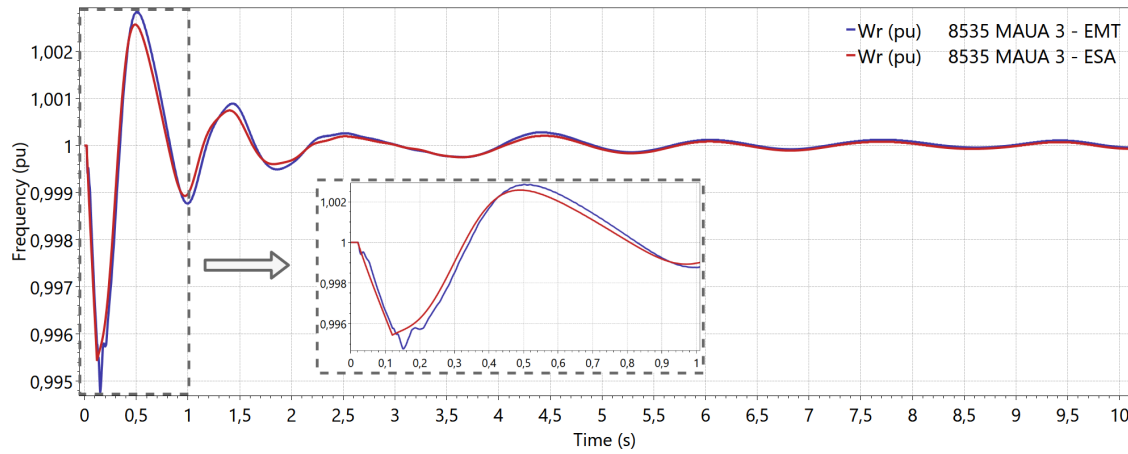
257

Figure 7.50: Frequency (pu) of the TPS Mauá 3 following a short-circuit at the AC bus Lechuga 500 kV

Due to the inherently slow dynamics of the rotor mass, it is slightly affected by the representation of the network fast transients. On the other hand, the electrical power reflects the fast transients of the network since it is an electrical quantity of the machine that can be directly obtained by the network quantities. Therefore the representation of both the electrical and mechanical dynamics of the synchronous machine supports a comprehensive nonlinear analysis concerning a wide frequency range of phenomena that impact its dynamic behavior.

In this context, the dynamic behavior of multiples machines are evaluated. For the sake of illustration, Figures 7.51 and 7.52, respectively, show the active power of the HPS Balbina (salient pole synchronous machine) and TPS Aparecida 2 (cylindrical pole synchronous machine), following the short-circuit at Lechuga 500 kV.
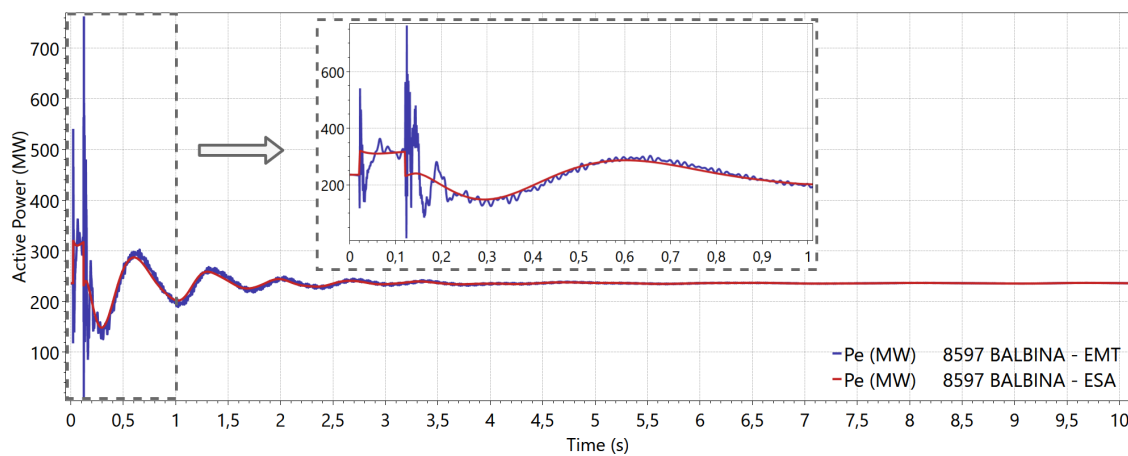

Figure 7.51: Active power (MW) of the HPS Balbina following a short-circuit at the AC bus Lechuga 500 kV
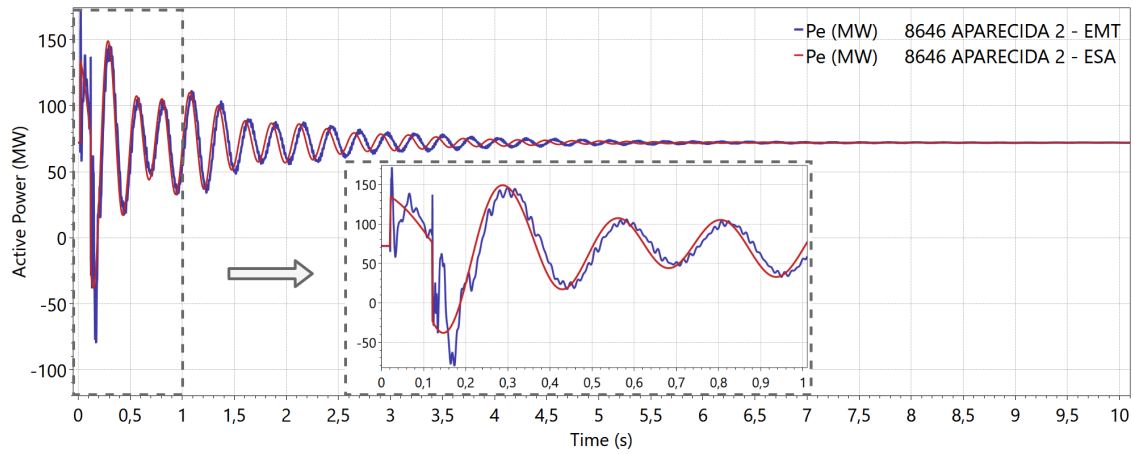
Figure 7.52: Active power (MW) of the TPS Aparecida 2 following a short-circuit at the AC bus Lechuga 500 kV

It is observed that the long-term dynamics from the EMT and ESA modeling are in consonance. This dynamic behavior is expected, and it justifies the premise of neglecting the network dynamics, the stator flux dynamics, and the rotor speed variation in traditional ESA studies. Moreover, the EMT simulation requires a small time step size for the time-domain simulation, and it expands the dimension of the network solution algorithm, which significantly increases the total simulation time. At this stage, the simple and convenient DSS interface routines of the MKL library have been applied, resulting in a total EMT simulation time close to 3 hours to run a 10-second EMT simulation with a time step size equal to 10 μs. Therefore, future research must be conducted to investigate more efficient techniques for the ordination and factorization of the electrical network solution. It is also envisioned: the parallelization of the EMT time-domain simulation, variable time step size, and a hybrid EMT-ESA simulation environment, which detects when the fast transients are settled and, then, only the ESA representation might be considered for the time-domain solution with larger time step size.

Representation of Long Transmission Lines by Using the Bergeron Model

In this item, the EMT simulation results are compared considering long transmission lines by: (i) the equivalent-π model (blue curves); (ii) the Bergeron model (red curves). In this regard, the EMT simulations with the Bergeron model have been carried out with the `BERG` execution option to identify long transmission lines as those with corresponding time travel τ higher than the `MINTAU` constant. In the present study, the `MINTAU` constant is equal to 10 times the time step size Δt.

Table 7.12 presents the parameters of the transmission lines, between Tucurui 500 kV and Lechuga 500 kV. It is noted that the time travel correspondent to these circuits is larger than 10 times the step-size. Therefore, these 500 kV circuits are all represented through the Bergeron model when the option `BERG` is enabled. On the other hand, medium-length transmission lines are ignored in this conversion since their respective line charging is not as large to result in a time-travel that fits into the `MINTAU` constant. An alternative study would be performed by considering the definition of only a specific set of circuits as the Bergeron model by employing the execution code `DTLT`, also implemented in this thesis.

Table 7.12: Parameters of the transmission lines between Tucuruí 500 kV and Lechuga 500 kV - $\Delta t = 10\mu s$

Transmission Line	$L\ (mH)$	$C\ (\mu F)$	$\tau\ (ms)$	$\lceil \tau / \Delta t \rceil$
Lechuga 500 kV - Silves 500 kV	155.693	3.757	0.76481	76
Silves 500 kV - Oriximiná 500 kV	228.845	5.668	1.13891	114
Oriximiná 500 kV - Jurupari 500 kV	241.305	5.898	1.19296	119
Jurupari 500 kV - Xingu 500 kV	171.231	4.075	0.83530	84
Xingu 500 kV - Tucuruí 500 kV	185.416	4.432	0.90653	91

The procedure to identify long transmission lines by the travel time (option `BERG` enabled) is a preliminary process. Afterward, the ANATEM software obtains the nominal parameters of long transmission lines from the static equivalent-π model [70]. Then, the Bergeron equivalent quadripole is constructed using the methodology detailed in Appendix A.1, for the steady-state initialization of the history sources associated with the long transmission lines.
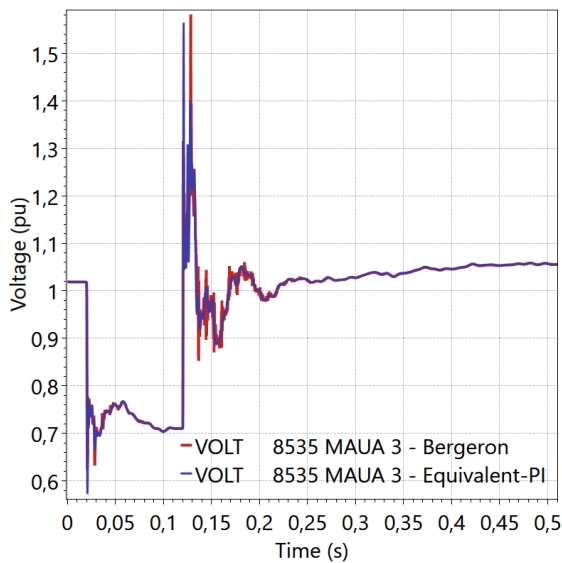
It is simulated a balanced three-phase short-circuit at Lechuga 500 kV through a resistance of 0.01 pu with 100 ms duration. Figure 7.53 presents the comparison of the RMS voltage at the AC buses Lechuga 500 kV, Tucuruí 500 kV, TPS Mauá 3, and HPS Balbina, following this disturbance.
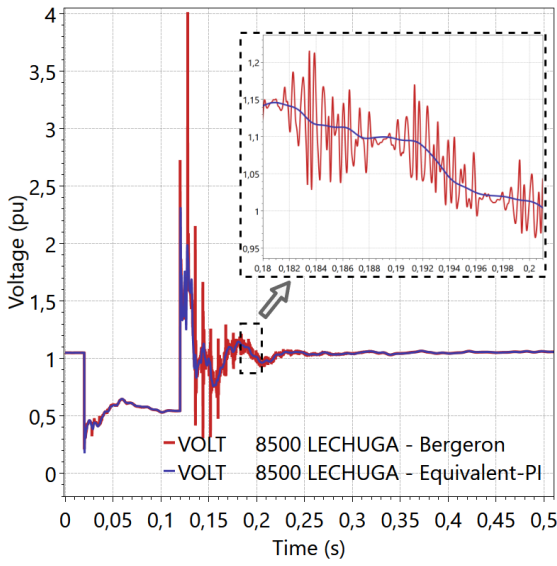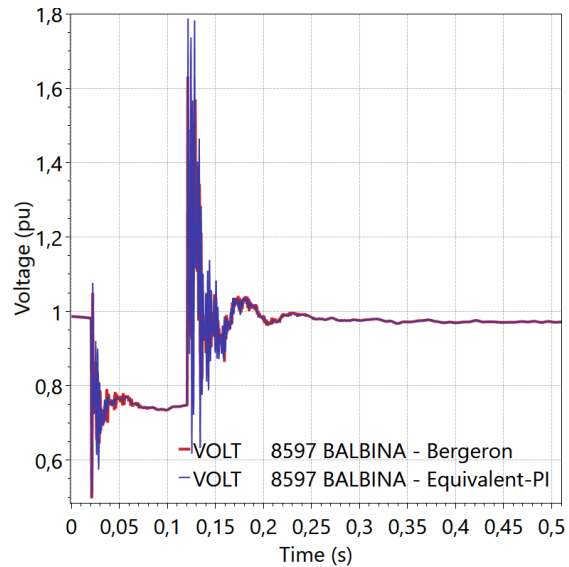

(a) Voltage (pu) at Lechuga 500 kV
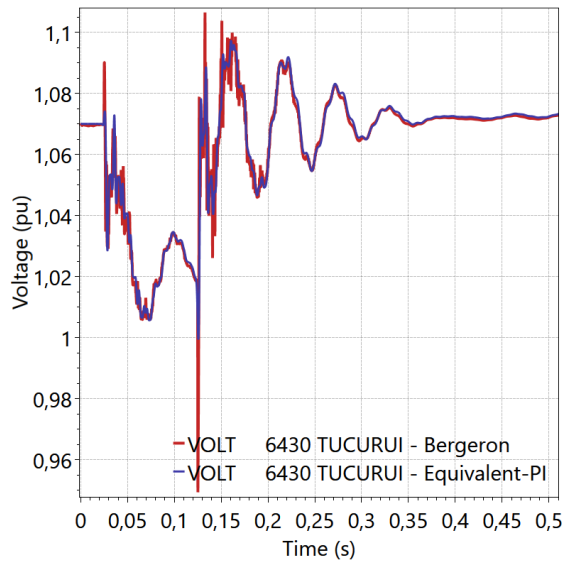
(b) Voltage (pu) at Tucuruí 500 kV

(c) Voltage (pu) at the TPS Mauá 3

(d) Voltage (pu) at the TPS Mauá 3

Figure 7.53: Bergeron x Equivalent-π model: comparison of the voltages at the Northern system, following a short-circuit at Lechuga 500 kV

From Figure 7.53, it is noted that the application of the Bergeron or the equivalent-π representation for long transmission lines presents differences in the dynamic response, mainly in the steps that follow the application of the disturbance. The Bergeron model results in more voltage spikes due to the reflection of the progres-

sive waves inherent to this model, which is adequately captured by its respective equivalent DPCM model, developed in Section 3.3.5.2.

Figure 7.54 illustrates the RMS current (pu) at the circuits Lechuga - Silves 500 kV, and Lechuga - J.Teixeira 230 kV, and Figures 7.55 and 7.56, respectively, illustrates the instantaneous current (pu) at the circuits Lechuga-Silves 500 kV and Lechuga-J.Teixeira 230 kV, following the short-circuit at Lechuga 500 kV.
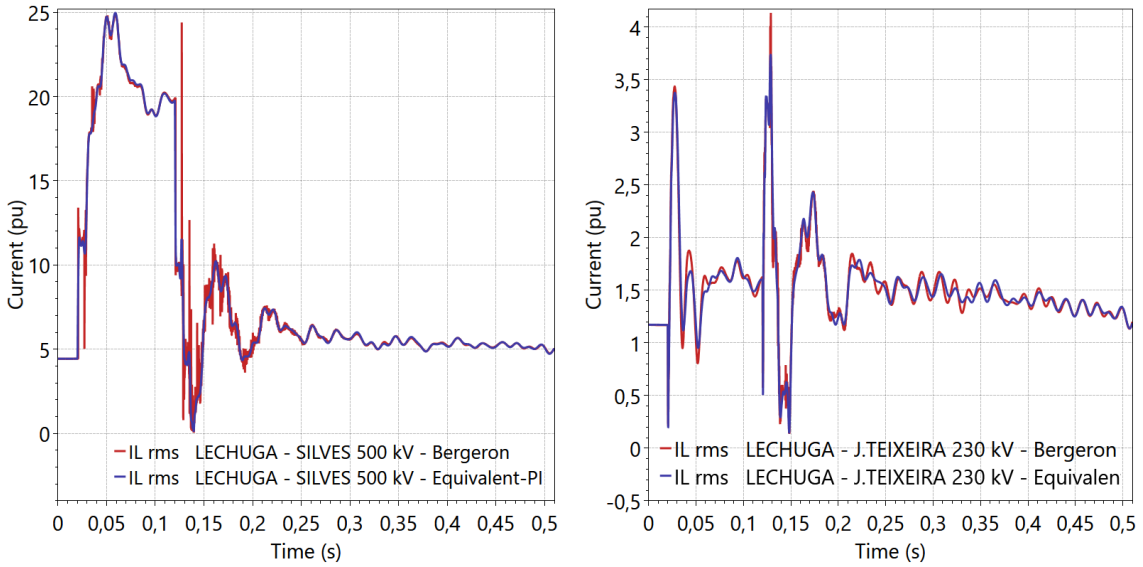
(a) Current (pu) at Lechuga - Silves 500 kV (b) Current (pu) at Lechuga - J.Teixeira 230 kV

Figure 7.54: Bergeron x Equivalent-π model: comparison of currents (pu) following a short-circuit at Lechuga 500 kV
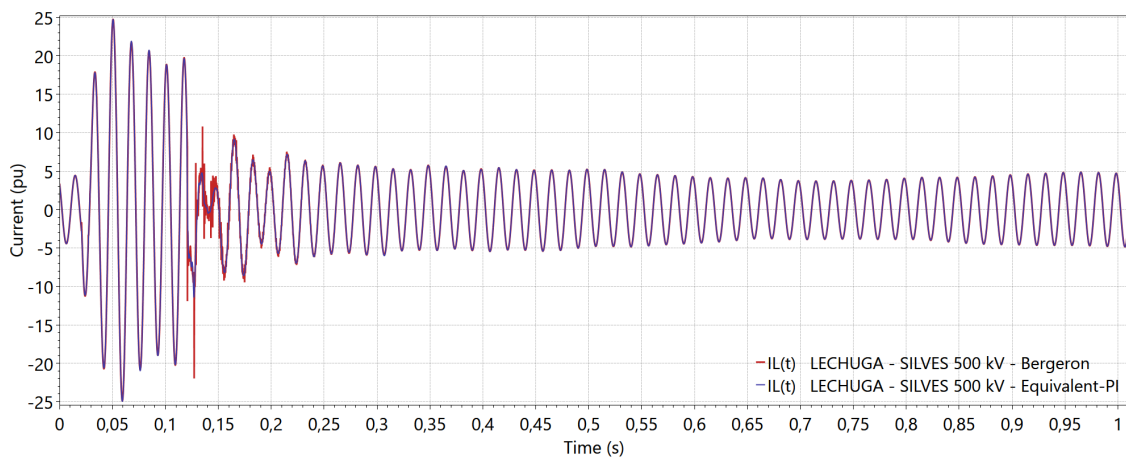

Figure 7.55: Current (pu) at the circuit Lechuga - Silves 500 kV following a short-circuit at the AC bus Lechuga 500 kV
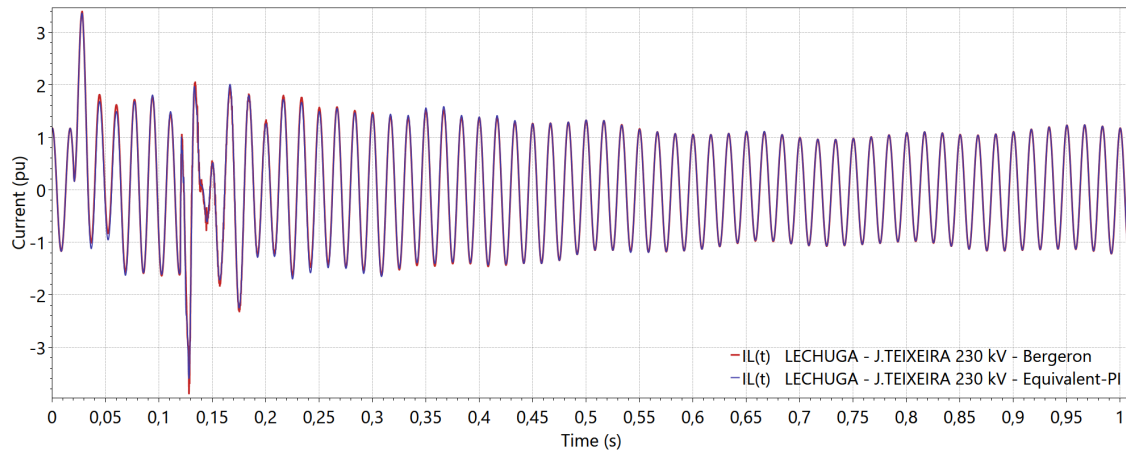
262

Figure 7.56: Current (pu) at the circuit Lechuga - J.Teixeira 230 kV following a short-circuit at the AC bus Lechuga 500 kV

One should note that the spikes, in the current waveform, due to the reflections of the traveling waves are more accentuated in the current of the circuit Lechuga-Silves 500 kV than in the Lechuga-J.Teixeira 230 kV. It should be pointed out that the Bergeron model has not been applied to Lechuga-J.Teixeira 230 kV because this circuit possesses a time travel smaller than `MINTAU`. For this reason, the current waveform of this circuit presents a reduced difference when comparing the two EMT simulations. In general, the farther a circuit is from long transmission lines, the smaller the difference in its dynamic response due to the use of the Bergeron or the equivalent-π model. In addition, the fast transients are attenuated due to the inductances of the circuits in the boundary, which mitigates the propagation of the traveling waves. This characteristic justifies the use of reduced equivalent networks in the study of high-frequency phenomena.

In order to evaluate the impact of employing the Bergeron model for long transmission lines over the dynamic behavior of the synchronous machine, Figure 7.57 presents the comparison of the direct and quadrature stator currents, the subtransient voltage of quadrature axis, and the field voltage of each generation unit at the TPS Mauá 3, following the short-circuit at Lechuga 500 kV.

263
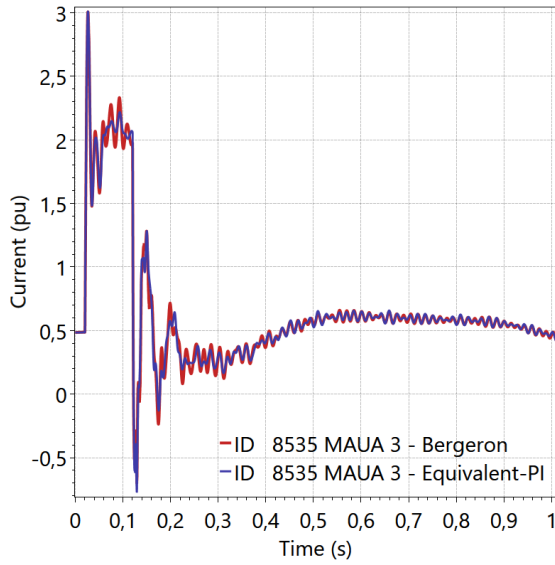
(a) Direct stator current (pu)
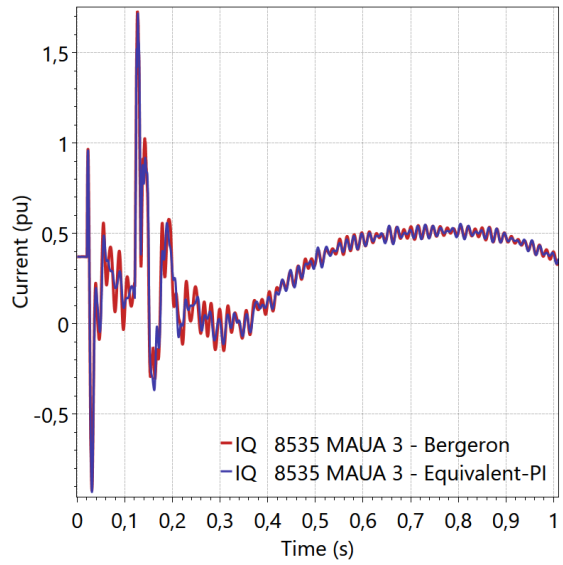
(b) Quadrature stator current (pu)
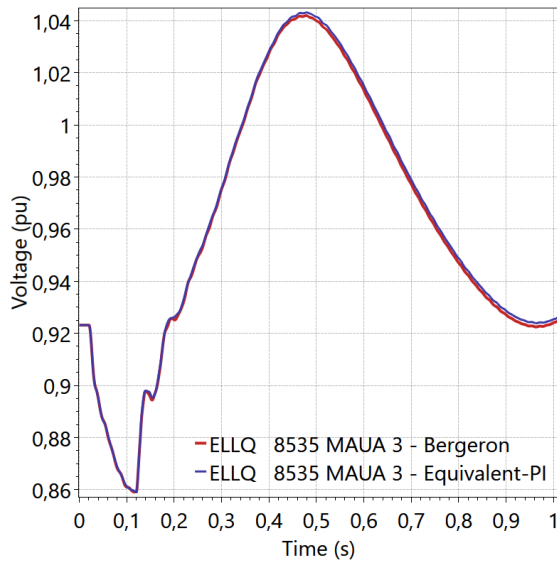
(c) Subtransient voltage (pu) of direct axis
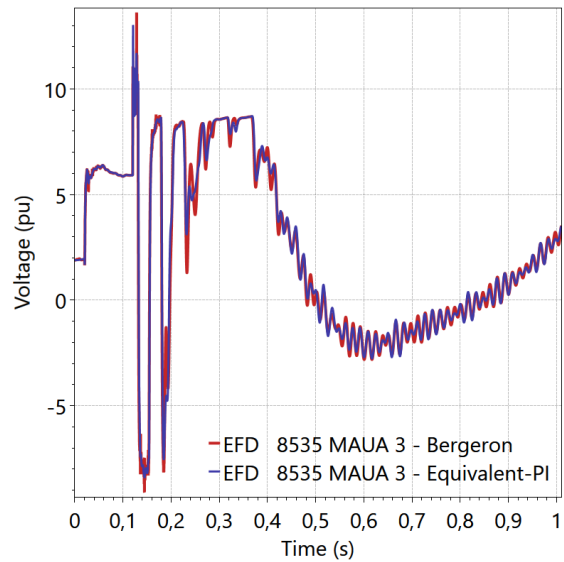
(d) Field voltage (pu)

Figure 7.57: Bergeron x Equivalent-π: internal quantities of the generation units at the TPS Mauá 3 following a short-circuit at Lechuga 500 kV

One should note that, for this type of disturbance, the simulation results obtained with lumped parameters are fairly close to the results of the Bergeron model.

At this point, the simulation time is increased to 10 seconds to investigate the long-term dynamic behavior of the synchronous machines, following the short-circuit at Lechuga 500 kV. Thus, Figures 7.58 and 7.59 show the active and reactive power at the TPS Mauá 3, respectively. These graphics also include the comparison with the ESA modeling (green curve), in order to provide a comprehensive validation of the general-purpose simulation environment that has been explored in this thesis.
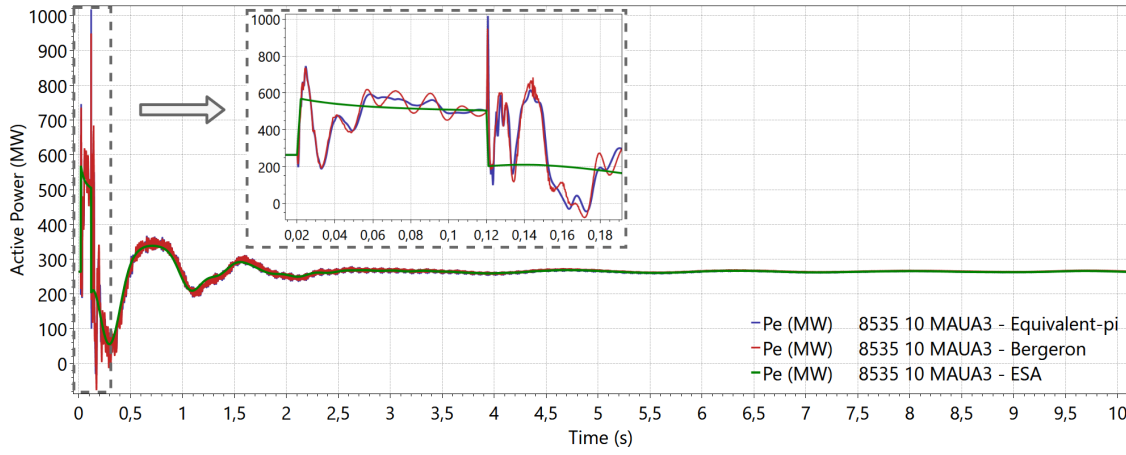
Figure 7.58: Active power (MW) of the TPS Mauá 3 following a short-circuit at the AC bus Lechuga 500 kV
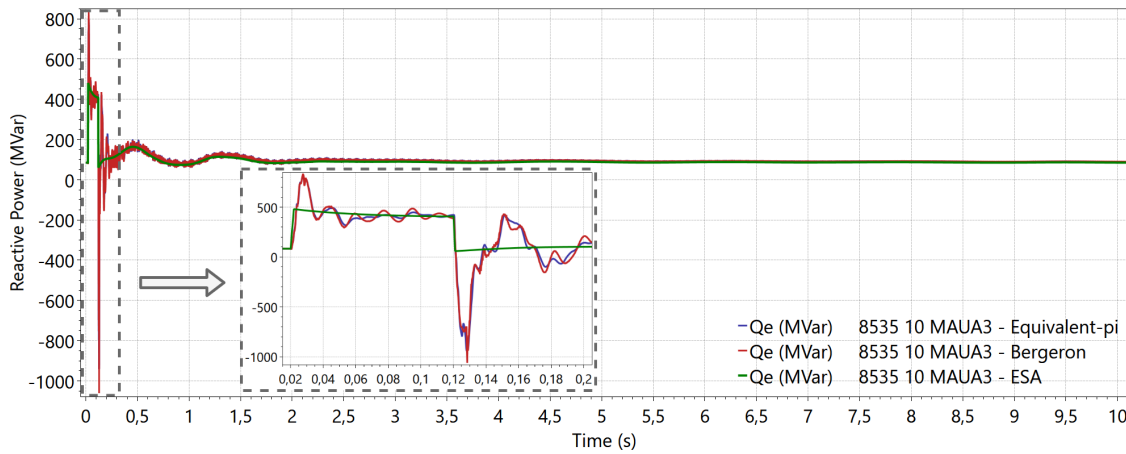
Figure 7.59: Reactive power (MW) of the TPS Mauá 3 following a short-circuit at the AC bus Lechuga 500 kV

As the present study accounts for multiple machine dynamics, Figures 7.60 and 7.61 illustrates the active power at the HPS Tucuruí and at the TPS Aparecida, following the short-circuit at Lechuga 500 kV. A 5-second window is applied in these graphics to allow the visualization of the fast transients during the short-circuit.
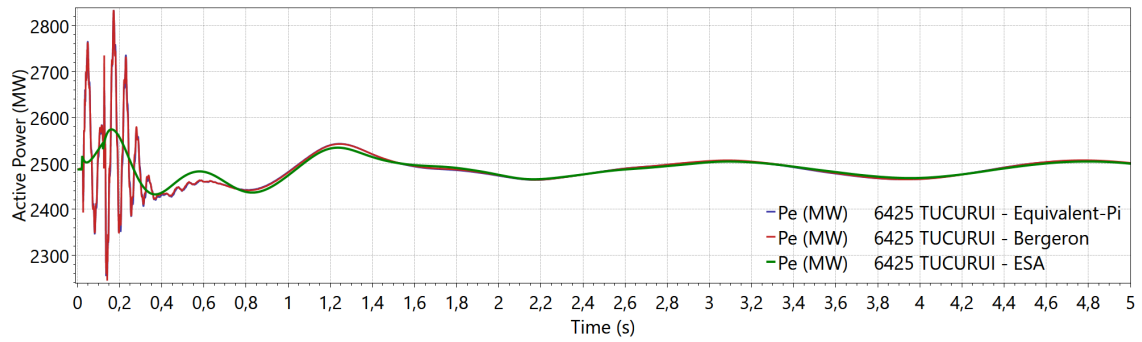
Figure 7.60: Active power (MW) of the HPS Tucurui following a short-circuit at the AC bus Lechuga 500 kV
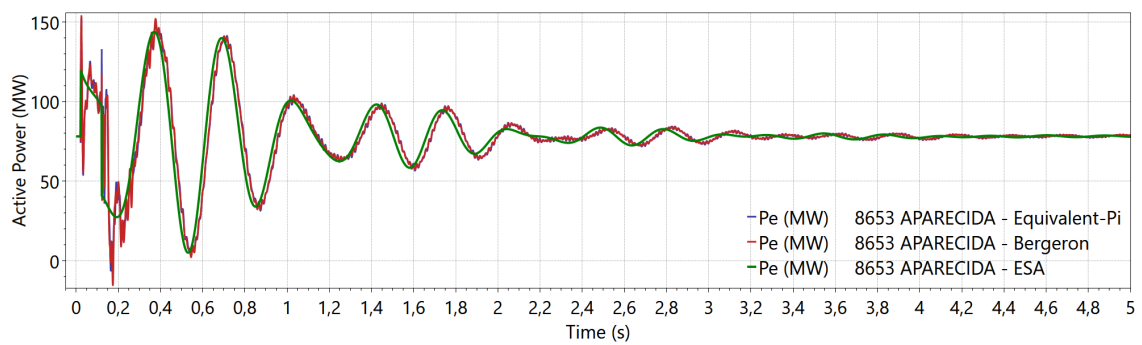
Figure 7.61: Active power (MW) of the TPS Aparecida 2 following a short-circuit at the AC bus Lechuga 500 kV

The simulation results presented in this item have shown that the synchronous machine detailed model considers the high-frequency transients of the electrical network. It is observed that the Bergeron, the equivalent-π, and the ESA modeling are in consonance for the long-term dynamic analysis, considering both the salient pole and the cylindrical pole synchronous machine.

Representation of the Turbine-Generator Shaft

In this item, a hypothetical subsynchronous resonance analysis is presented by employing the turbine-generator shaft described in Table 7.13 in the TPS Mauá 3 (bus 8535). It is important to point out the Electromechanical Stability Database does not account for the turbine-generator shaft data. Therefore, the turbine-generator shaft of the FBM test system is applied, in this study, for the purpose of illustrating the SSR phenomenon in a large-scale power system.

Table 7.13: Turbine-generator shaft applied in the TPS Mauá 3

Mass i	H_i (s)	D_i (pu/pu)	Torque (%)	Shaft ij	K_{ij} (pu/rad)
HP	0.092897	0.10500	30%	HP-IP	19.303
IP	0.155589	0.05850	26%	IP-LPA	34.929
LPA	0.858670	0.01970	22%	LPA-LPB	52.038
LPB	0.884215	0.00233	22%	LPB-GEN	70.858
GEN	0.868495	0.02480		GEN-EXC	2.822
EXC	0.0342165	0.01020			

Is should be noted that the damping factors (D_i) are dependent on the operating condition, and they are obtained by means of machine tests through the modal damping coefficients related to the shaft system [64]. However, the determination of these coefficients is out of the scope of this work. For this reason, the values assumed here are specified to allow the illustration of the SSR phenomenon when the series capacitive compensation is modified in the North-Northeast Interconnection (Figure 7.39).

The PAR 2023 case study is employed, in this item, regarding the same premises that have been explained in Section 7.3.1, and the long transmission lines are represented by the equivalent-π lumped parameter DPCM model.

It is simulated a balanced three-phase short-circuit at Lechuga 500 kV through a resistance of 0.01 pu with 100 ms duration. Figure 7.62 presents the comparison of the RMS voltage at the AC bus Lechuga 500 kV and at the TPS Mauá 3, following this disturbance. In these graphics, three cases are compared: (i) the EMT simulation (blue curve) using the multi-mass representation for the turbine-generator shaft of the TPS Mauá 3; (ii) the EMT simulation (red curve) using the rigid shaft representation; and (iii) the ESA simulation (green curve).
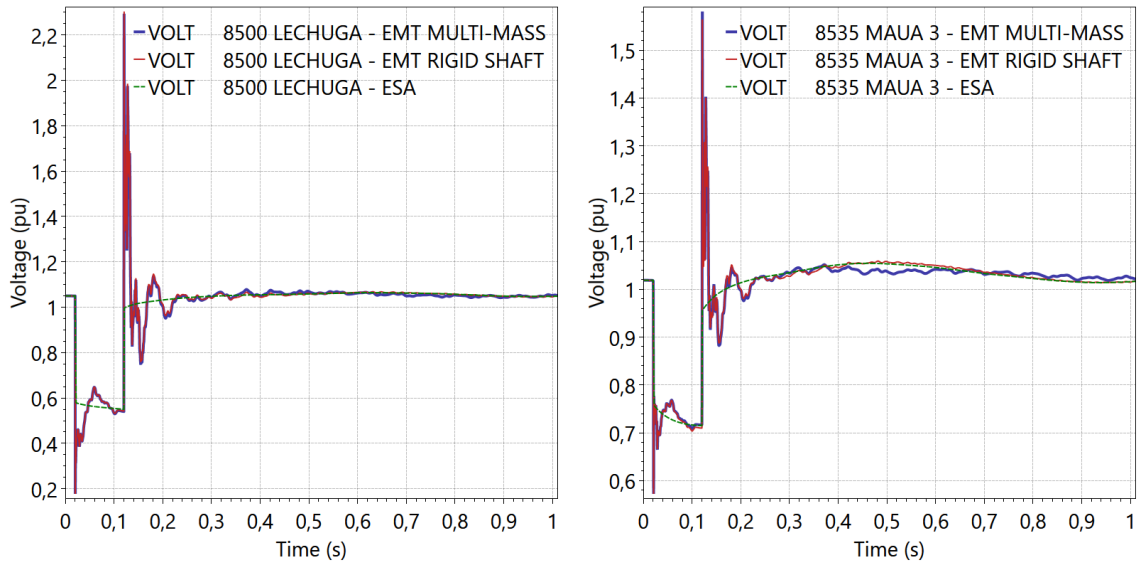
(a) Voltage (pu) at Lechuga 500 kV

(b) Voltage (pu) at the TPS Mauá 3

Figure 7.62: Multi-mass x rigid shaft x ESA: voltage comparison following a short-circuit at Lechuga 500 kV

As expected, Figure 7.62 shows that the fast transient due to the electrical network dynamics are in conformity regarding both EMT representations (rigid shaft and multi-mass). It is observed that the representation of the turbine-generator shaft by using the individualized spring-mass model reveals subsynchronous oscillations in the dynamic response. The subsynchronous oscillations are better observed in the synchronous machine quantities. Thus, Figures 7.63 and 7.64, respectively, illustrate the frequency (pu) and the active power (MW) of generation units at the TPS Mauá 3, following the short-circuit at Lechuga 500 kV.
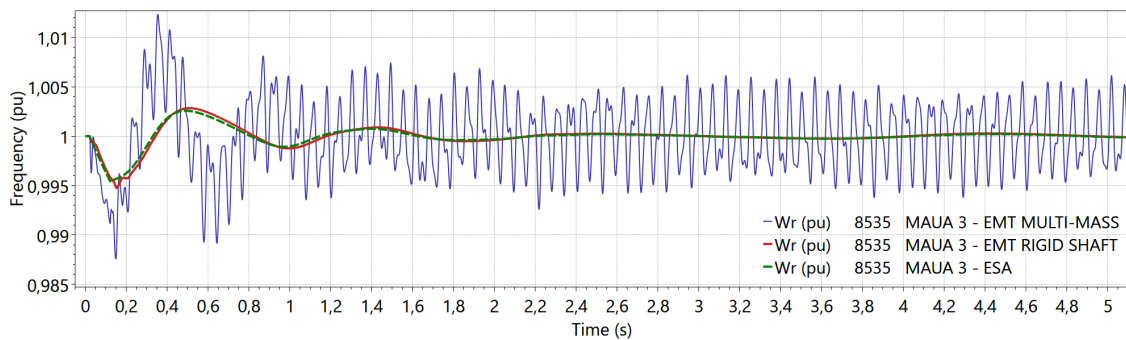
Figure 7.63: Multi-mass x rigid shaft x ESA: frequency (pu) of the TPS Mauá 3 following a short-circuit at Lechuga 500 kV

Figure 7.64: Multi-mass x rigid shaft x ESA: active power (MW) of the TPS Mauá 3 following a short-circuit at Lechuga 500 kV

One should note that the representation of the turbine-generator shaft reveals the subsynchronous interaction of the multi-mass system with the network dynamics, presenting a slightly damped behavior. In this analysis, an approximated subsynchronous oscillation frequency of 16.5 Hz is observed in the generator mass. The analysis of the interaction between the network dynamics and the shaft system has become possible due to the refinements of the synchronous machine model, such as the stator flux dynamics, which reflects the network transients in the synchronous machine rotor.

Figure 7.65 illustrates the active power (MW) at the TPS Aparecida 2. It shows that the representation of the shaft at the TPS Mauá 3 does not affect significantly the general dynamic behavior at other power stations, so that the EMT simulations, whether multi-mass or rigid shaft, result in a similar response for the active power of the TPS Aparecida 2.

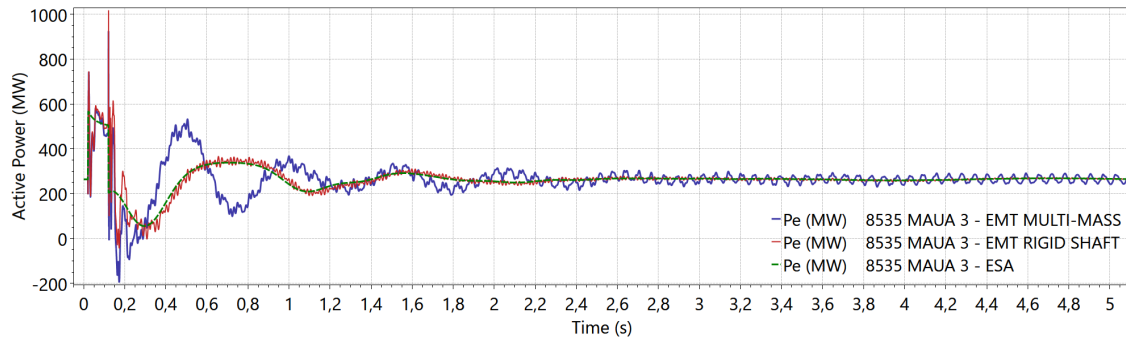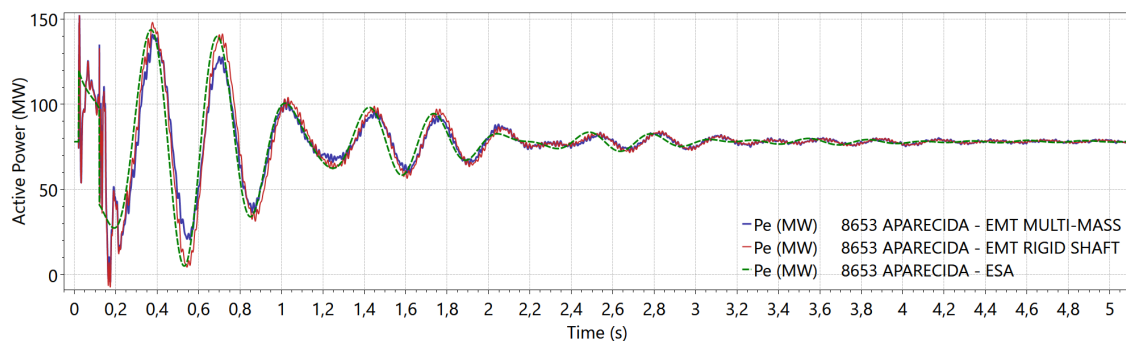Figure 7.65: Multi-mass x rigid shaft x ESA: active power (MW) of the TPS Aparecida 2 following a short-circuit at Lechuga 500 kV

The following item presents an example of subsynchronous resonance due to torsional interaction between the turbine-generator shaft of the TPS Mauá 3, and the series compensated transmission system of the Tucurui-Manaus interconnection.

Effect of the Variation of the Series Capacitive Compensation

In this item, it is evaluated the effect of the variation of the series capacitive reactance (X_{CS}) of the North-Northeast interconnection in the dynamic response of the turbine-generator shaft of the TPS Mauá 3. In the original case study, a series compensation level of 70% has been considered in the transmission lines between Lechuga 500 kV and Tucurui 500 kV.

At this point, the percentage of series compensation is modified in the line sections between Lechuga 500 kV and Jurupari 500 kV. Table 7.14 describes the values of the series capacitive reactance, employed in each line section, concerning a compensation level of 60%.

Table 7.14: Varying the series compensation from Lechuga 500kV to Jurupari 500 kV to $X_{CS} = 60\%$

Transmission Line	X_{CS} (pu)	(X_{CS}/X_L) (%)
Lechuga 500 kV - Silves 500 kV	-0.014086	60.0 %
Silves 500 kV - Oriximiná 500 kV	-0.020700	60.0 %
Oriximiná 500 kV - Jurupari 500 kV	-0.021840	60.0 %

Table 7.15 contains the series capacitive reactance values applied for a compensation level of 80%. The simulation results obtained with 60% and 80% of series compensation are compared to the original study case with 70 % of compensation.

Table 7.15: Varying the series compensation from Lechuga 500kV to Jurupari 500 kV to $X_{CS} = 80\%$

Transmission Line	X_{CS} (pu)	(X_{CS}/X_L) (%)
Lechuga 500 kV - Silves 500 kV	-0.018782	80.0 %
Silves 500 kV - Oriximiná 500 kV	-0.027600	80.0 %
Oriximiná 500 kV - Jurupari 500 kV	-0.029100	80.0 %

In the dynamic simulations, it is considered the EMT modeling, and the individualized turbine-generator shaft in the TPS Mauá 3. Then, the simulation results explores the series compensation between Lechuga 500 kV and Jurupari 500 kV, in the following levels: (i) 60% (green curve); (ii) 70% (red curve); and (iii) 80% (blue curve).

It is simulated a balanced three-phase short-circuit at Lechuga 500 kV through a resistance of 0.01 pu with 100 ms duration. Figures 7.66 and 7.67 presents the

comparison of the RMS voltage at the AC bus Lechuga 500 kV, and at the TPS Mauá 3, following this disturbance.
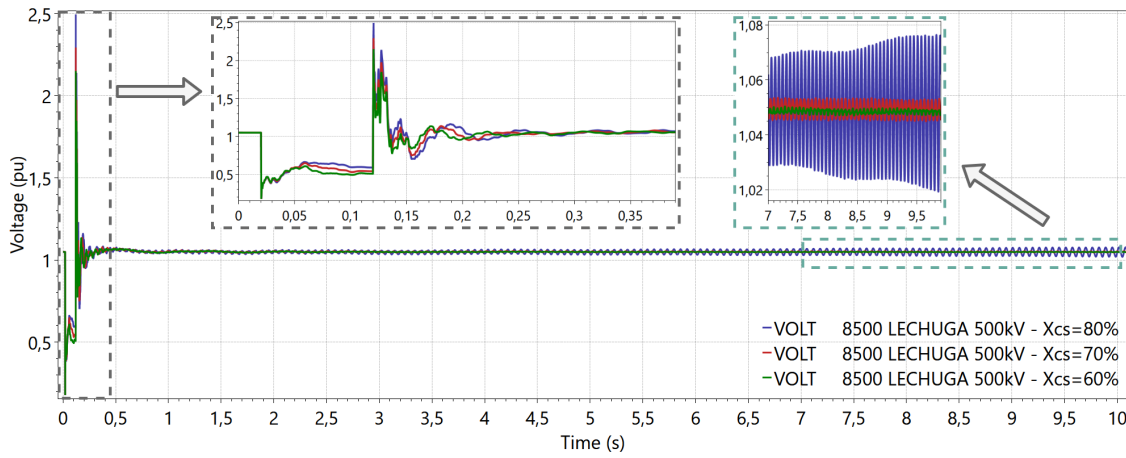
Figure 7.66: Voltage of the Lechuga 500 kV following a short-circuit at the AC bus Lechuga 500 kV
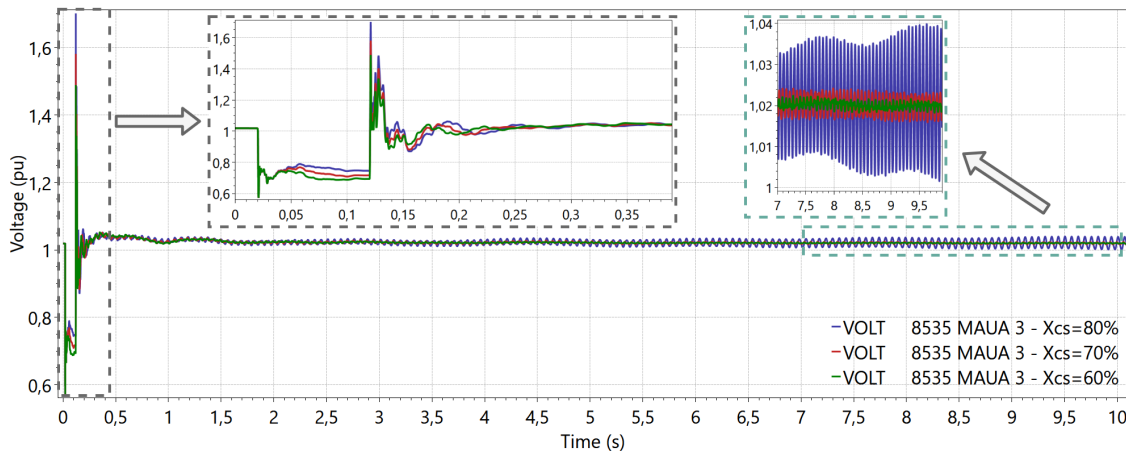
Figure 7.67: Voltage of the TPS Mauá 3 following a short-circuit at the AC bus Lechuga 500 kV

Figures 7.66 and 7.67 highlight both the period close to the event, to allow the visualization of the fast transients, and the final period of the simulation, which evidence the increasing oscillations in the subsynchronous range. From the time-domain response, it is possible to verify that the 80% compensation level exhibits unstable oscillations with an approximate frequency of 16 Hz.

Figures 7.68 and 7.69 presents the comparison of the active and reactive power at the TPS Mauá 3, following the short-circuit at the Lechuga 500 kV.
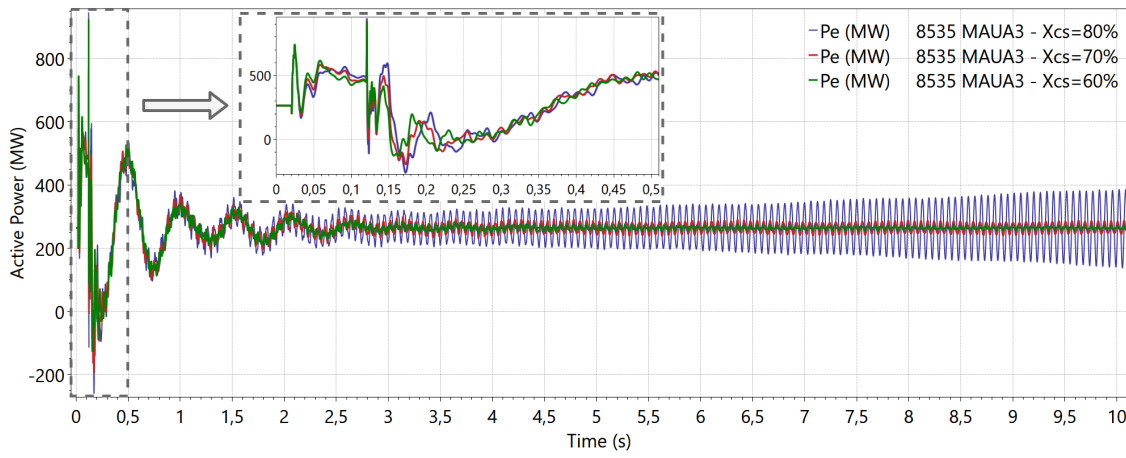
Figure 7.68: Active power (MW) of the Mauá 3 following a short-circuit at the AC bus Lechuga 500 kV
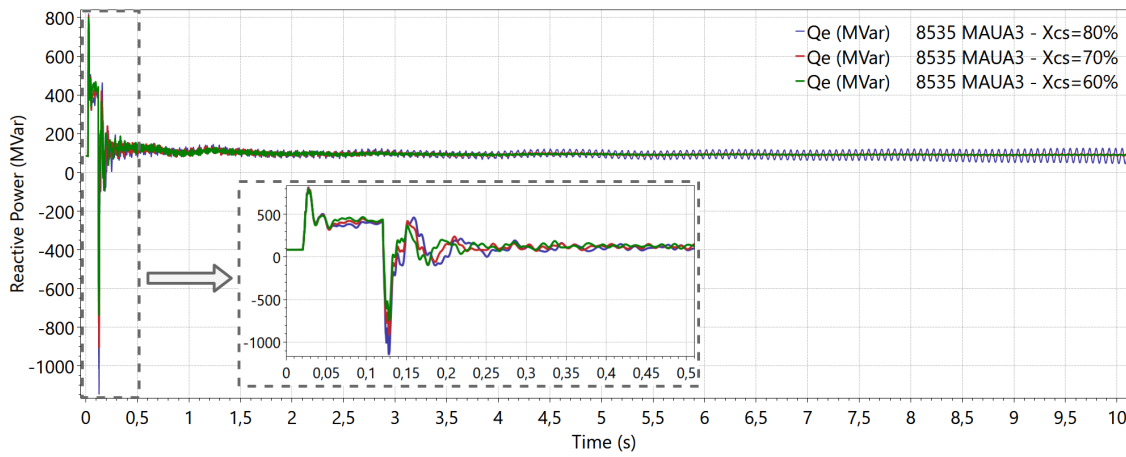
Figure 7.69: Reactive power (MVar) of the Mauá 3 following a short-circuit at the AC bus Lechuga 500 kV

This case study illustrates the occurrence of the subsynchronous resonance phenomenon at the compensation level of 80%. This occurs due to the interaction of the torsional modes of the turbine-generator shaft and natural oscillation frequencies of the series compensated transmission system.

The frequency of each rotor section is illustrated in Figure 7.70. It demonstrates that the dynamic phasor-based synchronous machine model with the representation of both the electrical and mechanical transients, the network dynamics, and the multi-mass shaft representation have provided a general purpose methodology for nonlinear time-domain simulation.
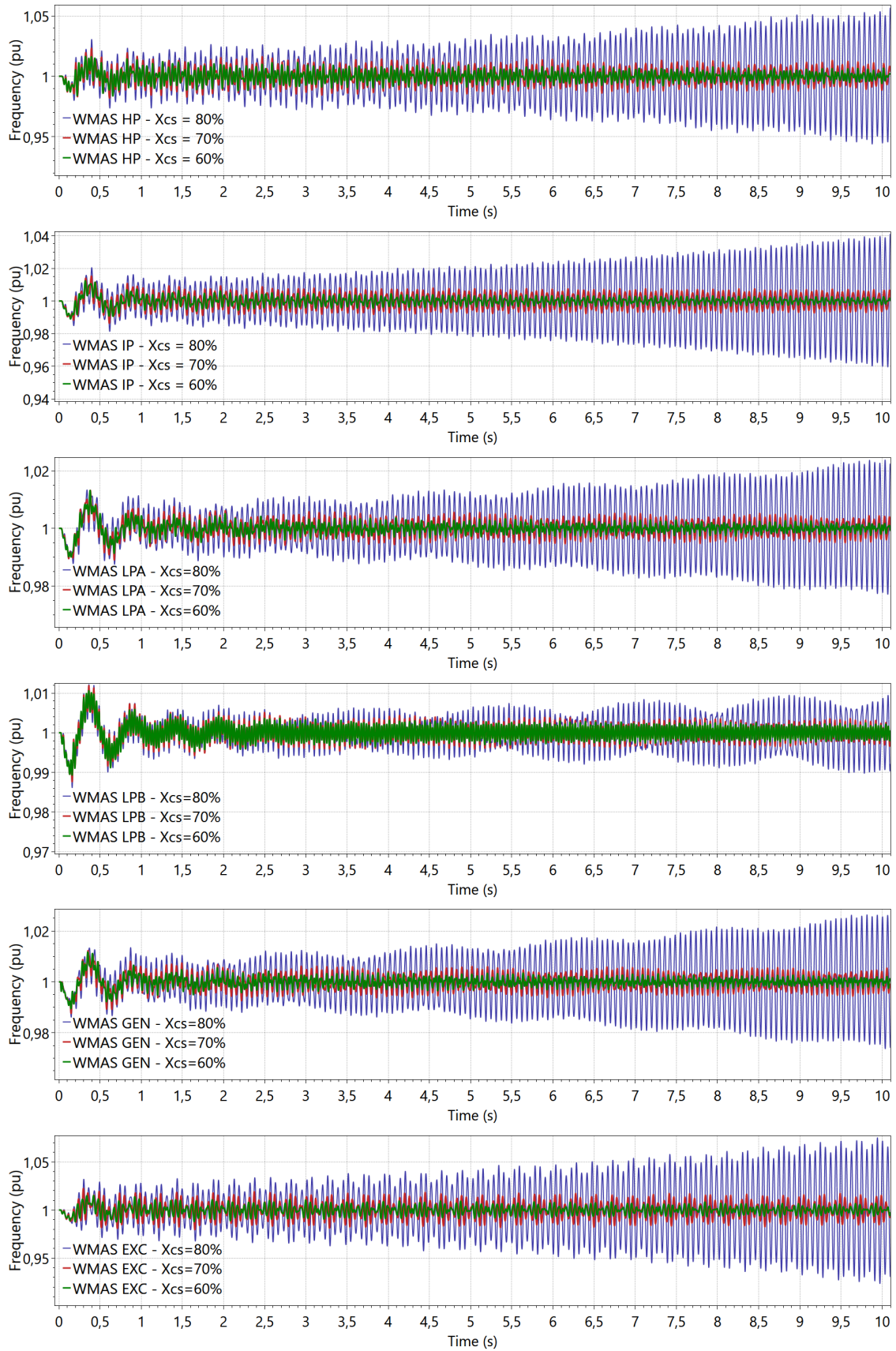
Figure 7.70: Frequency (pu) of the rotor masses following a short-circuit at Lechuga 500 kV

These results evidence the wider frequency range of the ANATEM software, considering the developments of this thesis. Therefore, it is demonstrated that this general-purpose simulation environment capture both electromechanical, subsynchronous, and electromagnetic oscillations, in a large scale power system.

Figure 7.71 compares the frequency (pu) of the generator mass, regarding the case with 80% of series compensation, in the following three configurations: (i) the EMT simulation (blue curve) using the multi-mass representation for the turbine-generator shaft of the TPS Mauá 3; (ii) the EMT simulation (red curve) using the rigid shaft representation; and (iii) the ESA simulation (green curve).
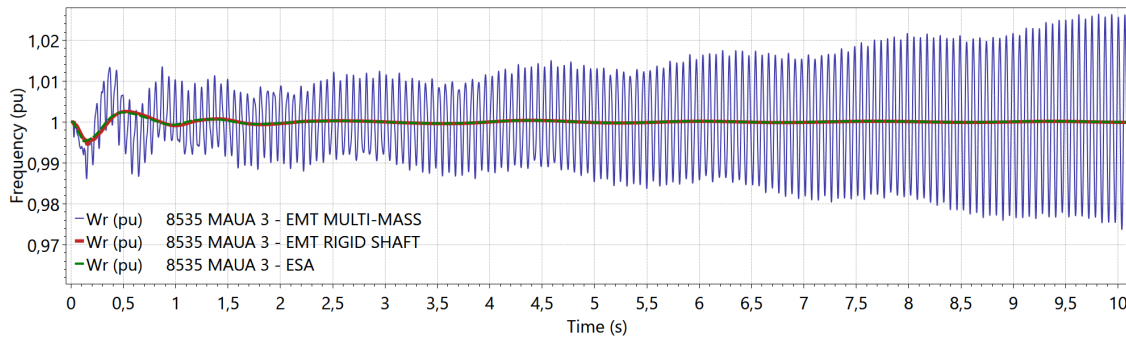
Figure 7.71: $X_{CS} = 80\%$: frequency (pu) of the generator mass from the TPS Mauá 3 following a short-circuit at Lechuga 500 kV

It is demonstrated that the representation of the turbine-generator shaft dynamics through the spring-mass model, in the ANATEM software, supports the analysis of subsynchronous resonance phenomenon. This achievement has been made possible via the development of the network dynamics, which reveals the natural oscillation frequencies of the series compensated transmission systems. Finally, the representation of the stator flux dynamics reflects the network transients in the rotor shaft and vice-versa. The interaction between the electrical and mechanical variables associated with turbogenerators when coupled to a series capacitive compensated transmission system can present **lightly damped**, **undamped**, **negatively damped** or **growing** oscillatory energy interchange. The present subsection has illustrated these categories of subsynchronous oscillations by using the dynamic phasor-based models extensively studied in this thesis.

Representation of Multiple Turbine-Generator Shaft

In this item, the general-purpose module of the ANATEM for the analysis of electromagnetic, subsynchronous, and electromechanical transients is explored in a multimachine simulation context. Therefore, the individualized model of the turbine-generator shaft, described in Table 7.13, is applied to multiple thermal power plants, which are identified in Table 7.16, as well as their total capacity and the number of units that are in operation in the PAR 2023 study case.

Table 7.16: TPS of the Northen system

AC bus number	Thermal Power Plant	Capacity (MVA)	Operating Units
8612	Jaraqui 1	11×4.450	10
8616	Jaraqui 2	12×4.450	11
8615	Tambaqui 1	12×4.450	11
8617	Tambaqui 2	11×4.450	10
8609	Manauara	5×21.345	4
8610	Ponta Negra	5×21.345	4
8611	Cristiano Rocha	5×21.345	4
8646	Aparecida 1	2×58.590	2
8653	Aparecida 2	2×71.18	2

It should be recalled that the TPS Mauá 3 has been represented with a rigid shaft, in this item, to allow a comparison between synchronous machines of smaller power capacity.

The simulation results compare the dynamic behavior of the multiple TPS shafts regarding the series capacitive compensation, between Lechuga 500 kV and Jurupari 500 kV, in the following levels: (i) 60% (green curve); (ii) 70% (red curve); and (iii) 80% (blue curve).

It is simulated a balanced three-phase short-circuit at Lechuga 500 kV through a resistance of 0.01 pu with 100 ms duration. Figures 7.72 to 7.74 presents the comparison of the RMS voltage at the AC buses Lechuga 500 kV (bus 8500), Tucuruí 500 kV (bus 6430), and at the TPS Aparecida 2 (bus 8653), following this disturbance.
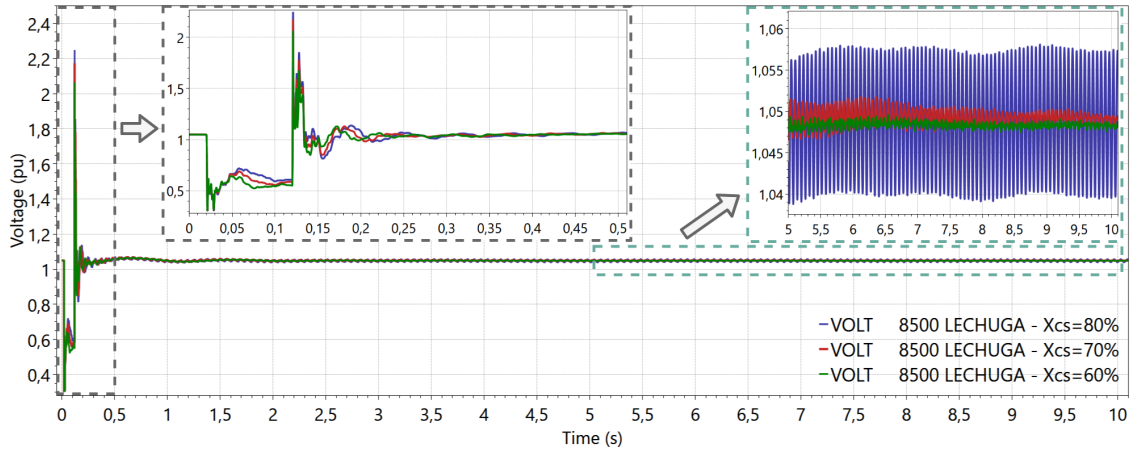
Figure 7.72: Voltage (pu) at Lechuga 500 kV following the short-circuit
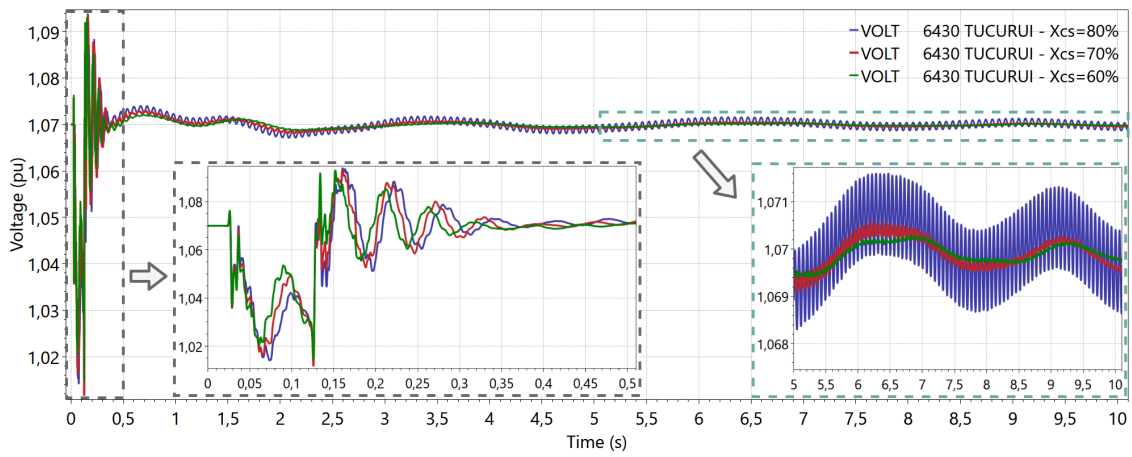
Figure 7.73: Voltage (pu) at Tucurui 500 kV following the short-circuit at Lechuga 500 kV
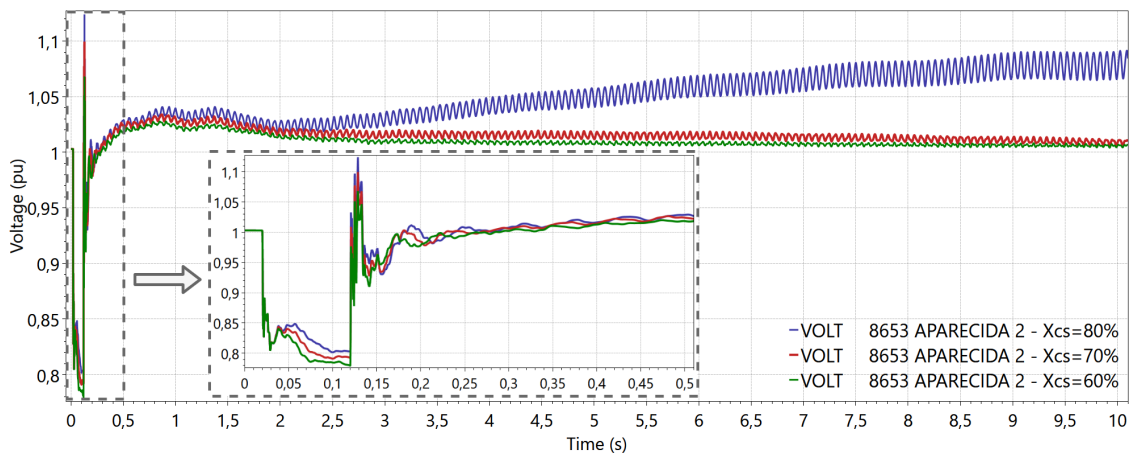
Figure 7.74: Voltage (pu) at the TPS Aparecida 2 following the short-circuit at Lechuga 500 kV

From Figures 7.72 and 7.73, it is noted that the 500 kV buses Lechuga (8500) and Tucurui (6430) exhibit the fast transients after the short-circuit, but they present small observability on the torsional modes in comparison to the terminal voltage of the TPS Aparecida 2. One can see that increasing the compensation level, from 60% to 80%, causes the torsional modes to present growing energy interchange with the electrical network in the subsynchronous frequency.

In this case, with multiple shaft representation, only a few machines experience the instability of torsional modes. For instance, Figures 7.75 and 7.76 present the comparison for the three compensation levels (60%, 70%, and 80%), of the frequency of the TPS Aparecida 2 and Tambaqui 1, following the short-circuit at Lechuga 500 kV.
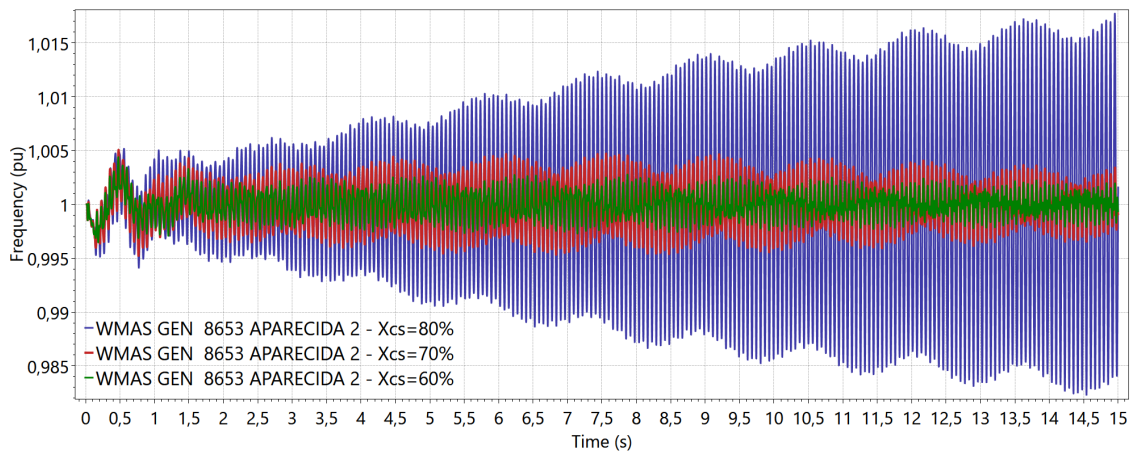
Figure 7.75: Frequency (pu) at the TPS Aparecida 2 following a short-circuit at Lechuga 500 kV
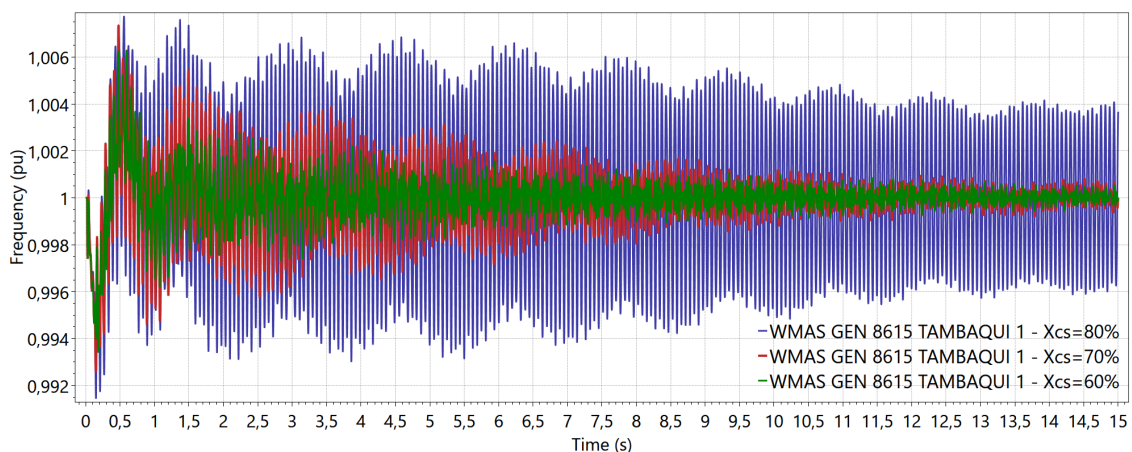
Figure 7.76: Frequency (pu) at the TPS Tambaqui 1 following a short-circuit at Lechuga 500 kV

It is noted that at 60% and 70% of series compensation, both the TPS Apare-

cida 2 and Tambaqui 1 present decreasing oscillations in the generator frequency. However, at 80% of series compensation, the TPS Aparecida 2 presents increasing oscillations, whereas the frequency of the generator mass of the TPS Tambaqui 1 presents decreasing oscillations at the frequency of 16 Hz.

As observed in Figure 7.77, the lack of representation of the turbine-generator shaft of the TPS Mauá 3 does not indicate growing subsynchronous oscillations in its corresponding generator frequency, contrasting with the dynamic behavior that has been observed in the previous item at 80% of series compensation. The application of the rigid shaft, in this item, has only revealed the electromechanical oscillation mode of this TPS.
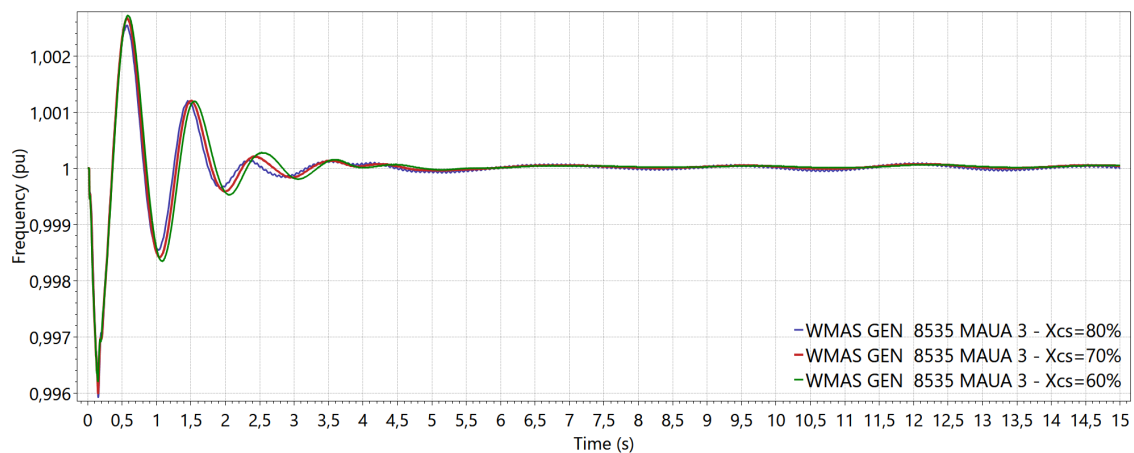
Figure 7.77: Frequency (pu) at the TPS Mauá 3 following a short-circuit at Lechuga 500 kV

An interesting issue, regarding the multiple turbine-generator shaft representation, is the situation in which the isolated SSR analysis does not present instability. However, in a context with multiple synchronous machines, numerous controllers, and individualized shaft representation, the nonlinear interaction between them could reveal adverse interactions in the subsynchronous range. The simulation results presented in this item, considering detailed controllers associated with multiple synchronous machines, show that the dynamic phasor-based models, developed in the ANATEM, support the SSR analysis in a large-scale power system with multiple turbine-generator shaft representation.

For the purpose of illustrating the dynamic behavior of the multiple TPS (listed in Table 7.16), Figure 7.78 presents the frequencies of the LPB, GEN, and EXC masses, following a short-circuit at Lechuga 500 kV and considering 60% of series compensation between Lechuga 500 kV and Jurupari 500 kV.
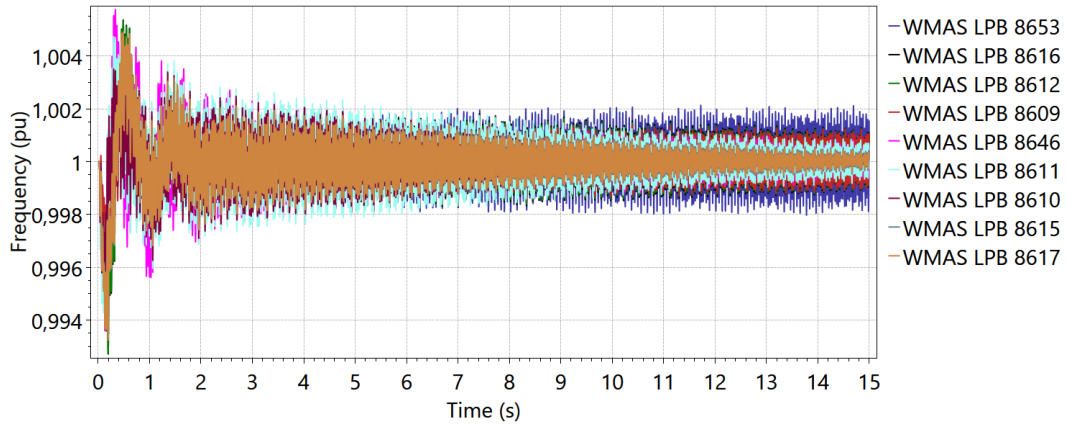
(a) $X_{CS} = 60\%$: frequency (pu) of the LPB mass
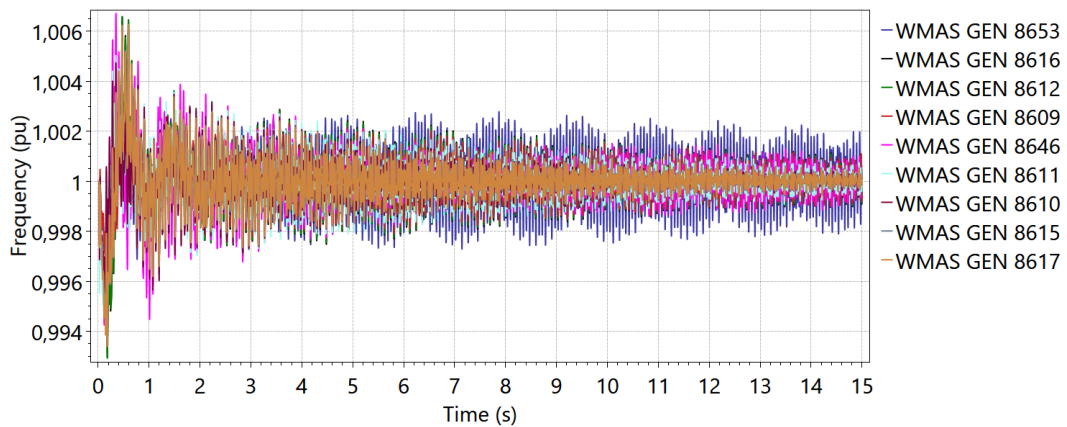
(b) $X_{CS} = 60\%$: frequency (pu) of the GEN mass
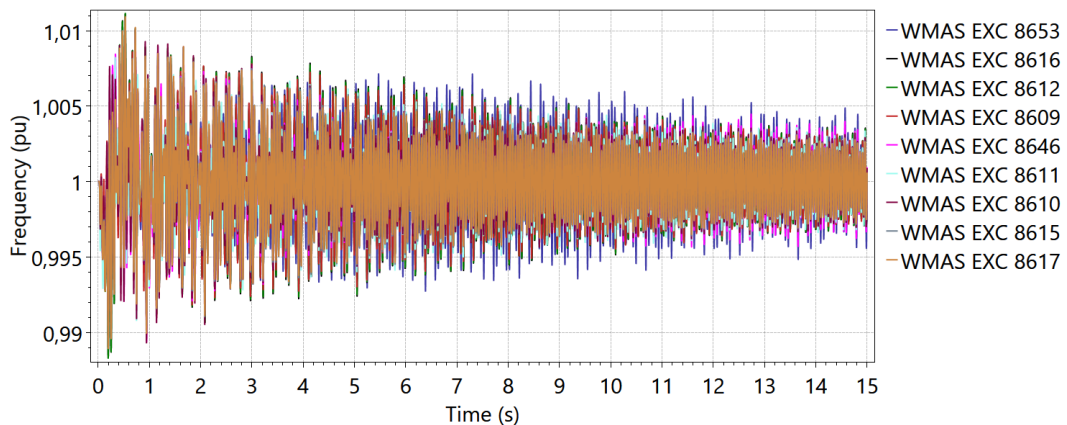
(c) $X_{CS} = 60\%$: frequency (pu) of the EXC mass

Figure 7.78: $X_{CS} = 60\%$: comparison of the frequency at multiple TPS following the short-circuit at Lechuga 500 kV

Figure 7.79 presents the comparison of the LPB, GEN, and EXC frequencies of the multiple TPS listed in Table 7.16, following a short-circuit at Lechuga 500 kV and considering 70% of series compensation between Lechuga 500 kV and Jurupari 500 kV.
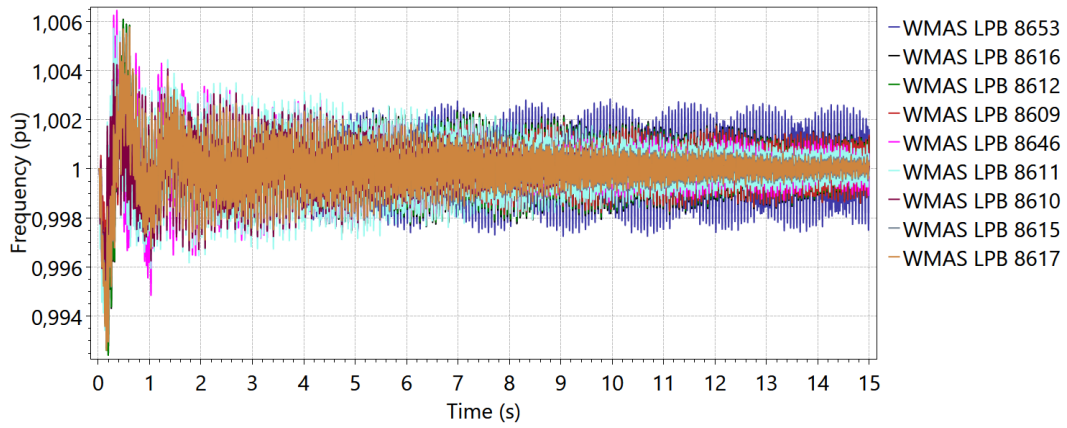
(a) $X_{CS} = 70\%$: frequency (pu) of the LPB mass
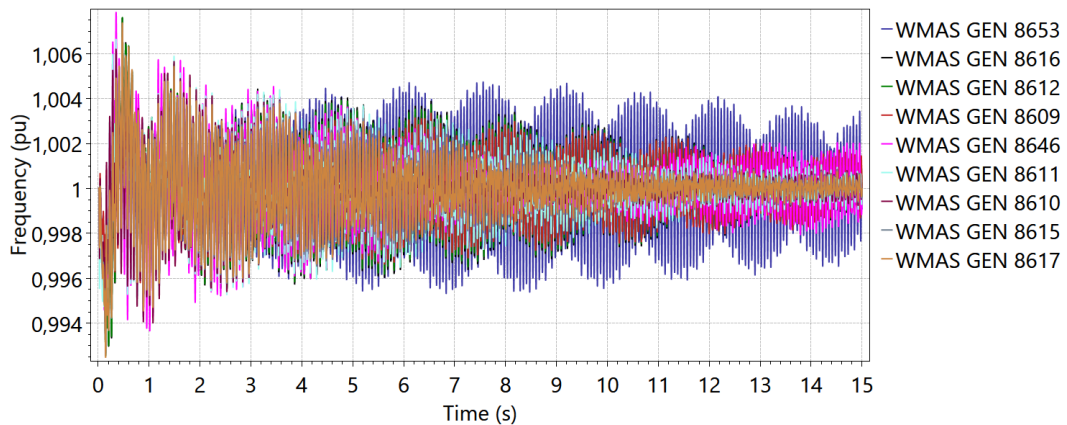
(b) $X_{CS} = 70\%$: frequency (pu) of the GEN mass
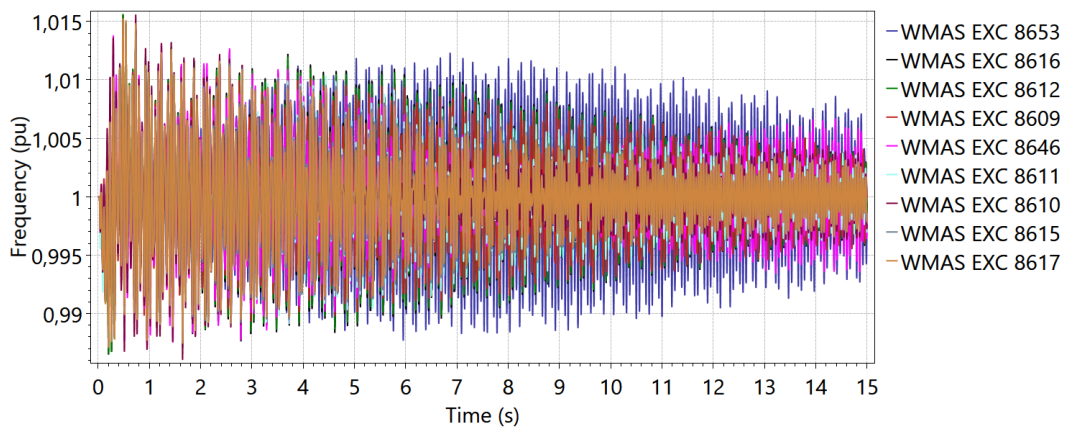
(c) $X_{CS} = 70\%$: frequency (pu) of the EXC mass

Figure 7.79: $X_{CS} = 70\%$: comparison of the frequency at multiple TPS following the short-circuit at Lechuga 500 kV

Figure 7.80 presents the comparison of the LPB, GEN, and EXC frequencies of the multiple TPS listed in Table 7.16, following a short-circuit at Lechuga 500 kV and considering 80% of series compensation between Lechuga 500 kV and Jurupari 500 kV.
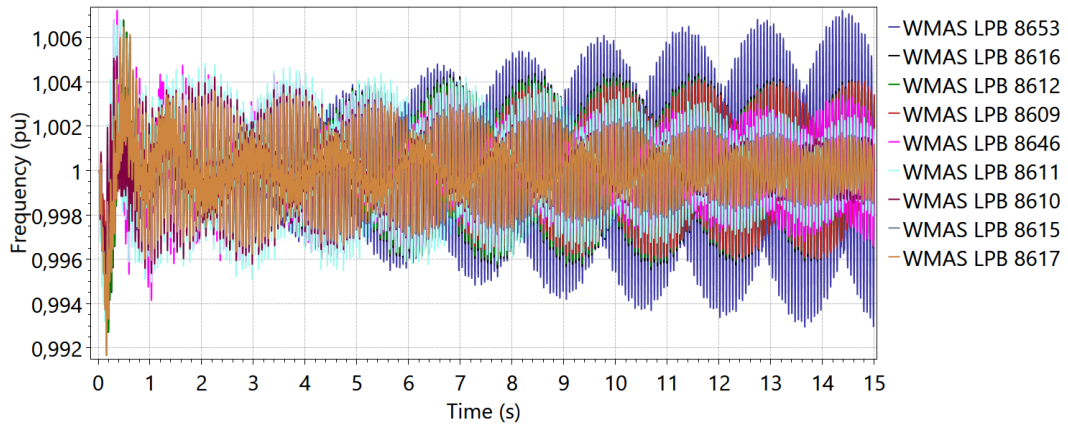
(a) $X_{CS} = 80\%$: frequency (pu) of the LPB mass
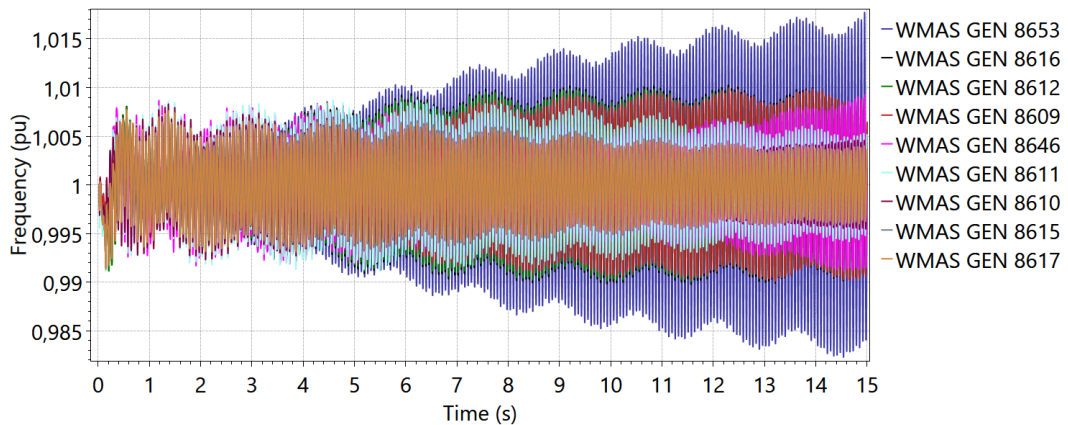
(b) $X_{CS} = 80\%$: frequency (pu) of the GEN mass
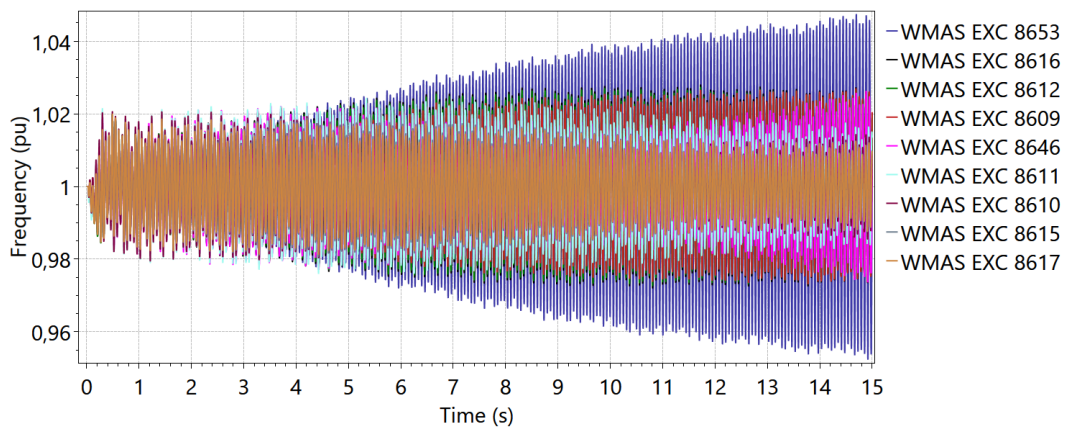
(c) $X_{CS} = 80\%$: frequency (pu) of the EXC mass

Figure 7.80: $X_{CS} = 80\%$: comparison of the frequency at multiple TPS following the short-circuit at Lechuga 500 kV

Figures 7.78 to 7.80 show that at 80% of series compensation, a clear unstable subsynchronous oscillation at 16 Hz can be observed in the rotor masses, most accentuated in the exciter mass. The modal analysis of this turbine-generator shaft (Section 7.1.2) has shown that the 16 Hz mode presented a more significant activity at the exciter (EXC) and high pressure turbine (HP), which could also be observed in this case study. One can see that the multiple turbine-generator shafts experience the SSR phenomenon on different levels, and that increasing the series compensation to 80% cause the damping of the torsional modes of 16 Hz to become negatively damped for most of the TPS.

It should be emphasized that the representation of the network dynamics, the stator flux dynamics, the rotor speed variation, the machine controllers, and multiple turbine-generator shaft models into an integrated simulation tool allows studying phenomena of multiple frequency ranges in a multi-machine power system. This general-purpose simulation environment has been validated and explored in this thesis by implementing the dynamic phasor-based models in the ANATEM software.

Chapter 8

Conclusions and Future Researches

8.1 Conclusions

In this thesis, a simulation methodology to perform nonlinear time-domain analysis of electromechanical and electromagnetic transients has been developed into a phasor-domain tool. A comprehensive theoretical review dealing with the dynamic phasor theory and the tensor analysis has been presented in Chapters 1 and 2. It has formed the basis for the development, in Chapter 3, of the Dynamic Phasor Companion Models (DPCM), which accurately represent fast transients in linear electrical networks.

The DPCM technique provides a direct interface with the phasor-domain synchronous machine model suitable for Electromagnetic Transient Analysis (EMT). In this thesis, the DPCM does not account for the three-phase representation; rather, it constitutes an intermediate simulation environment for the analysis of fast transients in balanced transmission systems along with steady-state initialization and compatibility with the electromechanical stability database for the synchronous machine and associated controllers. Therefore, a simulation model for synchronous machines have been extensively approached in Chapter 4, including the stator flux transients (the transformer effect), the rotor speed variation, and the subtransient saliency, which are details commonly neglected in conventional Electromechanical Stability Analysis (ESA). This level of detail makes possible the analysis of interactions between the synchronous machines, the electrical network, and controllers in a frequency band above the electromechanical range.

Therefore, the network dynamics and the detailed synchronous machine models have

been implemented in a traditional phasor-domain tool, the ANATEM software, considering the dynamic phasor approach and automatic initialization from the steady-state operating point provided by a power flow analysis tool - ANAREDE. It has been verified that the representation of the electrical network and the stator transients extended the ANATEM simulation scope towards the subsynchronous range. For this reason, the multi-mass turbine-generator shaft model, formulated in Chapter 5, has also been developed in the ANATEM software. As a result, the study of Subsynchronous Resonance (SSR) due to interactions between torsional oscillation frequencies of the rotor shaft and series compensated transmission systems also became possible through the ANATEM.

The simulation results, regarding the mathematical models developed in this thesis, have presented a good agreement with the results obtained through the three-phase instantaneous representation by using the PSCAD/EMTDC software, which is a traditional EMT tool. Therefore, it has been validated, in Chapter 6, that the fundamental dynamic phasor representation accurately captures fast transients following balanced disturbances in the electrical network and synchronous machines.

As demonstrated in Chapter 7, the dynamic phasor-based module of the ANATEM software provides an integrated simulation environment for the study of transients in multiple frequency ranges, so that it can accurately capture electromechanical, subsynchronous and electromagnetic phenomena in linear and balanced transmission systems. In this same chapter, the application of this general-purpose simulation tool in a test system adapted from the Brazilian Interconnected Power System (BIPS) has demonstrated that the developments of this thesis can handle large-scale power systems. In addition, the analytical expressions of the dynamic phasor-based models present a direct interface with linear analysis tools.

This thesis also concluded that the DPCM automatic initialization from the steady-state operating point supports the analysis of multiple power system scenarios without requiring a previous time-domain simulation to generate a snapshot file subsequent to the power system energizing. Apart from that, three-phase tools may require different adjustments of controllers in the initialization process, as well as the preparation of equivalent regions for the analysis of EMT and SSR phenomena, making it challenging to analyze multiple power system scenarios, topologies, and multi-machine systems.

In the SSR study of a large-scale power system adapted from the BIPS, it was shown that the compatibility of the dynamic phasor-based models of the ANATEM software with the ONS Electromechanical Database for the synchronous power plants permits evaluating the dynamic behavior of multi-machine power systems. Several other

works have presented linear and nonlinear SSR analysis through equivalent test systems, but in this thesis, an SSR study using a 6972-bus system showed that this tool could reveal valuable information concerning network switching and large disturbances. Furthermore, it can also reveal interactions between the mechanical system of turbogenerators with any network equipment or controller that presents oscillation frequencies in the subsynchronous range.

8.2 Future Researches

This work has developed a hybrid interface between ESA and EMT models for nonlinear time-domain simulation in the ANATEM software. It brings a series of advantages and possibilities for studying fast transients into complex power systems. Throughout the text, some limitations have been pointed out and they are enumerated below as directions for future researches:

- Evaluate the impact of a hybrid representation of the network dynamics by using the DPCM models and the static network representation in large-scale power systems. This study has been proposed, in Chapter 6, to represent a portion of the electrical network with dynamics by using the DPCM models, and the remainder with the conventional ESA modeling. This analysis could be conducted by using the `DRDN` execution code along with the `DINR` execution option, both developed in this thesis into the ANATEM software;

- In this thesis, the application of the DSS Interface Routines from the MKL library allowed the evaluation of the DPCM solution algorithm in a simple and didactic computational structure. However, in the nonlinear SSR analysis of a large-scale power system, the computational burden due to the small time step-size employed in the time-domain simulations, and the large number of components included in a 6972-bus system, demanded near to five hours to run a 15-second EMT simulation. Therefore, more efficient computational methods shall be explored for the sparse construction, ordination, and factorization in the electrical network solution algorithm. Furthermore, the parallelization of general alternating solution scheme of the ANATEM software, and the application of variable step-size algorithms are also envisioned to speed up the total simulation time;

- At this stage, the ANATEM software holds a hybrid ESA and EMT simulation environment within a compatible dynamic phasor interface. Therefore, it is possible to extend the dynamic phasor approach, in the ANATEM, considering high-frequency transients of other network equipment, for instance,

SVC, HVDC, and VSC models. As demonstrated in Chapter 7, it is expected that including the high-frequency model of the STATCOM using fundamental dynamic phasors would provide, in balanced transmission systems, dynamic behavior in good agreement with the time-domain response obtained using EMT tools. In this regard, significant future work could be carried out to increase the set of dynamic phasor-based models into the ANATEM;

- Study an adequate interface between the DPCM solution algorithm and the representation of wind and photovoltaic sources to allow the time-domain simulation using the ESA models of these sources. In addition, the EMT representation for these sources could also be evaluated by using the dynamic phasor approach;

- Considering the synchronous machine model for SSR analysis, a future work should investigate the slightly difference observed in the rotor speed in comparison with the three-phase synchronous machine of the PSCAD/EMTDC;

- In this thesis, a positive-sequence network representation is employed under the premise of a three-phase balanced system. This assumption allowed accurate simulation of fast transients induced in the network as a result of balanced faults. The detailed EMT analysis of unbalanced networks or fast transients following unbalanced faults could be addressed by applying a three-phase dynamic phasor representation, either using positive, negative, and zero sequence components or abc phase components.

Bibliography

[1] KUNDUR, P., BALU, N. J., LAUBY, M. G. *Power system stability and control*, v. 7. New York, McGraw-hill, 1994.

[2] DOMMEL, H. W. *Electromagnetic transients program: reference manual:(EMTP theory book)*. Bonneville Power Administration, 1986.

[3] MAHSEREDJIAN, J., DEWHURST, C. "EMTP-RV user manual", *Powersys, Jan*, 2016.

[4] *PSCAD/EMTDC user's manual*, tutorial manual ed. Manitoba, Research Centre, 1994.

[5] *Manual do Usuário do Programa de Análise de Transitórios Eletromecânicos - Anatem*, v11-07-00 ed. Cepel, 2019.

[6] SIEMENS, P. "Pss/e User-Manual", *Version 33.4, March 2013*, 2010.

[7] ANDERSON, P. M., AGRAWAL, B. L., VAN NESS, J. E. *Subsynchronous resonance in power systems*, v. 9. John Wiley & Sons, 1999.

[8] VERGHESE, G. C., ELBULUK, M. E., KASSAKIAN, J. G. "A general approach to sampled-data modeling for power electronic circuits", *IEEE Transactions on Power Electronics*, , n. 2, pp. 76–89, 1984.

[9] MATTAVELLI, P., VERGHESE, G. C., STANKOVIC, A. M. "Phasor dynamics of thyristor-controlled series capacitor systems", *IEEE Transactions on Power Systems*, v. 12, n. 3, pp. 1259–1267, 1997.

[10] GOMES JR, S., STANKOVIC, A. M. *Modeling of SVC and TCSC Using Dynamic Phasors*. Relatório técnico, DP/DSE-32962/04 Pós-doutorado na Northeastern University - Departamento de Sistemas Elétricos – Centro de Pesquisa de Energia Elétrica (Cepel), 2004.

[11] LIRIO, F. L. "Modelagem Tensorial de SVC e TCSC no Domínio s para Análise Linear de Transitórios Eletromagnéticos e Harmônicos". Universidade Federal do Rio de Janeiro, Rio de Janeiro, COPPE, 2007.

[12] DANIEL, L. D. O. *Simulador de Transitórios Eletromagnpeticos Utilizando Fasores Dinâmicos para Análise Não-Linear de Redes Elétricas com Equipamentos FACTS*. Tese de Doutorado, Universidade Federal do Rio de Janeiro, 2018.

[13] BURDEN, R. L., FAIRES, J. D. "Numerical Analysis, Brooks", *Cole Pub*, v. 7, 1997.

[14] DOMMEL, H. W. "Digital computer solution of electromagnetic transients in single-and multiphase networks", *IEEE transactions on power apparatus and systems*, , n. 4, pp. 388–399, 1969.

[15] DOMMEL, H. W., MEYER, W. S. "Computation of electromagnetic transients", *Proceedings of the IEEE*, v. 62, n. 7, pp. 983–993, 1974.

[16] ZANETTA JR, L. C. *Transitórios eletromagnéticos em sistemas de potência*. Editora EdUsp, São Paulo, 2003.

[17] UNDRILL, J. M. "Structure in the computation of power-system nonlinear dynamical response", *IEEE Transactions on Power Apparatus and Systems*, , n. 1, pp. 1–6, 1969.

[18] DOMMEL, H., SATO, N. "Fast transient stability solutions", *IEEE Transactions on Power Apparatus and Systems*, , n. 4, pp. 1643–1650, 1972.

[19] YOUNG, C. "Equipment and system modeling for large-scale stability studies", *IEEE Transactions on Power Apparatus and Systems*, , n. 1, pp. 99–109, 1972.

[20] STOTT, B. "Power system dynamic response calculations", *Proceedings of the IEEE*, v. 67, n. 2, pp. 219–241, 1979.

[21] SANDERS, S. R., NOWOROLSKI, J. M., LIU, X. Z., et al. "Generalized averaging method for power conversion circuits", *IEEE Transactions on Power Electronics*, v. 6, n. 2, pp. 251–259, 1990.

[22] PORTELA, C. M. "Análise de Redes Elétricas: Algumas Aplicações", *Lisboa, Portugal*, 1970.

[23] GOMES JR, S. "Modelagem e Métodos Numéricos para Análise Linear de Estabilidade Eletromecânica, Ressonância Subsíncrona, Transitórios Eletro-

magnéticos e Desempenho Harmônico de Sistemas de Potência". Universidade Federal do Rio de Janeiro, 2002.

[24] MIDDLEBROOK, R. "Small-signal modeling of pulse-width modulated switched-mode power converters", *Proceedings of the IEEE*, v. 76, n. 4, pp. 343–354, 1988.

[25] XU, J., YU, J. "Time-averaging equivalent circuit analysis of a resonant switching converter", *International Journal of Electronics Theoretical and Experimental*, v. 67, n. 6, pp. 937–948, 1989.

[26] DEMARCO, C. L. *Bringing phasor dynamics into the power system load flow.* University of Wisconsin, Engineering Experiment Station, 1993.

[27] MATTAVELLI, P., STANKOVIC, A. M., VERGHESE, G. C. "SSR analysis with dynamic phasor model of thyristor-controlled series capacitor", *IEEE Transactions on Power Systems*, v. 14, n. 1, pp. 200–208, 1999.

[28] STANKOVIĆ, A., MATTAVELLI, P., CALISKAN, V., et al. "Modeling and analysis of FACTS devices with dynamic phasors". In: *IEEE Power Engineering Society Winter Meeting*, 2000.

[29] GOMES JR, S., MARTINS, N., STANKOVIC, A. "Improved controller design using new dynamic phasor models of SVC's suitable for high frequency analysis". In: *Transmission and distribution conference and exposition, Dallas*, pp. 22–24, 2006.

[30] DE SOUZA, L. F. W. "Modelagem Analítica de um GCSC - Capacitor Série Controlado por Chave Autocomutada". Universidade Federal do Rio de Janeiro, Rio de Janeiro, COPPE, 2007.

[31] DEMIRAY, T., ANDERSSON, G. "Simulation of Power Systems Dynamics Using Dynamic Phasor Model". In: *X Simpósio de Especialistas em Planejamento da Operação e Expansão Elétrica, 2006. SNPTEE*, p. 10. X SNPTEE, 2006.

[32] DEMIRAY, T. *Simulation of power system dynamics using dynamic phasor models.* Tese de Doutorado, ETH Zurich, 2008.

[33] HENSCHEL, S. *Analysis of electromagnetic and electromechanical power system transients with dynamic phasors.* Tese de Doutorado, University of British Columbia, 1999.

[34] KULASZA, M. *Generalized dynamic phasor-based simulation for power systems.* Master thesis, University of Manitoba, 2014.

[35] GROUP, I. S. R. W., OTHERS. "Terms, definitions and symbols for subsynchronous oscillations", *IEEE Transactions on Power Apparatus and Systems*, v. 104, n. 6, pp. 1326–1334, 1985.

[36] JUSAN, F. C. *Análise Linear de Oscilações Subsíncronas em Sistemas Elétricos de Potência.* Tese de Mestrado, Universidade Federal do Rio de Janeiro, Rio de Janeiro, COPPE, 2007.

[37] *Manual do Usuário do Programa de Análise de Redes Elétricas - Anarede*, v11-02-00 ed. Cepel, 2019.

[38] ON TERMS & DEFINITIONS, T. F., SUBCOMMITTEE, S. D. P., COMMITTEE, P. S. E. "Proposed Terms and Definitions for Power System Stability", *IEEE Transactions on Power Apparatus and Systems*, v. 101, n. 7, pp. 1894–1898, 1982.

[39] KUNDUR, P., PASERBA, J., AJJARAPU, V., et al. "Definition and classification of power system stability", *IEEE Transactions on Power Systems*, v. 19, n. 2, pp. 1387–1401, 2004.

[40] CLOSE, C. M. *The analysis of linear circuits.* Harcourt Brace Jovanovich, 1966.

[41] DOMMEL, H. W. "Nonlinear and time-varying elements in digital simulation of electromagnetic transients", *IEEE Transactions on Power Apparatus and Systems*, , n. 6, pp. 2561–2567, 1971.

[42] BRANIN, F. H. "Computer methods of network analysis", *Proceedings of the IEEE*, v. 55, n. 11, pp. 1787–1801, 1967.

[43] GRAINGER, J. J., STEVENSON, W. D. *Power system analysis*, v. 67. McGraw-Hill New York, 1994.

[44] JOHNSON, W. *Transmission Lines and Networks.* McGraw-Hill, 1950.

[45] BEWLEY, L. V. *Traveling waves on transmission systems.* Dover, 1963.

[46] FUCHS, R. D. *Transmissão de energia elétrica: linhas aéreas*, v. 2. LTC, 1977.

[47] ANDERSON, P. M., FOUAD, A. A. *Power system control and stability.* John Wiley & Sons, 2008.

[48] KHAS' MINSKII, R. Z. "Necessary and sufficient conditions for the asymptotic stability of linear stochastic systems", *Theory of Probability & Its Applications*, v. 12, n. 1, pp. 144–147, 1967.

[49] MACHOWSKI, J., BIALEK, J. W., BUMBY, J. *Power system dynamics: stability and control.* John Wiley & Sons, 2011.

[50] GOMES JR, S., ALMEIDA, L. P., LIRIO, F. L., et al. "O novo Programa Computacional ANAHVDC para Simulação dos Múltiplos Elos HVDC do SIN considerando Transitórios Eletromecânicos e Eletromagnéticos". In: *XXV Simpósio de Especialistas em Planejamento da Operação e Expansão Elétrica, 2019. SNPTEE*, p. 9. XXV SNPTEE, 2019.

[51] LAUW, H. K., MEYER, W. S. "Universal machine modeling for the representation of rotating electric machinery in an electromagnetic transients program", *IEEE Transactions on Power Apparatus and Systems*, , n. 6, pp. 1342–1351, 1982.

[52] DE MELLO, F. *Dinâmica das Máquinas Elétricas I.* Eletrobras/UFSM, 1983.

[53] PARK, R. H. "Two-reaction theory of synchronous machines generalized method of analysis-part I", *Transactions of the American Institute of Electrical Engineers*, v. 48, n. 3, pp. 716–727, 1929.

[54] GROUP, I. S. R. W., OTHERS. "Proposed terms and definitions for subsynchronous oscillations", *IEEE Transactions on Power Apparatus and Systems*, v. 99, n. 2, pp. 506–511, 1980.

[55] GROUP, I. S. R. W., OTHERS. "Reader's guide to subsynchronous resonance", *IEEE Transactions on Power Systems*, v. 7, n. 1, pp. 150–157, 1992.

[56] WORKING GROUP, I. S., OTHERS. "First benchmark model for computer simulation of subsynchronous resonance", *IEEE transactions on power apparatus and systems*, v. 96, n. 5, pp. 1565–1572, 1977.

[57] BUTLER, J., CONCORDIA, C. "Analysis of series capacitor application problems", *Electrical Engineering*, v. 56, n. 8, pp. 975–988, 1937.

[58] CONCORDIA, C., CARTER, G. "Negative damping of electrical machinery", *Transactions of the American Institute of Electrical Engineers*, v. 60, n. 3, pp. 116–119, 1941.

[59] TWEEDIE, R., ABRAMS, H. "Electrical Features of the 1590 MW Coal-Slurry-Supplied Mohave Generating Station", *IEEE Transactions on Power Apparatus and Systems*, , n. 2, pp. 725–735, 1971.

[60] BALLANCE, J. W., GOLDBERG, S. "Subsynchronous resonance in series compensated transmission lines", *IEEE Transactions on Power Apparatus and Systems*, , n. 5, pp. 1649–1658, 1973.

[61] HEDIN, R., DANCY, R., STUMP, K. "An analysis of the subsynchronous interaction of synchronous machines and transmission networks". In: *Proceedings of the American Power Conference*, v. 35, pp. 1112–1119, 1973.

[62] WALKER, D., BOWLER, C., JACKSON, R., et al. "Results of subsynchronous resonance test at Mohave", *IEEE Transactions on Power Apparatus and Systems*, v. 94, n. 5, pp. 1878–1889, 1975.

[63] EREMIA, M., LIU, C.-C., EDRIS, A.-A. *Advanced solutions in power systems: HVDC, FACTS, and Artificial Intelligence.* John Wiley & Sons, 2016.

[64] TOMIM, M. A. *Análise de Estabilidade em Regime Permanente de Sistemas Elétricos Susceptíveis a Ressonância Subsíncrona.* Master thesis, Universidade Federal de Itajubá, 2004.

[65] AGRAWAL, B., FARMER, R. "Use of frequency scanning techniques for subsynchronous resonance analysis", *IEEE Transactions on Power Apparatus and Systems*, , n. 2, pp. 341–349, 1979.

[66] GROUP, I. S. R. W., OTHERS. "Countermeasures to subsynchronous resonance problems", *IEEE Transactions on Power Apparatus and Systems*, v. 99, n. 5, pp. 1810–1818, 1980.

[67] MORTENSEN, K., LARSEN, E., PIWKO, R. "Field tests and analysis of torsional interaction between the coal creek turbine-generators and the CU HVDC system", *IEEE Transactions on Power Apparatus and Systems*, , n. 1, pp. 336–344, 1981.

[68] *User's Manual: PacDyn Version 9.8.3*, v09.08.03 ed. Cepel, 2017.

[69] *Intel Math Kernel Library - Developer Reference*, revision: 021 ed. Intel, 2019.

[70] VARRICCHIO, S. L., GOMES JR., S., VÉLIZ, F. C., et al. "Método de Newton-Raphson para Utilização de Dados de Fluxo de Potência na Modelagem de Linhas de Transmissão para Estudos de Comportamento Har-

mônico de Sistemas de Potência", *V Seminário Brasileiro sobre Qualidade da Energia Elétrica*, 2003.

[71] VARRICCHIO, S., CAMPELLO, T. "Compatibility among Electrical Network Component Models of Computational Power System Analysis Programs", *IEEE Latin America Transactions*, v. 17, n. 05, pp. 833–842, 2019.

[72] FARMER, R., SCHWALB, A., KATZ, E. "Navajo project report on subsynchronous resonance analysis and solutions", *IEEE Transactions on Power Apparatus and Systems*, v. 96, n. 4, pp. 1226–1232, 1977.

[73] LEE, D., KUNDUR, P. "Advanced excitation controls for power system stability enhancement", *CIGRÉ paper*, v. 38, n. 1, 1986.

[74] RANGEL, R. D. *Modelagem de equipamentos FACTS baseados em inversores de tensão para análise de fluxo de potência e fenômenos eletromecânicos*. Tese de Doutorado, Tese de D. Sc., COPPE/UFRJ, Rio de Janeiro, RJ, Brasil, 2004.

[75] DA SILVA, M. P., LIRIO, F. L., GOMES, S., et al. "Evaluation of STATCOM model for electromagnetic and electromechanical transients". In: *2018 Simposio Brasileiro de Sistemas Elétricos (SBSE)*, pp. 1–6. IEEE, 2018.

[76] *Expansion and Reinforcement Planning - PAR2023*. Operador Nacional do Sistema Elétrico, March, 2019 (accessed March 25, 2019). Disponível em: <http://www.ons.org.br/>.

[77] *Electromechanical Stability Database*. Operador Nacional do Sistema Elétrico, March, 2019 (accessed November 3, 2019). Disponível em: <http://www.ons.org.br/>.

Appendix A

Demonstrations

A.1 Equivalent Quadripole of the Bergeron Model

This appendix describes the methodology adopted, in this work, to obtain an equivalent quadripole of long transmission lines compatible with the Bergeron model for steady-state analysis. The equivalent quadripole of the Bergeron model is acquired from standard steady-state parameters using the methodology proposed in [70, 71].

Long transmission lines are usually represented by the equivalent-π model in power flow analysis software, as illustrated in Figure A.1. In this regard, the line parameters are subject to the hyperbolic correction in terms of the line-length, the nominal parameters, and the nominal frequency of the electrical system.

Equivalent-pi model

$$z_s = \sqrt{(z_{nl}/y_{nl})}$$

$$\gamma = \sqrt{(z_{nl} \cdot y_{nl})}$$

Surge impedance and attenuation constant

$$z_l = z_s \cdot \sinh(\gamma l)$$

$$\frac{y_{sh}}{2} = \frac{1}{z_s} \cdot \tanh\left(\gamma l/2\right)$$

Parameters from the equivalent-pi model
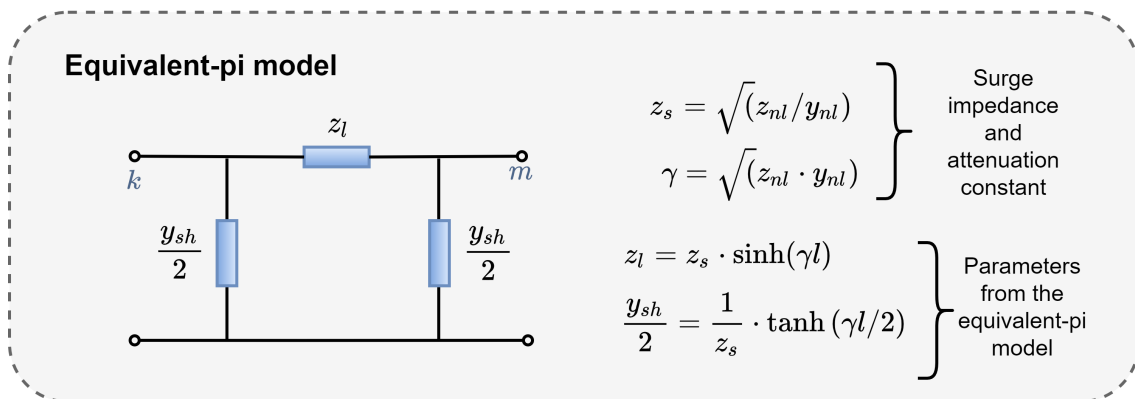
Figure A.1: Standard parameters of long transmission lines in power flows analysis tools

In this thesis, the new execution option `DINR` has been implemented in the ANAREDE software to obtain the nominal parameters of long transmission lines.

Thereby, the nominal parameters z_{nl} and y_{nl} (defined in Figure A.2) are inferred via the `PARNOM` method [70] from the standard steady-state parameters, which are the series inductance, series resistance and line-charging (input data for transmission lines in the ANAREDE software). In this operation, the `PARNOM` conversion is only applied over transmission lines that possess line-charging, and whose equivalent time travel τ is higher than the `MINTAU` parameter. In addition, the parameters z_{nl} and y_{nl} are obtained for the total line-length since the `PARNOM` method does not require the line-length to perform the per unit length calculation of the nominal parameters.
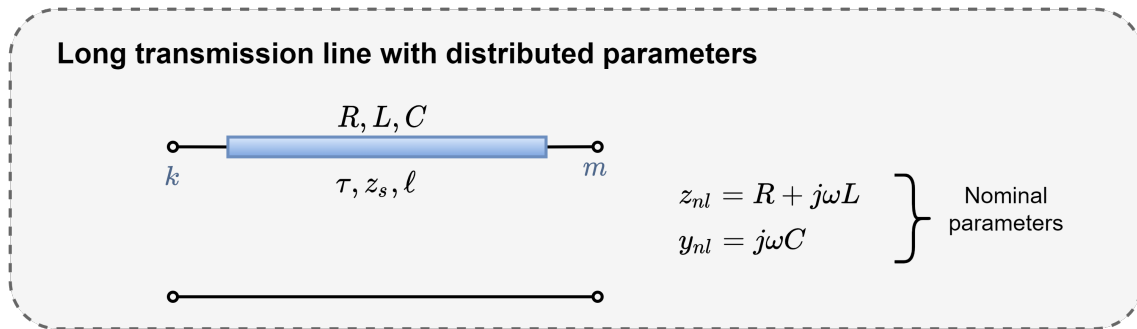
Figure A.2: Nominal parameters of a long transmission line

z_{nl} = total nominal series impedance

y_{nl} = total nominal series admittance

Therefore, the Bergeron model is built by using the nominal parameters, as illustrated in Figure A.3. The nodes 1 to 6 are defined in this same figure for the application of nodal analysis. In this case, the resistance losses are concentrated between two half lossless lines, as detailed in Section 2.4.4.2.
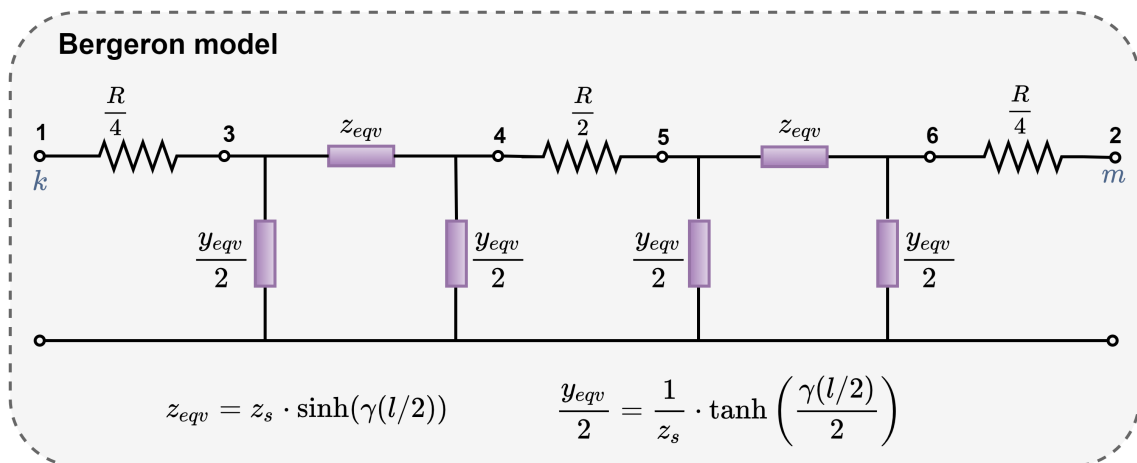
Figure A.3: Bergeron model

In Figure A.3, the nodes 1 and 2 are strategically placed in the line-ends in order to obtain an equivalent quadripole that directly correlates currents and voltages

between these two terminals. Therefore, the nodal admittance matrix corresponding to this system is given by:

$$
\mathbf{Y}_{\text{bus}} =
\left[
\begin{array}{cc|c|c|c|c}
\frac{4}{R} & 0 & -\frac{4}{R} & 0 & 0 & 0 \\
0 & \frac{4}{R} & 0 & 0 & 0 & -\frac{4}{R} \\
\hline
-\frac{4}{R} & 0 & \frac{4}{R} + \frac{1}{z_{eqv}} + \frac{y_{eqv}}{2} & -\frac{1}{z_{eqv}} & 0 & 0 \\
0 & 0 & -\frac{1}{z_{eqv}} & \frac{2}{R} + \frac{1}{z_{eqv}} + \frac{y_{eqv}}{2} & -\frac{2}{R} & 0 \\
\hline
0 & 0 & 0 & -\frac{2}{R} & \frac{2}{R} + \frac{1}{z_{eqv}} + \frac{y_{eqv}}{2} & -\frac{1}{z_{eqv}} \\
0 & -\frac{4}{R} & 0 & 0 & -\frac{1}{z_{eqv}} & \frac{4}{R} + \frac{1}{z_{eqv}} + \frac{y_{eqv}}{2}
\end{array}
\right]
$$
$$(\text{A.1})$$

From (A.1), the following submatrices are defined:

$$
Y_{\text{bus}} =
\left[
\begin{array}{cc}
\mathbf{M} & \mathbf{N} \\
\mathbf{O} & \mathbf{P}
\end{array}
\right]
\tag{A.2}
$$

Where:

$$
\mathbf{M} =
\left[
\begin{array}{cc}
\frac{4}{R} & 0 \\
0 & \frac{4}{R}
\end{array}
\right]
\tag{A.3}
$$

$$
\mathbf{N} =
\left[
\begin{array}{cccc}
-\frac{4}{R} & 0 & 0 & 0 \\
0 & 0 & 0 & -\frac{4}{R}
\end{array}
\right]
\tag{A.4}
$$

$$
\mathbf{O} =
\left[
\begin{array}{cc}
-\frac{4}{R} & 0 \\
0 & 0 \\
0 & 0 \\
0 & -\frac{4}{R}
\end{array}
\right]
= \mathbf{P}^{T}
\tag{A.5}
$$

$$
\mathbf{P} =
\left[
\begin{array}{cccc}
\left(\frac{4}{R} + \frac{1}{z_{eqv}} + \frac{y_{eqv}}{2}\right) & -\frac{1}{z_{eqv}} & 0 & 0 \\
-\frac{1}{z_{eqv}} & \left(\frac{2}{R} + \frac{1}{z_{eqv}} + \frac{y_{eqv}}{2}\right) & -\frac{2}{R} & 0 \\
0 & -\frac{2}{R} & \left(\frac{2}{R} + \frac{1}{z_{eqv}} + \frac{y_{eqv}}{2}\right) & -\frac{1}{z_{eqv}} \\
0 & 0 & -\frac{1}{z_{eqv}} & \left(\frac{4}{R} + \frac{1}{z_{eqv}} + \frac{y_{eqv}}{2}\right)
\end{array}
\right]
$$
$$(\text{A.6})$$

Then, the reduced admittance matrix $\mathbf{Y}'_{2\times2}$ corresponding to the equivalent quadripole of the Bergeron model is obtained by employing the Kron reduction over (A.1), and retaining the terminals respective to the line-ends. This procedure results in the following expression:

$$\mathbf{Y}'_{2\times2} = \mathbf{M} - \mathbf{N} \times \mathbf{P}^{-1} \times \mathbf{O} \tag{A.7}$$

At this point, it is noted that the submatrix $\mathbf{P}$ presents the symmetry property illustrated in (A.8).

$$\mathbf{P} = \begin{bmatrix} a & b & & \\ b & c & d & \\ & d & c & b \\ & & b & a \end{bmatrix} \tag{A.8}$$

Thus, the inverse matrix $\mathbf{P}^{-1}$ can be written, as follows:

$$\mathbf{P}^{-1} = \frac{1}{\Delta} \begin{bmatrix} \alpha_1 & \alpha_2 & \alpha_3 & \alpha_4 \\ \alpha_2 & \alpha_5 & \alpha_6 & \alpha_3 \\ \alpha_3 & \alpha_6 & \alpha_5 & \alpha_2 \\ \alpha_4 & \alpha_3 & \alpha_2 & \alpha_1 \end{bmatrix} \tag{A.9}$$

Where:

$$\Delta = a^2(c^2 - d^2) + b^2(b^2 - 2 \cdot a \cdot c) \tag{A.10}$$
$$\alpha_1 = a(c^2 - d^2) - b^2 \cdot c \tag{A.11}$$
$$\alpha_2 = b^3 - a \cdot c \cdot b \tag{A.12}$$
$$\alpha_3 = a \cdot b \cdot d \tag{A.13}$$
$$\alpha_4 = -b^2 \cdot d \tag{A.14}$$
$$\alpha_5 = a(-b^2 + a \cdot c) \tag{A.15}$$
$$\alpha_6 = -a^2 \cdot d \tag{A.16}$$

Therefore, according to the methodology proposed in [71], the reduced admittance matrix $\mathbf{Y}'_{2\times2}$ is given by:

$$\mathbf{Y}'_{2\times2} = \begin{bmatrix} \frac{4}{R} & 0 \\ 0 & \frac{4}{R} \end{bmatrix} - \frac{1}{\Delta} \cdot \left(-\frac{4}{R}\right)^2 \cdot \begin{bmatrix} \alpha_1 & \alpha_4 \\ \alpha_4 & \alpha_1 \end{bmatrix} \tag{A.17}$$

The following constants are defined:

$$k_1 = \frac{16}{\Delta \cdot R^2} \cdot \alpha_1 \tag{A.18}$$

$$k_4 = \frac{16}{\Delta \cdot R^2} \cdot \alpha_4 \tag{A.19}$$

Rearranging (A.17) in terms of the constants defined in (A.18) and (A.19), the equivalent admittance matrix of the Bergeron model is:

$$\mathbf{Y'} = \begin{bmatrix} \frac{4}{R} - k_1 & -k_4 \\ -k_4 & \frac{4}{R} - k_1 \end{bmatrix} \tag{A.20}$$

One should note that the equivalent admittance matrix of the Bergeron model allows defining the "equivalent Bergeron-π circuit" depicted in Figure A.4. This structure is compatible with the traditional nodal analysis formulation so that it is employed for the solution of the new steady-state operating point when the Bergeron model must be taken into account.
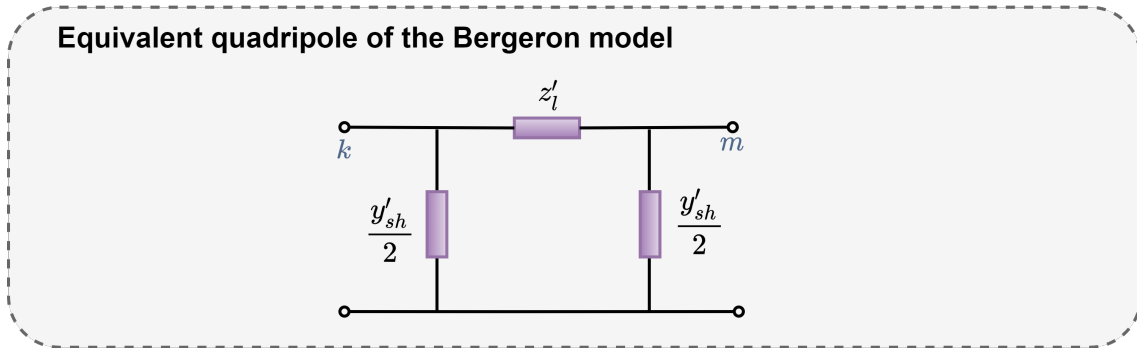
Figure A.4: Equivalent quadripole of the Bergeron model

Inferring the equivalent series impedance z'_l and parallel admittance y'_{sh} of the equivalent circuit of Figure A.4 by inspection of (A.20), yields the following equivalent parameters of the Bergeron-π model:

$$z'_l = \frac{1}{k_4} \tag{A.21}$$

$$\frac{y'_{sh}}{2} = \frac{4}{R} - k_1 - k_4 \tag{A.22}$$

After determining the nominal parameters of the line and building the equivalent Bergeron-π model, it is necessary to perform a new power flow solution with this

model to obtain a corresponding operating point to be utilized in the ANATEM time-domain solution. This representation is the most appropriate for the correct initialization of the Bergeron in the dynamic simulation of the ANATEM. However, if the power flow case utilized in the ANATEM does not account for the `DINR` conversion of the equivalent-π into the Bergeron-π model, then, the ANATEM performs this procedure using the `PARNOM` and the Kron reduction following the same steps detailed in this appendix; but, in this case, the ANATEM does not execute a new power flow solution, and the initial operating point of the dynamic simulation starts slightly different from the steady-state regime.

A.2   Linear Interpolation

In this thesis, the linear interpolation is employed to determine intermediary values of the time-domain response while performing the dynamic simulation with a fixed time-step size Δt. The intermediary values take place between two consecutive solution points.

In the ANATEM software, when the time-domain simulation considers network dynamics through Dynamic the Phasor Companion Models (DPCM), the history current sources (b_h) of distributed parameter lines hold a memory vector whose delay date back over the number of time steps that fits into the line travel time $[t - \tau]$, as shown in Figure A.5.
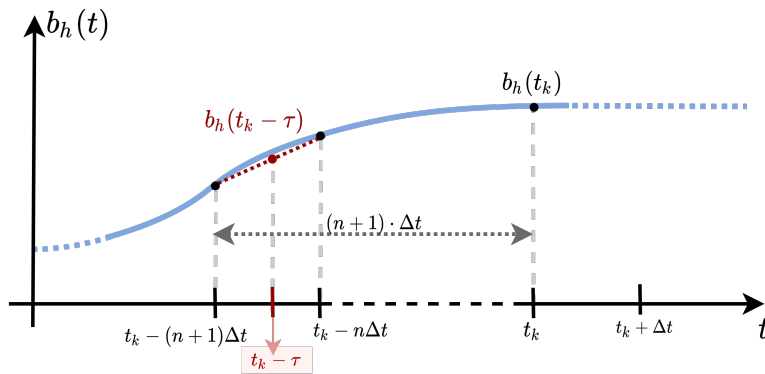
Figure A.5: Illustration of the Trapezoidal Integration

In this example, the travel time of a long transmission line is not a common multiple of Δt. In general terms, a travel time τ conforms x multiples of the time-step size, as follows:

$$x = \frac{\tau}{\Delta t} \tag{A.23}$$

From Figure A.5, one should note that if x is not an integer number, the travel

time τ would not be a common multiple of Δt. As a consequence, the line historical term $b_h(t_k - \tau)$ occurs between two subsequent discrete solutions at the instants $[t_k - (n+1) \cdot \Delta t]$ and $[t_k - n \cdot \Delta t]$, where t_k is the present simulation time, and the integer number n is defined as:

$$n = \lfloor x \rfloor \tag{A.24}$$

In other words, n is an integer number less than or equal to x. In such circumstances, the linear interpolation technique is employed to determine the intermediary value of the historical term $b_h(t_k - \tau)$. The size of the required memory vector to store the time-domain solutions of the line historical terms for linear interpolation is equal to $(n + 1)$.

For the sake of illustration, consider the generic function $f(t)$ shown in Figure A.6.
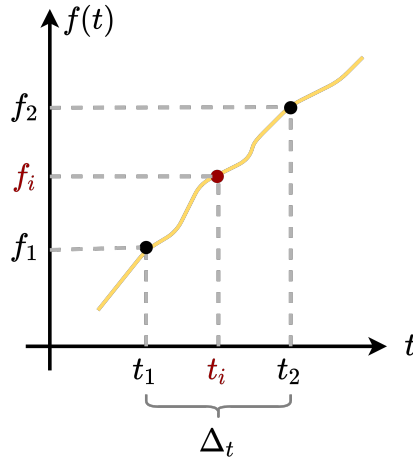
Figure A.6: Generic function $f(t)$

The intermediate value $f_i(t_i)$ at instant $t = t_i$ can be determined by the linear interpolation of the solutions determined at $t = t_1$ and $t = t_2$ through the triangle similarity property, as follows:

$$\frac{f_i - f_1}{f_2 - f_1} = \frac{t_i - f_1}{t_2 - t_1} \tag{A.25}$$

Resulting in the following expression for $f_i(t_i)$:

$$f_i = \left(\frac{t_i - t_1}{t_2 - t_1} \right) \cdot (f_2 - f_1) + f_1 \tag{A.26}$$

Applying this generic case to the interpolation problem of the history current sources $b_h(t - \tau)$, the following terms are recognized:

$$f_1 = b_h \left(t_k - (n+1) \cdot \Delta t \right) \tag{A.27}$$

$$f_2 = b_h(t_k - n \cdot \Delta t) \tag{A.28}$$

$$t_i - t_1 = (n+1) \cdot \Delta t - \tau \tag{A.29}$$

$$t_2 - t_1 = \Delta t \tag{A.30}$$

The following constant is defined:

$$\alpha = \frac{t_i - t_1}{t_2 - t_1} = \left(n + 1 - \frac{\tau}{\Delta t} \right) \tag{A.31}$$

Therefore, the linear interpolation expression for the history source $b_h(t - \tau)$ can be written, as follows:

$$b_h(t - \tau) = \alpha \cdot (f_2 - f_1) + f_1 \tag{A.32}$$

$$\boxed{b_h(t - \tau) = \alpha \cdot \left[b_h(t_k - n\Delta t) - b_h \left(t_k - (n+1)\Delta t \right) \right] + b_h \left(t_k - (n+1)\Delta t \right)} \tag{A.33}$$

Appendix B

Electrical Network Data

The dynamic database of the test systems that have been simulated in the ANATEM software are detailed in this appendix.

B.1   IEEE 14-Bus Test System

The ANATEM dynamic database used in the simulation of the IEEE 14-Bus Test System is presented below:

```
( Case Title
TITU
* IEEE 14-Bus Test System *
( Input and output files
DARQ
( Output Data
(Tipo) (C) ( Nome do Arquivo
   OUT     ..\out\
   LOG     ..\log\
   PLT     ..\plt\
( Input Data: ANAREDE SAVECASE
(Tipo) (C) ( Nome do Arquivo
   HIS   1 ..\sav\sis14b.his
999999
( Generator Models
DMDG MD01
(No)   (L'd)(Ra )( H )( D )(MVA)Fr C
0101                              ( infinity bus )
999999
(
```

```
DMDG MD02
(No)    (CS) (Ld )(Lq )(L'd)       (L"d)(Ll )(T'd)       (T"d)(T"q)
0201      1 100.3 59.9 35.7       28.3 19.8 7.28       .050 .100
(No)    (Ra )( H )( D )(MVA)Fr C
0201       2.474       50.
(No)    (CS) (Ld )(Lq )(L'd)       (L"d)(Ll )(T'd)       (T"d)(T"q)
0202      2  94.6 62.1 31.0       27.4 20.2 8.13       .048 .140
(No)    (Ra )( H )( D )(MVA)Fr C
0202       3.588       72.
999999
(AVR Models
DRGT MD01
(No)    (CS) (Ka )(Ke )(Kf )(Tm )(Ta )(Te )(Tf )(Lmn)(Lmx)LS
0101      31  300. 3.00 0.30  0.0  0.0 6.00 3.00 -1.1 8.05ED
0102      32  408. 1.00.1046  0.0  0.0 1.00 3.17 -1.1 8.05EI
999999
DRGT MD12
(No)    (CS) (Ka )(Ke )(Kf )(Kp )(Ki )(Kg )(Tq )(Ta )(Te )(Tf1)(Tf2)
1201      33  25.0 -.05 .080   .0  1.0  1.0   .0  .20  .50  1.0   .0
(No)    (Ln1)(Lx1)(Ln2)(Lx2)(Ln3)(Lx3)L
1201     -1.0  1.0 -4.6  4.6   .0   .0D
(
999999
( Saturation curves
DCST
(Nc)   T ( P1  ) ( P2  ) (  P3  )
0001   2    0.016     8.198      0.8
0002   2    0.013      7.92      0.8
0031   2    0.0147    1.206
0032   2    0.024     1.36
0033   2    0.016     1.54
(
999999
( Speed Governor Models
DRGV MD01
(No)    ( R )(Rp )(At )(Qnl)(Tw )(Tr )(Tf )(Tg )(Lmn)(Lmx)(Dtb)( D )(Pbg)(Pbt)
0101    0.05 0.381.200 0.15  1.5  7.0 0.05  0.5  0.0 .984  0.5  1.0  1.0  1.0
999999
( Assocation of machine models and controls
DMAQ
( Nb)   Gr (P) (Q) Und ( Mg ) ( Mt )u( Mv )u( Me )u(Xvd)(Nbc)
```

```
   01   10             3    202    102    101
   02   10             1    201    102    101
   03   10             1    201    102
   06   10             1    201    102    101
   08   10             1    201    101
   12   10             1    201    101
   14   10             1    202   1201    101
999999
( Induction motors
DMOT
( Nb)  Gr ( H ) ( K0 ) ( K1 ) ( K2 ) ( EXP) M ( Mt )
   4   10    4.                   1.   1.52
   4   20    4.                   1.   1.52
   5   10    4.                   1.   1.52
   5   20    4.                   1.   1.52
999999
( Voltage dependent loads
DCAR IMPR
(tp) ( no) C (tp) ( no) C (tp) ( no) C (tp) ( no)   (A) (B) (C) (D) (Vmn)
BARR    1 A BARR  9998                              0  40   0 100    70
999999
( Under-frequency Load Shedding Scheme
DERA
(Ne) (tp) ( no) C (tp) ( no) C (tp) ( no) C (tp) ( no) ( Nb) (Fs ) (Fc ) O
0001 AREA    10 A AREA    30                                          A
( (Tax) (Fr ) ( %C) (Ttx) (Tre) (Tdj)
A      .9917   10        0.10  0.10
A      .9833   10        0.20  0.10
A      .9800   10        0.40  0.10
A      .9667   10        0.80  0.10
A      .9583   10        1.60  0.10
A      .9500   10        3.20  0.10
A      .9417   10        6.40  0.10
A      .9333   10       12.80  0.10
FIMERAC
999999
( Output plot variables
DPLT
(Tipo)M( El ) ( Pa) Nc Gp ( Br) Gr ( Ex) (Bl) P
DELT        2         10     1 10
PELE        2         10
```

```
999999
( Relay
DREL MD02
( De)   ( Pa) Nc ( Ne) (Cor) ( Ang) (Tre) (Tdj) M
    2      3              1.5   45.0  0.20  0.01 A
999999
( Simulation Events
DEVT
(Tp) ( Tempo)( El )( Pa)Nc( Ex) ( % ) (ABS ) Gr Und
APCL       1.    2   3     2    50
RMGR       1.    1                          10   2
999999
( Simulation Parameters
DSIM
( Tmax ) (Stp) ( P ) ( I ) ( F )
   30.00  .005     5
EXSI MDSS
(Simulation end
FIM
```

B.2   Base Test System for DPCM Validation

The ANATEM dynamic database used in the validation of the DPCM is presented below:

```
( Case Title
TITU
** DPCM Validation Case **
(
( Input and output data
DARQ
(Tipo) (C) ( Nome do Arquivo
HIS    50    mbinf.his
OUT
LOG
PLT
999999
(
( Filter for RMS measurement
DCDU
(ncdu) ( nome cdu )
```

```
   1    VOLT_FILTER
(nb)i(tipo)o(stip)s(vent) (vsai) ( p1 )( p2 )( p3 )( p4 ) (vmin) (vmax)
  1   IMPORT VOLT           VOLT1      1
  2   LEDLAG         VOLT1  VOLT1F    1          1    0.002
  3   SAIDA         VOLT1F
FIMCDU
999999
DLOC
(Lc)   (Tipo)( El )( Pa)Nc( Ex)Gr(Bl)
  1    BARRAC    1
999999
DCNE
(Nc)   ( Mc )u
 1          1u
999999
(
( Representing generators by infinite buses
GINF
(
( Defining RLC group
DRLC
( Nb ) (Gp) (U) (Vdef) (    R   ) (    L   ) (    C   ) (T)
  1    10            1000.
999999
(
( Simulation Events
DEVT
(Tp) ( Tempo)( El )( Pa)Nc( Ex) ( % ) (ABS ) Gr Und
LRLC   0.0500   1                        10
RRLC   0.1500   1                        10
999999
(
( Output variables
DPLT IERR
(Tipo)M( El ) ( Pa) Nc Gp ( Br) Gr ( Ex) (Bl) P
VOLT        1
VOLT        2
ILIN        1   2   1
V(T)        1
IL(T)       2   1   1
V(T)        1
```

```
IL(T)      2   1   1
999999
(
( Simulation parameters
DSIM
( Tmax ) (Stp) ( P ) ( I ) ( F )
    0.20 1e-5    1
(
( Simulation considering the network dynamics
EXSI DINR
(
FIM
```

B.3   IEEE First Benchmark

The ANATEM dynamic database used in the simulation of the IEEE First Benchmark Model for Subsynchronous Resonance is presented below:

```
( Case Title
TITU
** The IEEE First Benchmark Model **
DARQ
(Tipo) (C) ( Nome do Arquivo
OUT         .\OUT\
PLT
SAV    12   fbm.sav
999999
( Infinite Bus Data
DMDG MD01
(No) O (L'd)(Ra )( H )( D )(MVA)Fr
0001                         60
999999
( SYnchronous Machine Model
DMDG MD03 MRSS
(No)   (CS) (Ld )(Lq )(L'd)(L'q)(L"d)(Ll )(T'd)(T'q)(T"d)(T"q)
(No)   (Ra )( H )( D )(MVA)Fr C (L"q)
0002       179. 171. 16.9 22.8 13.5  13.  4.3 0.85 .032 .050
0002       2.894    892.4    20.0
999999
( Turbine-Generator Shaft Model
DMAS
```

```
( No ) (   nome   )
10      turbogerador
( Ident ) ( Hmassa ) ( Dmassa ) ( Tmec ) ( Keixo ) ( Deixo )
HP       0.092897  0.40500      0.30     19.303      0.0
IP       0.155589  0.09850      0.26     34.929      0.0
LPA      0.858670  0.03970      0.22     52.038      0.0
LPB      0.884215  0.00433      0.22     70.858      0.0
GEN      0.868495  0.04480               2.822       0.0
EXC      0.0342165 0.02020
FIMMAS
999999
( Controlers
DCDU
(ncdu) ( nome cdu )
  0003 RV
(nb) (tipo) (stip)s(vent) (vsai) ( p1 )( p2 )( p3 )( p4 ) (vmin) (vmax)
  01 ENTRAD             TMEC
  06 EXPORT PMEC    TMEC
FIMCDU
999999
DLOC
(Lc)   (Tipo)( El )( Pa)Nc( Ex)Gr(Bl)
01     BARRAC  1
999999
( Association of Machine Models
DMAQ
( Nb)   Gr (P) (Q) Und ( Mg ) ( Mt )u( Mv )u( Me )u(Xvd)(Nbc) (Mrot)
    1   10          1       2            3u                        10
    5   10                  1
999999
( Output Variables
DPLT IMPR IERR
(Tipo)M( El ) ( Pa) Nc Gp ( Br) Gr ( Ex) (Bl)
VOLT        1
VOLT        2
VOLT        4
FMAQ        1          10
XMDG        1          10                 28
PTERM       1          10
999999
( Simulation Events
```

308

```
DEVT IMPR
(Tp) ( Tempo)( El )( Pa)Nc( Ex) ( % ) (ABS ) Gr Und          (Bl)
TCDU    .1     3                          .1                  1
999999
( Simulation Parameters
DSIM
( Tmax ) (Stp) ( P ) ( I )
   10.0  20e-6   11
EXSI DINR
FIM
```

B.4   System with a Voltage Source Converter

The ANATEM dynamic database used in the simulation of the VSC Test System is
given below:

```
( Case Title
TITU
System with a STATCOM
( Input and output files
DARQ
(Tipo) (C) ( Nome do Arquivo
OUT
LOG
PLT
SAV    16   Teste_Validacao.SAV
999999
(Infinite bus model
DMDG MD01
(No)   (L'd)(Ra )( H )( D )(MVA)Fr C
  04
999999
(
( VSC Control System
DCDU
(ncdu) ( nome cdu )
  121   VSI_SHUNT_2
(
(EFPAR (nome) (     valor      )
DEFPAR #Tf                0.005
DEFPAR #Kppll             50.
```

```
DEFPAR #Kipll                500.
DEFPAR #KP1                    8
DEFPAR #KI1                    5
DEFPAR #KP2                 0.05
DEFPAR #KI2                   1.
(nb)i(tipo) (stip)s(vent) (vsai) ( p1 )( p2 )( p3 )( p4 ) (vmin) (vmax)
0001 ENTRAD            Vref
0002 IMPORT VOLT       Vca
0003 LEDLAG       Vca   Vcamed 1.          1.    #Tf
0004 SOMA         Vref   ErrVca
                 -Vcamed ErrVca
0005 PROINT      Errvca Vcref  #KI1  #KP1      1.
0006 IMPORT VCEVS      Vc
0007 LEDLAG       Vc    Vcmed  1.          1.    #Tf
0008 SAIDA        Vcmed
0009 SOMA        -Vcref  ErrVcc
                 Vcmed  ErrVcc
0010 PROINT      ErrVcc X10   #KI2  #KP2      1.
0011 IMPORT ANGL       teta
0012 SOMA         teta   X12
                 -tetap  X12
0013 PROINT       X12    X13   #Kipll#Kppll   1.
0014 PROINT       X13    tetap    1.          1.
0015 SOMA         X10    psi
                 tetap  psi
0016 EXPORT PHSVSI psi
FIMCDU
999999
( Infinite Bus
DMAQ
( Nb)   Gr (P) (Q) Und ( Mg ) ( Mt )u( Mv )u( Me )u(Xvd)(Nbc)
   1   10          1    004
999999
( VSC Data
DEVS
(Ne)   (Vbdc) (Pbdc) (   Identificacao  ) ( Ccc) ( Rcc) (Vcci) ( Tipo)
  11     55.   100. FACTS VSI 1          500.          40. STATCOM
999999
DVSI
(Nv)   ( De) ( Pa) Nx np (  Cnvk  )M(Vb ) ( Rv)( Xv)(Vpt)(Vst)(St )(Tap) (Ne)
  21     2        10 1 .779696801N  120          5        30. 100.  1.    11
```

```
999999
( Associating VSC
DAVS
(Nv)    ( Mc )u
  21      121u
999999
( Remote locals
DLOC
(Lc)   (Tipo)( El )( Pa)Nc( Ex)Gr(Bl)
 108   MAQ        1            10          ( Wmaq   )
   2   BARRAC     2
999999
(Output variables
DPLT IERR
(
(Tipo)M( El ) ( Pa) Nc Gp ( Br) Gr ( Ex) (Bl) P
VOLT         1
VOLT         2
999999
( Simulation Events
DEVT
(Tp) ( Tempo)( El )( Pa)Nc( Ex) ( % ) (ABS ) Gr Und          (Bl)
TCDU     5.1   121                     0.05                  01
999999
( Simulation Parameters
DSIM
( Tmax ) (Stp) ( P ) ( I )
    8.0  20e-6    11
EXSI DINR
FIM
```